

# Synthesis and characterization of shear stress indicator supraparticles

Dissertation zur Erlangung des  
naturwissenschaftlichen Doktorgrades der  
Julius-Maximilians-Universität Würzburg



vorgelegt von

Sarah Wenderoth

aus St. Wendel

Würzburg 2023





Eingereicht bei der Fakultät für Chemie und Pharmazie am

\_\_\_\_\_

Gutachter der schriftlichen Arbeit

1. Gutachter: \_\_\_\_\_

2. Gutachter: \_\_\_\_\_

Prüfer des öffentlichen Promotionskolloquiums

1. Prüfer: \_\_\_\_\_

2. Prüfer: \_\_\_\_\_

3. Prüfer: \_\_\_\_\_

Datum des öffentlichen Promotionskolloquiums

\_\_\_\_\_

Doktorurkunde ausgehändigt am

\_\_\_\_\_



Die vorliegende Arbeit wurde am Lehrstuhl für Chemische Technologie der Materialsynthese an der Universität Würzburg in den Räumlichkeiten des Fraunhofer-Institut für Silicatforschung ISC durchgeführt. Bei der vorliegenden Arbeit handelt es sich um eine kumulative Dissertation, die nur eine verkürzte Darstellung der Forschungsergebnisse zeigt. Die ausführlichen Ergebnisse können in den entsprechenden Veröffentlichungen nachgelesen werden:

1. Veröffentlichung:

S. Wenderoth, T. Granath, J. Prieschl, S. Wintzheimer, K. Mandel

Abrasion Indicators for Smart Surfaces Based on a Luminescence Turn-On Effect in Supraparticles

*Adv. Photonics Res.*, **2020**, 1(1), 2000023

DOI: 10.1002/adpr.202000023 (CC BY 4.0)

---

2. Veröffentlichung:

S. Wenderoth, S. Müssig, J. Prieschl, E. Genin, K. Heuzé, F. Fidler, D. Haddad, S. Wintzheimer, K. Mandel

Optically sensitive and magnetically identifiable supraparticles as indicators of surface abrasion

*Nano Lett.*, **2022**, 22(7), 2762-2768

DOI: 10.1021/acs.nanolett.1c04773

---

3. Veröffentlichung:

S. Wenderoth, A. Eigen, S. Wintzheimer, J. Prieschl, A. Hirsch, M. Halik, K. Mandel

Supraparticles with a Mechanically Triggerable Color-Change-Effect to Equip Coatings with the Ability to Report Damage

*Small*, **2022**, 18(15), 2107513

DOI: 10.1002/smll.202107513 (CC BY 4.0)

---

4. Veröffentlichung:

S. Wenderoth, G. Bleyer, J. Endres, J. Prieschl, N. Vogel, S. Wintzheimer, K. Mandel

Spray-Dried Photonic Balls with a Disordered/Ordered Hybrid Structure for Shear-Stress Indication

*Small*, **2022**, 18(48), 2203068

DOI: 10.1002/smll.202203068 (CC BY 4.0)

---

5. Veröffentlichung:

S. Wintzheimer, S. Müssig, S. Wenderoth, J. Prieschl, T. Granath, F. Fidler, D. Haddad, K. Mandel

Hollow Superparamagnetic Nanoparticle-Based Microballoons for Mechanical Force Monitoring by Magnetic Particle Spectroscopy

*ACS Appl. Nano Mater.*, **2019**, 2(10), 6757-6762

DOI: 10.1021/acsanm.9b01693

---

6. Veröffentlichung:

S. Wintzheimer, J. Reichstein, S. Wenderoth, S. Hasselmann, M. Oppmann, M. T. Seuffert, K. Müller-Buschbaum, K. Mandel

Expanding the Horizon of Mechanochromic Detection by Luminescent Shear Stress Sensor Supraparticles

*Adv. Funct. Mater.*, **2019**, 29(19), 1901193

DOI: 10.1002/adfm.201901193

---

7. Veröffentlichung:

S. Wintzheimer, J. Reichstein, P. Groppe, A. Wolf, B. Fett, H. Zhou, R. Pujales-Paradela, F. Miller, S. Müssig, S. Wenderoth, K. Mandel

Supraparticles for Sustainability

*Adv. Funct. Mater.*, **2021**, 31(11), 2011089

DOI: 10.1002/adfm.202011089 (CC BY 4.0)

---

---

# Danksagung

Ein solches Projekt ist ohne Unterstützung nicht machbar. Daher möchte ich die Gelegenheit nutzen und mich an dieser Stelle bei allen bedanken, die mich in den letzten Jahren auf diesem Weg begleitet und unterstützt haben, sowohl im beruflichen als auch im privaten Umfeld.

Mein besonderer Dank gilt Herrn Prof. Dr. Karl Mandel, der mir die Promotion zu diesem interessanten Thema ermöglichte, mich über die gesamte Zeit betreute und immer mit Rat und Tat zur Seite stand.

Ebenso möchte ich mich bei Prof. Dr. Gerhard Sextl bedanken, der mir die Möglichkeit gab, am Lehrstuhl für Chemische Technologie der Materialsynthese und in den Räumlichkeiten des Fraunhofer ISC zu promovieren und für die Gutachtertätigkeit.

Ein ganz großes Dankeschön geht an Frau Dr. Susanne Wintzheimer. Danke, dass Du immer ein offenes Ohr für Diskussionen hattest, dass Du mich immer wieder motiviert hast, wenn gar nichts geklappt hat, und vor allem für Deine Unterstützung beim Schreiben der Veröffentlichungen.

Danke auch an das gesamte Team der OE280 des Fraunhofer ISC und die ehemalige NANO-ID Gruppe für den herzlichen Empfang in Würzburg und die Unterstützung während der letzten Jahre. Besonders bedanken möchte ich mich bei Doris Hanselmann, Johannes Prieschl und Maximilian Oppmann, ohne deren Hilfe im Labor und am Sprühtrockner vieles nicht möglich gewesen wäre. Danke an Rainer Jahn und Bastian Fett, mit denen ich mir das Labor teilen durfte. Danke auch an meine Mit-Doktoranden Dr. Stephan Müssig, Franziska Miller, Tim Granath, Jakob Reichstein, Bastian Fett und Thomas Zimmermann für die stets kollegiale und freundschaftliche Zusammenarbeit, die eine Promotionszeit erst erträglich macht.

---

---

Danke auch an die restlichen ISC-Kollegen, die mir immer hilfreich zur Seite gestanden haben (Heike Bleicher, Annette Burger, Katharina Emmert, Dr. Patrick Wenderoth, Dr. Ferdinand Somorowsky und alle, die ich jetzt hier vergessen habe).

Ein besonderer Dank geht an meinen Bürokollegen Bastian Fett. Danke für die zahlreichen wissenschaftlichen Diskussionen, die freitägliche Aufmunterungs-Quantendotsynthese und so vieles mehr.

Danke auch an Frau Erika Friedel für den sprachlichen Feinschliff in meinen Veröffentlichungen und die Unterstützung in den bürokratischen Feinheiten.

Danke auch an meine Studenten Natalie Bonakdar, Eva Beck, Jakob Endres, Leon Dyroff und Lukas Wald, die mich in meinen Arbeiten unterstützt haben. Ganz besonders auch an Jakob Reichstein für die Vorarbeiten, die Du während deiner Masterarbeit auf diesem Thema geleistet hast.

Ohne die zahlreichen Kooperationspartner wäre ein Großteil der Arbeit nicht möglich gewesen, zumindest nicht in dem hier gezeigten Umfang. Insbesondere möchte ich Dr. Emilie Genin und Dr. Karin Heuzé danken, die, nachdem mein Gastaufenthalt in Bordeaux durch Covid19 mehrfach abgesagt wurde, die Versuche zur Farbstoffmodifikation selbst durchführten.

Ich möchte auch meinen ehemaligen Kollegen/Mentoren und Freunden Christina Muth, Dr. Isabella Tavernaro, Dr. Christian Cavelius, Dr. Aljosha Jochum und Dr. Thibaut Thai danken. Danke, dass ich so vieles von euch lernen durfte, sowohl im Labor als auch in der allgemeinen wissenschaftlichen Arbeit.

Ein großes Dankeschön geht auch an meine Eltern Beate und Bernd Schmidt, ohne eure immerwährende Unterstützung wäre ich nicht so weit gekommen.

Schließlich möchte ich mich auch bei meinem Mann Patrick Wenderoth bedanken. Danke, dass Du in guten und in schlechten Zeiten immer für mich da bist und mich in allen Belangen unterstützt. Danke, dass Du jeden Tag wunderbar machst.

---

---

# List of abbreviations

APTES	(3-Aminopropyl)triethoxysilane
CIE	Commission internationale de l'éclairage
DLS	Dynamic light scattering
ICPTES	3-(Triethoxysilyl)propyl isocyanate
IUPAC	International Union of Pure and Applied Chemistry
LSM	Laser scanning microscopy
MOF	Metal organic framework
MPI	Magnetic particle imaging
MPS	Magnetic particle spectroscopy
PBI-PA	N-(1-hexylheptyl)-N'-(undecylphosphonic acid) perylene-3,4,9,10-tetracarboxylic bisimide
SAM	Self-assambled monolayer
SEM	Scanning electron microscope
TEOS	Tetraethoxy orthosilicate
UV	Ultraviolet

---

# Zusammenfassung

Die Erfassung kleinster mechanischer Belastungen spielt in vielen Bereichen der fortschreitenden Automatisierungs- und Fertigungstechnik, aber auch im täglichen Leben eine immer wichtigere Rolle. Im Rahmen dieser Doktorarbeit wurden verschiedene mikropartikuläre Systeme entwickelt, die in der Lage sind, mechanische Scherbelastungen über einfache Mechanismen anzuzeigen. Diese Systeme können mit einem Baukastenprinzip über das Sprühtrocknungsverfahren aus verschiedenen nanoskaligen Primärpartikeln (Silica und Eisenoxid) zu Mikrometergroßen Einheiten, sogenannten Suprapartikeln, aufgebaut werden. Durch den Aufbau von hierarchisch strukturierten Kern-Schale Suprapartikeln, die durch Variation der verschiedenen Bausteine und in Kombination mit unterschiedlichen Farbstoffen mechanische Belastungen durch einen leicht detektierbaren Farbumschlag anzeigen können, wurde eine neue Klasse von mechanochromen Scherstress-Indikatoren entwickelt. Dabei kann zwischen drei verschiedenen Mechanismen unterschieden werden. Wird ein Signal erst durch eine mechanische Belastung sichtbar, handelt es sich um *Turn-on* Indikatoren. Im umgekehrten Fall, den *Turn-off* Indikatoren, wird das Signal durch eine mechanische Belastung abgeschaltet. Beim dritten Mechanismus, den *Color-change* Indikatoren, ändert sich die Farbe durch eine mechanische Belastung. Diese Indikatoren können prinzipiell auf zwei verschiedene Arten eingesetzt werden. Zum einen können sie als Additive in eine Beschichtung eingearbeitet werden. Diese Schichten sind auf vielen Produkten applizierbar, wie z. B. auf Lebensmittelverpackungen, auf medizinischen Gütern oder allgemein auf allen sensiblen Oberflächen, bei denen mechanische Belastungen, wie z. B. Kratzer, schwierig zu detektieren sind, aber schwerwiegende Folgen haben können. Zum anderen sind diese Scherstress-Indikatoren auch direkt in Pulverform einsetzbar. So können sie z. B. in der Robotik, im 3D-Druck oder in Kugelmøhlen eingesetzt werden. Im Rahmen dieser Arbeit konnten insgesamt sechs verschiedene Scherstress-Indikatoren entwickelt werden, von denen drei als Additive in Beschichtungen und drei in Pulverform Verwendung finden. Diese suprapartikulären

Indikatoren können, je nach Zusammensetzung, mittels Fluoreszenz-, UV-Vis- oder Magnetischer Partikel Spektroskopie ausgelesen werden und dadurch mechanische Belastung anzeigen. Durch die Entwicklung dieser neuartigen Scherstress-Indikator-Suprapartikel ist es gelungen, die Molekülchemie mit der Welt der Nanoobjekte zu verbinden und makroskopische Systeme zu entwickeln, die intelligente und kommunizierende Materialien zur Anzeige von mechanischen Belastungen in einer Vielzahl von Anwendungen ermöglichen.

# Abstract

The detection of smallest mechanical loads plays an increasingly important role in many areas of advancing automation and manufacturing technology, but also in everyday life. In this doctoral thesis, various microparticle systems were developed that are able to indicate mechanical shear stress via simple mechanisms. Using a toolbox approach, these systems can be spray-dried from various nanoscale primary particles (silica and iron oxide) to micrometer-sized units, so-called supraparticles. By varying the different building blocks and in combination with different dyes, a new class of mechanochromic shear stress indicators was developed by constructing hierarchically structured core-shell supraparticles that can indicate mechanical stress via an easily detectable color change. Three different mechanisms can be distinguished. If a signal becomes visible only by a mechanical load, it is a *turn-on* indicator. In the opposite case, the *turn-off* indicator, the signal is switched off by a mechanical load. In the third mechanism, the *color-change* indicator, the color changes as a result of a mechanical load. In principle, these indicators can be used in two different ways. First, they can be incorporated into a coating as an additive. These coatings can be applied to a wide range of products, including food packaging, medical devices, and generally any sensitive surface where mechanical stress, such as scratches, is difficult to detect but can have serious consequences. Second, these shear stress indicators can also be used directly in powder form and for example then applied in 3D-printing or in ball mills. A total of six different shear stress indicators were developed, three of which were used as additives in coatings and three were applied in powder form. Depending on their composition, these indicators were readout by fluorescence, UV-Vis or Magnetic Particle Spectroscopy. The development of these novel shear stress indicator supraparticles were successfully combined molecular chemistry with the world of nano-objects to develop macroscopic systems that can enable smart and communicating materials to indicate mechanical stress in a variety of applications.

# Table of contents

<b>1</b>	<b>Introduction and aim of the work</b>	<b>1</b>
<b>2</b>	<b>Theoretical background</b>	<b>5</b>
2.1	Nanoparticles . . . . .	5
2.1.1	Fundamentals . . . . .	6
2.1.2	Silica . . . . .	9
2.1.3	Iron oxide . . . . .	14
2.2	Supraparticles . . . . .	17
2.2.1	Fundamentals . . . . .	18
2.2.2	Formation . . . . .	21
2.3	Characterization methods . . . . .	24
2.3.1	Fluorescence spectroscopy . . . . .	24
2.3.2	Confocal microscopy . . . . .	25
2.3.3	Magnetic Particle Spectroscopy . . . . .	26
<b>3</b>	<b>State of the art</b>	<b>28</b>
3.1	Shear stress indicators . . . . .	28
3.2	Functional coatings . . . . .	31
<b>4</b>	<b>Results</b>	<b>35</b>
4.1	Shear stress indicator supraparticles in thin coatings . . . . .	37
4.1.1	Turn-on indicators . . . . .	40
4.1.2	Turn-off indicators . . . . .	45
4.1.3	Color-change indicators . . . . .	51
4.2	Shear stress indicator supraparticles as powder . . . . .	58
4.2.1	Photonic balls . . . . .	58
4.2.2	Microballoons . . . . .	65
4.2.3	Multi-particle system . . . . .	67
<b>5</b>	<b>Conclusion and outlook</b>	<b>71</b>
	<b>References</b>	<b>80</b>
	<b>Appendix</b>	<b>98</b>

---

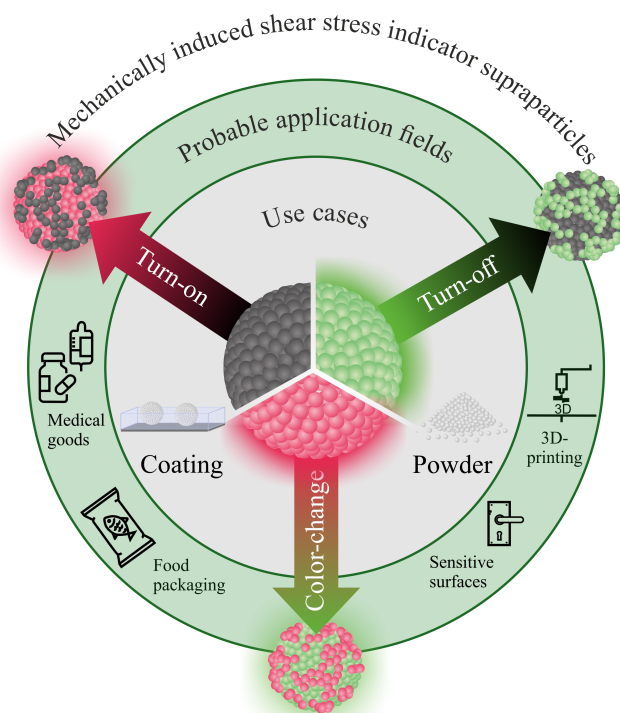
# Chapter 1

## Introduction and aim of the work

Due to the increasing automation of technical processes in the production of materials (“Industry 4.0”) and also in our daily lives (“Smart Home“), it has to be ensured that any faults or malfunctions can be detected and rectified timely – ideally before any damage occurs. Not only the usual environmental influences such as temperature, humidity or UV radiation should be detectable, but also mechanical stress should be taken into account. Even the smallest scratches can have a significant negative impact, if they are not technically easy to detect. For instance, a small scratch in the barrier layer of a food package can allow oxygen to penetrate. This can cause premature food spoilage which in turn may negatively impact the consumer. For medical products, a small tear in the packaging of sterile containers can have even more drastic consequences to human health (*e.g.*, infections). A new type of shear stress indicator is needed to easily and quickly detect such defects in the micrometer range. Traditional shear stress indicator systems sometimes involve large, very complex and thus expensive setups that are not suitable for commercial use (Chapter 3.1, Page 28). Similarly, although there are already ways for food packaging to indicate the freshness of the food, it has not yet been possible to verify the integrity of the packaging itself by simple means (Chapter 3.2, Page 31).

The aim of this work is to develop a miniaturized shear stress indicator in the micrometer range which can be used for various applications and indicate mechanical stress in a simple way. A (mainly) colorimetric change can be used to indicate the presence of a defect and thus ensure product safety in many applications. Therefore, nanostructured, hierarchical,

(predominantly) spherical particles in the micrometer range, so-called supraparticles, are used. Scheme 1.1 shows the main conceivable application areas (food packaging, packaging of medical goods, 3D-printing or on sensitive surfaces) of the developed indicators as well as different types of shear stress indicator supraparticles. Due to the core-shell structure of the individual supraparticles, the optical signal in the initial state differs from that in the mechanically stressed state. Depending on the composition of the different nanoparticle building blocks and the use of different fluorescence dyes, three different detection mechanisms can be realized. If an optical signal is detectable due to mechanical stress, it is a *turn-on* indicator. In the opposite case, the *turn-off* indicators, the signal disappears as a consequence of subsequent mechanical stress. The third type, *color-change* indicators, show a color change under mechanical stress. Basically, these indicators can be used in two different forms, either incorporated into a coating or directly in powder form.



**Scheme 1.1:** Schematic presentation of the core-shell structure of shear stress indicator supraparticles and the potential applications in medical products, food packaging, 3D-printing or on sensitive surfaces in general. Mechanical stresses initially applied to the surface of the supraparticle remove the shell material and expose the core of the supraparticle. By using different building blocks for the core or the shell of the supraparticles, three different mechanisms can be implemented, namely turn-on, turn-off and color-change. In principle, these indicator supraparticles can be used in two ways, either incorporated into a coating or in powder form.

In the present work, various indicators for the detection of mechanical stress were developed by varying different building blocks.<sup>1</sup> Herein, mainly silica and iron oxide nanoparticles were used, which were assembled into hierarchically structured supraparticles via a spray-drying process. Different types of shear stress indicator supraparticles were generated, by varying the nanoparticle size, the use of different dyes and the composition of the individual supraparticles. They can either be incorporated into thin films (Chapter 4.1, Page 37) or used in powder form (Chapter 4.2, Page 58).

By adapting the morphology, size and core-shell structure of the supraparticles, they can be incorporated into thin layers so that only the lower part of the particles is firmly anchored in the 3-5  $\mu\text{m}$  thick layer, and the upper part of the particle protrudes from this layer, creating a molehill-like structure. When this layer, in which the indicator supraparticles are embedded, is now successively abraded, the structure of the core-shell supraparticle changes in a way that first the shell is abraded and the core is exposed. Depending on the nanoparticle species used in the core or in the shell of the supraparticles, the different mechanisms can be realized. For the generation of an optical signal upon mechanical stress, the core must be made of optically active materials and the shell must be made of light-absorbing materials (Chapter 4.1.1, Page 40). In the reverse case, when a signal loss is detected, the supraparticle shell consists of optically active material and the core consists of light-absorbing material (Chapter 4.1.2, Page 45). If the light-absorbing material can additionally be readout via certain magnetic signals, similar to a fingerprint, not only a statement can be made about whether the surface has been subjected to mechanical stress, but the corresponding surface can also be uniquely identified. This means that coatings can become not only smart, but also communicating. By using two different optically active species in the core and shell of the supraparticle, color-change indicators can be produced (Chapter 4.1.3, Page 51). All of these indicator supraparticles can be incorporated into the barrier layer of food packaging, for instance. The change in the optical signals can be used to assess the gas permeability of the layer (*e.g.*, oxygen, carbon dioxide, water vapor). Therefore, it is possible to predict whether a packaged good is still intact or whether, *e.g.*, oxygen will penetrate and damage the product.

---

<sup>1</sup>In this work the terms mechanical stress, abrasion of surfaces and shear stress are used synonymously.

By varying the nanoparticulate building blocks, it is also possible to develop shear stress indicator supraparticles that indicate mechanical stress in different ways and can be used in powder form, enabling new areas of application. Photonic balls (Chapter 4.2.1, Page 58) based on silica and iron oxide nanoparticles can be used as indicator powders that lose their coloration when subjected to mechanical stress. The silica nanoparticles are in such an order of magnitude so that they can reflect light of a certain wavelength, while the iron oxide nanoparticles serve as broadband absorbers. The sensitivity of these systems can be affected by the size of the nanoparticles used. By using hollow spheres (also made of iron oxide and silicon dioxide), so-called microballoons (Chapter 4.2.2, Page 65), the degree of grinding of activated carbon in a ball mill can be determined easily and quickly via the change in the magnetic signal caused by the destruction of the hollow spheres under mechanical stress. In addition, the magnetic material can be completely removed afterwards from the ground material. Turn-off indicator supraparticles in powder form can also be used (Chapter 4.2.3, Page 67). Therefore, a multiparticle system is utilized, in which a light-absorbing core is surrounded by a shell of silica nanoparticles on the one hand, and on the other hand, supraparticles based on silica nanoparticles carrying a luminophore are arranged as satellites around the cores. By choosing a certain light-absorbing material, but also by using different luminophores, the sensitivity of these systems to mechanical stress can be adjusted.

## Chapter 2

# Theoretical background

In this chapter, nanoparticles in general are discussed first. Here, the focus is on silica and iron oxide nanoparticles. In particular, their syntheses, properties and modification possibilities are presented. Supraparticles are then the subject of discussion, with emphasis on their general properties, formation processes, and various applications. Afterwards, the main characterization techniques used in this thesis to determine the mechanical stability are shortly introduced.

### 2.1 Nanoparticles

Nanoparticles and nanomaterials have been the subject of modern research for many years and are being used in everyday life in numerous areas. The prefix "nano" (from Greek *nános*, meaning "dwarf") generally describes an order of magnitude of  $10^{-9}$ , or one in a billion.<sup>[1]</sup> There are definitions that describe a nanoparticle as: Anything between 10-20 nm<sup>[2]</sup>, 1-100 nm<sup>[3]</sup>, anything below 400 nm (smaller than the wavelength of visible light)<sup>[1]</sup>, or between 1-1000 nm.<sup>[1]</sup> The definition of what exactly a nanomaterial means is debated in the literature and depends in part on the material, the scientific field or the application area.<sup>[1, 4]</sup> On 10/18/2011, the European Commission officially defined the term nanomaterials in its Recommendation 2011/696/EU as: "*Nanomaterial' means a natural, incidental or manufactured material containing particles, in an unbound state*

or as an aggregate or as an agglomerate and where, for 50% or more of the particles in the number size distribution, one or more external dimensions is in the size range 1 nm - 100 nm." Thus, nanomaterials can be understood as entities in which at least one of their dimensions is in the nanometer range, or they consist of agglomerates containing such entities.<sup>[4]</sup> Nanoparticles, on the other hand, are then entities in which all three dimensions are in the range between 1 - 100 nm.<sup>[4]</sup>

However, nanoparticles are neither a development of modern times nor a purely man-made material. There are a variety of naturally occurring nanoparticles, *e.g.*, due to volcanic eruptions, forest fires or even different species of bacteria that are able to form nanoparticles.<sup>[5-7]</sup> Already in ancient times, gold and silver nanoparticles were used for glass coloring. One of the most famous examples is the 4<sup>th</sup> century Lycurgus Cup on display in the British Museum.<sup>[7, 8]</sup> As early as 2500 years before Christ, *soluble gold* was used for medicinal purpose in China and Egypt.<sup>[9]</sup> The father of modern colloid chemistry is *Michael Faraday*, who carried out investigations on the optical properties of colloidal gold films in 1857.<sup>[7, 10]</sup> In 1861, *Thomas Graham* introduced the term *colloid* for the first time.<sup>[11]</sup>

### 2.1.1 Fundamentals

The special properties of nanoparticles stem from their size.<sup>[2]</sup> The smaller the particles, the larger is the surface-to-volume ratio. This can be illustrated with the following thought experiment: A cube-shaped body with an edge length of 1 cm has a surface area of 6 cm<sup>2</sup>. If this cube was composed of smaller cubes with each an edge length of 1 μm, the volume would remain constant, but the surface area would increase to 6 m<sup>2</sup>. If the edge length of each single cube was further reduced to 1 nm, the surface area would increase to 6000 m<sup>2</sup>, while the volume of the entire body would still remain unchanged.<sup>[1]</sup> This means that the number of atoms which are on the surface of the particles increases massively, compared to the atoms in the interior.<sup>[1-3]</sup> With particles of 200 nm in size, only 0.6% of the entire number of atoms are located on the surface, while with 2 nm sized particles already nearly 50% of all atoms are located on the surface.<sup>[1, 2]</sup> This large number of surface accessible atoms results in new properties compared to bulk materials, as these atoms

have a higher energy and can be moved or removed more easily. These properties can be for instance magnetic, mechanical, optical, catalytic, or electronic. [12–14] For example, metallic nanoparticles exhibit size-dependent surface plasmon resonance [13], while iron oxide exhibits a variety of different magnetic properties depending on particle size. [15, 16] In principle, nanoparticles can be made from all kinds of materials, *e.g.*, metals, semi-metals or their oxides, but also from organic or polymer precursors. In the production of nanoparticles, a basic distinction can be made between two different processes: The "Top-Down" and the "Bottom-Up" process. [17] In the "Top-Down" method (Figure 2.1, left), starting from a bulk material, a nanoparticulate structure is successively generated by mechanical comminution processes (such as etching, laser lithography or grinding in a ball mill). The advantage of this method is that it can be performed on a large scale and thus, a large amount of nanoscaled material can be obtained relatively quickly. However, the major disadvantage is a usually wide particle size and morphology distribution. In contrast, with the "Bottom-Up" method (Figure 2.1, right), the nanoparticles are built up from molecular precursors (*e.g.*, via sol-gel processes, precipitation reactions, or vapor deposition), similar to the LEGO™ principle. [18] The major advantage is its capability of generating highly monodisperse systems by adjusting the synthesis parameters. Thus, a specific type of nanoparticles can be developed for different applications. As a result, the applications of nanoparticles have expanded in recent years and can be found in a wide variety of products, like in cosmetics [19, 20], pharmaceuticals [21, 22], data storage [23, 24], water treatment [25, 26], medicine [27, 28], or catalysis [29, 30]. Many applications require a specific particle size with the smallest possible particle size distribution. [31, 32]

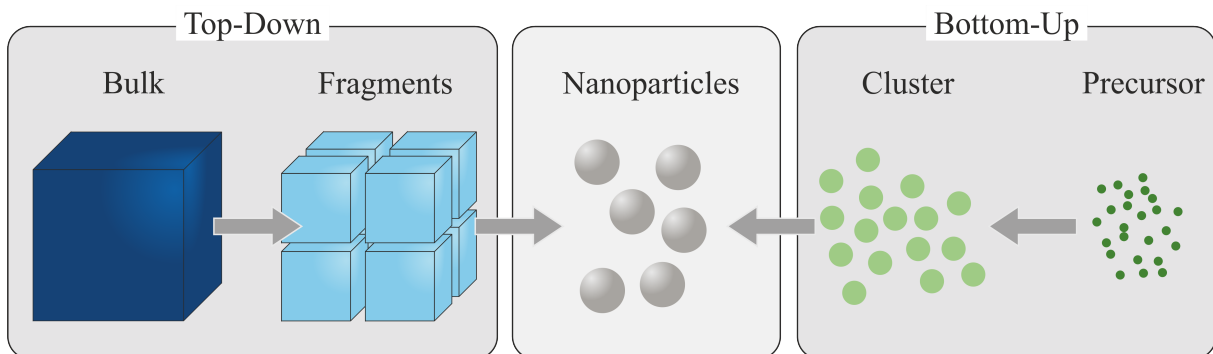


**Figure 2.1:** Schematic representation of the main methods of nanoparticle generation methods, namely: Top-Down process (left) and Bottom-Up process (right).

The formation and growth of nanoparticles was first described by *Victor LaMer* and *Robert Dinegar* in 1950.<sup>[33]</sup> This classical model is divided into three phases (Figure 2.2), where in the first phase a precursor is formed by a chemical reaction. The concentration of this precursor increases until the critical concentration for nucleation is exceeded (phase II). When this point is reached, the precursor aggregates spontaneously and the first nuclei are formed. During this nucleation process, the precursor concentration decreases again and falls below the critical nucleation concentration. In this phase III, the growth phase, these nuclei continue to grow by accumulating further precursor material until an equilibrium between the accumulation and release of precursors at the particle surface is reached. Afterwards, Ostwald ripening starts. This means small nanoparticles dissolve over time and the ions deposit on the surface of larger particles, which thus continue to grow. In order to form monodisperse nanoparticles, the nucleation process must be fast and the growth process must be slow.<sup>[34, 35]</sup>

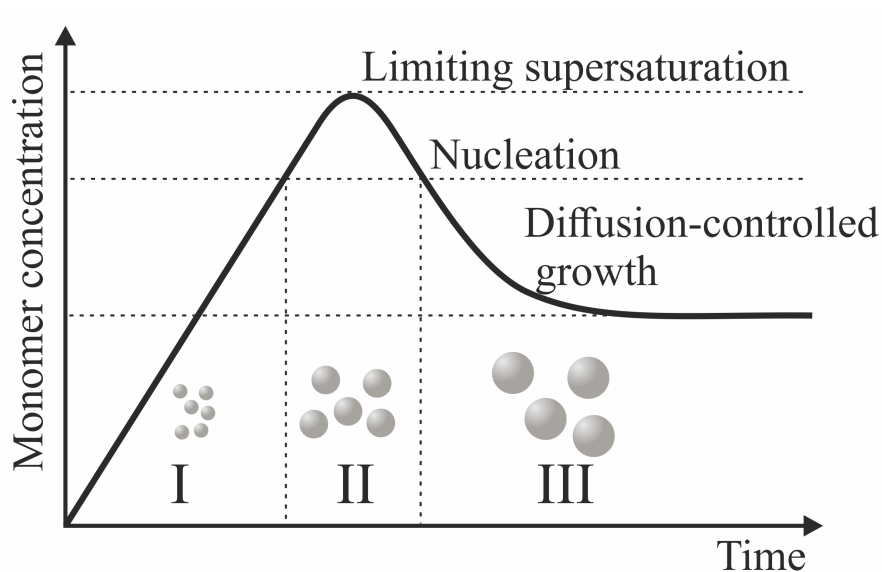


**Figure 2.2:** Schematic representation of particle creation and growth process based on the theory of *LaMer* and *Dinegar*.

Since nanoparticles, as mentioned earlier, have a very large surface-to-volume ratio and thus a high surface energy, they would aggregate immediately after their formation without surface stabilization and would continue to grow until they reach a thermodynamically favorable final stage, due to Van der Waals forces and Brownian motion. Basically, three types of stabilizer can be distinguished in general.<sup>[36]</sup> First, sterically demanding

molecules (*e.g.*, surfactants, polymers) can be adjusted to the surface of the individual nanoparticles, which is referred to as steric stabilization.<sup>[37]</sup> Due to the long molecular chains, the particles can no longer form a tight contact and aggregate. Second, molecules with a high charge (*e.g.*, citrate, amines) can be attached, which is called electrostatic stabilization.<sup>[38]</sup> In this case, the strong charge (negative or positive) causes a repulsion between individual nanoparticles. Third, a combination of the two methods is possible, as well. Therefore, sterically demanding molecules that additionally carry a charge (*e.g.*, sodium dodecyl sulfonate) are attached to the surface. This principle is called electrosteric stabilization.<sup>[39]</sup>

### 2.1.2 Silica

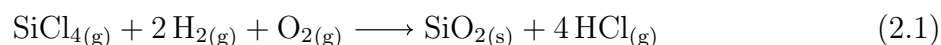
Since silica nanoparticles are used in every part of this thesis, this chapter first explains the fundamentals before presenting different synthesis methods and finally discussing different modification options.

#### Fundamentals

Silicon dioxide (with the molecular formula  $\text{SiO}_2$ ) is an oxide of silicon, which exists in nature in amorphous (known as silica) and crystalline form. While the crystalline form is found only in minerals (*e.g.*, quartz, cristobalit, coesite), the amorphous form is found in both, mineral (*e.g.*, geysersite, obsidian, opal) and biogenic (diatoms, radiolarians, sponges) matter.<sup>[40]</sup> In the vast majority of the cases, all of these silica species are composed of  $[\text{SiO}_4]^{4-}$  tetrahedrons. The tetrahedrons are connected by siloxane bridges (Si-O-Si).<sup>[41]</sup> The silicon atom at the surface is fully saturated only on the inside (towards the bulk), but still has free valences on the outside. These can form silanol groups (Si-OH) by reactions with water (liquid or vapor).<sup>[42]</sup> Colloidal silica has been used for many years in various fields (drug carriers<sup>[43]</sup>, biosensors<sup>[44]</sup>, catalyst support<sup>[45]</sup>, active coatings<sup>[46]</sup>, additives in paints<sup>[47]</sup>/food<sup>[48]</sup>/cosmetics<sup>[49]</sup>) due to its special properties (biocompatibility, chemical inertness, modifiability).<sup>[50]</sup>

## Synthesis

Nanoparticulate silica can be produced in a gaseous or liquid route (in terms of the phase of the silica precursor).<sup>[51]</sup> The gaseous route, also known as the aerosol process which includes flame hydrolysis or spray pyrolysis, was developed by the Degussa company as early as in the 1940s.<sup>[51]</sup> In this process, the precursor silicon tetrachloride ( $\text{SiCl}_4$ ) is atomized in a flame and pyrolyzed in the presence of hydrogen and oxygen. The hydrogen and oxygen react in a oxyhydrogen reaction to form water, which then reacts with the  $\text{SiCl}_4$  to form pyrogenic silica and hydrochloric acid (Equation 2.1).<sup>[52]</sup>



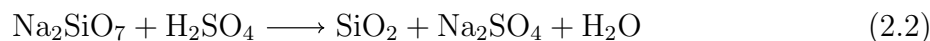
The resulting silica nanoparticles have a size of about 7-40 nm in their original form, but grow into larger hard agglomerates with a broader size distribution due to sintering processes at high temperatures.<sup>[53, 54]</sup> Particle size and its distribution can be affected by varying the concentration of reactants, temperature and residence time.<sup>[51]</sup> Although the flame pyrolysis method is energetically expensive, it is nevertheless used for several reasons: (i) the resulting silica is highly pure (>99.8 wt%  $\text{SiO}_2$ )<sup>[51]</sup>; (ii) the precursor  $\text{SiCl}_4$  is produced as a by-product in polysilicon industry and can therefore be further processed at low cost<sup>[55]</sup>; and (iii) the hydrochloric acid produced during the pyrolysis can be collected and reused.<sup>[53, 56]</sup>

Another way to synthesize silica nanoparticles is the ion exchange process. In a first step, sodium silicate is obtained from silica ores in a smelting process using alkali fluxes. Liquid sodium silicate solution, known as water glass, is then produced at high temperature and pressure. With the help of an ion exchange resin, the alkaline solution can be removed and silica nuclei are formed, which can then grow into silica particles under suitable reaction conditions (at least 60 °C, pH 8-10.5). This type of particle production is easily scalable and can thus be used for large-scale production of silica nanoparticles. Different particle sizes can be obtained by adjusting the concentration and alkali source.<sup>[41, 57]</sup>

In the liquid route, a basic distinction is made between the sol-gel synthesis and the microemulsion method. In the microemulsion method, two immiscible liquids (usually water and oil) are mixed together in a way that one liquid (water) is finely dispersed in small droplets in the second liquid (oil) (so-called reverse microemulsion method).<sup>[51, 58]</sup>

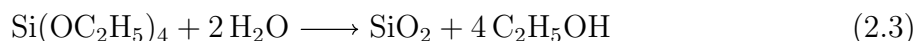
In order to stabilize these water droplets, a surfactant is added attaching to the droplet surface and assisting in the micelle formation.<sup>[59]</sup> The silica precursor and catalyst are located in the water droplets. The size of the final silica nanoparticles can be determined by the size and number of the droplets and can be affected through the water to surfactant ratio.<sup>[58]</sup> The surfactant serves as a steric surface stabilizer for the resulting silica nanoparticles.<sup>[60]</sup>

Sol-gel synthesis can again be divided into precipitated silica, biomimetic sol-gel synthesis, and the Stöber method.<sup>[51]</sup> In the precipitated silica synthesis, a dissolved silicate precursor is neutralized with an acid, leading to a decrease of the silica solubility limit. Thus, polymerization occurs, resulting in precipitation of silica particles from the solution.<sup>[61]</sup> One prominent silica precursor is sodium silicate. In the presence of sulfuric acid as precipitant, silica nanoparticles are precipitated (Equation 2.2).<sup>[61]</sup> Silica nanoparticles produced by the precipitation reaction have the largest market share and are mainly used in car tires, shoe soles, catalyst supports and adsorbers.<sup>[62–65]</sup>



The biomimetic sol-gel synthesis is inspired by various biological organisms (*e.g.*, diatoms, sponges) that build structures of silica to protect themselves or achieve structural stability.<sup>[66, 67]</sup> These organisms use various co-precipitating biomolecules (including long chain polyamides, specialized proteins (silaffins, silacidins, cingulium) and saccharides (*e.g.*, chitin)) to produce silica *in vivo* under mild conditions.<sup>[68–70]</sup>

The probably best-known sol-gel synthesis is named after its developer *Werner Stöber*. In 1968, Stöber *et al.* published a method for the synthesis of silica nanoparticles, which has been reproduced and modified ever since.<sup>[71]</sup> In Stöber's classical protocol, a silica alkoxide (like tetraethyl orthosilicate (TEOS)) is first hydrolyzed and then condensed in an aqueous alcoholic environment in the presence of ammonia as a catalyst to produce monodisperse nanoparticles with sizes between 50 nm and 2  $\mu\text{m}$  (Equation 2.3).<sup>[71]</sup>



At the beginning of the reaction, several intermediates are formed: From the monomer, first a dimer, then a circular structure, and finally the nanoparticles. Depending on the external pH conditions, not only the size of the resulting nanoparticles is determined, but

also the three dimensional structure, *i.e.*, whether individual, isolated nanoparticles form a sol, or whether they aggregate and form a gel network (Figure 2.3).<sup>[72]</sup> In addition, the presence of salts must be avoided under basic conditions, as they lead to a gelation process. The size of the resulting particles can be influenced by adjusting the synthesis conditions, *e.g.*, the ratio of water/alcohol/ammonia, the used alcohol and silica precursor, synthesis temperature as well as the reaction time.<sup>[58, 73–76]</sup>

In this work silica nanoparticles were synthesized based on the Stöber protocol. The reason for choosing this method is the uncomplicated and fast synthesis, the easily controllable size adjustments as well as the simple modification either during or after the synthesis.

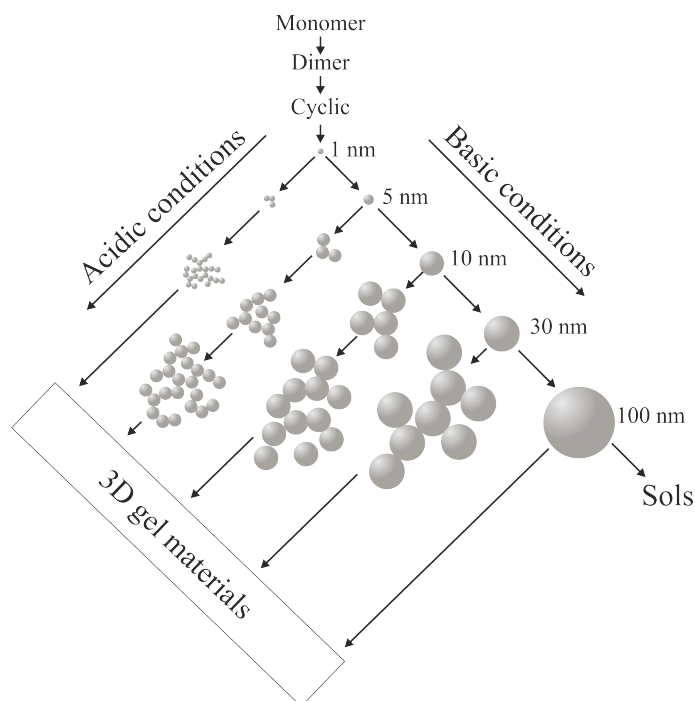


**Figure 2.3:** Schematic representation of silica particle growth processes to gels or sols based on pH conditions. Redrawn based on <sup>[42, 72]</sup>.

## Modification

Silica nanoparticles are used as model systems in many applications not only because of their variably tunable size but also because of their good modifiability. Due to the easily accessible silanol groups on the particle surface (between ca. 4.2 and 5.7 OH-groups per  $\text{nm}^2$ )<sup>[77]</sup>, a variety of silane linkers can be covalently attached to the surface. For example, molecules can be attached which carry a functional group (*e.g.*, silanes with an amino-<sup>[78]</sup>, thiol-<sup>[79]</sup>, or epoxy-<sup>[80]</sup> group) or the originally hydrophilic nanoparticles

can be converted into hydrophobic ones and thus can be rendered dispersible in nonpolar solvents (*e.g.*, polyethylene glycol [81]). [82, 83] The silane linkers attached in this way can then be used for further chemical reactions, where, for example, additional molecules but also other nanoparticles can be attached. Amino-functionalized silica nanoparticles can react with molecules that carry a carboxylate group to form a stable amide bond or with aldehyde- or N-hydroxysuccinimide ester-functionalized molecules. [58, 83] Another possibility for modification is the attachment of fluorescent dyes. These can be coupled to the surface via silane linkers [82, 83], but can also be incorporated into the interior of the particles during the synthesis. [74, 84, 85]

Since 2005, *Ulrich Wiesner's* research group has developed a series of dye-doped silica nanoparticles based on a modification of the classical Stöber method. This enabled a range of fluorescent dyes to be incorporated into silica nanoparticles with different primary particle sizes, known as Cornell-dots. [84, 86-88] For this purpose, core particles with an increased dye concentration were prepared in a first step and then coated with an additional silica shell to protect the dyes from leaching. [84] In order for dyes to be covalently incorporated into silica nanoparticles via the classical Stöber method, the dye molecules must contain an anchor group that can be incorporated into the network, like a silanol group (*e.g.*, APTES + rhodamine B [73, 85, 89], fluorescein [90], rhodamine 6G [91]; ICPTES + rhodamine 110 [92]; APTES + cysteic acid + Atto647 [74]). By incorporating the dyes into the silica matrix, the dyes can also be protected against external influences such as pH, temperature and bleaching compared to the pure dye molecules. [74] In addition, covalent incorporation has the advantage that the dye remains in the nanoparticle and does not leach into the surrounding medium over time. [74, 89, 93]

However, since the Stöber-like synthesis takes place in an alcoholic, ammonia environment, only molecules that are stable under such conditions can be used. Based on a protocol by Hartlen *et al.* [94], various dyes and even proteins can be incorporated into a silica matrix. [74, 93, 95]

In this work, Stöber-like synthesis was used to prepare various silica nanoparticles between 80-320 nm. By adding fluorescent dyes (rhodamine B and rhodamine 110) during the synthesis, the dyes were covalently incorporated into the silica network. After the nanoparticle formation, the surface was easily modified by APTES molecules.

### 2.1.3 Iron oxide

As a second system, iron oxide nanoparticles were employed in almost all of the projects of this thesis. Therefore, this section firstly describes some basics on iron oxide and secondly presents different syntheses routes for the preparation and modification of iron oxide nanoparticles.

#### Fundamentals

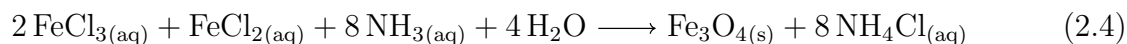
Iron occurs sporadically in pure form ( $\alpha$ -Fe), it is predominantly found in more than one hundred different iron minerals.<sup>[96]</sup> The iron oxides form a large series of different minerals. Various stoichiometric compositions of iron and oxygen, accompanied by the formation of different crystal lattices, can form a variety of minerals. The best known representatives of iron oxide are wüstite ( $\text{Fe}_{1-x}\text{O}$ ), hematite ( $\alpha$ - $\text{Fe}_2\text{O}_3$ ), maghemite ( $\gamma$ - $\text{Fe}_2\text{O}_3$ ), magnetite ( $\text{Fe}_3\text{O}_4$ ) and goethite ( $\alpha$ - $\text{FeOOH}$ ).<sup>[97]</sup> The uses of iron oxide are as varied as its occurrence, like as pigments<sup>[98]</sup>, catalysts<sup>[99, 100]</sup>, in food security<sup>[101, 102]</sup>, in waste water treatment<sup>[103, 104]</sup> or even in medical technology.<sup>[105, 106]</sup> Iron oxide also plays an important role in nature, for example in magnetotactic bacteria.<sup>[107]</sup>

#### Synthesis

Similar to silica nanoparticles, iron oxide nanoparticles can be produced by a variety of synthetic routes. Not only the size, but also the shape and the crystal structure can be influenced. These structural features are significantly driven by the reaction parameters during synthesis and thereby influence, *e.g.*, the electrical, mechanical, optical and magnetic properties of the resulting nanoparticles.<sup>[108–110]</sup> For this purpose, a number of different synthesis methods exist. Probably the best known and most widely used are co-precipitation<sup>[89, 111]</sup>, thermal decomposition<sup>[112]</sup>, hydrothermal synthesis<sup>[113]</sup>, and microemulsion methods.<sup>[114]</sup> However, electrochemical methods<sup>[115, 116]</sup>, microorganism syntheses<sup>[117]</sup>, or laser pyrolysis methods<sup>[118]</sup> can also be used to synthesize iron oxide nanoparticles. The applications and characterization possibilities of iron oxide nanoparticles are as diverse as the possibilities of their synthesis. Depending on

the kind of iron oxide nanoparticles or application, techniques such as magnetic particle spectroscopy (MPS), magnetic particle imaging (MPI), superconducting quantum interference device (SQUID) with vibrating sample magnetometry (VSM), x-ray diffraction (XRD), Mössbauer spectroscopy, transmission electron microscopy (TEM), scanning electron microscopy (SEM), or dynamic light scattering (DLS) (to name but a few) can be used to analyze particle size, morphology, composition, crystallinity or magnetic behavior of the particles as powder, in a medium or even in humans.

For the co-precipitation method, ferrous and ferric salts are precipitated in a stoichiometric ratio of 1:2 in the presence of a strong base and are surface modified after a washing step to produce a stable dispersion of magnetite (and maghemite) nanoparticles (Equation 2.4 by the example of iron chloride salts). [99, 108, 119] Nanoparticles in the size range of 5-20 nm can be synthesized. Sodium hydroxide or aqueous ammonia solution is used as a base. Depending on the choice of the iron salt (*e.g.*, chloride, sulfate, nitrate, or perchlorate), the ratio of the two salts to each other, and the choice of synthesis parameters (pH, temperature, ionic strength), different particle sizes and morphologies can be achieved. [99, 108, 120, 121]



When using the thermal decomposition method, an organometallic precursor (*e.g.*, ferric acetylacetonate, ferric N-nitrosophenylhydroxylamine, iron pentacarbonyl) is decomposed and oxidized in an organic solvent in the presence of stabilizer molecules (*e.g.*, oleylamine, steric acid, oleic acid) under the influence of temperature to form iron oxide nanoparticles. The advantage of this method is that highly monodispersed nanoparticles with a small particle size distribution can be achieved. However, the main problem of this method is that the synthesized nanoparticles can only be dispersed in non-polar solvents. [99, 119, 120] The hydrothermal synthesis route exploits the ability of water to hydrolyze and dehydrate metal salts under certain pressures and temperatures. [122] In an autoclave, aqueous solutions are typically heated above the boiling point (typically 130-250 °C) which increases the pressure in the vessel (typically 0.3-4 MPa). [120] However, the resulting metal oxides and hydroxides are insoluble in water under the given conditions, resulting in supersaturated solutions in which small crystals are formed. [113, 123, 124] The size and growth rate

of the iron oxide particles can be influenced by synthesis parameters such as pressure, temperature, reaction time, and the metal precursor itself. [125]

Another method of synthesizing iron oxide nanoparticles is the microemulsion method: Two immiscible phases of oil (*e.g.*, n-octane, cyclohexane) and water are mixed in the presence of a surfactant (*e.g.*, Triton-X) and co-surfactant (*e.g.*, hexanol, 1-butanol, glycol) to form very fine droplets. [99, 119, 126] In this process, the hydrophobic part of the surfactants remains in the oily phase and the hydrophilic part in the aqueous phase, so that segregation of the two phases no longer occurs. [120] By controlling the process parameters and thus the size of the finely dispersed droplets, monodisperse iron oxide nanoparticles can be generated.

The particle size, particle morphology, particle size distribution, and surface chemistry of iron oxide nanoparticles can be varied, as well as the crystallite size, crystal lattice, and as a result the nature of the iron oxide, and the specific incorporation of impurities by varying the synthesis parameters. [99, 119]

In this work, the co-precipitation method was mainly used to synthesize superparamagnetic iron oxide nanoparticles with a primary particle size of about 10 nm. This synthesis route is easily scalable and the resulting nanoparticles can be easily modified further.

### Modification

Depending on the subsequent application of the iron oxide nanoparticles, the surface can be functionalized with a variety of ligands. In this way, either new functionalities are generated, the stability in the medium is improved, or the binding of additional molecules can be realized. [101, 120] For this purpose, a number of different molecules can be used. For example, molecules with functional groups such as amines [127], ethylene glycol [128] or carboxylates [129], or molecules such as chitosane [130], cellulose [131], peptides [132], or polyglycerol [133] can be attached. It is also possible to modify the surface with polymer molecules such as polyethylene glycol [134], polyimide [135], polydopamine [136], or polylactic acid. [137] In addition to attaching various organic molecules, it is also possible to coat the iron oxide with other metals such as platinum [138], gold [139], or silver [140] to create core-shell nanoparticles.

Another way to modify iron oxide nanoparticles is to coat the particles with a silica shell. [89, 101, 120, 141] This silica layer has several advantages: i) It not only stabilizes the iron oxide nanoparticles in the dispersion, but also ensures that the attractive forces between the particles are reduced, thereby reducing agglomeration. [120] ii) On the silica surface various other ligands can be attached. [89, 101, 142] iii) The silica shell allows better protection of the iron oxide from external influences such as temperature. [143] iv) In addition, these composite particles are stable in dispersion, biocompatible and hydrophilic due to the silica surface. [5, 101] Such a silica shell can be achieved by classical sol-gel processes, such as the Stöber process described above, but also by aerosol pyrolysis. [120] In the Stöber process, shell thicknesses of 5-200 nm can be produced by varying the process conditions. The TEOS can attach to the hydroxyl groups of the iron oxide surface and form a three-dimensional silica network. [120]

In some of the work presented here, the superparamagnetic iron oxide nanoparticles were coated with a silica shell (via the Stöber route) for two specific reasons. First, the shell allows modification with molecules such as APTES to mimic the surface of the silica nanoparticles. Second, the light-absorbing effect of the black iron oxide is reduced by using the same mass of particles for the later experiments.

## 2.2 Supraparticles

Nanoparticles exhibit a whole range of new properties, due to their small size. However, the reduced size can lead to an increased reactivity, and nanoparticles tend to aggregate and agglomerate. This means that their intrinsic properties are partially lost and they can no longer be used for certain applications. If nanoparticles are combined into defined superstructures, not only can the intrinsic properties be retained, but also new ones can be generated. This is comparable to the developments in molecular chemistry towards supramolecular chemistry. *Jean-Marie Lehn* described supramolecular chemistry by saying that it is "*the buildup (synthesis!) of discrete or extended assemblies of chemical objects*" by "*designing and implementing functional chemical systems based on molecular components held together by noncovalent intermolecular forces.*". [144] According to *Sharon Glotzer* and *Michael Solomon*, nanoparticles can be understood as atoms and molecules of

tomorrow's materials and can be used to generate new meaningful structures. [145] Analogous to the definition of "supramolecules" (IUPAC: "*a system of two or more molecular entities held together and organized by means of intermolecular (noncovalent) binding interactions*" [146]), such structures built from smaller particulate units should be called "supraparticles". [147]

### 2.2.1 Fundamentals

Only a defined structure assembled from defined building blocks into a larger superstructure can be called a supraparticle, resulting in defined structural motifs. Nevertheless, not every agglomerate or aggregate based on nanoparticulate building blocks can be called a supraparticle. The selective assembly can create new properties/functionalities that are unique to supraparticles and cannot be found in single nanoparticles (Figure 2.4).

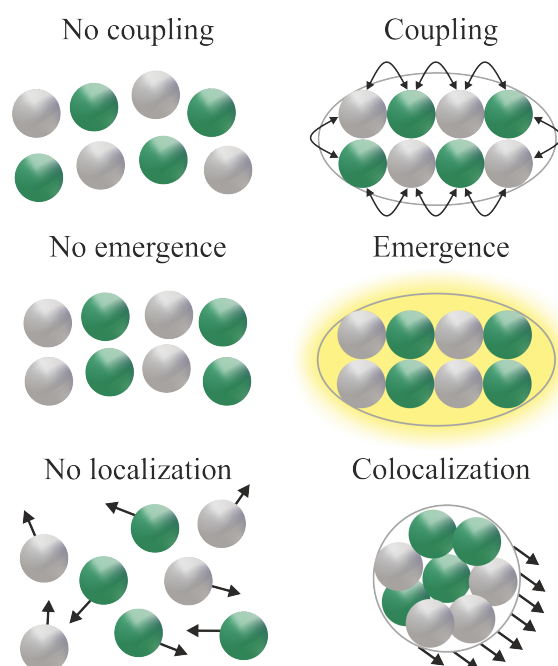


**Figure 2.4:** Schematic representation of properties arising in supraparticles in comparison to their building blocks (coupling, emergence and colocalization). Adapted and reprinted with permission. [148] Copyright 2021, Wiley-VCH GmbH.

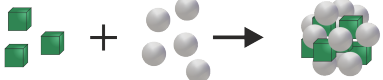
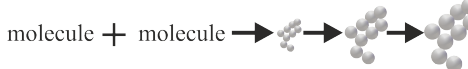
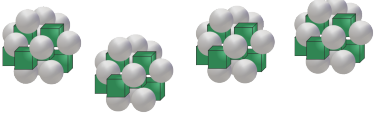
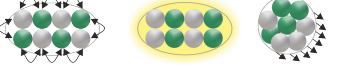
These phenomena are i) coupling (strong interaction of electrons from nanoparticles within a supraparticle due to forced proximity), ii) emergence (new properties occur due to a specific structure within the supraparticle), and iii) colocalization (different nanoparticles

with different properties form a distinguishable common entity in a supraparticle with either superimposed or combined properties that can be concentrated, removed, moved, and observed individually). [147, 148]

Figure 2.5 describes when a supraparticle can be designated as such: First, supraparticles are entities consisting of nanoparticulate building blocks. This excludes processes in which the particulate building blocks are only transition states and are not amenable to analysis, modification, or exchange. [149, 150] Second, supraparticles are obtained in dispersed form, *e.g.*, as powder, microcomposite, or colloid, and are thus distinct from nanoparticle arrays, which have infinite extents in one, two or three dimensions. [151, 152] Third, supraparticles have a specific structural motif, such as a defined averaged size, shape, internal structure, nearest neighbor junction, crystal packing, or fraction size, compared to randomly agglomerated nanoparticles. [153] These can lead to new additional functionalities (colocalization, emergence, coupling). [147, 148]

*Coupling* means that the physical properties of nanoparticles that are in close contact with each other change because electrons can interact between the nanoparticles. This includes effects such as changes in surface plasmon resonance or resonance energy transitions [154–156], upconversion [157, 158], and photocatalysis [159–161]. *Emergence* occurs when the nanoparticulate building blocks arrange themselves in a specific structure in the supraparticles and their characteristics differ from the intrinsic properties of the original nanoparticles. Examples include photonic effects [32, 162] (such as structural colors) or porosity. [163–165] *Colocalization* refers to nanoparticles within a supraparticle that move together and form a common, distinguishable entity that can be concentrated, observed individually, and removed. This includes, for example, supraparticles that can be understood as nanoparticle formulations [147], can be used as anti-counterfeiting agents, markers, or tracers by combining different optical or magnetic building blocks [166–169], or consist of magnetic building blocks with different properties. [170–172]

## 2.2. Supraparticles

Supraparticles:	Excluded particles:
Entity consisting of defined particles created from colloiddally dispersed nanoparticles as the starting material	Constituent particles are only transient stages that are not accessible for analysis, modification, or exchange
	
Are obtained in a dispersed form as colloid, powder, microcomposite, ...	Self-assembled nanoparticle arrangements infinitely extended in 1D, 2D or 3D as fibers, films, colloidal crystals, ...
	
A consistent structural motif prevails among all particles: size, shape or internal structure	Randomly agglomerated nanoparticles
	
Their structural motif creates additional functionality: colocalization, emergence, coupling	
	

**Figure 2.5:** Schematic representation of supraparticles and particle arrangements not fitting in this definition. Adapted and reprinted with permission. [148] Copyright 2021, Wiley-VCH GmbH.

Supraparticles can be used in many different fields due to the properties that result from their structure and building blocks. Science should contribute to sustainable living and resource use, both of which are increasingly important issues in today's world. Hereby, the use of supraparticles can play an important role to enable future generations to live on earth. [148, 173] In this context, there are already a variety of approaches using supraparticles, such as water [174–178] and air purification [179–181], detection of various gases in the environment [182–187], and agriculture. [188, 189] Beyond these basic needs of human life, supraparticles are applicable in energy storage and conversion [190–195], as well as in catalysis. [148, 194, 196–198] Supraparticles are also becoming increasingly important in the consumer sector of modern life. They can be used to extend the life of goods [32, 148, 199–201] or to make materials reusable or recyclable. [143, 148, 202]

## 2.2.2 Formation

### Fundamentals

Supraparticles are produced by the forced assembly of individual nanoparticulate building blocks and form a new entity.<sup>[147]</sup> In doing so, they must overcome the repulsive forces that exist between nanoparticles in a colloidally stable dispersion.<sup>[203, 204]</sup> Overcoming these repulsive forces can be accomplished by attractive interactions in several ways: i) Functional groups on the surface of nanoparticles react with certain groups on other nanoparticles; ii) Destabilization of the dispersion by changes in pH or ion strength; iii) Mixing of differently charged nanoparticles; iv) Or by entropy changes due to depletion attraction.<sup>[203–208]</sup> More or less dense structures can be generated, depending on how repulsive or attractive interactions are.<sup>[147]</sup> Another way to manufacture supraparticles is to choose and control the external conditions. On the one hand, if the processes are slow evaporation processes in which both the droplet size and the number of nanoparticulate building blocks in each droplet are controlled, the formation of supraparticles is thermodynamically controlled.<sup>[147]</sup> This process can produce colloidal clusters with highly ordered structures.<sup>[209–211]</sup> On the other hand, if the evaporation process is very fast, and the number of building blocks per droplet or even the droplet size cannot be influenced, these are kinetically controlled processes in which the arrangement of the individual nanobuilding blocks in the supraparticle is disordered.<sup>[147]</sup> In general, the structure formation of supraparticles depends on both the properties of the individual nanoparticulate building blocks and the fabrication process itself. There is a wide variety of methods for the manufacturing of supraparticles.<sup>[212–217]</sup> However, if the fabrication is based on droplets, two basic types can be distinguished. One is the wet self-assembly method, in which the liquid droplets are present in another liquid, and the other is the dry self-assembly method, in which the liquid droplets are generated in a gas atmosphere.<sup>[218]</sup> In both methods, a liquid with the nanoparticulate building blocks is first dispersed into fine droplets in a second medium (liquid or gas). Then, the liquid of the droplets is gradually removed, bringing the nanoparticles closer and closer, and forming a supraparticle that can be collected in solid form.<sup>[219, 220]</sup> Since the focus for the formation of supraparticles is set on spray-drying in this work, only this method will be explained in more detail.

## Spray-drying

Spray-drying is a process for converting dispersed solids into a powder form which can also be used on an industrial scale. The process is used, *e.g.*, in the pharmaceutical, food or chemical industry for the production of granulated drugs, instant coffee or washing detergents.<sup>[221-224]</sup> Figure 2.6 shows a schematic presentation of a spray-dryer on a laboratory scale.

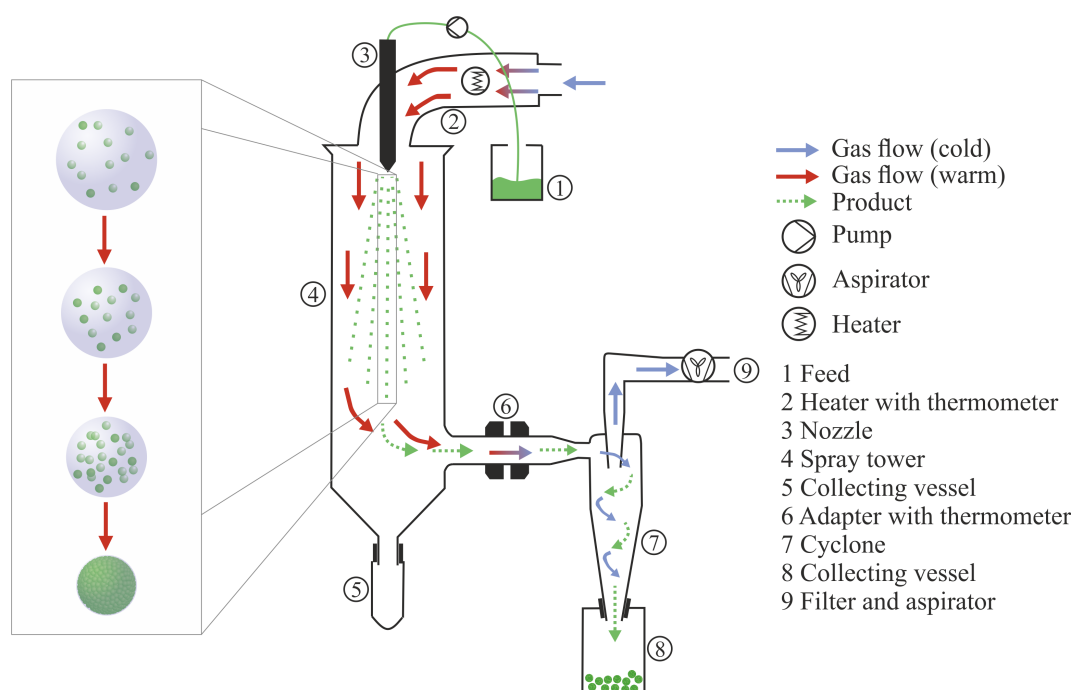


**Figure 2.6:** Schematic representation of a laboratory spray-dryer based on the Mini Spray-Dryer B-290 from Büchi, Switzerland. The gas flow (arrows) in the temperature profile (blue and red), the movement of the nanoparticle dispersion to the collected supraparticulate powder (green) and a labeling of the individual components are shown (1: nanoparticle dispersion, 2: heating element, 3: nozzle, 4: spray tower, 5: collecting vessel for large droplets and aggregates, 6: transition piece with outlet thermometer, 7: cyclone, 8: collecting vessel for sample, 9: filter and - connected to it - the aspirator). In the section on the left, the drying process of a droplet in which nanoparticles are present is shown schematically. Adapted and reprinted with permission.<sup>[162]</sup> Copyright 2022, Wiley-VCH GmbH.

Here, the nanoparticle dispersion is first transferred from a reservoir (1) via a peristaltic pump into a spray nozzle (3). Subsequently, the dispersion is finely atomized and enters the spray tower (4). The air in this cylinder is preheated by a heating element (2). A slight negative pressure is generated in the system via an aspirator (9), so that a constant gas flow is produced. The heated gas flow causes the solvent in the droplets to

evaporate and forces the nanoparticulate building blocks to approach each other ("forced assembly method") (Figure 2.6 excerpt left). [162, 225, 226] This results in densely packed supraparticulate structures, which are transported further via the gas flow to the cyclone (7), where they are separated by centrifugal forces and collected in the collecting vessel (8). The outlet temperature is recorded with a further thermometer (6) at the transition between spray tower and cyclone. Agglomerates or solvent droplets that are too heavy to be transported by the air stream or are not fully dried are collected in a further collecting vessel at the end of the spray tower (5). Between the cyclone and the aspirator a filter unit is placed (9) which collects the fine fraction that is not separated by the centrifugal forces in the cyclone.

The size and morphology of the supraparticles produced by this method depend on both the device parameters and the nanoparticle building blocks. [162, 227–229] The size of the resulting supraparticles is mainly determined by the droplet size generated in the nozzle. [225, 227] The droplet size, in turn, depends on several factors, including the type of nozzle, the pump rate, and the type and viscosity of the solvent. Basically, the larger the droplets are formed, the more nanoparticles they can contain and the larger the resulting supraparticle will be. The droplet size and the number of particles per droplet are affected by the solids concentration in the starting material. [225, 227, 230] Since droplet generation through the nozzle (in standard laboratory spray-dryers) is always accompanied by a broad distribution, the resulting supraparticles will also have a broad size distribution. [89, 143, 227] The morphology, as well as the size distribution of the resulting supraparticles, is influenced by both the properties of the nanoparticle dispersion used (particle size, physical and chemical properties, type of solvent, surface modifications or charges, ion concentration, stability, to mention just a few) and the process parameters (*e.g.*, temperature during the evaporation process, speed of the aspirator, cyclone size). [225, 227, 231–233] In a classical spray-drying process, usually, spherical morphologies are obtained, but they range from dense raspberry-like shapes to donut-shaped structures. [147, 225, 227, 234–236] The different morphologies can be controlled by the device parameters as well as by the used particle dispersion.

Starting from a system of two different particle species (as mainly used in this work), different morphologies can be obtained. In the simplest case, when both nanoparticle species

have similar sizes, densities and surface charges, supraparticles can be generated in which the nanoparticles are randomly distributed. [89, 143, 147, 162] Three different routes can be chosen to generate core-shell morphologies, depending on the initial particles. First, two consecutive spray-drying processes are performed. In the first step, core particles are generated which are coated with additional nanoparticles in a second step. [89, 92, 237] The advantage is that core-shell morphologies can also be assembled from nanoparticles of roughly the same size and density. Second, if nanoparticles with significantly different sizes or densities are used, segregation occurs in the droplet. The smaller, faster moving nanoparticles (Brownian molecular motion) are driven outward and the larger, heavier particles remain in the core. [230, 238] Third, a shell of nanoparticles can be built around a microscopic particle used as a template. [236]

## 2.3 Characterization methods

### 2.3.1 Fluorescence spectroscopy

Fluorescence spectroscopy uses the phenomenon of luminescence to characterize samples. [239] Basically, luminescence can be divided into two categories: Fluorescence and phosphorescence. [239] Here, only fluorescence is described, as this is the only phenomenon studied in this work. When a molecule is supplied with energy in the form of light, an electron can be excited from its ground state to a discrete singlet excited state by absorbing a photon. When this molecule collides with other molecules in its environment, some of its energy is lost. The excited electron falls back to its ground state and the remaining energy is released in the form of a photon. Thus, this photon has a lower energy than the original photon emitted, resulting in a shift of the energy to higher wavelengths. This emission of light can be measured as fluorescence. [240–242] Fluorescence typically occurs, *e.g.*, in aromatic molecules and was first described by *Sir John Frederick William Herschel* in 1845 when he observed the fluorescence of a solution of quinine in sunlight. [243] The first fluorescence spectrometers were developed in the 1950s. [239] The interaction between the absorption and the resulting emission of light is usually represented by the Jablonski diagram. [242] In fluorescence spectroscopy, typically two types of measurements are used.

On the one hand, an emission spectrum of the sample can be recorded. This means that light of a specific wavelength is irradiated on the sample and the emission intensity over a certain spectrum is recorded.<sup>[239]</sup> On the other hand, the excitation spectrum can be recorded by measuring the emission intensity at a given wavelength as a function of excitation.<sup>[239]</sup> This is possible because the emission spectrum of a sample remains constant regardless of the excitation wavelength, only the intensity of the signals changes (Khasa's rule).<sup>[244]</sup>

In principle, all fluorescence spectrometers are constructed in a similar way.<sup>[239]</sup> Starting with a light source (usually a xenon or mercury vapor lamp) the light is directed by mirrors through a monochromator. This monochromator can be adjusted with slits to allow only light of a certain wavelength to pass. The monochromated light then enters the sample chamber where it interacts with the sample. The emitted luminescence of the sample is then recorded at a 90° angle by a detector (usually a photomultiplier).<sup>[239]</sup> Fluorescence spectroscopy is used to examine different questions in chemistry and biology. The measurements can provide information about the molecules themselves, their interaction with solvents, for example, the motion, conformational changes and binding properties of biomolecules, or can determine the size of quantum dots.<sup>[95, 239, 245–247]</sup>

### 2.3.2 Confocal microscopy

The first confocal microscope was developed by *Marvin Minsky* in 1955 and patented in 1957.<sup>[248, 249]</sup> With these microscopes, it is possible to obtain a high-resolution image of, *e.g.*, a tissue sample with a high level of detail and better contrast than with conventional light microscopes.<sup>[240, 249, 250]</sup> In addition, these individual images are converted to a 3D image of the sample. This is possible because in confocal microscopy, the incident light is focused only on a specific point of the sample, rather than exposing the entire sample (as in classical fluorescence or light microscopy).<sup>[240, 249, 250]</sup> This is achieved by focusing the incident light (usually from a laser) through the microscope objective onto a very small spot in the sample. The light reflected or fluorescing from the sample is collected by the same objective. There is a small pinhole in the objective to ensure that only the light

emitted from the focal point is transmitted. [240, 249–251] Stray light reflected from outside the focal plane is filtered out. A detector (mostly a photomultiplier) which can collect the confocal light is placed behind the objective. [240, 249–251] Thus, information from a sample is obtained with pinpoint accuracy. By scanning the sample in both the  $xy$  and  $z$  directions, it is possible to first assemble the points as individual stacks in a 2D image, and then to generate a 3D image from these individual stacks by using a software module. The disadvantage of this method is that each point must be excited for a relatively long time to collect enough photons to distinguish the signal from the noise. This means that measurements can take a relatively long time and photobleaching cannot be neglected for sensitive samples. [240, 249, 250] The excitation light in confocal fluorescence microscopy is usually generated by different lasers. This makes it possible to excite a sample with different wavelengths. For example, if the individual components of a tissue sample are stained with different fluorescent dyes, it is possible to visualize and distinguish between them by using different lasers (or by varying the wavelength of a laser) or by detecting the emission bands at different wavelengths. [240, 249–251]

Confocal microscopy can be used to characterize, *e.g.*, cells [252, 253], tissue [251, 254], or bacteria. [255] Other applications include the study of nanoparticle uptake into human or animal cells [74, 93, 95] or, as done in this work, the characterization of supraparticles. [89, 237, 256]

#### 2.3.3 Magnetic Particle Spectroscopy

Magnetic Particle Spectroscopy (MPS) is a relatively new method, which was first mentioned in 2006. [257–259] This method was initially developed as an extension of Magnetic Particle Imaging (MPI) to characterize superparamagnetic iron oxide nanoparticles and to determine their applicability to MPI. [260] While MPI can measure superparamagnetic iron oxide nanoparticles quantitatively in three dimensions and with high spatial and temporal resolution, MPS can be thought of as a zero dimensional MPI scanner consisting of field coils and pick-up coils. [259–263] In MPS, sinusoidal alternating fields (amplitude of  $\pm 300$  Oe, frequency of 20 kHz) with sufficiently large amplitudes are applied to superparamagnetic iron oxide nanoparticles, periodically moving their magnetization into

and out of saturation. [263] After Fourier transforming these data, higher harmonics can be observed in the corresponding frequency spectrum due to the nonlinear behavior of various magnetic materials. [259, 263, 264] The absolute signal strength is directly proportional to the mass of the sample, the amplitude and frequency of the external magnetic field, and the sensitivity of the coil. [263] In order to analyze the relative behavior of the curves, the amplitude intensities are normalized to intensities relative to the fundamental intensity. [264] The higher harmonics are influenced [264] by the magnetic behavior of the sample in the alternating magnetic field. This means that by decreasing the magnetization amplitude as a function of the higher harmonics, changes in the environment of the magnetic sample can be detected and individual samples can be uniquely identified. [260] The major advantage of the MPS over conventional magnetometer measurements is the fast and simple measurement method, with results available in milliseconds to seconds, the ability to measure both powder and liquid samples, and the fact that the device does not have to be cooled at great expense to 4 K. [202]

MPS was originally designed for biological and biomedical applications. These include various assays, cell labeling and tracking, blood analysis, but also hyperthermia studies, mapping of temperature and viscosity changes. [263] Since the measurement method is very sensitive and can distinguish minute changes in magnetic material, it is possible to use the MPS for tracking or identifying objects in addition to biomedical applications, as well as for identifying the mechanical forces that prevail in a ball mill. [92, 169, 202, 259, 264, 265] This means that even the smallest changes in the magnetic material, such as the size, shape and composition of the nanoparticles, as well as the composition in a supraparticle, can greatly affect the magnetic signal, giving each material its own fingerprint that can be uniquely identified. [259]

# Chapter 3

## State of the art

Within this chapter, the state of the art of the detection of shear stress in general as well as the use of functional coatings with the focus on the detection of defects in food packaging is described.

### 3.1 Shear stress indicators

The human senses (smelling, hearing, tasting, seeing and touching) are able to perceive the environment and enable us to act quickly in dangerous situations. For all these senses, there have been attempts to reproduce them and create technical counterparts for a long period of time.<sup>[266]</sup> While most of them perform well in many areas, the sense of touch, *i.e.*, in its lateral resolution, has been difficult to be replicated yet.<sup>[266]</sup> The ongoing development of robots makes the development of an artificial skin equipped with sensitive tactile sensors inevitable. These robots are not only used industrially ("Industry 4.0")<sup>[267]</sup>, but are also expected to play an important role in our everyday life in the future, *e.g.*, for housekeeping assistance or entertainment purposes.<sup>[268]</sup>

In order to develop artificial skins for robotic applications that achieve sensitivities comparable to the human sense of touch, it is necessary to also consider the friction that occurs between the touched object and the robot's hand.<sup>[269]</sup> For this purpose, so-called pressure sensor matrices are used, which can determine not only the pressure but also

the shear stress by analyzing the pressure distribution. [268, 270, 271] In order to circumvent complex calculations, a contact sensor approach for shear stress has been developed using a cantilever embedded in an elastic material. [269] Another option is the utilization of electrically driven shear stress tactile sensors. Here, ultra thin ohmic platinum contacts are deposited around elastic nanopillars using an atomic layer deposition process. The nanopillars, in turn, are constructed from a series of InGaN/GaN multiple quantum plates that become optically active when biased by an electric field. External shear stress deforms the nanopillars, reducing the intensity of the light emitted from the InGaN. By observing the nanopillars (symmetry and elliptical cross-section), both the force and its direction can be directly determined. [272] By incorporating piezoelectric polyvinylidene fluoride polymer layers into soft materials, shear stress and its distribution can be measured. [273]

Other than in the robotics industry, tactile shear stresses also play an important role in modern medicine. [270] In this field, it is important to directly monitor shear stress, and the applied sensor must be flexible and attachable to curved surfaces or moving body parts. For this purpose, sensors are used to determine the interfacial forces (friction) between prostheses and stumps. [266, 270]

In general, sensors must be developed that are sensitive to mechanical stresses and can indicate them quickly and accurately. Furthermore, it is of great interest whether these sensors can be used not only on flexible, non-planar substrates, but also on large surfaces. [268, 274] In this context, the size of individual sensors plays an important role. The development of the so-called microelectromechanical systems (MEMS) made it possible to reduce the size of the traditional sensors that had been used until then by an order of magnitude. This initiated the next step of the silicon revolution, similar to the influence of silicon microelectronics that revolutionized the computer and semiconductor industries through integrated circuits. [275]

The detection of shear stresses induced by air flows is also very important, especially in aerodynamic technology. Sensors that determine shear stresses via temperature changes are very simple in design, but do not have sufficient resolution. [276] In order to overcome these obstacles, a variety of sensors have been developed, which can be broadly classified into three categories: based on optical [276], capacitive [277, 278] and piezoresistive [275, 276]

sensors. All of them have their own advantages and disadvantages. However, in general, it can be said that all these micromechanical sensors are often inflexible, large in size, expensive to manufacture, and susceptible to electromagnetic interferences. [270, 275, 276, 279]

Therefore, sensors that indicate mechanical stress with high spatial resolution, are easy to read-out, and can be incorporated into flexible components are needed. For this purpose, mechanochromic systems that indicate mechanical stress (such as grinding, squeezing, rubbing or extruding) via changes in their luminescence properties are very promising. [280, 281] Examples include crystalline solids [282–284], liquid crystals [285, 286] and dye-doped polymers. [287, 288]

Crystalline solids can either change their color or switch between a dark and a bright state upon external mechanical stress. [289] For this purpose, various complex compounds based on, *e.g.*, Au(I) [283], Cu(I) [284], Ag(I) [290], Zn(II) [291], Pt(II) [286], Al(III) [292], and Ir(III) [293] are used. [281] These metal complexes have a specific optical signal in the initial state (certain color or dark) and a grinding process changes the signal (the color changes or a color becomes visible). Many of these systems work reversibly. That is, a heating step can restore the crystal structure which was destroyed by the grinding process and the initial state reappears. [281]

Liquid crystals, such as a pyrene derivate, have yellow emission in the initial state (cubic phase). Due to the phase transformation during a milling process, new hydrogen bonds are formed, p-p stacking interactions occur and a blue shift of the optical signal can be observed. [294]

Detection of mechanical strain in polymeric materials (plastics, elastomers, composites, or coatings) is expensive. [295] Classical methods such as Raman spectroscopy [296] or bimetallic methods [297] are usually invasive, costly and cannot provide a real-time measurement in the application. However, this can be realized by using dye-doped polymers. In this case, a variety of different dye molecules (*e.g.*, derivatives of carbazole, anthracene, naphthalene, perylene, pyrene or p-phenylene vinylene) can be incorporated into the corresponding polymers. [295] A mechanical stress changes the orientation of the individual dye molecules in the polymers, resulting in a change in the optical signals. Depending on whether the polymer is elastic and returns to its initial state after shear stress exposure or is permanently deformed, the color change is reversible or irreversible. [295]

Such kinds of indicators can be used to open up new application fields, like data storage<sup>[298, 299]</sup>, security inks<sup>[281, 300]</sup>, security paper<sup>[281]</sup>, optoelectronic systems<sup>[281]</sup>, or mechanical indicators.<sup>[281]</sup> Nevertheless, incomplete conversion, luminescence loss due to temperature and solvent sensitivity, and photobleaching in these kinds of mechanochromic systems can lead to erroneous results and are therefore disadvantageous.<sup>[281, 283, 289]</sup>

## 3.2 Functional coatings

High-performance coatings which have special physical properties but may only be a few nanometers to micrometers thick do not only play an important role in numerous industrial application fields but also in everyday life. For example, an anti-scratch coating of only a few micrometer thickness enabled polycarbonate eyeglass lenses to replace the much thicker and heavier glass-based ones.<sup>[301]</sup> The application of such functional coatings are virtually unlimited. There are formulations used as easy-to-clean<sup>[302]</sup>, anti-corrosion<sup>[303]</sup>, anti-fouling<sup>[304]</sup>, anti-reflex<sup>[305]</sup>, anti-soiling<sup>[306]</sup>, anti-bacterial<sup>[307]</sup>, anti-wear<sup>[308]</sup>, or anti-fogging<sup>[309]</sup> coatings, to name but a few. All of these coatings have in common that they enhance the surface properties while ensuring that the underlying material is protected. For example, surfaces with a low-maintenance coating need to be cleaned less frequently and cleaning can be done under milder conditions (lesser use of chemicals and mechanical forces), which can significantly extend the life-time of the goods.<sup>[148]</sup>

In this context, especially in the field of food packaging coatings have become increasingly important in recent years. Here, special barrier layers are introduced into the multilateral structure of the packaging films. The aim is to develop ever thinner layers that provide a high oxygen barrier to keep the packaged goods fresh for longer time periods. Such multilayer films consist of a variety of different coatings and materials, all with different properties (*e.g.*, polyolefin as a base film with a good water vapor barrier, polyamide with good puncture resistance, ethyl vinyl alcohol for a good oxygen barrier).<sup>[310–312]</sup> This ultra-thin barrier layer (usually 3–5  $\mu\text{m}$ ) is mainly responsible for preventing oxygen from penetrating the packaging. This gives food a longer shelf-life and reduces food waste and wastage.<sup>[313]</sup> However, even the smallest imperfections, such as scratches caused by mechanical stress, are already sufficient to destroy this barrier. Technically, it is very

difficult or almost impossible to detect such tiny defects over a wide area with common sensors or indicators. [314]

Food safety has a major impact on the health of the society. [315] There are already some approaches in the literature to make food packaging smart and intelligent. [315–318] This involves using a combination of sensors and indicators to reversibly monitor the actual state of the packaging throughout the supply chain (sensor) and to indicate changes in the food quality via an irreversible shift (indicator). [315, 318]

Sensors in food monitoring are instruments that can reversibly detect, localize, physically or chemically identify a change in the environment – quantitatively if necessary – and emit corresponding signals. [315–317, 319, 320] Examples of sensors that can be used in food packaging are gas sensors, fluorescence-based oxygen sensors, or biosensors. [315, 321] CO<sub>2</sub> detectors are one example of common gas sensors. These can either have a luminescent dye that changes its fluorescence in the presence of CO<sub>2</sub>, or that can be used as pH indicators which show a color change via a pH-dependent colorimetric change. [322–325] One of the first attempts to use luminescent dyes was the use of pyranine in plastic films. [326] The stability of this system could be improved by incorporating it into a hydrophobic, organically modified silica matrix (ormosil) [323], but the used chemicals are mostly not food grade and possible leaching of the chemicals into the food can have critical consequences. [322] Fluorescence-based oxygen sensors can measure the presence of oxygen by altering the fluorescence lifetime of Ru(II) or Pt(II) octaethylporphyrine ketone dye complexes. [327, 328] Microbiological contamination can basically be divided into two areas. A distinction is made between normal microbiological growth, which occurs naturally and spoils the product over time, and the growth of pathogenic microorganisms, which can result from unclean work and contamination in the supply chain [315, 329] Since the classical, time-consuming laboratory methods of microbiological analysis are not practicable for food packaging [330, 331], a novel biosensor was developed. [332–334] In these studies, so-called lateral flow stripes are used. Bacterial cells are mixed with gold or palladium nanoparticles labeled with an antibody and applied to a test stripe. Through capillary interactions, the complex moves across the strip and can be captured by another antibody immobilized on the strip. In the process, a colored line becomes visible and can be detected with the naked eye. [335] While these sensors have some advantages over

invasive, expensive measurement methods such as gas chromatography with mass spectrometry<sup>[336]</sup>, they also have some challenges to overcome before they can be used as a mass product. These include making the sensors smaller while increasing their flexibility, lowering the development and manufacturing costs, and increasing their resistance as well as their sensitivity. The readout of these sensors is not always easy and sometimes requires complex and expensive measurement methods.

In contrast to sensors, indicators in packaging cannot provide quantitative information or store data, but can only indirectly provide qualitative information about the conditions within the packaging.<sup>[318–320]</sup> This information can be provided irreversibly, *e.g.*, by a change in color, an increase of color intensity, or the movement of a dye along a certain pathway.<sup>[337]</sup> Possible influences that can be indicated are, for example, the monitoring of cold chains during transport and production, the presence of gases (*e.g.*, oxygen or various decay gases), or, in general, the freshness of food.<sup>[318, 320, 327]</sup> So-called time-temperature indicators can show a deviating temperature (too high or too low) during the supply chain by simple color changes.<sup>[318]</sup> One example is an enzymatic time-temperature indicators based on an alkaline lipase that diffuses through a polyvinylalcohol gel substrate to indicate the freshness of milk.<sup>[338]</sup> The presence of oxygen, for instance, can be indicated by a color change of a redox dye (*e.g.*, N,N,N'N'-tetramethyl-*p*-phenylenediamines, methylene blue or 2,6-dichloroindophenol), while an alkaline component (like sodium hydroxide) and a reducing agent (*e.g.*, reducing sugar) are present.<sup>[327]</sup> The presence of CO<sub>2</sub> can be used, among other parameters, to make an indirect assessment about the freshness of the packed food.<sup>[318]</sup> By combining bromothymol blue and methyl red on a label, the real-time freshness of cut vegetables can be detected by a color change via an increase in CO<sub>2</sub> concentration.<sup>[339]</sup> However, the disadvantage of all these dye systems is that leaching effects (*e.g.*, due to moisture in the packaging) or bleaching effects (*e.g.*, due to UV radiation) can occur, and lead to false results.<sup>[327]</sup>

All these sensors and indicators have in common that they can only provide information about the condition of the packaged good, but cannot provide information about the integrity of the actual packaging. Although work has been done to detect defects in packaging through enhanced gas permeation measurements, there is currently no way to detect these defects, which are usually quite small, using simple methods.

However, in the case of other functional coatings, such as anti-corrosion coatings, investigations have been carried out to detect scratches on the surface of copper substrates. [340] For this purpose, capsules filled with a dye were incorporated into the coating, which was several hundreds micrometers thick. By irradiating a damaged sample with UV light, the progress of corrosion in the copper substrate can be visualized. In another work, a multilayer coating (a several hundred micrometer thick layer) is described in which capsules filled with different dyes were incorporated into each layer. [341] If a scratch is introduced into the layer, the detectable dye can be used to determine how deeply the scratch has penetrated the layer. However, these indicators also have the disadvantage that they only can be used in relatively thick layers (a few tens up to a few hundred micrometers), but they cannot be used in the thin barrier coatings typically used for food packaging.

# Chapter 4

## Results

In this chapter, a summary of the results of the following publications is given. The detailed results, the experimental parts as well as a detailed comparison with the literature can be found in the individual publications. All shown figures were reprinted or adapted with permission from the respective journals. Table 4.1 gives an overview of the publications presented in the mentioned chapters.

**Table 4.1:** Compilation of the publications presented in this thesis and the respective chapters.

Publication	Subchapter
<u>S. Wenderoth</u> , T. Granath, J. Prieschl, S. Wintzheimer, K. Mandel Abrasion Indicators for Smart Surfaces Based on a Luminescence Turn-On Effect in Supraparticles <i>Adv. Photonics Res.</i> , <b>2020</b> , 1(1), 2000023	4.1.1, 4.1.2
<u>S. Wenderoth</u> , S. Müssig, J. Prieschl, E. Genin, K. Heuzé, F. Fidler, D. Haddad, S. Wintzheimer, K. Mandel Optically sensitive and magnetically identifiable supraparticles as indicators of surface abrasion <i>Nano Lett.</i> , <b>2022</b> , 22(7), 2762-2768	4.1.2
<u>S. Wenderoth</u> , A. Eigen, S. Wintzheimer, J. Prieschl, A. Hirsch, M. Halik, K. Mandel Supraparticles with a Mechanically Triggerable Color-Change-Effect to Equip Coatings with the Ability to Report Damage <i>Small</i> , <b>2022</b> , 18(15), 2107513	4.1.3

- S. Wenderoth, G. Bleyer, J. Endres, J. Prieschl, N. Vogel, S. Wintzheimer, K. Mandel  
Spray-Dried Photonic Balls with a Disordered/Ordered Hybrid Structure for Shear-Stress Indication 4.2.1  
*Small*, **2022**, 18(48), 2203068
- S. Wintzheimer, S. Müssig, S. Wenderoth, J. Prieschl, T. Granath, F. Fidler, D. Haddad, K. Mandel  
Hollow Superparamagnetic Nanoparticle-Based Microballoons for Mechanical Force Monitoring by Magnetic Particle Spectroscopy 4.2.2  
*ACS Appl. Mater.*, **2019**, 2(10), 6757-6762
- S. Wintzheimer, J. Reichstein, S. Wenderoth, S. Hasselmann, M. Oppmann, M. T. Seuffert, K. Müller-Buschbaum, K. Mandel  
Expanding the Horizon of Mechanochromic Detection by Luminescent Shear Stress Sensor Supraparticles 4.2.3  
*Adv. Funct. Mater.*, **2019**, 29(19), 1901193
- S. Wintzheimer, J. Reichstein, P. Groppe, A. Wolf, B. Fett, H. Zhou, R. Pujales-Paradela, F. Miller, S. Müssig, S. Wenderoth, K. Mandel  
Supraparticles for Sustainability 2.2  
*Adv. Funct. Mater.*, **2021**, 31(11), 2011089
- 

The results chapter is divided into two main parts. In the first part, shear stress indicator supraparticles for use in thin films are described. First, the general challenges for such systems are discussed and the main mechanisms are presented. The relevant publications are then summarized. In the second part, shear stress indicator supraparticles in powder form are introduced. Again, an overview of the general mode of operation is given, followed by a summary of the individual publications.

## 4.1 Shear stress indicator supraparticles in thin coatings

The idea of this approach was to develop a new indicator system that could indicate mechanical forces acting on a surface. With this system, it will be possible to detect small scratches in ultra-thin layers, such as the barrier layer in food packaging, which can only be indirectly detected to date (Chapter 3.2, Page 31).<sup>[314]</sup> With the new type of mechanochromic shear stress indicator supraparticles in thin coatings developed herein, mechanical shear forces to the surface can be detected with simple methods even before the actual barrier coating is damaged, by detecting changes in the optical signals.

For this purpose, different nanoparticle building blocks were assembled into a hierarchical micrometer sized structure in such a way that a mechanical shear force applied to it results in an easily detectable optical signal change. In order to build such a structure, two different types of building blocks with different optical behavior were required. These were assembled into hierarchical microstructures via the spray-drying process (Chapter 2.2.2, Page 21). There is a total of three different basic mechanisms for determining shear stress on thin coatings (based on an optical detection mode). The mechanisms are only briefly and generally introduced here and will be further elaborated in the following chapters. These mechanisms are the turn-on (Chapter 4.1.1, Page 40), the turn-off (Chapter 4.1.2, Page 45), and the color-change (Chapter 4.1.3, Page 51) of an optical signal due to an increasing shear stress application. For the realization of such mechanisms, the respective supraparticles had to be structured in a certain way:

- They needed a predominantly spherical morphology.
- The different components had to be arranged in a core-shell structure. As the ratio of core to shell in all supraparticles was similar, a homogeneous macroscopic fluorescence signal was observed.
- They had to consist of an optically active and an optically inactive component in the core or shell (turn-on, turn-off) or of two optical components that were different from each other (color-change).

Therefore, the basic structure for all three mechanisms was identical and differed only in

the choice of nano building blocks or their arrangement within the supraparticle. Figure 4.1 shows the schematic structure of the three different systems. In the case of shear stress indicator supraparticles that demonstrated a turn-on effect (Figure 4.1a1), the core of the supraparticle consists of silica nanoparticles and was labeled with a fluorescent dye, while the shell consisted of black, light-absorbing iron oxide particles. In the case of turn-off supraparticles, this structure was exactly reversed (Figure 4.1b1). The core contained light-absorbing iron oxide nanoparticles, while the shell was composed of dye-doped silica nanoparticles. In the color-change shear stress indicator supraparticles, the core again was built up from dye-doped silica nanoparticles and the shell was made of alumina nanoparticles, which were surface functionalized with a second fluorescent dye (Figure 4.1c1). This means that in all three cases, the original optical signal changes as a result of mechanical stress affecting the surface as follows: In turn-on systems, the measurable fluorescence signal increased (Figure 4.1a2), in turn-off systems the signal decreased (Figure 4.1b2), and in color-change systems there was a peak shift from one dye signal to the other (Figure 4.1c2).

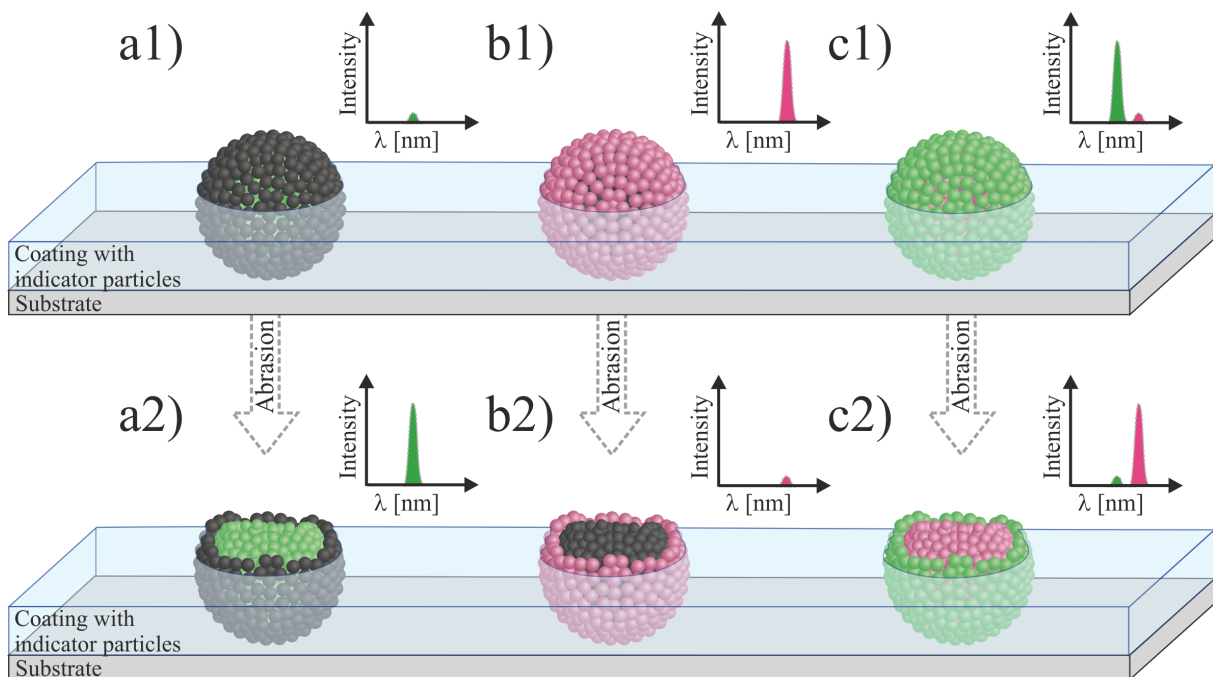


**Figure 4.1:** Schematic illustration of turn-on (a), turn-off (b) and color-change (c) indicator supraparticles embedded in thin coatings in the initial state (1) and after shear stress application (2). The diagrams symbolize the change of the fluorescence signal during the mechanical abrasion process.

In order to incorporate these shear stress indicator supraparticles into thin films, varying requirements had to met. First, there were specific requirements.

The coating matrix had to be:

- Applicable in layer thicknesses of a few  $\mu\text{m}$ .
- Optically inactive/transparent and was not allowed to optically interact with the supraparticles.
- Curable at temperatures that did not denature the used dyes.

In addition, there were challenges for the combination of supraparticles in the coating matrix:

- The supraparticles needed to be dispersible in the coating matrix (polarity, solvent, pH, salt concentration).
- The used dyes had to be covalently coupled in/onto the nanoparticles to prevent leaching of the dye into the coating.
- Besides the spherical morphology the supraparticles needed a minimum size so that they protruded clearly from the coating layer. This was the only way to create a molehill-like structure that ensured gradual abrasion of the supraparticles under mechanical stress.
- The supraparticles needed to be anchored in the coating matrix.

Only when all these requirements to the supraparticles and the coating were solved, an indicator layer for mechanical shear stress could be realized. In order to test the changes in the optical signals and thus the function of the indicator layers, the abrasion tests were carried out in the same way for all three models. A cube-shaped stamp with an edge length of  $1.5 \times 1.5 \text{ cm}^2$  was equipped with an abrasion paper and placed on a  $90^\circ$  angle on the surface of the coating (Figure 4.2). When selecting the abrasion paper, it was important to ensure that the used abrasive material does not interact with the supraparticles and can be removed from the coating without leaving any residues. With the aid of a crockmeter, this stamp was moved over the coating with a grinding pressure of 4 N in a linear motion. One shear cycle corresponds to the back and forth movement over a distance of 7 cm, adding up to a whole distance of 14 cm. Depending on the sample, between 1000 and 3000 shear cycles were performed. After each specified number of shear

cycles, the coatings were cleaned with compressed air and rinsed with ethanol to remove the residues of the abrasive material as well as any abraded particles. Subsequently, fluorescence measurements were conducted at three spots in each coating.

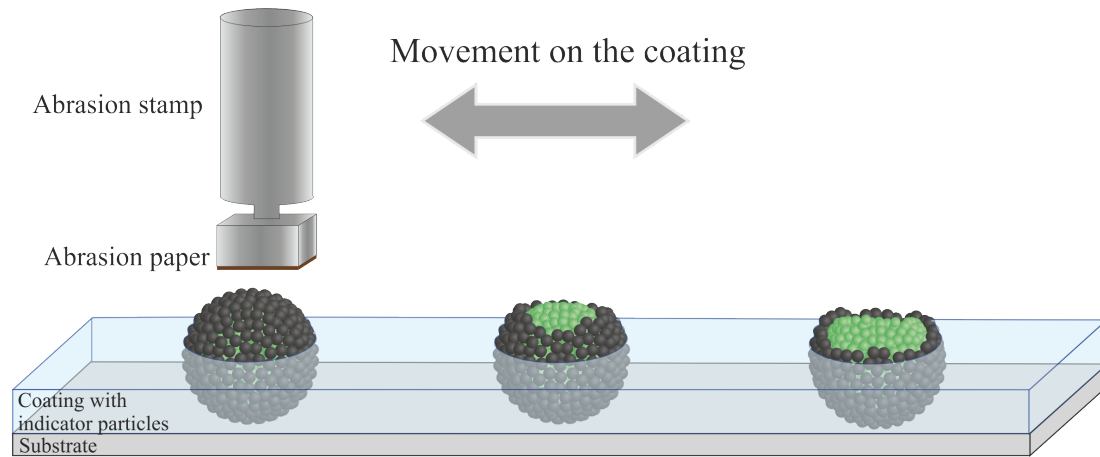


**Figure 4.2:** Schematic illustration of the abrasion process. An abrasion stamp equipped with an abrasion paper is placed in a 90° angle on the surface. The stamp moves in a linear movement over a distance of 7 cm (one way) over the surface and the supraparticles are abraded successively.

#### 4.1.1 Turn-on indicators

**Sarah Wenderoth**, Tim Granath, Johannes Prieschl, Susanne Wintzheimer, Karl Mandel, *Adv. Photonics Res.*, **2020**, 1(1), 200023

In this chapter, the structure and characterization of shear stress indicator supraparticles with a turn-on effect in thin films is described. As already mentioned, one characteristic of turn-on indicator supraparticles is the absence of an optical signal in the initial state. Only when the supraparticles are exposed to mechanical forces, *i.e.*, when they are slowly abraded layer by layer, an increase in the optical signal can be detected. Therefore, these indicator supraparticles consisted of two different building blocks. The core was made of an optically active material and the shell was built up from a light-absorbing material. Because of this core-shell structure, no signal of the supraparticles was measured when excited with light from the outside, since the light-absorbing shell absorbed most of the excitation light as well as the emitted light of the core. Only when the absorbing shell was destroyed, the excitation light from the outside could reach and excite the core. As a result, an optical signal could be detected.

However, the actual structure of the supraparticles was somewhat more complicated. As shown in Figure 4.3, the supraparticles consist of three different building blocks that were sprayed in two successive spray-drying processes to form core-shell supraparticles. The core of the indicator supraparticles was based on silica nanoparticles doped with a fluorescent dye (rhodamine B), whereas the shell of the supraparticles was composed of two different nanoparticle building blocks. One building block consisted of iron oxide nanoparticles which could absorb light and the other building block was made of pure silica nanoparticles. Since a shell of pure iron oxide would have too strong absorbing effects, it was diluted by pure silica nanoparticles.

In order to prevent the fluorescence dye from leaching into the layer during the coating process and coloring the lacquer completely, the dye had to be covalently incorporated into the silica matrix. The silanization of rhodamine B isothiocyanate (RITC) with APTES had allowed the dye to be covalently incorporated into the silica nanoparticles during a Stöber synthesis. This ensured that the subsequent detection of the fluorescent dye originated from the supraparticles only and was not detected across the entire layer.

The iron oxide nanoparticles used were first prepared by a precipitation reaction of ferrous and ferric salts in ammoniacal environment and were subsequently coated with a silica shell in a Stöber-like synthesis. This step has significant advantages. First, a silica coating surrounding the iron oxide nanoparticles can protect the iron oxide from external influences and hence possible oxidation processes that would convert the black, magnetic magnetite/maghemite mixture into the red, non-magnetic hematite. Second, all nanoparticles used then have the same chemical surface, and the same interactions can take place on all nanoparticle surfaces during subsequent modification and incorporation into the layer. In addition, the coating with a silica shell also increases the particle size of the iron oxide nanoparticles. The amount of added TEOS affected the thickness of the shell and thus the overall size of the nanoparticles. Furthermore, the addition of the silica shell reduced the "blackness" of the nanoparticles compared to the mass used, thus somewhat reducing the absorber performance. This was a positive side-effect for the optical characterization for the resulting indicator supraparticles.

Since all the used nanoparticles had the same chemical nature on the surface and approximately the same particle size, they were treated in the same way. In order to produce

spherical particles during spray-drying, the dye-labeled silica nanoparticles were surface modified with APTES. The linkage of the aminosilane on the surface of the nanoparticles had several advantages. First, the nanoparticles were destabilized in the aqueous environment, leading to the formation of spherical supraparticles during the spray-drying process. Second, the  $\zeta$ -potential of the nanoparticles was positive at slightly acidic pH values. In contrast, the non-amino functionalized nanoparticles of the shell had a negative  $\zeta$ -potential at the same pH value. Thus, the pre-assembly of the negatively charged shell nanoparticles onto the positively charged core-supraparticles occurred when the core-supraparticles were mixed with the nanoparticle dispersion of the shell nanoparticles prior to the second spray-drying process.

Figure 4.3a shows a schematic cross-section of a turn-on indicator supraparticle with a description of the individual components. The core of the supraparticle consisted of dye-labeled silica nanoparticles that emitted in the orange range of the visible spectra ( $\lambda_{em} = 580$  nm) when excited with light of the wavelength  $\lambda_{ex} = 545$  nm. The shell consisted of iron oxide@silica and pure silica nanoparticles. The theoretical representation corresponded quite well with the actual structure. As it can be seen in the scanning electron micrographs in Figure 4.3b (close-up) and 4.3c (overview), the silica nanoparticles in the core were slightly larger than the iron oxide@silica particles in the shell and, therefore, were clearly distinguishable. Furthermore, the iron oxide@silica and pure silica nanoparticles in the shell were statistically distributed without separation of the two particle types. A homogeneous fluorescence absorption by the supraparticle's shell ensured an uniform signal change during the shear off process. The supraparticle had a spherical morphology and the shell covered the entire core (Figure 4.3c).

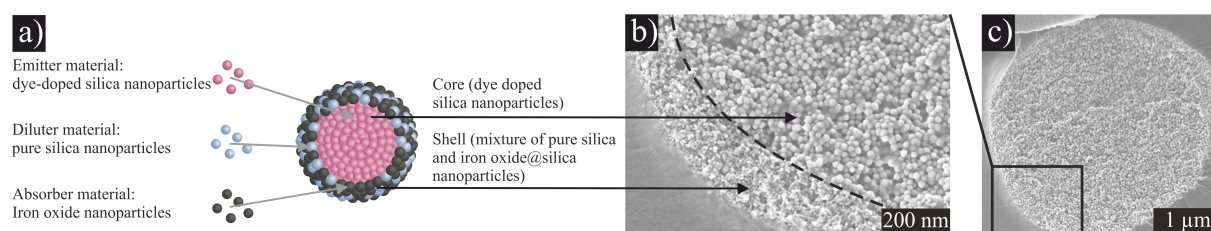


**Figure 4.3:** Schematic representation of a turn-on indicator supraparticle with labeling of the different building blocks and their functionality (a). Scanning electron microscopy images refer to the different parts of the supraparticle core and shell (b) as well as an overview image of the supraparticle in the cross-sectional mode. Adapted and reprinted with permission. [89] Copyright 2020, Wiley-VCH GmbH.

If these supraparticles were embedded in a coating layer, a molehill-like structure was formed, since the supraparticles with an average particle size of approximately  $15\ \mu\text{m}$  protrude clearly from the layer. In order to be able to adjust the optical sensitivity of the turn-on systems, the ratio of iron oxide@silica to pure silica in the shell was varied. Figure 4.4 shows confocal microscopy images of a concentration series of different ratios of iron oxide@silica to pure silica in the shell (the concentration iron oxide@silica decreases from a1 to e1). The more iron oxide@silica, *i.e.*, the more absorbing material was present, the less luminescence of the supraparticle occurred in the initial state. Conversely, the fewer iron oxide@silica particles in the shell, the less light was absorbed and the luminescence of the supraparticles was detected even in its initial state. However, if all the iron oxide@silica nanoparticles were replaced by pure silica ones, *i.e.*, if no absorbing material was left, the supraparticles were already very bright in their initial state.

If all these layers were subjected to a shear stress of 750 cycles, in samples 1 - 4 (with iron oxide@silica nanoparticles in the supraparticle shell) the fluorescence intensity increased, while in sample 5 (without iron oxide@silica) it decreased significantly. In all layers, a fluorescence signal was only detected for the supraparticulate structures and not by the layer itself. This was an indication for the successful covalent coupling of the dye to the silica nanoparticles and for the fact that the dye did not leak into the coating. Furthermore, the supraparticles were still present in the coating after the shear stress application and did not break off.

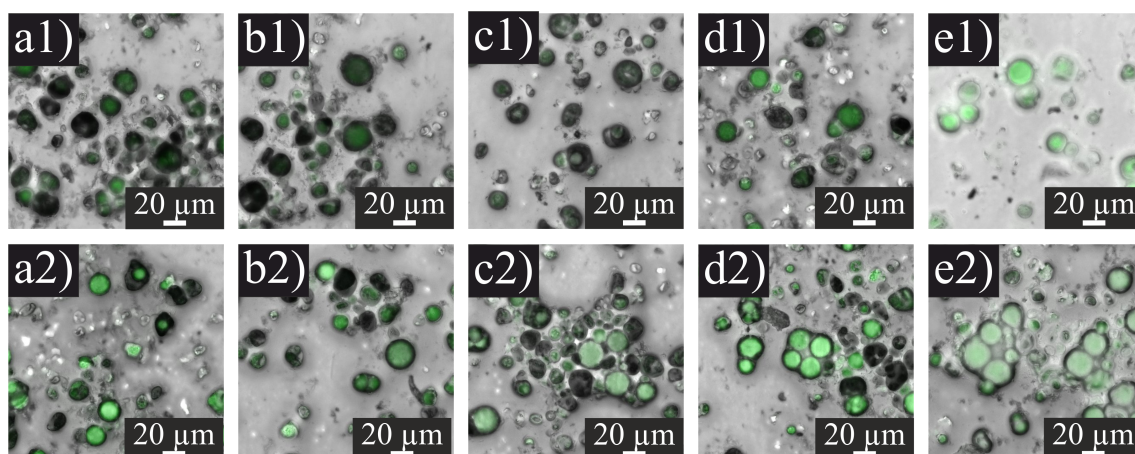


**Figure 4.4:** Confocal microscopy images of turn-on indicator supraparticles in a barrier coating with different iron oxide@silica concentrations in the supraparticle shell (decreasing from a to e) in the initial state (1) and after exposure to 750 shear cycles (2). Adapted and reprinted with permission. <sup>[89]</sup> Copyright 2020, Wiley-VCH GmbH.

In order to describe this effect of increasing or decreasing fluorescence intensity upon shear stress, the individual coatings were subjected to several successive shear cycles up to a total number of 1500 cycles (Figure 4.5). All four samples with iron oxide@silica nanoparticles in the shell of the supraparticles showed continuously increasing fluorescence signal up to a total number of 750 cycles.

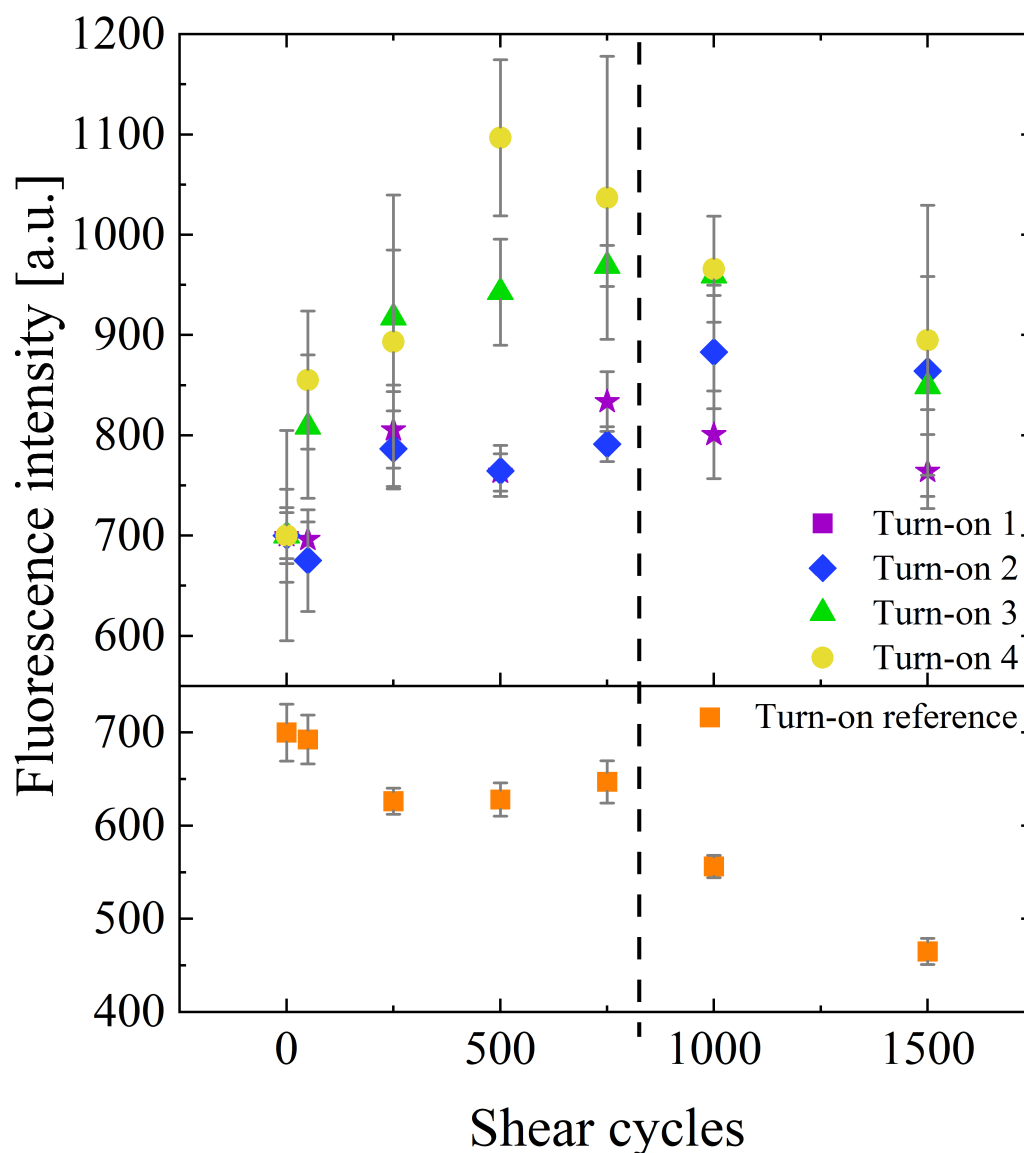


**Figure 4.5:** Normalized fluorescence intensities of turn-on indicator supraparticles in thin coatings are displayed against different number of shear cycles. Four different ratios between iron oxide@silica and pure silica nanoparticles in the shell are depicted (decreasing iron oxide@silica concentration from purple squares to blue diamonds to green triangles to yellow dots), as well as the reference sample without iron oxide@silica in the shell (orange squares). All samples were excited at  $\lambda_{ex} = 540$  nm and the emission maximum was measured at  $\lambda_{em} = 579$  nm. Adapted and reprinted with permission.<sup>[89]</sup> Copyright 2020, Wiley-VCH GmbH.

In the initial state, the turn-on supraparticles were surrounded by their respective shell. With each shear cycle, this shell was progressively removed, leading to an increase of the cross-sectional area visible in the top-view images. In the process, the ratio of the fluorescent core to the absorbing shell also increased, hence the resulting fluorescence signal increased. After about 750 shear cycles, about half of the supraparticles in the layer was sheared off. From this point on, two parallel mechanisms occurred leading to a decrease in fluorescence intensity for all samples. First, the ratio of fluorescent core to absorbing shell changed again as the cross-sectional area became smaller. Moreover, since the silica nanoparticles in the core are transparent, the iron oxide@silica nanoparticles from the lower half of the shell could also absorb more light again. Second, abrasion of the supraparticles also resulted in a general loss of luminescent material (detailed description in Chapter 4.1.2, Page 45). This mechanism of particle loss became more significant only after a certain point and played a minor role at the beginning of the abrasion of the supraparticles. In contrast, the sample without iron oxide@silica in the supraparticle shell had shown a decreasing fluorescence intensity with increasing abrasion due to the material loss. A turn-on effect was only possible if the optical signal of the supraparticle core was shielded in the initial state and was only exposed to a mechanical load.

### 4.1.2 Turn-off indicators

**Sarah Wenderoth**, Tim Granath, Johannes Prieschl, Susanne Wintzheimer, Karl Mandel, *Adv. Photonics Res.*, **2020**, 1(1), 200023

**Sarah Wenderoth**, Stephan Müssig, Johannes Prieschl, Emilie Genine, Karine Heuzé, Florian Fidler, Daniel Haddad, Susanne Wintzheimer, Karl Mandel, *Nano Lett.*, **2022**, 22(7), 2762-2768

The opposite mechanism to the turn-on effect is the turn-off effect. In this case, the optical signal of the coatings was detectable in the initial state, but this signal continued to decrease under mechanical stress. The light-absorbing part was placed in the supraparticle core and the light-emitting part was in the supraparticle shell. For the synthesis of these turn-off indicator supraparticles, the same building blocks as described in the previous chapter were used (Chapter 4.1.1, Page 40). In contrast to the turn-on indicator

supraparticles, the iron oxide@silica and pure silica nanoparticles formed the core of the turn-off supraparticle (Figure 4.6a). In order to obtain spherical supraparticles during the spray-drying process, both building blocks were surface functionalized with APTES. Due to the similar size and the same chemical nature of the surfaces of the iron oxide@silica and pure silica nanoparticles, a random distribution of both nanoparticle systems in the core was achieved (Figure 4.6b, c). The shell of dye-doped silica nanoparticles was then formed in a second spray-drying process. Slight acidification of the silica nanoparticle dispersion and addition of the amino-functionalized absorber cores to this dispersion resulted in pre-assembly of the dye-doped silica nanoparticles around the supraparticle core.

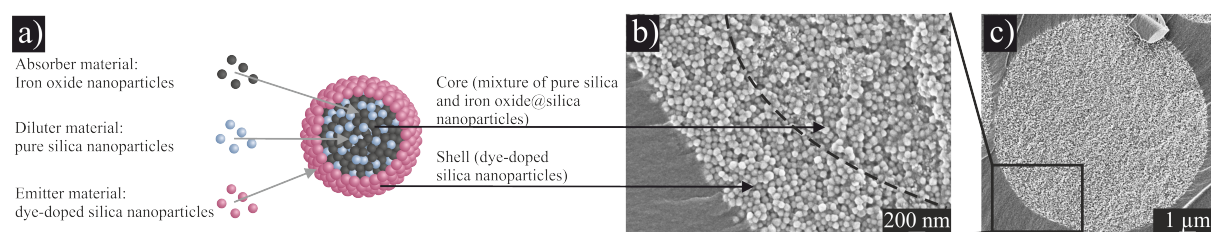


**Figure 4.6:** Schematic representation of a turn-off indicator supraparticle with labeling of the different building blocks and their functionality (a). Scanning electron microscopy images refer to the different parts of the supraparticle core and shell (b) as well as an overview image of the supraparticle in the cross-sectional mode (c). Adapted and reprinted with permission. [89] Copyright 2020, Wiley-VCH GmbH.

The iron oxide nanoparticles had further advantages in this turn-off system. In a two-step spray-drying process, the occurrence of side products cannot be prevented completely. In addition to the desired core-shell supraparticles, there might also be supraparticles of pure shell material or only core structures. While the pure core material would only decrease the overall fluorescence intensity in the initial state, supraparticles of pure shell material could affect the detection of the optical signal under mechanical stress. However, if this mixture was dispersed in water and separated magnetically before coating, the fraction of pure shell supraparticles could be removed, leaving back only the supraparticles with a magnetic component.

In Figure 4.7 different turn-off indicator systems are displayed. While in three of them the ratio of iron oxide@silica to pure silica nanoparticles in the shell were varied, the fourth sample consisted of only pure silica nanoparticles in the supraparticle core. Similar to the turn-on samples, the influence of the absorber material was investigated. During the shear process of turn-off indicator systems, two main mechanisms occurred concurrently.

On the one hand, the fluorescence intensity decreased during the layer-by-layer abrasion of the supraparticles because the cross-sectional area of the supraparticles changed. More and more of the absorbing core was exposed, while the fraction of the shell became less. On the other hand, the fluorescence intensity also decreased as more optically active material was removed. In order to make a statement about which of the two effects had the higher influence on the turn-off effect of the layers, the reference sample without iron oxide@silica in the core was considered. The reference sample had shown a much more pronounced and faster decrease in the fluorescence signal with increasing shear stress.

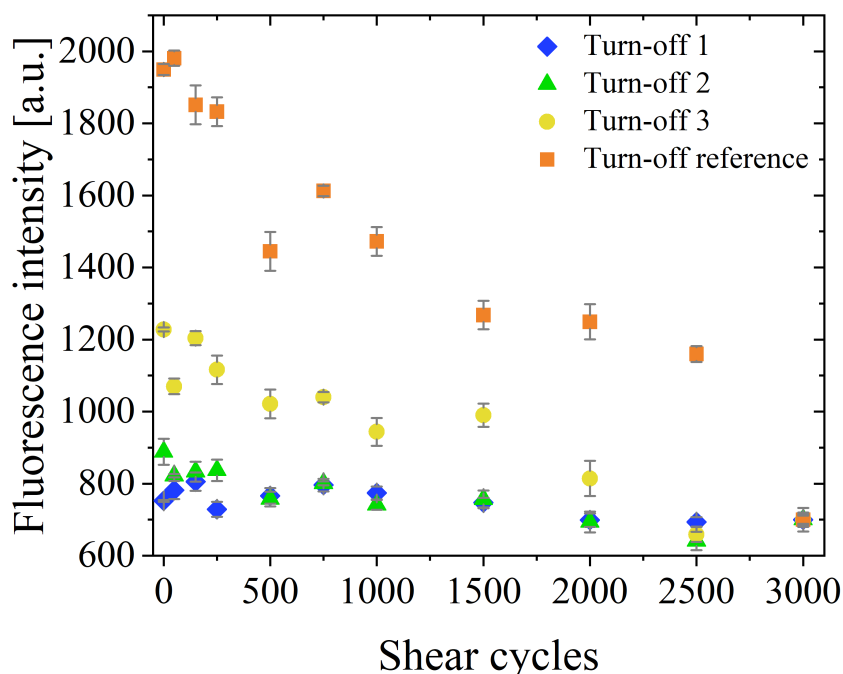


**Figure 4.7:** Normalized fluorescence intensities of turn-off indicator supraparticles in thin coatings are displayed against different shear cycles. Three different ratios between iron oxide@silica and pure silica nanoparticles in the core are shown (decreasing iron oxide@silica concentration from blue diamonds to green triangles to yellow dots), as well as the reference sample without iron oxide@silica in the core (orange squares). All samples were excited at  $\lambda_{ex} = 540$  nm and the emission maximum was measured at  $\lambda_{em} = 579$  nm. Adapted and reprinted with permission. [89] Copyright 2020, Wiley-VCH GmbH.

This indicated that the particle loss mechanism was stronger than the gradual exposure of the absorbing core. Nevertheless, the presence of iron oxide in the supraparticle core might affect the sensitivity of the indicator layer. The more iron oxide was present in the core, the more the fluorescence signal was reduced from the beginning, and the differences during the abrasion process were less clearly visible. Another disadvantage of

these turn-off coatings compared to the previously described turn-on coatings was that fragments from previous shear processes, if not completely removed, can lead to incorrect measurement results, since the overall change in the optical signal was not very high for the particle system shown here.

Since, as described, the particle loss mechanism was the dominant factor for the decrease in fluorescence intensity of turn-off indicator coatings, a multi-hierarchical structure as well as the use of iron oxide nanoparticles within the supraparticle were not mandatory. The hierarchical structure was only necessary if, in addition to intelligent, communicating coatings were to be generated in which several pieces of information could be read out simultaneously. Not only the state of the mechanical stress was displayed, but in addition the coating could be identified. The supraparticles were structured in such a way, that they had an identifiable component and a component that reacted irreversibly to mechanical stress (Figure 4.8). The high reliability and resolution was achieved because both type of information were implemented within one supraparticle. In order to create a coating with these properties, the nanoparticles had to fulfill several requirements. First, one component had to have a uniquely identifiable, always readable signal that did not change during shearing. Second, another component was required that irreversibly changes signal during the shear process. Therefore, a core-shell supraparticle system was developed where the core consisted of magnetic iron oxide nanoparticles with a unique, identifiable magnetic signal that was read out by means of its MPS signal. It was important that not only the layer was uniquely identified, but also that the signal remained constant throughout the life-time of the layer. Additionally, the signal had to be independent of the particle's total mass, since magnetic material was also removed during the shear process. In such a system, the shell of the supraparticle consisted of dye-doped silica nanoparticles that attenuated the fluorescent signal when the supraparticles were abraded step-by-step (Figure 4.8a, b, c). The dye had to be chosen and concentrated in a way that it was sufficiently detectable despite the presence of the iron oxide in the core. The fluorescent supraparticle shell indicated the mechanical stress of the layer while the magnetic supraparticle core had always shown the same signal in the MPS, so that the coating could be identified and distinguished from other coatings at the same time.

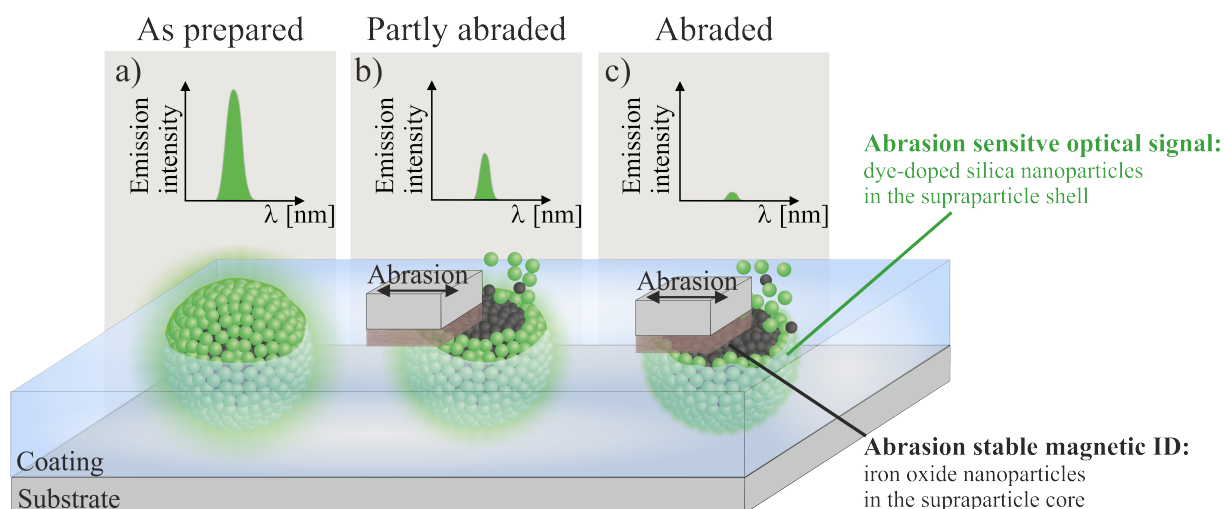


**Figure 4.8:** Schematic representation of turn-off indicator supraparticles. The core was based on iron oxide nanoparticles equipped with a magnetic ID and the shell was formed by dye-doped silica nanoparticles. The supraparticles formed a molehill-like structure in the coating. With an increasing shear stress application, the supraparticles were step-wise abraded (a, b, c). Simultaneously, the fluorescence signal of the entire coating decreases with increasing shear cycles. During the entire shear process, the magnetic signal of the core remained constant and therefore, the coating could be identified. Adapted and reprinted with permission. [92] Copyright 2022, American Chemical Society.

In this work, iron oxide nanoparticles were synthesized by a precipitation reaction in which different amounts of cobalt ions were incorporated into the crystal lattice. As a result, the magnetic signals of the two samples in the MPS were significantly different from each other. The used silica nanoparticles were labeled with a rhodamine 110 dye that was previously functionalized with ICP TES to ensure covalent incorporation into the silica matrix. It was the first time that this dye was incorporated in a silica matrix while keeping its fluorescence activity. These building blocks were further processed into core-shell supraparticles in a two-step spray-drying process. In order to ensure that the supraparticles have a spherical morphology, calcium chloride was added in the first spray-drying step to destabilize the nanoparticle dispersion. In the second spray-drying process, the dye-doped silica nanoparticles were sprayed around the iron oxide cores to form a shell. The excess of supraparticles consisting only of shell-forming material produced in the second spray-drying step could be removed, if the supraparticles were dispersed in water and separated with a magnet before incorporation into a coating. The decrease in normalized fluorescence intensity of the two samples over 1000 shear cycles was recorded (Figure 4.9a). The decrease of the fluorescence intensity was again explained by the two

mechanisms mentioned above. First, the fluorescence decreased because fluorescent material was ablated and removed during each shear step. Second, more light was absorbed by exposing the absorbing core to light. The fact that two different iron oxide nanoparticle species with different absorption properties were used causes the fluorescence signals to decrease at different rates during the abrasion process. The more the magnetic component was able to absorb light, the faster the fluorescence in the layer decreased with an increasing shear stress application.

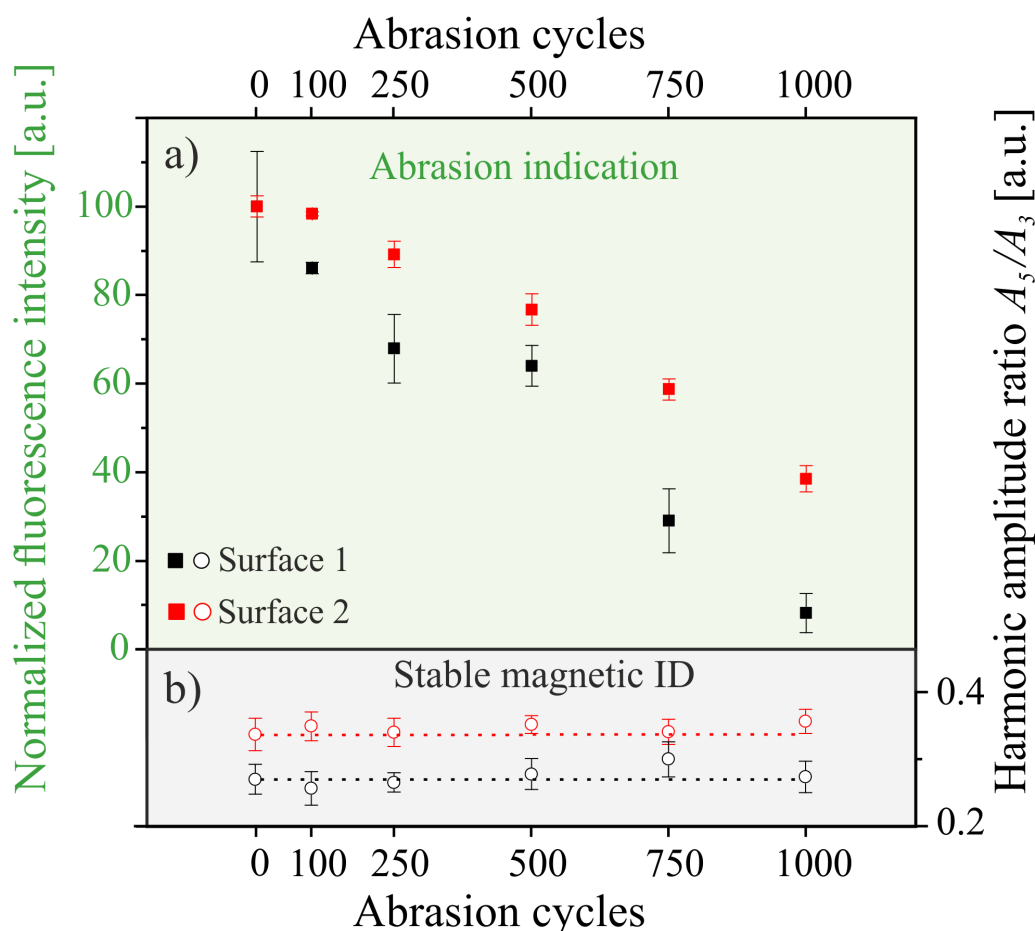


**Figure 4.9:** Normalized fluorescence intensities of turn-off indicator supraparticles in thin coatings are displayed against different shear cycles (a). Two surfaces with different iron oxide species in the core are displayed (red and black filled squares). All samples were excited at  $\lambda_{ex} = 490$  nm and the emission maximum was measured at  $\lambda_{em} = 521$  nm. The magnetic ID signal recorded via MPS over the different shear cycles (b) are displayed in red and black empty circles. The dashed lines are just to guide the reader's eye and represent the MPS value of the as prepared state. Adapted and reprinted with permission.<sup>[92]</sup> Copyright 2022, American Chemical Society.

In Figure 4.9b, the MPS signal was shown as the ratio of the amplitude of the fifth and the third harmonic with respect to the shear stress cycles. Here, it could be seen that the two coatings obtained distinctly different signals in the initial state, allowing the two coatings to be clearly identified. Furthermore, the MPS signals remained constant with respect to their standard deviation over the entire shear process, so that the coating could be identified over its entire lifetime. In this work, the MPS signals were measured using a hand-held sensor that measured non-destructively by placing it on top of the coating. In addition, only small amounts of magnetic material were required, and loss of mass due the removal upon mechanical stress did not affect the identifiability of the coating using this method. The amount of the magnetic material in the initial state was about  $7 \mu\text{g} \cdot \text{cm}^{-2}$ .

### 4.1.3 Color-change indicators

**Sarah Wenderoth**, Andreas Eigen, Susanne Wintzheimer, Johannes Prieschl, Andreas Hirsch, Marcus Halik, Karl Mandel, *Small*, **2022**, 18(15), 2107513

In addition to simply turning a signal on or off, a color-change mechanism was developed. Therefore, the supraparticles were constructed in such a way that first the core was built up from silica nanoparticles labeled with a rhodamine B dye (Figure 4.10a). This core was then coated with a shell of alumina nanoparticles in a second spray-drying process (Figure 4.10b). In a next step, a monolayer based on two different molecules was attached to the surface of the alumina shell in a self-assembly process. This monolayer consisted of two molecules with a phosphate end group (Figure 4.10c). One molecule additionally carried a chromophore and the other molecule was responsible for changing the hydrophilicity of the supraparticle's surface so that it could be subsequently incorporated into the coating matrix. In addition, the second molecule was responsible for separating the dye molecules on the surface and shifting the equilibrium of the dye from an excimer to a monomer state. Hence, the two dyes, in the core and shell of the supraparticle, were clearly distinguishable in their fluorescence signals. After incorporation of the core-shell supraparticles into a coating matrix, layers with oxygen barrier properties were achieved. These coatings displayed a molehill-like structure with a large part of the supraparticles protruding from the coating. In the initial state, mainly the dye in the shell was detectable, and only

through the gradual removal during the abrasion test the second dye in the core became visible (Figure 4.10d). The resulting color change thus allowed to draw conclusions about the state of the coating.

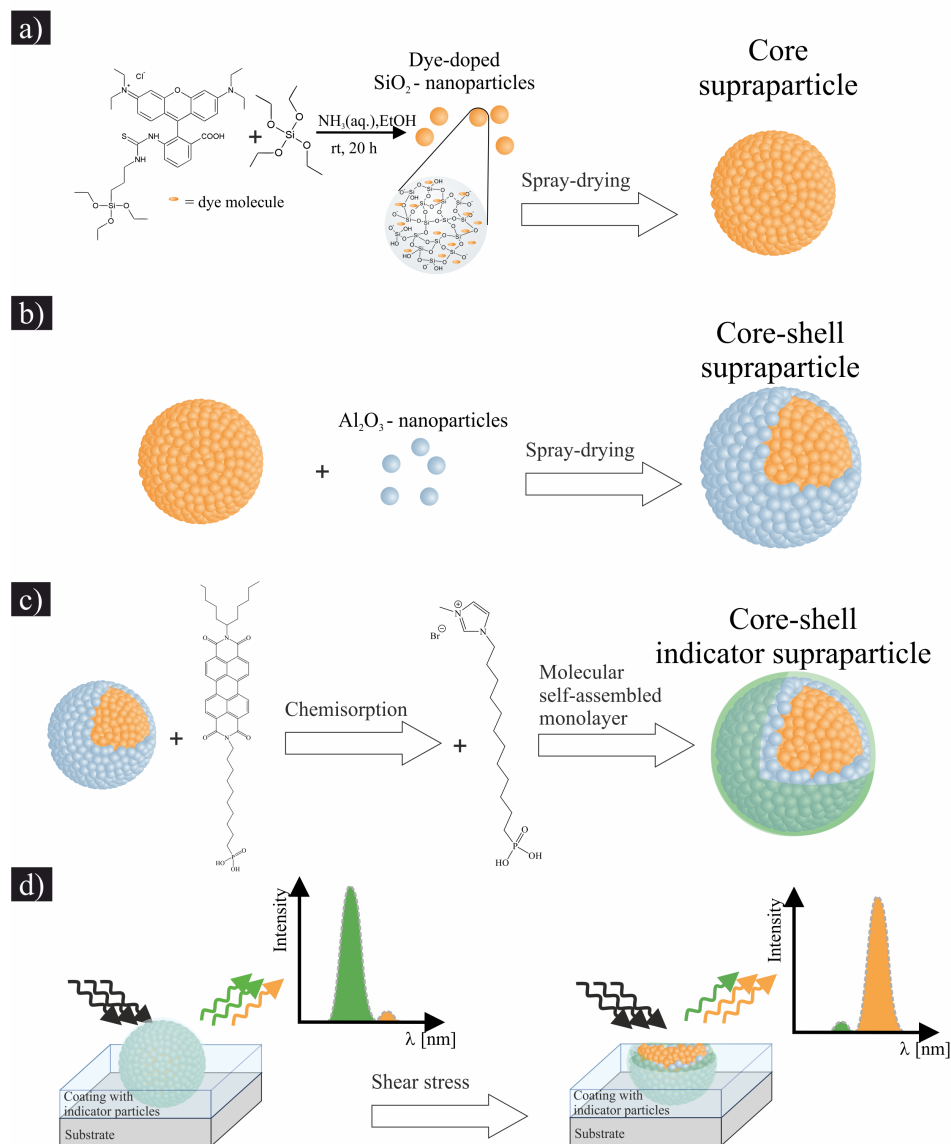


**Figure 4.10:** Schematic illustration of the step-wise synthesis of shear stress indicator coatings with a color-change effect. First, based on a Stöber process, dye-doped silica nanoparticles were formed and via the spray-drying process, core supraparticles were built up (a). Second, the core supraparticles were mixed with alumina nanoparticles and spray-dried again to form core-shell supraparticles (b). Third, the core-shell supraparticles were modified with a PBI dye via a chemisorption process of the phosphate group of the molecule on the alumina nanoparticle surface. In order to separate the chromophore molecules and to build a monolayer, a spacer molecule was attached (c). Fourth, the resulting supraparticles were incorporated into a coating and the fluorescence signals were recorded. After the application of shear stress to this surface, the recorded signals changed and a color change of the coating was observed (d). Adapted and reprinted with permission. [237] Copyright 2022, Wiley-VCH GmbH.

As already described (Chapter 4.1, Page 37), the shape, size, composition and structuring of the supraparticles have an enormous influence on whether the supraparticles could be used as an indicator of mechanical stress in a barrier coating. For color-change indicators, the choice of the used dyes and their position in the supraparticle core or shell also plays a crucial role. The most important properties the two dyes had to fulfill were:

- The emission bands of the dyes had to be clearly distinguishable.
- The emission maxima had to be at similar intensities so that one dye did not completely outshine the other.
- Both dyes needed to be covalently coupled to their support nanoparticles and had not to have a degradation with time or by external influences.
- An interaction of the two dyes with each other, the supporting nanoparticles or the coating matrix needed to be avoided.
- Both dyes had to be detectable with the same excitation wavelength.

Another crucial point in the synthesis of these color-change indicator supraparticles was that the dye molecules, which were coupled on the shell, had to be chosen in a way that they only interact with the alumina nanoparticles. All of these specifications were met when the silica nanoparticles in the core of the supraparticles were labeled with a rhodamine B dye and the alumina nanoparticles in the shell were labeled with a PBI-PA<sup>1</sup> dye. The rhodamine B dye was already firmly incorporated into the matrix via silanol groups during the synthesis of the silica nanoparticles. The phosphonic acid group of the PBI-PA dye was responsible for the fact that only a reaction with alumina nanoparticles was allowed.<sup>[342, 343]</sup> In addition, the alumina-phosphate bond is also covalent and cannot be easily broken. The addition of a second molecule into the self-assembled monolayer (SAM) also ensured that the PBI-PA dye remained in its excimer state and, moreover, it prevented the formation of dimers. This guaranteed that the PBI-PA dye had only one fluorescence maximum ( $\lambda_{em} = 537$  nm), which thus was clearly distinguished spectroscopically from the one of the rhodamine B dye ( $\lambda_{em} = 578$  nm). Since both dyes had quite broad excitation spectra, it was also possible to find a wavelength at which both dyes were excitable simultaneously ( $\lambda_{ex} = 520$  nm). The concentration of the PBI-PA dye was kept rather low, which means that the emission maxima of the two dyes were of the same order

---

<sup>1</sup>N-(1-hexylheptyl)-N'-(undecylphosphonic acid) perylene-3,4,9,10-tetracarboxylic bisimide

of magnitude even at a rather unfavorable excitation wavelength for the rhodamine B dye. In order to ensure that the two dyes were only in the respective supraparticle structure (rhodamine B in the core, PBI-PA in the shell) and that leaching into the coating matrix was ruled out, coatings were prepared with only one of the two dyes in the core and shell, respectively, and examined by confocal microscopy (Figure 4.11). Thus, in the first case, a core based on rhodamine B labelled silica nanoparticles coated with alumina nanoparticles was recorded (Figure 4.11a). In the second case, pure silica nanoparticles were used for the core and the alumina shell was labeled with the PBI-PA dye (Figure 4.11c). The supraparticles were then chopped off, leaving only hemispheres and revealing the interior of the supraparticles. The insets show schematic representations of the particle systems used in each case. In the case of the sample where the core consisted of silica nanoparticles labeled with rhodamine B, fluorescence has been detected already in the initial state, which was due to the fact that the alumina shell is optically transparent. In the sheared state, in addition to the highly stained interior of the supraparticle, a dark, unstained shell was observed, the alumina shell (Figure 4.11b). In the second sample, in which the core was unstained and the shell was labeled with the PBI dye, staining of the entire supraparticle surface was visible in the initial state. In the sheared state, however, only the shell of the supraparticle was colored and the core remained unstained (Figure 4.11d). In both cases, only the structures of the supraparticles were fluorescent, but the surrounding layer was unstained, indicating that the dyes were covalently coupled to their respective carriers and no leaching occurred during incorporation into the coating matrix. Since both dyes can be excited at the same wavelength and the emission bands partially overlap, it was not possible to image a supraparticle with both dyes simultaneously by confocal microscopy to achieve a sharp delineation of the two dyes in the core and shell, respectively.

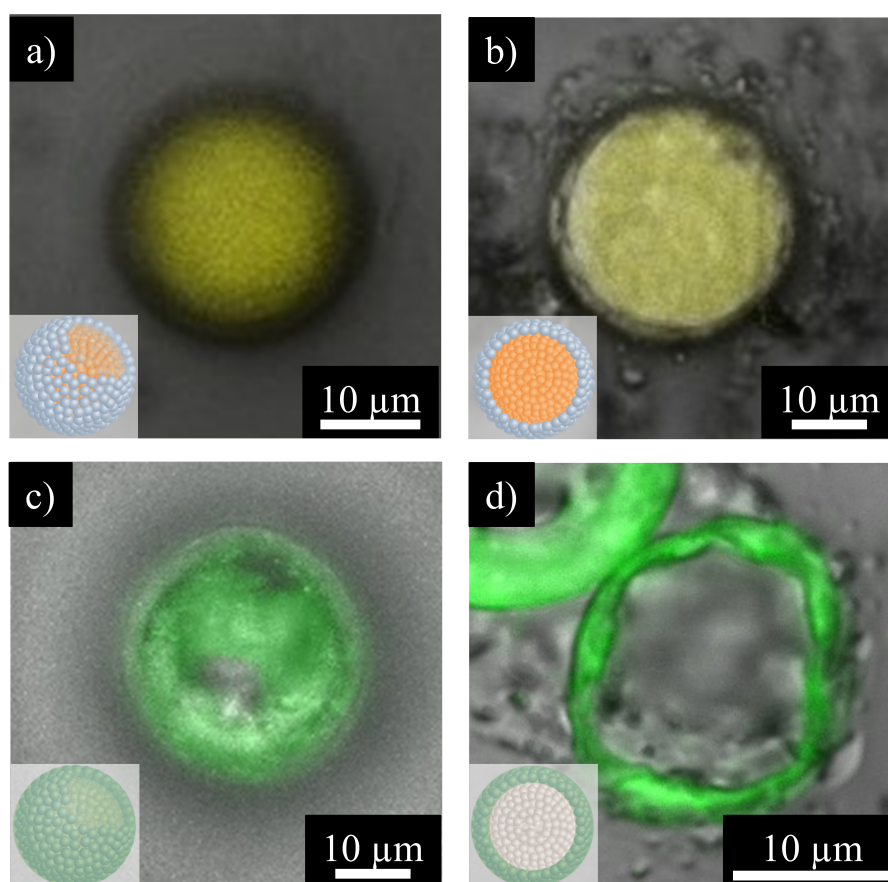


**Figure 4.11:** Confocal microscopy images of core-shell supraparticles where either the core (a, b) or the shell (c, d) is labeled with a rhodamine (core) or PBI-PA (shell) dye, respectively. The supraparticles are shown in the as prepared (a, c) and in the abraded state (b, d). Insets illustrate the state and colorization of the imaged supraparticle. Adapted and reprinted with permission. <sup>[237]</sup> Copyright 2022, Wiley-VCH GmbH.

After the supraparticles (with both dyes in the core and in the shell) were incorporated into a coating layer, a molehill-like structure was obtained (Figure 4.12a1). This structure was visualized by SEM micrographs (Figure 4.12a2). In a cross-cut of such a molehill, the supraparticle was still intact and the coating process did not destroy the supraparticle (Figure 4.12a3). In a next step, shear experiments were performed (for experimental details see Chapter 4.1, Page 37) on these surfaces (Figure 4.12b1). After investigating the abraded surfaces with an SEM, the supraparticles were only gradually removed and not completely torn out of the layer, although the shear stress experiments were quite stressful for the samples (Figure 4.12b2). Also, in the cross-cut image of such an abraded supraparticle (Figure 4.12b3), the part of the supraparticle which still sticks in the coating was intact and only the top of the supraparticle was abraded flat.

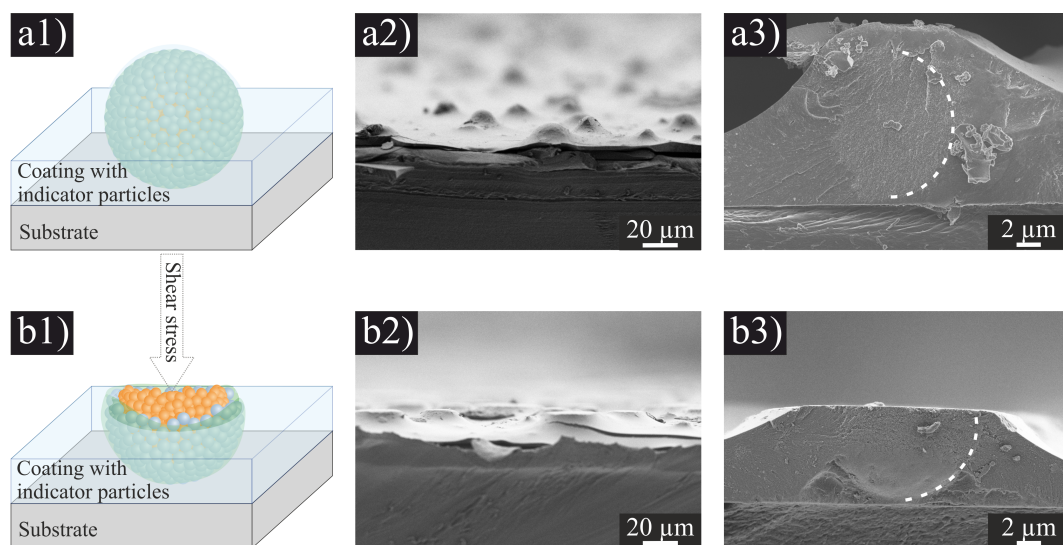


**Figure 4.12:** Schematic illustration of color-change supraparticles in a thin coating in the as prepared (a1) and in the abraded state (b1). SEM micrographs of the coatings in the as prepared (a2) and in the abraded state (b2), as well as cross-section images in the as prepared (a3) and in the abraded state (b3). Adapted and reprinted with permission. [237] Copyright 2022, Wiley-VCH GmbH.

In the shear experiment, the fluorescence behavior of the sample was determined after different shear cycles (0, 100, 250, 500, 1000, 1250, 1500). Since both dyes have had overlapping excitation spectra, they were excited with the same excitation wavelength at  $\lambda_{ex} = 520$  nm, whereas the emission spectra remained distinguishable from each other. The influence of the shear experiments on the supraparticles was detected simultaneously in one measurement (Figure 4.13a). The first emission band at  $\lambda_{em} = 537$  nm (green background) corresponds to the PBI-PA dye in the shell and the maximum at  $\lambda_{em} = 579$  nm (orange background) occurred from the rhodamine B dye in the supraparticle core. Since both used nanoparticle systems (silica in the core, alumina in the shell) were optically transparent, both dyes could be detected in their initial state. However, the peak for the PBI-PA dye decreased faster with an increased number of shear cycles than the peak for the rhodamine B dye. The purple dotted line illustrated the difference between the two peaks in the initial state and after 1500 shear cycles. Although the mechanism of particle loss (Chapter 4.1.2, Page 45) caused both dye signals to be decreased during the shear process, their individual signal change was different. This was explained by the fact that during the shear process, initially, the cross-sectional area of the core increases, while the cross-sectional area of the shell as seen from the top-view decreased. The ratio of the two

peak maxima to each other became smaller throughout the shear process (Figure 4.13b). This results in an overall color change from green to orange observed over the entire shear process.

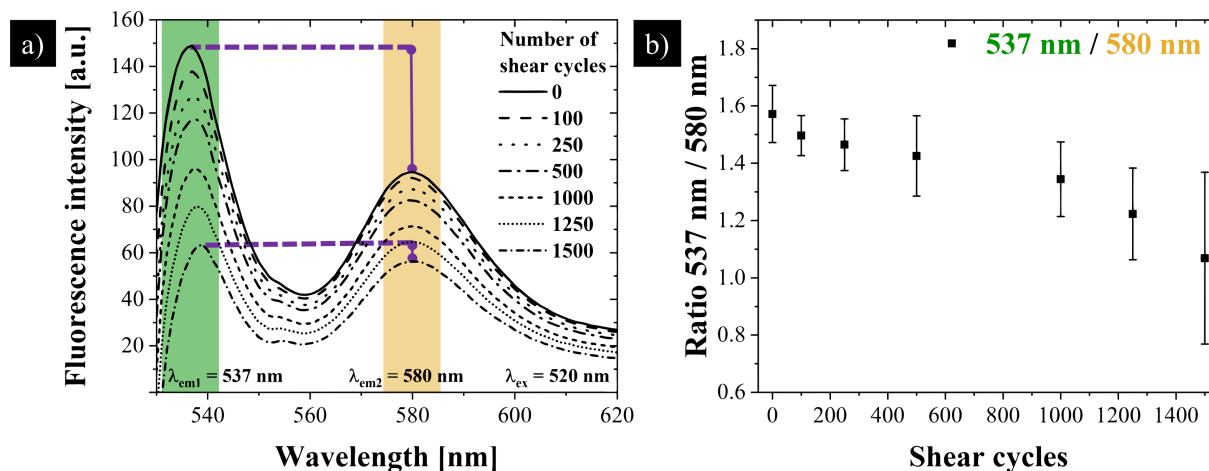


**Figure 4.13:** Fluorescence intensity of color-change indicator supraparticle in a thin coating, excited at  $\lambda_{ex} = 520$  nm, as a function of the recorded wavelength over different shear cycles (a). The green and orange bars highlight the maxima of the PBI-PA dye in the shell (green,  $\lambda_{em} = 537$  nm) and the rhodamine B dye in the core (orange,  $\lambda_{em} = 579$  nm), respectively. The purple line shows the decrease of fluorescence intensities of the two dyes in the as prepared state and after 1500 shear cycles. In b), the ratio between the fluorescence maximum of the PBI-PA dye and the rhodamine B dye is shown for the different shear cycles. Adapted and reprinted with permission. <sup>[237]</sup> Copyright 2022, Wiley-VCH GmbH.

In addition to the microscopy and fluorescence measurements, the oxygen barrier properties of the coating were also measured in the initial state and after 1000 shear cycles. In the initial state, the coating exhibited a value of  $520 \text{ cm}^3 \cdot (\text{m}^2 \cdot \text{d} \cdot \text{bar})^{-1}$  and after 1000 shear cycles a value of  $4972 \text{ cm}^3 \cdot (\text{m}^2 \cdot \text{d} \cdot \text{bar})^{-1}$ . This increase in oxygen permeability by a factor of 10 was due to the destruction of the coating during the shear stress experiment. Thus, the use of shear stress indicator supraparticles in thin films is a way to easily detect mechanical stress on a packaging by a change in an optical signal. This means that conclusions about the oxygen barrier can be drawn directly from the color of the coating.

## 4.2 Shear stress indicator supraparticles as powder

In addition to using shear stress indicator supraparticles in thin coatings to detect the damage of a packaging, it is also possible to use such supraparticles in powder form. These kinds of shear stress indicator supraparticles could be used to localize shear forces, *e.g.*, in 3D-printing or to monitor a ball-milling reaction. Therefore, the structure of the supraparticles as well as the characterization methods slightly differ from those used in coatings. In this chapter, three different systems, in which shear stress indicator supraparticles in powder form are used, are described. Common to all three systems was the way they were subjected to shear stress. In all systems, a ball-mill (commercial and/or self-made) was used to gradually destroy the structure of the supraparticles. The collision of the supraparticles with the milling balls during the milling process destroyed the supraparticles (Figure 4.14). Thus, their intrinsic properties such as optical or magnetic response changed.

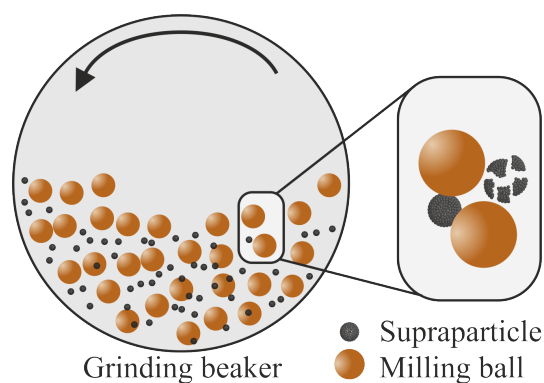


**Figure 4.14:** Schematic representation of the ball milling process. The grinding beaker rotates while the milling balls collide and the supraparticles are fragmented.

### 4.2.1 Photonic balls

**Sarah Wenderoth**, Gudrun Bleyer, Jakob Endres, Johannes Prieschl, Nicolas Vogel, Susanne Wintzheimer, Karl Mandel, *Small*, **2022**, 18(48), 2203068

One possibility for shear stress indicator supraparticles in powder form is to use so-called photonic balls. Photonic balls are described as optically active supraparticles that obtain their color due to physical interaction of light with the defined arrangement of the nanoparticles within the supraparticles. The major advantage of such structural coloring

compared to using organic dyes or pigments is that they are insensitive to external influences such as UV light, temperature, humidity or pH value. Monodisperse nanoparticles made of *e.g.*, silica or polymer in the size range of 180-350 nm are used to prepare such photonic balls. A highly ordered structure at the surface of the supraparticle allows light to interact with the particles in such a way that there is constructive interference at the surface if the specific wavelength equals approximately twice the size of the nanoparticles (similar to the Bragg Law in crystals). However, since all incident wavelengths are incoherently scattered inside the supraparticle, all supraparticles would appear white. By using a broadband or spectrally selective absorber in the form of nanoparticles (*e.g.*, iron oxide, melanin, gold, or silver), this incoherently scattered light can be absorbed.

In this work, photonic balls were synthesized from silica nanoparticles in the size range of 214-325 nm via a modified Stöber process. Iron oxide nanoparticles synthesized by an oxidative precipitation reaction were used as broadband absorbers for incoherently scattered light. The advantages of using silica and iron oxide as building blocks for the photonic balls were that both can be obtained in large quantities at low cost. In order to ensure that the used iron oxide is also protected against external influences such as temperature and pH value, it was coated with a silica shell. Spray-drying was used to assemble the nanoparticle building blocks to photonic balls (Figure 4.15a). The fact that the drying process in a spray-dryer takes only a few milliseconds enables the production of large quantities of photonic balls in a short time (compared to conventional synthesis methods such as micropipette injection, microfluidics, or electrospray-assisted fabrication). As the drying process in the spray-dryer is kinetically dominated, a very specific structure of the supraparticles was achieved (Figure 4.15b). SEM micrographs were used to determine the structure of these supraparticles. The outer structure of the supraparticle was highly ordered and this order extended over several planes into the inner part of the supraparticle (top view: Figure 4.15c, e (higher magnification), cross-sectional images: Figure 4.15d, f (higher magnification)). However, the inside of the supraparticle was disordered and the iron oxide nanoparticles were statistically distributed throughout the entire supraparticle.

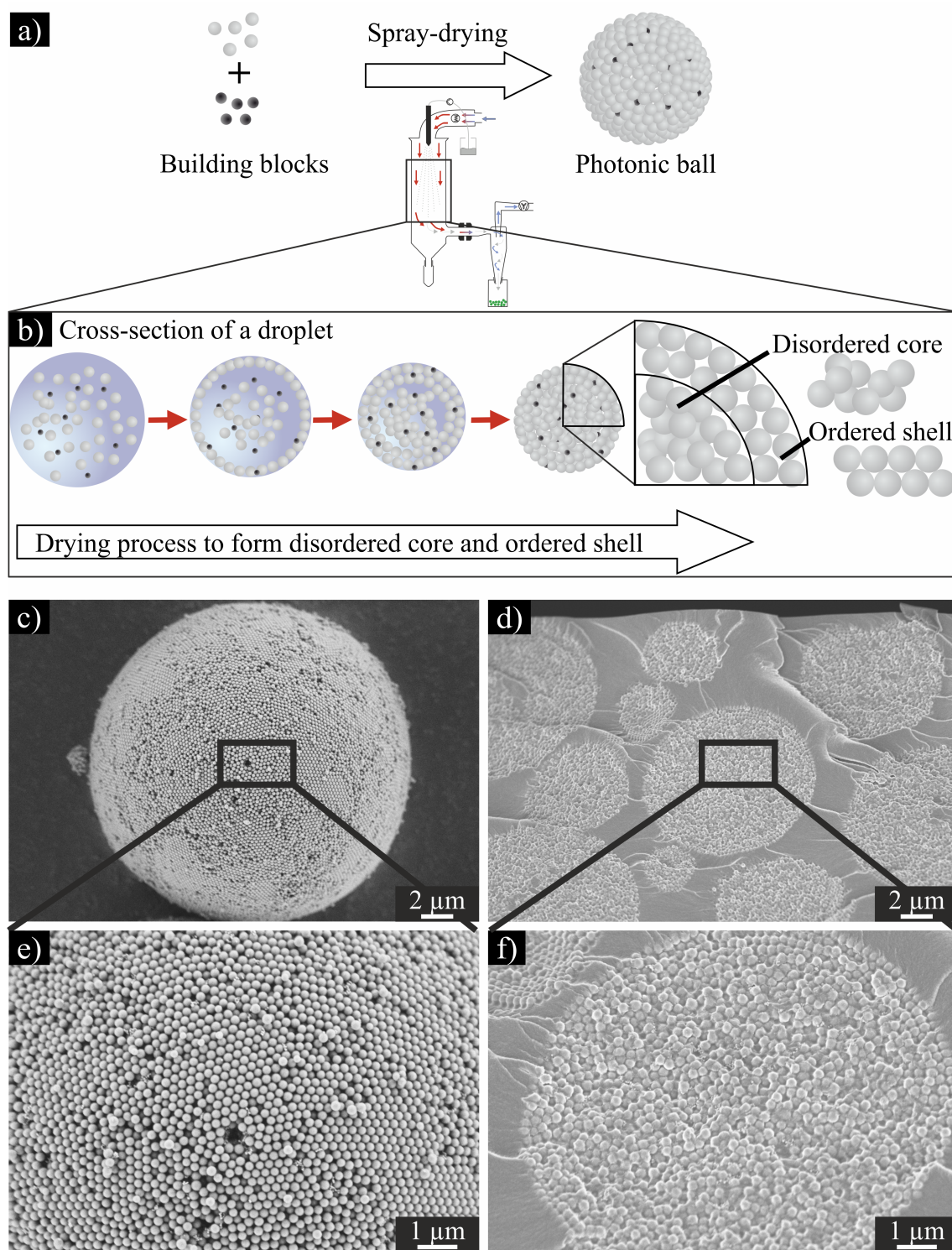


**Figure 4.15:** Schematic representation of the assembling from silica and iron oxide nanoparticles via the spray-drying process to photonic balls (a). Through the kinetically controlled assembly process, the nanoparticles within a droplet were forced together which resulted in a supraparticle with a highly ordered shell and a disordered core based on silica nanoparticles, whereas the iron oxide nanoparticles are randomly distributed in the whole supraparticle (b). SEM images of a whole photonic ball with a highly ordered shell (c, e with higher magnification) and cross-section of a photonic ball (d, f with higher magnification). Adapted and reprinted with permission. <sup>[162]</sup> Copyright 2022, Wiley-VCH GmbH.

By varying the ratio of silica to iron oxide nanoparticles, the intensity of the color impression was influenced (Figure 4.16, ratio silica:iron oxide: 500:1, 100:1, 50:1, 20:1, 10:1, 1:1). If no or only few amounts of absorber was added, the incoherent scattering of the light predominates and a whitish color was obtained (Figure 4.16a, left). By increasing the amount of absorber nanoparticles, this incoherent scattering was reduced and the color resulting from constructive interference at the outer ordered layers became more dominant. However, if the amount of absorber nanoparticles was increased too much, absorption dominates and the powder appeared black (Figure 4.16a, right). Furthermore, as the amount of absorber was increased, the quantity of highly ordered zones on the supraparticle surface was changed (Figure 4.16c). Therefore, the more absorber material was present, the more disordered areas on the surface were created. The reflection maximum for all samples was at around 660 nm determined by spectroscopic examinations. The grey line in Figure 4.16b visualized the photonic stop band (ratio of reflection minimum and maximum) and was most pronounced at a silica:iron oxide ratio of 50:1.

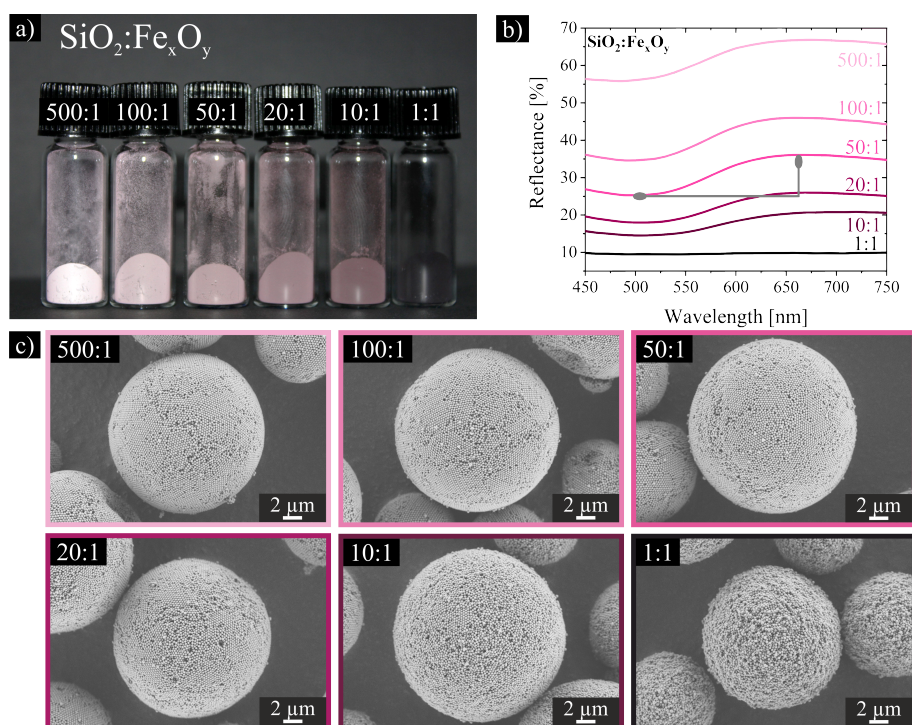


**Figure 4.16:** Photography of photonic ball powders with different ratios of silica and iron oxide (500:1, 100:1, 50:1, 20:1, 10:1, 1:1) (a). Reflectance spectra of the powders against the wavelength (b). The grey line displays the largest photonic stop band of the sample with a ratio of 50:1 silica:iron oxide. SEM images of the respective samples show an increase in disorder on the photonic ball surface with increasing iron oxide content (c). Adapted and reprinted with permission. <sup>[162]</sup> Copyright 2022, Wiley-VCH GmbH.

While the ratio of silica to iron oxide nanoparticles affected the intensity of the resulting color, the size of the silica nanoparticles influenced the color of the photonic balls itself (Figure 4.17 a). The smaller the used nanoparticles, the more the color shifted to blue. Thus, by using silica nanoparticles in the range of 214 - 325 nm (sizes determined by DLS measurements), almost every color in the visible spectrum was covered (Figure 4.17b) (1: 214 nm, blue; 2: 229 nm, green; 3: 258 nm, yellow; 4: 282 nm, orange; 5: 325 nm, red). If these powders were examined spectroscopically, the reflectance maximum was corresponding to about twice the size of the silica nanoparticles. By converting the reflectance spectra into x-y-values and transferring them to a CIE-1931 chromaticity diagram, the color impression of the powders was observed (Figure 4.17c).

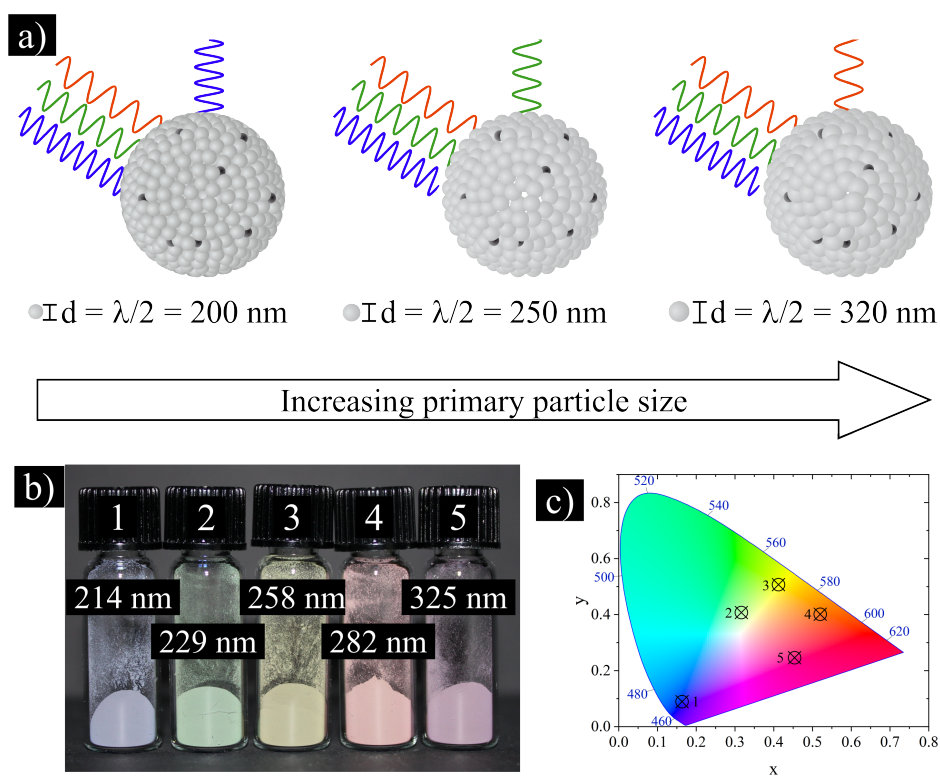


**Figure 4.17:** Schematic illustration of the influence of silica primary particles and the color of the resulting photonic balls (a). Photography of photonic balls powder samples with different colors based on different primary particle sizes measured by DLS (b). Corresponding CIE chromaticity diagram of the different powder samples (c). Adapted and reprinted with permission. <sup>[162]</sup> Copyright 2022, Wiley-VCH GmbH.

Since the color appearance of the photonic balls is solely based on the interaction of the incidental light with the outer highly ordered layers, the coloration of the photonic balls was lost when these outer layers were destroyed and the inner disorder was exposed

(Figure 4.18a). In order to demonstrate this effect, the samples were mixed with  $\text{ZrO}_2$  grinding balls for specific time intervals at specific milling speeds on a vortex device. This means, with increasing grinding time, the ordered surface of the supraparticles was successively destroyed. Following the grinding process, the structural investigation of the supraparticles was carried out by means of SEM analysis (Figure 4.18b1-b4). First of all, the supraparticles have had a certain strength and do not completely disintegrate due to the load in the mill. With increasing grinding time, the supraparticles were successively eroded from the outside. Spectroscopic measurements of the grinded powders show that with an increasing shear load the intense coloration of the powder disappeared (Figure 4.18c1-c3) and the data points in the CIE chromaticity diagram were moved towards the white spot at 0.3333, 0.3333 (Figure 4.18d1-d3) in the center. Due to increasing destruction of the ordered surface of the supraparticles, the fraction being capable of constructively interfering with the incident light became less. As a result, the proportion of disordered nanoparticles that scatter the incident light increases inside the supraparticle. However, the center of the white spot (in the CIE chromaticity diagram) cannot be reached in these samples because the used iron oxide nanoparticles were not totally black but slightly red-brownish. Additionally, the size of the used silica nanoparticles did not only have an effect on the color of the resulting photonic spheres (Figure 4.18d1-d3), but also on the mechanical stability. The larger the silica nanoparticles are, the lower the reactive surface area, and thus fewer Si-O-Si bonds were formed between the individual nanoparticles, resulting in a lower mechanical stability. For sample 1 (blue coloring, Figure 4.18d1) all measurement points were distinguished from each other which means that the destruction progresses successively with increasing shear stress. In the case of sample 3 (yellow coloring, Figure 4.18d2), no color change was detected after the third measuring point. In the case of sample 5 (red-pinkish coloration, Figure 4.18d3), no change was recorded after the second measuring point.

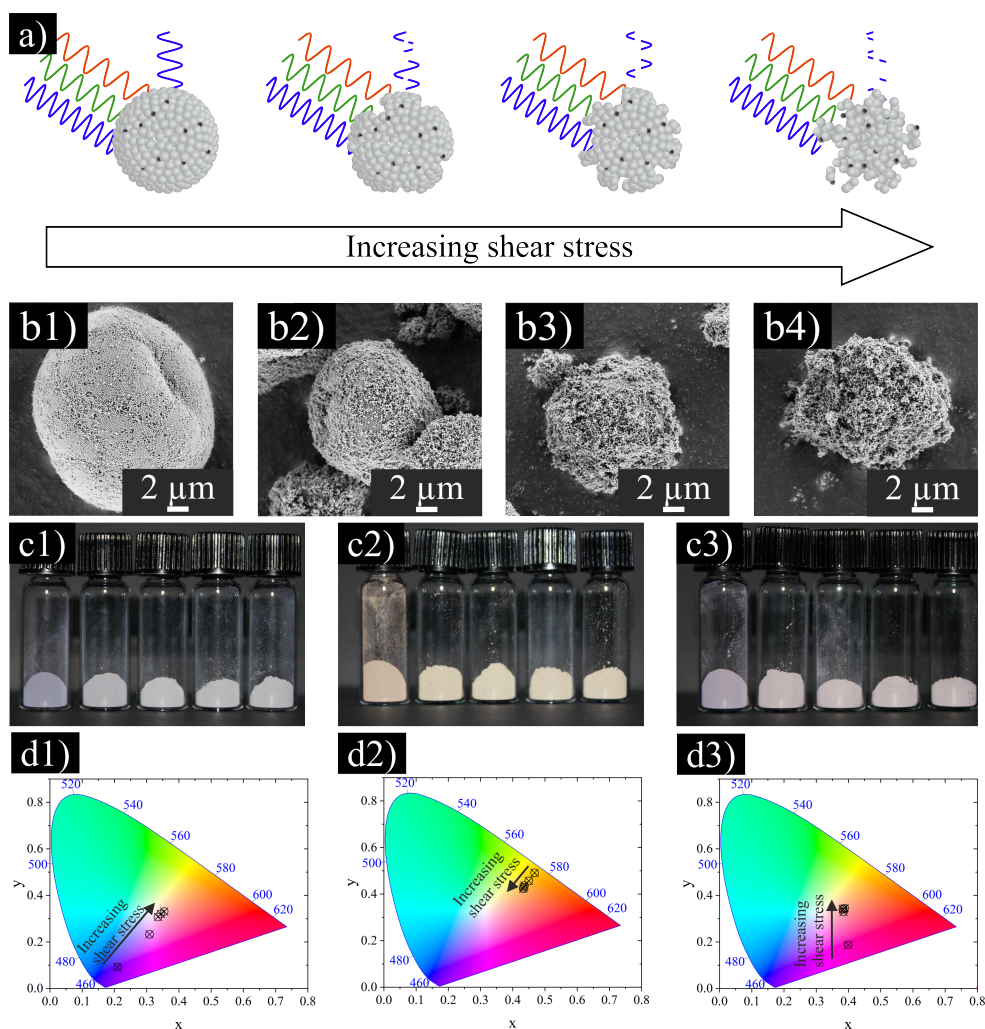


**Figure 4.18:** Schematic representation of the fragmentation process of a photonic ball (a) and SEM images of sample 1 (blue color impression) during the ball-milling process (b1: initial state, b2: 15 s, b3: 45 s, b4: 90s). c) Photographs of powder sample 1 (blue color impression, c1), sample 3 (yellow color impression, c2) and sample 5 (red-pinkish color impression, c3) with increasing shear stress during the ball-milling process, from left to right (initial state, after 30, 60, 90, 120 s) and the corresponding reflectance spectra shown in the CIE chromaticity diagrams of the powder samples (d1: sample 1, blue color, d2: sample 3, yellow color, d3: sample 5, red-pinkish color). Adapted and reprinted with permission. [162] Copyright 2022, Wiley-VCH GmbH.

In summary, by choosing the appropriate nanoparticular building blocks (monodisperse silica nanoparticles in the size range of 200 - 350 nm, iron oxide nanoparticles in the right crystal phase, shape and size) and suitable spray-drying conditions, it was possible to produce shear stress indicator supraparticles whose inner structure was disordered while the outer layers were highly ordered. Only through this hierarchical structure, a color change occurred under mechanical stress, as the outer ordered structure was successively

destroyed. By choosing the size of the utilized silica nanoparticles, not only the color of the resulting supraparticles was adjusted, but also their sensitivity towards mechanical load.

### 4.2.2 Microballoons

Susanne Wintzheimer, Stephan Müssig, **Sarah Wenderoth**, Johannes Prieschl, Tim Granath, Florian Fidler, Daniel Haddad, Karl Mandel, *ACS Appl. Nano Mater.*, **2019**, 2(10), 6757-6762

Another possibility to create shear stress indicator supraparticles was the use of so-called microballoons. These were hollow particles with a size of about 40  $\mu\text{m}$ . Superparamagnetic iron oxide nanoparticles partially modified with a patchy silica shell based on condensed tetraethoxysilane were used as building blocks to form spherical hollow microparticles in a self-directing Pickering emulsion method by surface modification with methacryloxypropyltrimethoxysilane (Figure 4.19). The resulting supraparticles possess a specific magnetic signal that was detected by MPS. The balloon-like structure of the supraparticles was visualized by LSM and SEM (Figure 4.19b1, c1). If the supraparticles were subjected to mechanical stress, *e.g.*, in a ball mill, they were successively fragmented (Figure 4.19a2). These fragments were visualized by microscopic methods (LSM: Figure 4.19b2, SEM: Figure 4.19c2). The following applied: The longer the grinding process lasts, *i.e.*, the more energy was introduced into the system, the smaller were the resulting fragments. The size distribution was thereby changed during the milling process from  $41 \pm 27 \mu\text{m}$  in the initial state to  $8 \pm 8 \mu\text{m}$  after the mechanical force application. This gradual reduction in the size of the microballoons was detected using MPS (Figure 4.19d).

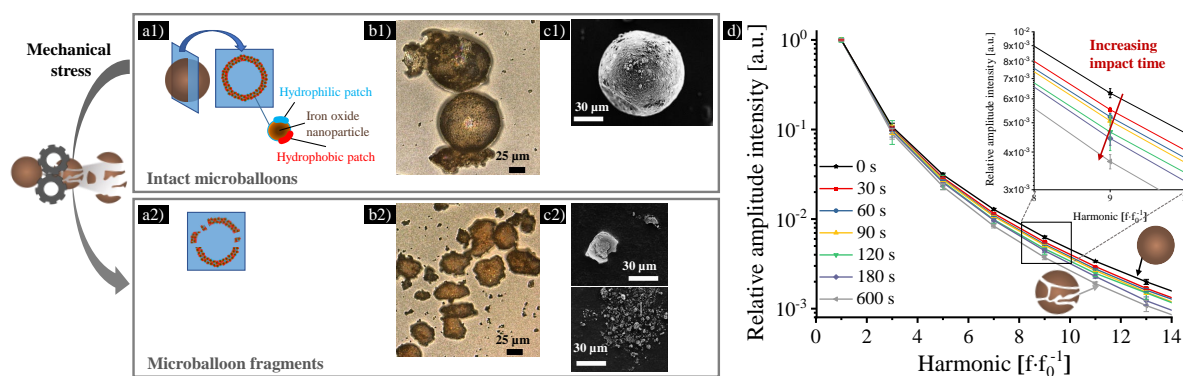


**Figure 4.19:** Schematic illustration of an intact microballoon with its building blocks (a1) and in the destroyed state after mechanical stress (a2). LSM images of the intact (b1) and of the destroyed state (b2). SEM images of the intact (c1) and the destroyed microballoons (c2). MPS curves of the microballoons after different ball milling times (d). Adapted and reprinted with permission. [264] Copyright 2019, American Chemical Society.

A possible application for this type of shear stress indicator supraparticles was the grinding of activated carbon for use in water or gas purification. At this stage, certain active surface areas were required, which were achieved by grinding agglomerate structures. The required particle size of the activated carbon was monitored by using microballoons, which were non-reactive, chemically inert and non-toxic due to their composition of silica and iron oxide and which were removable from the ground material by magnetic separation. By observing the MPS signals after different milling times (Figure 4.20a), the fragmentation of the microballoons and also the ground material was investigated. The gradual reduction of the grain size of the ground material before (Figure 4.20 1) and after mechanical stress (Figure 4.20 2) was determined macroscopically (Figure 4.20b), microscopically (LSM: Figure 4.20c, SEM: Figure 4.20d) and by laser diffraction measurements (Figure 4.20e). During the milling process, not only the ground material but also the used microballoons were successively crushed. Once the targeted size was reached, the microballoons were removed from the ground material by magnetic separation.

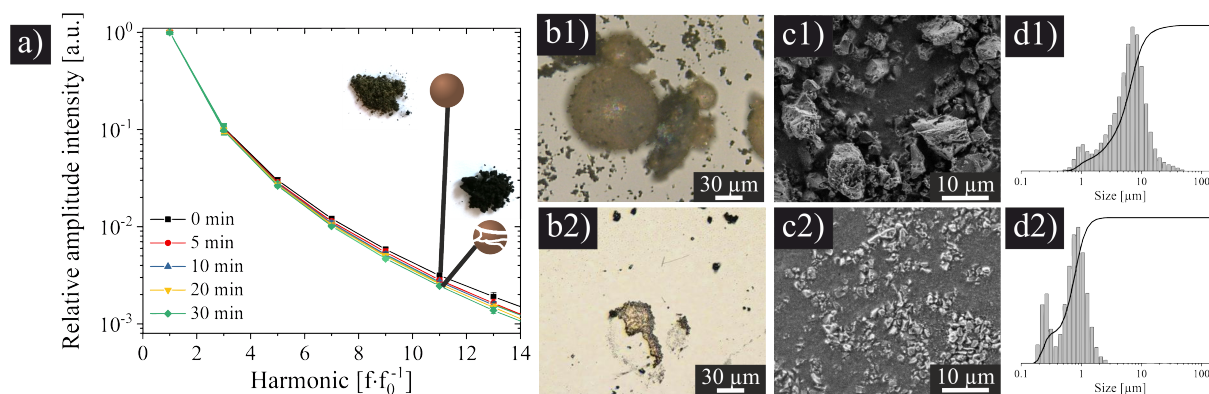


**Figure 4.20:** MPS curve of microballoons mixed with charcoal in a ball mill for different time periods and photographs of the powders in the as prepared state and after 30 min of milling (a). LSM (b1), SEM (c1) images and laser diffraction measurements (d1) of the as prepared powder. LSM (b2), SEM (c2) images and laser diffraction measurements (d2) after 30 min of milling. Adapted and reprinted with permission. [264] Copyright 2019, American Chemical Society.

In summary, the microballoons presented here can be used as an indicator for mechanical stress in a ball mill due to the systematic fragmentation of their hollow sphere structure. These structural changes correlated directly with a change in magnetic properties and were detected quickly and easily using MPS. Due to the high resolution of the MPS method, only small amounts of the indicator material were required (1 wt%). By using microballoons, the material to be ground did not have to be constantly cleaned during the grinding process in order to analytically determine whether the grinding process has already been completed. In addition, due to their magnetic properties, the supraparticles were removed completely after the grinding process was completed.

### 4.2.3 Multi-particle system

Susanne Wintzheimer, Jakob Reichstein, **Sarah Wenderoth**, Sebastian Hasselmann, Maximilian Oppmann, Marcel T. Seuffert, Klaus Müller-Buschbaum, Karl Mandel, *Adv. Funct. Mater.*, **2019**, 29(19), 1901193

Contrary to the single-particle shear stress indicator systems presented so far, this chapter presents a multi-particle system. In contrast to the previously presented systems, not only a single, hierarchically constructed particle, namely a supraparticle with a defined core-shell structure, but a more complex supraparticulate structure was generated. For

this purpose, an absorbing core was surrounded by a layer of silica nanoparticles that carried a luminophore. Additionally, this covered absorber core had numerous supraparticles consisting of silica nanoparticles and luminophores attached to it. Here, too, the modular principle of a building block toolbox was applied and different particle systems were assembled from different building blocks, so that the sensitivity to shear stress was adjusted by choosing different materials. The shear stress detection mechanism was a turn-off effect, comparable to the one already described in coatings (Chapter 4.1.2, Page 45). These multi-particle systems consisted of three different components, similar to the turn-off indicator supraparticles (Figure 4.21). The core of these particles was based on a material capable of absorbing light (charcoal, carbon or iron oxide). Surrounding this core, a layer of pure silica nanoparticles was formed in the spray-drying process, which ensures that the absorbing properties of the core were somewhat minimized in their initial state. In addition, these silica nanoparticles form satellite supraparticles around the core. The third component was the coloring part. In this work, various organic dyes (fluorescein and rhodamine B) and complexed lanthanoids of  $\text{Eu}^{3+}$  (in LuminoRed) and  $\text{Tb}^{3+}$  (used in the form of a metal organic framework (MOF)) were used.

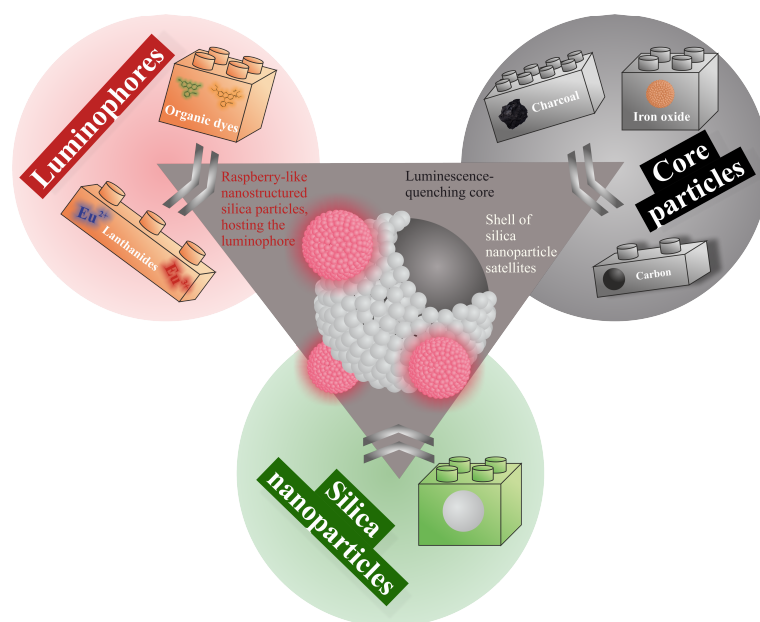


**Figure 4.21:** Schematic illustration of the toolbox to create mechanochromic shear stress indicator supraparticles based on different luminophores, core particles and silica nanoparticles. All of these are assembled via the spray-drying process into a multicomponent system with a light absorbing core, a shell of silica nanoparticles and luminescent satellite particles. Adapted and reprinted with permission. <sup>[256]</sup> Copyright 2019, Wiley-VCH GmbH.

Due to the flexible composition of the individual building blocks (different core materials in combination with different luminophores), a variety of different turn-off indicators were obtained. All combinations had in common that in the initial state, the luminescence of the dyes/lanthanides was detected. During the experiments in the ball mill, *i.e.*, under continuous shear stress, this optical signal was successively decreased. Only the combination of the three different building blocks (light-absorbing core, silica particles as shell and satellite particles, and a luminophore) resulted in a turn-off indicator supraparticle system (characterized with SEM-EDX (scanning electron microscopy with energy dispersive X-ray analysis) and fluorescence microscopy). The structure of this multi-particle system played a crucial role. The system only provided an optical signal in the initial state, through the luminescent satellite particles. If during the grinding process the particles were successively abraded and thus the distance between the luminescent components and the absorbing core became less and less, the luminescence was no longer detectable because it was directly absorbed by the core material. Although the system still consisted of the same basic building blocks, a decrease in optical signals was detected with increasing shear stress, for the sole reason that the macroscopic structure of the supraparticle array was changed.

The variation of the core material had the largest influence on the sensitivity of the indicator supraparticles with respect to their turn-off effect under shear stress application. The three different core materials iron oxide, charcoal, and carbon particles have shown significant differences in their behavior during the milling process (Figure 4.22a). The system with a core of iron oxide nanoparticles pre-assembled into supraparticles was disintegrated the fastest and had shown the strongest turn-off effect. After just 3.5 min, half of the originally measured signal was lost. This was due to the fact that the iron oxide nanoparticles in the core were held together only by physical interactions and therefore, they were more susceptible to mechanical stress. In contrast, the carbon cores had shown enhanced resistance to shear stress, and half of the original fluorescence signal was retained after 24.6 min. The charcoal, which had a higher porosity compared to the carbon particles and which therefore was easier to grind, had already shown a decay to half of the original signal intensity after 5.4 min.

In addition to varying the core materials, the choice and amount of the luminophores also

affected the sensitivity of supraparticles to mechanical stress (Figure 4.22b). Here, the core system was kept the same (charcoal) and the four different luminophores were varied. The system with the Tb-MOF had shown the fastest decay rate of its luminescence and half of the output signal was reached after less than 1 min. MOFs are generally known for their low mechanical stability, which is one of the reasons why this system was abraded fastest. The different luminophores also lead to different repulsive forces between the silica nanoparticles in the satellites, which can favor the detachability of these satellite particles from the core. As a result, the light absorption effect of the core came into play more quickly, leading to a more rapid onset of the turn-off effect and thus compromising the sensitivity of the turn-off system. If the luminophore system itself was mechanically unstable, this also led to a faster degradation of the entire system.

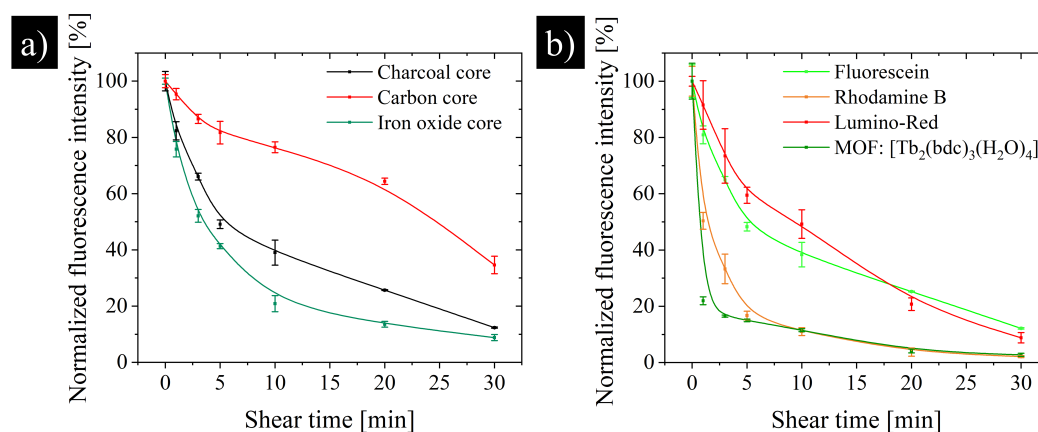


**Figure 4.22:** a) Normalized fluorescence intensity of turn-off samples with different cores (charcoal, carbon or iron oxide core), surrounded by a silica nanoparticle shell, silica satellites and a fluorescein dye, during the application of shear stress in a ball mill over a period of 30 min. b) Normalized fluorescence intensity of turn-off samples with a charcoal core surrounded by silica nanoparticles and silica satellites labeled with different dyes (fluorescein, rhodamine B, Lumino-Red, MOF [Tb<sub>2</sub>(bdc)<sub>3</sub>(H<sub>2</sub>O)<sub>2</sub>]) during application of shear stress in a ball mill over a period of 30 min. Adapted and reprinted with permission. [256] Copyright 2019, Wiley-VCH GmbH.

In summary, the multihierarchical system described here was modularized so that both the core material (light absorbing behavior) and the luminophores were used to prepare different supraparticle systems so that the shear stress capacity could be adjusted depending on the used materials. Thus, by using a MOF-based luminophore and a charcoal core, a system was achieved that lost half of the initial fluorescence signal within one minute, while a system based on a carbon core and fluorescein as dye had shown the same loss only after more than 24 min.

# Chapter 5

## Conclusion and outlook

The aim of this doctoral thesis was the development of micron-scaled shear stress indicators. It was possible to develop a new additive that is versatile, can easily and quickly indicate mechanical stress in different ways, and is made from low-cost materials. These systems were used in powder form or as part of a coating. By combining different material properties in a single micron-scale unit, it was possible to combine several types of information in one supraparticle.

By combining different nanoparticulate building blocks, a hierarchical nanostructured entity in the micrometer range, a so-called supraparticle, was assembled in a spray-drying process. The nanoparticles used in this work were essentially limited to systems of silica and iron oxide. By varying the synthesis conditions (temperature, reaction time, reactant composition), the size of the resulting silica nanoparticles were tuned between 80 - 320 nm in a classical Stöber process. In addition, fluorescent dyes such as rhodamine B or rhodamine 110 were covalently incorporated into the silica network during nanoparticle synthesis, and the surface of the nanoparticles was functionalized with APTES molecules. The iron oxide nanoparticles were prepared by different synthetic routes (precipitation reaction and oxidative ripening) resulting in different particle sizes (10 - 100 nm). In addition, the magnetic properties of the synthesized nanoparticles were influenced by incorporating cobalt atoms into the iron oxide lattice. Furthermore, the iron oxide nanoparticles were coated with a silica shell under Stöber conditions. These iron oxide@silica nanoparticles were also surface modified with APTES molecules. In the spray-drying process, the

equipment (cyclone size, nozzle type), the spray parameters (temperature, pump rate, aspirator speed), as well as the type and composition of the nanoparticle dispersion (viscosity, solids content, nanoparticle size, dispersion stability) influenced the morphology, size distribution, and particle size of the resulting supraparticles.

In order for the created shear stress indicator supraparticles to be used in a coating, various requirements were imposed on their composition, morphology and size:

- The dyes must be covalently coupled into the silica nanoparticles to prevent leakage into the coating.
- The supraparticles must have a predominantly spherical morphology and a core-shell structure to ensure uniform exposure of the cross-sectional area during the abrasion process so that a change in optical signals can be detected.
- The supraparticles must form a molehill-like structure in the layer so that they are held firmly in the layer but protrude far enough to be abraded. On average, the supraparticles must be about twice as large as the thickness of the coating.

When these conditions were met, three different detection mechanisms could be realized: *turn-on*, *turn-off* and *color-change*. In the first case, *turn-on* indicators, the core of the supraparticle consisted of fluorescent silica nanoparticles and the shell of light-absorbing iron oxide nanoparticles. The optical properties (luminescence and light absorption), which at first glance appear to be opposite, lead to a gradual change in the optical signals when the supraparticles were abraded after being incorporated into a layer. As more of the core was exposed, the fluorescence signal became more intense. This was detected in a spectrometer and was visualized by confocal microscopy. In the opposite case, for *turn-off* indicator supraparticles, the structure was reversed, with light-absorbing iron oxide nanoparticles in the core and fluorescent silica nanoparticles in the shell. Therefore, after incorporation into a layer and subsequent mechanical stress, the fluorescence intensity was gradually decreased. Not only the change in the cross-sectional area of the supraparticles, but also the loss of material due to abrasion caused this decrease in intensity. If, in addition, the light-absorbing magnetic material in an MPS provided distinguishable, clearly identifiable signals due to its material composition (cobalt doping), such a layer was not only intelligent but also communicative at the same time. The third was the *color-change* indicator. Here, the color of the system changed under mechanical stress. Two different

dyes were coupled in the core or shell of the supraparticle. When selecting the dyes, it was important that their extinction bands overlapped to the extent that they were excited simultaneously, but the emission bands remained clearly separated. After incorporating such supraparticles into a coating, a shift in the color was observed in abrasion tests. Abrasion also changed the oxygen permeability of the coating. The color of the coating was therefore used to assess the integrity and thereby the oxygen barrier of the coating. These three systems succeeded in combining the chemistry of molecules with the world of nano-objects to create macroscopic systems that enable smart surfaces.

In addition to smart and communicating coatings, this work also developed supraparticle systems that were used in powder form as shear stress indicators. For this purpose, three fundamentally different indicator systems were fabricated that can indicate mechanical stress using different detection methods (UV-vis spectroscopy, MPS, and fluorescence spectroscopy). The first system consisted of photonic balls composed of silica and iron oxide nanoparticles. During the spray-drying process, a high order of silica nanoparticles was formed on the outer surface of the supraparticles, while the interior remained disordered. The iron oxide nanoparticles were statistically distributed throughout the supraparticle. By varying the ratio of silica to iron oxide nanoparticles, the intensity of the coloration was controlled, while the size of the silica nanoparticles affects the color itself. When subjected to mechanical stress, these systems showed a loss of color due to the irreversible destruction of the outer highly ordered structure. Due to the exclusive use of physical ordering effects for color generation, the photonic balls were stable against chemical interactions or environmental influences (*e.g.*, UV light, pH, solvent, temperature), in contrast to organic dyes. In the second system, superparamagnetic hollow spheres, so-called microballoons, were used to determine mechanical stress and the degree of comminution in a ball mill. The increasing fragmentation of the microballoons during the grinding process changed the magnetic signal of the sample, which was read out by MPS. The microscopically investigated comminution of a sample was correlated with the MPS values, eliminating the need for time-consuming analysis to determine if the desired result was achieved. After grinding, the microballoon fragments were removed from the actual ground material using a magnet. In the third system, a toolbox-like approach was used to create various indicators that exhibit a *turn-off* effect in powder form. Light-absorbing materials (activated

carbon, charcoal, iron oxide) were combined with luminophores (fluorescein, rhodamine B, Lumino-red, Tb-MOF) and pure silica nanoparticles in a spray-drying process to form supraparticles. By combining the different components, shear stress indicators were produced that respond to mechanical stress at different rates. Due to the different decay curves of the respective luminescence, the appropriate system can be selected for different applications, depending on whether a minimum load was to be tolerated or even the smallest loads were to be indicated.

This flexibility and the variety of possibilities in terms of color, sensitivity, detection methods and applications formed the basis for a completely new type of hierarchically structured supraparticle indicators for the determination of mechanical stress. Based on different indicator systems which are similar mainly in the type of materials used (silica and iron oxide), the size and structure of the individual supraparticles (nanostructured, hierarchically structured supraparticles in the size range of 5 - 100  $\mu\text{m}$ ), further systems can be developed in the future. With the systems presented here, only a qualitative statement about the shear stress was possible so far. The mechanical stress was calculated for several systems, but only in a very vague way and with simplifying assumptions. In order to be able to use these systems in a real application, it would be helpful not only to get a yes/no answer, but also to be able to draw direct conclusions about the acting force by displaying a corresponding color or MPS signal. A supraparticle could be designed so that a certain minimum mechanical force is required to destroy it completely. This could be achieved by modifying the individual building blocks with different surface molecules that either bind more strongly or repel each other, making it easier or harder for the supraparticles to disintegrate. It would also be conceivable to use a binder during the spray-drying process to create more stable supraparticles and thus more robust systems. Systems consisting of several shells, each containing different colors, are also conceivable. The different cohesion of the individual shells could then be used to infer the degree of destruction of the supraparticle and thus the necessary force via the detected optical signal.

## Zusammenfassung und Ausblick

Ziel dieser Doktorarbeit war die Entwicklung von Mikrometer großen Scherstress-Indikatoren. Es ist dabei gelungen, ein neues Additiv zu entwickeln, das vielseitig einsetzbar ist, mechanische Belastungen einfach und schnell auf unterschiedliche Weise anzeigt und zudem aus kostengünstigen Materialien aufgebaut wurde. Diese Indikatorsysteme können in Pulverform oder als Teil einer Beschichtung eingesetzt werden. Durch die Kombination verschiedener Materialeigenschaften in einer einzigen mikroskaligen Einheit war es möglich, mehrere Informationen in einem Suprapartikel zu vereinen.

Durch die Kombination verschiedener nanopartikulärer Bausteine wurde in einem Sprühtrocknungsprozess eine hierarchisch nanostrukturierte Einheit im Mikrometerbereich, ein so genannter Suprapartikel, aufgebaut. Die in dieser Arbeit verwendeten Nanopartikel waren im Wesentlichen auf Systeme aus Silica und Eisenoxid beschränkt. Durch Variation der Synthesebedingungen (Temperatur, Reaktionszeit, Reaktantenzusammensetzung) konnte die Größe der entstehenden Silica-Nanopartikel in einem klassischen Stöberverfahren zwischen 80-320 nm eingestellt werden. Darüber hinaus wurden während der Nanopartikelsynthese Fluoreszenzfarbstoffe wie Rhodamin B oder Rhodamin 110 kovalent in das Silica-Netzwerk eingebaut und die Oberfläche der Nanopartikel mit APTES Molekülen funktionalisiert. Die verwendeten Eisenoxid-Nanopartikel wurden über verschiedene Synthesewege (Fällungsreaktion und oxidative Reifung) in unterschiedlichen Partikelgrößen (10-100 nm) hergestellt. Durch den Einbau von Cobaltatomen in das Eisenoxidgitter waren zudem die magnetischen Eigenschaften der hergestellten Nanopartikel beeinflussbar. Darüber hinaus ließen sich die Eisenoxid-Nanopartikel unter Stöber-Bedingungen mit einer Silica-Schale ummanteln. Diese Eisenoxid@Silica Nanopartikel konnten wiederum mit APTES Molekülen oberflächenmodifiziert werden.

Bei der Sprühtrocknung hatten sowohl das verwendete Equipment (Zyklongröße, Düsentyp), die Sprühparameter (Temperatur, Pumprate, Aspiratorgeschwindigkeit) als auch die Art und Zusammensetzung der Nanopartikeldispersionen (Viskosität, Feststoffgehalt, Größe der Nanopartikel, Stabilität der Dispersion) einen Einfluss auf die Morphologie, Größenverteilung und Partikelgröße der entstandenen Suprapartikel.

Damit die hergestellten Scherstress-Indikator-Suprapartikel in einer Beschichtung verwendet werden konnten, wurden verschiedene Anforderungen an ihre Zusammensetzung, Morphologie und Größe gestellt:

- Der verwendete Farbstoff musste kovalent in die Silica Nanopartikel eingebunden sein, um ein Austreten in die Beschichtung zu verhindern.
- Die Suprapartikel mussten eine vorwiegend sphärische Morphologie und eine Kern-Schale Struktur aufweisen, um eine gleichmäßige Freilegung der Querschnittsfläche während des Abrasionsprozesses zu gewährleisten, damit eine Änderung der optischen Signale detektiert werden konnte.
- Die Suprapartikel mussten in der Schicht eine maulwurfshügelartige Struktur bilden, so dass sie einerseits fest in der Schicht gehalten wurden, andererseits aber weit genug herausragten, um abgetragen zu werden. Dazu mussten die Suprapartikel im Mittel etwa doppelt so groß sein wie die Schichtdicke.

Waren diese Voraussetzungen erfüllt, konnten drei verschiedene Detektionsmechanismen realisiert werden: *turn-on*, *turn-off* und *color-change*. Im ersten Fall, den *turn-on* Indikatoren, bestand der Kern der Suprapartikel aus fluoreszierenden Silica Nanopartikeln und die Schale aus lichtabsorbierenden Eisenoxid Nanopartikeln. Die auf den ersten Blick gegensätzlichen optischen Eigenschaften (Lumineszenz und Lichtabsorption) führten zu einem graduellen Anstieg der optischen Signale, wenn die Suprapartikel nach dem Einbau in eine Schicht abgetragen wurden. Je mehr der Kern freigelegt wurde, desto intensiver wurde das Fluoreszenzsignal. Dies konnte sowohl in einem Spektrometer detektiert, als auch durch konfokale Mikroskopie sichtbar gemacht werden. Im umgekehrten Fall, den *turn-off* Indikator Suprapartikeln, war die Struktur invers aufgebaut, das heißt lichtabsorbierende Eisenoxid Nanopartikel im Kern und fluoreszierende Silica Nanopartikel in der Schale. Nach Einbau in eine Schicht und anschließender mechanischer Belastung nahm die Fluoreszenzintensität folglich allmählich ab. Diese Intensitätsabnahme wurde nicht

nur die Veränderung der Querschnittsfläche der Suprapartikel, sondern auch der Materialverlust durch den Abrasionsprozess verursacht. Wenn das lichtabsorbierende magnetische Material aufgrund seiner Materialzusammensetzung (Cobaltdotierung) in einer MPS unterschiedliche, aber eindeutig identifizierbare Signale liefert, kann eine solche Schicht intelligent und gleichzeitig auch kommunikativ sein. Die dritte Variante waren die *color-change* Indikator Suprapartikel. Hier änderte sich die Farbe des Systems bei mechanischen Belastung. Dazu mussten zwei unterschiedliche Farbstoffe im Kern beziehungsweise in der Schale des Suprapartikels angebunden werden. Wichtig bei deren Auswahl war, dass sich ihre Extinktionsbanden so weit überlappen, dass sie gleichzeitig angeregt werden konnten, die Emissionsbanden aber klar voneinander getrennt blieben. Nach dem Einbau solcher Suprapartikel in eine Beschichtung konnte bei Abriebtests eine Farbänderung beobachtet werden. Durch den Abrieb änderte sich auch die Sauerstoffdurchlässigkeit der Schicht. Die Farbe der Beschichtung konnte daher zur Beurteilung der Integrität und damit der Sauerstoffbarriere der Schicht herangezogen werden. Mit diesen drei Systemen war es gelungen, die Chemie der Moleküle mit der Welt der Nanoobjekte zu verbinden und makroskopische Systeme zu schaffen, die es ermöglichen, Oberflächen intelligent zu gestalten.

Neben intelligenten und kommunizierenden Beschichtungen wurden in dieser Arbeit auch Suprapartikelsysteme entwickelt, die in Pulverform als Scherstress-Indikatoren eingesetzt wurden. Dazu wurden drei grundlegend verschiedene Indikatorsysteme hergestellt, bei denen die mechanische Belastung mit unterschiedlichen Detektionsmethoden (UV/Vis Spektroskopie, MPS, Fluoreszenzspektroskopie) anzeigbar waren. Das erste System bestand aus photonischen Bällen, aufgebaut aus Silica und Eisenoxid Nanopartikeln. Während des Sprühtrocknungsprozesses bildete sich eine hohe Ordnung der Silica Nanopartikel auf der äußeren Oberfläche der Suprapartikel, während das Innere ungeordnet blieb. Die Eisenoxid Nanopartikel waren statistisch im gesamten Suprapartikel verteilt. Durch Variation des Verhältnisses von Silica zu Eisenoxid Nanopartikeln konnte die Intensität der Färbung gesteuert werden, während die Größe der Silica Nanopartikel die Farbe selbst beeinflusste. Während einer mechanischen Belastung konnte in diesen Systemen ein Farbverlust beobachtet werden, der auf eine irreversible Zerstörung der hoch geordneten äußeren Struktur zurückzuführen war. Im Gegensatz zu organischen Farbstoffen sind die photonischen Bälle stabil gegenüber chemischen Wechselwirkungen oder Umwelteinflüssen (z. B.

UV-Licht, pH-Wert, Lösemittel, Temperatur), da die Farberzeugung ausschließlich durch physikalischer Ordnungseffekte erfolgt. Im zweiten System wurden superparamagnetische Hohlkugeln, sogenannte Microballoons, verwendet, um die mechanische Beanspruchung und den Mahlgrad in einer Kugelmühle zu bestimmen. Durch die zunehmende Fragmentierung der Hohlkugeln während des Mahlvorgangs änderte sich das magnetische Signal der Probe, das mittels MPS ausgelesen wurde. Der mikroskopisch ermittelte Mahlgrad einer Probe wurde mit den MPS-Werten korreliert, so dass zeitaufwändige Analysen, ob das gewünschte Ergebnis erreicht wurde, entfielen. Nach Beendigung des Mahlvorganges wurden die Hohlkugelfragmente mit Hilfe eines Magneten aus dem eigentlichen Mahlgut wieder entfernt. Im dritten System wurden nach einem Baukastenprinzip verschiedene Indikatoren hergestellt, die in Pulverform einen *turn-off* Effekt zeigten. Dazu wurden lichtabsorbierende Materialien (Aktivkohle, Kohlenstoff, Eisenoxid) mit Luminophoren (Fluorescein, Rhodamin B, Lumino-Red, Tb-MOF) und reinen Silica Nanopartikeln in einem Sprühtrocknungsprozess zu Suprapartikeln assembliert. Durch die Kombination der verschiedenen Bausteine wurden Scherstress-Indikatoren hergestellt, die unterschiedlich schnell auf mechanische Belastung reagierten. Durch die unterschiedlichen Abklingkurven der jeweiligen Lumineszenz kann für verschiedene Anwendungen das passende System ausgewählt werden, je nachdem ob eine Mindestbelastung toleriert werden soll oder schon kleinste Belastungen angezeigt werden sollen.

Diese Flexibilität und Vielfalt an Möglichkeiten in Bezug auf Farbe, Empfindlichkeit, Detektionsmethoden und Einsatzgebieten bildeten die Grundlage für eine völlig neue Art von hierarchisch strukturierten suprapartikulären Indikatoren zur Bestimmung mechanischer Belastungen. Auf der Basis verschiedener Indikatorsysteme, die sich vor allem in der Art der verwendeten Materialien (Silica und Eisenoxid), der Größe und der Struktur der einzelnen Suprapartikel (nanostrukturierte, hierarchisch aufgebaute Suprapartikel im Größenbereich von 5- 100  $\mu\text{m}$ ) ähneln, können in Zukunft weitere Systeme entwickelt werden. Mit den hier vorgestellten Systemen ist bislang nur eine qualitative Aussage über die Scherbelastung möglich. Eine Berechnung der mechanischen Beanspruchung wurde zwar an verschiedenen Systemen durchgeführt, ist jedoch nur sehr vage und zum Teil mit vereinfachenden Annahmen möglich. Um diese Systeme dennoch in einer realen Anwendung einsetzen zu können, wäre es hilfreich, nicht nur eine Ja/Nein-Antwort zu

erhalten, sondern durch die Anzeige eines entsprechenden Farb- oder MPS-Signals direkte Rückschlüsse auf die wirkende Kraft ziehen zu können. Ein Suprapartikel könnte so konstruiert werden, dass eine bestimmte minimale mechanische Kraft erforderlich ist, um ihn überhaupt erst zu zerstören. Dies könnte erreicht werden, indem die einzelnen Bausteine mit unterschiedlichen Oberflächenmolekülen modifiziert werden, die sich entweder stärker aneinander binden oder abstoßen, so dass die Suprapartikel leichter oder schwerer zerfallen. Denkbar wäre auch die Verwendung eines Binders während des Sprühtrocknungsprozesses, um stabilere Suprapartikel und damit robustere Systeme zu erzeugen. Auch Systeme aus mehreren Schalen, die jeweils unterschiedliche Farben enthalten, sind denkbar. Durch die unterschiedliche Kohäsion der einzelnen Schalen könnte so über das detektierte optische Signal auf den Zerstörungsgrad des Suprapartikels und damit auf die notwendige Kraft geschlossen werden.

# References

- [1] Naito, M.; Yokoyama, T.; Hosokawa, K.; Nogi, K. *Nanoparticle technology handbook*, third edition ed.; Elsevier: Amsterdam, Netherlands, **2018**.
- [2] Hanemann, T.; Szabó, D. V. *Materials* **2010**, *3*, 3468–3517.
- [3] Nagarajan, R. In *ACS Symposium Series*; American Chemical Society: Washington, DC, **2008**; pp 2–14.
- [4] Boholm, M.; Arvidsson, R. *Nanoethics* **2016**, *10*, 25–40.
- [5] Oberdörster, G.; Oberdörster, E.; Oberdörster, J. *Environ. Health Perspect.* **2005**, *113*, 823–839.
- [6] Sadowski, Z.; Maliszewska, I. H.; Grochowalska, B.; Polowczyk, I.; Koźlecki, T. *Mater. Sci.-Poland* **2008**, *26*, 419–424.
- [7] Heiligtag, F. J.; Niederberger, M. *Mater. Today* **2013**, *16*, 262–271.
- [8] Talapin, D. V.; Shevchenko, E. V. *Chem. Rev.* **2016**, *116*, 10343–10345.
- [9] Thakor, A. S.; Jokerst, J.; Zavaleta, C.; Massoud, T. F.; Gambhir, S. S. *Nano Lett.* **2011**, *11*, 4029–4036.
- [10] Michael Faraday *Phil. trans. R. Soc.* **1857**, *147*, 145–181.
- [11] Thomas Graham *Phil. Trans. R. Soc.* **1861**, *151*, 183–224.
- [12] Kango, S.; Kalia, S.; Celli, A.; Njuguna, J.; Habibi, Y.; Kumar, R. *Prog. Polym. Sci.* **2013**, *38*, 1232–1261.
- [13] Zhao, P.; Li, N.; Astruc, D. *Coordin. Chem. Rev.* **2013**, *257*, 638–665.
- [14] Gill, R.; Zayats, M.; Willner, I. *Angew. Chem.* **2008**, *120*, 7714–7736.
- [15] Chatterjee, J.; Haik, Y.; Chen, C.-J. *J. Magn. Magn. Mater.* **2003**, *257*, 113–118.
- [16] Demortière, A.; Panissod, P.; Pichon, B. P.; Pourroy, G.; Guillon, D.; Donnio, B.; Bégin-Colin, S. *Nanoscale* **2011**, *3*, 225–232.
- [17] Gale, P. A.; Steed, J. W. *Supramolecular Chemistry*; John Wiley & Sons, Ltd: Chichester, UK, **2012**.
- [18] Talapin, D. V. *ACS nano* **2008**, *2*, 1097–1100.

- 
- [19] Kokura, S.; Handa, O.; Takagi, T.; Ishikawa, T.; Naito, Y.; Yoshikawa, T. *Nanomed. Nanotechnol.* **2010**, *6*, 570–574.
- [20] Carrouel, F.; Viennot, S.; Ottolenghi, L.; Gaillard, C.; Bourgeois, D. *Nanomaterials* **2020**, *10*, 140.
- [21] Farjadian, F.; Roointan, A.; Mohammadi-Samani, S.; Hosseini, M. *Chem. Eng. J.* **2019**, *359*, 684–705.
- [22] Narmani, A.; Rezvani, M.; Farhood, B.; Darkhor, P.; Mohammadnejad, J.; Amini, B.; Refahi, S.; Abdi Goushbolagh, N. *Drug Develop. Res.* **2019**, *80*, 404–424.
- [23] Reiss, G.; Hütten, A. *Nat. Mater.* **2005**, *4*, 725–726.
- [24] Wang, L.; Hasanzadeh Kafshgari, M.; Meunier, M. *Adv. Funct. Mater.* **2020**, *30*, 2005400.
- [25] Kumari, P.; Alam, M.; Siddiqi, W. A. *Sustain. Mater. Technol.* **2019**, *22*, e00128.
- [26] Masunga, N.; Mmelesi, O. K.; Kefeni, K. K.; Mamba, B. B. *J. Environ. Chem. Eng.* **2019**, *7*, 103179.
- [27] Jordan, A.; Scholz, R.; Wust, P.; Fählng, H.; Felix, R. *J. Magn. Magn. Mater.* **1999**, *201*, 413–419.
- [28] Ghitman, J.; Biru, E. I.; Stan, R.; Iovu, H. *Mater. Des.* **2020**, *193*, 108805.
- [29] Gao, C.; Lyu, F.; Yin, Y. *Chem. Rev.* **2021**, *121*, 834–881.
- [30] Astruc, D. *Chem. Rev.* **2020**, *120*, 461–463.
- [31] Frey, N. A.; Peng, S.; Cheng, K.; Sun, S. *Chem. Soc. Rev.* **2009**, *38*, 2532–2542.
- [32] Vogel, N.; Utech, S.; England, G. T.; Shirman, T.; Phillips, K. R.; Koay, N.; Burgess, I. B.; Kolle, M.; Weitz, D. A.; Aizenberg, J. *Proc. Natl. Acad. Sci. USA* **2015**, *112*, 10845–10850.
- [33] LaMer, V. K.; Dinegar, R. H. *J. Am. Chem. Soc.* **1950**, *72*, 4847–4854.
- [34] Wang, F.; Richards, V. N.; Shields, S. P.; Buhro, W. E. *Chem. Mater.* **2014**, *26*, 5–21.
- [35] Shevchenko, E. V.; Talapin, D. V.; Schnablegger, H.; Kornowski, A.; Festin, O.; Svedlindh, P.; Haase, M.; Weller, H. *J. Am. Chem. Soc.* **2003**, *125*, 9090–9101.
- [36] Christian, P.; von der Kammer, F.; Baalousha, M.; Hofmann, T. *Ecotoxicology* **2008**, *17*, 326–343.
- [37] Barsbay, M.; Çaylan Özgür, T.; Sütekin, S. D.; Güven, O. *Eur. Polym. J.* **2020**, *134*, 109811.
- [38] Restrepo, C. V.; Villa, C. C. *Environ. Nanotechnol. Monit. Manag.* **2021**, *15*, 100428.
-

- 
- [39] Segets, D.; Marczak, R.; Schäfer, S.; Paula, C.; Gnichwitz, J.-F.; Hirsch, A.; Peukert, W. *ACS nano* **2011**, *5*, 4658–4669.
- [40] Sommer, M.; Kaczorek, D.; Kuzyakov, Y.; Breuer, J. *J. Plant Nutr. Soil Sc.* **2006**, *169*, 310–329.
- [41] Bergna, H. E. *The colloid chemistry of silica: Developed from a Symposium sponsored by the Division of Colloid and Surface Chemistry, at the 200th National Meeting of the American Chemical Society, Washington, DC, August 26 - 31, 1990*; National Meeting of the American Chemical Society, Vol. 200; ACS: Washington, DC, **1994**.
- [42] Iler, R. K. *The chemistry of silica: Solubility, polymerization, colloid and surface properties, and biochemistry*; A Wiley-Interscience publication; Wiley: New York, NY, **1979**.
- [43] Mehmood, A.; Ghafar, H.; Yaqoob, S.; Gohar, U. F.; Ahmad, B. *J. Dev. Drugs* **2017**, *06*, 1000174.
- [44] Ornelas-Hernández, L. F.; Garduno-Robles, A.; Zepeda-Moreno, A. *Nanoscale Res. Lett.* **2022**, *17*, 56.
- [45] Schätz, A.; Reiser, O.; Stark, W. J. *Chem. Eur. J.* **2010**, *16*, 8950–8967.
- [46] Bahattab, M. A.; Alhomoudi, I. A.; Alhussaini, M. I.; Mirza, M.; Hegmann, J.; Glaubitt, W.; Löbmann, P. *Sol. Energ. Mat. Sol. C.* **2016**, *157*, 422–428.
- [47] Zuin, S.; Massari, A.; Ferrari, A.; Golanski, L. *Sci. Total Environ.* **2014**, *476-477*, 298–307.
- [48] Go, M.-R.; Bae, S.-H.; Kim, H.-J.; Yu, J.; Choi, S.-J. *Front. Microbiol.* **2017**, *8*, 1013.
- [49] Morais, R. P.; Hochheim, S.; de Oliveira, C. C.; Riegel-Vidotti, I. C.; Marino, C. E. B. *Int. J. Pharm.* **2022**, *614*, 121439.
- [50] Slowing, I. I.; Vivero-Escoto, J. L.; Wu, C.-W.; Lin, V. S.-Y. *Adv. Drug Deliver. Rev.* **2008**, *60*, 1278–1288.
- [51] Hyde, E. D. E. R.; Seyfaee, A.; Neville, F.; Moreno-Atanasio, R. *Ind. Eng. Chem. Res.* **2016**, *55*, 8891–8913.
- [52] Wagner, E.; Brünner, H. *Angew. Chem.* **1960**, *72*, 744–750.
- [53] Katz, H. S., Milewski, J. V. *Handbook of fillers for plastics*, 2nd ed.; Van Nostrand Reinhold: New York, **1987**; Vol. 165-201.
- [54] Boldridge, D. *Aerosol Sci. Tech.* **2010**, *44*, 182–186.
- [55] Xiao, Y.; Wang, Y.; Luo, G.; Bai, S. *Chem. Eng. J.* **2016**, *283*, 1–8.
- [56] White, L.; Duffy, G. *Ind. Eng. Chem.* **1959**, *51*, 232–238.
-

- 
- [57] Lim, H. M.; Lee, J.; Jeong, J.-H.; Oh, S.-G.; Lee, S.-H. *Eng.* **2010**, *02*, 998–1005.
- [58] Taylor-Pashow, K. M. L.; Della Rocca, J.; Huxford, R. C.; Lin, W. *Chem. Commun.* **2010**, *46*, 5832–5849.
- [59] Guerrero-Martínez, A.; Pérez-Juste, J.; Liz-Marzán, L. M. *Adv. Mater.* **2010**, *22*, 1182–1195.
- [60] Chang, C.-L.; Fogler, H. S. *AIChE J.* **1996**, *42*, 3153–3163.
- [61] Drummond, C.; McCann, R.; Patwardhan, S. V. *Chem. Eng. J.* **2014**, *244*, 483–492.
- [62] Idrus, S. S.; Ismail, H.; Palaniandy, S. *Polym. Test.* **2011**, *30*, 251–259.
- [63] Hewitt, N. *Compounding precipitated silica in elastomers*; PDL handbook series; Andrew Publ: Norwich, NY, **2007**.
- [64] Wijzen, F.; Koch, B.; Rocha, J.; Esculcas, A.; Liégeois-Duyckaerts, M.; Rulmont, A. *J. Catal.* **1998**, *177*, 96–104.
- [65] Lutz, W.; Weber, M.; Bertram, R.; Kurzhals, R.; Kryukova, G. *Z. Anorg. Allg. Chem.* **2011**, *637*, 421–425.
- [66] Hildebrand, M. *Prog. Org. Coat.* **2003**, *47*, 256–266.
- [67] Hartman, W. D. In *Silicon and Siliceous Structures in Biological Systems*; Simpson, T. L.; Volcani, B. E., Eds.; Springer New York: New York, NY, 1981; pp 453–493.
- [68] Sumper, M.; Brunner, E. *Adv. Funct. Mater.* **2006**, *16*, 17–26.
- [69] Lechner, C. C.; Becker, C. F. W. *Mar. drugs* **2015**, *13*, 5297–5333.
- [70] Patwardhan, S. V. *Chem. Commun.* **2011**, *47*, 7567–7582.
- [71] Stöber, W.; Fink, A.; Bohn, E. *J. Colloid Interface Sci.* **1968**, *26*, 62–69.
- [72] Dronskowski, R.; Kikkawa, S.; Stein, A. *Handbook of Solid State Chemistry*; Wiley-VCH Verlag GmbH & Co. KGaA: Weinheim, Germany, **2017**.
- [73] Oppmann, M.; Wenderoth, S.; Ballweg, T.; Schug, B.; Mandel, K. *Adv. Mater. Technol.* **2021**, *6*, 2100235.
- [74] Tavernaro, I.; Cavelius, C.; Peuschel, H.; Kraegeloh, A. *Beilstein J. Nanotech.* **2017**, *8*, 1283–1296.
- [75] Gao, W.; Rigout, M.; Owens, H. *Appl. Surf. Sci.* **2016**, *380*, 12–15.
- [76] Rahman, I. A.; Padavettan, V. *J. Nanomater.* **2012**, *2012*, 1–15.
- [77] Zhuravlev, L. T. *Colloid. Surface. A* **2000**, *173*, 1–38.
- [78] Bagwe, R. P.; Hilliard, L. R.; Tan, W. *Langmuir* **2006**, *22*, 4357–4362.
- [79] Maria Claesson, E.; Philipse, A. P. *Colloid. Surface. A* **2007**, *297*, 46–54.
-

- 
- [80] Zhang, Q.; Huang, R.; Guo, L.-H. *Sci. Bull.* **2009**, *54*, 2620–2626.
- [81] Ma, K.; Mendoza, C.; Hanson, M.; Werner-Zwanziger, U.; Zwanziger, J.; Wiesner, U. *Chem. Mater.* **2015**, *27*, 4119–4133.
- [82] Biju, V. *Chem. Soc. Rev.* **2014**, *43*, 744–764.
- [83] Gubala, V.; Giovannini, G.; Kunc, F.; Monopoli, M. P.; Moore, C. J. *Cancer Nano.* **2020**, *11*, 1–43.
- [84] Ow, H.; Larson, D. R.; Srivastava, M.; Baird, B. A.; Webb, W. W.; Wiesner, U. *Nano Lett.* **2005**, *5*, 113–117.
- [85] Wang, Y.; Li, Z.; Zhong, W.; Li, H.; Xu, D.; Chen, H. *Sci. China Chem.* **2010**, *53*, 747–751.
- [86] Burns, A.; Ow, H.; Wiesner, U. *Chem. Soc. Rev.* **2006**, *35*, 1028–1042.
- [87] Choi, J.; Burns, A. A.; Williams, R. M.; Zhou, Z.; Flesken-Nikitin, A.; Zipfel, W. R.; Wiesner, U.; Nikitin, A. Y. *J. Biomed. Opt.* **2007**, *12*, 064007.
- [88] Herz, E.; Burns, A.; Lee, S.; Sengupta, P.; Bonner, D.; Ow, H.; Liddell, C.; Baird, B.; Wiesner, U. *Proc. of SPIE* **2006**, 609605.
- [89] Wenderoth, S.; Granath, T.; Prieschl, J.; Wintzheimer, S.; Mandel, K. *Adv. Photonics Res.* **2020**, *1*, 2000023.
- [90] van Blaaderen, A.; Vrij, A. *Langmuir* **1992**, *8*, 2921–2931.
- [91] Wang, L.; Tan, W. *Nano Lett.* **2006**, *6*, 84–88.
- [92] Wenderoth, S.; Müssig, S.; Prieschl, J.; Genin, E.; Heuzé, K.; Fidler, F.; Haddad, D.; Wintzheimer, S.; Mandel, K. *Nano Lett.* **2022**, *22*, 2762–2768.
- [93] Schmidt, S.; Tavernaro, I.; Cavelius, C.; Weber, E.; Kümper, A.; Schmitz, C.; Fleddermann, J.; Kraegeloh, A. *Nanoscale Res. Lett.* **2017**, *12*, 545.
- [94] Hartlen, K. D.; Athanasopoulos, A. P. T.; Kitaev, V. *Langmuir* **2008**, *24*, 1714–1720.
- [95] Clasen, A.; Wenderoth, S.; Tavernaro, I.; Fleddermann, J.; Kraegeloh, A.; Jung, G. *RSC Adv.* **2019**, *9*, 35695–35705.
- [96] Gocht, W. *Handbuch der Metallmärkte*; Springer Berlin Heidelberg: Berlin, Heidelberg, **1985**.
- [97] Cornell, R. M.; Schwertmann, U. *The iron oxides: Structure, properties, reactions, occurrences and uses*, 2nd ed.; Wiley-VCH: Weinheim, **2003**.
- [98] Hradil, D.; Grygar, T.; Hradilová, J.; Bezdička, P. *Appl. Clay Sci.* **2003**, *22*, 223–236.
-

- 
- [99] Campos, E. A.; Stockler Pinto, D. V. B.; de Oliveira, J. I. S.; Da Mattos, E. C.; Dutra, R. D. C. L. *J. Aerosp. Technol. Manag.* **2015**, *7*, 267–276.
- [100] Roy, S. D.; Das, K. C.; Dhar, S. S. *Inorg. Chem. Commun.* **2021**, *134*, 109050.
- [101] Bagheri, S.; Julkapli, N. M. *J. Magn. Magn. Mater.* **2016**, *416*, 117–133.
- [102] Khan, F.; Pandey, P.; Upadhyay, T. K. *Agriculture* **2022**, *12*, 1672.
- [103] Mandel, K.; Hutter, F.; Gellermann, C.; SEXTL, G. *Sep. Purif. Technol.* **2013**, *109*, 144–147.
- [104] Xu, P.; Zeng, G. M.; Huang, D. L.; Feng, C. L.; Hu, S.; Zhao, M. H.; Lai, C.; Wei, Z.; Huang, C.; Xie, G. X.; Liu, Z. F. *Sci. Total Environ.* **2012**, *424*, 1–10.
- [105] Laurent, S.; Dutz, S.; Häfeli, U. O.; Mahmoudi, M. *Adv. Colloid Interfac.* **2011**, *166*, 8–23.
- [106] Mahmoudi, M.; Sant, S.; Wang, B.; Laurent, S.; Sen, T. *Adv. Drug Deliver. Rev.* **2011**, *63*, 24–46.
- [107] Lin, W.; Bazylnski, D. A.; Xiao, T.; Wu, L.-F.; Pan, Y. *Environ. Microbiol.* **2014**, *16*, 2646–2658.
- [108] Gupta, A. K.; Gupta, M. *Biomaterials* **2005**, *26*, 3995–4021.
- [109] Mohapatra, M.; Anand, S. *Int. J. Eng. Sci. Tech.* **2011**, *2*, 127–146.
- [110] Chaturvedi, S.; Dave, P. N.; Shah, N. K. *J. Saudi Chem. Soc.* **2012**, *16*, 307–325.
- [111] Sun, S.; Zeng, H. *J. Am. Chem. Soc.* **2002**, *124*, 8204–8205.
- [112] Hyeon, T.; Lee, S. S.; Park, J.; Chung, Y.; Na, H. B. *J. Am. Chem. Soc.* **2001**, *123*, 12798–12801.
- [113] Jiang, Y. f.; Zheng, A.; Zheng, S. j.; Liu, W. m.; Zhuang, L. *J. Appl. Phys.* **2020**, *128*, 103106.
- [114] Vidal-Vidal, J.; Rivas, J.; López-Quintela, M. A. *Colloid. Surface. A* **2006**, *288*, 44–51.
- [115] Pascal, C.; Pascal, J. L.; Favier, F.; Elidrissi Moubtassim, M. L.; Payen, C. *Chem. Mater.* **1999**, *11*, 141–147.
- [116] Cabrera, L.; Gutierrez, S.; Menendez, N.; Morales, M. P.; Herrasti, P. *Electrochim. Acta* **2008**, *53*, 3436–3441.
- [117] Bharde, A. A.; Parikh, R. Y.; Baidakova, M.; Jouen, S.; Hannoyer, B.; Enoki, T.; Prasad, B. L. V.; Shouche, Y. S.; Ogale, S.; Sastry, M. *Langmuir* **2008**, *24*, 5787–5794.
- [118] Bomati-Miguel, O.; Mazeina, L.; Navrotsky, A.; Veintemillas-Verdaguer, S. *Chem. Mater.* **2008**, *20*, 591–598.
-

- 
- [119] Teja, A. S.; Koh, P.-Y. *Prog. Cryst. Growth Ch.* **2009**, *55*, 22–45.
- [120] Wu, W.; He, Q.; Jiang, C. *Nanoscale Res. Lett.* **2008**, *3*, 397–415.
- [121] Granath, T.; Löbmann, P.; Mandel, K. *Part. Part. Syst. Charact.* **2021**, *38*, 2000307.
- [122] Tavakoli, A.; Sohrabi, M.; Kargari, A. *Chem. Pap.* **2007**, *61*, 151–170.
- [123] Cabañas, A.; Darr, J. A.; Lester, E.; Poliakoff, M. *J. Mater. Chem.* **2001**, *11*, 561–568.
- [124] Sue, K.; Suzuki, M.; Arai, K.; Ohashi, T.; Ura, H.; Matsui, K.; Hakuta, Y.; Hayashi, H.; Watanabe, M.; Hiaki, T. *Green Chem.* **2006**, *8*, 634.
- [125] Burda, C.; Chen, X.; Narayanan, R.; El-Sayed, M. A. *Chem. Rev.* **2005**, *105*, 1025–1102.
- [126] Fernandes, M. T. C.; Garcia, R. B. R.; Leite, C. A. P.; Kawachi, E. Y. *Colloid. Surface. A* **2013**, *422*, 136–142.
- [127] Huang, S.-H.; Chen, D.-H. *J. Hazard. Mater.* **2009**, *163*, 174–179.
- [128] Karaoğlu, E.; Kavas, H.; Baykal, A.; Toprak, M. S.; Sözeri, H. *Nano-Micro Lett.* **2011**, *3*, 79–85.
- [129] Liu, X.; Hu, Q.; Fang, Z.; Wu, Q.; Xie, Q. *Langmuir* **2009**, *25*, 7244–7248.
- [130] Qu, J.; Liu, G.; Wang, Y.; Hong, R. *Adv. Powder Technol.* **2010**, *21*, 461–467.
- [131] Zhou, J.; Li, R.; Liu, S.; Li, Q.; Zhang, L.; Zhang, L.; Guan, J. *J. Appl. Polym. Sci.* **2009**, *111*, 2477–2484.
- [132] Palani, A.; Lee, J.-S.; Huh, J.; Kim, M.; Lee, Y.-J.; Chang, J. H.; Lee, K.; Lee, S.-W. *J. Proteome Res.* **2008**, *7*, 3591–3596.
- [133] Li, J.; Zhao, X.; Shi, Y.; Cai, Y.; Mou, S.; Jiang, G. *J. Chromatogr. A* **2008**, *1180*, 24–31.
- [134] Zhang, J.; Rana, S.; Srivastava, R. S.; Misra, R. D. K. *Acta Biomater.* **2008**, *4*, 40–48.
- [135] Zhan, J.; Tian, G.; Jiang, L.; Wu, Z.; Wu, D.; Yang, X.; Jin, R. *Thin Solid Films* **2008**, *516*, 6315–6320.
- [136] Wang, Y.; Wang, S.; Niu, H.; Ma, Y.; Zeng, T.; Cai, Y.; Meng, Z. *J. Chromatogr. A* **2013**, *1283*, 20–26.
- [137] Pérez, A.; Mijangos, C.; Hernández, R. *Macromol. Symp.* **2014**, *335*, 62–69.
- [138] Tzitzios, V. K.; Petridis, D.; Zafiropoulou, I.; Hadjipanayis, G.; Niarchos, D. *J. Magn. Magn. Mater.* **2005**, *294*, e95–e98.
-

- 
- [139] Yu, H.; Chen, M.; Rice, P. M.; Wang, S. X.; White, R. L.; Sun, S. *Nano Lett.* **2005**, *5*, 379–382.
- [140] Hsu, J.-H.; Chen, S.-Y.; Chang, W.-M.; Jian, T. S.; Chang, C.-R.; Lee, S.-F. *J. Appl. Phys.* **2003**, *93*, 7702–7704.
- [141] Kralj, S.; Drogenik, M.; Makovec, D. *J. Nanopart. Res.* **2011**, *13*, 2829–2841.
- [142] Yi, D. K.; Selvan, S. T.; Lee, S. S.; Papaefthymiou, G. C.; Kundaliya, D.; Ying, J. Y. *J. Am. Chem. Soc.* **2005**, *127*, 4990–4991.
- [143] Miller, F.; Wenderoth, S.; Wintzheimer, S.; Mandel, K. *Adv. Optical Mater.* **2022**, *10*, 2201642.
- [144] Lehn, J.-M. *Chem. Soc. Rev.* **2017**, *46*, 2378–2379.
- [145] Glotzer, S. C.; Solomon, M. J. *Nat. Mater.* **2007**, *6*, 557–562.
- [146] Muller, P. *Pure Appl. Chem.* **1994**, *66*, 1077–1184.
- [147] Wintzheimer, S.; Granath, T.; Oppmann, M.; Kister, T.; Thai, T.; Kraus, T.; Vogel, N.; Mandel, K. *ACS nano* **2018**, *12*, 5093–5120.
- [148] Wintzheimer, S.; Reichstein, J.; Groppe, P.; Wolf, A.; Fett, B.; Zhou, H.; Pujales-Paradela, R.; Miller, F.; Müssig, S.; Wenderoth, S.; Mandel, K. *Adv. Funct. Mater.* **2021**, *31*, 2011089.
- [149] Othman, A.; Vargo, P.; Andreescu, S. *ACS Appl. Nano Mater.* **2019**, *2*, 7008–7018.
- [150] Zhang, Y.; Qiu, W.; Ma, Y.; Luo, Y.; Tian, Z.; Cui, G.; Xie, F.; Chen, L.; Li, T.; Sun, X. *ACS Catal.* **2018**, *8*, 8540–8544.
- [151] Mao, Z.; Xu, H.; Wang, D. *Adv. Funct. Mater.* **2010**, *20*, 1053–1074.
- [152] Xue, Z.; Yan, C.; Wang, T. *Adv. Funct. Mater.* **2019**, *29*, 1807658.
- [153] Lim, E. W. C.; Feng, R. *J. Chem. Phys.* **2012**, *136*, 124109.
- [154] Pazos-Perez, N.; Wagner, C. S.; Romo-Herrera, J. M.; Liz-Marzán, L. M.; García de Abajo, F. J.; Wittemann, A.; Fery, A.; Alvarez-Puebla, R. A. *Angew. Chem. Int. Ed.* **2012**, *51*, 12688–12693.
- [155] Pons, T.; Medintz, I. L.; Sapsford, K. E.; Higashiya, S.; Grimes, A. F.; English, D. S.; Mattoussi, H. *Nano Lett.* **2007**, *7*, 3157–3164.
- [156] Uddayasankar, U.; Krull, U. J. *Langmuir* **2015**, *31*, 8194–8204.
- [157] Zhou, D.; Liu, D.; Jin, J.; Chen, X.; Xu, W.; Yin, Z.; Pan, G.; Li, D.; Song, H. *J. Mater. Chem. A* **2017**, *5*, 16559–16567.
- [158] Teitelboim, A.; Meir, N.; Kazes, M.; Oron, D. *Accounts Chem. Res.* **2016**, *49*, 902–910.
-

- 
- [159] Zhang, Q.; Wang, W.-Z.; Yu, J.-J.; Qu, D.-H.; Tian, H. *Adv. Mater.* **2017**, *29*, 1604948.
- [160] Swearer, D. F.; Zhao, H.; Zhou, L.; Zhang, C.; Robotjazi, H.; Martinez, J. M. P.; Krauter, C. M.; Yazdi, S.; McClain, M. J.; Ringe, E.; Carter, E. A.; Nordlander, P.; Halas, N. J. *P. Natl. Acad. Sci. USA* **2016**, *113*, 8916–8920.
- [161] Tou, M.; Mei, Y.; Bai, S.; Luo, Z.; Zhang, Y.; Li, Z. *Nanoscale* **2016**, *8*, 553–562.
- [162] Wenderoth, S.; Bleyer, G.; Endres, J.; Prieschl, J.; Vogel, N.; Wintzheimer, S.; Mandel, K. *Small* **2022**, *18*, e2203068.
- [163] Egly, S.; Fröhlich, C.; Vogel, S.; Gruenewald, A.; Wang, J.; Detsch, R.; Boccaccini, A. R.; Vogel, N. *Langmuir* **2018**, *34*, 2063–2072.
- [164] Sultan, U.; Götz, A.; Schlumberger, C.; Drobek, D.; Bleyer, G.; Walter, T.; Löwer, E.; Peuker, U. A.; Thommes, M.; Spiecker, E.; Apeleo Zubiri, B.; Inayat, A.; Vogel, N. *Small* **2023**, e2300241.
- [165] Bollhorst, T.; Grieb, T.; Rosenauer, A.; Fuller, G.; Maas, M.; Rezwan, K. *Chem. Mater.* **2013**, *25*, 3464–3471.
- [166] Shikha, S.; Salafi, T.; Cheng, J.; Zhang, Y. *Chem. Soc. Rev.* **2017**, *46*, 7054–7093.
- [167] Paunescu, D.; Stark, W. J.; Grass, R. N. *Powder Technol.* **2016**, *291*, 344–350.
- [168] Miller, F.; Wintzheimer, S.; Prieschl, J.; Strauss, V.; Mandel, K. *Adv. Optical Mater.* **2021**, *9*, 2001972.
- [169] Müssig, S.; Reichstein, J.; Prieschl, J.; Wintzheimer, S.; Mandel, K. *Small* **2021**, *17*, e2101588.
- [170] Haw, C.; Chiu, W.; Abdul Rahman, S.; Khiew, P.; Radiman, S.; Abdul Shukor, R.; Hamid, M. A. A.; Ghazali, N. *New J. Chem.* **2016**, *40*, 1124–1136.
- [171] Mandel, K.; Granath, T.; Wehner, T.; Rey, M.; Stracke, W.; Vogel, N.; Sextl, G.; Müller-Buschbaum, K. *ACS nano* **2017**, *11*, 779–787.
- [172] Granath, T.; Sanchez-Sanchez, A.; Shmeliov, A.; Nicolosi, V.; Fierro, V.; Celzard, A.; Mandel, K. *ACS nano* **2016**, *10*, 10347–10356.
- [173] P. E. Shaw, L. Newby *Regul. Stud.* **1998**, 863.
- [174] Chandra, V.; Park, J.; Chun, Y.; Lee, J. W.; Hwang, I.-C.; Kim, K. S. *ACS nano* **2010**, *4*, 3979–3986.
- [175] Mishra, A. K.; Ramaprabhu, S. *J. Phys. Chem. C* **2010**, *114*, 2583–2590.
- [176] Ai, L.; Zhang, C.; Chen, Z. *J. Hazard. Mater.* **2011**, *192*, 1515–1524.
- [177] Ai, L.; Huang, H.; Chen, Z.; Wei, X.; Jiang, J. *Chem. Eng. J.* **2010**, *156*, 243–249.
-

- 
- [178] Oliveira, L. C. A.; Gonçalves, M.; Oliveira, D. Q. L.; Guerreiro, M. C.; Guilherme, L. R. G.; Dallago, R. M. *J. Hazard. Mater.* **2007**, *141*, 344–347.
- [179] Harada, T.; Hatton, T. A. *Chem. Mater.* **2015**, *27*, 8153–8161.
- [180] Liu, Z.; Li, Z.; Xie, X.; Yang, S.; Fei, J.; Li, Y.; Xu, Z.; Liu, H. *Environ. Sci. Technol.* **2020**, *54*, 604–612.
- [181] Ren, H.; Koshy, P.; Chen, W.-F.; Qi, S.; Sorrell, C. C. *J. Hazard. Mater.* **2017**, *325*, 340–366.
- [182] Pannek, C.; Vetter, T.; Oppmann, M.; Weber, C.; Eberhardt, A.; Dold, M.; Bauersfeld, M.-L.; Henfling, M.; Trupp, S.; Schug, B.; Wöllenstein, J.; Mandel, K. *Sensor Actuat. B-Chem.* **2020**, *306*, 127572.
- [183] Singh, N.; Gupta, R. K.; Lee, P. S. *ACS Appl. Mater. Inter.* **2011**, *3*, 2246–2252.
- [184] Zhang, Y.; Xiang, Q.; Xu, J.; Xu, P.; Pan, Q.; Li, F. *J. Mater. Chem.* **2009**, *19*, 4701.
- [185] Reichstein, J.; Schötz, S.; Macht, M.; Maisel, S.; Stockinger, N.; Collados, C. C.; Schubert, K.; Blaumeiser, D.; Wintzheimer, S.; Görling, A.; Thommes, M.; Zahn, D.; Libuda, J.; Bauer, T.; Mandel, K. *Adv. Funct. Mater.* **2022**, *32*, 2112379.
- [186] Wintzheimer, S.; Oppmann, M.; Dold, M.; Pannek, C.; Bauersfeld, M.-L.; Henfling, M.; Trupp, S.; Schug, B.; Mandel, K. *Part. Part. Syst. Character.* **2019**, *36*, 1900254.
- [187] Koren, K.; Mistlberger, G.; Aigner, D.; Borisov, S. M.; Zankel, A.; Pölt, P.; Klimant, I. *Monatsh. Chem.* **2010**, *141*, 691–697.
- [188] Kohane, D. S. *Biotechnol. Bioeng.* **2007**, *96*, 203–209.
- [189] Mattos, B. D.; Tardy, B. L.; Magalhães, W. L. E.; Rojas, O. J. *J. Control. Release* **2017**, *262*, 139–150.
- [190] Vanmaekelbergh, D.; van Vugt, L. K.; Bakker, H. E.; Rabouw, F. T.; de Nijs, B.; van Dijk-Moes, R. J. A.; van Huis, M. A.; Baesjou, P. J.; van Blaaderen, A. *ACS nano* **2015**, *9*, 3942–3950.
- [191] van der Burgt, J. S.; Geuchies, J. J.; van der Meer, B.; Vanrompay, H.; Zanaga, D.; Zhang, Y.; Albrecht, W.; Petukhov, A. V.; Fillion, L.; Bals, S.; Swart, I.; Vanmaekelbergh, D. *J. Phys. Chem. C* **2018**, *122*, 15706–15712.
- [192] Cui, J.; Kramer, M.; Zhou, L.; Liu, F.; Gabay, A.; Hadjipanayis, G.; Balasubramanian, B.; Sellmyer, D. *Acta Mater.* **2018**, *158*, 118–137.
- [193] Balgis, R.; Widiyastuti, W.; Ogi, T.; Okuyama, K. *ACS Appl. Mater. Inter.* **2017**, *9*, 23792–23799.
- [194] Ro, G.; Hwang, D. K.; Kim, Y. *J. Ind. Eng. Chem.* **2019**, *79*, 364–369.
- [195] Liu, W.; Gao, P.; Mi, Y.; Chen, J.; Zhou, H.; Zhang, X. *J. Mater. Chem. A* **2013**, *1*, 2411–2417.
-

- 
- [196] Parveen, K.; Banse, V.; Ledwani, L. *AIP Conf. Proc.* **2016**, *1724*, 020048.
- [197] Ndolomingo, M. J.; Bingwa, N.; Meijboom, R. *J. Mater. Sci.* **2020**, *55*, 6195–6241.
- [198] Luo, D.; Qin, X.; Song, Q.; Qiao, X.; Zhang, Z.; Xue, Z.; Liu, C.; Mo, G.; Wang, T. *Adv. Funct. Mater.* **2017**, *27*, 1701982.
- [199] Sun, G.; Fan, M.; Chen, L.; Luo, J.; Liu, R. *Colloid. Surface. A* **2020**, *589*, 124458.
- [200] Reichstein, J.; Müssig, S.; Bauer, H.; Wintzheimer, S.; Mandel, K. *Adv. Mater.* **2022**, *34*, e2202683.
- [201] Osterloh, F.; Hiramatsu, H.; Porter, R.; Guo, T. *Langmuir* **2004**, *20*, 5553–5558.
- [202] Müssig, S.; Fidler, F.; Haddad, D.; Hiller, K.-H.; Wintzheimer, S.; Mandel, K. *Adv. Mater. Technol.* **2019**, *4*, 1900300.
- [203] Duguet, E.; Désert, A.; Perro, A.; Ravaine, S. *Chem. Soc. Rev.* **2011**, *40*, 941–960.
- [204] Manoharan, V. N. *Science* **2015**, *349*, 1253751.
- [205] Wang, Y.; Wang, Y.; Breed, D. R.; Manoharan, V. N.; Feng, L.; Hollingsworth, A. D.; Weck, M.; Pine, D. J. *Nature* **2012**, *491*, 51–55.
- [206] Vogel, N.; Retsch, M.; Fustin, C.-A.; Del Campo, A.; Jonas, U. *Chem. Rev.* **2015**, *115*, 6265–6311.
- [207] Hubert, C.; Chomette, C.; Désert, A.; Sun, M.; Treguer-Delapierre, M.; Mornet, S.; Perro, A.; Duguet, E.; Ravaine, S. *Faraday Discuss.* **2015**, *181*, 139–146.
- [208] Gong, Z.; Hueckel, T.; Yi, G.-R.; Sacanna, S. *Nature* **2017**, *550*, 234–238.
- [209] Zhao, Y.; Shang, L.; Cheng, Y.; Gu, Z. *Accounts Chem. Res.* **2014**, *47*, 3632–3642.
- [210] de Nijs, B.; Dussi, S.; Smallenburg, F.; Meeldijk, J. D.; Groenendijk, D. J.; Filion, L.; Imhof, A.; van Blaaderen, A.; Dijkstra, M. *Nature Mater.* **2015**, *14*, 56–60.
- [211] Manoharan, V. N.; Elsesser, M. T.; Pine, D. J. *Science* **2003**, *301*, 483–487.
- [212] Xue, Z.; Wang, P.; Peng, A.; Wang, T. *Adv. Mater.* **2019**, *31*, e1801441.
- [213] Xu, K.; Xu, J.-H.; Lu, Y.-C.; Luo, G.-S. *Cryst. Growth Des.* **2013**, *13*, 926–935.
- [214] Liu, W.; Kappl, M.; Butt, H.-J. *ACS nano* **2019**, *13*, 13949–13956.
- [215] Wang, R.; Bao, S.; Liu, F.; Jiang, X.; Zhang, Q.; Sun, B.; Zhu, M. *Mat. Sci. Eng. C-Mater.* **2013**, *33*, 4759–4766.
- [216] Ribeiro, R. F.; Motta, M. H.; Härter, A. P. G.; Flores, F. C.; Beck, R. C. R.; Schaffazick, S. R.; de Da Bona Silva, C. *Mat. Sci. Eng. C-Mater.* **2016**, *59*, 875–884.
- [217] Zhang, S.; Yan, S.; Lu, K.; Qiu, S.; Chen, X. D.; Wu, W. D. *Powder Technol.* **2023**, *415*, 118168.
-

- 
- [218] Rastogi, V.; Melle, S.; Calderón, O. G.; García, A. A.; Marquez, M.; Velev, O. D. *Adv. Mater.* **2008**, *20*, 4263–4268.
- [219] Dendukuri, D.; Doyle, P. S. *Adv. Mater.* **2009**, *21*, 4071–4086.
- [220] Brugarolas, T.; Tu, F.; Lee, D. *Soft Matter* **2013**, *9*, 9046.
- [221] Vehring, R. *Pharm. Res.* **2008**, *25*, 999–1022.
- [222] Homayoonfal, M.; Malekjani, N.; Baeghbali, V.; Ansarifar, E.; Hedayati, S.; Jafari, S. M. *Crit. Rev. Food Sci. Nutr.* **2022**, 1–41.
- [223] Gharsallaoui, A.; Roudaut, G.; Chambin, O.; Voilley, A.; Saurel, R. *Food Res. Int.* **2007**, *40*, 1107–1121.
- [224] Farshchi, A.; Hassanpour, A.; Bayly, A. E. *Powder Technol.* **2019**, *355*, 738–754.
- [225] Nandiyanto, A. B. D.; Okuyama, K. *Adv. Powder Technol.* **2011**, *22*, 1–19.
- [226] Oppmann, M.; Wozar, M.; Reichstein, J.; Mandel, K. *Chem. Nano. Mat.* **2018**, 230–240.
- [227] Yang, D.-L.; Liu, R.-K.; Wei, Y.; Sun, Q.; Wang, J.-X. *Particuology* **2023**, *85*, 22–48.
- [228] Liu, W.; Chen, X. D.; Selomulya, C. *Particuology* **2015**, *22*, 1–12.
- [229] Cotabarren, I. M.; Bertín, D.; Razuc, M.; Ramírez-Rigo, M. V.; Piña, J. *Chem. Eng. Res. Des.* **2018**, *132*, 1091–1104.
- [230] Zhou, H.; Pujales-Paradela, R.; Groppe, P.; Wintzheimer, S.; Mandel, K. *Part. Part. Syst. Charact.* **2022**, *39*, 2200127.
- [231] Okuyama, K.; Wuled Lenggoro, I. *Chem. Eng. Sci.* **2003**, *58*, 537–547.
- [232] Suhendi, A.; Nandiyanto, A. B. D.; Munir, M. M.; Ogi, T.; Gradon, L.; Okuyama, K. *Langmuir* **2013**, *29*, 13152–13161.
- [233] Balgis, R.; Ernawati, L.; Ogi, T.; Okuyama, K.; Gradon, L. *AIChE J.* **2017**, *63*, 1503–1511.
- [234] Iskandar, F.; Gradon, L.; Okuyama, K. *J. Colloid Interf. Sci.* **2003**, *265*, 296–303.
- [235] Ballweg, T.; Gellermann, C.; Mandel, K. *ACS Appl. Mater. Inter.* **2015**, *7*, 24909–24914.
- [236] Oppmann, M.; Miller, F.; Thürauf, S.; Groppe, P.; Prieschl, J.; Stauch, C.; Mandel, K. *ACS Appl. Mater. Inter.* **2018**, *10*, 14183–14192.
- [237] Wenderoth, S.; Eigen, A.; Wintzheimer, S.; Prieschl, J.; Hirsch, A.; Halik, M.; Mandel, K. *Small* **2022**, *18*, e2107513.
- [238] Iskandar, F.; Chang, H.; Okuyama, K. *Adv. Powder Technol.* **2003**, *14*, 349–367.
-

- 
- [239] Lakowicz, J. R. *Principles of fluorescence spectroscopy*, 3rd ed.; Springer: New York, NY, **2006**.
- [240] Wnek, G.; Bowlin, G. *Encyclopedia of Biomaterials and Biomedical Engineering*; CRC Press, **2008**.
- [241] Guilbault, G. G. *Practical fluorescence*; Marcel Dekker: New York, NY, **1990**.
- [242] Jabłoński, A. *Z. Physik* **1935**, *94*, 38–46.
- [243] Herschel, J. F. *Phil. Trans. Roy. Soc.* **1845**, *135*, 143–145.
- [244] Kasha, M. *Disc. Faraday Soc.* **1950**, *9*, 14.
- [245] Schuler, B. *Chem. Phys. Chem.* **2005**, *6*, 1206–1220.
- [246] Holehouse, A. S.; Pappu, R. V. *Ann. Rev. Biophys.* **2018**, *47*, 19–39.
- [247] Mutavdžić, D.; Xu, J.; Thakur, G.; Triulzi, R.; Kasas, S.; Jeremić, M.; Leblanc, R.; Radotić, K. *Analyst* **2011**, *136*, 2391–2396.
- [248] Minsky, M. *Scanning* **1988**, *10*, 128–138.
- [249] Jerome, W. G.; Price, R. L. *Basic Confocal Microscopy*; Springer International Publishing: Cham, **2018**.
- [250] Nwaneshiudu, A.; Kuschal, C.; Sakamoto, F. H.; Anderson, R. R.; Schwarzenberger, K.; Young, R. C. *J. Invest. Dermatol.* **2012**, *132*, e3.
- [251] Bayguinov, P. O.; Oakley, D. M.; Shih, C.-C.; Geanon, D. J.; Joens, M. S.; Fitzpatrick, J. A. J. *Curr. Protoc. Cytom.* **2018**, *85*, e39.
- [252] French, A. P.; Mills, S.; Swarup, R.; Bennett, M. J.; Pridmore, T. P. *Nat. Protoc.* **2008**, *3*, 619–628.
- [253] Jonkman, J.; Brown, C. M.; Wright, G. D.; Anderson, K. I.; North, A. J. *Nat. Protoc.* **2020**, *15*, 1585–1611.
- [254] Martinez-Santibañez, G.; Cho, K. W.; Lumeng, C. N. *Method. Enzymol.* **2014**, *537*, 17–30.
- [255] Kolenbrander, P. E.; Andersen, R. N.; Blehert, D. S.; Eglund, P. G.; Foster, J. S.; Palmer, R. J. *Microbiol. Mol. Biol. R.* **2002**, *66*, 486–505.
- [256] Wintzheimer, S.; Reichstein, J.; Wenderoth, S.; Hasselmann, S.; Oppmann, M.; Seuffert, M. T.; Müller-Buschbaum, K.; Mandel, K. *Adv. Funct. Mater.* **2019**, *29*, 1901193.
- [257] Nikitin, P. I.; Vetoshko, P. M.; Ksenevich, T. I. *J. Magn. Magn. Mater.* **2007**, *311*, 445–449.
- [258] Krause, H.-J.; Wolters, N.; Zhang, Y.; Offenhäusser, A.; Miethe, P.; Meyer, M. H.; Hartmann, M.; Keusgen, M. *J. Magn. Magn. Mater.* **2007**, *311*, 436–444.
-

- 
- [259] Wu, K.; Liu, J.; Chugh, V. K.; Liang, S.; Saha, R.; Krishna, V. D.; Cheeran, M. C.-J.; Wang, J.-P. *Nano Futures* **2022**, *6*, 022001.
- [260] Wu, K.; Su, D.; Saha, R.; Liu, J.; Chugh, V. K.; Wang, J.-P. *ACS Appl. Nano Mater.* **2020**, *3*, 4972–4989.
- [261] Barrera, G.; Allia, P.; Tiberto, P. *Phys. Rev. Appl.* **2022**, *18*, 024077.
- [262] Knopp, T.; Gdaniec, N.; Möddel, M. *Phys. Med. Biol.* **2017**, *62*, R124–R178.
- [263] Wu, K.; Su, D.; Saha, R.; Wong, D.; Wang, J.-P. *J. Phys. D: Appl. Phys.* **2019**, *52*, 173001.
- [264] Wintzheimer, S.; Müssig, S.; Wenderoth, S.; Prieschl, J.; Granath, T.; Fidler, F.; Haddad, D.; Mandel, K. *ACS Appl. Nano Mater.* **2019**, *2*, 6757–6762.
- [265] Müssig, S.; Granath, T.; Schembri, T.; Fidler, F.; Haddad, D.; Hiller, K.-H.; Wintzheimer, S.; Mandel, K. *ACS Appl. Nano Mater.* **2019**, *2*, 4698–4702.
- [266] Maheshwari, V.; Saraf, R. *Angew. Chem.* **2008**, *120*, 7926–7945.
- [267] Wittenberg, C. *IFAC-PapersOnLine* **2016**, *49*, 420–425.
- [268] Someya, T.; Sekitani, T.; Iba, S.; Kato, Y.; Kawaguchi, H.; Sakurai, T. *Proc. Natl. Acad. Sci. USA* **2004**, *101*, 9966–9970.
- [269] Noda, K.; Hoshino, K.; Matsumoto, K.; Shimoyama, I. *Sensor. Actuat. A-Phys.* **2006**, *127*, 295–301.
- [270] Missinne, J.; Bosman, E.; van Hoe, B.; van Steenberge, G.; Kalathimekkad, S.; van Daele, P.; Vanfleteren, J. *IEEE Photon. Technol. Lett.* **2011**, *23*, 771–773.
- [271] Engel, J.; Chen, J.; Liu, C. *J. Micromech. Microeng.* **2003**, *13*, 359–366.
- [272] Dvorak, N. A.; Ku, P.-C. *IEEE Electr. Device L.* **2022**, *43*, 1081–1084.
- [273] Li, F.; Akiyama, Y.; Wan, X.; Okamoto, S.; Yamada, Y. *IEEE Access* **2022**, *10*, 319–327.
- [274] Xu, Y.; Tai, Y.-C.; Huang, A.; Ho, C.-M. *J. Microelectromech. Syst.* **2003**, *12*, 740–747.
- [275] Löfdahl, L.; Gad-el Hak, M. *Meas. Sci. Technol.* **1999**, *10*, 665–686.
- [276] Nguyen, T.-V.; Kazama, R.; Takahashi, H.; Takahata, T.; Matsumoto, K.; Shimoyama, I. *J. Micromech. Microeng.* **2017**, *27*, 075017.
- [277] Zhe, J.; Modi, V.; Farmer, K. R. *J. Microelectromech. S.* **2005**, *14*, 167–175.
- [278] Lv, H.; Jiang, C.; Xiang, Z.; Ma, B.; Deng, J.; Yuan, W. *Flow. Meas. Instrum.* **2013**, *30*, 66–74.
- [279] Suresh, R.; Tjin, S. C. *Sens. Actuators, A* **2005**, *120*, 26–36.
-

- 
- [280] Nguyen, N. D.; Zhang, G.; Lu, J.; Sherman, A. E.; Fraser, C. L. *J. Mater. Chem.* **2011**, *21*, 8409.
- [281] Zhang, X.; Chi, Z.; Zhang, Y.; Liu, S.; Xu, J. *J. Mater. Chem. C* **2013**, *1*, 3376.
- [282] Sagara, Y.; Mutai, T.; Yoshikawa, I.; Araki, K. *J. Am. Chem. Soc.* **2007**, *129*, 1520–1521.
- [283] Ito, H.; Saito, T.; Oshima, N.; Kitamura, N.; Ishizaka, S.; Hinatsu, Y.; Wakeshima, M.; Kato, M.; Tsuge, K.; Sawamura, M. *J. Am. Chem. Soc.* **2008**, *130*, 10044–10045.
- [284] Perruchas, S.; Le Goff, X. F.; Maron, S.; Maurin, I.; Guillen, F.; Garcia, A.; Gacoin, T.; Boilot, J.-P. *J. Am. Chem. Soc.* **2010**, *132*, 10967–10969.
- [285] Sagara, Y.; Kato, T. *Angew. Chem.* **2008**, *120*, 5253–5256.
- [286] Kozhevnikov, V. N.; Donnio, B.; Bruce, D. W. *Angew. Chem.* **2008**, *120*, 6382–6385.
- [287] Löwe, C.; Weder, C. *Adv. Mater.* **2002**, *14*, 1625–1629.
- [288] Kinami, M.; Crenshaw, B. R.; Weder, C. *Chem. Mater.* **2006**, *18*, 946–955.
- [289] Luo, X.; Li, J.; Li, C.; Heng, L.; Dong, Y. Q.; Liu, Z.; Bo, Z.; Tang, B. Z. *Adv. Mater.* **2011**, *23*, 3261–3265.
- [290] Tsukuda, T.; Kawase, M.; Dairiki, A.; Matsumoto, K.; Tsubomura, T. *Chem. Commun.* **2010**, *46*, 1905–1907.
- [291] Mizukami, S.; Houjou, H.; Sugaya, K.; Koyama, E.; Tokuhisa, H.; Sasaki, T.; Kanetsato, M. *Chem. Mater.* **2005**, *17*, 50–56.
- [292] Bi, H.; Chen, D.; Di Li, Yuan, Y.; Xia, D.; Zhang, Z.; Zhang, H.; Wang, Y. *Chem. Commun.* **2011**, *47*, 4135–4137.
- [293] Szerb, E. I.; Talarico, A. M.; Aiello, I.; Crispini, A.; Godbert, N.; Pucci, D.; Pugliese, T.; Ghedini, M. *Eur. J. Inorg. Chem.* **2010**, *2010*, 3270–3277.
- [294] Sagara, Y.; Yamane, S.; Mutai, T.; Araki, K.; Kato, T. *Adv. Funct. Mater.* **2009**, *19*, 1869–1875.
- [295] Roberts, D. R. T.; Holder, S. J. *J. Mater. Chem.* **2011**, *21*, 8256.
- [296] Davis, D. A.; Hamilton, A.; Yang, J.; Cremer, L. D.; van Gough, D.; Potisek, S. L.; Ong, M. T.; Braun, P. V.; Martínez, T. J.; White, S. R.; Moore, J. S.; Sottos, N. R. *Nature* **2009**, *459*, 68–72.
- [297] Schönberg, A.; Elkaschef, M.; Nosseir, M.; Sidky, M. M. *J. Am. Chem. Soc.* **1958**, *80*, 6312–6315.
- [298] Hirata, S.; Watanabe, T. *Adv. Mater.* **2006**, *18*, 2725–2729.
- [299] Lim, S.-J.; An, B.-K.; Jung, S. D.; Chung, M.-A.; Park, S. Y. *Angew. Chem. Int. Ed.* **2004**, *43*, 6346–6350.
-

- 
- [300] Kishimura, A.; Yamashita, T.; Yamaguchi, K.; Aida, T. *Nat. Mater.* **2005**, *4*, 546–549.
- [301] Charitidis, C.; Laskarakis, A.; Kassavetis, S.; Gravalidis, C.; Logothetidis, S. *Superlattice Microst.* **2004**, *36*, 171–179.
- [302] Zhang, X.; Liu, X.; Laakso, J.; Levänen, E.; Mäntylä, T. *Appl. Surf. Sci.* **2012**, *258*, 3102–3108.
- [303] Cui, G.; Bi, Z.; Wang, S.; Liu, J.; Xing, X.; Li, Z.; Wang, B. *Prog. Org. Coat.* **2020**, *148*, 105821.
- [304] Maan, A. M. C.; Hofman, A. H.; Vos, W. M.; Kamperman, M. *Adv. Funct. Mater.* **2020**, *30*, 2000936.
- [305] Glaubitt, W.; Löbmann, P. *J. Eur. Ceram. Soc.* **2012**, *32*, 2995–2999.
- [306] de Jesus, M. A. M. L.; Timò, G.; Agustín-Sáenz, C.; Braceras, I.; Cornelli, M.; Ferreira, A. d. M. *Sol. Energ. Mat. Sol. C.* **2018**, *185*, 517–523.
- [307] Elbourne, A.; Crawford, R. J.; Ivanova, E. P. *J. Colloid Interf. Sci.* **2017**, *508*, 603–616.
- [308] Zhang, J.; Li, S.; Lu, C.; Sun, C.; Pu, S.; Xue, Q.; Lin, Y.; Huang, M. *Surf. Coat. Technol.* **2019**, *364*, 265–272.
- [309] Durán, I. R.; Laroche, G. *Adv. Colloid Interfac.* **2019**, *263*, 68–94.
- [310] Schiessl, S.; Kucukpinar, E.; Cros, S.; Miesbauer, O.; Langowski, H.-C.; Eisner, P. *Front. Nutr.* **2022**, *9*, 790157.
- [311] Morris, B. A. *The Science and Technology of Flexible Packaging: Multilayer Films from Resin and Process to End Use*, 2nd ed.; *Plastics Design Library*; Elsevier Science & Technology Books: San Diego, **2022**.
- [312] Kaiser, K.; Schmid, M.; Schlummer, M. *Recycling* **2018**, *3*, 1.
- [313] Rovera, C.; Ghaani, M.; Farris, S. *Trends Food Sci. Tech.* **2020**, *97*, 210–220.
- [314] Duncan, T. V. *J. Colloid Interf. Sci.* **2011**, *363*, 1–24.
- [315] Yousefi, H.; Su, H.-M.; Imani, S. M.; Alkhaldi, K.; M Filipe, C. D.; Didar, T. F. *ACS Sens.* **2019**, *4*, 808–821.
- [316] Sari, A. N. A.; Warsiki, E.; Kartika, I. A. *Conf. Ser.: Earth Environ. Sci.* **2021**, *749*, 012009.
- [317] Yam, K. L.; Takhistov, P. T.; Miltz, J. *J. Food. Sci.* **2005**, *70*, R1–R10.
- [318] Kalpana, S.; Priyadarshini, S. R.; Maria Leena, M.; Moses, J. A.; Anandharamakrishnan, C. *Trends Food Sci. Tech.* **2019**, *93*, 145–157.
- [319] Sohail, M.; Sun, D.-W.; Zhu, Z. *Crit. Rev. Food Sci. Nutr.* **2018**, *58*, 2650–2662.
-

- 
- [320] Vanderroost, M.; Ragaert, P.; Devlieghere, F.; de Meulenaer, B. *Trends Food Sci. Tech.* **2014**, *39*, 47–62.
- [321] Lee, S. Y.; Lee, S. J.; Choi, D. S.; Hur, S. J. *J. Sci. Food Agr.* **2015**, *95*, 2799–2810.
- [322] Saliu, F.; Della Pergola, R. *Sensor Actuat. B-Chem.* **2018**, *258*, 1117–1124.
- [323] von Bultzingslöwen, C.; McEvoy, A. K.; McDonagh, C.; MacCraith, B. D.; Klimant, I.; Krause, C.; Wolfbeis, O. S. *Analyst* **2002**, *127*, 1478–1483.
- [324] Wang, J.; Wen, Z.; Yang, B.; Yang, X. *Results Phys.* **2017**, *7*, 323–326.
- [325] Jung, J.; Puligundla, P.; Ko, S. *Food Chem.* **2012**, *135*, 2170–2174.
- [326] Mills, A.; Chang, Q. *Analyst* **1993**, *118*, 839.
- [327] Ghaani, M.; Cozzolino, C. A.; Castelli, G.; Farris, S. *Trends Food Sci. Tech.* **2016**, *51*, 1–11.
- [328] Fitzgerald, M.; Papkovsky, D. B.; Smiddy, M.; Kerry, J. P.; O’Sullivan, C. K.; Buckley, D. J.; Guilbault, G. G. *J. Food. Sci.* **2001**, *66*, 105–110.
- [329] Fang, Z.; Zhao, Y.; Warner, R. D.; Johnson, S. K. *Trends Food Sci. Tech.* **2017**, *61*, 60–71.
- [330] Gupta, V.; Gulati, P.; Bhagat, N.; Dhar, M. S.; Viridi, J. S. *Eur. J. Clin. Microbiol.* **2015**, *34*, 641–650.
- [331] Gokduman, K.; Avsaroglu, M. D.; Cakiris, A.; Ustek, D.; Gurakan, G. C. *J. Microbiol. Meth.* **2016**, *122*, 50–58.
- [332] Tominaga, T. *Food Sci. Technol.* **2017**, *86*, 566–570.
- [333] Ramos, A. C.; Gales, A. C.; Monteiro, J.; Silbert, S.; Chagas-Neto, T.; Machado, A. M. O.; Carvalhaes, C. G. *J. Microbiol. Meth.* **2017**, *142*, 1–3.
- [334] Yang, X.; Tang, Y.; Alt, R. R.; Xie, X.; Li, F. *Analyst* **2016**, *141*, 3473–3481.
- [335] Kim, G.; Lim, J.; Mo, C. *J. Biosyst. Eng.* **2015**, *40*, 277–283.
- [336] Llobet, E. *Sensor Actuat. B-Chem.* **2013**, *179*, 32–45.
- [337] Kerry, J. P.; O’Grady, M. N.; Hogan, S. A. *Meat Sci.* **2006**, *74*, 113–130.
- [338] Lu, L.; Zheng, W.; Lv, Z.; Tang, Y. *Packag. Technol. Sci.* **2013**, *26*, 80–90.
- [339] Chen, H.-Z.; Zhang, M.; Bhandari, B.; Guo, Z. *Postharvest Biol. Tec.* **2018**, *140*, 85–92.
- [340] Salaluk, S.; Jiang, S.; Viyanit, E.; Rohwerder, M.; Landfester, K.; Crespy, D. *ACS Appl. Mater. Inter.* **2021**, *13*, 53046–53054.
- [341] Lu, X.; Li, W.; Sottos, N. R.; Moore, J. S. *ACS Appl. Mater. Inter.* **2018**, *10*, 40361–40365.
-

## References

---

- [342] Pujari, S. P.; Scheres, L.; Marcelis, A. T. M.; Zuilhof, H. *Angew. Chem. Int. Ed.* **2014**, *53*, 6322–6356.
- [343] Hanson, E. L.; Schwartz, J.; Nickel, B.; Koch, N.; Danisman, M. F. *J. Am. Chem. Soc.* **2003**, *125*, 16074–16080.

# Appendix

# Abrasion Indicators for Smart Surfaces Based on a Luminescence Turn-On Effect in Supraparticles

Sarah Wenderoth, Tim Granath, Johannes Prieschl, Susanne Wintzheimer, and Karl Mandel\*

Slight mechanical damage on surfaces or coatings caused, for example, by shear stress, is hardly detectable by simple means. Therefore, shear stress indicator particles for the creation of “interactive and communicating” coatings are presented. These are core-shell supraparticles obtained by a two-step spray-drying assembly process from nanoparticle dispersions. Three different types of nanoparticles are used to create the supraparticles: dye-doped silica nanoparticles responsible for the fluorescence signal, iron oxide nanoparticles acting as a fluorescence absorber, and pure silica nanoparticles regulating the indicator sensitivity. The creation of two different types of indicator systems is feasible by changing the nanoparticle arrangements within the supraparticle: A turn-off and a turn-on system, which indicate—after incorporation into a coating—shear stress by the decrease or the increase in the fluorescence intensity, respectively. Herein, two different mechanisms compete with each other: on the one hand, the change in the fluorescence signal due to physical light-absorbing effects, and on the other hand, the abrasion of luminescent material. The clear superiority of the turn-on system to achieve a reliable signal is demonstrated in this work. With the particle systems, interactive and communicating surface coatings are established.

## 1. Introduction

Many surfaces of man-made objects are equipped with a coating. The coating fulfills specific functions, for instance, as easy-to-clean,<sup>[1]</sup> scratch-resistant,<sup>[2]</sup> antireflexive,<sup>[3]</sup> or antimicrobial<sup>[4]</sup> agent. These functional properties are usually achieved via molecular building blocks, by nanoparticulate coating additives or by imprinting a surface texture. A certain degree of “smartness” can also be achieved by combining several additives<sup>[5,6]</sup> which may turn a surface into a gas sensor,<sup>[7]</sup> a corrosion protection layer,<sup>[8]</sup> or a self-healing layer.<sup>[9]</sup> Although there have always been

solutions to identify deformations in components, such as in metals<sup>[10]</sup> or polymer parts,<sup>[11]</sup> the detection of damages within a surface coating which is only a few micrometers thick still remains a challenge.<sup>[12]</sup> Such a “scratch-detecting” surface indicator must be cheap, easy to manufacture, easy to detect and should be applicable to any type of surface. Some additives for bulk materials have already been presented which are able to detect scratches and repair them directly.<sup>[13]</sup> A disadvantage of these systems is, however, that they only do work in a bulk material and not in a coating of a few microns thickness.

In this study, we report on shear stress indicators in the form of so-called supraparticles that can be used as damage detectors in thin coatings. These indicator supraparticles are micron-sized, hierarchically structured particles and are composed of nanoparticles. The great advantage of such supraparticles is that a number of very different properties can be combined by assembling different nanoparticle building

blocks which carry specific attributes (e.g., magnetism, fluorescence, catalytic activity, etc.).<sup>[14]</sup> Forced assembly of nanoparticles can be achieved by spray-drying. This process is well-known and well established, for instance, in the pharmaceutical or food industry, to obtain dry powder products (such as granular drugs or instant coffee).<sup>[15]</sup> Complex architectures can be achieved by repeating this process: In a first spray-drying cycle, supraparticles can be formed from a nanoparticle dispersion. Within a second spray-drying cycle, the supraparticles resulting from the first spray-drying cycle can be coated with other nanoparticles to ultimately obtain core-shell supraparticles.

S. Wenderoth, T. Granath  
Chair of Chemical Technology of Materials Synthesis  
Julius-Maximilians-University Würzburg  
Röntgenring 11, D97070 Würzburg, Germany

The ORCID identification number(s) for the author(s) of this article can be found under <https://doi.org/10.1002/adpr.202000023>.

© 2020 The Authors. Published by Wiley-VCH GmbH. This is an open access article under the terms of the Creative Commons Attribution License, which permits use, distribution and reproduction in any medium, provided the original work is properly cited.

DOI: 10.1002/adpr.202000023

T. Granath, J. Prieschl, Dr. S. Wintzheimer, Prof. K. Mandel  
Departement of Chemistry and Pharmacy  
Inorganic Chemistry  
Friedrich-Alexander University Erlangen-Nürnberg (FAU)  
Egerlanderstrasse 1, D91058 Erlangen, Germany  
E-mail: karl.mandel@fau.de

Prof. K. Mandel  
Fraunhofer Institute for Silicate Research  
ISC  
Neunerplatz 2, D97082 Würzburg, Germany

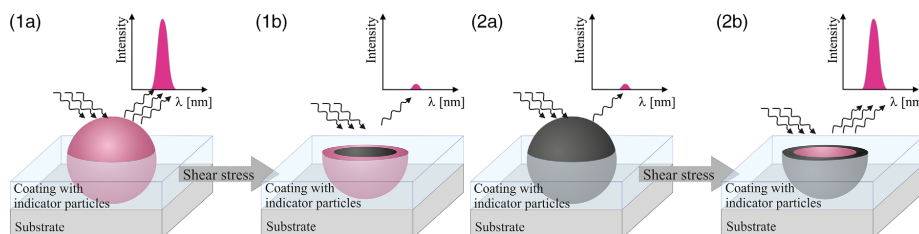
Such a core-shell supraparticle system was developed herein as a shear indicator. The indication of damage is realized through the irreversible change in an optical signal from bright to dark (turn-off) or from dark to bright (turn-on). To achieve this, an emitter and an optical absorber are arranged within the supraparticle core or the shell. In a first approach, the optical absorber part forms the supraparticle core and the emitter part forms the supraparticle shell. The resulting indicator supraparticles are called “turn-off supraparticles”. Conversely, with the emitter in the supraparticle core and the optical absorber in the supraparticle shell, “turn-on supraparticles” are obtained in a second approach. If the indicator supraparticles are then embedded in a coating, they form a molehill-like structure.<sup>[5]</sup> This means that the particles are only embedded (held) in a thin lacquer layer at their bottom, whereas their “heads” stand out of the coating. During the shearing process, the heads of the particles are chopped off stepwise. This abrasion process can be measured by changes in the optical signal from the emitter part of the indicator supraparticles. In this way, not only a damage of the obtained coating can be measured but, moreover, the process of increasing damage can be recorded.

## 2. Results and Discussion

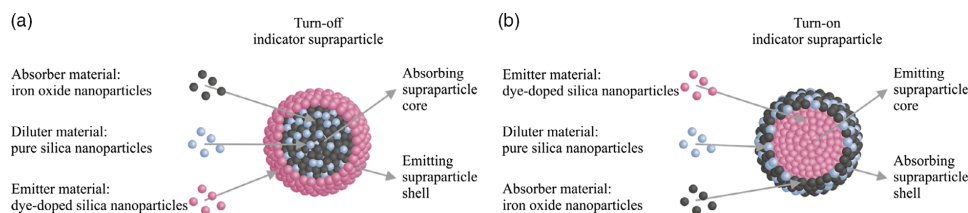
By the tailored combination of an emitting nanoparticle system and an optical absorbing one, a core-shell supraparticle was assembled, where either the optical absorber part is in the supraparticle core and the emitter part in the supraparticle shell (so-called “turn-off indicator supraparticles”), or vice versa (so-called “turn-on indicator supraparticles”). Both supraparticle types can

be embedded in a coating. By analyzing the fluorescence of the intact, as-prepared turn-off system, a fluorescence signal of a certain intensity can be detected (Scheme 1 (1a)). During an abrasion process, the optical signal decreases to an endpoint of significantly less intensity (Scheme 1(1b)). In contrast to this, the mechanism for the turn-on indicator supraparticles is exactly the other way round, as they exhibit nearly no fluorescence in the intact state (Scheme 1(2a)), while in the sheared state, they yield a bright fluorescence signal (Scheme 1(2b)).

In practice, the structure of the indicator supraparticles is more complex than described previously in a simplified way for a better understanding. The indicator supraparticles used herein consist of three different nanoparticle components (Scheme 2). First, these are dye-doped silica nanoparticles, which are responsible for the optical signal; second, iron oxide nanoparticles, which act as an optical absorber material, and third, pure silica nanoparticles that dilute the optical absorber material to adjust the sensitivity of the whole indicator particle. (The fluorescence spectra of all building blocks in comparison to the achieved supraparticles are shown in Figure S1, Supporting Information, as well as the UV-vis spectra of the nanoparticle dispersions and the rhodamine B dye in Figure S2, Supporting Information). In principle, these building blocks might seem very similar to the ones described by us in a previous publication.<sup>[16]</sup> However, the resulting indicator system of this preliminary work was based on a rather complex multi-particle-object-system, whereas herein, a single-entity-system is established, i.e., all three indicator components are hierarchically collocated within one single supraparticle entity. In addition to this clear difference, the newly developed indicator supraparticles come with further significant advantages.



**Scheme 1.** Indicator supraparticles embedded in coatings and their fluorescence signal in case of 1a) an intact turn-off supraparticle, 1b) a sheared-off turn-off supraparticle, 2a) an intact turn-on supraparticle, and 2b) a sheared-off turn-on supraparticle. For each state, the corresponding theoretical/expected fluorescence intensity graph is shown.



**Scheme 2.** Schematic structure of a) a turn-off indicator supraparticle and b) a turn-on indicator supraparticle. Black spheres: iron oxide nanoparticles acting as optical absorber, blue spheres: pure silica nanoparticles acting as “diluter”, pink spheres: dye-doped silica nanoparticles acting as emitter.

First, the dye (rhodamine B) responsible for the fluorescence of the indicator supraparticles is covalently bound to the silica particle matrix. This prevents leaching of the dye from the nanoparticle (see Section 1 in the Supporting Information) and subsequent dissipation into the entire coating. Therefore, it can be ensured that the obtained fluorescence signal really originates from the indicator particles and is not a nonreliable fluorescence response of the system. Furthermore, by having selected nano iron oxide as optical absorber material, the system was also equipped with magnetic properties, as the iron oxide nanoparticles are superparamagnetic.<sup>[17]</sup> That enables a magnetic purification process, i.e., washing the samples after assembly in water and separating only the magnetic fraction of the supraparticle with a magnet. This guarantees that excess pure silica supraparticles, that might have formed and do not contain any magnetic fraction (and therefore contain no optical absorber either), can be removed from the desired core-shell supraparticle entities (see Figure S3, Supporting Information). The magnetic purification step is crucial, as bare silica supraparticles are always a side product of twofold spray-drying processes, and their presence would deteriorate the indicator function of the coating.

To be able to transfer the theoretical illustration as described earlier into real samples, further issues must be addressed.

First, it is important that the supraparticle core is covered fully by the shell material to guarantee a homogenous turn-off or turn-on behavior during abrasion processes. This is why the nanoparticles that had been designed to form the future supraparticle core of the desired supraparticle entity, were surface functionalized with (3-aminopropyl)triethoxysilane (APTES) molecules. Through this modification, the particles are positively charged at an acidic pH value, which was found in this study—and also in another work earlier<sup>[18]</sup>—to be crucial to enhance the proper assembly of the negatively charged shell-particles around the core particles.

Second, the iron oxide nanoparticles used are coated with silica. These nanoparticles will be referred to further in the manuscript as iron oxide@silica nanoparticles. The idea of this step is to camouflage the iron oxide nanoparticles with silica so that their surfaces are silica and thus the “perception” of the surroundings (solvent, other particles, silane molecules, etc.) toward this particle system is the same as for pure silica nanoparticles. Moreover, by adjusting the shell thickness of silica (of which the adjustment of the necessary parameters during shell formation are well-known),<sup>[17,19]</sup> the primary nanoparticle diameters of iron oxide and pure silica can be matched for the iron oxide@silica nanoparticles to be comparable to the sizes of pure silica nanoparticles. This is crucial to be able to conduct the spray-drying process of the two sorts of nanoparticles without risking to obtain a certain structural arrangement caused by different sizes, as it would otherwise be the case for a bimodally size-distributed system during spray-drying.<sup>[20]</sup> Furthermore, as the silica shell surrounds the iron oxide nanoparticles, modification with APTES can be done in the same way as for pure silica nanoparticles. Therefore, both systems can be considered as equal with respect to their surface nature and can both be treated in the same way.

In **Figure 1**, the schematic cross-section of indicator supraparticles is assigned to real samples imaged via scanning electron microscope (SEM) (further cross-sections of supraparticles are shown in Figure S4, Supporting Information). The theoretical sketches of the envisaged supraparticles (Figure 1(1a,2a)) correspond quite well to the real samples obtained from the designed assembly process (Figure 1(1b,2b)). The iron oxide@silica nanoparticles and the pure silica nanoparticles within the supraparticle core (turn-off, Figure 1(1)), and in the supraparticle shell (turn-on, Figure 1(2)) respectively, are distributed statistically. Thus, no preferred arrangement is detectable, as it was originally intended (see aforementioned explanation). This statistical

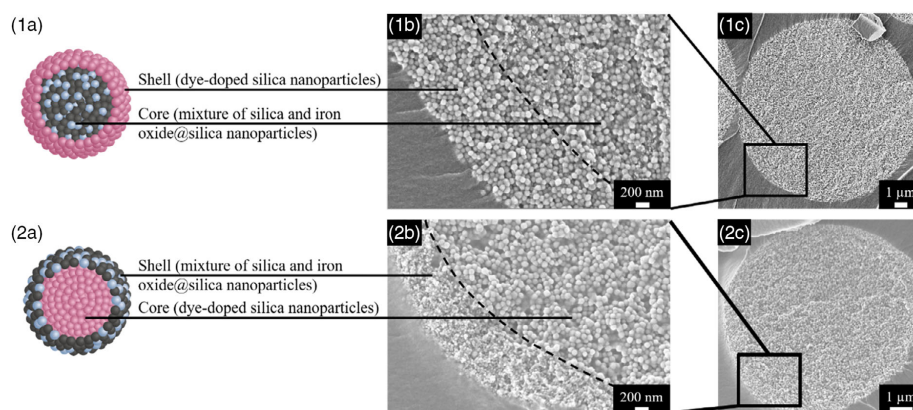


**Figure 1.** a) Comparison between schematic cross-section of supraparticles and b) real SEM images with description of the different parts in case of 1b) a turn-off supraparticle (“turn-off sample 3”) and 2b) turn-on supraparticle (“turn-on sample 2”) edged by a lacquer matrix. c) The SEM images on the right-hand side depict the whole cross-section of the supraparticles. (Color code of the scheme on the left-hand side: pink spheres: dye-doped silica nanoparticles, blue spheres: pure silica nanoparticles, black spheres: iron oxide@silica nanoparticles).

distribution ensures a homogenous absorbance of the fluorescence over the entire system during the shear-off process. The core and the shell sections of the supraparticles can be well distinguished, and the shell covers the entire core. The supraparticle cores, as well as the entire supraparticles, exhibit a spherical morphology (Figure 1 (1c,2c)). The supraparticle size distributions are shown in Figure S5, Supporting Information. The morphology of spray-dried supraparticles depends on different parameters. Not only do the technical parameters of the used spray-dryer (temperature, gas flow, nozzle, ...) have an eminent influence but also the sample properties (material, concentration, solvent, viscosity, ...) as well.<sup>[20,21]</sup> Interestingly, the spherical morphology, which is of advantage for our approach, is crucially enhanced by the APTES-functionalization of the nanoparticles of the supraparticle core. Nonmodified nanoparticles only resulted in nonspherical supraparticles (Figure S6, Supporting Information). Only with the help of spherical supraparticles, it is possible, that during the abrasion process, the supraparticles are evenly sheared. As they all have the same shell thickness, the ratio of absorber to emitter in each particle is the same, yielding homogeneous macroscopic fluorescence signals.

After integration into coatings, no difference between both systems can be found at the first glance (SEM studies, Figure 2 and Figure S7, Supporting Information). Their visible appearance is shown in Figure S8, Supporting Information (supraparticle-loaded coatings on a transparent film). Prior to abrasion, both samples provide the targeted molehill-like

structure (Figure 2 (1a,2a)) which is caused by the application of the coating with a spiral doctor blade (for more details see the Experimental Section). The supraparticles are partly embedded in the coating layer and partly stick out of it while still being covered by a thin coating film. For abrasion tests of the coatings, a cube-shaped stamp was used and up to either 1500 (for the turn-on samples) or 3000 shear cycles (for the turn-off samples) were carried out. One cycle denotes the movement of the stamp forward and backward over a length of 7 cm (for more information see Experimental Section). After 750 shear cycles, large parts of the supraparticles are evenly sheared-off/chopped-off and removed, laying open the particles' cross-sections (Figure 2 (1b,2b)). This indicates that during the abrasion process, the nonembedded part of the supraparticles is removed stepwise.

Although no differences in the particle structures of the two systems can be detected in SEM studies, fluorescence spectroscopy reveals that, in fact, the two systems react very differently (Figure 3 and 4). In Figure 3, the fluorescence intensity is normalized to the last value measured after 3000 shear cycles, which corresponds to the number of shear cycles where the coating is still intact macroscopically (beyond 3000 cycles, macroscopic cracks start to appear). The fluorescence intensity normalized to the initial fluorescence value of each sample is shown in Figure S9, Supporting Information.

In general, for the turn-off system, two different mechanisms compete during the abrasion process: On the one hand, the

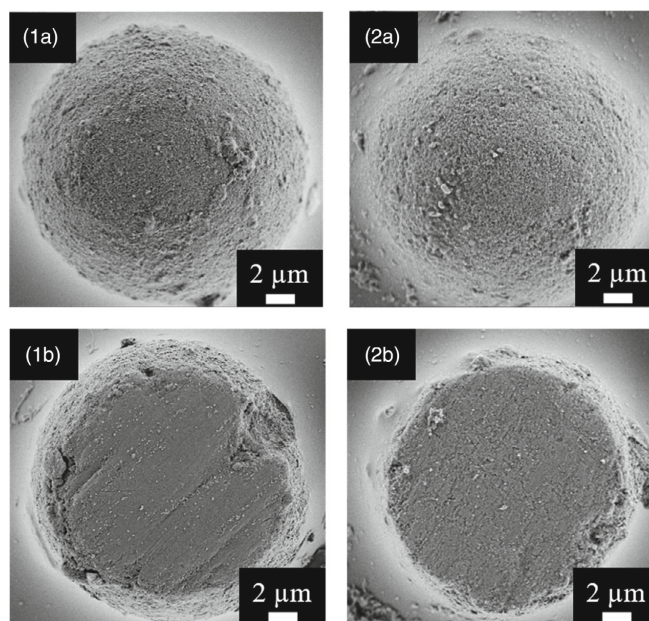


**Figure 2.** SEM images of supraparticles embedded in a coating, a) before and b) after the shear process for both systems (turn-off: 1a, 1b; turn-on: 2a, 2b).

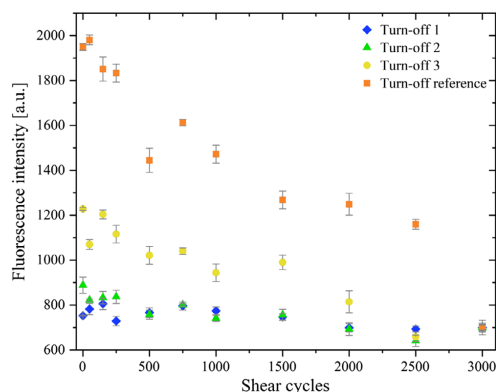


**Figure 3.** Normalized fluorescence intensities of turn-off indicator supraparticles as a function of shear cycles (blue diamonds, green triangles, yellow dots (Turn-off 1–3): different ratios between iron oxide@silica optical absorber to silica diluter nanoparticles in the core of the supraparticles; orange squares: reference sample, i.e., only pure silica nanoparticles without optical absorbing part are spray-dried for the supraparticle core). The samples were excited at 540 nm and the emitted signal was measured at 579 nm.

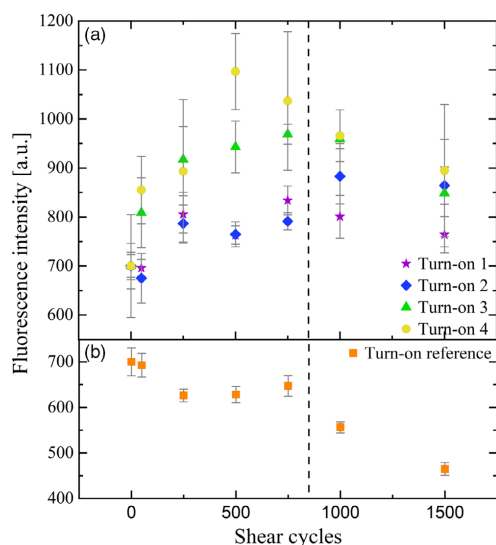


**Figure 4.** Normalized fluorescence intensities of turn-on indicator supraparticles as a function of shear cycles (a) purple stars, blue diamonds, green triangles, yellow dots (Turn-on 1–4): different ratios between iron oxide@silica optical absorber to silica diluter nanoparticles in the shell of the supraparticle system; b) orange squares: reference sample, i.e., only pure silica nanoparticles without optical absorbing part spray-dried to the supraparticle shell). The black dashed line indicates the start of particle loss domination. The sample was excited at 540 nm and the emitted signal was measured at 579 nm.

fluorescence decreases by the stepwise uncovering of the supraparticle optical absorbing core, as this causes light absorption. On the other hand, the fluorescence decreases, simply because luminescent components are removed from the supraparticle. To determine which effect predominates, a reference sample was prepared that does not contain an optical absorbing component, i.e., a supraparticle system that is exclusively composed of dye-doped silica nanoparticles. As it is evident (Figure 3, orange squares), this sample shows an even stronger decrease in fluorescence intensity than the other optical absorber-containing samples (blue diamonds, green triangles, and yellow dots in Figure 3). This leads to the conclusion that the turn-off effect is mainly caused by the loss of particles and not by the uncovering of light-absorbing cores. Due to different amounts of optical absorber, i.e., iron oxide@silica within the supraparticles, the samples turn-off 1 to turn-off 3 logically show a lower initial fluorescence intensity than the reference sample without iron oxide and consequently, a lower fluorescence intensity decline. The more iron oxide@silica is present in the supraparticle core, the lower are the fluorescence losses during the abrasion process, as most of the fluorescence has already been absorbed from the very beginning. Therefore, the turn-off effect detected herein is not caused by the light-absorbing core, but mainly by the loss of fluorescent particles. The major disadvantage of the turn-off system is that it cannot reliably monitor the damaging process as there is always the risk of obtaining interference signals if the sheared-off luminescent particle fragments are not completely removed from the sample.

In contrast to the turn-off indicator supraparticles, the effect of particle loss seems to play a subordinate role for the turn-on indicator supraparticles; at least in the beginning of an abrasion process, which is of main interest for the indication of damages arising.

As a compact layer of optical absorber material initially shields the fluorescence from the supraparticle core, a fluorescent cross-section, constantly growing in size, is exposed during the abrasion process. This consequently increases the overall fluorescence of the sample (Figure 4 and Figure S10 in the Supporting Information). In Figure 4, the fluorescence of the samples is normalized to the lowest detectable intensity, which is in this case the initial intensity. In the beginning, the extent of the gain in fluorescence mainly depends on the ratio of optical absorber to nonoptical-absorber material in the supraparticle shell: The more nonoptical-absorber material is present, the stronger is the increase in fluorescence (yellow dots, Figure 4). This is due to the higher overall amount of optical absorbing material. The maximum fluorescence intensity can be achieved for all samples (turn-on 1—turn-on 4) when supraparticles are sheared down to hemispheres. At this point, the emitting area is largest and the optical absorbing shell area is quite small. If abrasion continues, two mechanisms play a role: first, the distance of the measured surface on top to the optical absorbing shell at the bottom of each supraparticle, so that the fluorescence can be more efficiently optical absorbed again and second, the overall particle loss caused by abrasion. When comparing the reference sample, i.e., supraparticles composed of dye-doped silica core and pure silica shell (Figure 4b), with the turn-on samples, the “particle loss mechanism” becomes evident: The reference (orange squares, Figure 4b), which does not contain

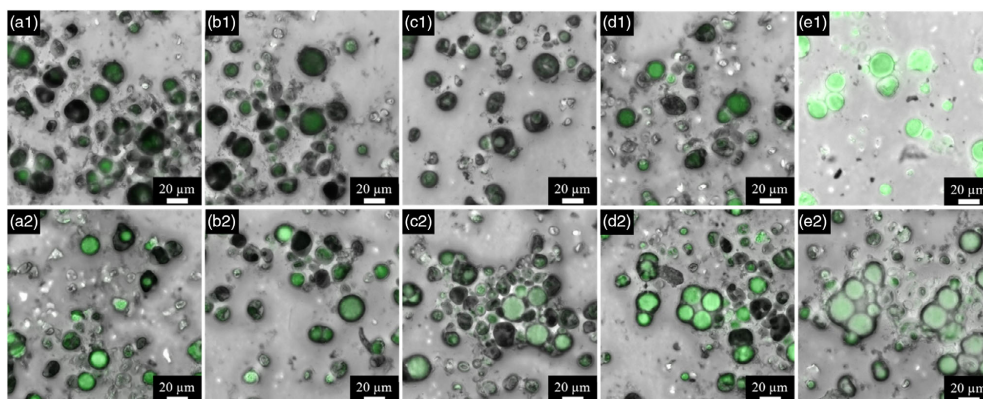


**Figure 5.** Confocal microscopy images of turn-on indicator supraparticles before (upper row/1) and after 750 shear cycles (bottom row/2). Images a–d) show turn-on supraparticles (samples “Turn-on 1 to 4”) with decreasing amounts of optical absorber material in the shell. Images e) show the reference sample without any optical absorber part.

any optical absorber, shows a decrease in the optical signal with increasing abrasion. This decrease remarkably steepens to a certain extent after 750 abrasion cycles, which can be explained by the loss of luminescent nanoparticles. A similar luminescence loss after an initial increase can be observed for the turn-on samples beyond 500–1000 shear cycles (Figure 4a). Furthermore, after 1500 shear cycles, the fluorescence intensity of the turn-on samples (purple stars, blue diamonds, green triangles, and yellow dots, Figure 4a) is clearly converging and drops almost back to the initial level of fluorescence of the samples. At this point, it is very probable that the ratio between optical absorbing and emitting material changes in each supraparticle. With proceeding shear, more and more emitting core nanoparticles are sheared-off, while the amount of optical absorbing materials stays nearly constant, as the bottom of the particles is not removed.

When using confocal microscopy (Figure 5), the increase in fluorescence intensity upon shear can be visualized on the microscale for the turn-on samples as well as the decrease in fluorescence for the reference sample, giving a visible support for the process described herein.

The focus of the presented work was on delivering a proof-of-principle that shear stress can be indicated via single, complex particles. As a detailed application evaluation and test study would go beyond the scope of this work, we herein restrict ourselves in the following to only outlining the potential of the developed particles:

One possibility of applying the supraparticles could be as an additive in barrier coatings for food packaging. In food conservation, already very small micro-scratches cause gases such as oxygen to penetrate through the protective foil, either yielding food that is no longer fresh and tasty, or worse, causing sickness when eaten.<sup>[12]</sup> With the indicator supraparticle presented here, an on-the-fly detection is possible. With a simple UV lamp, a quality check can be performed and a potential presence of scratches is indicated—in particular, obvious in case of

the turn-on shear stress indicator supraparticles where the coating would suddenly “glow colorful” due to the switched-on fluorescence. In the same way, another conceivable application of these indicator supraparticles could be for the packaging of biological or medical products, where it must be ensured that the interior is kept sterile. Again, an instant, quick and easy UV-lamp-check could be sufficient so that, e.g., users can assure themselves that the packaging is intact and thus the interior sterile.

### 3. Conclusion

In conclusion, this work presents shear stress indicator supraparticles in thin coatings, enabling smart surfaces. Via the spray-drying process, highly structured core-shell supraparticle systems were achieved based on nanoparticle building blocks, incorporating directly opposed properties (luminescence or light absorbance). By embedding those in a thin coating, a molehill-like structure was obtained, which can be sheared-off by mechanical forces. During the study of turn-on and turn-off indicators, i.e., supraparticles showing increasing or decreasing luminescence intensities upon shear stress, respectively, two possible force indication mechanisms were elucidated: The turn-off effect is mainly caused by the simple loss of material during the shear-off process. The turn-on mechanism, however, bases on the stepwise uncovering of the fluorescent supraparticle cores. The enlargement of the luminous cross-sectional area with simultaneous reduction of the light-absorbing parts enables a reliable monitoring of damage. The straightforward integration of the newly developed indicator supraparticles into coatings enables the conversion of arbitrary objects into smart and communicating items. A possible application for these indicator supraparticles could be their integration into coatings of packages of sensible goods to indicate damage of the package, for instance, due to micro-scratches.

#### 4. Experimental Section

**Materials:** All chemicals were purchased from Aldrich (Germany), except for FeCl<sub>3</sub>·6 H<sub>2</sub>O, which was purchased from Honeywell. All chemicals were used without further purification. For all syntheses, deionized water was used. Nanoparticle suspension purification steps were performed by dialysis, using a cellulose hydrate membrane (molecular weight cut-off: 10 kDa, Nadir-dialysis tubing, Roth, Germany).

**Nanoparticle Synthesis:** The synthesis of silica nanoparticles is based on the Stöber protocol.<sup>[22]</sup> In a typical experiment, 300 mL of ethanol was mixed with 15 g of 25% aqueous ammonia solution. After 5 min of stirring, 15 g (0.072 mol) tetraethoxysilane (TEOS) was added rapidly. This mixture was stirred for 24 h. 100 mL water was added; the ethanolic-ammoniacal solution was first removed by rotary evaporation and further the particle suspension was purified by subsequent dialysis against water (4 L, water exchanges after 30, 90, 240, 480 min) for 24 h.

For dye-doped silica nanoparticles, 9 mg (0.017 mmol) of rhodamine B isothiocyanate was dissolved in 2 mL of dimethyl sulfoxide. Then, 13 µL (0.055 mmol) of APTES was added and mixed for 24 h. An aliquot of 300 µL of this dye solution was added 30 min after TEOS had been added to the particle reaction. The purification of the dye-doped nanoparticle suspension was done as described previously.

The synthesis of iron oxide nanoparticles and their silica shell was done according to literature<sup>[17]</sup> and is just shortly described here as follows: 21.6 g (80 mmol) FeCl<sub>3</sub>·6 H<sub>2</sub>O and 7.9 g (40 mmol) FeCl<sub>2</sub>·4 H<sub>2</sub>O were dissolved in 1 L water. The precipitation of iron oxide nanoparticles was initiated by addition of 50 mL of 25% aqueous ammonia solution. The obtained precipitate was washed with water until reaching a neutral pH value and further stabilized with 1 L of citric acid solution (0.05 M). Afterward, the nanoparticles obtained were washed several times to remove the excess of citric acid and were then redispersed in water.

For the silica shell, 700 mg dispersed iron oxide nanoparticles were mixed with water to reach a final weight of 80 g and were then mixed with 320 mL of ethanol and 4 mL of 25% aqueous ammonia solution. TEOS was added in six steps every 8 h (300, 450, 600 µL, ...). The purification was done in the same way as described for silica nanoparticles.

The calculation of the APTES modification was carried out according to Stauch et al.<sup>[23]</sup> Therefore, a theoretical number of 4.6 OH groups per nm<sup>2</sup> was chosen for a full APTES modification of silica as well as iron oxide@silica nanoparticles.<sup>[24]</sup> In both cases, 1 g nanoparticles were mixed with 12 g ethanol and 120 µL of 25% aqueous ammonia solution (to generate a Stöber-like environment). After 5 min stirring, either 100 µL APTES in case of silica or 150 µL APTES in case of iron oxide@silica were added. After 24 h of stirring, the particles were purified via dialysis (as described previously).

**Supraparticle Preparation and Coating:** Core-shell supraparticles, consisting of a core supraparticle and coated with a nanostructured shell were obtained in a two-step spray-drying process. In general, the weight ratio of core to shell was set to 1:1. During all shell-creation processes, 25 mg citric acid monohydrate was added to set the pH to 4, to obtain a positively charged surface of the supraparticles. For both systems, the iron oxide@silica phase was diluted with pure silica nanoparticles in different weight ratios. Furthermore, two reference samples were created: one consisting of a pure dye-doped silica core and unmodified silica shell, for the turn-on series, and other an unmodified silica core with a dye-doped silica shell, for the turn-off series. In Table 1, a detailed list of mixing ratios for the iron oxide@silica to silica is outlined.

For all spray-drying steps, in both cases (turn-off and turn-on), a B-290 mini spray-dryer (Büchi, Switzerland) with an ultrasonic nozzle was used. The inlet temperature was set to 140 °C and the outlet temperature was 80–90 °C during the whole process. The power of the ultrasonic nozzle was set to 5 W.

For the coating preparation, a polyolefin film was first treated two times by corona application (Arcotec treater, Germany) at 0.8 kV and then coated with a lacquer. The lacquer formulation utilized herein is described in previous work.<sup>[5]</sup> 1.5 mL of this lacquer were mixed with 150 mg supraparticles and applied onto the polyolefin film with a 20 µm spiral doctor blade on a Coatmaster 509 MC (Erichsen Testing Equipment, Germany).

**Table 1.** Summary of mixing ratios for the iron oxide@silica optical absorber to silica diluter nanoparticles in turn-off (core) and turn-on (shell) supraparticles.

Sample	Ratio iron oxide@silica optical absorber to silica diluter nanoparticles	m	
		(iron oxide@silica)	(pure silica)
		[mg]	[mg]
Turn-off 1	1:1	1000	1000
Turn-off 2	1:3	500	1500
Turn-off 3	1:7	250	1750
Turn-off-reference	0:1	0	2000
Turn-on 1	1:0	2000	0
Turn-on 2	20:1	1905	95
Turn-on 3	10:1	1819	181
Turn-on 4	5:1	1667	333
Turn-on-reference	0:1	0	2000

The curing of the coatings was done for 10 min at room temperature and then for 30 min at 90 °C.

**Analyses:** For coating tests, an automated crockmeter (Tomsic, Italy) was used. For this purpose, the coated substrates were fixed on a rigid metal plate and the abrasion finger was set in a 90° angle on top of the film. This 1.5 cm thick finger was covered by a SiC abrasion paper with a roughness of #4000 and a grain size of 5 µm (Struers, Germany). The test parameters were set as follows: load of the finger = 4 N, track length = 7 cm, cycling numbers = 0–1500 for turn-on, and 0–3000 for turn-off samples.

Fluorescence spectroscopy was conducted using a spectrofluorometer FP8600 (Jasco, Japan) with a cuvette sample holder for the washing steps and nanoparticle testing (Figure S1–S3 Supporting Information), and with a solid sample holder (FDA-808, Jasco, Japan) for coating measurements. The excitation wavelength was set to 540 nm and the fluorescence signal was measured in a range between 560 and 650 nm.

The examination of the supraparticle surface as well as cross-section morphologies of turn-off and turn-on indicator supraparticles was performed using a Supra 25 SEM (Zeiss, Germany) SEM at 2 kV (field emission) and a working distance of 3.7 mm. Powder samples were prepared on a carbon pad which was placed on a SEM sample holder. The cross-section samples were prepared by dispersing 10 mg of supraparticles in 500 µL lacquer, curing then at 100 °C and cutting them with a scalpel. Furthermore, these samples were fixed on a SEM sample holder with conductive silver and sputtered with platinum for 5 s at 50 mA (MED 010, Balzers Union).

Confocal microscopy measurements were performed using a Leica TCS SP8 (Leica Microsystems GmbH, Germany) with a 63×/1.40 water immersion objective and a white light laser SuperK Extreme EXW. The rhodamine B dye was excited at 540 nm and the fluorescence signal was detected in a range between 560 and 750 nm. A transmission light image was recorded simultaneously to detect the nonfluorescent parts of the sample.

#### Supporting Information

Supporting Information is available from the Wiley Online Library or from the author.

#### Acknowledgements

This work was financially supported by the BMBF (NanoMatFutur grant 03XP0149) and the DFG (grant MA 7252/4-2), which are gratefully

acknowledged. The authors thank BÜCHI Labortechnik AG for providing the spray-dryer equipment.

### Conflict of Interest

The authors declare no conflict of interest.

### Keywords

abrasion indicators, communicating materials, smart surfaces, supraparticles, turn-on fluorescence

Received: August 3, 2020

Revised: August 25, 2020

Published online: September 16, 2020

- [1] X. Zhang, X. Liu, J. Laakso, E. Levänen, T. Mäntylä, *Appl. Surf. Sci.* **2012**, 258, 3102.
- [2] D. K. Hwang, J. H. Moon, Y.-G. Shul, K. T. Jung, D. H. Kim, D. W. Lee, *J. Sol-Gel Sci. Techn.* **2003**, 26, 783.
- [3] W. Glaubitt, P. Löbmann, *J. Eur. Ceram. Soc.* **2012**, 32, 2995.
- [4] A. Elbourne, R. J. Crawford, E. P. Ivanova, *J. Colloid Interf. Sci.* **2017**, 508, 603.
- [5] T. Ballweg, C. Gellermann, K. Mandel, *ACS Appl. Mater. Inter.* **2015**, 7, 24909.
- [6] a) R. P. Wool, *Soft Matter* **2008**, 4, 400. b) M. Oppmann, F. Miller, S. Thürauf, P. Groppe, J. Prieschl, C. Stauch, K. Mandel, *ACS Appl. Mater. Inter.* **2018**, 10, 14183.
- [7] S. Wintzheimer, M. Oppmann, M. Dold, C. Pannek, M.-L. Bauersfeld, M. Henfling, S. Trupp, B. Schug, K. Mandel, *Part. Part. Syst. Char.* **2019**, 36, 1900254.
- [8] M. F. Montemor, *Surf. Coat. Tech.* **2014**, 258, 17.
- [9] B. J. Blaiszik, S. L. B. Kramer, S. C. Olugebefola, J. S. Moore, N. R. Sottos, S. R. White, *Ann. Rev. Mat. Res.* **2010**, 40, 179.
- [10] A. Augustyniak, J. Tsavalas, W. Ming, *ACS Appl. Mater. Inter.* **2009**, 7, 2618.
- [11] M. Stratigaki, R. Göstl, *ChemPlusChem* **2020**.
- [12] T. V. Duncan, *J. Colloid Interf. Sci.* **2011**, 363, 1.
- [13] S. R. White, N. R. Sottos, P. H. Geubelle, J. S. Moore, M. R. Kessler, S. R. Sriram, E. N. Brown, S. Viswanathan, *Nature* **2001**, 409, 794.
- [14] S. Wintzheimer, T. Granath, M. Oppmann, T. Kister, T. Thai, T. Kraus, N. Vogel, K. Mandel, *ACS nano* **2018**, 12, 5093.
- [15] a) A. Gharsallaoui, G. Roudaut, O. Chambin, A. Voilley, R. Saurel, *Food Res. Int.* **2007**, 40, 1107. b) R. Vehring, *Pharm. Res.* **2008**, 25, 999.
- [16] S. Wintzheimer, J. Reichstein, S. Wenderoth, S. Hasselmann, M. Oppmann, M. T. Seuffert, K. Müller-Buschbaum, K. Mandel, *Adv. Funct. Mater.* **2019**, 29, 1901193.
- [17] K. Mandel, M. Straßer, T. Granath, S. Dembski, G. SEXTL, *Chem. Commun.* **2015**, 51, 2863.
- [18] a) S. Wintzheimer, F. Miller, J. Prieschl, M. Retter, K. Mandel, *Nanoscale Adv.* **2019**, 1, 4277. b) A. B. D. Nandiyanto, T. Ogi, W.-N. Wang, L. Gradon, K. Okuyama, *Adv. Powder Technol.* **2019**, 30, 2908.
- [19] H. L. Ding, Y. X. Zhang, S. Wang, J. M. Xu, S. C. Xu, G. H. Li, *Chem. Mater.* **2012**, 24, 4572.
- [20] A. B. D. Nandiyanto, K. Okuyama, *Adv. Powder Technol.* **2011**, 22, 1.
- [21] F. Iskandar, L. Gradon, K. Okuyama, *J. Colloid Interf. Sci.* **2003**, 265, 296.
- [22] W. Stöber, A. Fink, E. Bohn, *J. Colloid Interf. Sci.* **1968**, 26, 62.
- [23] C. Stauch, S. Süß, R. Luxenhofer, B. P. Binks, D. Segets, K. Mandel, *Part. Part. Syst. Char.* **2018**, 35, 1800328.
- [24] L. T. Zhuravlev, *Colloid Surface A* **2000**, 173, 1.

**WILEY-VCH**

Copyright WILEY-VCH Verlag GmbH & Co. KGaA, 69469 Weinheim, Germany, 2016.

## Supporting Information

### **Abrasion indicators for smart surfaces based on a luminescence turn-on effect in supraparticles**

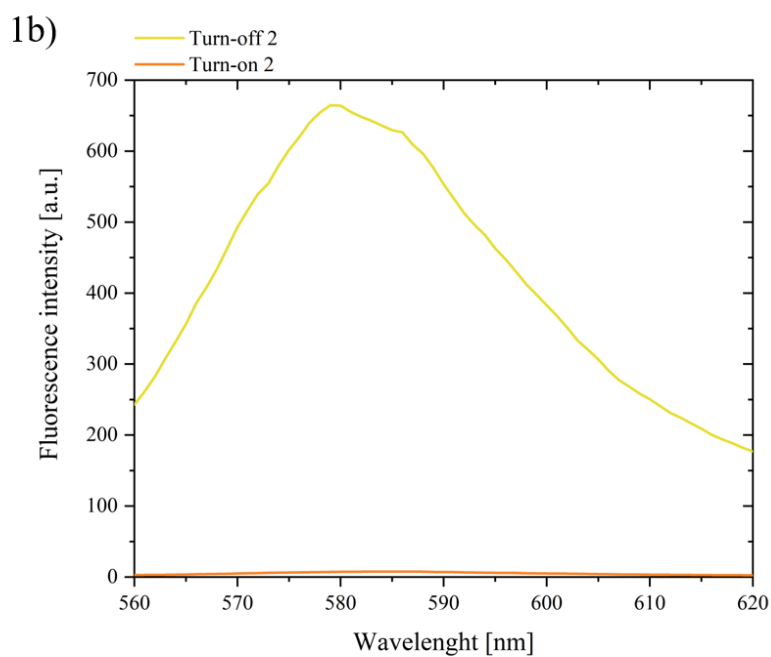
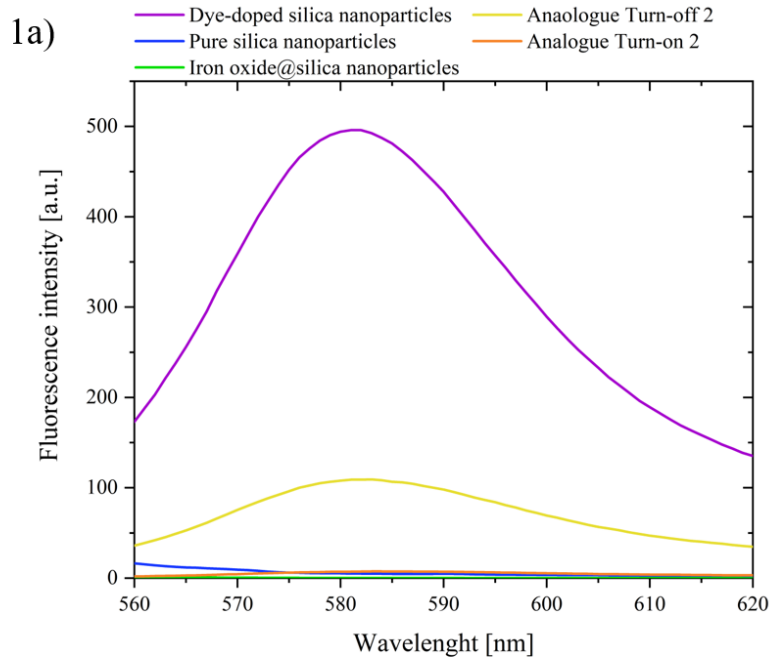
*Sarah Wenderoth, Tim Granath, Johannes Prieschl, Susanne Wintzheimer, and Karl Mandel\**

WILEY-VCH

**1. Leaching experiments of dye-doped silica nanoparticles and fluorescence and UV-vis spectra of pure nanoparticles and mixtures**

Leaching experiments were performed to ensure that the dye molecules were covalently bound within the silica nanoparticles. Therefore, 500  $\mu\text{L}$  of dye-doped silica nanoparticle suspension were filtered through a membrane with a cut-off of  $\sim 30$  kDa by centrifugation (16000 g, 5 min). In the filtrate, less than 1 % of the initial fluorescence intensity was detected via fluorescence spectroscopy. This indicates a permanent coupling of the dye to the particles. Thus, it is assumed that also in the supraparticles and coatings prepared thereof, the dye cannot leach from the nanoparticles and dissipate into the coating lacquer.

WILEY-VCH



## WILEY-VCH

**Figure S1:** Fluorescence spectra of nanoparticle dispersions with 10 mg particle content in 3 mL of water. The amounts of dye-doped silica nanoparticles are the same for the turn-off and turn-on sample (1a) (purple: dye-doped silica nanoparticles, blue: pure silica nanoparticles, green: iron oxide@silica nanoparticles, yellow: mixture of nanoparticles in the same ratio as Turn-off 2 sample, orange: mixture of nanoparticles in the same ratio as Turn-on 2 sample). Fluorescence spectra of the supraparticles dispersed in water (2.5 mg in 3 mL of water) (1b, yellow; Turn-off 2, orange: Turn-On 2).

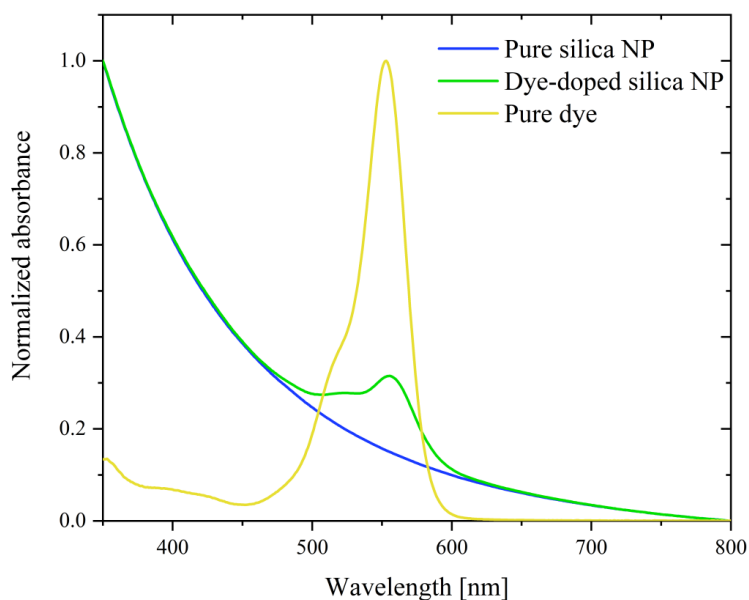


**Figure S2:** UV-vis spectra of pure silica nanoparticles (blue), dye-doped silica nanoparticles (green) and pure rhodamine B dye (yellow).

## 2. Fluorescence spectroscopy analyzers after supraparticle washing steps

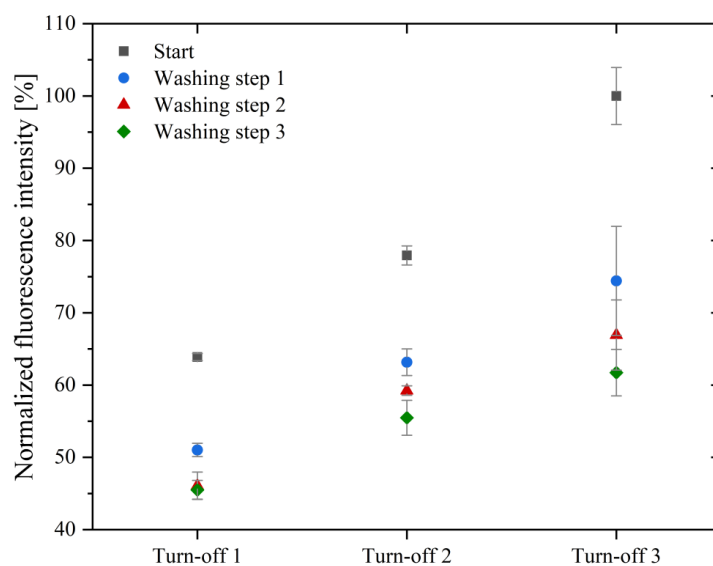


**Figure S3:** Normalized fluorescence intensities of turn-off supraparticles in water ( $1 \text{ mg mL}^{-1}$ ). Black squares symbolize the start fluorescence of each supraparticle system, blue dots the fluorescence of the redispersed dispersion after a first washing step and magnetic separation, red triangles symbolize the fluorescence after the second washing step and green diamonds after the third washing step.

## 3. SEM images of supraparticle cross-sections (turn-off, turn-on)

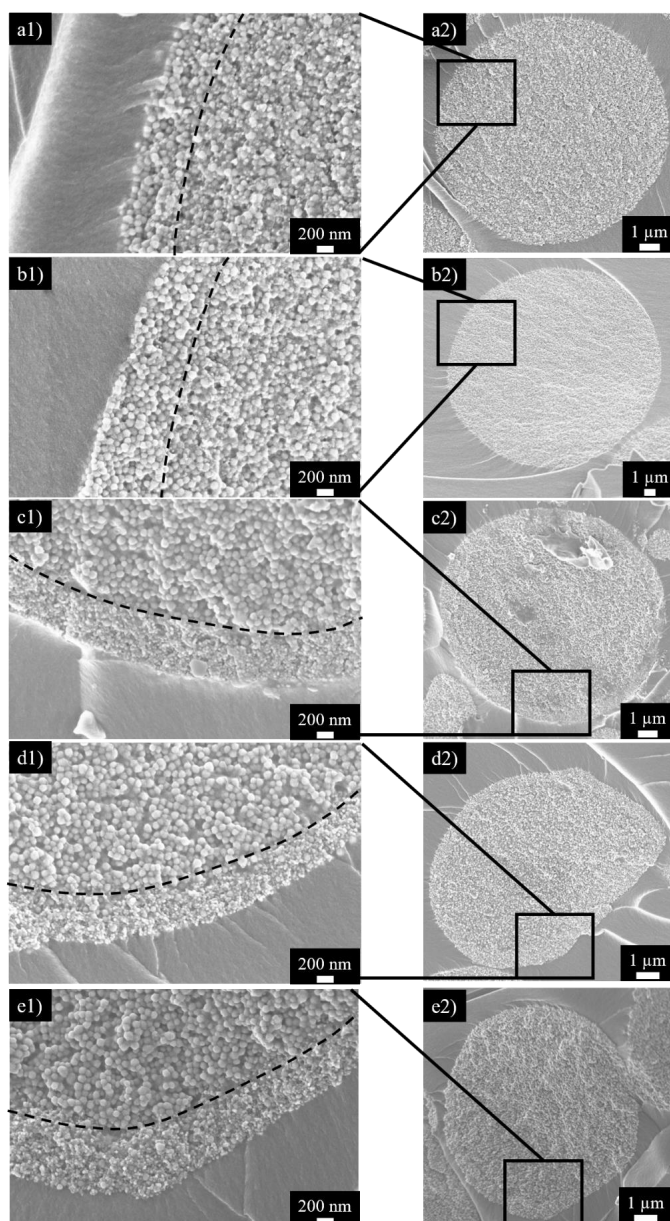


**Figure S4:** SEM cross-sections of turn-off 1 (a1 and a2), turn-off 2 (b1 and b2) supraparticles and turn-on 1 (c1 and c2), turn-on 3 (d1 and d2) and turn-on 4 (e1 and e2) supraparticles.

#### 4. Particle size distribution by laser diffraction

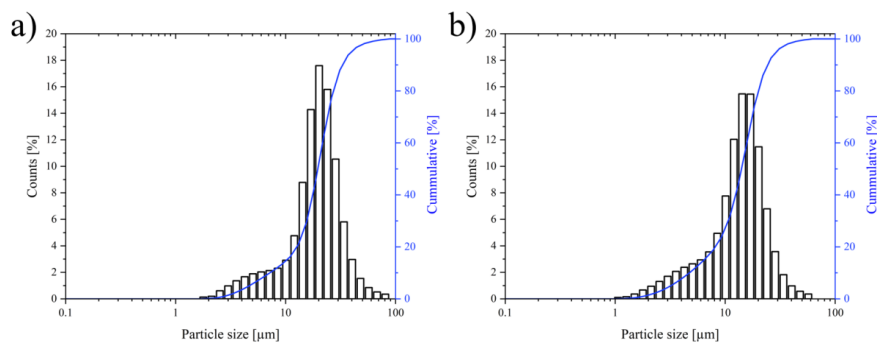


**Figure S5:** Particle size distribution determined via laser diffraction of turn-off (a) and turn-on (b) samples.

#### 5. SEM comparison of supraparticles with/without APTES

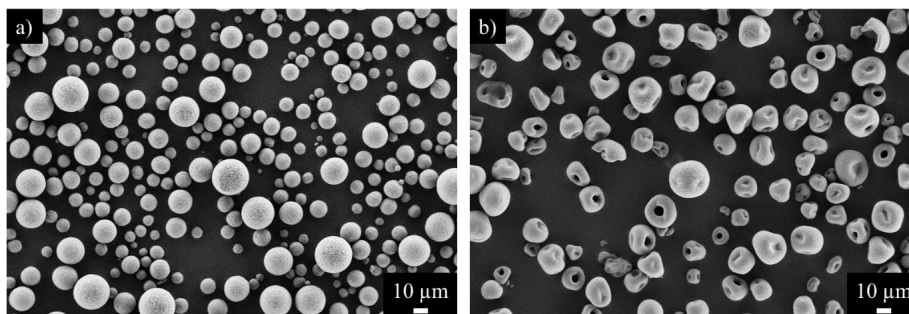


**Figure S6:** Spherical silica core supraparticles consisting of APTES modified nanoparticles (a) and non-spherical, donut-like silica supraparticles built up from pure silica nanoparticles (b).

#### 6. SEM images of embedded supraparticles before and after shearing

WILEY-VCH

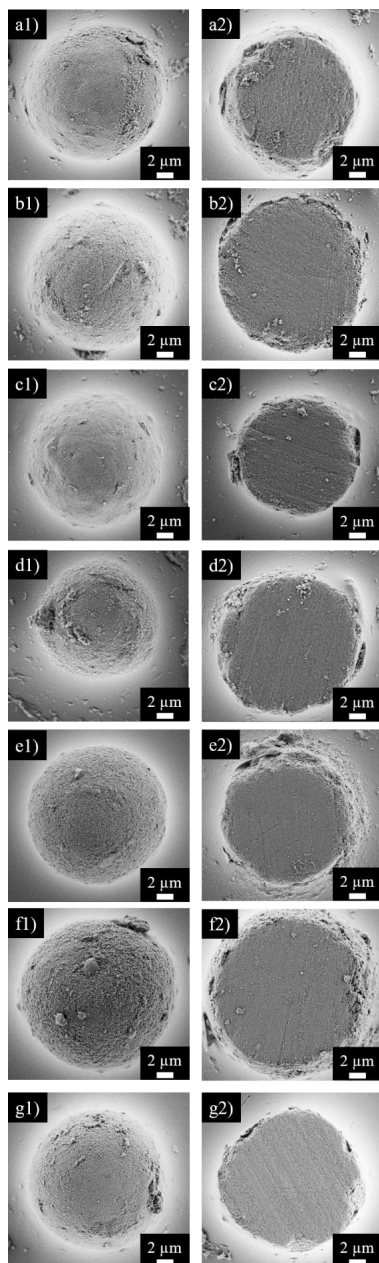


**Figure S7:** SEM images of embedded supraparticles of the samples: turn-on 2 (a), turn-on 3 (b) turn-on 4 (c), turn-on reference (d), turn-off 2 (e), turn-off 3 (f) and turn-off reference (g) before (1) and after 750 shear cycles (2).

## 7. Photographs of coated films before and after shear process

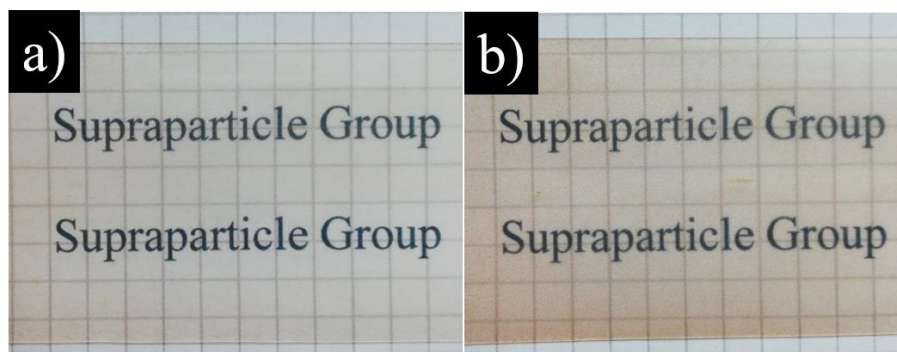


**Figure S8:** Photographs of turn-off supraparticles (a) and turn-on supraparticles (b) in the coating. On top, the as prepared state is shown and below, the situation after 1500 shear cycles.

WILEY-VCH

## 8. Fluorescence spectroscopy of turn-off and turn-on shear cycle experiments

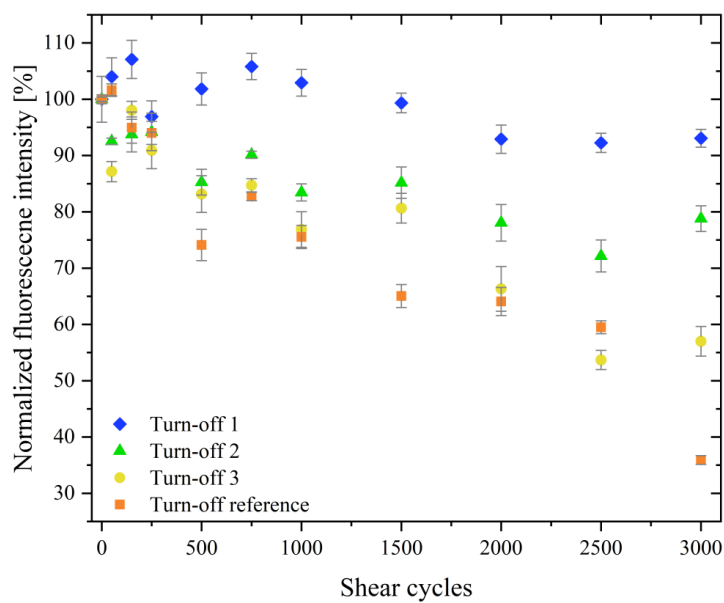


**Figure S9:** Normalized fluorescence intensities of turn-off indicator supraparticles as a function of shear cycles (blue diamonds, green triangles, yellow dots: different ratios between iron oxide@silica optical absorber to silica diluter nanoparticles in the core of the supraparticle system, orange squares: reference sample, i.e., only pure silica nanoparticles spay-dried to supraparticle cores, without optical absorbing part). The fluorescence intensities are normalized to the initial fluorescence intensity. The samples were excited at 540 nm and the emitted signal was measured at 579 nm.

WILEY-VCH

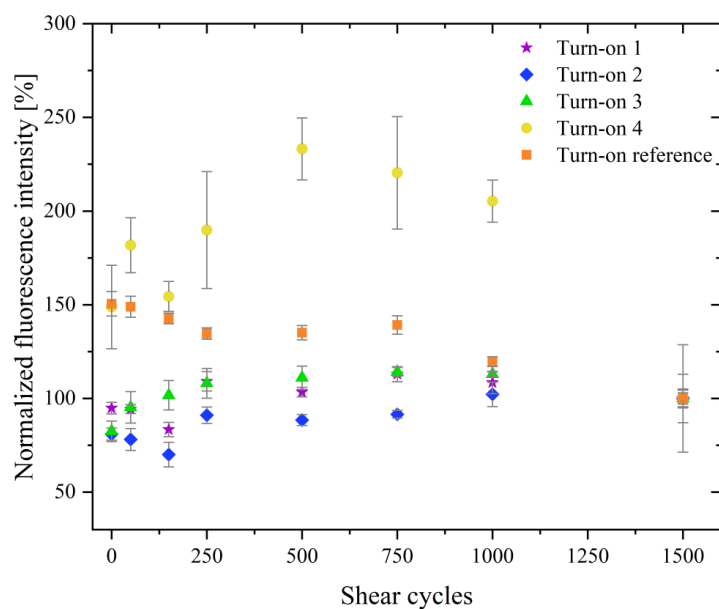


**Figure S10:** Normalized fluorescence intensities of turn-on indicator supraparticles as a function of shear cycles (purple stars, blue diamonds, green triangles, yellow dots: different ratios between iron oxide@silicaoptical absorber to silica diluter nanoparticles in the shell, orange squares: reference sample, i.e. only pure silica nanoparticles spay-dried to supraparticle shell, without optical absorbing part). The fluorescence intensities are normalized to the last shear cycle step. The sample was excited at 540 nm and the emitted signal was measured at 579 nm.

## Optically Sensitive and Magnetically Identifiable Supraparticles as Indicators of Surface Abrasion

Sarah Wenderoth,<sup>¶</sup> Stephan Müssig,<sup>¶</sup> Johannes Prieschl, Emilie Genin, Karine Heuzé, Florian Fidler, Daniel Haddad, Susanne Wintzheimer, and Karl Mandel\*



Cite This: <https://doi.org/10.1021/acs.nanolett.1c04773>



Read Online

ACCESS |



Metrics & More



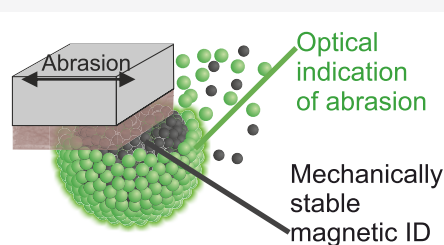
Article Recommendations



Supporting Information

**ABSTRACT:** Identifying and ensuring the integrity of products plays an important role in today's globalized world. Miniaturized information taggants in the packaging surface are therefore required to monitor the product itself instead of applying external labels. Ideally, multiple types of information are stored in such additives. In this work, micrometer-sized core-shell particles (supraparticles) were developed to provide material surfaces with both an identifier and a surface abrasion indication functionality. The core of the supraparticles contains iron oxide nanoparticles that allow identification of the surface with a spectral magnetic code resolved by magnetic particle spectroscopy. The fluorescent silica nanoparticles in the supraparticle shell can be abraded by mechanical stress and resolved by fluorescence spectroscopy. This provides information about the mechanical integrity of the system. The application as surfaces, that contain several types of information in one supraparticle, was demonstrated here by incorporating such bifunctional supraparticles as additives in a surface coating.

**KEYWORDS:** surface coatings, abrasion indicator, supraparticles, magnetic particle spectroscopy, identification



### 1. INTRODUCTION

In increasingly complex global supply chains, backtracing the true origin of products is essential to guarantee the high quality of manufactured goods. Improved traceability of even the smallest subcomponents is only achieved when identifiers are linked with materials rather than being applied on macroscopically attached external labels. Macroscopic barcodes or radio frequency identifiers (RFIDs)<sup>1</sup> thus have to be replaced by miniaturized taggants.<sup>2,3</sup> Besides nanoparticulate taggants,<sup>4,5</sup> which have their advantages and shortcomings, one promising alternative are specifically designed additives in the form of supraparticles<sup>6</sup> (i.e., nanostructured, micron-sized particles), which are equipped with information.<sup>4,7–10</sup> Such additives could contain information used for object identification or for an irreversible recording of external influences such as temperature,<sup>11</sup> moisture,<sup>12,13</sup> gases,<sup>14,15</sup> or mechanical stress<sup>16,17</sup> that may have affected the material previously.

Thinking further ahead, the creation of a supraparticle with properties that enables multiple levels of information to be read out from a single unit would open up numerous possibilities. These are, for instance, multiencoded identification,<sup>18–21</sup> recording of several different environmental influences at once, or identification of the material while simultaneously recording environmental influences.<sup>11</sup> Such micron-sized particles with multiple physical signals are demanded for applications such as recycling of waste streams,<sup>22</sup> repair

measures of electronic devices,<sup>11</sup> anticounterfeiting,<sup>18</sup> or biomedical applications.<sup>19–21</sup> Yet, success in the read out of multiple levels of information has been very rarely reported to date.

In this work, bifunctional supraparticles are presented; they enable identification and irreversible recording of mechanical stress, simultaneously. Both types of information are stored in one micron-sized unit, resulting in high reliability and resolution of the two types of information. The working principle of the smart supraparticles is successfully demonstrated after their integration into a coating. Coatings represent an ideal use case for the embedment of such (micro)particles, as coatings can be flexibly applied onto diverse product components and are routinely employed in modern materials' production to refine surface properties. In order to obtain surfaces that are equipped with additives providing two types of information, several demands for both the used supraparticles and the resulting surface itself must be addressed. A summary of numerous important challenges that had to be addressed compared with

Received: December 10, 2021

Revised: March 15, 2022



ACS Publications

© XXXX American Chemical Society

A

<https://doi.org/10.1021/acs.nanolett.1c04773>  
Nano Lett. XXXX, XXX, XXX–XXX

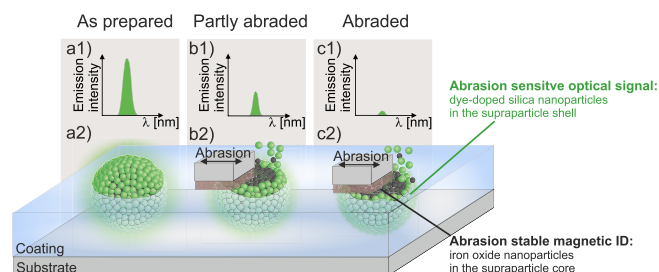


**Figure 1.** Conception to achieve surfaces based on supraparticles, equipped with a magnetic ID and an optical abrasion indicator functionality, integrated into coatings in a molehill-like arrangement. With increasing abrasion, a fluorescent, nanoparticulate shell (dye-doped silica nanoparticles, see results part) of initially intact supraparticles (a2) is gradually abraded (b2 and c2), letting a black core (the magnetic ID material, iron oxide nanoparticles, see results part) appear. This mechanical degradation of the supraparticles is optically monitored by a decrease in fluorescence intensity (a1, b1, c1). The iron oxide nanoparticles in the supraparticle core are used to identify the surface magnetically. Importantly, this functionality is unaffected by mechanical forces. Thereby, an abrasion sensitive functionality is combined with an abrasion stable ID, equipping the surface with both types of information.

recently published surfaces that allow obtaining information either about their abrasion<sup>23</sup> or enable their magnetic identification<sup>24,25</sup> is provided in the electronic Supporting Information (SI).

First, the optically detectable abrasion indication functionality yields an optical signal change upon surface abrasion. Further, it provides an optical signal although optically absorbing magnetic materials are present. Second, the magnetic identification (ID) functionality must enable the unique identification of the surface, ensuring that different surfaces are distinguishable. Moreover, the magnetic ID functionality provides a magnetic signal that remains stable upon abrasion, thus making identification possible at any time during the lifespan of the surface. Third, the coating, which carries the indicator supraparticles should not interact with neither the optical nor the magnetic signal. In addition, the coating thickness and supraparticle size has to fit in a way that a molehill-like structure arises (see Figure 1).

A working concept for a complex supraparticle structure was developed to address all of the above-mentioned challenges. A multihierarchical structure is envisioned, where both the ID signal carrier and the abrasion indicator are combined within one supraparticle (Figure 1). In the proposed concept, the shell of the supraparticles should be based on dye-doped silica nanoparticles, which would indicate the abrasion. The supraparticle core should carry the ID, which could be provided by magnetic iron oxide nanoparticles and resolved by magnetic particle spectroscopy (MPS).<sup>24–26</sup> After integration of the supraparticles into a coating, the luminescent nanoparticulate shell (Figure 1 a2) should progressively be destroyed (Figure 1 b2, c2) upon surface abrasion. This could yield a decreased relative intensity in their optical response (Figure 1 a1, b1, and c1). As the magnetically readable ID, provided by the supraparticle core, has to be capable of being read out during the whole lifespan of the coating, it has to be unaffected by mechanical forces. Thus, the supraparticle shell would indicate mechanical forces due to a decrease in luminescent signal intensity, and simultaneously, magnetic identification should be possible independent of mechanical destruction. In this way, many different spots could provide both types of information, namely, the ID and information about the mechanical integrity of the coating. When two powder additives would have to be

incorporated into a coating lacquer, their segregation is in principle possible, depending on many aspects including hydrophilicity, dispersibility, size, wetting, and so on. This might lead to coatings in which the additives are dispersed inhomogeneously, that is, only parts of the coatings could contain luminescent or magnetic particles. By combination of both functionalities within one micron-sized particle as presented herein, both types of information can be correlated to each other with enhanced lateral resolution. Another advantage is the close distance of the silica shell to the dark iron oxide core, which causes the often desired mitigation of dark color caused by iron oxide particles. Finally, from a procedural perspective, it is in general easier to handle only one additive compared with introducing two types of additives into a surface coating.

## 2. RESULTS AND DISCUSSION

In order to turn the concept, as depicted in Figure 1, into reality, two types of nanoparticulate building blocks are needed. First, a special type of dye-doped luminescent silica nanoparticles was developed. In a first step, rhodamine hydrochloride was silanized with 3-(triethoxysilyl)propyl isocyanate (ICPTES) and prehydrolyzed in an ethanolic ammonia solution to create dye-clusters.<sup>27</sup> In a second step, tetraethoxysilane was added and silica nanoparticles were formed. Through this prehydrolyzation process, the dye-clusters built the center of the formed silica nanoparticles. Because of this crucial step, dye molecule leakage from the silica nanoparticles was prevented during both further processing steps and in the supraparticulate form within the coating lacquer. Overall, the dye coupling to the silica/silane system turned out to be very complex and at the same time crucial to achieve the ultimately desired properties. This exhaustive study on the dye-system (fundamental characterization of the dye coupling reactions (Figures S1, S3) with optical spectroscopy (Figures S2, S6), nuclear magnetic resonance (NMR) (Figures S4, S5) and mass spectrometry (MS) can be found in the SI. Second, the used iron oxide nanoparticles in the supraparticle core are designated to provide a magnetic ID that enables identification of the equipped surfaces. In order to do so, different nanoparticles were synthesized that vary in their magnetic properties because of doping the iron oxide with cobalt ions during their synthesis (see

B

<https://doi.org/10.1021/acs.nanolett.1c04773>  
Nano Lett. XXXX, XXX, XXX–XXX

Material and Methods section). These optical and magnetic signal carriers were subsequently structured into core-shell supraparticles to obtain the desired bifunctionality. This was done by assembling the magnetic nanoparticles as a core and the luminescent nanoparticles as a shell, using spray-drying in two subsequent steps. In the first step, two cores were manufactured, each containing one of the two iron oxide nanoparticle types, respectively. During the second spray-drying event, dye-doped silica nanoparticles were arranged as a luminescent nanoparticulate shell around the previously synthesized cores.

Sensitivity of the surface toward external abrasion is obtained by embedding the supraparticles only partly in the coating and partly leaving them to stick out of it (Figure 1a2) (see Materials and Methods section). On the created coatings, abrasion tests were subsequently conducted by shearing a commonly used cube-shaped stamp (1.5 × 1.5 cm), equipped with an abrasion paper, for up to 1000 cycles over the surface (schematically illustrated in Figure 1b2, c2). One cycle represents the movement forward and backward over a length of 7 cm (see Materials and Methods section). As indicated by scanning electron microscopy images (Figure 2a1–a6), large parts of the supraparticles that stuck out of the surface, got progressively chopped off. It is unlikely that individual nanoparticles are cut in-between with the utilized grains. Rather, we hypothesize that the nanoparticles are removed as whole particles. This mechanical destruction of the supraparticles is utilized for the abrasion indication. With increasing abrasion cycles, a progressive fluorescence intensity reduction up to approximately 90% was obtained for surface 1 after normalization to its initial fluorescence intensity (Figure 2b1, black squares). The sensitive reaction after only 100 abrasion cycles arises from the supraparticles partly sticking out of the surface coating. Surface 2 exhibits a reduction of fluorescence intensity of around 60% after 1000 abrasion cycles (Figure 2b1, red squares). With increasing surface abrasion, a larger share of light absorbing iron oxide nanoparticles, previously hidden within the core, is revealed. This yields the observed decrease of normalized fluorescence intensity, mainly because of two different processes. First, due to the uncovering of the light absorbing supraparticle core, the emitted light of the dye-doped supraparticle shell is absorbed. The reduction of the fluorescence intensity thus depends on the light absorption properties of the supraparticle composition. As the two different iron oxide core nanoparticles have a different chemical composition, their fluorescence intensity reduction also differs. Second, the reduction of fluorescence intensity is caused by the loss of dye-doped shell nanoparticles after mechanical abrasion.<sup>23</sup>

Identification of the surface with magnetic IDs was achieved by utilizing magnetic particle spectroscopy (MPS). In contrast to data from other magnetometers, the measured time-dependent voltage, which originates from the magnetic samples after their excitation in an alternating current magnetic field, is Fourier transformed. This yields a spectral harmonic amplitude decay as a function of frequency that describes the response of magnetic samples toward an external magnetic field.<sup>28</sup> This powerful spectral description is essential for the presented concept, because other identification principles, such as magnetic readout of defined geometrical patterns<sup>29,30</sup> might be unsuitable for this application because of their mechanical destruction. As no sophisticated cooling systems are required for MPS, a relatively inexpensive device with measurement times in the order of (milli)seconds is feasible with a geometrically customizable detection coil. Thus, MPS provides a powerful

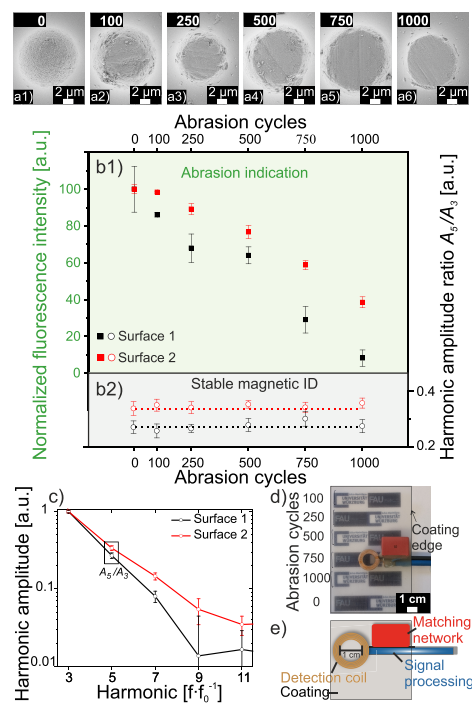


**Figure 2.** Scanning electron microscopy images of synthesized supraparticles incorporated into surfaces after 0, 100, 250, 500, 750, and 1000 abrasion cycles (a1–a6). The initially spherical shape is progressively damaged due to applied mechanical forces. This mechanical destruction yields a decrease in normalized fluorescence intensity (b1), demonstrating that abrasion is optically monitored for two different surfaces (red and black filled squares). The two magnetic IDs (b2), which originate from different magnetic cores of the supraparticles in the respective surfaces (red and black empty circles), remain constant despite surface abrasion. The dotted line is a guide for the eye that represents the values after 0 cycles. Upon normalization to the amplitude of the third harmonic  $A_3$ , the harmonic amplitude as a function of multiples of the fundamental frequency  $f_0$  of both surfaces (c) allows their magnetic discrimination. The transparent appearance of the surface coating (d, black frame marks the edge) shows almost no undesired visual constraint originating from the supraparticles as observed by the clearly visible printed background (university labels). The sensitivity to resolve the magnetic IDs by the presented mobile MPS sensor (d) is noteworthy, especially because of the unsophisticated physical hardware utilized (as schematically shown in e).

analytical tool to be utilized beyond a laboratory environment. The combination of defined luminescent signals with defined spectral magnetic signals adds another read out option to store information compared to solely optically resolved information.<sup>31</sup> As it is desired to put more and more functionalities in a single spot, it will eventually be challenging to distinguish several solely optically resolved signals from each other. The spectral nature of the utilized magnetic signal allows for identification independent of the taggant's orientation within the coating (in contrast to a required defined orientation for spatially resolved

C

<https://doi.org/10.1021/acs.nanolett.1c04773>  
Nano Lett. XXXX, XXX, XXX–XXX

magnetic tags<sup>32</sup> or their magnetic separation in liquids before ID detection<sup>33</sup>).

Moreover, the harmonic spectrum is self-referenced with respect to the harmonic amplitude  $A_3$  of the third harmonic (Figure 2c), enabling identification independent of marker concentration and external influences such as readout sensitivity or the presence of paramagnetic or diamagnetic material. Significantly different signal decays for surfaces 1 and 2 are observed, as they contain different magnetic nanoparticles (Figure 2c). Thus, unique spectral IDs were generated by variation of the utilized magnetic particles. In order to simplify the ID, which is determined by its spectral magnetization amplitude decay, the ratio of the fifth harmonic amplitude  $A_5$  to the third harmonic amplitude  $A_3$  ( $A_5/A_3$ ) is used. This ratio describes the (negative) slope of each spectrum and is used, herein, as a very simplified magnetic ID parameter. Inspection of these ID parameters as a function of abrasion cycles (Figure 2b2, black and red circles) reveals two important aspects. First, the respective ID parameter remains constant over all abrasion cycles (within the limits of the error bars, which represent the standard deviation of five averaged measurements). This means that the magnetic ID is independent of the observed abrasion, which is an essential feature for identification of the surface during its complete lifespan. Second, the signals of the two different surfaces are distinguishable, thereby allowing their identification and distinction due to their respective magnetic spectral ID. It is likely, that a larger variety of different magnetic IDs is distinguishable within such surfaces. However, this work focuses on demonstrating that it is in general possible to combine different *mechanically stable* magnetic IDs with an abrasion indication functionality. A discussion about the number of possible magnetic codes and more information about the magnetic data processing and analysis is provided in the SI.

The potential for applications is expressed as the fabricated surface (coating) is visually almost unaffected by the incorporation of supraparticles (see digital photograph in Figure 2d) as observed by the clearly visible printed background (university labels). Furthermore, the applied abrasion (see the marking of cycle numbers in Figure 2d) cannot be observed by eye, confirming the sensitivity of the abrasion indication. The luminescence signals can be detected by hand-held fluorescence spectrometer devices outside a defined sample geometry, enabling analysis of various object geometries. In addition to the luminescence read out, the magnetic functionality is identified sensitively by a hand-held device with adjustable geometry, as well. Noteworthy, the mass of magnetic material in the surface is as low as in the order of  $7 \mu\text{g cm}^{-2}$ , which reveals the remarkable sensitivity of this hand-held MPS detector. As schematically illustrated (Figure 2e), a sending and detection coil, which is connected to power supply and data processing, is all that is required from a user's perspective for very simple read out. Spectral evaluation as well as all necessary adjustments prior to or in between measurements are automatized by a home written code.

The provided proof-of-principle for surfaces with ID and abrasion indication functionalities opens up the possibility to equip objects with such information, as the information is stored within bifunctional supraparticles that can be used as universally applicable additives. The utilized supraparticles are especially attractive to be incorporated directly into barrier coatings with thicknesses of 3–5  $\mu\text{m}$  without the requirement of an additional working step. Other reported mechanical force indicator

concepts<sup>34–36</sup> require their incorporation into coating thicknesses above 100  $\mu\text{m}$  and are typically applied as an underlying secondary coating and are not sensitive toward mechanical forces unless the superficial coating is completely pierced.

### 3. CONCLUSION

In this work, a coating containing supraparticles that carry two different types of information was demonstrated. The presented bifunctionality originates from a core–shell supraparticle design. The luminescent, particulate shell provides a luminescent signal, which changes irreversibly upon abrasion. This was utilized to gain information about mechanical damage that might have deteriorated the quality of the surface coating. The cores of the supraparticles carry a mechanically unaffected spectrally resolved magnetic ID, enabling identification by magnetic particle spectroscopy. The utilized iron oxide nanoparticles have the main function of magnetic identification but also to absorb light emission for the abrasion indication. The feasibility to create surfaces with such bifunctional supraparticles was demonstrated after their incorporation into a coating. The presented sensitive detection of the luminescent and magnetic signals increases the relevance of the presented system for backtracing of global supply chains and quality control applications.

### 4. MATERIALS AND METHODS

Chemicals were purchased from Sigma-Aldrich (Germany) unless stated otherwise. Ammonium hydroxide solution was purchased from Merck (Germany), rhodamine hydrochloride from abcr (Germany), and iron chloride tetrahydrate from Fluka (Germany). All chemicals were used without further purification. All syntheses were done in deionized water.

**Iron Oxide Syntheses.** Superparamagnetic iron oxide nanoparticles (SPIONs) were obtained during a coprecipitation reaction. In order to synthesize SPION1, iron(III) chloride hexahydrate ( $\text{FeCl}_3 \cdot 6 \text{H}_2\text{O}$ , 10.80 g, 40 mmol, Sigma-Aldrich, >99%) and iron(II) chloride tetrahydrate ( $\text{FeCl}_2 \cdot 4 \text{H}_2\text{O}$ , 3.98 g, 20 mmol, Fluka, >99%) were dissolved in deionized water (225 mL) at room temperature and mixed with 30% aqueous ammonia solution  $\text{NH}_3(\text{aq})$  (25 mL). SPION2, which was used to fabricate the second surface, was synthesized by partial substitution of  $\text{FeCl}_3 \cdot 6 \text{H}_2\text{O}$  with  $\text{CoCl}_2 \cdot 6 \text{H}_2\text{O}$  (Sigma-Aldrich, > 98%). For SPION2, 10.0 g of  $\text{FeCl}_3 \cdot 6 \text{H}_2\text{O}$  (37 mmol) and 0.72 g of  $\text{CoCl}_2 \cdot 6 \text{H}_2\text{O}$  (3 mmol) were used, while the amount of  $\text{FeCl}_2 \cdot 4 \text{H}_2\text{O}$  was unchanged. Subsequently, the black precipitate was magnetically separated after 60 s of stirring, washed three times with deionized water, and redispersed in deionized water (250 mL) for 2 min. The nanoparticles were redispersed in a 50 mM aqueous citric acid solution ( $\text{C}_6\text{H}_8\text{O}_7$ , Panreac AppliChem, ACS reagent, 500 mL) and washed 3 times with deionized water and redispersed in water to obtain a stable ferrofluid.

**Dye-Doped Silica Nanoparticles.** The dye stock solution was prepared by dissolving 10 mg (1 equiv) of rhodamine 110 in 2 mL of dimethyl sulfoxide and mixed with 40.9  $\mu\text{L}$  (6 equiv) of 3-(triethoxysilyl) propyl isocyanate. The reaction mixture was stirred for a further 24 h.

The synthesis of silica nanoparticles is primarily based on a modified Stöber process and is done according to the literature.<sup>27</sup> Initially, 300 mL of ethanol was mixed with 15 g of aqueous ammonia solution (25 wt %) before 300  $\mu\text{L}$  of the dye suspension was added. The mixture was allowed to stir

D

<https://doi.org/10.1021/acs.nanolett.1c04773>  
Nano Lett. XXXX, XXX, XXX–XXX

overnight before 15 g of tetraethoxysilane were added under vigorous stirring. After 20 h of reaction time, the particle dispersion was purified by vacuum evaporating and dialyses (molecular weight cutoff: 10 kDa, cellulose acetate membrane, Nadir, Roth, Germany).

**Supraparticle Preparation.** The indicator supraparticles were prepared in a two-step spray-drying process using a B-290 mini spray-dryer (Büchi, Switzerland). In a first step, the iron oxide core particles were prepared as follows: SPION1 or SPION2, respectively, were dispersed with silica nanoparticles (Köstrosol K9550, Chemiewerk Bad Köstritz, Germany) in a weight ratio 1:9 with subsequent addition of 30 wt % (referred to the total particle mass) calcium chloride (CaCl<sub>2</sub>, Supelco). This dispersion was spray-dried with an ultrasonic nozzle with an inlet temperature of 80 °C, resulting in an outlet temperature of 51 °C and aspirator power of 80%. The resulting spherical supraparticles were mixed in a second step in a weight ratio of 1:1 with dispersed dye-doped silica nanoparticles. Thereby, the inlet temperature was set to 140 °C which results in an outlet temperature of 85–90 °C, whereas the aspirator power was at 75%.

**Coating.** Indicator supraparticles (150 mg) were suspended and mixed in 1.5 mL coating lacquer<sup>37</sup> and coated with a 20 μm doctor blade on a polyolefin foil using a Coatmaster 590 MC (Erichsen Testing Equipment, Germany). After 10 min of curing at room temperature, the foils were heated up to 90 °C for 30 min.

**Characterization. Magnetic Particle Spectroscopy.** Magnetic particle spectroscopy (MPS) measurements of powders and coatings were performed similar to a recent work<sup>38</sup> with a self-built spectrometer based on the electronics of a commercial magnetic particle spectrometer (MPS Unit, Pure Devices GmbH, Rimpfing, Germany) and a probehead designed similar to patent WO2014068303. Excitation field strength was 17 mT at a working frequency of 20 kHz. Before each measurement, calibration without probe was done, consisting of zero adjustment of the residual signal at the excitation frequency and recording of an empty spectrum that was subtracted automatically from the consecutive measured spectra. In addition to the spectral information, an errorbar is calculated on the basis of the measured signal. Data acquisition time for a single measurement was 8 ms, and an averaging factor of 5 was applied here.

**Fluorescence Spectroscopy.** Emission spectra were measured using a FP-8600 (Jasco, Japan) equipped with a solid sample holder (FDA-808, Jasco, Japan). The excitation wavelength was set to 490 nm, and the spectra were recorded from 500 to 620 nm.

**Scanning Electron Microscopy.** Scanning electron microscopy images were recorded using a Supra 25 SEM (Zeiss, Germany) at 2 kV (field emission) and a working distance of 4 mm. The samples were sputtered with platinum for 5 s at 50 mA (MED 010, Balzers Union).

**Abrasion Experiments.** Abrasion experiments were done using an automated crockmeter (Tomsic, Italy). On a glass slide, the film was fixed and a squared test finger (1.5 × 1.5 cm) equipped with an abrasion paper (SiC, roughness #4000, grain size 5 μm, Struers, Germany) was set in a 90° angle on top of the film. The track length was set to 7 cm, with a finger load of 4 N and a cycle number between 0 and 1000 abrasion cycles.

## ■ ASSOCIATED CONTENT

### Supporting Information

The Supporting Information is available free of charge at <https://pubs.acs.org/doi/10.1021/acs.nanolett.1c04773>.

Information about challenges that were faced during the combination of abrasion functionality and magnetic identification within one entity, fundamental characterization of the dye coupling reaction and discussion about magnetic data processing, analysis and the number of possible magnetic codes (PDF)

## ■ AUTHOR INFORMATION

### Corresponding Author

Karl Mandel – *Fraunhofer-Institute for Silicate Research ISC, D97082 Würzburg, Germany; Department of Chemistry and Pharmacy, Inorganic Chemistry, Friedrich-Alexander-Universität Erlangen-Nürnberg (FAU), D91058 Erlangen, Germany; [orcid.org/0000-0002-1445-0702](https://orcid.org/0000-0002-1445-0702); Email: [karl.mandel@fau.de](mailto:karl.mandel@fau.de)*

### Authors

Sarah Wenderoth – *Chair of Chemical Technology of Materials Synthesis, Julius-Maximilians-University Würzburg, D97070 Würzburg, Germany; Fraunhofer-Institute for Silicate Research ISC, D97082 Würzburg, Germany*

Stephan Müssig – *Department of Chemistry and Pharmacy, Inorganic Chemistry, Friedrich-Alexander-Universität Erlangen-Nürnberg (FAU), D91058 Erlangen, Germany*

Johannes Prieschl – *Department of Chemistry and Pharmacy, Inorganic Chemistry, Friedrich-Alexander-Universität Erlangen-Nürnberg (FAU), D91058 Erlangen, Germany*

Emilie Genin – *University Bordeaux, ISM, UMR-5255, F-33400 Talence, France; CNRS, ISM, UMR5255, F-33400 Talence, France; [orcid.org/0000-0002-5536-1933](https://orcid.org/0000-0002-5536-1933)*

Karine Heuzé – *University Bordeaux, ISM, UMR-5255, F-33400 Talence, France; CNRS, ISM, UMR5255, F-33400 Talence, France*

Florian Fidler – *Magnetic Resonance and X-ray Imaging Department, Development Center X-ray Technology, Fraunhofer-Institute for Integrated Circuits IIS, 97074 Würzburg, Germany*

Daniel Haddad – *Magnetic Resonance and X-ray Imaging Department, Development Center X-ray Technology, Fraunhofer-Institute for Integrated Circuits IIS, 97074 Würzburg, Germany*

Susanne Wintzheimer – *Fraunhofer-Institute for Silicate Research ISC, D97082 Würzburg, Germany; Department of Chemistry and Pharmacy, Inorganic Chemistry, Friedrich-Alexander-Universität Erlangen-Nürnberg (FAU), D91058 Erlangen, Germany*

Complete contact information is available at: <https://pubs.acs.org/doi/10.1021/acs.nanolett.1c04773>

### Author Contributions

¶S.We. and S.M. contributed equally to this work. Overarching research goals were developed by S.We., S.M., S.Wi., and K.M. Supervision of the whole project was done by S.We., S.M., S.Wi., and K.M. Preceding experiments, knowledge acquisition, and identification of key problems was performed by S.We., S.M. and F.F. Magnetic nanoparticles were synthesized by S.M. Dye-doped silica nanoparticles were conceptualized, synthesized and characterized by S.We. S.Wi., E.G., and K.H (SI). Interpretation

E

<https://doi.org/10.1021/acs.nanolett.1c04773>  
Nano Lett. XXXX, XXX, XXX–XXX

and conclusions were drawn by S.We., Dye-coupling experiments were synthesized, characterized and interpreted by S.We., E.G., K.H., and S. Wi. Utilized supraparticles were conceptualized by S.We. with support of S.M. and S.Wi. Supraparticles were synthesized by S.We., S.M., and J.P. Incorporation of supraparticles into the coating and abrasion tests were performed, optically characterized and interpreted by S.We. and discussed with S.M. Magnetic sensor development was done by F.F. and D.H. Magnetic measurements were performed by F.F. Magnetic data analysis, interpretation, and conclusions were drawn by S.M. and discussed with S.We. SEM characterization was done by J.P. Figures were created by S.We. and S.M. Original publication draft was written equally by S.We. and S.M. with input from F.F. Reviewing and editing was performed by S.We., S.M., S.Wi., E.G., K.H., F.F., and K.M. All authors proof-read and commented on the publication. Funding was acquired by S.M. and K.M.

#### Funding

This work was financially supported by the BMBF (Nano-MatFutur grant 03XP0149) who is gratefully acknowledged. S.M. thankfully acknowledges the German federal environmental foundation (DBU) for his doctoral scholarship.

#### Notes

The authors declare no competing financial interest.

#### ACKNOWLEDGMENTS

We thank BÜCHI Labortechnik AG for providing the spray-dryer equipment. This work was financially supported by Bordeaux University and the CNRS who are gratefully acknowledged. We thank the analytical facilities CESAMO (NMR, HRMS) of Bordeaux University. We thank G. Clermont for his help with the UV measurements.

#### ABBREVIATIONS

RFID, radio frequency identifiers; ID, identification; MPS, magnetic particle spectroscopy; ICPTES, 3-(triethoxysilyl)propyl isocyanate; SPION, superparamagnetic iron oxide nanoparticle

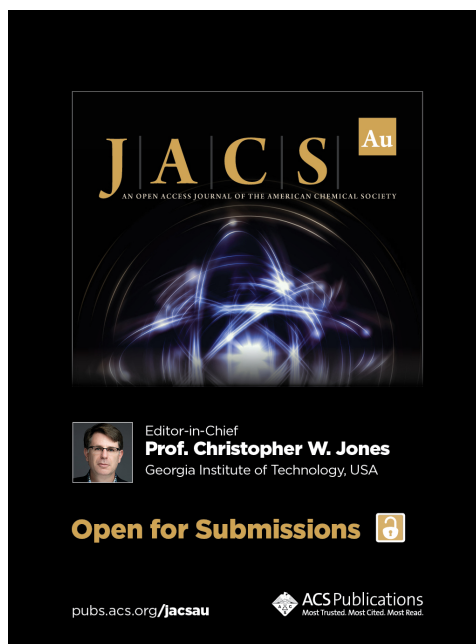
#### REFERENCES

- (1) Koelle, A. R.; Depp, S. W.; Freyman, R. W. Short-range radio-telemetry for electronic identification, using modulated RF backscatter. *Proceedings of the IEEE* **1975**, *63* (8), 1260–1261.
- (2) Vollath, D. Bifunctional nanocomposites with magnetic and luminescence properties. *Adv. Mater.* **2010**, *22*, 4410–4415.
- (3) Shikha, S.; Salafi, T.; Cheng, J.; Zhang, Y. Versatile design and synthesis of nano-barcode. *Chem. Soc. Rev.* **2017**, *46* (22), 7054–7093.
- (4) Puddu, M.; Paunescu, D.; Stark, W. J.; Grass, R. N. Magnetically recoverable, thermostable, hydrophobic DNA/silica encapsulates and their application as invisible oil tags. *ACS Nano* **2014**, *8* (3), 2677–2685.
- (5) Paunescu, D.; Stark, W. J.; Grass, R. N. Particles with an identity: tracking and tracing in commodity products. *Powder Technol.* **2016**, *291*, 344–350.
- (6) Wintzheimer, S.; Granath, T.; Oppmann, M.; Kister, T.; Thai, T.; Kraus, T.; Vogel, N.; Mandel, K. Supraparticles: Functionality from uniform structural motifs. *ACS Nano* **2018**, *12* (6), 5093–5120.
- (7) Bao, L.; You, H.; Wang, L.; Li, L.; Qiao, R.; Zhang, Y.; Zhong, Y.; Xiong, Y.; Li, Z. Self-assembly of LaF<sub>3</sub>: Yb, Er/Tm nanoplates into colloidal spheres and tailoring their upconversion emissions with fluorescent dyes. *J. Mater. Chem. C* **2014**, *2* (42), 8949–8955.
- (8) Miller, F.; Wintzheimer, S.; Reuter, T.; Groppe, P.; Prieschl, J.; Retter, M.; Mandel, K. Luminescent Supraparticles Based on CaF<sub>2</sub>-Nanoparticle Building Blocks as Code Objects with Unique IDs. *ACS Appl. Nano Mater.* **2020**, *3* (1), 734–741.
- (9) Song, F.; Tang, P. S.; Durst, H.; Cramb, D. T.; Chan, W. C. W. Nonblinking plasmonic quantum dot assemblies for multiplex biological detection. *Angew. Chem., Int. Ed.* **2012**, *124* (35), 8903–8907.
- (10) Zhang, Q.; Wang, X.; Zhu, Y. Multicolor upconverted luminescence-encoded superparticles via controlling self-assembly based on hydrophobic lanthanide-doped NaYF<sub>4</sub> nanocrystals. *J. Mater. Chem.* **2011**, *21* (32), 12132–12138.
- (11) Reichstein, J.; Miller, F.; Wintzheimer, S.; Mandel, K. Communicating Particles: Identification Tag and Temperature Recorder in One Single Supraparticle. *Adv. Funct. Mater.* **2021**, *31*, 2104189.
- (12) Wehner, T.; Seuffert, M. T.; Sorg, J. R.; Schneider, M.; Mandel, K.; SEXTL, G.; Müller-Buschbaum, K. Composite materials combining multiple luminescent MOFs and superparamagnetic microparticles for ratiometric water detection. *J. Mater. Chem. C* **2017**, *5* (39), 10133–10142.
- (13) Wehner, T.; Mandel, K.; Schneider, M.; SEXTL, G.; Müller-Buschbaum, K. Superparamagnetic luminescent MOF@ Fe<sub>3</sub>O<sub>4</sub>/SiO<sub>2</sub> composite particles for signal augmentation by magnetic harvesting as potential water detectors. *ACS Appl. Mater. Interfaces* **2016**, *8* (8), 5445–5452.
- (14) Wintzheimer, S.; Oppmann, M.; Dold, M.; Pannek, C.; Bauersfeld, M.-L.; Henfling, M.; Trupp, S.; Schug, B.; Mandel, K. Indicator Supraparticles for Smart Gasochromic Sensor Surfaces Reacting Ultrafast and Highly Sensitive. *Part. Part. Syst. Char.* **2019**, *36* (10), 1900254.
- (15) Pannek, C.; Vetter, T.; Oppmann, M.; Weber, C.; Eberhardt, A.; Dold, M.; Bauersfeld, M.-L.; Henfling, M.; Trupp, S.; Schug, B.; Wollenstein, J.; Mandel, K. Highly sensitive reflection based colorimetric gas sensor to detect CO in realistic fire scenarios. *Sensor Actuat. B-Chem.* **2020**, *306*, 127572.
- (16) Wintzheimer, S.; Reichstein, J.; Wenderoth, S.; Hasselmann, S.; Oppmann, M.; Seuffert, M. T.; Müller-Buschbaum, K.; Mandel, K. Expanding the horizon of mechanochromic detection by luminescent shear stress sensor supraparticles. *Adv. Funct. Mater.* **2019**, *29* (19), 1901193.
- (17) Wintzheimer, S.; Müssig, S.; Wenderoth, S.; Prieschl, J.; Granath, T.; Fidler, F.; Haddad, D.; Mandel, K. Hollow Superparamagnetic Nanoparticle-Based Microballoons for Mechanical Force Monitoring by Magnetic Particle Spectroscopy. *ACS Appl. Nano Mater.* **2019**, *2* (10), 6757–6762.
- (18) Li, R.; Zhang, Y.; Tan, J.; Wan, J.; Guo, J.; Wang, C. Dual-mode encoded magnetic composite microsphere based on fluorescence reporters and raman probes as covert tag for anticounterfeiting applications. *ACS Appl. Mater. Interfaces* **2016**, *8* (14), 9384–9394.
- (19) Alvarez-Puebla, R. A.; Pazos-Perez, N.; Guerrini, L. SERS-fluorescent encoded particles as dual-mode optical probes. *Applied Materials Today* **2018**, *13*, 1–14.
- (20) Niu, X.; Chen, H.; Wang, Y.; Wang, W.; Sun, X.; Chen, L. Upconversion fluorescence-SERS dual-mode tags for cellular and in vivo imaging. *ACS Appl. Mater. Interfaces* **2014**, *6* (7), 5152–5160.
- (21) Wang, Z.; Zong, S.; Li, W.; Wang, C.; Xu, S.; Chen, H.; Cui, Y. SERS-fluorescence joint spectral encoding using organic-metal-QD hybrid nanoparticles with a huge encoding capacity for high-throughput biodetection: putting theory into practice. *J. Am. Chem. Soc.* **2012**, *134* (6), 2993–3000.
- (22) Ahmad, S. R. A new technology for automatic identification and sorting of plastics for recycling. *Environ. Technol.* **2004**, *25* (10), 1143–1149.
- (23) Wenderoth, S.; Granath, T.; Prieschl, J.; Wintzheimer, S.; Mandel, K. Abrasion Indicators for Smart Surfaces Based on a Luminescence Turn-On Effect in Supraparticles. *Adv. Photonics Res.* **2020**, *1* (1), 2000023.
- (24) Müssig, S.; Fidler, F.; Haddad, D.; Hiller, K.-H.; Wintzheimer, S.; Mandel, K. Supraparticles with a Magnetic Fingerprint Readable by Magnetic Particle Spectroscopy: An Alternative beyond Optical Tracers. *Adv. Mater. Technol.* **2019**, *4* (9), 1900300.

F

<https://doi.org/10.1021/acs.nanolett.1c04773>  
Nano Lett. XXXX, XXX, XXX–XXX

- (25) Müssig, S.; Reichstein, J.; Prieschl, J.; Wintzheimer, S.; Mandel, K. A Single Magnetic Particle with Nearly Unlimited Encoding Options. *Small* **2021**, *17*, 2101588.
- (26) Rauwerdink, A. M.; Giustini, A. J.; Weaver, J. B. Simultaneous quantification of multiple magnetic nanoparticles. *Nanotechnology* **2010**, *21* (45), 455101.
- (27) Wang, L.; Tan, W. Multicolor FRET silica nanoparticles by single wavelength excitation. *Nano Lett.* **2006**, *6* (1), 84–88.
- (28) Biederer, S.; Knopp, T.; Sattel, T. F.; Lüdtke-Buzug, K.; Gleich, B.; Weizenecker, J.; Borgert, J.; Buzug, T. M. Magnetization response spectroscopy of superparamagnetic nanoparticles for magnetic particle imaging. *J. Phys. D Appl. Phys.* **2009**, *42* (20), 205007.
- (29) Park, B. C.; Kim, Y. K. Synthesis, microstructure, and physical properties of metallic barcode nanowires. *Met. Mater. Int.* **2017**, *23* (3), 413–425.
- (30) Wang, D.-S.; Mukhtar, A.; Wu, K.-M.; Gu, L.; Cao, X. Multi-segmented nanowires: a high tech bright future. *Materials* **2019**, *12* (23), 3908.
- (31) Müssig, S.; Reichstein, J.; Miller, F.; Mandel, K. Colorful Luminescent Magnetic Supraparticles: Expanding the Applicability, Information Capacity, and Security of Micrometer-Scaled Identification Taggants by Dual-Spectral Encoding. *Small* **2022**, 2107511.
- (32) Lee, J. H.; Wu, J. H.; Liu, H. L.; Cho, J. U.; Cho, M. K.; An, B. H.; Min, J. H.; Noh, S. J.; Kim, Y. K. Iron-gold barcode nanowires. *Angew. Chem., Int. Ed.* **2007**, *46* (20), 3663–3667.
- (33) Xie, M.; Hu, J.; Wen, C.-Y.; Zhang, Z.-L.; Xie, H.-Y.; Pang, D.-W. Fluorescent–magnetic dual-encoded nanospheres: A promising tool for fast-simultaneous-addressable high-throughput analysis. *Nanotechnology* **2012**, *23* (3), 035602.
- (34) Lu, X.; Li, W.; Sottos, N. R.; Moore, J. S. Autonomous damage detection in multilayered coatings via integrated aggregation-induced emission luminogens. *ACS Appl. Mater. Interfaces* **2018**, *10* (47), 40361–40365.
- (35) Salaluk, S.; Jiang, S.; Viyanit, E.; Rohwerder, M.; Landfester, K.; Crespy, D. Design of Nanostructured Protective Coatings with a Sensing Function. *ACS Appl. Mater. Interfaces* **2021**, *13* (44), 53046–53054.
- (36) Hu, M.; Peil, S.; Xing, Y.; Dohler, D.; Caire da Silva, L.; Binder, W. H.; Kappel, M.; Bannwarth, M. B. Monitoring crack appearance and healing in coatings with damage self-reporting nanocapsules. *Mater. Horiz.* **2018**, *5* (1), 51–58.
- (37) Ballweg, T.; Gellermann, C.; Mandel, K. Coatings with a Molehill Structure of Nanoparticle-Raspberry Containers for Surfaces with Abrasion-Refreshable Reservoir Functionality. *ACS Appl. Mater. Interfaces* **2015**, *7* (44), 24909–24914.
- (38) Müssig, S.; Kuttich, B.; Fidler, F.; Haddad, D.; Wintzheimer, S.; Kraus, T.; Mandel, K. Reversible magnetism switching of iron oxide nanoparticle dispersions by controlled agglomeration. *Nanoscale Adv.* **2021**, *3* (10), 2822–2829.



G

<https://doi.org/10.1021/acs.nanolett.1c04773>  
Nano Lett. XXXX, XXX, XXX–XXX

## Supporting Information

### Optically sensitive and magnetically identifiable supraparticles as indicators of surface abrasion

*Sarah Wenderoth<sup>‡</sup>, Stephan Müssig<sup>‡</sup>, Johannes Prieschl, Emilie Genin, Karine Heuzé, Florian Fidler, Daniel Haddad, Susanne Wintzheimer, Karl Mandel\**

S. Wenderoth  
Chair of Chemical Technology of Materials Synthesis, Julius-Maximilians-University Würzburg,  
Röntgenring 11, D97070 Würzburg, Germany

S. Wenderoth, S. Wintzheimer, K. Mandel  
Fraunhofer-Institute for Silicate Research ISC, Neunerplatz 2, D97082 Würzburg, Germany

S. Müssig, J. Prieschl, S. Wintzheimer, K. Mandel  
Department of Chemistry and Pharmacy, Inorganic Chemistry, Friedrich-Alexander-Universität  
Erlangen-Nürnberg (FAU), Egerlandstrasse 1, D91058 Erlangen, Germany  
E-mail: karl.mandel@fau.de

E. Genin, K. Heuzé,  
University Bordeaux, ISM, UMR-5255, F-33400 Talence, France  
CNRS, ISM, UMR5255, F-33400 Talence, France

F. Fidler, D. Haddad,  
Magnetic Resonance and X-ray Imaging Department, Development Center X-ray Technology,  
Fraunhofer-Institute for Integrated Circuits IIS, Am Hubland, 97074 Würzburg, Germany

### 1. Challenges that were faced during the combination of abrasion functionality and magnetic identification within one entity

Three recent publications<sup>1-3</sup> from our group provide the foundation for this publication. In the herein presented work, an optically detected abrasion indicator functionality is combined with a magnetic identification (ID) functionality within one supraparticle entity. In order to obtain different magnetic ID signals, different magnetic nanoparticles had to be used. In the recently reported publication on abrasion indicators<sup>3</sup>, only one type of magnetic nanoparticle was used.

Perspectively, a large variety of different superparamagnetic nanoparticles (SPIONs) should be used in order to distinguish a variety of different surfaces, ideally with little preparation effort for the SPIONs. This is why the silica shell, that was used in <sup>3</sup> in order to reduce the light absorption of the utilized SPIONs, was not synthesized around the SPIONs in this work to minimize demanded synthetic expertise. But typically, dark magnetic materials hamper the optical properties of surrounding materials due to their light absorption. Absence of the silica shell led to much more luminescence absorption of the utilized SPIONs, so that the ratio of SPIONs to “diluter silica nanoparticles” in the core had to be reduced as much as possible to obtain sufficient luminescence intensity. From a magnetic perspective, however, a higher SPION concentration yields smaller error bars during magnetic identification, so that a high SPION concentration was desired.

While many publications report on the combination of luminescent and magnetic signals in one entity, a *defined spectral* luminescent signal and *defined spectrally* resolved magnetic properties from one entity, which is mechanically abraded, was never reported to the best of our knowledge. It is thus unknown how they affect each other. Thus, it was essential to find a suitable mediocrity in order to resolve both, spectral luminescent and spectral magnetic signals, sufficiently intense.

This is why we demonstrated in this work that it is possible to obtain a spectral luminescent signal and a spectral magnetic signal from one supraparticle entity. Moreover, the supraparticle design



In this work, the rhodamine 110 dye was modified with 3-(triethoxysilyl)propyl isocyanate (ICPTES) and the resulting product is (still) showing fluorescence. Thus, the question arises of firstly, the coupling of these educts via urea formation has been successful at all and if the resulting main product is obtained as mono- or disubstituted dye. As the ICPTES is a multi type reactive molecule due to the triethoxysilyl moiety, it tends to also perform side reactions with itself developing silanol-bridges and ultimately forming aggregates (polycondensation of the silane), which makes any precise reaction analysis difficult. This is why, propyl-isocyanate was chosen as model substance to confirm the reaction behavior of rhodamine 110 with an isocyanate. Furthermore, the propyl isocyanate can be easily evaporated and thus, removed from the reaction mixture, which makes a purification of the product feasible. In order to demonstrate that propyl isocyanate acts an adequate model for ICPTES, both compounds were reacted with rhodamine 110 under the same reaction conditions and spectroscopically examined (**Figure S2**). The synthesis protocols were as follows: 10 mg (27.2  $\mu\text{mol}$ , 1 eq) of rhodamine 110 were dissolved in 2 mL of  $\text{DMSO-d}_6$ . Secondly, mixed with either 15.3  $\mu\text{L}$  (163.2  $\mu\text{mol}$ , 6 eq) of propyl isocyanate (Acros, 99%) or 40.9  $\mu\text{L}$  (165.2  $\mu\text{mol}$ , 6 eq) of ICPTES and allowed to shake overnight. Both syntheses were performed under argon atmosphere.

Examining the optical properties of both obtained (crude) products, it is evident that the absorbance (Figure S2a), excitation and emission spectra (Figure S2b) of the two modifications are indeed very similar. More precisely, the wavelength of the absorbance, excitation and emission maxima coincide. The shoulder observed on the red absorbance spectrum around 550 nm corresponds to the formation of non-emissive aggregates due to the polycondensation of the silane in water. For these reasons, propyl-isocyanate is a good model substance to examine the coupling reaction of rhodamine 110 with an isocyanate.

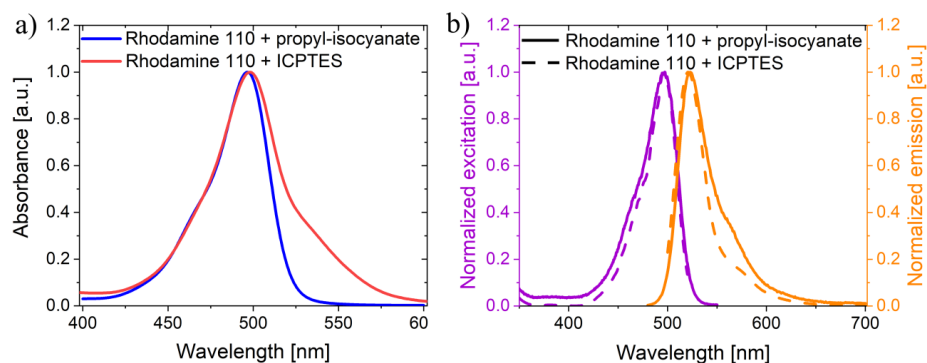


Figure S2: UV-vis spectra of rhodamine 110 coupled with propyl-isocyanate (blue) and ICPTES (red) with an absorbance maximum at 498 nm (a). Excitation (red) and emission (blue) spectra of rhodamine 110 coupled with propyl-isocyanate (line) and ICPTES (dotted line) with an excitation maxima at 496 nm and an emission maxima at 521 nm (b). All measurements were performed in water.

Performing the reaction of rhodamine 110 as described above (and removing excess of propyl isocyanate), two products are conceivable, additional to the pure dye (**Figure S3a**). In case the propyl-isocyanate only couples to one amine group of the dye, the monosubstituted product (Figure S3b) is obtained. If both amine groups are coupled to the ligand, the disubstituted product results (Figure S3c). Additionally, it is possible that the propyl-isocyanate undergoes hydrolysis under the chosen reaction conditions, resulting in a side product that cannot be removed from the crude product mixture. This is why the aging of propyl-isocyanate was also examined by dissolving propyl-isocyanate in DMSO- $d_6$ , analyzing the sample right away and performing again  $^1\text{H-NMR}$  analysis after storing it at room temperature for 8 days.

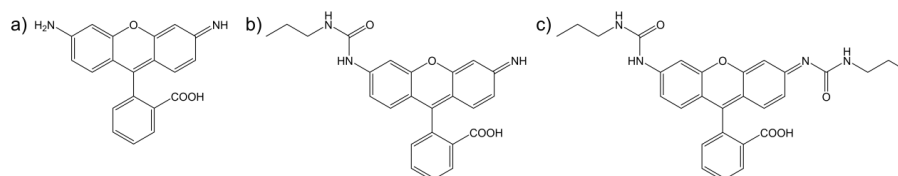


Figure S3: Molecular structure of pure rhodamine 110 dye (a), the monosubstituted rhodamine 110 (b) and the disubstituted rhodamine 110 (c).

In the following <sup>1</sup>H-NMR analyses were used to determine which of the two targeted products were formed. In **Figure S4**, the summarized <sup>1</sup>H-NMR spectra of the reactants are shown (rhodamine 110 (pink), fresh propyl-isocyanate (red), aged propyl-isocyanate (blue)) and the product (rhodamine 110 + propyl-isocyanate (green)). The aged sample of propyl isocyanate indeed showed hydrolysis of the reagent, resulting in propylcarbamic acid, shown by the doubling of signals of the hydrogen atoms of the propyl in the NMR spectra and the appearance of a new signal at around 5.8 ppm caused by the formed amine group (green box). This hydrolyzed compound can also be detected in the product NMR spectrum (orange, red, yellow box), as it cannot be removed after synthesis through evaporation in contrast to propyl-isocyanate (no triplet signal of the CH<sub>2</sub>-group next to the nitrogen of the propyl-isocyanate (purple box) is detectable in the product). The broad singlet (gray box) in the dye spectra (crude product, as well as rhodamine 110 educt), which has a similar chemical shift as the CH<sub>2</sub>-group, is caused by the aniline group. The new signal (found in the crude product), highlighted in the blue box, is caused by the CH<sub>2</sub>-group next to the nitrogen of the propyl-isocyanate coupled to the rhodamine 110 molecule, which indicates the successful modification of the rhodamine 110 molecule with propyl-isocyanate.

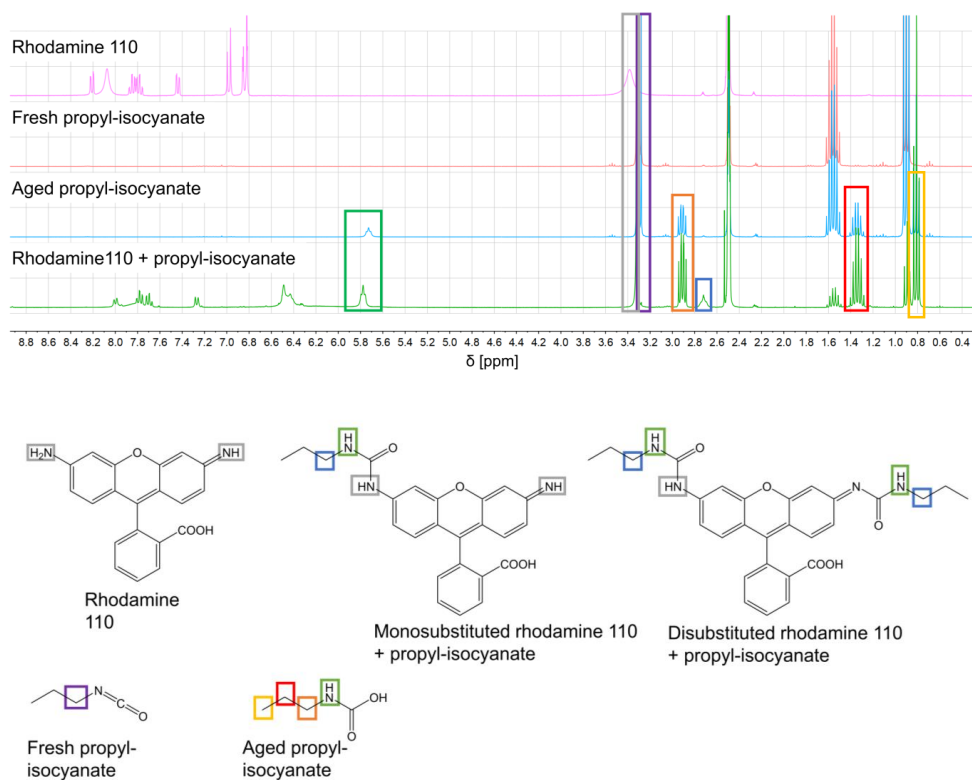


Figure S4: Summarized <sup>1</sup>H-NMR spectra of pure rhodamine 110 (pink), fresh propyl-isocyanate (red), aged propyl-isocyanate (blue) and rhodamine 110 coupled with propyl-isocyanate (green). Furthermore, the structure formula of the different molecules are shown with an allocation of the signals to the respected hydrogen atoms.

In **Figure S5**, the  $^1\text{H-NMR}$  spectra of the rhodamine 110 coupled with propyl-isocyanate is shown, again with highlighted signals (peak picking and integration) of the product molecule (leaving aside the signals of the hydrolyzed propyl isocyanate). As the ratio of the signals from the hydrogen atoms of the propyl-group is nearly 2:2:3, caused by the  $\text{CH}_2:\text{CH}_2:\text{CH}_3$  moieties and 1:2 from the aromatic CH to the  $\text{CH}_2$  groups at 2.7 ppm, it can be reasoned that the monosubstituted product is the main product. Furthermore, some representative signals in the aromatic area for disubstituted rhodamine dyes are missing, which reaffirms the assumption that the monosubstituted product is the main product.<sup>4,6,8,9</sup>

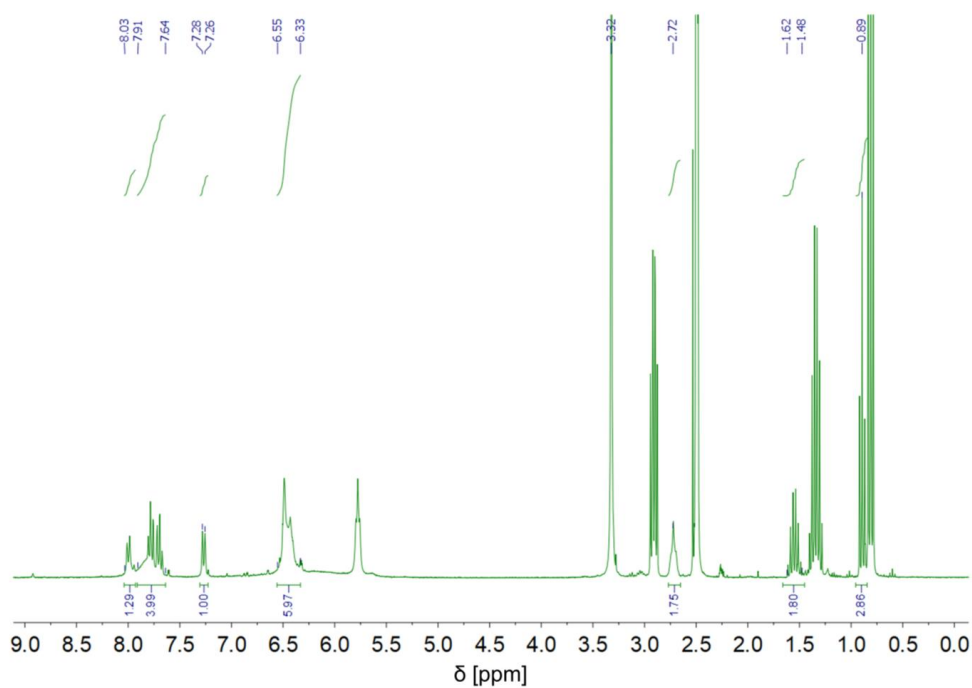


Figure S5:  $^1\text{H-NMR}$  spectra of rhodamine 110 coupled with propyl-isocyanate.

Additionally mass spectrometry analysis was performed (not shown) with an electrospray technique and negative ionization detection. The pure dye cannot be detected in the MS. The monosubstituted rhodamine 110 is observed with  $m/z = 414$  and  $m/z = 449$  also corresponds to the monosubstituted dye with an associated chloride as the starting material is introduced as HCl salt. Furthermore, the disubstituted dye molecule ( $m/z = 499$ ) can be observed. Consequently, the mass spectroscopy analysis supports the finding from NMR spectrometry.

Summing up the characterization results, the coupling of the rhodamine 110 with propylisocyanate was successful. Furthermore, the monosubstituted compound is the main product.

Finally, to demonstrate that for this research the dye coupling with ICPTES is necessary in order to develop covalent integration of the dye molecule into the silica nanoparticles, leaching experiments were performed. For this, two syntheses were carried out. As described in the main manuscript, particles were synthesized with the dye-ICPTES linker and with the pure dye in the same concentration. After the synthesis and purification of the particle dispersion by dialysis, the fluorescence intensity of both products was measured (**Figure S6**). It is evident that the unlinked dye can almost completely be washed out from the silica nanoparticle dispersion, as it cannot be incorporated into the silica matrix during the synthesis. The functionalization of rhodamine 110 with ICPTES as a linker ensures that the dye is covalently linked to the silica matrix and remains by around 90% within the sample after purification.

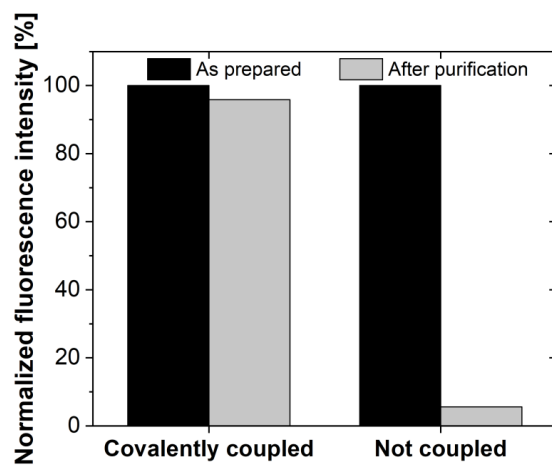


Figure S6: Normalized fluorescence intensity measurements of silica nanoparticle dispersions after synthesis and after purification via dialyses. The dye is coupled with an ICPTES as linker (left) or alternatively added without further functionalization (right).

3. Discussion about magnetic data processing, analysis and the number of possible magnetic codes

In MPS, a harmonic spectrum as function of harmonics is typically analyzed as shown in Fig. 2c. In MPS spectra, the harmonic amplitude of the fundamental frequency is affected by the signal response of materials with non-linear magnetization curves (such as the utilized superparamagnetic iron oxide nanoparticles) but also by linear magnetization curves (such as omnipresent diamagnetic or paramagnetic materials). It is possible to eliminate the influence of non-magnetic materials by normalizing the spectra to the amplitude of the third harmonic and analyze higher harmonics as done herein (see Fig. 2c). This self-referenced characterization of magnetic properties is a powerful advantage compared to many other magnetic characterization techniques and enables to identify the magnetic identification taggants when they are detected exclusively, but also when the identification taggant is incorporated into macroscopic objects such as the herein presented surface coating. After normalization with respect to the amplitude of the third harmonic ( $f_0^{-1} = 3$ ), the observed signal deviations can be reliably used for identification of ID taggants within the respective surface coating. For discrimination of different IDs, their amplitude at a chosen higher harmonic needs to be different, as demonstrated herein exemplarily for  $A_5/A_3$  (Fig. 2b2). Thus, the two surfaces exhibit different harmonic amplitudes, which reliably enables their identification and additionally remain constant with respect to the amplitudes before abrasion.

Although in this work the focus was put on demonstrating the feasibility of the general principle, it is likely that several dozens or hundreds of different magnetic IDs (rather than the two demonstrated IDs) are possible with this concept. This could be achieved in several ways: firstly, by utilizing not only a single code value (as done herein ( $A_5/A_3$ ) for demonstration of the concept in a simple way), but rather utilize several harmonic amplitude ratios in a mathematical algorithm,

the identification reliability could be enhanced, enabling the discrimination of more similar particles. Secondly, the utilization of very different magnetic nanoparticles might yield more exceptional MPS spectra, facilitating their easier distinction. Thirdly, by utilizing more magnetic material within the surface coating, the errors will decrease drastically, also allowing the discrimination of more different IDs. However, the feasibility for this approach certainly depends on the coating demands. Fourthly, as this comparatively new technology further develops, more sensitive MPS devices will be available, which will also decrease the measurement errors.

**Literature (Supporting Information part)**

- (1) Müssig, S.; Reichstein, J.; Prieschl, J.; Wintzheimer, S.; Mandel, K. A Single Magnetic Particle with Nearly Unlimited Encoding Options. *Small* **2021**, 2101588.
- (2) Müssig, S.; Fidler, F.; Haddad, D.; Hiller, K.-H.; Wintzheimer, S.; Mandel, K. Supraparticles with a Magnetic Fingerprint Readable by Magnetic Particle Spectroscopy: An Alternative beyond Optical Tracers. *Adv. Mater. Technol.* **2019**, 4 (9), 1900300.
- (3) Wenderoth, S.; Granath, T.; Prieschl, J.; Wintzheimer, S.; Mandel, K. Abrasion Indicators for Smart Surfaces Based on a Luminescence Turn-On Effect in Supraparticles. *Adv. Photonics Res.* **2020**, 1 (1), 2000023.
- (4) Lavis, L. D.; Chao, T.-Y.; Raines, R. T. Fluorogenic label for biomolecular imaging. *ACS Chem. Biol.* **2006**, 1 (4), 252–260.
- (5) Watkins, R. W.; Lavis, L. D.; Kung, V. M.; Los, G. V.; Raines, R. T. Fluorogenic affinity label for the facile, rapid imaging of proteins in live cells. *Org. Biomol. Chem.* **2009**, 7 (19), 3969–3975.

(6) Gorska, K.; Manicardi, A.; Barluenga, S.; Winssinger, N. DNA-templated release of functional molecules with an azide-reduction-triggered immolative linker. *Chem. Comm.* **2011**, *47* (15), 4364–4366.

(7) Grimm, J. B.; English, B. P.; Chen, J.; Slaughter, J. P.; Zhang, Z.; Revyakin, A.; Patel, R.; Macklin, J. J.; Normanno, D.; Singer, R. H. A general method to improve fluorophores for live-cell and single-molecule microscopy. *Nat. Methods* **2015**, *12* (3), 244–250.

(8) Grimm, J. B.; Lavis, L. D. Synthesis of rhodamines from fluoresceins using Pd-catalyzed C–N cross-coupling. *Org. Lett.* **2011**, *13* (24), 6354–6357.

(9) Banala, S.; Maurel, D.; Manley, S.; Johnsson, K. A caged, localizable rhodamine derivative for superresolution microscopy. *ACS Chem. Biol.* **2012**, *7* (2), 289–293.

# Supraparticles with a Mechanically Triggerable Color-Change-Effect to Equip Coatings with the Ability to Report Damage

Sarah Wenderoth, Andreas Eigen, Susanne Wintzheimer, Johannes Prieschl, Andreas Hirsch, Marcus Halik,\* and Karl Mandel\*

Small scratches and abrasion cause damage to packaging coatings. Albeit often invisible to the human eye, such small defects in the coating may ultimately have a strong negative impact on the whole system. For instance, gases may penetrate the coating and consequently the package barrier, thus leading to the degradation of sensitive goods. Herein, the indicators of mechanical damage in the form of particles are reported, which can readily be integrated into coatings. Shear stress-induced damage is indicated by the particles via a color change. The particles are designed as core-shell supraparticles. The supraparticle core is based on rhodamine B dye-doped silica nanoparticles, whereas the shell is made of alumina nanoparticles. The alumina surface is functionalized with a monolayer of a perylene dye. The resulting core-shell supraparticle system thus contains two colors, one in the core and one in the shell part of the architecture. Mechanical damage of this structure exposes the core from the shell, resulting in a color change. With particles integrated into a coating lacquer, mechanical damage of a coating can be monitored via a color change and even be related to the degree of oxygen penetration in a damaged coating.

and often, they need to possess excellent barrier properties against the permeation of gases or moisture.<sup>[3]</sup> Such high-performance coatings can thereby for instance improve the sustainability of food in the sense that it can be stored longer, which ultimately contributes to less waste.<sup>[2,4]</sup> In addition to the increasing development of high-performance packagings, there are also a large number of studies that deal with the development of intelligent packagings.<sup>[5,6]</sup> This involves the development of intelligent systems, consisting of sensors and indicators, respectively, that can, on the one hand, record the actual state of the packaging throughout the entire supply chain (via sensors) and, on the other hand, provide an irreversible indication of changes regarding the food quality (via indicators).<sup>[1,2,5-7]</sup> Sensors are described as instruments that are able to detect an event or a change in their environment, to localize it, or even to quantify

## 1. Introduction

High-performance coatings become more and more important in the field of packaging.<sup>[1,2]</sup> Due to growing demands from the packaging industry and the large number of different wrapping types, coating materials have to meet ever more specific requirements. The coatings need to be very thin, highly flexible,

in order to send signals that this change can be investigated in terms of its physical or chemical nature.<sup>[1,2]</sup> These types of sensors can be, for example, gas sensors, fluorescence-based oxygen sensors, or biosensors.<sup>[8]</sup> Such fluorescence-based oxygen sensors for example could determine the oxygen content by measuring the fluorescence lifetime of ruthenium(II) or platinum(II)-octaethylporphyrine-ke-ton dye complexes.<sup>[9,10]</sup>

S. Wenderoth  
 Chair of Chemical Technology of Materials Synthesis  
 Julius-Maximilians-University Würzburg  
 Röntgenring 11, D97070 Würzburg, Germany  
 S. Wenderoth, S. Wintzheimer, K. Mandel  
 Fraunhofer-Institute for Silicate Research  
 ISC  
 Neunerplatz 2, D97082 Würzburg, Germany  
 E-mail: karl.mandel@fau.de

 The ORCID identification number(s) for the author(s) of this article can be found under <https://doi.org/10.1002/smll.202107513>.

© 2022 The Authors. Small published by Wiley-VCH GmbH. This is an open access article under the terms of the Creative Commons Attribution License, which permits use, distribution and reproduction in any medium, provided the original work is properly cited.

DOI: 10.1002/smll.202107513

A. Eigen, M. Halik  
 Organic Materials & Devices  
 Department of Material Science, Interdisciplinary Center for Nanostructured Films (IZNF)  
 Friedrich-Alexander University Erlangen-Nürnberg (FAU)  
 Cauerstrasse 3, D91058 Erlangen, Germany  
 E-mail: marcus.halik@fau.de  
 S. Wintzheimer, J. Prieschl, K. Mandel  
 Department of Chemistry and Pharmacy  
 Inorganic Chemistry  
 Friedrich-Alexander University Erlangen-Nürnberg (FAU)  
 Egerlandstrasse 1, D91058 Erlangen, Germany  
 A. Hirsch  
 Institute of Organic Chemistry II  
 Friedrich-Alexander University Erlangen-Nürnberg (FAU)  
 Nikolaus-Fiebiger-Strasse 10, D91058 Erlangen, Germany

Even though these sensors bring significant advantages over invasive analytical measurements techniques (such as gas chromatographic mass spectrometry),<sup>[11]</sup> there are still some challenges which need to be overcome to permit widespread use. The requirements include the reduction of size by increasing the flexibility, reducing development and production costs, and increasing both resistance and sensitivity.<sup>[2]</sup> Furthermore, the read-out of such sensors is difficult and not practicable for the end user.<sup>[2,9]</sup>

Indicators in packaging, as opposed to sensors, are instruments that cannot provide quantitative information or store data, but can give a direct, qualitative indication in the form of a color change, increased color intensity, or the diffusion of a dye along a specified path.<sup>[12]</sup> Application examples for such indicators include monitoring of cold chains, of the atmosphere (presence of oxygen or various putrefactive gases, etc.), or the presence of microorganisms (bacteria, yeast, fungi).<sup>[2,9]</sup> For example, gas indicators determine the oxygen concentration by means of a visible color change of redox dyes (e.g., methylene blue, 2,6-dichloroindophenol or *N,N,N',N'*-tetramethyl-*p*-phenylenediamines), a reduction component (e.g., reduced sugar) and an alkaline component (such as sodium hydroxide).<sup>[9,13]</sup> The disadvantage of such indicators is that leaching effects can always occur (e.g., due to moisture inside the packaging) which can lead to false results.<sup>[9]</sup>

All these indicators have in common that they can only determine whether the food is still edible, but cannot provide information about the integrity of the packaging itself. There are studies describing the influence of damage in the packaging coating on the increased permeation of gases, but to the best of our knowledge, there is no way to detect these minor damages on the surface of a package with simple methods.<sup>[14]</sup>

More general, studies on the detection of scratches in functional coatings (but not in/for packaging materials) have been made: For example, the use of dye-filled capsules in an anti-corrosive coating on a copper substrate was shown.<sup>[15]</sup> Here, destruction of the surface coating and subsequent UV irradiation reveals fluorescence that can indicate the progress of corrosion in the copper substrate. Another study shows the development of a multilayer coating in which the different layers have capsules filled with different dyes.<sup>[16]</sup> Depending on how deep the scratches penetrate the coating different colors can be detected. Another work on self-healing coatings to prolong the use of coated opponents also describes the use of dye-filled capsules.<sup>[17]</sup> If the capsules are destroyed by cracks in the coating (cuts), the dye can escape and the color indicates the damage. If the dye now reacts with reactive groups on the capsule surface, the self-healing process starts and the color disappears, which in turn indicates that the layer is intact again. However, these kinds of systems only work if rather deep scratches (several tens of microns up to hundreds of microns) are induced in the respective layers.

In this study, we present an intelligent surface that is able to detect shear induced stress on the surface before there is any effect on the integrity of the packaging itself, even in coatings of a few microns in size (<10 μm). This effect can be detected using shear stress indicator supraparticles that exhibit a mechanically triggered color change effect.

The use of dyes, like rhodamines and perylene bisimides, that are widely used and whose stability has been extensively studied in areas such as solar cell technology, organic light-emitting diodes and which are even used as standards for photoluminescence quantum yield measurements enables the production of highly stable films that can be used for practical packaging applications.<sup>[18]</sup>

Supraparticles are micrometer-sized, hierarchically structured particles assembled from nanoparticulate building blocks, where the intrinsic properties of the nanoparticles remain active.<sup>[19]</sup> Core-shell structures can be formed by selectively assembling the nanobuilding blocks into a supraparticle (e.g., by spray-drying).<sup>[20]</sup>

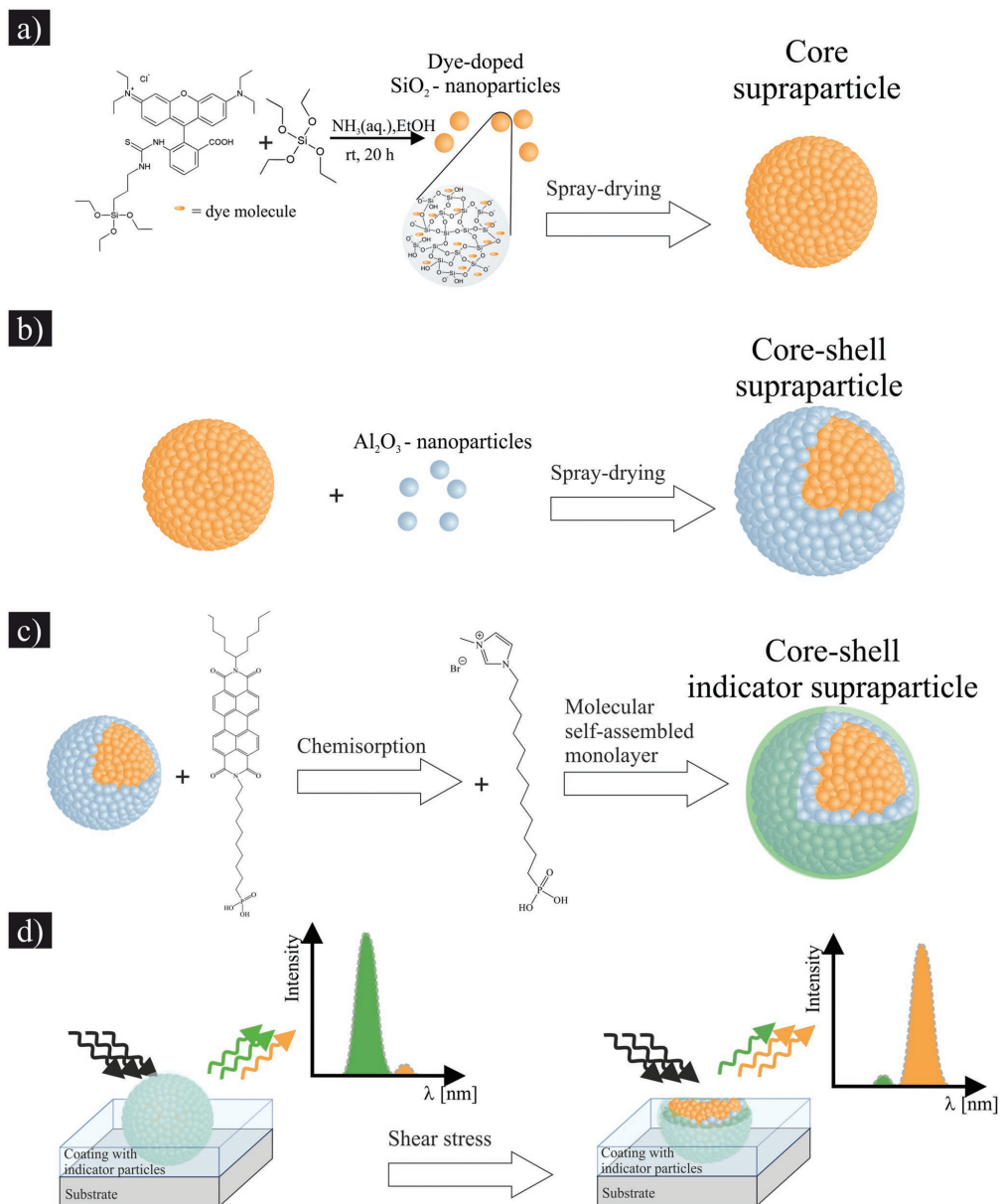
In the novel concept, the supraparticle core is based on dye-doped silica nanoparticles surrounded by a shell of dye-decorated alumina nanoparticles. This dye on alumina is applied as a monolayer in a self-assembling process. The self-assembled monolayer itself is composed of two different molecules, both based on phosphonic acid derivatives. One provides the chromophore and is thus responsible for the color change itself. The second one changes the hydrophilicity of the whole system and thus the processability of the supraparticles. Furthermore, it tunes the chromophores absorption and emission from excimer to monomer signature in order to gain a clear contrast to the dye of the inner core.

After incorporating these supraparticles into a thin coating of around 5 μm, a molehill-like structure can be observed. In these coatings, only the tip of the supraparticles sticks out of the lacquer film. A defined abrasion slightly changes the ratio between shell and core on the upper side of the coating, thus causing a color change between the two dye systems. This spectral shift can be used as a measure of the integrity of the packaging material and is, therefore, suitable for industries with high throughput due to the simple measuring process. A further benefit of this work in contrast to, for example, the use of capsules in a polymer film described above is that no additional layer needs to be applied to a package, as the indicator supraparticles can be incorporated directly into the barrier coating of the packaging.

## 2. Results and Discussion

The supraparticles that respond to mechanical stress via a color change have to be constructed very specifically when used for the development of smart coatings. The most important prerequisites for the successful production of such supraparticles are the morphology (spherical) and size (>10 μm) of the supraparticles, the use of different dyes (rhodamine B and *N*-(1-hexylheptyl)-*N'*-(undecylphosphonic acid) perylene-3,4,9,10-tetracarboxylic bisimide (PBI-PA)) that can be excited at the same wavelength and, above all, an extremely precise hierarchical structure within the supraparticles. The step-by-step process (four steps, **Scheme 1**) to create a smart surface is as follows:

First, a silanized rhodamine B dye is covalently incorporated into the silica network of 80 nm silica nanoparticles in a modified Stöber synthesis and the dye-doped nanoparticles are assembled into spherical supraparticles via spray-drying (**Scheme 1a**).<sup>[21]</sup>



**Scheme 1.** Schematic process of the investigation of color change indicator supraparticles. The process is divided into 4 steps. a) In a first step, dye-doped silica nanoparticles are synthesized via the Stöber process and spray-dried to core supraparticles. b) In a second step, core-shell supraparticles are obtained via a second spray-drying process with alumina nanoparticles. c) In a third step, PBI-PA is chemically adsorbed onto the supraparticles, followed by the formation of a self-assembled monolayer consisting of Imi-PA. d) The core-shell indicator supraparticles are then embedded into a coating, in a way that a molehill-like structure is received. Due to a shear stress on the surface, the emission of the intact state in green switches to orange in the sheared-off state.

Second, commercially available alumina nanoparticles with a primary particle size <50 nm are spray-dried around the dyed silica core supraparticles to form core-shell supraparticles (Scheme 1b). The alumina nanoparticles serve as a binding site for the subsequent growth of a self-assembled monolayer (SAM).

Third, the SAM, consisting of the second dye molecule PBI-PA and the matrix molecule 1-Methyl-3-(dodecylphosphonic acid)imidazolium bromide (Imi-PA) is self-assembled on the alumina nanoparticle surface on the supraparticle shell (Scheme 1c).

Forth, the produced core-shell indicator supraparticles are incorporated into a coating lacquer. Due to the size of the supraparticles, a molehill-like structure is formed (Scheme 1d).<sup>[22]</sup>

When observing the emission behaviour, the fluorescence of the perylene dye at the particle surface predominates in the intact initial state. However, when the layer is subjected to shear stress, the supraparticles are successively removed. When observing the emission behaviour, a shift from the perylene dye to the rhodamine B dye in the supraparticle core can be seen.

In previous studies we showed, that PBI-PA together with matrix SAM-molecules form stable mixed self-assembled monolayers.<sup>[23]</sup> It was demonstrated, that the mixing ratio determines the amount of aggregated PBI-PA molecules, which exhibit excimer fluorescence.<sup>[23]</sup> To create a sharp optical monomer fluorescence the number of aggregates needs to be minimized. Therefore, we used a two-step process to maximize the distance between the PBI-PA molecules and to hinder aggregation. As a demonstration, pristine alumina nanoparticles (FTIR spectra in the supplementary Figure S1, Supporting Information), which were not assembled into supraparticles, were functionalized with 10  $\mu$ M PBI-SAM in a first step (Figure 1). The resulting particles showed three peaks in fluorescence measurements at 530, 578, and 630 nm, where the first two narrow peaks belong to the monomer, and the third broad peak belongs to the excimer fluorescence (Figure 1a).<sup>[23]</sup> The fluorescence of the excimer clearly outweighs the fluorescence of the monomers. Since the molecules move individually in a dissolved state, it can be assumed that their anchoring on

the surface takes place in a disordered manner. As the concentration is well below that required for a saturated surface, the molecules can move freely around their anchor point and thus come into contact with other PBI-PA molecules. This leads to the formation of the undesired excimers (Figure 1b). In a second step, 10 mM Imi-PA was added to the prefunctionalized particles with the chemisorbed PBI-PA. This concentration exceeds the necessary concentration for a full surface coverage as was shown in previous work.<sup>[23]</sup> Fluorescence measurements revealed that the excimer peak vanished at 630 nm and a clear monomer signal remained afterwards. The Imi-PA molecules function as matrix molecules. These occupy the remaining free surface spaces towards a fully saturated monolayer. The filling with the IMI-PA restricts the radius of movement of the PBI-PA significantly so that the aggregated chromophores become isolated and all molecules in mixed SAM occur more perpendicular oriented.<sup>[24]</sup> Fluorescence spectra of core-shell supraparticles with only rhodamine B dye doped silica nanoparticles in the supraparticle core are shown in the supplementary information (Figure S2, Supporting Information).

The supraparticles used herein are produced via spray drying. During this process, several parameters influence the size and morphology of the resulting supraparticles. These for example are the nozzle used to generate the spray mist, the viscosity, solids concentration, and the solvent of the nanoparticle dispersion, but also the temperature in the plant. For the production of shear stress indicator supraparticles, several of these factors must be carefully adjusted. On the one hand, spherical supraparticles are required, which also have a highly ordered core-shell structure (Figure S3, Supporting Information). On the other hand, the supraparticles must also be large enough to protrude significantly from the lacquer layer to form a molehill-like structure, which is crucial for shear stress detection. Achieving these targets is possible by using an ultrasonic nozzle and by adding salt to the precursor dispersion. An ultrasonic nozzle generates larger droplets compared to the conventional two-fluid nozzle, which usually results in larger supraparticles (for the same spray parameters). The supraparticles used in this work were analyzed by dynamic laser diffraction and an average

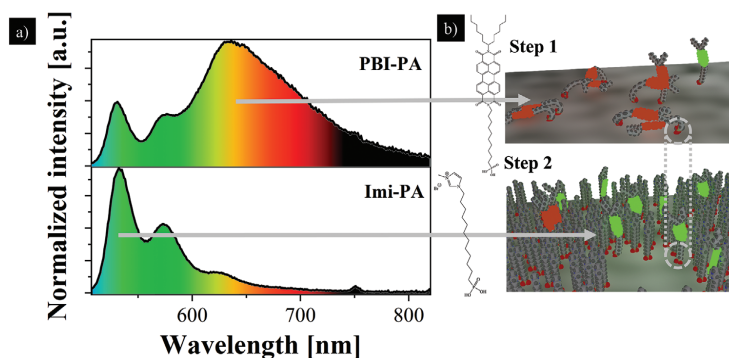


**Figure 1.** Fluorescence spectra ( $\lambda_{\text{ex}} = 500$  nm) of alumina nanoparticles after first and secondary functionalization with PBI-PA and Imi-PA in THF:MeOH 2:1 (a) and the schematic process leading to the formation of a dense, self-assembled monolayer with incorporated but isolated PBI-PA molecules (b). The grey circle indicates the same anchoring group on the surface as a guide for the eye.

particle diameter of  $23 \mu\text{m} \pm 16 \mu\text{m}$  was obtained (Figure S4, Supporting Information). Salt addition to the nanoparticle dispersion helps to adjust the supraparticle morphology. Nanoparticles that form stable dispersions (showing no agglomeration) tend to be spaced as far apart as possible in droplets. If the solvent is now gradually evaporated, a “crust” of nanoparticles first forms at the outer edge of the drop and the solvent is trapped in the center. Given the external temperature is high enough to evaporate the solvent, the outer crust will eventually crack and donut-shaped supraparticles will result. However, if the particle dispersion is destabilized before the spray drying process, as done in this work with calcium chloride, small agglomerates are already formed in the dispersion. Consequently, a generated drop contains several of these agglomerates, which facilitates solvent evaporation and decreases disintegration, ultimately resulting in spherical supraparticles.<sup>[25]</sup> Regarding the spray drying process, one has to mention that a perfectly homogeneous droplet size distribution cannot be achieved, which results in supraparticles with a rather broad size distribution.

An important point for the application of spray-dried supraparticles as shear stress indicators in layers, besides size and shape, is their mechanical stability. The stability of

supraparticles has already been investigated in various publications and it was stated that, depending on their composition, they are very robust against static pressure, and even quite resilient to shear stress to a certain degree.<sup>[26]</sup> In the present work, this was confirmed, as both strong magnetic stirring of supraparticle dispersions as well as the coating application with a spiral doctoral blade did not affect the supraparticles inertness.

Furthermore, the localization of the two dyes either in the core or in the shell, respectively, must be determined. Confocal microscopy images were taken to visualize the localization of the two different dyes in the core-shell structure of the supraparticle (Figure 2). For this purpose, supraparticles were prepared where either the core or the shell was labelled with rhodamine B or PBI-PA, respectively. The supraparticles were incorporated into a coating (“as prepared state”, Figure 2a,c) and then chopped-off to see the cross-section (Figure 2b,d). The inlets in each image (bottom left) are intended to schematically illustrate the aforementioned type of supraparticle in the microscopic image. The rhodamine B dye (Figure 2a,b), which is located in the core of the supraparticle, is also visible in the as prepared state, as the alumina nanoparticle-based shell is optically transparent. In both images of the labelled core supraparticles, a

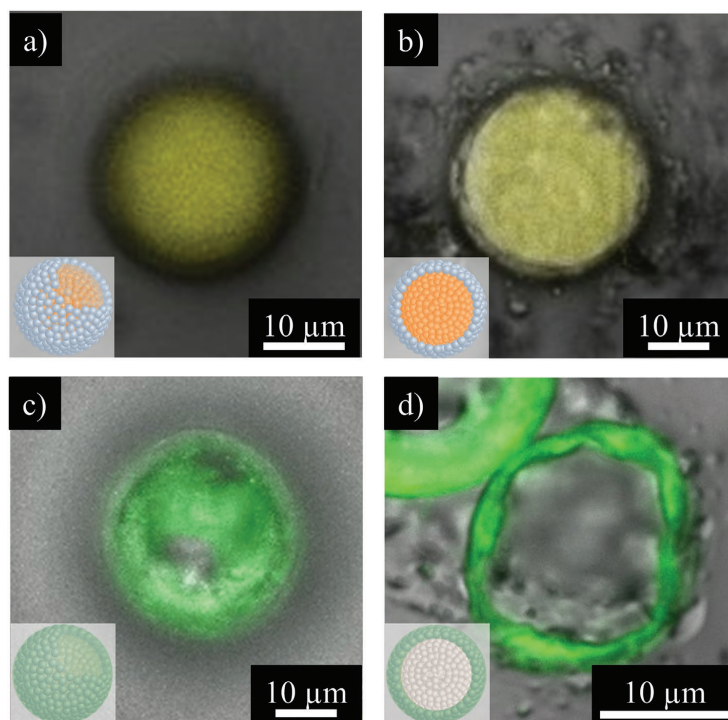


**Figure 2.** Confocal microscopy images of supraparticles where only the core (a,b) or the shell (c,d) is labelled with the corresponding dyes. The as-prepared core labelled supraparticle (a) and the corresponding cross-section (b) are labelled with rhodamine B. The shell labelled supraparticles in the as-prepared (c) and cross-sectioned (d) state are functionalized with the PBI-PA-dye. The schematic illustrations on the bottom left of each panel visualize the supraparticle state schematically.

dark, non-fluorescent shell is visible, which is the shell of the alumina nanoparticles. In the case of the PBI-PA dye located in the shell of the supraparticles (Figure 2c,d), it can be seen that the dye is located exclusively in the shell, and the core of the supraparticle, based on silica nanoparticles, does not fluoresce. While phosphonic acids bind covalently on alumina surfaces with almost no tendency of desorption, they weakly physisorb on silica and can be easily removed by solvent.<sup>[27]</sup> Therefore, the SAM is only bound to the outer shell. Due to the similar excitation and emission spectra of the two dyes, it is not possible to detect both dyes in confocal microscopy within one supraparticle with sharp boundaries.

The supraparticles are coated onto a polyolefin film with a 20  $\mu\text{m}$  doctor blade. During curing, a molehill-like structure is obtained with the supraparticles sticking out from the layer (Figure 3a). The schematic presentation in Figure 3a1 shows that the supraparticle is envisioned to be completely embedded in the lacquer layer in the lower area, while only a thin layer of lacquer covers the entire supraparticle at the top. SEM reveals that the desired molehill-like structure could indeed be obtained (Figure 3a2). The cross-section of a supraparticle in the initial state (Figure 3a3) reveals that the supraparticle represents an elevation within the coating, while the entire supraparticle is still covered by a thin lacquer layer. It can also be noticed that the coating process did not negatively affect the stability of the supraparticles as the spherical supraparticles remain intact within the layer. After shear stress (Figure 3b), the supraparticles, as envisaged in the schematic drawing (Figure 3b1), are indeed chopped-off, as confirmed via SEM (Figure 3b2). The cross-section depiction of the sheared state (Figure 3b3) reveals that the molehill-like structure at the upper edge is flattened, but the rest of the supraparticle itself remains intact without completely breaking out of the layer during shear stress

conditions. The dashed lines in Figure 3a3 and Figure 3b3 are for illustrative purposes only to guide the reader's eye. The original image can be found in Figure S5, Supporting Information.

After having incorporated the indicator supraparticles into a coating, shear stress experiments were carried out. For this purpose, the coated film was fixed on a glass slide and a cube-shaped stamp (15  $\times$  15 mm) was equipped with an abrasion paper and placed on it at a 90° angle (see Experimental Methods section for more details). The finger was moved over the sample in a linear motion on a 7 cm long path up to 1500 times with a load of 4 N. Since this is a rather hard treatment of the coating surface, it is worth mentioning that the supraparticles cannot be removed from the coating by simply touching, wiping or unrolling/bending. After several shear cycles (0, 100, 250, 500, 1000, 1250, and 1500), fluorescence spectroscopy measurements were performed (Figure 4). Both dyes can be excited at the same wavelength, but possess different emission spectra, which can be distinguished from each other. Thus, with simultaneous excitation, the different emission behavior during the shearing process can also be detected at the same time. The excitation wavelength was set to 520 nm and the emission spectra were recorded between 530 and 620 nm. Caused by the two different dyes in the supraparticles, two different emission maxima were detected. The first maximum at 537 nm (green line) is caused by the PBI-PA on the supraparticle shell, and the maximum at 580 nm (orange line) relates to the rhodamine B dye in the supraparticle core (Figure 4a). Both dyes can also be detected in the initial state at 0 shear cycles (black line). The nanoparticles, in the system used here, for the core material (silica) as well as for the shell material (alumina) are optically transparent in the visible range. In addition, both dyes can be excited with the same wavelength, which means that both can be detected simultaneously even in the as prepared state. During the shearing

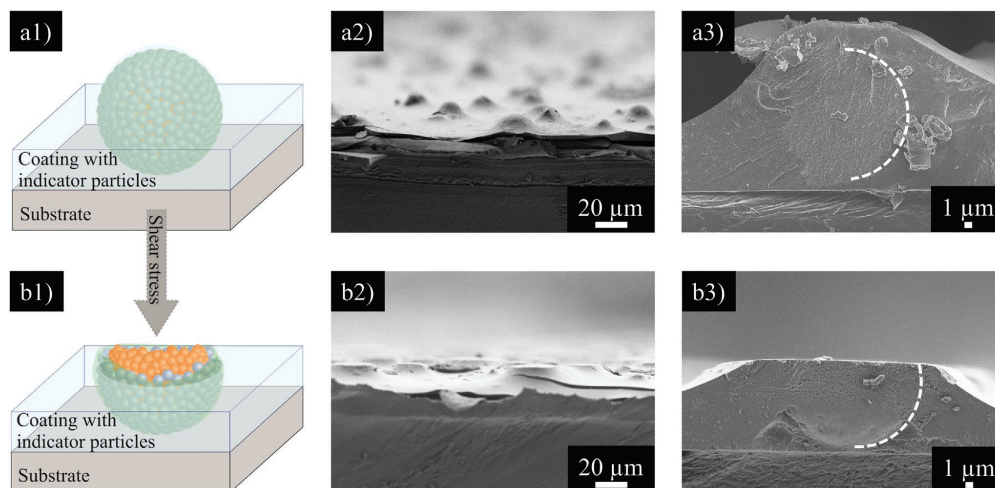


**Figure 3.** Schematic illustrations of the a1) embedded indicator supraparticle in a coating in the as-prepared and the b1) and the sheared-off state. a2) SEM images of the real sample in the as-prepared b2) and in the sheared-off state, a3) as well as cross-section images of an indicator supraparticle in the as-prepared b3) and the sheared-off state. The white dashed line was added to guide the reader's eye for better visibility of the supraparticles.

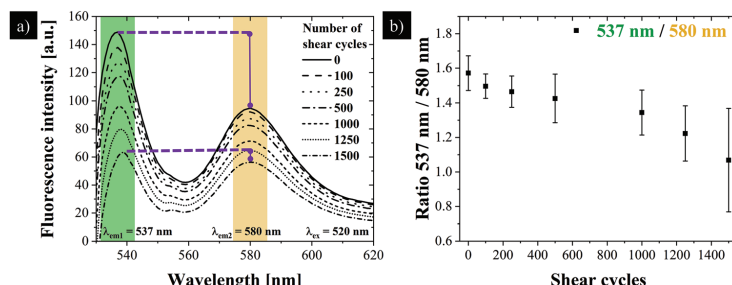


**Figure 4.** Fluorescence spectroscopy measurements of embedded indicator supraparticles: a) Fluorescence intensity as a function of wavelength of the supraparticles during a shear process over 1500 shear cycles ( $\lambda_{\text{ex}} = 520$  nm,  $\lambda_{\text{em1}} = 537$  nm,  $\lambda_{\text{em2}} = 580$  nm). b) The ratio between the two dye maxima is plotted as function of the shear cycles.

process, however, it can be observed that the emission peak of the PBI-PA in the supraparticle shell decreases faster than the peak of the rhodamine B dye. The purple lines are added to emphasize the massively changed intensity ratio between the two peaks. Consequently, a color change from green to orange can be detected. The gradual removal of the supraparticles initially causes the shell to be removed faster than the core. Due to the change in the cross-sectional area, whereby more of the core is visible than of the shell, the fluorescence of the core dye is decreasing more slowly.

The overall detected decrease of fluorescence intensity—also with the rhodamine B dye—can be explained by particle loss mechanisms during the shear-off process.<sup>[21]</sup> Figure 4b depicts the relationship between the PBI-PA and rhodamine B dyes over the shear cycles. It can be seen that the ratio decreases over the entire shear process. This ultimately results in a net change in color.

In addition to the fluorescence spectroscopy measurements, the abrasion of the supraparticles in the coating can also be detected by measuring the oxygen transmission rate. In the as-prepared state, the coating has an oxygen transmission rate of  $520 \text{ cm}^3 (\text{m}^2 \text{ d bar})^{-1}$ , after 1000 shear cycles this value increased to  $4972 \text{ cm}^3 (\text{m}^2 \text{ d bar})^{-1}$ . This increase of the oxygen transmission by a factor of 10 is caused by the destruction of the entire coating by the mechanical shear forces. Thus, the use of the developed indicator supraparticles is a possibility to create a smart surface which can indicate damage caused to a surface by changing its color. As this coating will be part of a packaging system, the color of the surface can ultimately give a hint to the oxygen transmission properties of the coating.

### 3. Conclusion

In summary, this work demonstrated the development of an intelligent surface that is capable of indicating mechanical damage, caused by shear forces, by means of a color change. The system is based on hierarchically constructed supraparticles with two different dyes situated either in the core or in the shell of the supraparticle, respectively. Using supraparticles in which either the core or the shell is labelled with the corresponding dyes, the localization of the individual dyes within the

supraparticle could be visualized via confocal microscopy. It was also possible to ensure that the PBI-PA dye in the mixed monolayer shell of the supraparticle exhibit monomer emission. After embedment of these supraparticles in a thin coating, a molehill-like structure could be achieved, in which the measured fluorescence of the supraparticles changed from green to orange as a result of a shear process (mechanical damage). The color change of the coating during the shearing process could also be correlated with the oxygen permeability of the intact and damaged coating, respectively. In the sample study, a color change from green to orange indicated an increase of oxygen permeability from  $520$  to  $4972 \text{ cm}^3 (\text{m}^2 \text{ d bar})^{-1}$ . Overall, this work demonstrates how the chemistry of molecules can be combined with the world of nanoobjects to create macroscopic systems that can be used as smart surfaces

### 4. Experimental Section

The chemicals were purchased from the following companies: tetraethoxysilane (TEOS), rhodamine B isothiocyanate, (3-aminopropyl) triethoxysilane, dimethyl sulfoxide, alumina nanoparticle-dispersion ( $<50$  nm in isopropanol), tetrahydrofuran, methanol (Sigma-Aldrich, Germany), aqueous ammonia solution (VWR, Germany), ethanol (CSC Jäcklechemie, Germany), 1-Methyl-3-(dodecylphosphonic acid) imidazolium bromide (Imi-PA). The synthesis of *N*-(1-hexylheptyl)-*N'*-(undecylphosphonic acid) Perylene-3,4,9,10-tetracarboxylic bisimide (PBI-PA) has previously been published elsewhere.<sup>[28]</sup> All chemicals were used without further purification.

**Synthesis of Dye-Doped Silica Nanoparticles:** The synthesis of 80 nm silica nanoparticles was carried out according to the literature,<sup>[21]</sup> based on the Stöber process.<sup>[29]</sup> In a normal experiment, 300 ml of ethanol was mixed with 15 ml of aqueous ammonia solution (25 wt%). With vigorous stirring, 15 g (0.072 mol) of TEOS was added, and after 30 min, 300  $\mu\text{L}$  of a previously prepared dye solution was added and the mixture was stirred overnight. Purification was carried out by rotatory evaporation to remove the ethanol/ammonia solution and was additionally dialyzed for 24 h with multiple water changes (dialysis membrane: molecular weight cut-off 10 kDa, cellulose hydrate membrane, Nadir-dialysis tubing, Roth, Germany).

For the dye solution, 9 mg (0.017 mmol) of rhodamine B isothiocyanate were dissolved in 2 ml of dimethyl sulfoxide and mixed with 13  $\mu\text{L}$  (0.055 mmol) of (3-aminopropyl)triethoxysilane. This mixture was stirred for 24 h.

**Spray Drying of Core-Shell Indicator Supraparticles:** In the first step, the silica nanoparticle dispersion was mixed with 10 wt%  $\text{CaCl}_2$  and

spray-dried by using a B-280 mini spray-dryer (Büchi, Switzerland). The spray-dryer was equipped with an ultrasonic nozzle and the inlet temperature was set at 140 °C, with an outlet temperature of about 80 °C. The ultrasonic nozzle has a power of 5 W. In a second step, the shell formation step, the previously built-up core supraparticles were again spray-dried with alumina nanoparticles in a weight ratio of 1:1, whereby the same spray-drying conditions were selected as for the core supraparticles.

**Supraparticle Functionalization with Self-Assembled Monolayers:** In a first step, the core-shell supraparticles were dispersed in a THF solution of 10 µM of PBI-PA to form a 1 mg ml<sup>-1</sup> dispersion and stirred for 5 min. The mixture was left to rest for 10 min, during which time the functionalized particles sedimented. The supernatant containing the unbound PBI-PA molecules was removed and the supraparticles were washed twice in THF to remove any unbound PBI-PA molecules. One washing step consisted of redispersing the particles in THF, stirring for 5 min, and sedimentation for 10 min. In a second step, the supraparticles were redispersed in a THF/Methanol mixture (v/v, 2:1) 10 mM Imi-PA solution to form a 2 mg ml<sup>-1</sup> dispersion and stirred for 5 min. Again, the mixture was allowed to rest for 10 min for sedimentation and washed in a THF/methanol mixture two times as described in the previous step. Afterwards the particles were dried in an oven over night at 80 °C.

**Coating of Color Change Supraparticles as Thin Films:** The substrate is a polyolefin film that was treated twice by a corona application (Arotec treater, Germany) at 0.6 kV and then coated with the lacquer particle mixture. The lacquer used is described in earlier work.<sup>[22]</sup> 150 mg of the color-change indicator supraparticles were suspended in 1.5 ml of the lacquer and applied to the polyolefin film using a 20 µm spiral doctor blade on a Coatmaster 509 MC (Erichsen Testing Equipment, Germany). The coated films were cured for 10 min at room temperature and for 30 min at 90 °C.

**Characterization of Color Change Supraparticles and Coatings:** Abrasion experiments were carried out with an automated crockmeter (Tomsic, Italy). For this purpose, the coated film was fixed on a glass plate, and the squared abrasion finger (1.5 × 1.5 cm) was placed on it at a 90° angle. The finger was covered with an abrasion paper (SIC, roughness #4000, grain size 5 µm, Struers, Germany). The parameters for the tests were set as follows: track length: 7 cm, load of the finger: 4 N, cycle numbers: 0–1500.

An FP8600 spectrofluorometer (Jasco, Japan) with a solid sample holder (FDA-808, Jasco, Japan) was used for the fluorescence spectroscopy measurements. The excitation wavelength was set to 520 nm and the spectra were recorded from 530–620 nm.

In addition, a RF-6000 spectrofluorometer (Shimadzu, Japan) with a quartz cuvette was used for fluorescence spectroscopy measurements on particle dispersions. The excitation wavelength was set to 500 nm.

The overview images of the morphology of supraparticles, the cross-sections of supraparticles, and the coatings were taken with a Supra 25 SEM (Zeiss, Germany) at 2 kV (field emission) and a working distance of 4 mm. The cross-sections were prepared by dispersing 10 mg of core-shell supraparticles in 500 µL of lacquer, curing at 90 °C, and cutting with a scalpel. The cut sample was placed on an SEM sample holder by using conductive silver and sputtered with platinum for 5 s at 50 mA (MED 010, Balzers Union).

Confocal microscopy measurements were performed using a Leica TCS SP8 (Leica Microsystems GmbH, Germany) with a 63 × 1.4 water immersion objective and a SuperK Extreme EXW white light laser. The core labelled coatings were excited at 540 nm and the resulting fluorescence signals were recorded between 560–750 nm. For the shell labelled coatings, the excitation wavelength was set to 520 nm and the emission signals were recorded between 540–580 nm. The non-fluorescent parts of the sample were recorded simultaneously by transmission light imaging.

Oxygen transmission rates were recorded using a Mocon Ox-Tran 2/21 oxygen permeation measuring device (AMETEK GmbH, Germany). The relative humidity was set to 50% and the measurement temperature was 23 °C.

Fourier Transform Infrared Spectroscopy (FT-IR) measurements on dried nanoparticles were obtained by a IR Presitge-21 (Shimadzu, Japan) with a resolution of 4 cm<sup>-1</sup> in a range of 400 to 4000 cm<sup>-1</sup>.

## Supporting Information

Supporting Information is available from the Wiley Online Library or from the author.

## Acknowledgements

This work was financially supported by the BMBF (NanoMatFutur grant 03XP0149) and the Deutsche Forschungsgemeinschaft (DFG) in the scope of the SFB 953 (182849149) who are gratefully acknowledged. The authors thank BÜCHI Labortechnik AG for providing the spray-dryer equipment.

Open access funding enabled and organized by Projekt DEAL.

## Conflict of Interest

The authors declare no conflict of interest.

## Author Contributions

S.W. and A.E. contributed equally to this work. Overarching research goals were developed by S.We., A.E., S.Wi., M.H. and K.M. Supervision of the whole project was done by S.We., A.E., M.H., and K.M. Preceding experiments, knowledge acquisition, and identification of key problems was performed by S.We. and A.E. Dye-doped silica nanoparticles and supraparticles were synthesized by S.We.. Surface Incorporation of supraparticles into the coating, abrasion tests, and confocal microscopy were performed, optically characterized and interpreted by S.We. Synthesis of PBI-PA was done by A.H.. Surface functionalization of core-shell supraparticles was done by A.E.. SEM characterization was done by J.P.. Figures were created by S.We. with support from A.E.. Original paper draft was written by S.We. with the input of A.E.. Reviewing and editing was performed by S.We., A.E., S.Wi., M.H., and K.M. All authors proof-read and commented on the publication.

## Data Availability Statement

The data that support the findings of this study are available in the supplementary material of this article.

## Keywords

abrasion indicators, color changes, smart surfaces, supraparticles, self-assembled monolayers

Received: December 3, 2021

Revised: February 11, 2022

Published online: March 6, 2022

[1] M. Sohail, D.-W. Sun, Z. Zhu, *Crit. Rev. Food Sci. Nutr.* **2018**, *58*, 2650.

[2] M. Vanderroost, P. Ragaert, F. Devlieghere, B. de Meulenaer, *Trends Food Sci. Technol.* **2014**, *39*, 47.

- [3] J. Wang, D. J. Gardner, N. M. Stark, D. W. Bousfield, M. Tajvidi, Z. Cai, *ACS Sustainable Chem. Eng.* **2018**, *6*, 49.
- [4] L. Mei, Q. Wang, *Annu. Rev. Food Sci. Technol.* **2020**, *11*, 339.
- [5] A. N. A. Sari, E. Warsiki, I. A. Kartika, *Conf. Ser.: Earth Environ. Sci.* **2021**, *1*, 012009.
- [6] K. L. Yam, P. T. Takhistov, J. Miltz, *J. Food Sci.* **2005**, *70*, R1.
- [7] B. Bayram, G. Ozkan, T. Kostka, E. Capanoglu, T. Esatbeyoglu, *Molecules* **2021**, *26*, 4031.
- [8] S. Y. Lee, S. J. Lee, D. S. Choi, S. J. Hur, *J. Sci. Food Agric.* **2015**, *95*, 2799.
- [9] M. Ghaani, C. A. Cozzolino, G. Castelli, S. Farris, *Trends Food Sci. Technol.* **2016**, *51*, 1.
- [10] M. Fitzgerald, D. B. Papkovsky, M. Smiddy, J. P. Kerry, C. O'Sullivan, D. J. Buckley, G. G. Guilbault, *J. Food Sci.* **2001**, *66*, 105.
- [11] E. Llobet, *Sensor Actuators, B* **2013**, *179*, 32.
- [12] J. P. Kerry, M. N. O'grady, S. A. Hogan, *Meat Sci.* **2006**, *74*, 113.
- [13] B. Kuswandi, Y. Wicaksono, A. Abdullah, L. Y. Heng, M. Ahmad, *Sens. Instrum. Food Qual. Saf.* **2011**, *5*, 137.
- [14] a) A. R. A. Hammam, *SN Appl. Sci.* **2019**, *1*, 632; b) d. Costa, M. V. Tavares, E. K. Garnstedt, *Surf. Coat. Technol.* **2021**, *426*, 127746.
- [15] S. Salaluk, S. Jiang, E. Viyanit, M. Rohwerder, K. Landfester, D. Crespy, *ACS Appl. Mater. Interfaces* **2021**, *13*, 53046.
- [16] X. Lu, W. Li, N. R. Sottos, J. S. Moore, *ACS Appl. Mater. Interfaces* **2018**, *10*, 40361.
- [17] M. Hu, S. Peil, Y. Xing, D. Döhler, L. C. da Silva, W. H. Binder, M. Kappel, M. B. Bannwarth, *Mater. Horiz.* **2018**, *5*, 51.
- [18] a) C. Li, H. Wonneberger, *Adv. Mater.* **2012**, *24*, 613; b) M. Sun, K. Müllen, M. Yin, *Chem. Soc. Rev.* **2016**, *45*, 1513; c) A. M. Brouwer, *Pure Appl. Chem.* **2011**, *83*, 2213; d) C. Huang, S. Barlow, S. J. Marder, *J. Org. Chem.* **2011**, *76*, 2386; e) S. Prabhpreet, S. M. Lalit, V. Vanita, K. J. Kapil, *Mater. Chem. B* **2016**, *4*, 3750; f) C. Wang, B. Bunes, M. Xu, N. Wu, X. Yang, D. Gross, L. Zang, *ACS Sens.* **2016**, *5*, 552; g) C. Chang, H. Tsai, K. Chen, *Materials* **2014**, *7*, 5488; h) E. M. Calzado, J. M. Villalvilla, P. G. Boj, J. A. Quintana, R. Gómez, J. L. Segura, M. A. Díaz-García, *J. Phys. Chem. C* **2007**, *111*, 13595.
- [19] S. Wintzheimer, T. Granath, M. Oppmann, T. Kister, T. Thai, T. Kraus, N. Vogel, K. Mandel, *ACS Nano* **2018**, *12*, 5093.
- [20] a) A. B. D. Nandiyanto, K. Okuyama, *Adv. Powder Technol.* **2011**, *22*, 1; b) F. Iskandar, H. Chang, K. Okuyama, *Adv. Powder Technol.* **2003**, *14*, 349.
- [21] S. Wenderoth, T. Granath, J. Prieschl, S. Wintzheimer, K. Mandel, *Adv. Photonics Res.* **2020**, *1*, 2000023.
- [22] T. Ballweg, C. Gellermann, K. Mandel, *ACS Appl. Mater. Interfaces* **2015**, *7*, 24909.
- [23] C. Henkel, J. E. Wittmann, J. Träg, J. Will, L. M. S. Stiegler, P. Strohmriegel, A. Hirsch, T. Unruh, D. Zahn, M. Halik, *Small* **2020**, *16*, 1903729.
- [24] J. E. Wittmann, L. M. S. Stiegler, C. Henkel, J. Träg, K. Götz, T. Unruh, D. Zahn, A. Hirsch, D. Guldi, M. Halik, *Adv. Mater. Interfaces* **2019**, *6*, 1801930.
- [25] a) M. Sperling, O. D. Velev, M. Gradzielski, *Angew. Chem., Int. Ed.* **2014**, *53*, 586; b) E. Lintingre, G. Ducouret, F. Lequeux, L. Olanier, T. Périé, L. Talini, *Soft Matter* **2015**, *11*, 3660; c) N. Tsapis, E. R. Dufresne, S. S. Sinha, C. S. Riera, J. W. Hutchinson, L. Mahadevan, D. A. Weitz, *Phys. Rev. Lett.* **2005**, *94*, 18302; d) W. Liu, M. Kappel, W. Steffen, H.-J. Butt, *J. Colloid Interfaces Sci.* **2022**, *607*, 1661.
- [26] a) J. Wang, E. Kang, U. Sultan, B. Merle, A. Inayat, B. Graczykowski, G. Fytas, N. Vogel, *J. Phys. Chem. C* **2021**, *125*, 23445; b) J. Wang, J. Schwenger, A. Ströbel, P. Feldner, P. Herre, S. Romeis, W. Peukert, B. Merle, N. Vogel, *Sci. Adv.* **2021**, *7*, eabj0954; c) S. Wintzheimer, J. Reichstein, S. Wenderoth, S. Hasselmann, M. Oppmann, M. T. Seuffert, K. Müller-Buschbaum, K. Mandel, *Adv. Funct. Mater.* **2019**, *29*, 1901193; d) S. Wintzheimer, S. Müssig, S. Wenderoth, J. Prieschl, T. Granath, F. Fidler, D. Haddad, K. Mandel, *ACS Appl. Nano Mater.* **2019**, *2*, 6757.
- [27] a) E. L. Hanson, J. Schwartz, B. Nickel, N. Koch, M. F. Danisman, *J. Am. Chem. Soc.* **2003**, *125*, 16074; b) S. P. Pujari, L. Scheres, A. T. M. Marcelis, H. Zuilhof, *Angew. Chem., Int. Ed.* **2014**, *53*, 6322; c) T. Bauer, T. Schmaltz, T. Lenz, M. Halik, B. Meyer, T. Clark, *ACS Appl. Mater. Interfaces* **2013**, *5*, 6073; d) L. Zeininger, L. Portilla, M. Halik, A. Hirsch, *Chem-Eur J.* **2016**, *22*, 13506.
- [28] A. Ringk, X. Li, F. Gholamrezaie, E. C. P. Smits, A. Neuhold, A. Moser, C. van der Marel, G. H. Gelinck, R. Resel, D. M. de Leeuw, *Adv. Funct. Mater.* **2013**, *23*, 2016.
- [29] W. Stöber, A. Fink, E. Bohn, *J. Colloid Interfaces Sci.* **1968**, *26*, 62.



## Supporting Information

for *Small*, DOI: 10.1002/smll.202107513

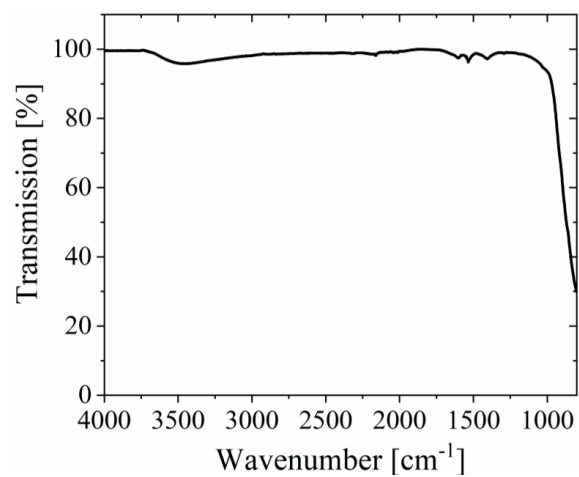
Supraparticles with a Mechanically Triggerable Color-Change-Effect to Equip Coatings with the Ability to Report Damage

*Sarah Wenderoth, Andreas Eigen, Susanne Wintzheimer, Johannes Prieschl, Andreas Hirsch, Marcus Halik,\* and Karl Mandel\**

## Supporting Information

**Supraparticles with a mechanically triggerable color-change-effect to equip coatings with the ability to report damage**

*Sarah Wenderoth<sup>‡</sup>, Andreas Eigen<sup>‡</sup>, Susanne Wintzheimer, Johannes Prieschl, Andreas Hirsch, Marcus Halik\*, Karl Mandel\**

**1. FTIR spectra of pristine alumina nanoparticles**

**Figure S1.** FTIR spectra of pristine alumina nanoparticles.

WILEY-VCH

## 2. Fluorescence spectra of only rhodamine B dye doped core-shell supraparticles

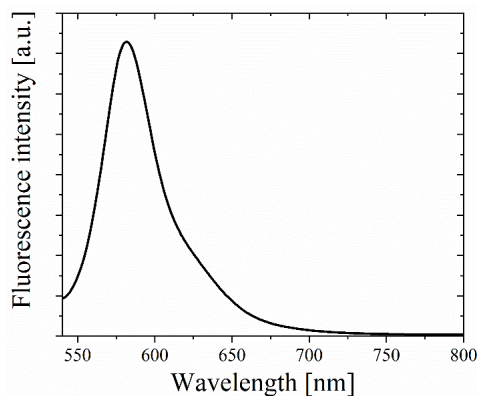


**Figure S2.** Fluorescence spectra of color change indicator supraparticles only with rhodamine B dye in the supraparticle core. The excitation wavelength was set to 520 nm.

## 3. SEM images of core-shell supraparticles

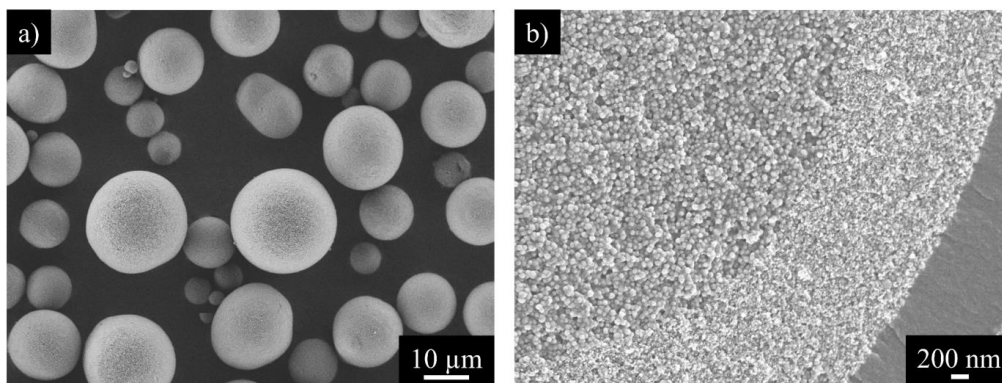


**Figure S3.** SEM images of core-shell indicator supraparticles (a) and cross section of a core-shell supraparticle (b). The core is based on dye-doped silica-nanoparticles and the shell is based on alumina oxide nanoparticles.

## 4. Laser diffraction to determine particle size distribution

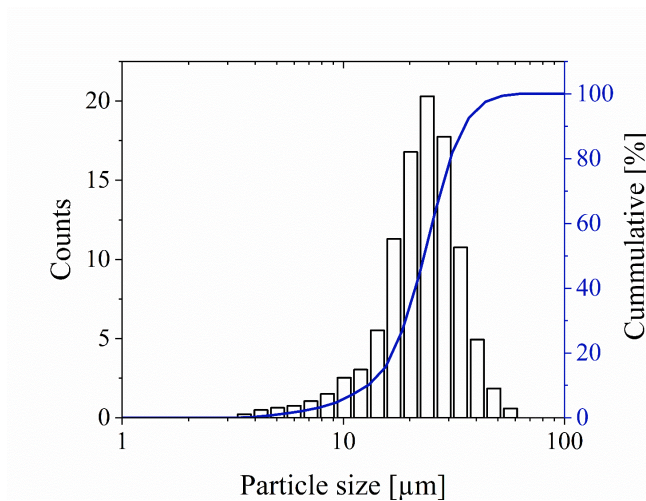


**Figure S4.** Particle size distribution determined by laser diffraction of color change indicator supraparticles.

## 5. Original image of Figure 3 without the dashed line

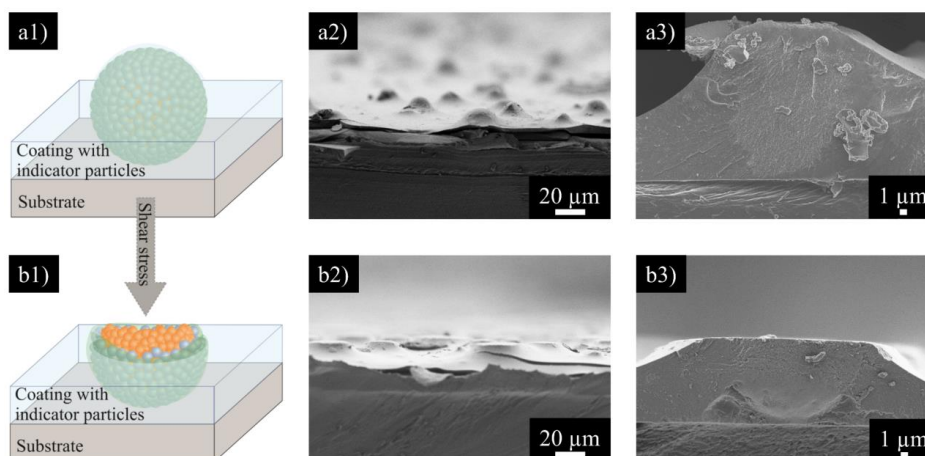


**Figure S5.** Schematic illustrations of the embedded indicator supraparticle in a coating in the as-prepared (a1) and the sheared-off state (b1). SEM images of the real sample in the as-prepared (a2) and in the sheared-off state (b2), as well as cross-section images of an indicator supraparticle in the as-prepared (a3) and the sheared-off state (b3).

WILEY-VCH

6. Photographs of coated films before and after shear process



**Figure S6.** Photographs of the embedded indicator supraparticle in a coating. In the marked area of 1.5 x 7 cm between the black lines the sheared-off state after 750 shear cycles is shown and outside this area the coating is still in its as prepared state.

## RESEARCH ARTICLE

Check for updates

NANO - MICRO  
small

www.small-journal.com

## Spray-Dried Photonic Balls with a Disordered/Ordered Hybrid Structure for Shear-Stress Indication

Sarah Wenderoth, Gudrun Bleyer, Jakob Endres, Johannes Prieschl, Nicolas Vogel, Susanne Wintzheimer, and Karl Mandel\*

Optical microscale shear-stress indicator particles are of interest for the in situ recording of localized forces, e.g., during 3D printing or smart skins in robotic applications. Recently developed particle systems are based on optical responses enabled by integrated organic dyes. They thus suffer from potential chemical instability and cross-sensitivities toward humidity or temperature. These drawbacks can be circumvented using photonic balls as shear-stress indicator particles, which employ structural color as the element to record forces. Here, such photonic balls are prepared from silica and iron oxide nanoparticles via the scalable and fast spray-drying technique. Process parameters to create photonic balls with a disordered core and an ordered particle structure toward the exterior of the supraparticles are reported. This hybrid disordered–ordered structure is responsible for a color loss of the indicator particles during shear-stress application because of irreversible structural destruction. By adjusting the primary silica particle sizes, nearly all colors of the visible spectrum can be achieved and the sensitivity of the response to shear stress can be adjusted.

## 1. Introduction

With the transformation of industry regarding their digitalization and automatization, a localized in situ recording of

S. Wenderoth, J. Endres  
Chair of Chemical Technology of Materials Synthesis  
Julius-Maximilians-University Würzburg  
Röntgenring 11 D97070, Würzburg, Germany

S. Wenderoth, S. Wintzheimer, K. Mandel  
Fraunhofer-Institute for Silicate Research ISC  
Neunerplatz 2 D97082, Würzburg, Germany  
E-mail: karl.mandel@fau.de

G. Bleyer, N. Vogel  
Institute of Particle Technology  
Friedrich-Alexander Universität Erlangen-Nürnberg (FAU)  
Cauerstrasse 4 D91058, Erlangen, Germany

J. Prieschl, S. Wintzheimer, K. Mandel  
Department of Chemistry and Pharmacy  
Inorganic Chemistry  
Friedrich-Alexander Universität Erlangen-Nürnberg (FAU)  
Egerlandstrasse 1 D91058, Erlangen, Germany

 The ORCID identification number(s) for the author(s) of this article can be found under <https://doi.org/10.1002/smll.202203068>.

© 2022 The Authors. Small published by Wiley-VCH GmbH. This is an open access article under the terms of the Creative Commons Attribution License, which permits use, distribution and reproduction in any medium, provided the original work is properly cited.

DOI: 10.1002/smll.202203068

acting mechanical forces is of interest in different applications, from additive manufacturing processes to robotics.<sup>[1]</sup> Microscale particles are a promising material class, potentially enabling shear-stress indication during 3D printing or the creation of shear-stress-sensitive skins for robots.<sup>[2]</sup> It has recently been shown that optical supraparticles, i.e., particles consisting of organic dye-carrying nanoparticles, can reliably detect shear stress by an optical signal response.<sup>[3–6]</sup> However, the use of organic molecules as optical probes brings along disadvantages, such as chemical instability (e.g., photo-bleaching) and cross-sensitivities toward other environmental influences such as temperature or humidity.<sup>[7]</sup> This is why the use of materials providing their color not through molecular chemistry (as with pigments and organic dyes) but through their physical structure and

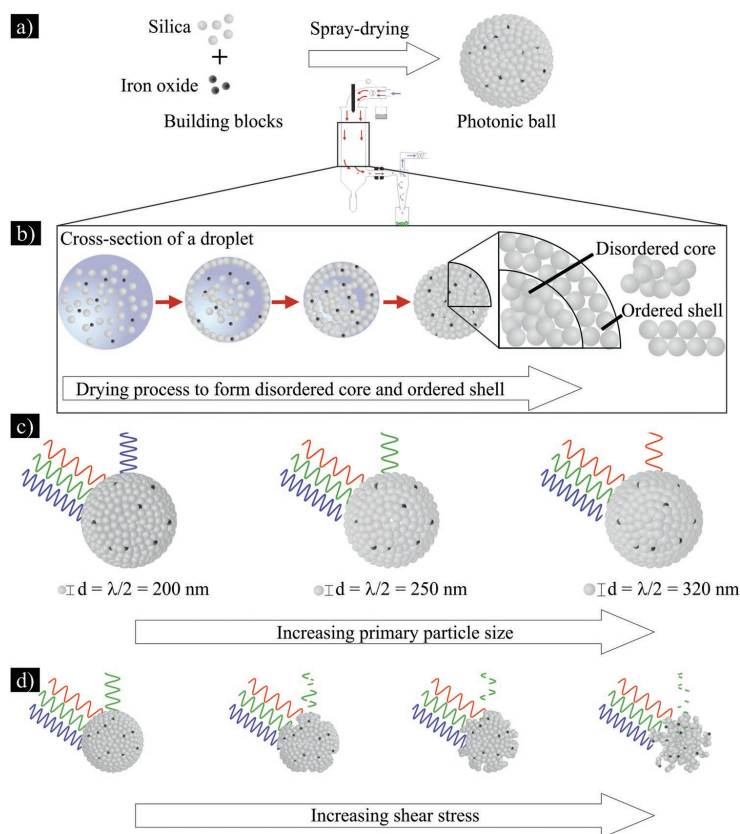
thus, a color response only to mechanical triggers, would be favorable.<sup>[8]</sup> Photonic balls (an optically active class of supraparticles<sup>[9]</sup>) are such materials that exhibit structural coloration from a defined arrangement of primary particles.<sup>[10,11]</sup> They consist of monodisperse nanoparticles (mostly silica or different polymer nanoparticles with sizes of typically 150–300 nm), and typically exhibit a well-ordered arrangement of the primary particles near the surface,<sup>[11,12]</sup> while their interior can be disordered.<sup>[11,13–15]</sup> When such a supraparticle is illuminated with white light, constructive interference of light of a defined wavelength given by the size of the individual primary particle produces a macroscopically visible structural coloration.<sup>[11,14]</sup> However, all wavelengths of the incoming light are incoherently scattered inside of the supraparticle. This ultimately yields a whitish appearance of the supraparticle powder.<sup>[11,14,15]</sup> By incorporating broadband or spectrally selective light absorbers in form of nanoparticles (e.g., melanin,<sup>[16]</sup> polydopamin,<sup>[15]</sup> carbon black,<sup>[17,18]</sup> iron oxide,<sup>[19,20]</sup> gold,<sup>[11,18]</sup> or silver<sup>[18]</sup>) within the supraparticle, the incoherently scattered light is absorbed, so that the constructive interference from the ordered layers toward the surface create a more homogenous color impression. Various manufacturing processes are described in the literature for the creation of photonic balls, such as microfluidics,<sup>[15,21]</sup> electrospray-assisted fabrication,<sup>[22]</sup> or micropipette injection.<sup>[23]</sup> However, the disadvantage of all these methods is that only small quantities can be produced.<sup>[22]</sup> This is why recently, spray-drying has been selected

as a fabrication process for photonic balls, providing good scalability and high production speed (of a few ms).<sup>[24]</sup>

In the work presented herein, spray-dried photonic balls are developed for mechanical shear stress indicated by a loss of color, which is readily detectable by the bare eye without the need for complex, time-consuming, or expensive measurement methods. In this context, shear stress can be defined as abrasion, i.e., the process of rubbing away the surface of a material or product. The scalable and fast spray-drying method may pave the way to a facile transfer of photonic ball production to industry and thus, its commercialization as a product. The supraparticulate nature of such photonic balls allows tailoring the resultant coloration as well as the sensitivity range, simply by changing the primary particle size and composition.

## 2. Results and Discussion

The photonic balls with shear-stress indication functionality are based on the concept of a disordered/ordered hybrid supraparticle structure. The building blocks for this structure are solely silica and iron oxide nanoparticles (Scheme 1a). By varying the size of the silica building blocks, different structural colors are obtained. The wavelength of the resultant color impression is determined by the optical path difference between light reflected at different lattice planes in the supraparticle and roughly correlates with the primary nanoparticle building block size by a factor of two.<sup>[14,25]</sup> The broadband absorption properties of the iron oxide building blocks further allow optimization of color perception.<sup>[19]</sup>



**Scheme 1.** a) Schematic illustration of the disordered/ordered structure of the photonic balls, based on silica and iron oxide nanoparticle building blocks and obtained via forced assembly in a kinetically controlled regime via spray-drying. b) At the beginning of the spray-drying process, the nanoparticles are randomly distributed in the water droplet. During the evaporation process, highly ordered structures form shell by shell on the droplet surface. Since this evaporation process is fast, there is no time for the entire supraparticle to form an ordered structure and the core, therefore, remains disordered. c) Depending on the choice of the size of the silica nanobuilding blocks, the structural color of the photonic balls can be adjusted over the entire visible spectrum. d) Upon exposure to shear stress, stepwise destruction of the highly ordered shell destroyed would cause a diminishing of the structural color.

In the spray-drying process, a dispersion of silica and iron oxide nanoparticles is nebulized. Upon drying, the nanoparticles in the fine droplets are forced together ("forced assembly").<sup>[26,27]</sup> Regarding the spray-drying device, a commercial B-290 mini spray-dryer by BÜCHI Labortechnik AG was utilized for this research. A schematic illustration showing its setup and working principle is presented in the Supporting Information (Figure S1, Supporting Information). As this assembly process proceeds within a few milliseconds, the self-assembly process is kinetically controlled and does not allow for the formation of a fully ordered supraparticle. Thus, the inner core of such a supraparticle remains disordered (Scheme 1b). Upon careful parameter adjustment (such as the choice of the nanoparticle building blocks, their dispersion properties, and surface functionality, as well as the careful adjustment of the spray-drying parameters), it is however possible to obtain an ordered structure for the outermost nanoparticle layers of such supraparticles. An overview of these parameters and different nanoparticle compositions is given later in the text.

The ordered arrangement on the outside of the supraparticles is essential for the coloring of the as-synthesized intact photonic balls.<sup>[11,15,19]</sup> The color appearance can be tuned by the choice of the primary particle size (Scheme 1c).

Altogether, the approach of spray-drying—executed carefully, using the right parameters—can produce the disordered core/ordered shell structure system, which is desired for our application. It is well conceivable that destruction of the order of the shell subsequently destroys the functionality that is caused by this region in the system. The presence of shear stress, which would in nearly all cases cause an attack at the surface first, could be expected to destroy the surface order, and thus the coloration effect in the system (Scheme 1d). Hence, with increasing destruction of the ordered outer shell, the perceivable structural color should be gradually lost. Therefore, this type of supraparticle can be used as a shear-stress indicator, where the stress can be determined readily by the human eye thanks to a color loss. In this context, it has to be mentioned that the color change of the samples can be qualitatively detected with the naked eye while with the help of reflectance spectroscopy quantitative monitoring is possible.

In order to realize this indicator concept, first, supraparticles with the desired morphology need to be prepared. For this purpose, silica nanoparticles with a primary particle size of  $d_{\text{DLS}} = 258 \pm 72$  nm were synthesized according to a modified Stöber process.<sup>[25,28]</sup> Iron oxide nanoparticles ( $d_{\text{DLS}} = 77 \pm 17$  nm) were obtained via an oxidative-precipitation reaction.<sup>[29]</sup> After these two nanoparticle dispersions were mixed in a different ratios (see below), they were spray-dried, using a commercially available spray-dryer (for details see the Experimental Section). The morphology, i.e., structure, size, and shape of spray-dried supraparticles is influenced by several parameters.

On the one hand, parameters regarding the building blocks themselves, such as composition, primary particle size, surface functionalization, and colloidal stability of the nanoparticles, solvent of the dispersion, and concentration of nanoparticles in dispersion do crucially influence the result. On the other hand, there are spray-dryer device parameters such as feed rate, temperature, flying speed (aspirator), and nozzle-type that have a strong impact on the finally resulting structures.

If all these parameters are not orchestrated in the right way, the resulting supraparticle powders do not show the desired structure and thus no color. In order to give an idea on this challenge, a selection of failed attempts, i.e., supraparticles with an undefined structure, is displayed in Figure S2 in the Supporting Information and summarized in Table S1 in the Supporting Information. These examples show a variation on the different parameters regarding the building blocks with fixed device parameters. For example, the type of absorbing iron oxide nanoparticles (size of the individual nanoparticles and their structure) has a significant influence on the morphology of the subsequent supraparticles. When using iron oxide cluster particles from a hydrothermal synthesis according to the literature,<sup>[19]</sup> the resulting supraparticles form many different shapes. While some of the surfaces provide ordered regions, the sample in its entirety does not show any structural color (Figure S2a, Supporting Information). Consequently, and in agreement with literature, we assume that the sphericity of the supraparticles is essential for the color appearance of the sample.<sup>[14]</sup> If the iron oxide is added as very small nanoparticles (around 10 nm),<sup>[4]</sup> during the spray-drying process, the larger silica nanoparticles were located in the core and the iron oxide nanoparticles formed the shell (Figure S2b, Supporting Information). This shell formation is caused by segregation of binary dispersions their segregation with large-size distribution during fast droplet evaporation in a spray-dryer.<sup>[30]</sup> Additionally, the composition of the solvent plays a crucial role in supraparticle formation. Since the silica nanoparticles are synthesized by the Stöber method, traces of ethanol can remain in the dispersion. In this case, the presence of ethanol reduces the boiling point of water, thus droplet evaporation is accelerated resulting in a deformation of the droplet which causes a crumbled shape of the supraparticle.<sup>[31]</sup> Thereby, the high order on the surface is interrupted by indentations (Figure S2c, Supporting Information). In order to form spherical supraparticles in general, which is a necessary but not sufficient condition to achieve photonic balls, the addition of a surface functionalization (like amino silanes on the silica nanoparticle surface<sup>[4]</sup>) or a salt (such as  $\text{CaCl}_2$ )<sup>[3]</sup> is suggested in literature. These modifications slightly destabilize the nanoparticle dispersion, which avoids the formation of a crust at the outermost layers of the droplet that forms during spray-drying. This would ultimately lead to a collapse of the droplet, being the cause of a buckled supraparticles structure.<sup>[32]</sup> Exemplarily, the resulting supraparticle structure that is obtained when  $\text{CaCl}_2$  is added to the dispersion during spray-drying is depicted in Figure S2d in the Supporting Information. As can be seen, the supraparticles are indeed spherical, however, unfortunately, the surface is entirely disordered. In this case, the preagglomerated state of the primary particles cannot independently move within the drying droplet, which prevents their self-organization into an ordered arrangement. Regarding the spray-dryer device parameters such as feed rate, temperature, flying speed (aspirator), and nozzle-type, there are already several studies showing their influence on the sphericity of the resulting supraparticles.<sup>[3,4,9,26,33]</sup> Based on these reports, the ideal parameters were selected as following: inlet temperature of 140 °C (resulting in an outlet temperature of around 80 °C), aspirator power at 75%, ultrasonic nozzle power at 5 W, vacuum at -30 mbar, 2 mm tube, and pump rate at 15%.

Only if all parameters are optimized in a way as detailed in the Experimental Section, ultimately spray-dried photonic balls with the desired structure can be obtained. The scanning electron micrographs of these supraparticles (Figure 1a), as well as of their cross-sections (Figure 1b), reveal the successful formation of the disordered/ordered core-shell structure. Large size deviations of the photonic balls as well as slight deformations of their spherical shapes are both common drawbacks of the fast spray-drying method but do not seem to interfere with their structural color properties. The ordered arrangement of the silica nanoparticles on the surface of the supraparticle is clearly visible in the higher magnification in Figure 1c and reaches approximately three layers into the interior of the supraparticle (Figure 1d, upper part of the supraparticle). At the same time, the inner region of the supraparticle is disordered. As evidenced from the scanning electron microscope (SEM) images, the iron oxide particles seem to be randomly distributed (see Figure S3, Supporting Information). The surface of the supraparticles generally exhibits an ordered arrangement of primary particles, with the typical defects, grain boundaries, and irregularities expected from the fast kinetics of the self-assembly process, which prevents a global equilibration of the particles.

The spherical nature of the supraparticles with their characteristic internal morphology interacts with visible light in characteristic ways.<sup>[11]</sup> The ordered particle layers toward the surface, seen clearly in Figure 1d, cause constructive interference of light by Bragg diffraction at the individual layers. The amount of reflected light (~10–15%) can be accounted for by the presence of only several ordered layers of particles,<sup>[11]</sup> as formed in our supraparticles during the fast evaporation process. This interference causes a uniform structural color with a hue that is determined by the size of the primary particles (as discussed below). In addition, the disordered interior causes

incoherent scattering of light of all wavelengths, creating a whitish appearance, which can dominate the overall optical response (Figure 2a, left). In order to suppress this scattering by absorbing stray light, so that the constructively interfered light can be observed more clearly, the presence of absorbing moieties is needed.<sup>[14]</sup> However, with high concentrations of the absorbing components, the absorption becomes dominant while additionally the overall order in the supraparticle is reduced as revealed by SEM imaging of the resulting supraparticles (Figure 2b and Figure S4, Supporting Information). Such powders, therefore, appear black (Figure 2a, right). Thus, the macroscopically visible coloration of the resultant photonic balls can be optimized by the iron oxide absorber concentration (Figure 2) for supraparticles with mass ratios silica:iron oxide of 500:1, 100:1, 50:1, 20:1, 10:1, and 1:1. The size of the structure-forming silica nanoparticle building blocks in this set of experiments was  $d_{\text{DLS}} = 288 \pm 75$  nm. The acquired reflectance spectrum shows that the absolute light reflectance increases with increasing silica content in all spectral regions (Figure 2b). A maximum of reflectance at 660 nm is visible for almost all samples, indicating the spectral position of constructive interference. The intensity of this photonic stop band (i.e., difference between reflectance maximum and minimum) is most pronounced at a ratio of 50:1 silica to iron oxide (gray lines). This ratio thus provided the most pronounced coloration, it was selected for all further experiments. We support the macroscopic reflectance properties of the entire powder sample with a microspectroscopic analysis of individual supraparticles via correlative microscopy. For each sample, individual supraparticles were identified via electron microscopy and subsequently correlated with optical microscopy and single-particle spectroscopy. In Figure 2c, SEM images of the individual supraparticles are shown. The insets in each image show

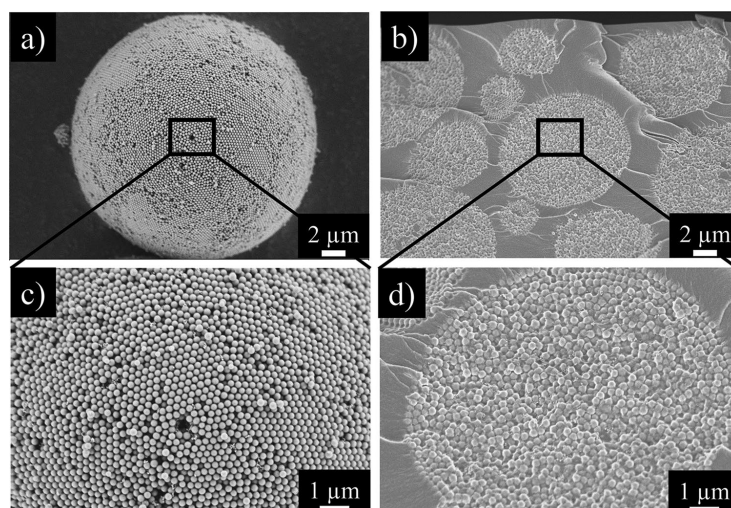


**Figure 1.** SEM images on the outer surface appearance of a,c) a whole spray-dried supraparticle and b,d) cross-sections thereof at a,b) lower and c,d) higher magnification.

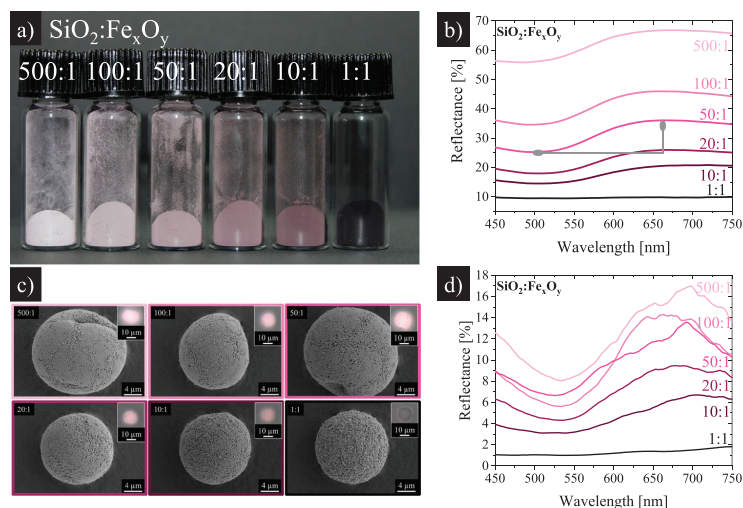


**Figure 2.** a) A photograph of the powder samples containing silica and iron oxide nanoparticles in different mass ratios of 500:1, 100:1, 50:1, 20:1, 10:1, and 1:1. b) Macroscopic reflectance spectra of these powder samples. The gray line was added as an aid to see the difference between the reflectance line maximum and minimum for the 50:1 sample. c) SEM images of single supraparticles of each sample with insets of the corresponding optical microscopy image. d) Reflectance spectra of the individual supraparticles shown in (c). For the reflectance spectra of the powder sample, three measurements of each sample were recorded and their average was calculated.

the optical microscopy image of the respective supraparticle. In these images, the decrease in order with increasing iron oxide content becomes evident. Concurrently, the intensity of the reflection decreases. The reflectance spectra of the individual supraparticles follow the same trend as for the individual powder (Figure 2d). With the increasing iron oxide content, the reflectance intensity decreases. In order to obtain better statistics of these individual measurements, spectra were recorded on ten individual supraparticles and the mean values were calculated (see Figure S5, Supporting Information). A slight red shift can be observed between macroscopically measured spectra of a film of supraparticles and the single particle spectroscopy. This could stem from differences in the measurement method. The macroscopic film was measured using an integrating sphere, while the single-particle spectra were measured in an optical microscope with a limited numerical aperture (0.55), which only probes angles below  $33^\circ$ . As such photonic materials exhibit a blueshift with increasing angles,<sup>[14]</sup> deviations in the spectral distribution of light may arise. In addition, differences between the optical response of a single supraparticle and a whole film of supraparticles may contribute to the deviations.<sup>[34]</sup>

Figure 3a shows five powder samples of the spray-dried photonic balls providing structural colors from blue to red (dynamic light scattering measurements (DLS) of the primary particles silica and iron oxide, see Figure S6 in the Supporting Information, SEM images of the different samples: Figure S7, Supporting Information). The primary particle size (measured by DLS) of the silica building blocks increases from left to right (1: blue, 214 nm; 2: green, 229 nm; 3: yellow, 258 nm; 4: orange,

282 nm; 5: red, 325 nm). The ratio of silica:iron oxide was set to 50:1 for all samples. The recorded reflectance spectra on these powder samples confirm that the wavelengths of the reflectance maxima of the individual curves correspond to about twice the primary particle size of the respective silica nanoparticles (Figure 3b). These spectra can be transferred into a CIE 1931 chromaticity diagram by converting them into  $x$ - $y$  coordinates (Figure 3c). This type of diagram helps to determine the real color impression of the powder samples, as the photographs are affected by the illumination conditions.<sup>[19]</sup> It can be seen that the individual powder samples are capable of representing colors throughout the visible spectrum. We further investigate the angle-dependent coloration of the supraparticles. To this end, we disperse the samples 1 (blue), 2 (green), and 5 (red) in a fluorinated oil and measure the reflectance properties with increasing angle between illuminating light beam and detector (Figure S8a, Supporting Information). The spectral position of the photonic stop band blue-shifted with increasing angles, as expected for Bragg-type reflection (Figure S8b, Supporting Information).<sup>[15,35]</sup> Indicating that the observed structural coloration indeed originates from the ordered surface-near layers of primary particles. In addition, this experiment shows that the supraparticle powder can be dispersed in liquids while retaining coloration, which increases the versatility of the system.

We now elucidate the indicator function of the supraparticles. If the ordered structure near the surface is destroyed, e.g., by mechanical stress, the supraparticles are expected to lose their color. This can be demonstrated by experiments in a ball mill-like setup.<sup>[36]</sup> For this purpose, a defined amount of powder sample 1, exhibiting a blue color, is mixed with zirconium

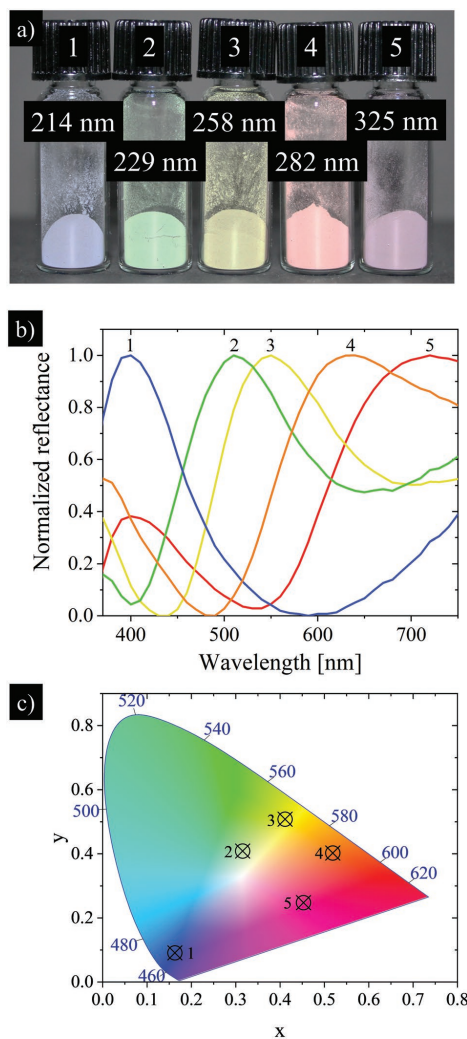


**Figure 3.** a) Photograph of powder samples in different colors with the corresponding silica primary particle sizes measured by DLS (numbered from 1 to 5). b) Normalized reflectance spectra of the powders (numbering corresponds with the one in (a)). c) Presentation of the reflection maxima in a CIE chromaticity diagram (numbering corresponds with the one in (a)). Three reflectance spectra of each sample were recorded and their average was calculated. The transformation to the CIE chromaticity diagram was performed by normalization of the reflectance spectra and the use of the software OriginPro 2021.

oxide balls in a centrifuge tube (for details, see the Experimental Section). These are then mixed with a vortex device for different time intervals. The resulting particle structures after

the particles have been exposed to the shear-stress process, were studied with SEM and reflectance measurements (Figure 4). At the initial state (0 s), the structural order on the surface of the supraparticles is intact (Figure 4a) and causes their blue visual appearance, evident also in the spectroscopic analysis (Figure 4e). Having been exposed the powder to 15 s of shear stress, the supraparticle surfaces clearly reveal a less smooth and ordered structure, although large, ordered areas remain visible (Figure 4b). Consequently, the resulting color of the sample shifted into the blue-violet range (Figure 4e). The longer the exposure to the shear stress (45 s (Figure 4c) or 90 s (Figure 4d)), the more the surface is destroyed, and hardly (45 s) to nearly no (90 s) ordered regions remain on the supraparticles. This also leads to a decrease in distances between the coordinates in the CIE chromaticity diagram and the sample color approaches the white spot at the center of the CIE color space (Figure 4e). With increasing destruction of the ordered surface structure of the supraparticles, the propensity of constructive interference of the reflected incident light decreases and the light is only scattered by the disordered supraparticle structure, which was formerly only present in its core. This results in a whitish color of the powder sample (a pure white color impression is prevented by the presence of the iron oxide nanoparticles). Further measurement points, higher magnification SEM images, as well as the corresponding CIE chromaticity diagram are shown in Figures S9–S11 in the Supporting Information.

Additionally, the influence of the size of the individual supraparticles within the powder sample was investigated for sample 1 in the initial state (Figure S12a, Supporting Information) and after 120 s of shear-stress application (Figure S12b, Supporting Information). Three different particle sizes were chosen for the initial state and two particle sizes for the sheared state, representing the overall composition of the sample (initial: large:  $25 \pm 3 \mu\text{m}$ , medium:  $20 \pm 2 \mu\text{m}$ , small:  $11 \pm 1 \mu\text{m}$ ; 120 s shear stress: large:  $37 \pm 2 \mu\text{m}$ , medium:  $14 \pm 1 \mu\text{m}$ ). The spectral measurement of Figure S12 in the Supporting Information indicates that in the initial state, the reflected light intensity of the large and medium supraparticles is similar, while a significant difference occurred for the small supraparticles. Presumably, the number of ordered layers formed in the fast spray-drying process is inherently limited by the kinetics, but is also affected by the size of the confinement. While comparably large droplets produce similar levels of order, the higher curvature and fast drying kinetics of the smaller droplets decrease the order within the supraparticles. This hypothesis is supported by a small peak shift to smaller wavelengths for larger supraparticles, which is typical for increasing amounts of ordered layers.<sup>[11]</sup> However, care needs to be taken with the interpretation of these size-dependent properties as the ratio of measuring spot size ( $5 \mu\text{m} \times 5 \mu\text{m}$  in the center of the supraparticle) to the supraparticle size (as shown as dotted squares in the SEM images, Figure S12c, Supporting Information) can influence the measurement. The Bragg reflection of the ordered layers is only detected in a circular spot in the center of the supraparticle and the reflectance conditions in the microscope.<sup>[11,21]</sup> This circular spot grows proportionally with the supraparticle size. If the measuring spot is larger than the circular spot showing reflected color, lower color intensities are

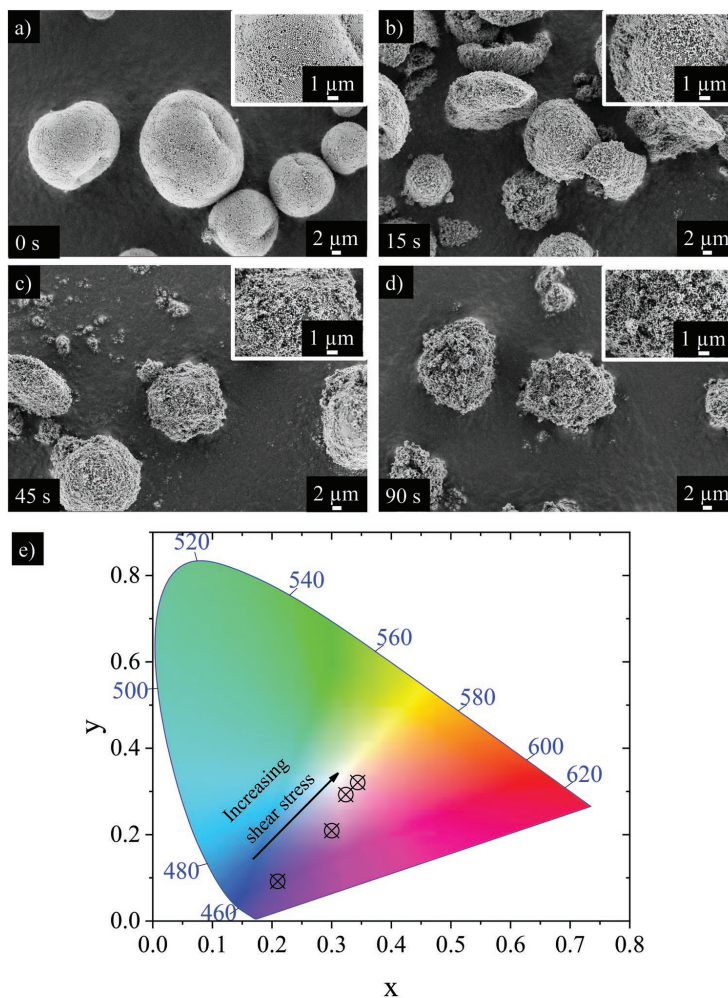


**Figure 4.** SEM images of supraparticles after shear-stress treatment in the ball mill-like setup. A sample with an originally blueish appearance was chosen for this experimental series. The resulting particle structures in SEM for four different shear-stress exposure times are depicted, namely, at a) the initial state, as well as the states after b) 15, c) 45, and d) 90 s of shear-stress treatment. The insets display a higher magnification of the supraparticles' surfaces. e) All samples have been measured by reflectance spectroscopy and the results are presented in form of a CIE chromaticity diagram. Three reflectance spectra of each sample were recorded and their average was calculated. The transformation to the CIE chromaticity diagram was performed by normalization of the reflectance spectra and the use of the software OriginPro 2021.

measured. After exposure to mechanical stress, the spectra of the individual particles were less defined and show lower reflection, indicating the compromised order and shape of the particles (Figure S12b,d, Supporting Information).

An important point for the application of spray-dried silica-based supraparticles as shear-stress indicators is their general mechanical stability, which allows their handling and processing in the as-prepared state. The stability of supraparticles

has already been investigated in various publications and it was stated that, depending on their composition, they are very robust against static pressure, and moderately resilient to shear stress.<sup>[5,6,36–38]</sup>

After having successfully demonstrated the use of spray-dried photonic balls as shear-stress indicators, we explored whether the composition of the supraparticles, i.e., their silica building blocks size and consequently their structural color, affects their

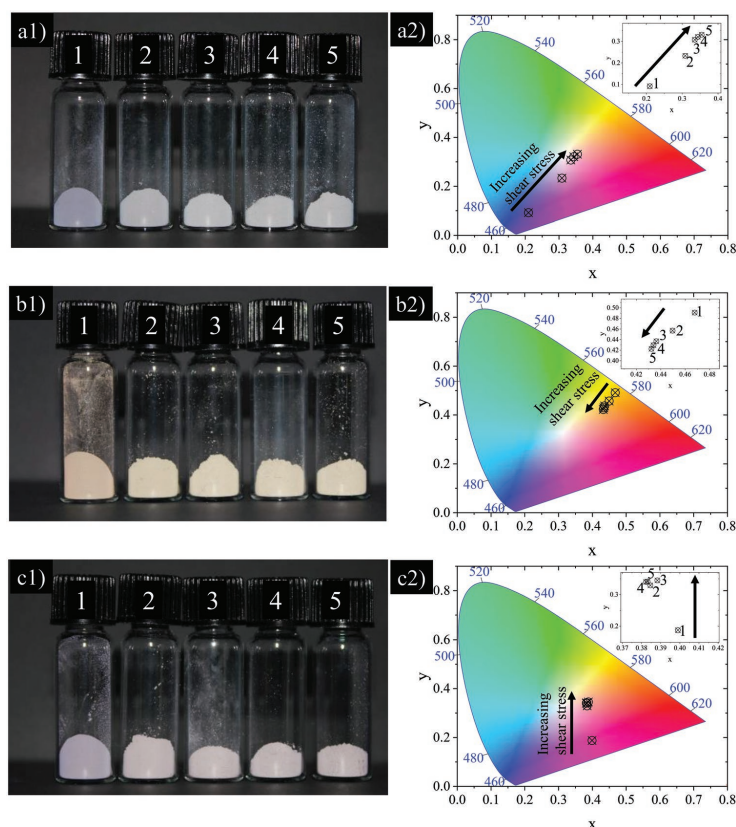


**Figure 5.** Photographs of powder samples 1 (blue color impression (a)), sample 3 (yellow color (b)), and sample 5 (red-pinkish color (c)) in 1) the initial state, and 2) after 30, 3) 60, 4) 90, and 5) 120 s shear-stress application in a1,b1,c1) the ball mill-like setup. a2,b2,c2) The reflection measurements of each powder are displayed in the CIE chromaticity diagram. The insets on the top left corners show the single measurement points correlated to measurement points (1 to 5) during shear-stress application. Three reflectance spectra of each sample were recorded and their average was calculated. The transformation to the CIE chromaticity diagram was performed by normalization of the reflectance spectra and the use of the software OriginPro 2021.

sensitivity to shear stress. For this purpose, shear-stress experiments on samples 1, 3, and 5 (resulting in blue, yellow, and red-pinkish supraparticles), containing increasing sizes of silica nanoparticles, were carried out (Figure 5). Figure 5a1,b1,c1 shows photographs of the individual powder samples after shear times of 0, 30, 60, 90, and 120 s (from left to right, numbered 1 to 5). Note that the photographs were not post-processed with an image editing software to enable accurate comparison. Thus, the colors appear less bright. This is why their color change appears less pronounced than the values calculated from reflectance spectra indicate (Figure 5a2,b2,c2). In general, all samples show sensitivity to shear stress. Their initial color is lost during shear-stress application, visually expressed by approaching the middle of the CIE chromaticity diagram, i.e., a white coloring. In this context, it needs to be mentioned that the samples do not precisely reach the coordinates of the white point (0.3333,

0.3333), which is due to the contained iron oxide which is not totally black but reddish-brown. Noteworthy, in the case of sample 1 (blue color impression), a successive decrease in color can be seen from the time point 1 to 5 (Figure 5a1), while for the sample 3 (yellow color) (Figure 5b1) and sample 5 (red-pinkish color) (Figure 5c1), no differences between sample points 2 and 5 are visible to the eye. This visual impression is also confirmed by reflectance spectroscopy. Only in the case of sample 1 (blue color), the individual measuring points can be clearly distinguished from one another (Figure 5a2), indicating higher resistance to shear stress compared to the other samples containing larger silica nanoparticles. With increasing silica building block size, the color loss proceeds faster; sample 3 (yellow color) already shows no more color change after the third measurement point and the sample 5 (red-pinkish color) after the second one. This indicates a destruction of the supraparticles

already after 30 s of shear-stress application to such an extent that no more color changes take place. As the supraparticles are grinded successively during the ball milling process, laser diffraction measurements were performed to determine the size reduction during the shear experiments (Figure S13, Supporting Information). The faster color loss of the samples with larger primary particle size corroborates with recent reports on the stability of supraparticles under compression.<sup>[38]</sup> There, it was found that the fracture stress of supraparticles of similar morphology is inversely proportional to the primary particle size, so that smaller primary particle sizes exhibit increased mechanical stability.

As above, we investigated the angle-dependent coloration of dispersed supraparticles. Figure S14a in the Supporting Information shows the spectra of sample 5 at 30° measuring angle before and after milling for 120 s. After milling, the peak intensity became lower and the peak broadened, which is indicative for less ordered systems.<sup>[39]</sup> Due to agglomerates forming in the sample during milling, the sample becomes less uniform and stable, leading to a higher error in the measurements. Figure S14b in the Supporting Information shows the shift in peak position of both samples as a function of angle between light source and detector. Here, it becomes apparent that the damaged sample is less angle-dependent, as the ordered structure, that is responsible for the angle dependent Bragg scattering, is damaged. The ability to detect changes in the spectra upon shearing in liquid, different stress indicator scenarios can be envisioned.

In order to determine the approximate work a supraparticle is experiencing in the ball mill-like setup, a conventional ball mill was used. Based on the used parameters in a classical ball-mill, the impact energy is known and therefore the approximate work needed to produce a certain color can be calculated. These results can be transferred to the used ball mill-like setup used in this study. Additionally, the influence of the number of balls in the ball mill-like setup was investigated in the same way. The calculations and results are displayed in Figure S15 in the Supporting Information.

It can thus be deduced that the smaller the primary particle size of the silica nanoparticles, the lower the supraparticles are destroyed by shear stress resulting in a lower loss of structural color. The smaller primary particle size increases the reactive surface area within a supraparticle. Therefore, more Si—O—Si bridges can be formed between the individual nanoparticles, making the individual supraparticles more cohesive.<sup>[40]</sup> By the right choice of primary particle size, the shear-stress indicator supraparticles can thus be equipped with a tuned sensitivity against shear-stress applications. Regarding a potential practical application, the more sensitive samples should be further tested in experimental setups that allow the application of lower mechanical forces onto the samples to obtain gradual color losses or to define the threshold values for the color loss of each sample.

### 3. Conclusion

A careful selection of silica and iron oxide nanoparticle building blocks and spray-drying parameters yields photonic

balls capable to detect shear stress. They provide a disordered arrangement of primary particles on the inside and a highly ordered one on the surface. This hybrid structure is responsible for a color loss of the indicator particles during shear-stress application due to the irreversible destruction of the highly ordered outer structure. Since physical ordering effects are exploited to create the color, a change in optical properties is only caused by mechanical forces, which is advantageous compared to organic dye-based systems that often suffer from chemical degradation or cross-sensitivities. By adjusting the primary silica particle sizes, nearly all colors of the visible light spectrum can be achieved but also the sensitivity of their response to shear stress can be adjusted. These photonic shear-stress indicators may find application as mechanical indicators in 3D printing or may allow the creation of smart surfaces.<sup>[3–5]</sup>

### 4. Experimental Section

The following chemicals were used without further purification: tetraethoxysilane (TEOS, 99%, Sigma-Aldrich, Germany), aqueous ammonia solution (NH<sub>3</sub>(aq), 25 wt%, abcr, Germany), 3-aminopropyltriethoxysilane (APTES, 97%, abcr, Germany), sodium hydroxide (NaOH, 99%, Roth, Germany), sodium nitrate (NaNO<sub>3</sub>, 99%, Roth, Germany), ferrous sulfate heptahydrate (FeSO<sub>4</sub> · 7H<sub>2</sub>O, 99.5%, Roth, Germany), ethanol (EtOH, 99%, Jäckle-Chemie, Germany), fluorinated oil (3M Novec 7500, >99%, io-li-tec, Germany), Krytox 157 FSH (Costenoble, Germany).

**Synthesis of Silica Nanoparticles:** The syntheses of silica nanoparticles with sizes between 200 and 350 nm were carried out according to the literature.<sup>[25]</sup> In a normal experiment, 3 g deionized water was mixed with 7.22 g of aqueous ammonia solution and 37.1–56.0 g ethanol (more ethanol—smaller particles). The mixture was heated to 60 °C. Under vigorous stirring, 5.6 g of TEOS was added and the mixture was allowed to stir for 2 h. After cooling to room temperature, the particles were collected by centrifugation and washed at least three times with deionized water. Further purification was done by dialysis against deionized water for 24 h with multiple water exchanges (dialysis membrane: molecular weight cut-off 10 kDa, cellulose hydrate membrane, Nadir-dialysis tubing, Roth, Germany).

**Synthesis and Functionalization of Iron Oxide Nanoparticles:** The synthesis of iron oxide nanoparticles was carried out following the literature.<sup>[29]</sup> 111.2 g FeSO<sub>4</sub> · 7H<sub>2</sub>O was dissolved in 900 g of deionized water. In addition, 452 g of an aqueous 3 M NaNO<sub>3</sub> solution was mixed with 332 g of deionized water and 296 g of an aqueous 3 M NaOH solution. Using a peristaltic pump with a static mixer, the two solutions were mixed to precipitate the Fe(OH)<sub>2</sub> intermediate. This dispersion was oxidized in an oven at 90 °C for 24 h. The resulting particles were collected and washed with deionized water by magnetic separation.

**Spray-Drying of Supraparticles:** Silica and iron oxide nanoparticles were mixed in different weight ratios and all dispersions were diluted with deionized water to a final concentration of 3 wt%. A B-290 mini spray-dryer (Büchi, Switzerland) equipped with an ultrasonic nozzle and an inlet temperature of 140 °C was used. The power of the nozzle was set to 5 W.

**Characterization of Supraparticles:** The particle size of the nanoparticle building blocks was determined by measuring the hydrodynamic particle diameter with a ZetaSizer ZS (Malvern Instruments, United Kingdom). The measurements were performed at 25 °C in a triplicate run with 12 measurements per run.

An overview of the morphology and cross-sections of the supraparticles was made, using a Supra 25 SEM (Zeiss, Germany) at 2 kV (field emission) and a working distance of 3.7 mm. The cross-sections were prepared by mixing 10 mg of the supraparticles onto 500 µL of lacquer and cured at 90 °C for 30 min, followed by cutting with a scalpel. The samples were placed on an SEM sample holder

with conductive silver and sputtered with platinum for 5 s at 50 mA (MED 010, Balzers Union, Germany).

Shear-stress experiments were conducted with a ball-mill-like setup. For this purpose, 100 mg of supraparticle powder was mixed with 50 ZrO<sub>2</sub> ball-mill balls (1 mm diameter) in a centrifuge tube (5 mL, Eppendorf). This tube was mixed on a vortex device (HSB03710, Heathrow Scientific, USA) at 3000 rpm for 5–120 s.

In order to determine the approximated work during the shear-stress experiment, a ball mill Pulverisette Premium Line 7 (Fritsch, Germany) was used. The parameters were set as 1 g supraparticle powder, 0.045 L grinding beaker, nine 10 mm ZrO<sub>2</sub> balls, 650 rpm rotational speed, and speed interval of 5, 10, 15, 30 s.

All powders (as prepared and after shear-stress experiments) were spectroscopically characterized using a spectrophotometer Color i7 (X-Rite, USA). All measurements were carried out in the reflection mode.

For the correlative single particle spectrometry, small amounts of samples were deposited on carbon pads for the measurement. The microscopy images were taken in reflection mode, using a custom-modified (A.S. & Co.) Zeiss Axio Imager.Z2 with a Zeiss-Epiplan-Neofluor 50x/NA0.55 objective and a CMOS camera (Zeiss AxioCam 208 color) with both field diaphragm and aperture completely open. The white balance was set, using a diffusive white standard (SRS-99-010, Labsphere). Spectra were taken with a partially closed field diaphragm using a CCD spectrometer (Zeiss MCS CCD/UV-NIR) with a fused silica mirror reference (BB2-E02, Thorlabs). The measurement spot of the outcoupled light supplied to the spectrometer was adjusted to 5 μm × 5 μm. A minimum of eight spectra were averaged per measurement. The integration time was adjusted to the size of the measurement spot. The spectra were always measured in the center of the supraparticle. For the SEM images, a Zeiss Gemini 500 SEM with an SE2 detector was used. The acceleration voltage was 2 kV. Due to a special correlative microscopy sample holder and software from Zeiss (Zeiss Shuttle and Find), the same supraparticles were identified and imaged as in the microscopy imaging and spectroscopic measurements.

For the spectroscopy measurements in liquid, 1 mg of sample was added in 600 μL in fluorinated oil (FO, 3M Novec 7500, >99%) with 1 wt% surfactant (Krytox 157 FSH) in 1.5 mL clear cylindrical glass vial. The supraparticles were dispersed by shaking the vial by hand and remained homogeneously dispersed for more than 1 min (which was sufficient to record the spectra). After this time, the supraparticles started to sediment due to their higher density.

The sample was illuminated by a tungsten halogen light source (HL-2000-FSHA, ocean optics), using a self-built lens-aperture system to achieve an illumination with a spot size of 2 mm within the supraparticle suspension. The scattered light was collected via collimator connected to a spectrometer (Flame-T-VIS-NR-ES spectrometer, ocean optics) with a glass fiber. Both the glass vial and the collimator were mounted on a rotational stage, so that the angle in which the scattered light was collected could be varied from 30° to 90°. The direction of the light source remained fixed. A clear glass vial containing only FO was used as a 0%-reference. For a 100%-reference, the collimator was angled close to 90° to collect parts of the light directly from the source. Due to the arbitrary value of the 100%-reference, the reflectance was not given in absolute values. As the 100%-reference was the same for each measurement, the values could be compared between samples. For each individual measurement, 20 spectra (integration time 30 ms) were averaged. For each measured angle, five measurements were taken. Before each of these measurements, the vial was shaken by hand and placed back into the setup to prevent the influence of sedimentation.

**Statistical Analysis:** The displayed reflectance spectra of the powder sample were the average of three individual measurements from the same batch. In order to present the color of the powder samples in the CIE chromaticity diagram, the average of three individual measurements was calculated and normalized. Subsequently, the reflectance spectra of the samples were normalized and then transferred in a CIE diagram with the help of the software OriginPro 2021. Within the CIE chromaticity diagram, the x and y values for each sample could be identified. The DLS spectra represented an average of three individual measurements

with 15 single measurements each from the same batch. The particle size distribution of the supraparticles during shear-stress experiments obtained by laser diffraction was displayed as the average of five individual measurements from the same batch.

## Supporting Information

Supporting Information is available from the Wiley Online Library or from the author.

## Acknowledgements

This work was financially supported by the BMBF (Nano-MatFutur grant 03XP0149). The project was also supported by the Deutsche Forschungsgemeinschaft (DFG, German Research Foundation)—Project-ID: 416229255–SFB 1411. The authors thank BÜCHI Labortechnik AG for providing the spray-dryer equipment. The authors thank Felix Häring and Benedikt Schug for providing the iron oxide nanoparticles and Selina Kosdik for the photographs of the powder samples.

Open access funding enabled and organized by Projekt DEAL.

## Conflict of Interest

The authors declare no conflict of interest.

## Authors Contribution

General research goals were developed by S.W., S.W., and K.M. The supervision of the whole project was done by S.W., S.W., and K.M. Performance of the syntheses and characterization were carried out by S.W., G.B., J.E., and J.P. Interpretation and conclusion of the results was done by S.W. in discussion with G.B., N.V., S.W., and K.M. Figures were created by S.W. The original manuscript draft was written by S.W. with the contribution of S.W. Reviewing and editing were performed by S.W., G.B., N.V., S.W., and K.M. All authors proof-read and commented on the publication.

## Data Availability Statement

The data that support the findings of this study are available in the supplementary material of this article.

## Keywords

disordered/ordered core-shell structures, hybrid materials, photonic balls, shear-stress indicators, supraparticles

Received: May 17, 2022  
Revised: September 27, 2022  
Published online:

- [1] a) H. Lasi, P. Fettke, H.-G. Kemper, T. Feld, M. Hoffmann, *Bus. Inf. Syst. Eng.* **2014**, *6*, 239; b) T. Ageyeva, S. Horváth, J. G. Kovács, *Sensors* **2019**, *19*, 3551.  
[2] a) S. Li, Y. Zhang, Y. Wang, K. Xia, Z. Yin, H. Wang, M. Zhang, X. Liang, H. Lu, M. Zhu, *InfoMat* **2020**, *2*, 184; b) M. Nadgorny, A. Ameli, *ACS Appl. Mater. Interfaces* **2018**, *10*, 17489.

- [3] S. Wenderoth, S. Müssig, J. Prieschl, E. Genin, K. Heuzé, F. Fidler, D. Haddad, S. Wintzheimer, K. Mandel, *Nano Lett.* **2022**, *22*, 2762.
- [4] S. Wenderoth, T. Granath, J. Prieschl, S. Wintzheimer, K. Mandel, *Adv. Photonics Res.* **2020**, *1*, 2000023.
- [5] S. Wenderoth, A. Eigen, S. Wintzheimer, J. Prieschl, A. Hirsch, M. Halik, K. Mandel, *Small* **2022**, *18*, e2107513.
- [6] S. Wintzheimer, J. Reichstein, S. Wenderoth, S. Hasselmann, M. Oppmann, M. T. Seuffert, K. Müller-Buschbaum, K. Mandel, *Adv. Funct. Mater.* **2019**, *29*, 1901193.
- [7] a) J. M. Clough, E. Guimard, C. Rivet, J. Sprakel, T. E. Kodger, *Adv. Opt. Mater.* **2019**, *7*, 1900218; b) U. Resch-Genger, M. Grabolle, S. Cavaliere-Jaricot, R. Nitschke, T. Nann, *Nat. Methods* **2008**, *5*, 763; c) A. Steinegger, I. Klimant, S. M. Borisov, *Adv. Opt. Mater.* **2017**, *5*, 1700372; d) H. S. Jung, P. Verwilt, W. Y. Kim, J. S. Kim, *Chem. Soc. Rev.* **2016**, *45*, 1242.
- [8] G. von Freymann, Y. Kitaev, B. V. Lotsch, G. A. Ozin, *Chem. Soc. Rev.* **2013**, *42*, 2528.
- [9] S. Wintzheimer, T. Granath, M. Oppmann, T. Kister, T. Thai, T. Kraus, N. Vogel, K. Mandel, *ACS Nano* **2018**, *12*, 5093.
- [10] a) Y. Zhao, L. Shang, Y. Cheng, Z. Gu, *Acc. Chem. Res.* **2014**, *47*, 3632; b) O. D. Velev, A. M. Lenhoff, E. W. Kaler, *Science* **2000**, *287*, 2240.
- [11] N. Vogel, S. Utech, G. T. England, T. Shirman, K. R. Phillips, N. Koay, I. B. Burgess, M. Kolle, D. A. Weitz, J. Aizenberg, *Proc. Natl. Acad. Sci. U. S. A.* **2015**, *112*, 10845.
- [12] a) C. I. Aguirre, E. Reguera, A. Stein, *Adv. Funct. Mater.* **2010**, *20*, 2565; b) J. Wang, C. F. Mbah, T. Przybilla, B. Apeleo Zubiri, E. Spiecker, M. Engel, N. Vogel, *Nat. Commun.* **2018**, *9*, 5259.
- [13] Y. Takeoka, *J. Mater. Chem. C* **2013**, *1*, 6059.
- [14] E. S. A. Goerlitzer, R. N. Klupp Taylor, N. Vogel, *Adv. Mater.* **2018**, *30*, 1706654.
- [15] L. R. P. Areias, G. Marcelo, J. P. S. Farinha, *ACS Appl. Nano Mater.* **2021**, *4*, 13185.
- [16] M. Xiao, Z. Hu, Z. Wang, Y. Li, A. D. Tormo, N. Le Thomas, B. Wang, N. C. Gianneschi, M. D. Shawkey, A. Dhinojwala, *Sci. Adv.* **2017**, *3*, e1701151.
- [17] D.-S. Choi, J.-H. Choi, C.-Y. Lee, *Appl. Sci.* **2020**, *10*, 420.
- [18] C.-F. Lai, Y.-C. Wang, *Crystals* **2016**, *6*, 61.
- [19] Y. f. Jiang, A. Zheng, S. J. Zheng, W. m. Liu, L. Zhuang, *J. Appl. Phys.* **2020**, *128*, 103106.
- [20] M. Teshima, T. Seki, R. Kawano, S. Takeuchi, S. Yoshioka, Y. Takeoka, *J. Mater. Chem. C* **2015**, *3*, 769.
- [21] J.-G. Park, S.-H. Kim, S. Magkiriadou, T. M. Choi, Y.-S. Kim, V. N. Manoharan, *Angew. Chem., Int. Ed.* **2014**, *53*, 2899.
- [22] J. H. Moon, G.-R. Yi, S.-M. Yang, D. J. Pine, S. B. Park, *Adv. Mater.* **2004**, *16*, 605.
- [23] W. Luo, J. Yan, Y. Tan, H. Ma, J. Guan, *Nanoscale* **2017**, *9*, 9548.
- [24] a) C. Avcı, M. L. de Marco, C. Byun, J. Perrin, M. Scheel, C. Boissière, M. Faustini, *Adv. Funct. Mater.* **2021**, *33*, 2104450; b) Q. Yang, M. Li, J. Liu, W. Shen, C. Ye, X. Shi, L. Jiang, Y. Song, *J. Mater. Chem. A* **2013**, *1*, 541.
- [25] W. Gao, M. Rigout, H. Owens, *Appl. Surf. Sci.* **2016**, *380*, 12.
- [26] A. B. D. Nandiyanto, K. Okuyama, *Adv. Powder Technol.* **2011**, *22*, 1.
- [27] a) M. Oppmann, M. Wozar, J. Reichstein, K. Mandel, *ChemNanoMat* **2018**, *6*, 141; b) C. Stauch, C. Hobbs, A. Shmeliov, V. Nicolosi, T. Ballweg, R. Luxenhofer, K. Mandel, *Part. Part. Syst. Charact.* **2018**, *35*, 1800096.
- [28] W. Stöber, A. Fink, E. Bohn, *J. Colloid Interface Sci.* **1968**, *26*, 62.
- [29] M. Mündlein, B. Schug, S. Wintzheimer, K. Mandel, *J. Magn. Magn. Mater.* **2019**, *488*, 165350.
- [30] S. Zellmer, G. Garnweitner, T. Breinlinger, T. Kraft, C. Schilde, *ACS Nano* **2015**, *9*, 10749.
- [31] F. Iskandar, L. Gradon, K. Okuyama, *J. Colloid Interface Sci.* **2003**, *265*, 296.
- [32] a) W. Liu, M. Kappl, W. Steffen, H.-J. Butt, *J. Colloid Interface Sci.* **2022**, *607*, 1661; b) M. Sperling, O. D. Velev, M. Gradzielski, *Angew. Chem., Int. Ed.* **2014**, *53*, 586.
- [33] F. Iskandar, A. B. D. Nandiyanto, W. Widiyastuti, L. S. Young, K. Okuyama, L. Gradon, *Acta Biomater.* **2009**, *5*, 1027.
- [34] A. B. Stephenson, M. Xiao, V. Hwang, L. Qu, P. A. Odoriso, M. Burke, K. Task, T. Deisenroth, S. Barkley, R. H. Darji, V. N. Manoharan, e-print, arXiv:2207.03033, **2022**.
- [35] a) J. Wang, Y. Liu, G. Bleyer, E. S. A. Goerlitzer, S. Englisch, T. Przybilla, C. F. Mbah, M. Engel, E. Spiecker, I. Imaz, D. Maspoch, N. Vogel, *Angew. Chem., Int. Ed.* **2022**, *61*, e202117455; b) R. Ohnuki, M. Sakai, Y. Takeoka, S. Yoshioka, *Langmuir* **2020**, *36*, 5579.
- [36] S. Wintzheimer, S. Müssig, S. Wenderoth, J. Prieschl, T. Granath, F. Fidler, D. Haddad, K. Mandel, *ACS Appl. Nano Mater.* **2019**, *2*, 6757.
- [37] J. Wang, J. Schwenger, A. Ströbel, P. Feldner, P. Herre, S. Romeis, W. Peukert, B. Merle, N. Vogel, *Sci. Adv.* **2021**, *7*, eabj0954.
- [38] J. Wang, E. Kang, U. Sultan, B. Merle, A. Inayat, B. Graczykowski, G. Fytas, N. Vogel, *J. Phys. Chem. C* **2021**, *125*, 23445.
- [39] a) Y. Takeoka, S. Yoshioka, A. Takano, S. Arai, K. Nueangnoraj, H. Nishihara, M. Teshima, Y. Ohtsuka, T. Seki, *Angew. Chem.* **2013**, *125*, 7402; b) A. Patil, C. M. Heil, B. Vanthournout, M. Bleuel, S. Singla, Z. Hu, N. C. Gianneschi, M. D. Shawkey, S. K. Sinha, A. Jayaraman, *Adv. Opt. Mater.* **2022**, *10*, 2102162.
- [40] C. Stauch, T. Ballweg, W. Stracke, R. Luxenhofer, K. Mandel, *J. Colloid Interface Sci.* **2017**, *490*, 401.



## Supporting Information

for *Small*, DOI: 10.1002/smll.202203068

Spray-Dried Photonic Balls with a Disordered/Ordered Hybrid Structure for Shear-Stress Indication

*Sarah Wenderoth, Gudrun Bleyer, Jakob Endres, Johannes Prieschl, Nicolas Vogel, Susanne Wintzheimer, and Karl Mandel\**

WILEY-VCH

Supporting Information

**Spray-dried photonic balls with a disordered/ordered hybrid structure for shear stress indication**

*Sarah Wenderoth, Gudrun Bleyer, Jakob Endres, Johannes Prieschl, Nicolas Vogel, Susanne Wintzheimer, and Karl Mandel\**

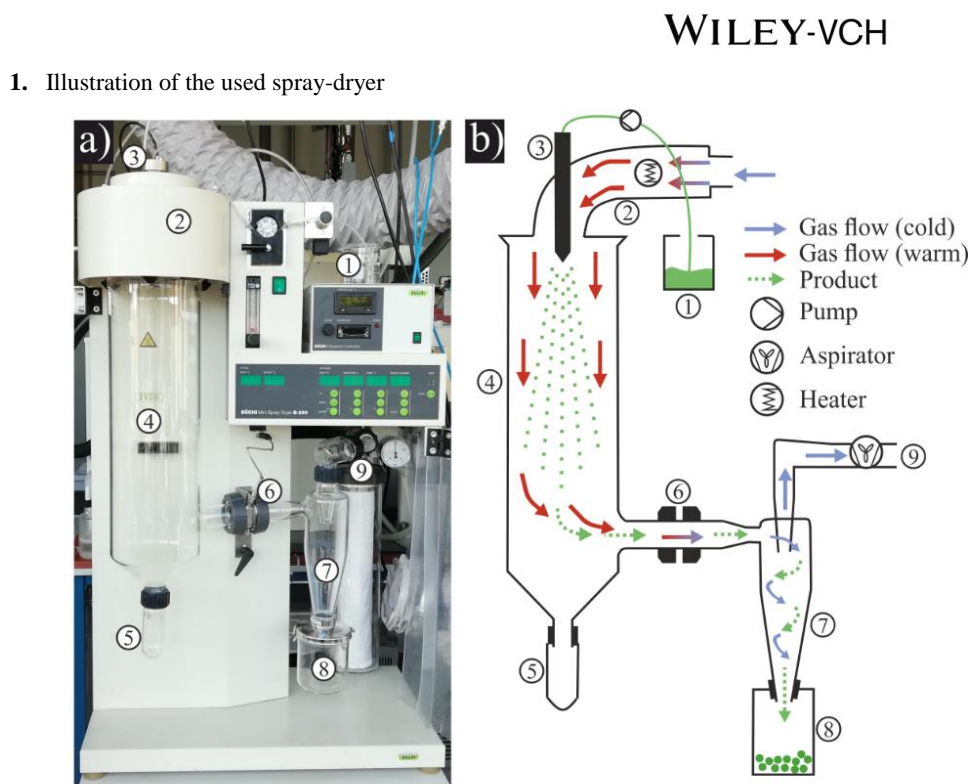


**Figure S1:** a) Photography of the used Mini Spray-Dryer B-290 from Büchi, Switzerland and b) a schematic illustration to visualize the gas and particle flow. The different parts of the device are numbered in both images (1: nanoparticle dispersion, 2: heater with the inlet thermometer, 3: ultrasonic nozzle, 4: spray tower, 5: collecting vessel, 6: adapter with outlet thermometer, 7: cyclone, 8: collecting vessel for supraparticles, 9: filter and behind the aspirator).

## 2. SEM images of undefined supraparticles

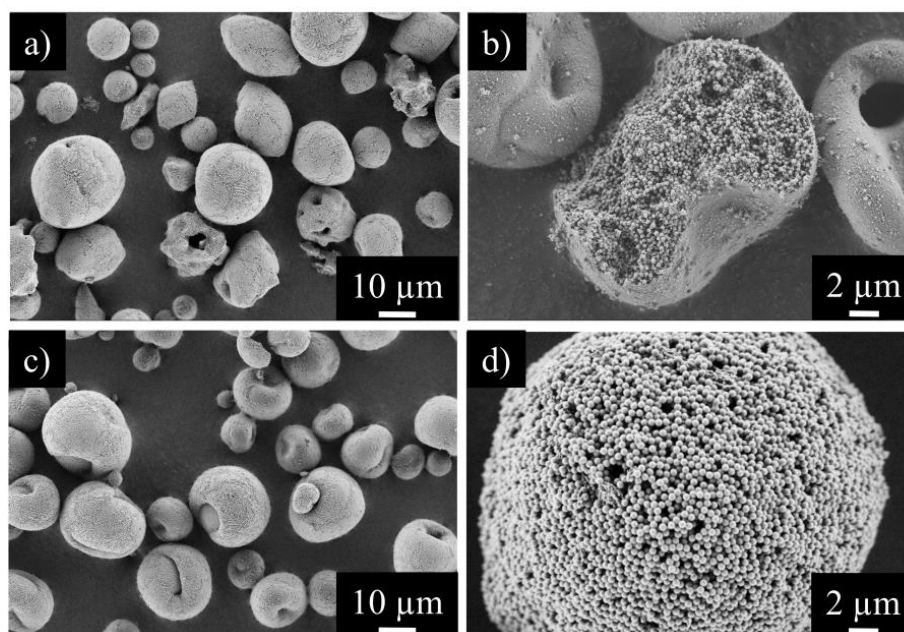
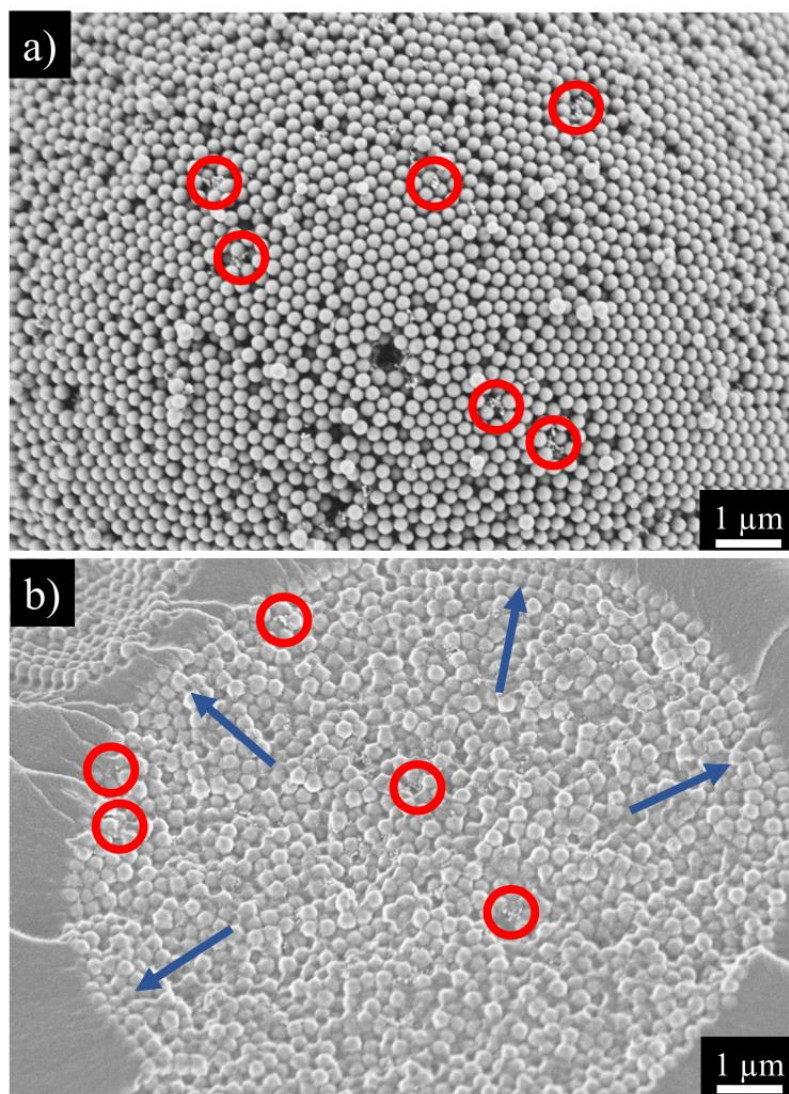


**Figure S2:** SEM images of spray-dried supraparticles showing no structural color, although they were also composed of iron oxide and silica nanoparticles. In a), iron oxide nanoparticles based on a hydrothermal synthesis were used, which in dispersion form agglomerates and thus, yield supraparticles with undefined shapes. In b), small iron oxide nanoparticles (~10 nm) were used, which form a dense shell around the larger silica nanoparticles during the spray-drying process. In c), the dispersion of the silica nanoparticles contained some ethanol residues from the synthesis, causing a crumbled shape of the supraparticles. In d)  $\text{CaCl}_2$  was added to enhance the spherical shape of the supraparticles. This resulted in disordered arrangement of the nanoparticle building blocks over the entire supraparticle.

**Table S1:** Summary of the spray-dryer conditions for the above mentioned supraparticles.

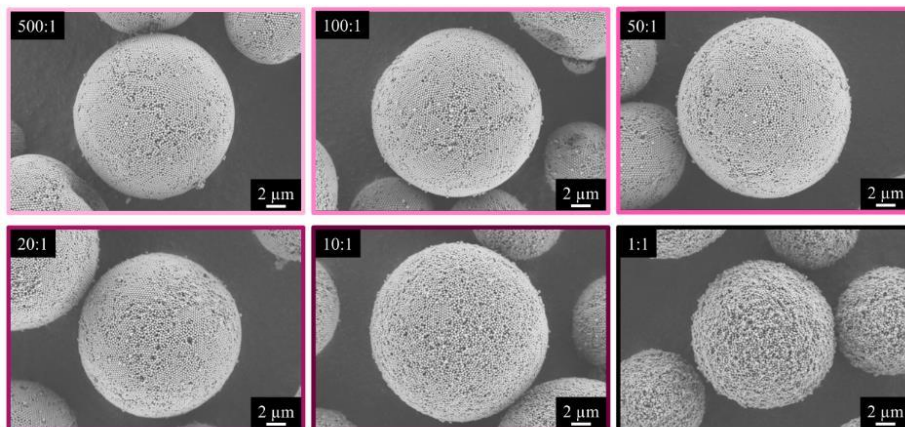
Inlet temperature:	140 °C	Weight concentration:	3 wt%
Outlet temperature:	75-85 °C	Nozzle power:	5 W
Aspirator power:	75%	Vacuum:	-30 mbar

## 3. SEM images of higher magnifications of photonic balls



**Figure S3:** Reprint of SEM images of Figure 1 in a larger scale of the photonic ball (a) as received after spray-drying and (b) in cross-section. The red circles highlight some of the iron oxide nanoparticles, which are randomly distributed on the whole supraparticle (core and outer shell). The blue arrows highlight the area of high order on the outer shell of the photonic ball in the cross-section.

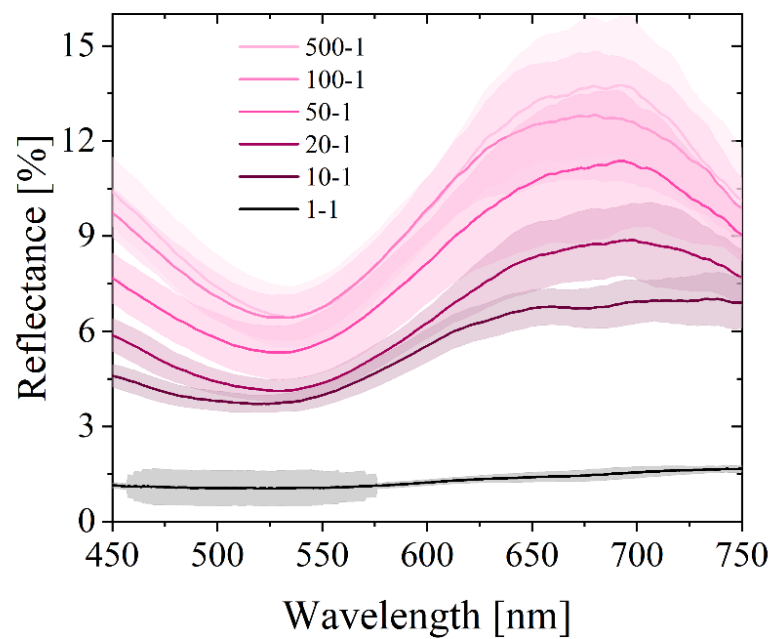
## 4. SEM images of supraparticles with different ratios of silica and iron oxide



**Figure S4:** SEM images of photonic balls with different ratios of silica:iron oxide (500:1, 100:1, 50:1, 20:1, 10:1, 1:1). With an increasing amount of iron oxide, the number of defects on the supraparticle surface is increasing.

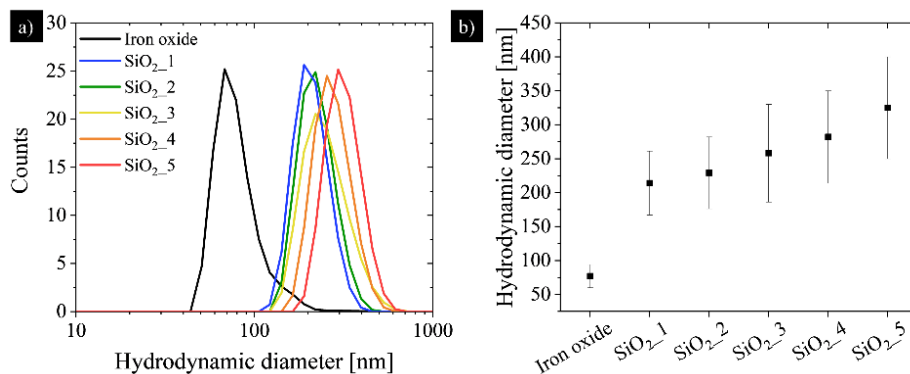
WILEY-VCH

5. Reflectance spectra of single supraparticles with different ratios of silica and iron oxide



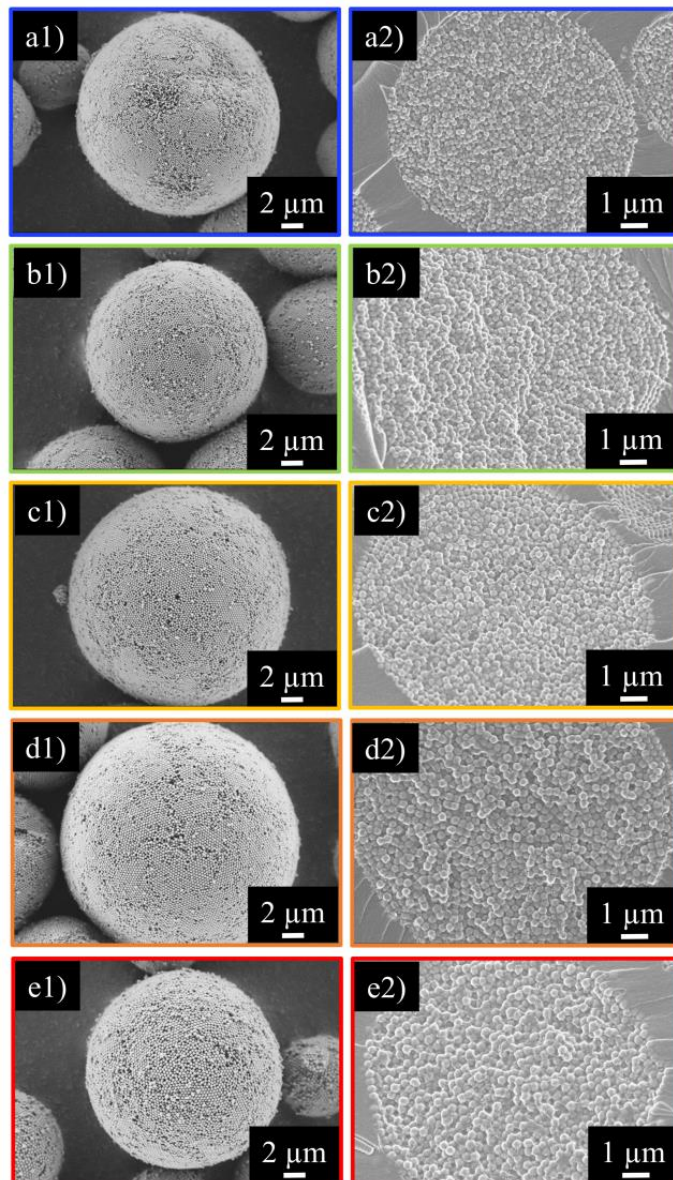
**Figure S5:** Reflectance spectra of 10 single supraparticles with different ratios of silica: iron oxide (500:1, 100:1, 50:1, 20:1, 10:1, 1:1). With an increasing amount of iron oxide, the intensity of the reflectance signal is decreasing.

## 6. DLS measurements of iron oxide and silica nanoparticles



**Figure S6:** a) DLS measurements of the primary nanoparticles iron oxide (black) and silica (blue, green, yellow, orange, red). The colors of the different silica graphs refer to the later visible colors of the corresponding photonic balls. b) The primary nanoparticle sizes of the individual nanoparticles are as follows: iron oxide:  $d_{\text{DLS}} = 77 \pm 17$  nm, SiO<sub>2</sub>\_1:  $d_{\text{DLS}} = 214 \pm 47$  nm, SiO<sub>2</sub>\_2:  $d_{\text{DLS}} = 229 \pm 53$  nm, SiO<sub>2</sub>\_3:  $d_{\text{DLS}} = 258 \pm 72$  nm, SiO<sub>2</sub>\_4:  $d_{\text{DLS}} = 282 \pm 68$  nm, SiO<sub>2</sub>\_5:  $d_{\text{DLS}} = 325 \pm 75$  nm. The DLS spectra represents an average of three individual measurements with 15 single measurements each from the same batch.

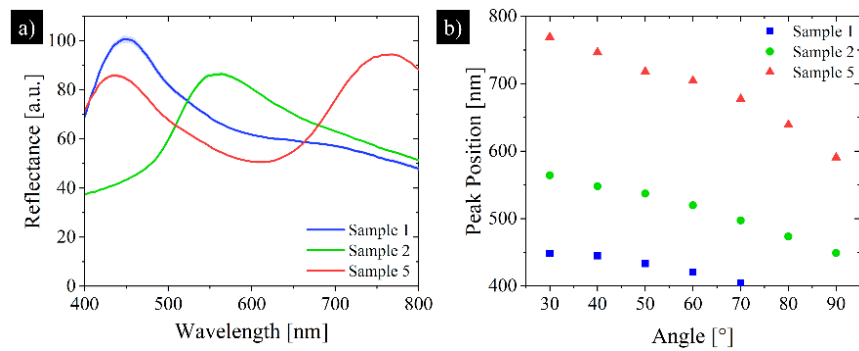
## 7. SEM images of photonic balls with different sizes of silica nanoparticles



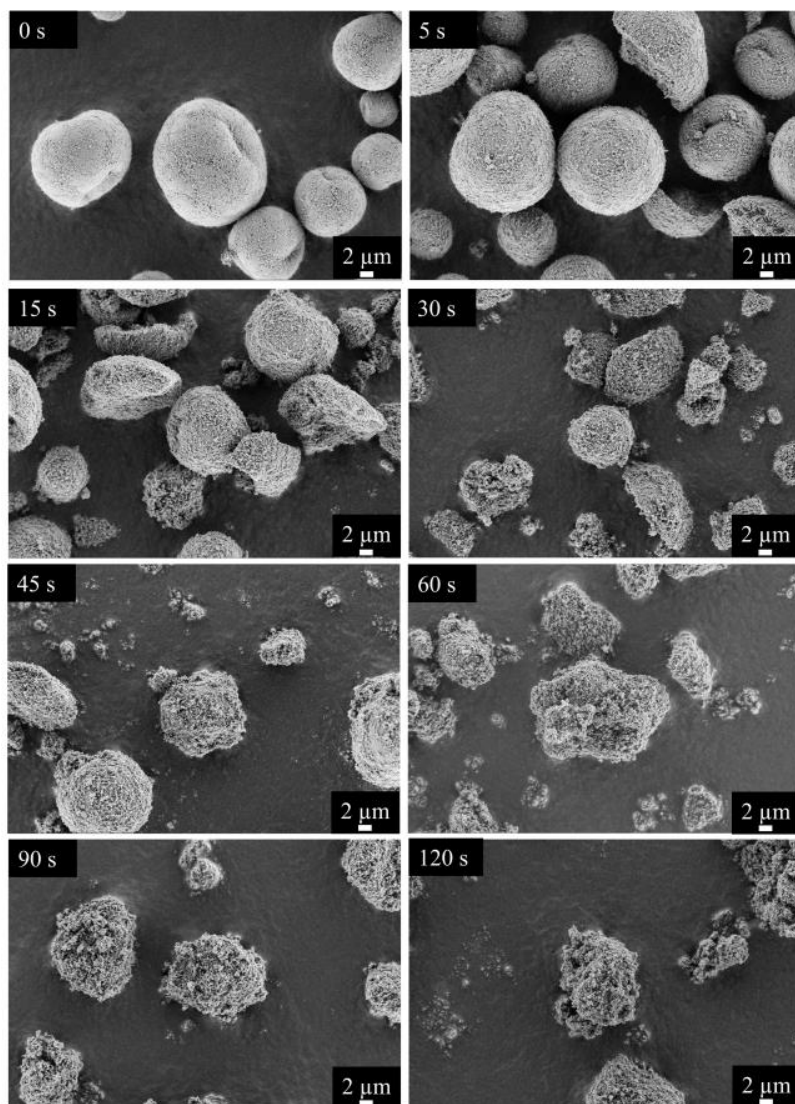
**Figure S7:** SEM images of the different photonic balls (1) as prepared and (2) in cross-section. The frames of each image refer to the visible colors from Figure 3 (a: blue, b: green, c: yellow, d: orange, e: red).

WILEY-VCH

## 8. Angle dependent spectroscopy measurement in liquid



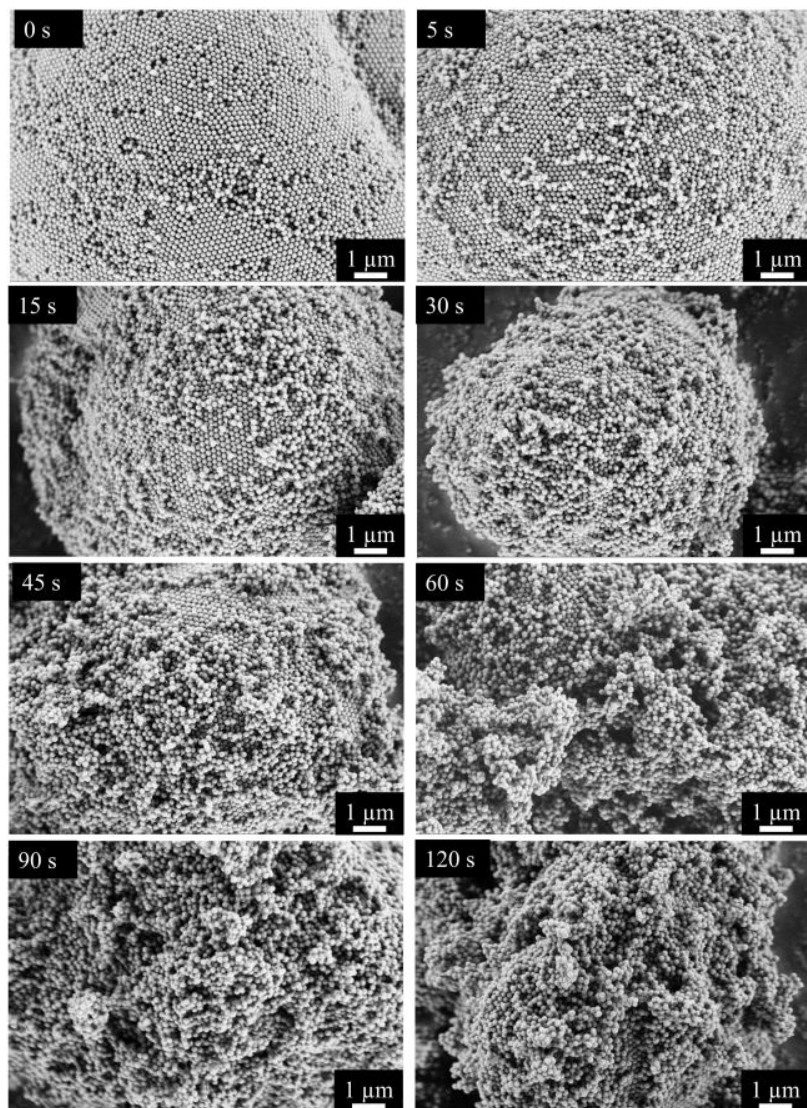
**Figure S8:** a) Spectra of samples 1 (blue), 2 (green) and 5 (red), respectively, measured at 30° observation angle relative to the incident light in fluorinated oil. b) Change in peak position over observation angle for all samples.

**9. SEM images of photonic balls during shear stress application**

**Figure S9:** SEM images of photonic balls with the smallest silica particle size ( $d_{DLS} = 214 \pm 47$  nm) which appear blueish in the as-prepared state (0 s), as well as after different shear stress exposure times (5 s, 15 s, 30 s, 45 s, 60 s, 90 s, 120 s) whereas an increasing deformation of the supraparticles can be obtained.

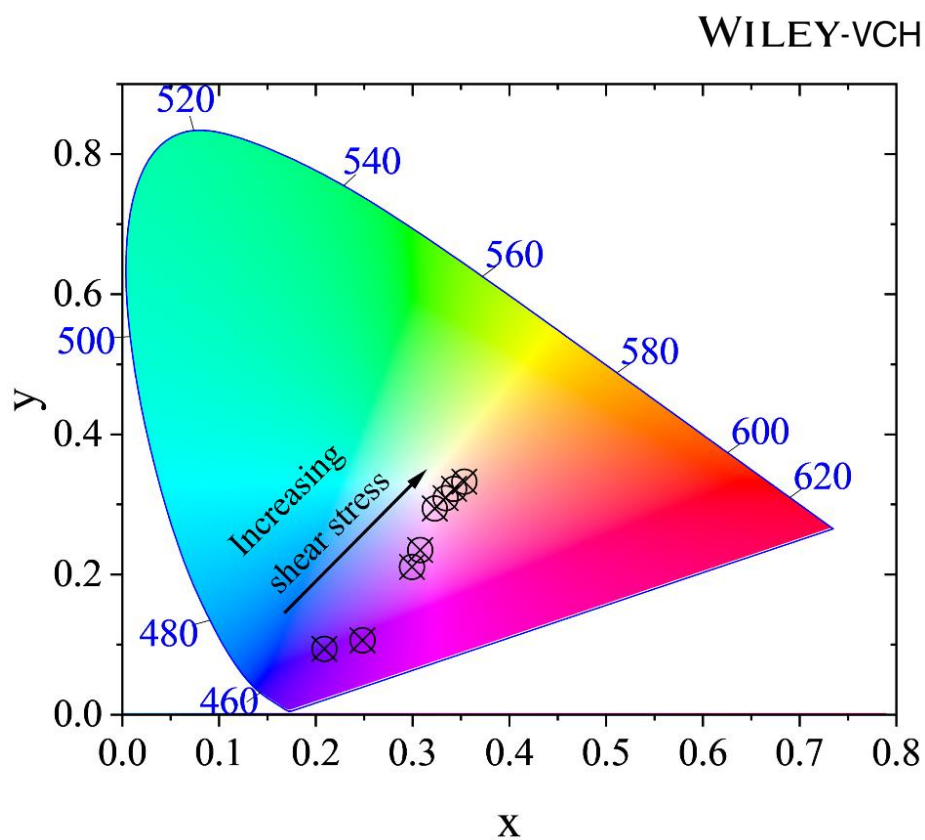
**10. SEM images of photonic balls during shear stress application in higher magnification**

WILEY-VCH



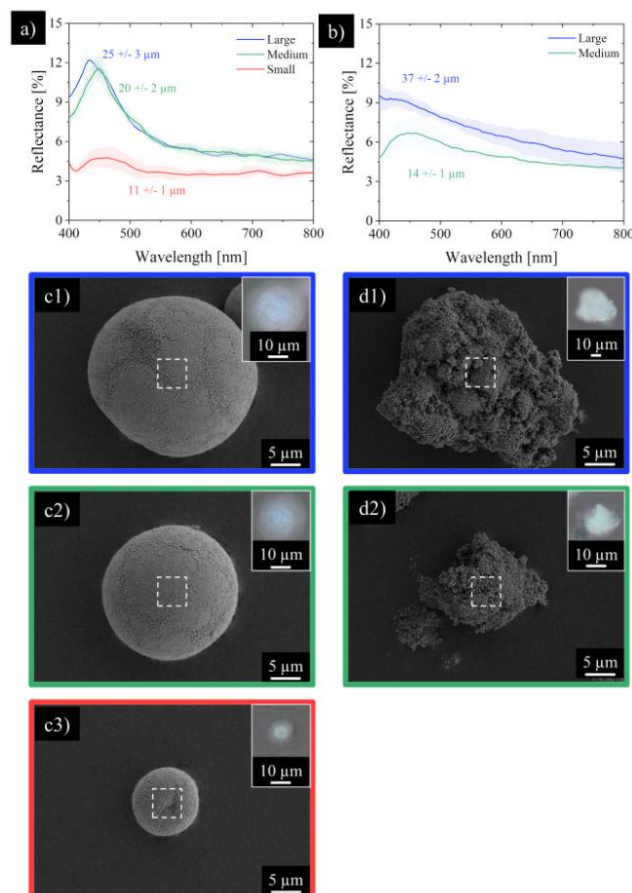
**Figure S10:** SEM images of the photonic balls from Figure S9 in higher magnification. The reduction of highly ordered areas on the supraparticle surface is clearly visible.

#### 11. CIE chromaticity diagram of photonic balls during shear stress application



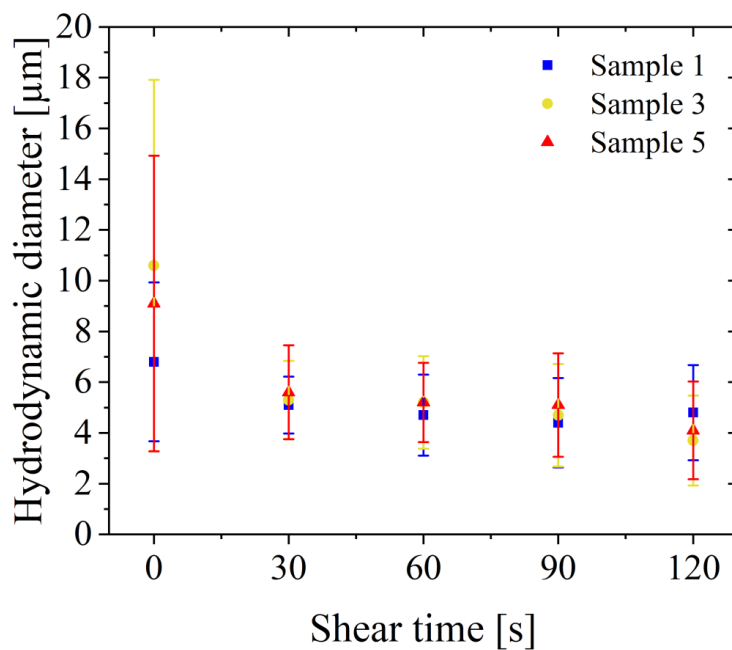
**Figure S11:** CIE chromaticity diagram of the photonic balls which appear blueish during shear stress application. The different coordinates in the diagram refer from left to right to the SEM images in Figure S9+S10. Three reflectance spectra of each sample were recorded and their average was calculated. The transformation to the CIE chromaticity diagram was performed by normalization of the reflectance spectra and the use of the software OriginPro 2021.

## 12. Determination of the size dependence of the individual supraparticles on the optical signal before and after shear stress application



**Figure S12:** a) Reflectance spectra of individual supraparticles of sample 1 in the initial state. Three different particle sizes (large:  $25 \pm 3 \mu\text{m}$ , medium:  $20 \pm 2 \mu\text{m}$ , small:  $11 \pm 1 \mu\text{m}$ ) were selected and 10 supraparticles were measured per size. b) Reflectance spectra of individual supraparticles from sample 1 after 120 s of shear stress application. Two different particle sizes were selected and measured (large: agglomerates of multiple supraparticles that were formed during the shear stress application:  $37 \pm 2 \mu\text{m}$ , medium:  $14 \pm 1 \mu\text{m}$ ). c) SEM images of three different particle sizes of the sample 1 in the initial state (1: large, 2: medium, 3: small). The dashed square in the center of the supraparticles is to illustrate the measurement spot size of the spectrometer in the optical microscope. The inset in each image shows the optical microscopy image. d) SEM images of the sample 1 after 120 s of shear stress application in the two different sizes (1: large, 2: medium). The dashed square shows the spot size of the spectrometer in the optical microscope. The insets show the supraparticle in the optical microscope.

WILEY-VCH

**13. Laser scattering measurements to determine the supraparticle size after shear stress application**

**Figure S13:** Laser scattering measurement to determine the hydrodynamic particle size of supraparticles during shear stress application for sample 1 (blue color), sample 3 (yellow color) and sample 5 (red color) in the initial state as well as after 30, 60, 90, and 120 s in the ball mill like setup. The particle size distribution of the supraparticles during shear stress experiments obtained by laser diffraction are displayed as the average of 5 individual measurements from the same batch.

#### 14. Influence of shear stress application on optical signal in angle dependent spectroscopy measurements in liquid

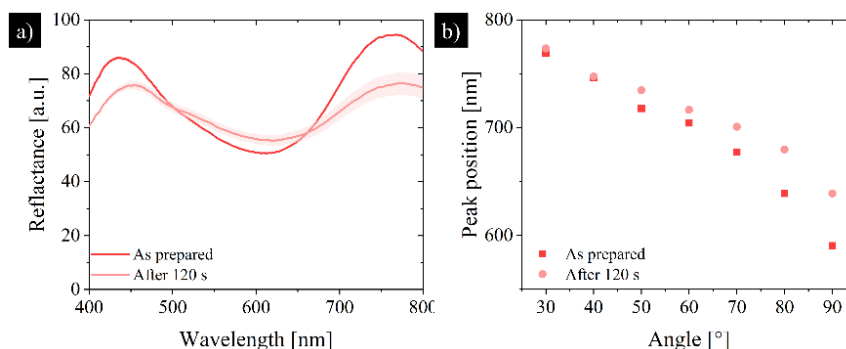


**Figure S14:** a) Spectra of sample 5 as prepared and after 120 s of milling measured at 30° observation angle respective to incident light in fluorinated oil. b) Change in peak position over observation angle for all respective samples.

#### 15. Determination of the impact energy and the approximate work, loaded on the sample during ball milling experiments

Based on various studies, an approximation of the impact energy acting on the supraparticle samples during ball milling experiments was calculated.<sup>[S1, S2, S3]</sup> Several assumptions were necessary to calculate the impact energy  $E_i$ , which is independent of the milling sample.<sup>[S2]</sup> In the ball mill, the rotational speed of the mill is equal to the rotational speed of the vessel.<sup>[S1, S2]</sup> Here, the impact energy is linearly dependent on the volume of the used grinding beaker.<sup>[S1]</sup> Furthermore, the impact energy is proportional to the grinding speed.<sup>[S2, S3]</sup>

In this work, the following parameter settings were chosen: beaker filling ratio: 0.1 (9 balls and 1 g sample); rotational speed: 650 rpm; beaker volume: 0.045 L; ball size and material: 10 mm  $ZrO_2$  balls. Based on these parameters and calculations from a previous work<sup>[S4]</sup>, the impact energy  $E_i$  can be estimated as  $20 \text{ J s}^{-1}$ .

In order to calculate the approximate work during the ball milling experiment, a supraparticle sample was milled for a total of 30 s. Reflectance spectra of the sample were recorded in the initial state, after 5, 10, 15 and 30 s of grinding. Using the resulting CIE chromaticity diagram, the x and y values of the different samples were determined. Since the impact energy is given as  $20 \text{ J s}^{-1}$ , the approximate work for each time point can be calculated using equation 1:

$$W = E_i \cdot t \quad (1)$$

This gives the approximate work for each sample as follows: Start = 0 J; 5 s = 100 J, 10 s = 200 J, 15 s = 300 J, and 30 s = 600 J. These values can be plotted in an xy-diagram,

WILEY-VCH

where the x and y values are from the CIE chromaticity diagram (Figure S15). Since they exhibit linear behavior, the distance between two points can be calculated using the Pythagoras theorem (equation 2):

$$z=(x^2+y^2)^{1/2} \quad (2)$$

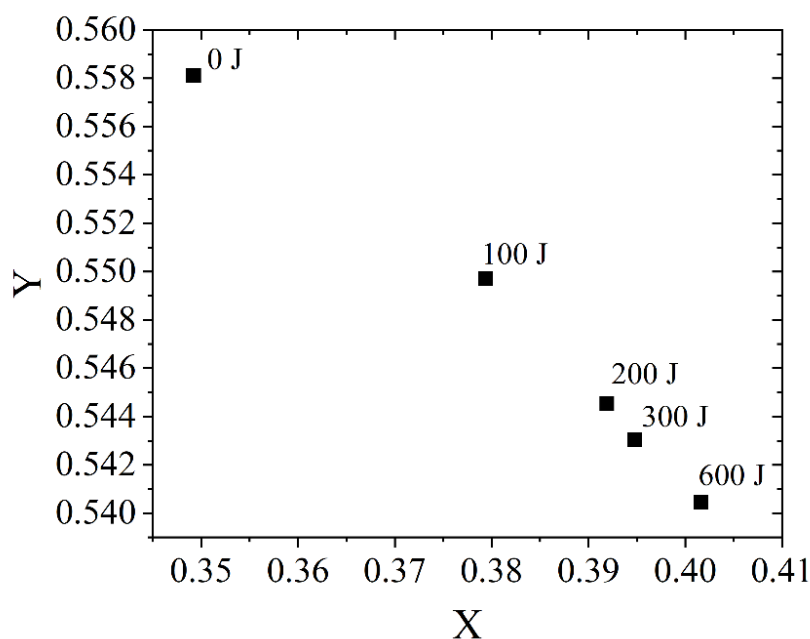


**Figure S15:** Plotted values from the CIE chromaticity diagram of the samples grinded in the ball mill. The approximate work is assigned to the respective grinding time (initial state = 0 s, 5 s = 100 J, 10 s = 200 J, 15 s = 300 J, 30 s = 600 J).

By assuming that the color change occurring during the destruction of the supraparticles is only dependent on the work introduced, starting from the distances between the different points in the xy-diagram calculated above, the approximate work for the samples in the ball mill like setup can also be calculated. For this purpose, 100 mg of the supraparticle powder was mixed with 50 ZrO<sub>2</sub> balls with a diameter of 1 mm in the ball mill like setup and grinded for a total of 120 s. A reflectance spectra of the sample was recorded after 30, 60, 90 and 120 s of milling. Based on the above calculations, the approximate work done in this system can be calculated as follows: 30 s = 165 J, 60 s = 549 J, 90 s = 463 J and 120 s = 532 J. It should be mentioned that after 60 s of grinding, the sample is already almost completely

## WILEY-VCH

destroyed and the slight changes in the approximate work done may also be due to measurement errors.

In a further experiment, the influence of the number of balls in the ball mill like setup was investigated. A reduction in the degree of filling leads to a reduction in the number of grinding balls and thus to a reduction in the number of impacts responsible for energy transfer. Increasing the grinding ball fill ratio affects the grinding media motion and reduces the transmissive power, although the number of grinding balls and thus the potential impact partners increase. Therefore, 100 mg of the supraparticle powder was mixed with 0, 25, 50 and 100 ZrO<sub>2</sub> balls of 1 mm diameter. After 30 s of grinding in the ball mill like setup, the reflectance spectra were recorded. Using the above calculations, the approximate work was calculated as 0 balls = 16 J, 25 ball = 29 J, 50 balls = 165 J, 100 balls = 195 J. These results again emphasize that the number of grinding balls chosen in this work is in a range that, on the one hand, adequate times can be used for the overall experiment (fewer balls means longer experiment time) and, on the other hand, the effects that occur in the shear experiments can still be detected (too many balls destroy the sample too quickly).

**References**

- [S1] B. Funk, DBU-final report-AZ-29622-31, Ressourceneffiziente chemische Synthese – Prozessentwicklung in Kugelmöhlen für lösungsmittelfreie Reaktionen (RESPEKT), Jena, **31.12.2015**.
- [S2] H. Mio, J. Kano, F. Saito, *Chem. Eng. Sci.* **2004**, *59*, 5909–5916.
- [S3] a) J. Kano, H. Mio, F. Saito, *AIChE J.*, **2000** *46* (8), 1694–1697; b) J. Kano, H. Mio, F. Saito, M. Miyazaki, *Min. Eng.*, **2001** *14* (10), 1213–1223, c) H. Mio, J. Kano, F. Saito, K. Kaneko, *Int. J. Miner. Process* **2004**, *74S*, 85–92.
- [S4] S. Wintzheimer, J. Reichstein, S. Wenderoth, S. Hasselmann, M. Oppmann, M. T. Seuffert, K. Müller-Buschbaum, K. Mandel, *Adv. Funct. Mater.* **2019**, *29*, 1901193.

## Hollow Superparamagnetic Nanoparticle-Based Microballoons for Mechanical Force Monitoring by Magnetic Particle Spectroscopy

Susanne Wintzheimer,<sup>†</sup> Stephan Müssig,<sup>†</sup> Sarah Wenderoth,<sup>†</sup> Johannes Prieschl,<sup>†</sup> Tim Granath,<sup>†</sup> Florian Fidler,<sup>§</sup> Daniel Haddad,<sup>§</sup> and Karl Mandel<sup>\*,†,‡,§</sup>

<sup>†</sup>Chair of Chemical Technology of Materials Synthesis, Julius-Maximilians-University Würzburg, Röntgenring 11, D97070 Würzburg, Germany

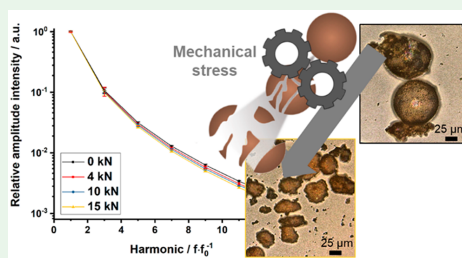
<sup>‡</sup>Fraunhofer Institute for Silicate Research ISC, Neunerplatz 2, D97082 Würzburg, Germany

<sup>§</sup>Magnetic Resonance and X-ray Imaging Department, Development Center X-ray Technology EZRT, Fraunhofer Institute for Integrated Circuits IIS, Am Hubland, D97074 Würzburg, Germany

### Supporting Information

**ABSTRACT:** The determination of induced mechanical forces in ball mills is an ongoing problem, which is so far mainly addressed by simulations. Herein, we suggest utilizing superparamagnetic microballoons as sensor particles for mechanical stress. The defined assembly of superparamagnetic nanoparticles yields microballoons with hollow cores, which makes them susceptible to mechanical forces. It is shown that the hollow structure is continuously fragmented under static or dynamic force application. By use of magnetic particle spectroscopy, these structural changes are readily detected and enable the quantification of the applied mechanical forces in ball mills.

**KEYWORDS:** magnetic particles, supraparticles, magnetic particle spectroscopy, sensor, ball milling



Ball mills typically apply shear and impact forces on powder samples by collision of accelerated balls in rotating pots. This leads to grinding of the processed material into smaller down to nanometer-scale particles. Furthermore, ball milling enables mechanical alloying, which refines the structure of metals and alloys.<sup>1</sup> Mechanochemistry has quickly developed into another important application area in recent years. It describes the (physico)chemical transformation of substances by mechanical energy. This includes the reactivity increase of solids, the realization of reactions under nonequilibrium conditions, or solvent-free one-step syntheses.<sup>2</sup> The ball milling process, i.e., the energy transfer from the milling tools to the powder, is the determining factor for grinding rates or mechanochemical reaction yields.<sup>3,4</sup> It is influenced by several factors including milling speed and time, ball to powder ratio, filling grade of the milling pot, milling atmosphere, or size and material of balls used.<sup>2–4</sup> Thus, a change of ball milling parameters, for example, for upscaling purposes or synthesis transfer to other laboratories, always implicates varied acting energies and consequently different milling outcomes.<sup>5</sup>

As the actions inside ball mills are complex and strongly influenced by the treated material, the amount of energy acting on a sample is hardly measurable.<sup>4</sup> Up to now (as far as the authors know), only simulations such as discrete element method-based<sup>4–7</sup> or particle element method-based simulations,<sup>8,9</sup> as well as response surface modeling,<sup>10</sup> are used to

predict the effect of parameter variations on the transferred energy and thus the obtained results. However, mathematical models are complex and rely on assumptions to reduce the unknown parameters to an acceptable amount.

Instead of this impracticable and often unreliable procedure, we suggest the use of a sensor, which is placed along with the sample in the milling pot. It should enable the fast and easy monitoring and quantification of acting mechanical forces during the milling process and is magnetically separated from the processed material after milling. This herein presented approach can be realized by superparamagnetic microballoons combined with magnetic particle spectroscopy (MPS). These magnetic supraparticles,<sup>11</sup> i.e., micrometer-sized particles of around 40 μm, which are assembled from individual nanoparticles, are hollow and thus susceptible to mechanical forces. Their deformation and subsequent fragmentation depend on the amount of acting forces and result in a modification of their magnetization properties and thus their MPS signal.

The primary building blocks for superparamagnetic microballoons are patchy silica–iron oxide nanoparticles obtained by a partial coverage of iron oxide nanoparticles with condensed tetraethoxysilane (TEOS).<sup>12</sup> Their silanization with

Received: September 5, 2019

Accepted: September 24, 2019

Published: September 24, 2019

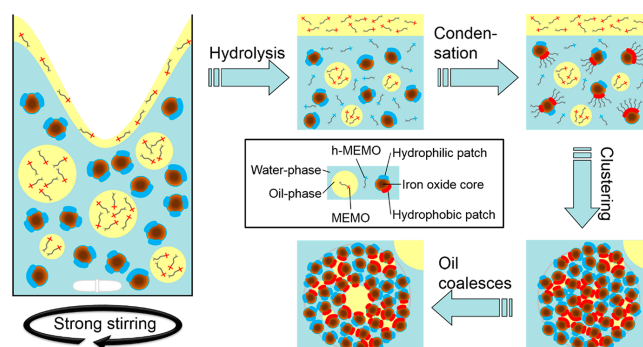


**Figure 1.** Silica–iron oxide nanoparticles carrying hydrophilic TEOS-derived patches are reacted with MEMO in an oil–water mixture. Hydrolysis and condensation of MEMO onto the nanoparticles yield hydrophobic patches and initiate the clustering of the patchy nanoparticles. Subsequent oil coalescence in the center of the cluster and continuing condensation of MEMO yield hollow microballoons. Figure adapted from ref 13.

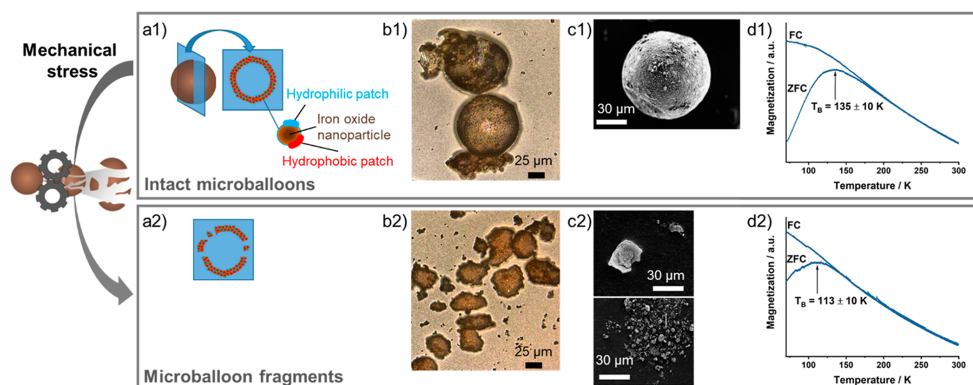


**Figure 2.** Superparamagnetic supraparticles consisting of patchy silica (TEOS-derived) iron oxide nanoparticles embedded into a silica matrix (MEMO-derived). In their as-prepared state a hollow spherical balloon-like shape is observed as depicted in schematic (a1) as well as LSM (b1) and SEM (c1) images. After application of mechanical forces, the microballoons are fragmented due to their hollow structure, which is also shown in the schematic, LSM and SEM images (a2, b2, and c2, respectively). ZFC/FC measurements indicate slight changes in the magnetic properties of intact (d1) and fragmented (d2) microballoon samples after mechanical force application.

methacryloxypropyltrimethoxysilane (MEMO) and subsequent clustering via a self-directing Pickering emulsion yield spherical hollow supraparticles (Figure 1).<sup>13</sup>

Their balloon-like appearance (Figure 2a1) can be visualized by laser scanning (LSM) and scanning electron microscopy (SEM, Figures 2b1 and 2c1, respectively). It should be mentioned that as the supraparticle material consists of sole silica and iron oxide, it is nonreactive, chemically inert, nontoxic, readily separable from nonmagnetic materials (due to its superparamagnetic nature, Figure S1 in the Supporting Information), and low-priced, which is ideal for its use as sensor material within a targeted substance.<sup>14,15</sup> Application of mechanical forces, for example, dynamical shear and impact forces (for further information see experimental details in the Supporting Information), on the microballoons leads to their fragmentation (Figures 2a2, 2b2, and 2c2).

It seems logical that the extent of fragmentation, i.e., the size and number of fragments, depends on the extent of applied

forces. However, an optical quantification of the shattering and, thus, of the applied mechanical forces is not convenient at all. This is why the magnetic properties of the supraparticles were exploited for this purpose. To study the influence of mechanical fragmentation of the microballoons on their magnetic properties, zero-field-cooled/field-cooled (ZFC/FC) measurements were carried out, which are conventionally utilized to determine magnetic interactions between individual nanoparticles within supraparticles as described elsewhere.<sup>16–18</sup> When analyzing the blocking temperature  $T_B$ , which represents the onset temperature for superparamagnetic behavior, of intact and mechanically deformed microballoons, we observe a change in interparticle interaction (Figures 2d1 and 2d2). The average iron oxide nanoparticle distance stays the same within the aggregates, i.e., within the microballoons and their fragments. This is why the slight shift of  $T_B$  toward lower temperatures may be caused by the decreasing size of the nanoparticle aggregates due to microballoon fragmentation.

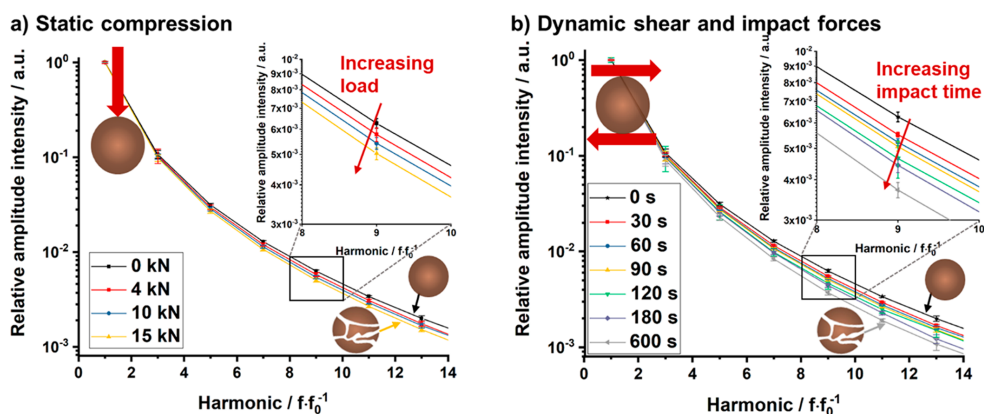


**Figure 3.** Drop of the MPS signal curves of microballoons during the application of quasi-static compression in a ZwickRoell GmbH & Co. KG materials testing machine (a) or of dynamic shear and impact forces in a ball mill-like setup (b) increases significantly with increasing load or milling time, respectively.

On average, the number of nearest neighbors is decreased, and therefore the frequency of magnetic interparticle interactions is reduced as indicated by a lower  $T_B$ .<sup>19</sup> Thus, ZFC/FC measurements can detect microballoon fragmentation. However, this analysis method is time-consuming and requires elaborate sample preparation as well as expensive measurement equipment, which makes it unsuitable for the monitoring of mechanical forces acting on the microballoons.

Contrastingly, MPS has the advantage of displaying a fast and simple “press one button, get the result unambiguously and within a few seconds” method with off-shelf devices.<sup>20</sup> Examples for its straightforward application as read-out technique for magnetic supraparticles have been recently published by our group.<sup>19,21</sup> The working principle of MPS, in which an alternating magnetic field is applied and the magnetization behavior of the sample is detected, has already been described in several publications<sup>22–25</sup> and is therefore only briefly discussed in the [Supporting Information](#) (Figure S2). [Figures 3a](#) and [3b](#) depict MPS signals of the microballoons after application of quasi-static compression in a ZwickRoell GmbH & Co. KG materials testing machine or dynamic shear and impact forces in a ball mill-like setup, respectively. In both cases, the steepening of the signal curve drop with increasing mechanical energy is evident, especially if one considers the logarithmic scale of the  $y$ -axes. Significant difference tests of the measured values at the ninth harmonics ([Figure S3](#)) showed that the measurement points are typically significantly different ( $p < 0.05$ ) from the next but one. As a continuous process is monitored, it is not surprising that a measurement point is rarely significantly different from the next one. Nevertheless, the test confirms that the MPS signals are clearly distinguishable in the course of mechanical force application.

By use of laser diffraction to measure the mean particle size and size distribution of the samples ([Figure 4](#)), the fragmentation of the microballoons can be well correlated to the steepening of the MPS signal curve drop with increasing mechanical energy during dynamic impact force application. The intact microballoons ([Figures 2a1](#) to [2c1](#)) possess a

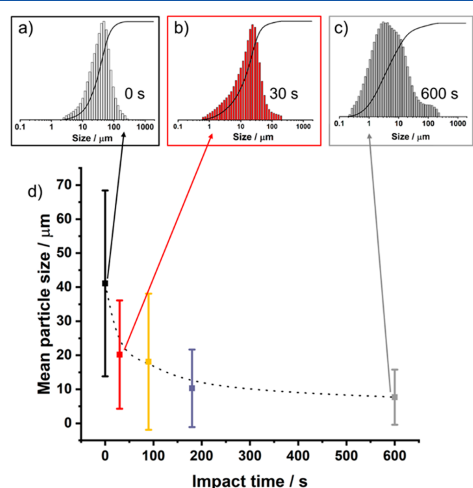


**Figure 4.** Mean particle size and standard deviation obtained from laser diffraction measurements of the hollow microballoons dispersed in water at different time points during dynamic shear and impact force application.

diameter of  $41 \pm 27 \mu\text{m}$  (mean  $\pm$  standard deviation) ([Figure 4a](#)). With increasing duration of force application, the average particle size drops down to  $8 \pm 8 \mu\text{m}$  at 600 s ([Figures 4b–d](#)) due to fragmentation of the microballoons ([Figures 2a2](#) to [2c2](#)) corresponding to 600 s dynamic force application. Consequently, the MPS signal curve drop steepens with decreasing mean particle size, i.e., increasing fragmentation of the microballoons.

If one plots the MPS amplitude signal intensities, for example, of the ninth harmonic as a function of the applied static compression forces ([Figure 5a](#)), the curve progression

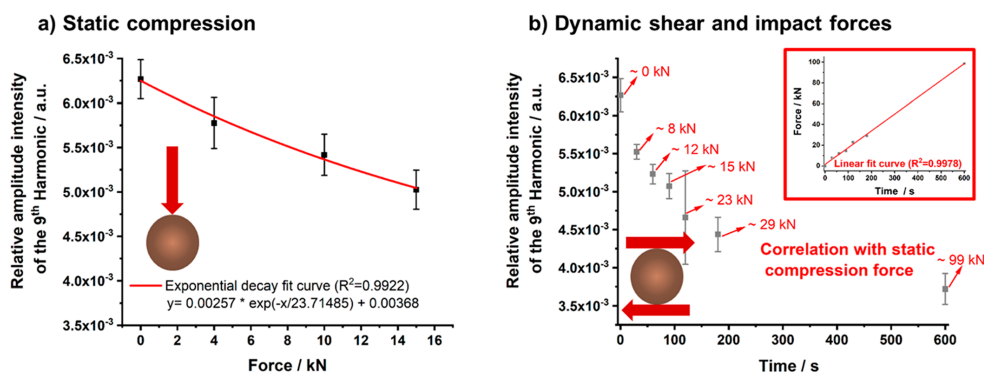


**Figure 5.** Relative amplitude intensity of the 9th harmonic acquired by MPS over the applied force during quasi-static compression (a) or the time of dynamic shear and impact forces application (b). Determining the exponential decay function (from the fit curve in part a) enables the quantification of theoretically acting force during the dynamic force application (red indications in part b). The determined theoretically acting force is proportional to the milling time (inset of part b).

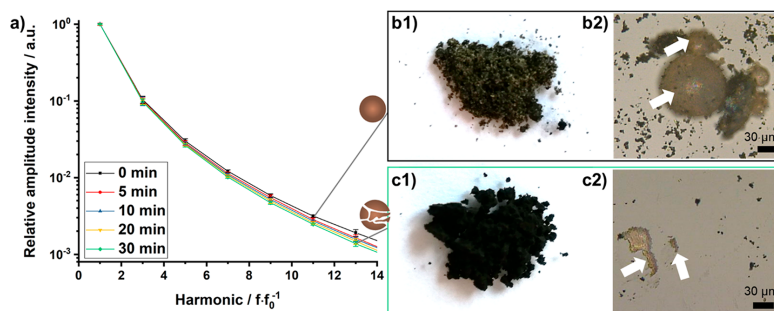


**Figure 6.** Drop of MPS signal curves of microballoons (a) steepens during the ball milling of activated carbon (with 1.0 g of  $\text{ZrO}_2$  balls of 1 mm in diameter and 800 rpm velocity) over 30 min. Photographs and LSM images display the sample morphologies before milling (b) and after 30 min milling time (c). Microballoons within the activated carbon sample are indicated by white arrows.

can be fitted by an exponential decay function. By use of this function, it is possible to quantify an applied force based on a MPS signal; i.e., a measured amplitude intensity can be correlated to the acting static force. Consequently, the measured amplitude intensities during dynamic force application (Figure 5b) can also be correlated to the theoretically acting static forces (given in red font in Figure 5b) on the microballoon sample. As the inset shows, the correlated theoretically acting (static) force is proportional to the milling time, which confirms the reliability of the correlation via the fitted function: if constant treatment parameters are used, the amount of acting force over a certain period of time must always be constant.

Consequently, MPS is not only able to detect the fragmentation of microballoons caused by the application of mechanical forces but even suitable to monitor and quantify them. This is of interest for applications such as ball milling processes, where the determination of acting forces on a sample is crucial. This MPS-based mechanical force detection is only possible due to the superparamagnetic supraparticle nature of the studied microballoons. While common super-

paramagnetic nanoparticles would not be susceptible to mechanical stress, ferromagnetic materials would agglomerate within a sample, preventing a homogeneous force monitoring, and paramagnetic materials cannot be measured by MPS.

To prove the proposed concept to monitor acting mechanical forces during the ball milling process of an arbitrary sample with microballoons via MPS, activated carbon powder was selected as model substance as it is frequently milled to obtain larger active surface areas for water treatment and gas cleaning applications.<sup>26</sup> Figure 6a shows the expected steepening of the MPS signal curve drops with increasing milling time, which indicates the fragmentation of the microballoons and enables the monitoring of acting mechanical forces on the processed activated carbon during the milling process. The comparison of photographs (Figures 6b1 and 6c1) and LSM (Figures 6b2 and 6c2) images initially and after 30 min milling time (Figures 6b and 6c, respectively) leads to the conclusion that the microballoons fragmented while the carbon powder was milled. After a completed milling process the microballoon sensors are no longer needed, and their fragments can be readily separated magnetically. The

morphology and size of the milled carbon powder are compared to the untreated one in Figure S4. Based on the determined exponential decay function, the measured MPS relative amplitude intensities of the ninth harmonic can be used to correlate the theoretically acting static force with the milling time. Consequently, 5, 10, 20, and 30 min correspond to 9, 13, 17, and 22 kN acting force on the sample, respectively.

Summing up, the herein presented superparamagnetic hollow microballoons are utilized as a mechanical force sensor during a ball milling process due to the destruction of their hollow shape. These structural variations are resolved fast and easily with MPS, enabling the quantification of acting mechanical forces on an arbitrary sample. As MPS is highly sensitive (1.0 wt% of magnetic material is sufficient),<sup>17</sup> the sensor does not necessarily have to be separated from the processed material for measurements, which may enable a future inline monitoring. However, because of its magnetic properties, the supraparticle sensor can be removed from it after milling.

#### ■ ASSOCIATED CONTENT

##### ● Supporting Information

The Supporting Information is available free of charge on the ACS Publications website at DOI: 10.1021/acsanm.9b01693.

VSM magnetization curve, description of MPS, significant differences of measurement points, SEM and laser diffraction of carbon powder and experimental details (PDF)

#### ■ AUTHOR INFORMATION

##### ✉ Corresponding Author

\*E-mail karl-sebastian.mandel@isc.fraunhofer.de.

##### ORCID

Susanne Wintzheimer: 0000-0003-3791-8117

Tim Granath: 0000-0001-9390-4807

Karl Mandel: 0000-0002-1445-0702

##### Notes

The authors declare no competing financial interest.

#### ■ ACKNOWLEDGMENTS

This work was financially supported by the BMBF Nano-MatFutur Grant 03XP0149, which is gratefully acknowledged. K.M. and T.G. gratefully acknowledge funding by the DFG within Project MA 7252/4-2. S.M. acknowledges funding of the German Federal Environmental Foundation for his doctoral scholarship. F.F. and D.H. acknowledge financial support by the Bavarian Ministry of Economic Affairs, Regional Development and Energy.

#### ■ REFERENCES

- R, S.; Chaira, D. Development of nano-structured duplex and ferritic stainless steels by pulverisette planetary milling followed by pressureless sintering. *Mater. Charact.* **2015**, *99*, 220–229.
- Baláz, P.; Achimovičová, M.; Baláz, M.; Billik, P.; Cherkezova-Zheleva, Z.; Criado, J. M.; Delogu, F.; Dutková, E.; Gaffet, E.; Gotor, F. J. Hallmarks of mechanochemistry: from nanoparticles to technology. *Chem. Soc. Rev.* **2013**, *42*, 7571–7637.
- Mio, H.; Kano, J.; Saito, F.; Kaneko, K. Optimum revolution and rotational directions and their speeds in planetary ball milling. *Int. J. Miner. Process.* **2004**, *74*, S85–S92.
- Burmeister, C. F.; Kwade, A. Process engineering with planetary ball mills. *Chem. Soc. Rev.* **2013**, *42*, 7660–7667.
- Mio, H.; Kano, J.; Saito, F. Scale-up method of planetary ball mill. *Chem. Eng. Sci.* **2004**, *59*, 5909–5916.
- Funk, B. Ressourceneffiziente chemische Synthese – Prozessentwicklung in Kugelmöhlen für lösungsmittelfreie Reaktionen (RE-SPEKT). DBU-final report-AZ-29622-31, Jena, 2015.
- Mio, H.; Kano, J.; Saito, F.; Kaneko, K. Optimum revolution and rotational directions and their speeds in planetary ball milling. *Int. J. Miner. Process.* **2004**, *74*, 85–92.
- Kano, J.; Mio, H.; Saito, F. Correlation of grinding rate of gibbsite with impact energy of balls. *AIChE J.* **2000**, *46*, 1694–1697.
- Kano, J.; Mio, H.; Saito, F.; Miyazaki, M. Correlation of grinding rate of gibbsite with impact energy in tumbling mill with mono-size balls. *Miner. Eng.* **2001**, *14*, 1213–1223.
- Erdemir, F. Study on particle size and X-ray peak area ratios in high energy ball milling and optimization of the milling parameters using response surface method. *Measurement* **2017**, *112*, 53–60.
- Wintzheimer, S.; Granath, T.; Oppmann, M.; Kister, T.; Thai, T.; Kraus, T.; Vogel, N.; Mandel, K. Supraparticles: Functionality from Uniform Structural Motifs. *ACS Nano* **2018**, *12*, S093–S120.
- Mandel, K.; Straßer, M.; Granath, T.; Dembski, S.; SEXTL, G. Surfactant free superparamagnetic iron oxide nanoparticles for stable ferrofluids in physiological solutions. *Chem. Commun.* **2015**, *51*, 2863–2866.
- Granath, T.; Sanchez-Sanchez, A.; Shmeliov, A.; Nicolosi, V.; Fierro, V.; Celzard, A.; Mandel, K. Hollow Superparamagnetic Microballoons from Lifelike, Self-Directed Pickering Emulsions Based on Patchy Nanoparticles. *ACS Nano* **2016**, *10*, 10347–10356.
- Xu, P.; Zeng, G. M.; Huang, D. L.; Feng, C. L.; Hu, S.; Zhao, M. H.; Lai, C.; Wei, Z.; Huang, C.; Xie, G. X. Use of iron oxide nanomaterials in wastewater treatment: a review. *Sci. Total Environ.* **2012**, *424*, 1–10.
- De Vries, A. J.; LePage, M.; Beau, R.; Guillemin, C. L. Evaluation of porous silica beads as a new packing material for chromatographic columns. Application in gel permeation chromatography. *Anal. Chem.* **1967**, *39*, 935–939.
- Stauch, C.; Späth, S.; Ballweg, T.; Luxenhofer, R.; Mandel, K. Nanostructured micro-raspberries from superparamagnetic iron oxide nanoparticles: Studying agglomeration degree and redispersibility of nanoparticulate powders via magnetisation measurements. *J. Colloid Interface Sci.* **2017**, *505*, 605–614.
- Rajan, G. S.; Stromeyer, S. L.; Mauritz, K. A.; Miao, G.; Mani, P.; Shamsuzzoha, M.; Nikles, D. E.; Gupta, A. Superparamagnetic nanocomposites based on poly(styrene-*b*-ethylene/butylene-*b*-styrene)/cobalt ferrite compositions. *J. Magn. Mater.* **2006**, *299*, 211–218.
- de Julian, C.; Sangregorio, C.; Mattei, G.; Battaglin, G.; Cattaruzza, E.; Gonella, F.; Lo Russo, S.; D’Orazio, F.; Lucari, F.; De, G.; Gatteschi, D.; Mazzoldi, P. Nanostructure and magnetic properties of CoNi-alloy-based nanoparticles dispersed in a silica matrix. *J. Magn. Mater.* **2001**, *226–230*, 1912–1914.
- Müssig, S.; Fidler, F.; Haddad, D.; Hiller, K.-H.; Wintzheimer, S.; Mandel, K. Supraparticles with a Magnetic Fingerprint Readable by Magnetic Particle Spectroscopy: An Alternative beyond Optical Tracers. *Adv. Mater. Technol.* **2019**, *4*, 1900300.
- Pure Devices. Benchtop MRI Systems; <https://www.pure-devices.com/> (accessed July 2019).
- Müssig, S.; Granath, T.; Schembri, T.; Fidler, F.; Haddad, D.; Hiller, K.-H.; Wintzheimer, S.; Mandel, K. Anisotropic Magnetic Supraparticles with a Magnetic Particle Spectroscopy Fingerprint as Indicators for Cold-Chain Breach. *ACS Appl. Nano Mater.* **2019**, *2*, 4698.
- Fidler, F.; Steinke, M.; Kraupner, A.; Grüttnner, C.; Hiller, K.-H.; Briel, A.; Westphal, F.; Walles, H.; Jakob, P. M. Stem Cell Vitality Assessment Using Magnetic Particle Spectroscopy. *IEEE Trans. Magn.* **2015**, *51*, 1–4.
- Biederer, S.; Knopp, T.; Sattel, T. F.; Lüdtkke-Buzug, K.; Gleich, B.; Weizenecker, J.; Borgert, J.; Buzug, T. M. Magnetization response spectroscopy of superparamagnetic nanoparticles for magnetic particle imaging. *J. Phys. D: Appl. Phys.* **2009**, *42*, 205007.

(24) Biederer, S.; Sattel, T.; Knopp, T.; Lüdtke-Buzug, K.; Gleich, B.; Weizenecker, J.; Borgert, J.; Buzug, T. M. A Spectrometer for Magnetic Particle Imaging. In *4th European Conference of the International Federation for Medical and Biological Engineering: ECFMBE 2008 23–27 November 2008 Antwerp, Belgium*; Magjarevic, R., Hauelsen, J., Nagel, J. H., Nysen, M., Sloten, J. V., Verdonck, P., Eds.; IFMBE Proceedings 22; Springer: Berlin, 2009; pp 2313–2316.

(25) Kuhlmann, C.; Khandhar, A. P.; Ferguson, R. M.; Kemp, S.; Wawrzik, T.; Schilling, M.; Krishnan, K. M.; Ludwig, F. Drive-field Frequency Dependent MPI Performance of Single-Core Magnetite Nanoparticle Tracers. *IEEE Trans. Magn.* **2015**, *51*, 1.

(26) CARBOTECH AC GmbH. Powdered Activated Carbons; <https://www.carbotech.de/aktivkohle/?lang=en> (accessed July 2019).

## SUPPORTING INFORMATION

**Hollow Superparamagnetic Nanoparticle-Based Microballoons for Mechanical Force Monitoring by Magnetic Particle Spectroscopy**

Susanne Wintzheimer<sup>†</sup>, Stephan Müssig<sup>†</sup>, Sarah Wenderoth<sup>†</sup>, Johannes Prieschl<sup>†</sup>, Tim Granath<sup>†</sup>, Florian Fidler<sup>§</sup>, Daniel Haddad<sup>§</sup>, Karl Mandel<sup>\*†‡</sup>

<sup>†</sup>Chair of Chemical Technology of Materials Synthesis, Julius-Maximilians-University Würzburg, Röntgenring 11, D97070 Würzburg, Germany

<sup>‡</sup>Fraunhofer Institute for Silicate Research ISC, Neunerplatz 2, D97082 Würzburg, Germany

<sup>§</sup>Magnetic Resonance and X-ray Imaging Department, Development Center X-ray Technology EZRT, Fraunhofer Institute for Integrated Circuits IIS, Am Hubland, D97074 Würzburg, Germany

\*karl-sebastian.mandel@isc.fraunhofer.de

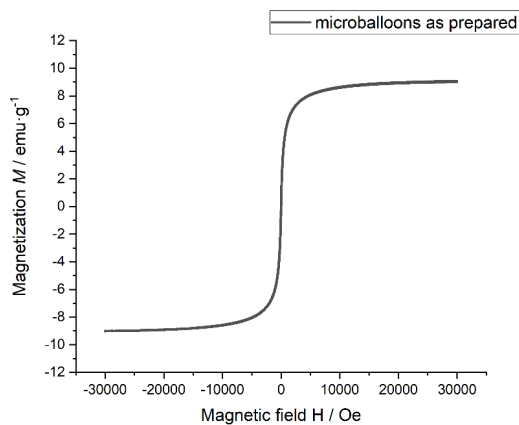


Figure S1. VSM magnetization curve of hollow microballoons showing their superparamagnetism.

Description of magnetic particle spectroscopy (MPS):

In magnetic particle spectroscopy the dynamic properties of magnetic particles are measured. After applying a sinusoidal alternating field (Figure S2a), the non-linearity of the time-dependent magnetization curve (Figure S2b) induces a voltage, which is exploited to characterize ferro-, ferri-, and superparamagnetic particles. After Fourier-transform of the thereby induced voltage, higher harmonics are found and yield a spectrum which is typically analyzed. To investigate the shape of the resulting curves, the amplitude intensities are normalized to intensities relative to the fundamental intensity and subsequently analyzed.<sup>1</sup>

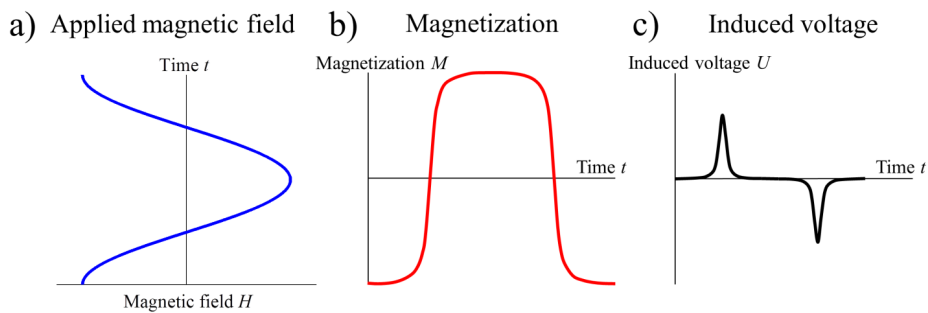


Figure S2. Principle of MPS: When a sinusoidal magnetic field is applied to ferro-, ferri-, or superparamagnetic samples (a), their time-dependent magnetization (b) induces a voltage (c). After Fourier-transform of the induced voltage, typically the amplitude intensity as a function of higher harmonics is studied. Adapted with permission from Müssig, S.; Fidler, F.; Haddad, D.; Hiller, K.-H.; Wintzheimer, S.; Mandel, K.. Supraparticles with a Magnetic Fingerprint Readable by Magnetic Particle Spectroscopy: An Alternative beyond Optical Tracers. *Adv. Mater. Technol.* **2019**, *291*, 1900300.<sup>1</sup> Copyright 2019 WILEY-VCH Verlag GmbH & Co. KGaA.

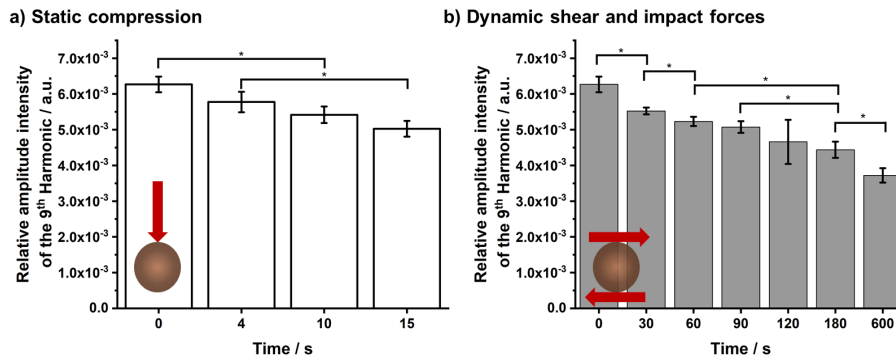


Figure S3. The relative amplitude intensity of the 9<sup>th</sup> Harmonic acquired by MPS over the applied force during quasi-static compression (a) or the time of dynamic shear and impact force application (b) with asterixes (\*) indicating significant difference (two sample T-test,  $p < 0.05$ ,  $n = 3$ ).

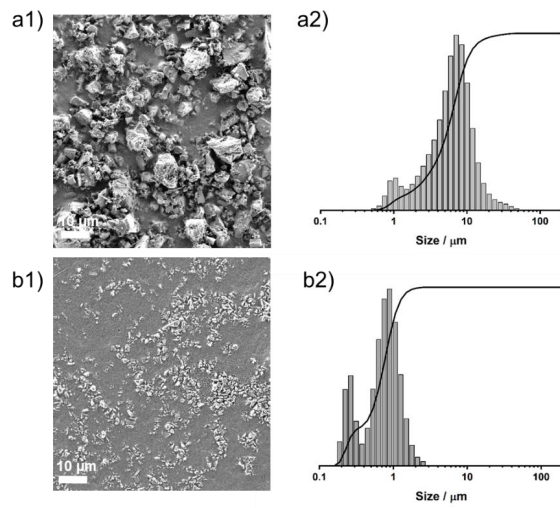


Figure S4. SEM images (a1, b1) and particle size distributions determined via laser diffraction (a2, b2) of untreated (a1, a2) and milled (b1, b2) carbon powder.

### Experimental details

#### Synthesis:

Superparamagnetic hollow microballoons were obtained by a three-step synthesis as already described elsewhere.<sup>2</sup> In brief, superparamagnetic iron oxide nanoparticles were precipitated by dissolving  $\text{FeCl}_3 \cdot 6 \text{H}_2\text{O}$  (2.160 g, 8 mmol, Sigma Aldrich, >99%) and  $\text{FeCl}_3 \cdot 4 \text{H}_2\text{O}$  (0.795 g, 4 mmol, Fluka, >99%) in deionized water (100 mL) and mixing it with aqueous ammonia solution (28-30 %, 5 mL). The obtained precipitate was washed until neutral pH, stabilized with  $\text{HNO}_3$  (1 M, 10 mL) and diluted with water (90 mL). Subsequently, a patchy silica shell was created around the iron oxide nanoparticles by adding tetraethoxysilane (5 mL, abcr GmbH, 99%) under stirring, proceeding the reaction for 1 h and aging it for a day. For the microballoon synthesis, the nanoparticle dispersion (21 mL) was carefully covered with cyclohexane (20 mL) and methacryloxypropyltrimethoxysilane (1.24 mL, 5.2 mmol, VWR International, 98%) was slowly dropped into the organic phase. After that, vigorous stirring was performed for 9 hours, followed by aging for 24 hours. The obtained microballoons were washed and dried at 45 °C for 18 h.

#### Mechanical force application:

Static compression was applied on microballoons with a ZwickRoell GmbH & Co. KG universal materials testing machine Z100 (load cell 20 kN). 5 mg of the sample were filled into a common KBr pellet press form and placed under the testing machine. The applied force was increased from 4 to 15 kN. For dynamic force application in a ball mill-like setup, microballoons (10 mg) and 50  $\text{ZrO}_2$  balls (1 mm in diameter) were filled into a 2 mL microcentrifuge tube. To induce dynamic shear and impact forces onto the microballoons, the tube was inserted into a series HSB03710 vortexer (Heathrow Scientific) and the balls were rotationally accelerated with 3000 rpm for 30 s up to 10 min. After milling, the balls were removed and the remaining powder was further characterized. For the proof-of-concept experiment, microballoons (200 mg) were carefully intermixed with activated carbon (800 mg, Kuraray YP-50F) and placed into a Pulverisette Premium Line 7 ball mill from Fritsch equipped with 45 mL grinding beakers containing 1.0 g  $\text{ZrO}_2$  balls of 1 mm in diameter. The sample was treated for 30 min at 800 rpm and after 0, 5, 10, 20, and 30 min milling time small samples were taken.

#### Characterization:

Scanning electron and confocal laser scanning micrographs were acquired using a Zeiss Supra 25 SEM at 2 keV and a Keyence color 3D VK-X210, respectively. Magnetization measurements were performed at 300 K with a vibrating sample magnetometer VersaLabTM 3T from Quantum Design by cycling the applied field from -30 kOe to +30 kOe for two times with a step rate of 100 Oe  $\text{s}^{-1}$  at 20 °C. For zero-field-cooled field-cooled (ZFC/FC) measurements, the samples were cooled to 60 K without external field before heating to 300 K and subsequent cooling to 60 K with 12  $\text{K} \cdot \text{min}^{-1}$  with a field of 10 Oe. Furthermore, the samples were characterized with a MPS unit from Pure Devices GmbH in a sinusoidal alternating field of 20.1 kHz from -300 Oe to 300 Oe at room temperature. Laser diffraction measurements were carried out on a Microtrak Bluewave using FLEX version 11.0.0.3 as analysis software. The mean particle size was taken from the graphic mean  $M_z$ . The Standard Deviation is the Graphic Standard Deviation SD calculated by  $(84\% - 16\%)/2$ .

#### References:

- (1) Müssig, S.; Fidler, F.; Haddad, D.; Hiller, K.-H.; Wintzheimer, S.; Mandel, K. Supraparticles with a Magnetic Fingerprint Readable by Magnetic Particle Spectroscopy: An Alternative beyond Optical Tracers. *Adv. Mater. Technol.* 2019, 291, 1900300, DOI: 10.1002/admt.201900300.
- (2) Granath, T.; Sanchez-Sanchez, A.; Shmeliov, A.; Nicolosi, V.; Fierro, V.; Celzard, A.; Mandel, K. Hollow Superparamagnetic Microballoons from Lifelike, Self-Directed Pickering Emulsions Based on Patchy Nanoparticles. *ACS nano* 2016, 10, 10347–10356, DOI: 10.1021/acsnano.6b06063.

## FULL PAPER

Sensors

## Expanding the Horizon of Mechanochromic Detection by Luminescent Shear Stress Sensor Supraparticles

Susanne Wintzheimer, Jakob Reichstein, Sarah Wenderoth, Sebastian Hasselmann, Maximilian Oppmann, Marcel T. Seuffert, Klaus Müller-Buschbaum, and Karl Mandel\*

Novel sensor particles have been developed that expand the variety of today's mechanochromic systems. The developed supraparticles consist of several different components to enable the sensor function. First, a luminescence-quenching core material is coated with silica nanoparticles. Second, this structure is surrounded by raspberry-like nanostructured silica particles, which host luminophore moieties. Upon shear stress, components spatially separated in the original supraparticles, namely quencher and luminophore components, come into contact. This causes an irreversible quenching of the luminescence (sensor turn-off). Different options to select core, quencher, and luminophore components allow to drive the sensors to different sensing options regarding response time, sensitivity, and operation time. The sensors can be sensitive and rapid in response or generated to monitor the influence of shear stress over longer periods of time. Thus, a rapid, visible, "on-the-fly" sensing of shear stress is possible as well as monitoring the impact of prolonged shear stress. The particles are assembled by spray-drying. This affords flexibility when choosing the type of quencher and luminophore moiety. As such, the sensitivity of this robust, particle-based shear stress sensor system can be deliberately configured. Furthermore, the supraparticle sensor can be integrated in surfaces to create interactive, communicating materials.

## 1. Introduction

Touch is one of the human senses essential for orientation and interaction. Impinging mechanical forces transmit valuable information about the external environment to mechanosensory cells that communicate with the brain to initiate response

Dr. S. Wintzheimer, J. Reichstein, S. Wenderoth, Dr. K. Mandel  
Chair of Chemical Technology of Materials Synthesis  
Julius-Maximilians-University Würzburg  
Röntgenring 11, D97070 Würzburg, Germany  
E-mail: karl-sebastian.mandel@isc.fraunhofer.de

S. Hasselmann, M. Oppmann, Dr. K. Mandel  
Fraunhofer Institute for Silicate Research  
ISC Neunerplatz 2, D97082 Würzburg, Germany

M. T. Seuffert, Prof. K. Müller-Buschbaum  
Institute of Inorganic Chemistry  
Julius-Maximilians-University Würzburg  
Am Hubland, 97074 Würzburg, Germany

 The ORCID identification number(s) for the author(s) of this article can be found under <https://doi.org/10.1002/adfm.201901193>.

DOI: 10.1002/adfm.201901193

to the input.<sup>[1–3]</sup> Transferring this concept to a technical context is one of the major challenges when it comes to the future of industrial manufacturing with devices that shall be able to interact with the environment.<sup>[4–9]</sup> One of the crucial steps toward this vision is to create smart surfaces with internal sensor functionality, most importantly mechanosensors such as shear stress sensors.<sup>[7,10–14]</sup>

To date, most of the developed mechanosensors are based on micro-electromechanical systems (e.g., capacitive or piezo resistive sensors embedded in polymers).<sup>[15–17]</sup> These sensors are often bulky, non-flexible, immobile, cost-intensive, and susceptible to electromagnetic interferences.<sup>[18–21]</sup> Additionally, they possess a high defect ratio and insufficient spatial resolution.<sup>[11,22]</sup> Therefore, mechanosensing devices with a high spatial resolution and easy transduction mechanisms, applicable in flexible devices, are needed. Mechanochromic systems (e.g., liquid-crystalline and crystalline solids or dye-doped polymers) can meet these requirements.<sup>[23–26]</sup> Exposed to a direct

mechanical force, they react with a change in their luminescence emission. The mechanically induced change in luminescence emission of the mechanochromic systems is caused by conversions at the molecular-level and is not yet well understood.<sup>[27–30]</sup> The drawbacks of these compounds are that they may show insufficient conversion or luminescence loss as well as susceptibility to temperature or solvents.<sup>[24,31,32]</sup>

One strategy to overcome the downsides of molecular sensors is to increase the sensor dimensions from the molecular level to the nano- or microscale with the help of nanoparticle assemblies. Nanoparticles provide a substantial functional diversity due to their unique optical, catalytic, and electronic properties.<sup>[33,34]</sup> Recently, the concept of combining distinct nanoparticles to create more complex particulate entities, known as supraparticles, was shown to result in new functional properties due to the cooperative interplay of the building blocks in the supraparticle.<sup>[34,35]</sup> The use of nanoparticles and particle assemblies as sensor materials or as carriers for sensing molecules has already been demonstrated for gas or chemical sensors.<sup>[33,34,36–39]</sup> However, they have—to the best of our knowledge—not yet been applied in the fabrication of shear

stress sensors. The approach closest to ours is the implementation of particle aggregates, which disintegrate when shear stress of a certain intensity is applied.<sup>[40–42]</sup> Korin et al.<sup>[40]</sup> showed that particle aggregates labelled with luminescent tags are suitable to monitor shear stress when the luminescence of released single nanoparticles is measured. However, the quantification of the response was still too complex, that is, no immediately visible sensor signal, suitable for an “on-the-fly” sensing principle, could be achieved.

Herein, we describe a route toward luminescent turn-off shear stress sensor supraparticles (TOSs), prepared by assembling nanoparticle and chemical moiety building blocks via spray-drying. The thereby obtained hierarchical, nanostructured sensor supraparticles are straight-forward in their use. They yield a directly measurable, visible, optical signal-change upon shear stress, thus expanding the horizon of the mechanochromic concept.

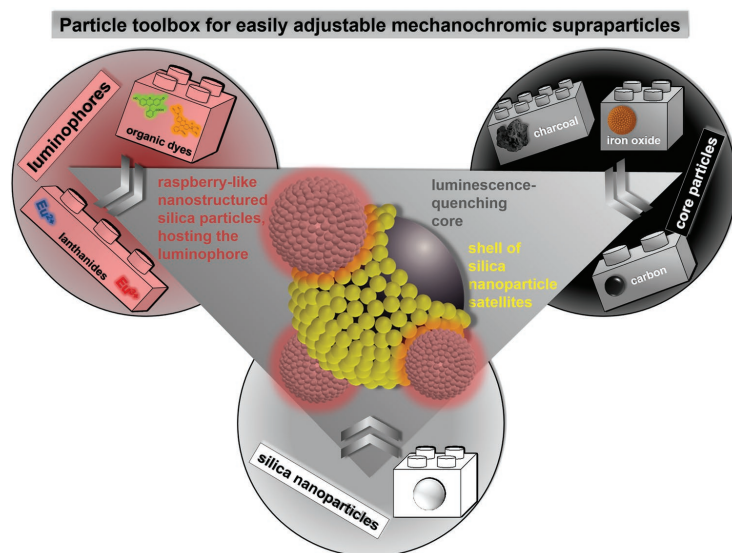
## 2. Results and Discussion

The novel TOS consist of three essential, but also adjustable components that synergistically sum up in their functionality (Scheme 1). The first component is the core of the particle, which is a luminescence quencher. This core is coated with a shell of silica nanoparticle satellites, enveloping the quencher core. Finally, this quencher-core silica nanoparticle satellite system is surrounded by raspberry-like nanostructured silica particles, hosting the luminophore.

The above described, complex and highly hierarchical particle structure was obtained by co-spray-drying a dispersion

of silica nanoparticles with quencher particles (see below) and luminophore moieties. It is well known that spray-drying of pure silica nanoparticle dispersions yields nanostructured (supra)particles that have a raspberry-like appearance, as discussed in earlier publications.<sup>[41–45]</sup> The addition of two more components, that is, the quencher particles and luminophore moieties, results in the more complex particle architecture as described above and depicted in Scheme 1.

As conceptualized in Scheme 1, the core and luminophore materials can be flexibly changed, resulting in various TOS types. The systems which were studied herein are summarized in Figure 1. As core materials, charcoal, carbon particles, and iron oxide supraparticles have been investigated (the resulting supraparticles are denoted as TOS-f, TOS-c, and TOS-i, respectively). These materials are known to be good luminescence quenchers due to their broad absorbance in the visible light wavelength range and possible electronic interaction by Förster and Dexter mechanisms, respectively.<sup>[46,47]</sup> As luminophores the xanthenes dyes fluorescein and rhodamine B, as well as two coordination compounds containing the lanthanide ions  $\text{Eu}^{3+}$  and  $\text{Tb}^{3+}$  as emitters, Lumino-Red and the metal-organic framework  ${}^3[\text{Tb}_2(\text{bdc})_3(\text{H}_2\text{O})_4]$  ( $\text{bdc}^{2-} = 1,4\text{-benzo-dicarboxylate}$ ), were selected. The fluorescence of the organic fluorophores fluorescein and rhodamine B can be observed by exciting the molecules to a high vibrational level of an excited singlet state. Fluorescein is a luminophore with good quantum yield and broad absorption and emission ranges depending on pH value, being fluorescent in nature.<sup>[48–51]</sup> The neutral form of fluorescein, as used in this work, shows a maximum of absorption around 490 nm and light emission with a maximum intensity



**Scheme 1.** Toolbox for the synthesis of a turn-off sensor supraparticle (TOS), consisting of a quencher core particle, coated by silica satellite nanoparticles, surrounded by raspberry-like nanostructured silica supraparticles which carry different luminophores.

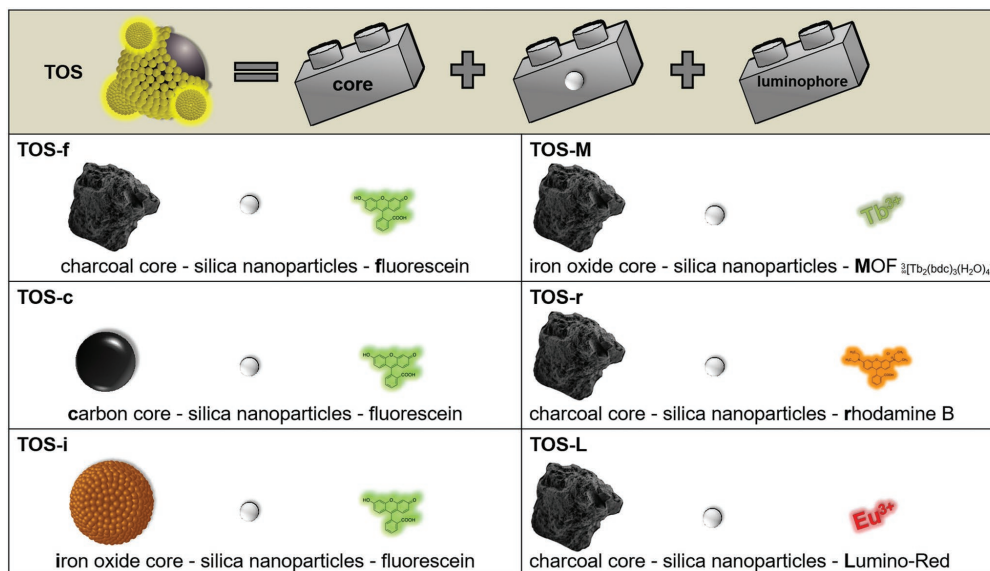


**Figure 1.** Nomenclature and composition of all synthesized TOSs, demonstrating the flexible, toolbox-like approach to assemble these types of supraparticles.

at 510 nm and therefore is of green color. The fluorescence properties of rhodamine B are condition-dependent (concentration, pH, solvent viscosity). In its zwitterionic form it strongly absorbs light with wavelengths around 540 nm by  $\pi$ - $\pi^*$  transitions.<sup>[52]</sup> Subsequently, rhodamine B emits light within a broad wavelength range and an emission maximum at 570 nm being yellow-orange in color by fluorescence.<sup>[53–55]</sup> For the Eu-complex Lumino-Red and the Tb-containing MOF  $[\text{Tb}_2(\text{bdc})_3(\text{H}_2\text{O})_4]$ , ion specific emission by intra-4f-transitions is observed,<sup>[56–58]</sup> sensitized by excitation through the respective ligands. For Lumino-Red,  $\text{Eu}^{3+}$  emission consists of the transitions  ${}^5\text{D}_0 \rightarrow {}^7\text{F}_n$  ( $n = 0–4$ ). Emission of  $[\text{Tb}_2(\text{bdc})_3(\text{H}_2\text{O})_4]$  is caused by characteristic transitions of the  $\text{Tb}^{3+}$  ions from  ${}^5\text{D}_0 \rightarrow {}^7\text{F}_n$  ( $n = 6–2$ ).<sup>[58]</sup> The characteristic emissions are of low line width and result in red and green light emission, respectively, being phosphorescence in nature due to the parity forbidden character of the intra-4f-transitions.

Altogether, the supraparticles act as luminescent sensors, which are susceptible to shear stress. In the as prepared, that is, non-sheared state, the sensor supraparticles possess a strong luminescence, stemming from the incorporated luminophores. Upon application of shear stress, the TOS reacts with a significant reduction of the luminescence emission intensity. That means, a luminescent turn-off behavior is observed, which correlates with the applied shear stress (i.e., time of shear stress application). **Figure 2a** depicts the luminescence decay as function of shear time of TOS-L as example. The turn-off response is even visible by eye “on-the-fly,” that is, instantly at one glance (**Figure 2b**).

The shear stress experiments on the TOS powder samples to obtain the described luminescence decay results were carried out with a ball mill, rotated at a fixed frequency (see experimental section for details). Samples were taken at different times during milling. Investigation of the fluorescence intensity decay in relation to the non-sheared fluorescence intensity enables correlation of sensor luminescence intensity with the time of shear stress application. The determination of the absolute magnitude of impact energy  $E_i$ , acting on the particles during ball milling, was possible in approximation. For the system depicted in **Figure 2**, it was found to be  $E_{i,200\text{rpm}} = 3.5 \text{ J s}^{-1}$ . A detailed explanation can be found in **Figures S1, S2**, and **Table S1**, Supporting Information.

Based on the determined impact energy, the applied work could be determined. This was exemplarily done for the condition that the shear work yielded 50% decrease of the initial TOS emission intensity  $I$  after a certain time  $t_{I=50\%}$ . This was used to compare the shear sensitivity of different sensor particle architectures with each other in a quantitative, reliable, and reproducible way (**Table S2**, Supporting Information).

A quantification of the applied shear stress was also possible after incorporation of the developed TOS in a matrix to form a shear stress sensor surface. This is exemplarily shown in the last section of this manuscript. The quantification is achievable by means of a so-called crockmeter test (see experimental section for details), which is a standardized measurement to determine forces acting especially on surfaces.

In order to understand the turn-off mechanism of the TOS on the microscopic scale and to be able to determine the role of each component, a sample of TOS-L (consisting

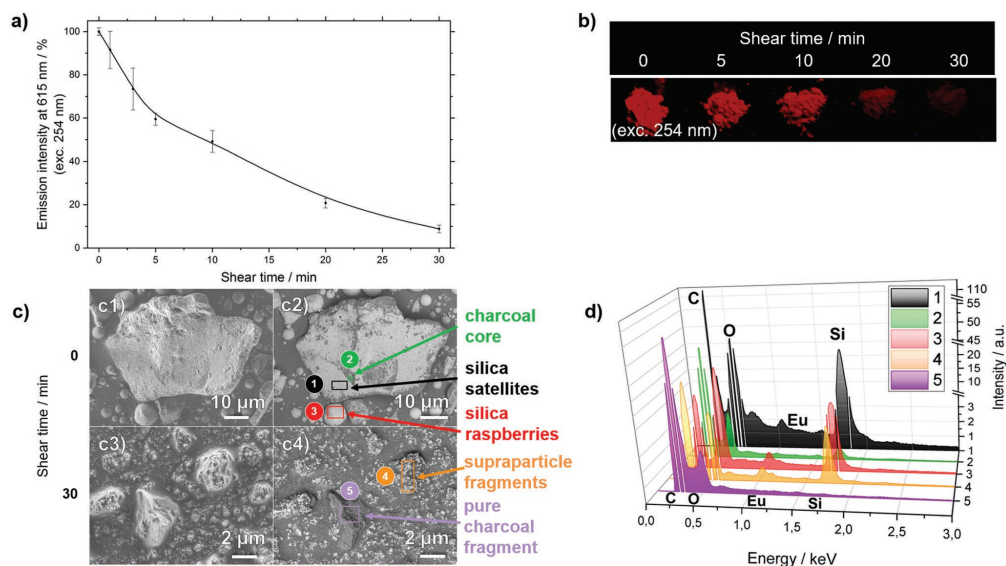


**Figure 2.** a) Shear sensing by emission intensity reductions at 615 nm (excited at 254 nm) and b) photographs under UV light (excited at 254 nm), as well as c) SEM of TOS-L (for all: charcoal core, 10 nm silica particles, excess Lumino-Red) depending on the shear time. c1) and c3) SE, as well as c2) and c4) BSE images showing the TOS-L in non-sheared and sheared state, respectively, with marked areas where EDX analysis has been carried out. d) EDX of different areas of TOS-L in the non-sheared and sheared state.

of charcoal, 10 nm silica particles, and Lumino-Red) was sheared and subsequently studied by means of scanning electron microscopy (SEM). The morphology and composition of this TOS sample before and after shearing is depicted in Figure 2c. The non-sheared TOS-L is shown in Figure 2c1,c2 in secondary electron (SE) and back scattered electron (BSE) imaging mode. The sheared TOS-L in both modes is depicted in Figure 2c3,c4, respectively. The material composition was examined via energy dispersive X-ray spectroscopy (EDX) (spot 1 to 5) and is depicted in Figure 2d. It is evident that the non-sheared TOS sample mainly consists of supraparticles with a charcoal core and raspberry-like shaped particles. The charcoal has a typical microscale size and bumpy shape. Moreover, this particle is almost completely covered by silica nanoparticles (satellites), which possess a brighter material contrast in comparison to charcoal (Figure 2c2, spot 1). Raspberry-like silica supraparticles can be found in close proximity/surrounding the charcoal supraparticles and they contain Lumino-Red ( $\text{Eu}^{3+}$ , Figure 2c2, spot 3). It is worth noting that also the silica satellites, coating/enveloping the charcoal as a thin layer, carry Lumino-Red which is detectable via EDX ( $\text{Eu}^{3+}$ , spot 1). The surface of the charcoal that stays uncovered by silica does not carry any adsorbed luminophore (Figure 2c2, spot 2).

Thus, the findings reveal that the luminophore adsorbs on any silica particle in the first place, be it either the silica nanoparticle satellites which coat the quencher core, or the raspberry-like supraparticles which surround the quencher-core-silica-satellite particles.

After exposure to shear stress, the supraparticle architectures were found to be merely disintegrated. Only undefined particle fragments are left, consisting of charcoal, silica, and Lumino-Red (Figure 2c4, spot 4 and spot 5).

All in all, these microscopy studies could reveal the architecture of the supraparticles and their structural destruction upon shear stress.

To understand the contribution of the luminescent moieties and their fate upon shear stress, fluorescence microscopy (Figure 3) on TOS-f (consisting of charcoal, 10 nm silica particles, and fluorescein) before and after shearing was conducted. TOS-f was selected as the system of choice here, as fluorescein is a model fluorophore in fluorescence microscopy as it responds ideally to the typically applied excitation wavelengths in the microscope. The fluorescence microscopy images of the TOS-f in non-sheared state (Figure 3a,b) clearly demonstrate that the raspberry-like silica particles which carry the luminophore (and show in contrast to the black charcoal particles less contrast in transmission light mode), are principally responsible for the strong luminescence of the TOS. In contrast to this, the charcoal cores, directly coated by a shell of silica nanoparticle satellites, onto which luminophores are adsorbed as well (compare Figure 2c2, spot 1), yield no detectable luminescence.

Thus, as revealed by fluorescence micrographs, the silica satellite nanoparticle coating on the quencher particles does not contribute to the luminescence of the whole system. Therefore, it can be concluded that it is the raspberry-like silica supraparticles, which play the crucial role for the luminescence of the system (compare Scheme 1). They act as carrier structures for

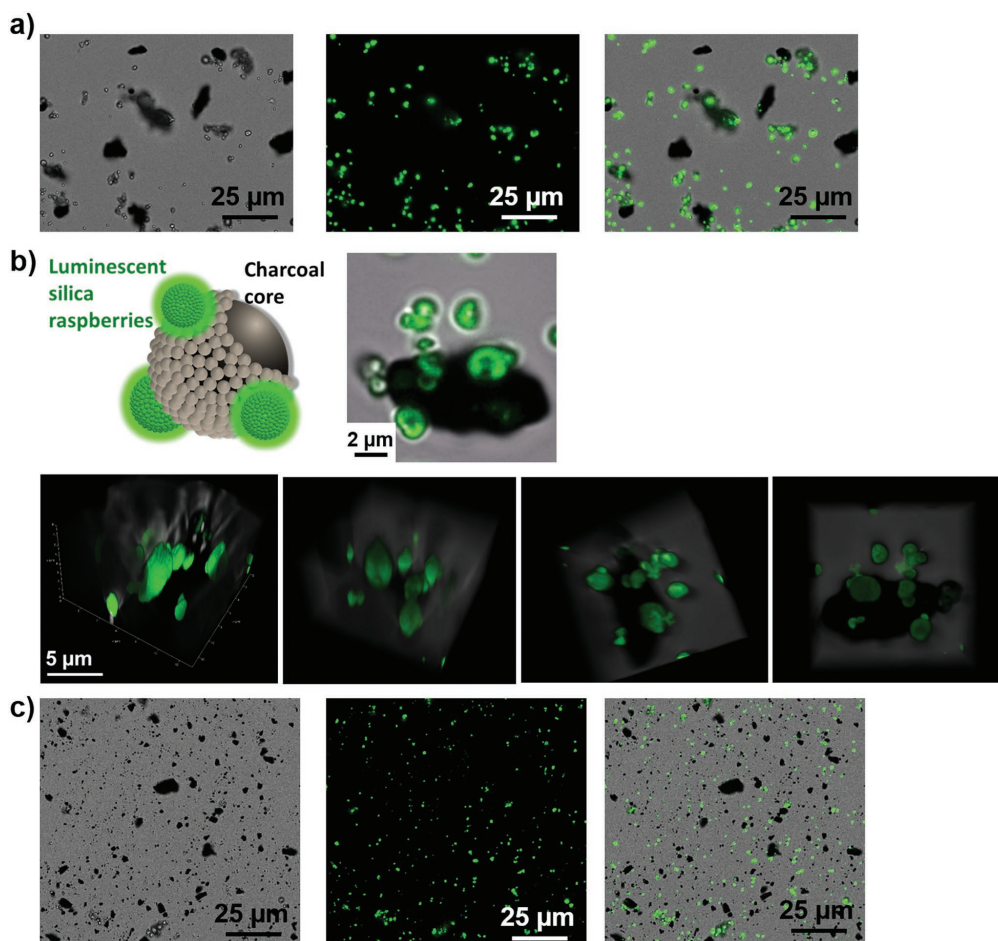


**Figure 3.** Confocal fluorescence microscopy of TOS-f (charcoal core, 10 nm silica particles, fluorescein) in non-sheared a), b) and sheared state c) with a) and c) showing from left to right the transmission light, fluorescence and merged image, while b) shows a close-up view of one supraparticle, as scheme (for a better understanding of the following images), as 2D and as 3D images from different viewing angles (for a video, see Supporting Information V1).

the luminophore and ensure that self-quenching of the dye is avoided, as the particle structure reduces the aggregation of dye molecules.<sup>[46,59,60]</sup> Furthermore, the system ensures an appropriate spacing between the luminescence-quenching particles and the luminophores in order to prevent energy transfer processes, which may otherwise result in unwanted radiation-less decay.<sup>[46,61]</sup> After exposure to shear stress (Figure 3c), the structurally destroyed TOS-f system shows significantly less luminescence detectable via fluorescence microscopy. Only a few, still intact and luminescing raspberry-silica-particles can be found, among non-luminescent fragments, consisting of black charcoal and rather transparent silica.

Combining the outcomes of scanning electron and fluorescence microscopy, it becomes obvious that the developed TOS only works due to the synergy of all three components and their assembly to the specific supraparticle structures. A simple combination of just two components does not result in a reliable, reproducible TOS (in this regard, also see the results of further experiments depicted in Figure S3, Supporting Information). In the non-sheared state, the luminophore-carrying raspberry-like particles provide the luminescence of the TOS. During and after shear stress exposure, the luminophore is still present in the sample but its emission is efficiently quenched. This is caused by intermixing and interaction of charcoal

quencher and luminophore-carrying silica nanoparticles. The distance between the luminescence-quenching charcoal and luminophore is minimized and luminescence quenching through electronic coupling and energy transfer can take place.<sup>[47,62,63]</sup> Additionally, the charcoal covers the luminophore and due to the strong absorbance of the charcoal in the excitation and emission wavelength ranges of the luminophores, the quencher can further attenuate the luminescence intensity of the TOS.<sup>[47]</sup> These effects result in the overall turn-off response of the sensor luminescence when shear stress is applied.

A unique feature of the developed TOS is its modularity: The luminescence-quenching core (Figure 4), the type of luminophore (Figure 5), the size of the silica nanoparticle satellites/raspberry building blocks (Figure S4, Supporting Information) as well as the ratios of all three components can be freely varied. Most importantly, the variation of the core (charcoal, carbon, or iron oxide) influences the sensitivity of the TOS (Figure 4a) toward shear stress in terms of luminescence reduction. As a side effect, also the morphology of the supraparticles (Figure 4b) as well as the color (Figure 4c) are slightly modified.

The ability to vary the TOS sensitivity can be deduced from the different core materials. As the luminescence-quenching particle is sheared and intermixed with the silica-luminophore raspberry particles, the tendency of this core material to fragment, affects the turn-off speed of the sensor (e.g., the shearing time  $t_{i=50\%}$  that is necessary to yield a relative emission intensity drop by 50%). The carbon quencher particle, on the one hand, possesses a lower porosity than charcoal, which results in the

more shear stress resistive TOS-c ( $t_{i=50\%} = 24.6$  min) compared to TOS-f ( $t_{i=50\%} = 5.4$  min). The iron oxide raspberries containing TOS-I, on the other hand, have a higher tendency to disintegrate ( $t_{i=50\%} = 3.5$  min), compared to the dense micro-particle core comprising TOS-c and TOS-f. The reason here is that nanoparticles within the iron oxide raspberries are only kept together by physical interactions, resulting in a TOS sample that is more susceptible to shear stress.

Besides the core variation, the luminophore variation (fluorescein, rhodamine B, Lumino-Red, and the Tb-MOF) was used to modify the excitation and emission wavelength ranges and thus the chromaticity of the luminescence (Figure 5b,c) of the TOS (TOS-f, TOS-r, TOS-L, and TOS-M, respectively). It is worth noting that the variation of the luminophore type (and amount) also has a significant impact on the sensor sensitivity as well as on the time scale, the respective TOS is functioning on (Figure 5a). The fastest TOS system is the Tb-MOF containing TOS-M, which shows a loss of about 80% in luminescence intensity in only 2 min and of 50% in less than a minute, qualifying as turn-off sensor suitable for observation by the eye. As MOFs are known for limited mechanical stability, this may explain the vast difference to the Eu-complex Lumino-Red and the organic dye fluorescein containing TOSs. For them (TOS-L and TOS-f), a lesser initial intensity reduction can be observed of only 20–25%, respectively, in the first 2 min. However, these TOS can be utilized over a longer period of time, as they can monitor continuing shear stress via an ongoing intensity reduction over 30 min. For TOS-M, there is no reasonable change

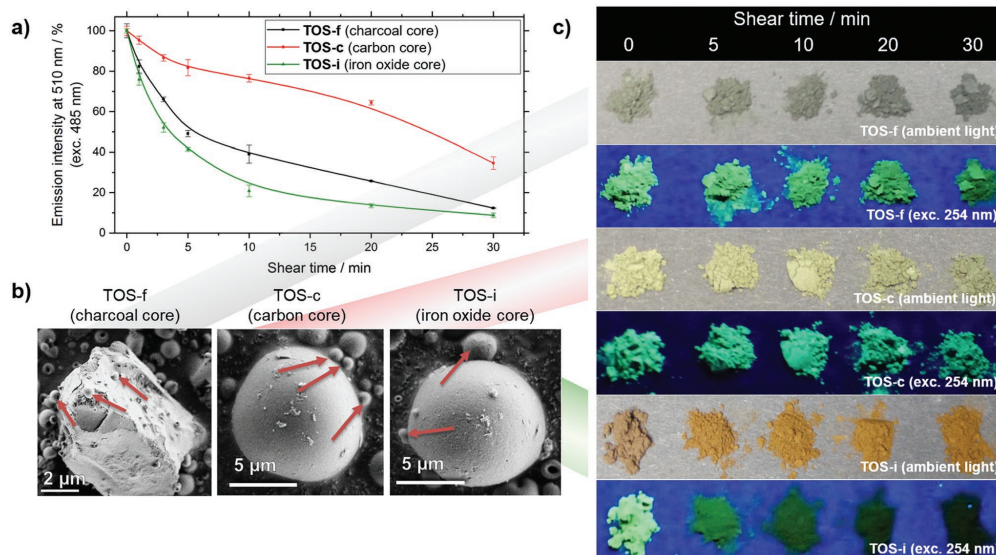


**Figure 4.** a) Shear sensing by emission intensity reductions for TOS with charcoal, carbon and iron oxide quencher particles (10 nm silica particles and fluorescein) for emission at 510 nm (excited at 485 nm) depending on the shear time the systems were exposed to (see experimental section for details). b) SEM of the TOS systems with respective quencher particles in the as-prepared state with red arrows indicating the silica raspberries. c) The influence of different shear times by photographs of TOSs under ambient light and under UV light (excited at 254 nm).

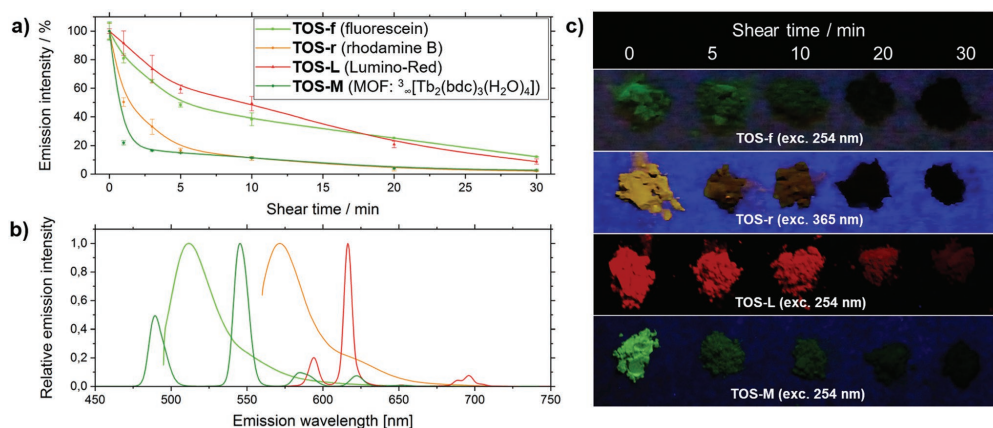


**Figure 5.** a) Shear sensing by emission intensity reductions of TOS containing different dye moieties (charcoal core, 10 nm silica particles): fluorescein (TOS-f), rhodamine B (TOS-r), Lumino-Red (TOS-L) and  ${}^3\text{[Tb}_2(\text{bdc})_3(\text{H}_2\text{O})_4]$  (TOS-M), as well as b) their photoluminescence spectra (TOS-f: exc. 485 nm,  $\text{max}_{\text{em}} = 510$  nm; TOS-r: exc. 550 nm,  $\text{max}_{\text{em}} = 570$  nm; TOS-L: exc. 254 nm,  $\text{max}_{\text{em}} = 615$  nm; TOS-M: exc. 254 nm,  $\text{max}_{\text{em}} = 545$  nm) and c) their photographs.

observable after 5 min of shear stress. Thereby, the different luminophores can be utilized to steer the sensor systems either to rapid response or toward continuous monitoring options over longer shear stress influence times.

Depending on the luminophore type, the adsorbed luminophores add a steric repulsion force to the nanoparticles and prevent bridging between individual silica nanoparticles. This leads to satellites whose removability from the core correlates with the degree of dye modification.<sup>[43]</sup> An energetically easier and thus faster exposition of the core consequently results in a faster turn-off response and therefore TOSs with a higher sensitivity. In addition, also the mechanical stability of the luminophore has an influence on the luminescence upon shear stress. Mechanic decomposition can be another mechanism to reduce the luminescence intensity.

Altogether, the herein created TOS can be easily adjusted in terms of shear sensitivity. Based on the approximated impact energy  $E_{i,200 \text{ rpm}} = 3.5 \text{ J s}^{-1}$ , the shear work, to which a TOS needs to be exposed in order to yield an emission intensity drop by 50%, can be quantified for each sample (see Table S2, Supporting Information). Thus, on the one hand, shear-labile sensor particles (TOS-M) are obtained, showing an emission intensity drop to 50% within already 0.74 min, that is, work of 155 J has to be applied, only. On the other hand, shear-resistant sensors (TOS-c) can be created, coming with an emission intensity drop to 50% after 24.6 min, that is, work of as much as 5.2 kJ has to be applied in this case. Additionally, the optical appearance of the TOS can be modified. This affords the adaptation of the TOS to the properties of diverse matrix materials and application requirements.

In addition, the successful operation of the developed TOS in a matrix material was also demonstrated. Therefore, TOS-f (consisting of charcoal, 10 nm silica particles and fluorescein) were incorporated in a coating lacquer for foils. The coating was carried out via spiral blade technique, by casting a TOS

containing thermally curable hybridpolymeric lacquer onto a flexible polyolefin (PO) foil substrate. The sensing ability of the TOS within the coating is shown in Figure 6a (crocker-meter test—see experimental section for details). In this proof of principle experiment, it was demonstrated that the green luminescence of the TOS decreases with increasing crocking cycles on the coating, reliably monitoring the shear stress on its matrix. This can also be easily detected under a UV lamp by eye as an “on-the-fly”-sensing (Figure 6b). Furthermore, the work  $W_{I=90\%}$  done to decrease the emission intensity of the TOS-f within the coating by 10% was calculated (Table S3, Supporting Information). The obtained value of 80 J is comparable to the  $W_{I=90\%}$  of the TOS-f powder sample (treated in the ball mill), which is 105 J. It is reasonable to attribute this slight difference between these two values to the influence of the matrix around the TOS. The matrix, for instance, fixes the position of the supraparticles. Therefore, the particles cannot evade to the applied force. Thus, less shear work needs to be done in order to decrease the emission intensity by 10%. Finally, with respect to potential applications, it is worth noting that this experiment shows a successful application of the novel shear stress sensor on a substrate, which is even flexible.

### 3. Conclusion

In this work, hierarchical, nanostructured supraparticles that expand the horizon of traditional mechanochromic detection were developed for use as shear stress sensors. The TOS have an intense luminescence that is quenched upon the influence of shear stress. The irreversible luminescence loss during exposure to shear stress allows for a rapid “on-the-fly” sensing and monitoring. Assembly via spray-drying enables adjustment of the composition, as the building blocks can be selected from a variable toolbox. Thus, the sensor

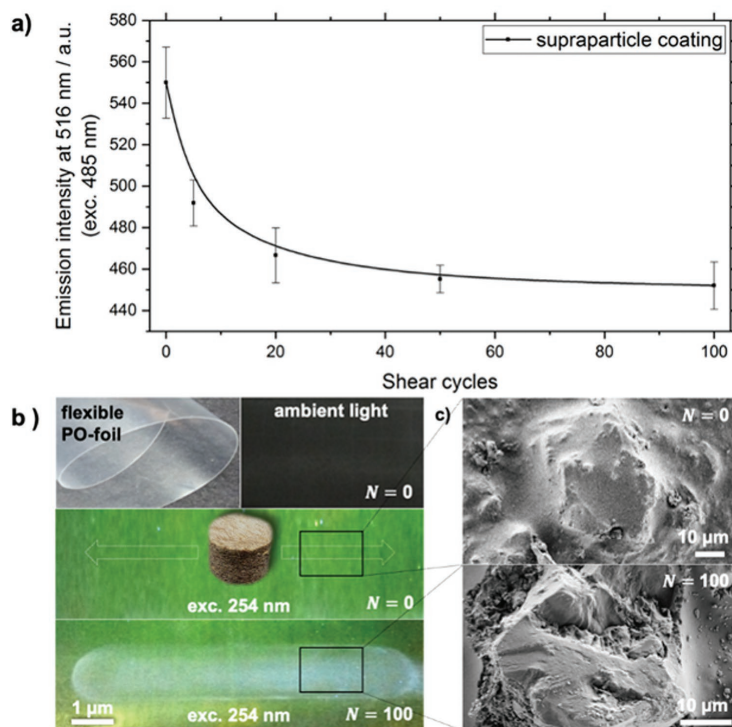


**Figure 6.** a) Emission intensity reduction for an emission at 510 nm (excited at 485 nm) of TOS-f incorporated into a coating on a PO foil depending on the applied shear forces in crocking cycles, b) Photographs under ambient light and under UV irradiation (254 nm) and c) SEM images showing the TOS-containing coating on PO foil before and after shear stress application.

sensitivity and optical properties can be readily adjusted via the choice of luminescence quencher and luminophore material. The sensors can be further incorporated into different matrices, which was herein shown as first proof of principle for a coating. The TOS can therefore also be used to create novel smart surfaces for variable applications. In addition, the different options to select and arrange core, quencher, and luminophore allow to drive the sensors into different sensing options regarding response time, sensitivity, and operation time. Thanks to the variability of the sensor sensitivity, that is, high susceptibility to shear stress ( $W_{1=50\%} = 155$  J) and fast turn-off response ( $t_{1=50\%} = 0.74$  min) or low susceptibility ( $W_{1=50\%} = 5166$  J) and slow turn-off response ( $t_{1=50\%} = 24.6$  min), the sensors can find use in a vast variety of applications. In contrast to most of the already existing micro-electromechanical and mechanochromic shear stress sensors, the novel sensors also tolerate high impact energies of several kJ. This makes it, for example, highly suitable for the monitoring of mechanical stress acting on a screw during the tightening or on a car tire during acceleration and deceleration. Besides the irreversibility of the TOS affording an “on-the-fly”

sensing, another unique feature is its flexibility in terms of color and sensitivity. Overall, the herein presented TOS are the start of an entire new group of hierarchical structured mechanical sensor supraparticles.

#### 4. Experimental Section

**Materials:** Silica nanoparticles as aqueous nanoparticle dispersion (Köstrosol 1030 (K1030)), containing 30 wt% silica with a hydrodynamic diameter of  $10 \text{ nm} \pm 5 \text{ nm}$  (DLS measurements) were received from Chemiewerke Bad Köstritz. Iron(III) chloride hexahydrate ( $\text{FeCl}_3 \cdot 6\text{H}_2\text{O}$ , 97.0% purity) and iron(II) chloride tetrahydrate ( $\text{FeCl}_2 \cdot 4\text{H}_2\text{O}$ , 99.0% purity) were purchased from Honeywell. Sodium hydroxide (NaOH, 99.0% purity) and hydrochloric acid (HCl, 36 wt%) were obtained from Carl Roth. Citric acid mono-hydrate ( $\text{C}_6\text{H}_8\text{O}_7 \cdot \text{H}_2\text{O}$ , 99.5% purity) was provided from PanReac. Charcoal (NORIT SA ULTRA PAH) was purchased from Cabot Norit. Resorcinol ( $\text{C}_6\text{H}_6\text{O}_2$ ,  $\geq 99.0\%$  purity), sodium carbonate monohydrate ( $\text{Na}_2\text{CO}_3 \cdot \text{H}_2\text{O}$ , 99.5% purity), fluorescein ( $\text{C}_{20}\text{H}_{12}\text{O}_5$ , 95.0% purity) and rhodamine B ( $\text{C}_{28}\text{H}_{31}\text{ClN}_2\text{O}_3$ ,  $\geq 95.0\%$  purity) were received from Sigma-Aldrich and formaldehyd ( $\text{CH}_2\text{O}$ , 37 wt% in aqueous solution stabilized by 10% methanol) was

obtained from Merck. Lumino-Red was purchased from Luminochem and terephthalic acid ( $C_8H_6O_4$ , 98% purity) was received from abcr GmbH. Terbium oxide ( $Tb_2O_3$ , 99.9% purity) was purchased from Auer-Remy and sodium hydroxide (NaOH, 99% purity) for the synthesis of disodium terephthalate was obtained from VWR International BVBA. All substances were used without further purification. Water was deionized before use. Terbium nitrate hydrate ( $Tb(NO_3)_3 \cdot x H_2O$ ) was synthesized by dissolving the metal oxide in concentrated nitric acid followed by removing the liquid phase under vacuum.<sup>[64]</sup> Disodium terephthalate ( $Na_2C_8H_4O_4$ ) was synthesized by dissolving sodium hydroxide in deionized water followed by the addition of terephthalic acid. The reaction mixture was heated and mixed with additional water until a clear solution was obtained. Subsequently, ethanol was added to the solution until a colorless precipitate formed. The reaction mixture was refluxed for 30 min and the resulting colorless precipitate was separated by filtration over sintered glass and dried under vacuum.<sup>[65]</sup> The synthesized chemicals were used without further purification.

**Synthesis of quenching cores for TOSs:** While charcoal was commercially purchased, the carbon particles were synthesized via carbonization of organic resorcinol–formaldehyde precursors.<sup>[66]</sup> The nanostructured iron oxide supraparticles (which—like the silica nanoparticle luminophore carriers—resemble raspberries in structure) were obtained via spray-drying an aqueous iron oxide nanoparticle dispersion.<sup>[67,68]</sup>

For the fabrication of iron oxide raspberry-like supraparticles as quenching core material, first iron oxide nanoparticles were synthesized. This synthesis was based on procedures according to the literature.<sup>[69–71]</sup> For the precipitation of iron oxide nanoparticles,  $FeCl_3 \cdot 6H_2O$  (8.0 mmol, 2.162 g),  $FeCl_2 \cdot 4H_2O$  (4.0 mmol, 0.792 g) were dissolved in water ( $H_2O$ , 50 mL) and mixed with sodium hydroxide dissolved in water (50 mL, 1.5 M) by pumping the two fluids with a peristaltic pump (Ismatec MCP, flow rate: 100 mL  $min^{-1}$ ). The resulting black precipitate was separated with a permanent handheld magnet after 1 min, washed four times with water (100 mL), redispersed in citric acid (50 mL, 0.01 M) and stirred for 30 min. The dispersion was destabilized by adding sodium hydroxide (100  $\mu$ L, 1.5 M), magnetically separated and washed four times with 4:1 ethanol ( $EtOH$ )/ $H_2O$  (200 mL). The precipitate was redispersed in water and treated with a sonifier (Branson, Model 450, Output: 20) for 5 min to obtain a 5 wt% stable ferrofluid ( $Fe_3O_4$ ). To obtain nanostructured raspberry-like iron oxide microparticles, the synthesized ferrofluid was spray-dried with a “B-290” mini spray dryer (Büchi). The inlet air temperature was chosen to be 130 °C and the outlet temperature was 60–65 °C during the spray-drying process.

The carbon particles as quenching core material were synthesized, as reported.<sup>[66]</sup> The organic precursor Resorcinol (117 mmol, 12.9 g) was dissolved in a formaldehyde solution (231 mmol, 18.8 g) under continuous stirring. Subsequently, deionized water (67.5 g) and  $Na_2CO_3$  solution (31.2 mmol, 0.78 g, 0.1 N) were added. After heavy stirring for about 5 min, the solution was heated to 85 °C and kept at this temperature for 24 h yielding a beige-orange liquid with an orange colored sediment. The sediment was dried under ambient pressure and room temperature for about 30 h. The resulting red-orange powder was carbonized at 800 °C (heat rate: 10 K  $min^{-1}$ ) for 1 h under nitrogen atmosphere. The obtained carbon particles had a particle size of  $9 \pm 3 \mu$ m (Fraunhofer diffraction and SEM measurements).

For the use of charcoal as quenching core, the described charcoal was sifted with a 45- $\mu$ m test sieve obtained from Retsch. After sieving more than 90% of the charcoal possessed a particle size below 40  $\mu$ m (laser diffraction measurement).

**Synthesis of the luminescent MOF  $3_4[Tb_2(bdc)_3(H_2O)_4]$ :** The luminescent, 3D metal-organic framework  $3_4[Tb_2(bdc)_3(H_2O)_4]$  was synthesized according to the literature.<sup>[58]</sup> Therefore, terbium nitrate hydrate (2.0 mmol, 403 mg) and disodium terephthalate (2.0 mmol, 420 mg) were dissolved separately in deionized water (10 mL) each.

**Table 1.** Precursors (core material, satellite material, and luminophore) used for TOS synthesis via spray-drying.

TOS type	Core material: amount	Satellite material: amount	Luminophore type: amount
TOS-L	charcoal: 1 g	K1030: 3.33 g	Lumino-Red: 100 mg
TOS-f	charcoal: 1 g	K1030: 3.33 g	fluorescein: 2 mg
TOS-c	carbon particles: 1 g	K1030: 3.33 g	fluorescein: 2 mg
TOS-i	iron oxide supraparticles: 1 g	K1030: 3.33 g	fluorescein: 2 mg
TOS-r	charcoal: 1 g	K1030: 3.33 g	rhodamine B: 66.6 mg
TOS-M	charcoal: 1 g	K1030: 3.33 g	$3_4[Tb_2(bdc)_3(H_2O)_4]$ : 33 mg

Subsequently, the terbium nitrate solution was added dropwise to the disodium terephthalate solution under intense stirring. Immediately a colorless solid precipitates. After stirring the reaction mixture for 3 h the product was separated by filtration over sintered glass, washed with deionized water, and dried under vacuum. The identity and purity of the obtained product was confirmed by powder X-ray diffraction (see Figure S5, Supporting Information) and elemental analysis (calculated: C: 32.67%, H: 2.29%; found: C: 32.39%, H: 2.27%).

**TOS synthesis:** For TOS synthesis, three types of precursors (core material, satellite material and luminophore) are mixed in one dispersion and combined in a spray-drying process (Scheme S1, Supporting Information). The applied materials and amounts of each precursor to form the different TOSs can be found in Table 1. For the preparation of the spray-drying dispersion, the luminophore was dissolved in the silica particle dispersion, and water was added under intense stirring for 15 min to form a 5 wt% dispersion. At the same time, the core particles were dispersed either in isopropanol (charcoal and carbon particles) or water (iron oxide supraparticles) using an ultrasonic bath for 15 min resulting in a 5 wt% particle dispersion. Subsequently, both core and satellite particle dispersions were mixed under intense stirring for about 2 min. This final precursor dispersion was spray-dried with a “B-290” mini spray dryer from Büchi. The inlet air temperature was chosen to be 130 °C and the outlet temperature was 60–65 °C during the spray-drying process. Regarding the TOS-L, excess Lumino-Red was used herein in order to guarantee the detectability of the luminophore with energy dispersive X-ray (EDX) spectroscopy, which is the case for this commercial rare-earth ion  $Eu^{3+}$  containing complex. In order to obtain an optimized luminescence emission intensity of each TOS system, the amount of luminophore content was always adjusted. This is necessary due to different quenching efficiencies of each dye by the quencher in proximity to the dye-hosting raspberry-shaped supraparticles. It is exemplarily shown for fluorescein in Figure S6, Supporting Information.

**Formulation of a TOS-containing coating on a PO foil:** Pretreatment of the obtained PO foil starts with corona application for about 20 s under continuous movement in a continuous Arcotec treater at 0.8 kV. After that, the foil was cleaned with air to avoid defects from contaminations. The formulation of the lacquer consisting of 25% solids content in ethanol was prepared as described elsewhere.<sup>[41]</sup> To this lacquer, a total amount of 20–25 wt% TOS was added and dispersed. The coatings were prepared using 1 mL of TOS-lacquer and a 50  $\mu$ m spiral blade on a Coatmaster 509 MC (Erichsen Testing Equipment), resulting in layers of about 38  $\mu$ m, respectively after solvent evaporation. The curing was conducted thermally for 30 min at 120 °C.

**Characterization:** Shear experiments on all examined TOSs were carried out by milling the powder samples with a Pulverisette Premium Line 7 ball mill from Fritsch equipped with 45 mL grinding beakers containing 50 ZrO<sub>2</sub> grinding balls (with a diameter of 5 mm and 0.37 g weight). Generally, 1 g of sample was treated for 30 min at 200 rpm (chosen as adequate speed of rotation while the TOS would also work for higher frequencies—see Figure S2, Supporting Information). After 0, 1, 2, 3, 5, 10, 20, and 30 min of milling time a three small sample were taken and analyzed via fluorescence spectroscopy in order to correlate the relative luminescence emission intensity drop

of the sensor system with the applied shear time. Application of shear stress on a TOS-containing coating via abrasion was performed with an automated TOMSIC crockmeter. Its setup consisted of a rigid platform on which the coated foil is fixed and an abrading finger covered with an abradant fabric. The test parameters were as follows: diameter of the circular rubbing finger  $d = 15$  mm; grinding pressure  $P = 4$  bar; track length  $l = 8$  cm; density of abrasive felt,  $0.52$  g cm<sup>-3</sup>; cycling number  $c = 100$ . Based on these parameters, the grinding work  $W = P \cdot (0.5d)^2 \cdot \pi \cdot 2l \cdot c$  can be calculated. Fluorescence spectroscopic analyses were conducted on a spectrofluorometer FP 8600 from Jasco equipped with a Sapre powder sample cell FP-1061 (Jasco). The confocal images were captured using a Leica TCS SP8X (Leica Microsystems GmbH) equipped with a white light laser SuperK Extreme EXW (NKT Photonics GmbH) and a HC PL APO 63x/1.40 Oil CS2 objective (Leica Microsystems GmbH). The fluorescein dye was excited at 491 nm with a fluorescent detection range from 496 to 750 nm. Simultaneously a transmission light image was recorded in order to visualize the non-fluorescent parts of the sample. The 3D images were post-processed using a 3D median filter with a radius of three pixels. Sample morphology was either studied on a SEM using a Zeiss Supra 25 SEM at 3 kV (field emission) and 3 mm working distance or on a Zeiss Ultra 55 at 1.5 kV or 5 kV and 2 mm working distance and SE and BSE sensitive detectors. EDX analysis was carried out with an Ametek EDAX detector at 15 kV and 8 mm working distance. The powder X-ray diffraction patterns were recorded on a Bruker D8 Discover DaVinci diffractometer with focussing Göbel mirrors and a linear LynxEye detector. The sample was ground to a fine powder and placed on a silicon wafer. The diffraction pattern was recorded in parallel beam geometry in transmission mode using CuK<sub>α</sub> radiation ( $\lambda = 1.54056$  Å). Elemental analysis was carried out on a Vario micro cube (Elementar Analysensysteme GmbH).

### Supporting Information

Supporting Information is available from the Wiley Online Library or from the author.

### Acknowledgements

This work was financially supported by BMBF NanoMatFutur grant 03XP0149, which is gratefully acknowledged. Karl Mandel and Klaus Müller-Buschbaum gratefully acknowledge funding by the DFG within the projects MA 7252/4-2 and MU-1562/7-2. The authors would also like to thank Tim Granath for the development of the synthesis protocol for citrate-stabilized iron oxide nanoparticles and Sabine Amberg-Schwab, Heike Bleicher, and Anette Burger for providing the lacquer for the coating.

### Conflict of Interest

The authors declare no conflict of interest.

### Keywords

luminescence, mechanochromic, sensor, shear stress, supraparticles

Received: February 8, 2019  
Published online: March 7, 2019

- [1] P. G. Gillespie, R. G. Walker, *Nature* **2001**, 413, 194.  
[2] E. D. Adrian, *Br. Med. J.* **1954**, 1, 287.

- [3] B. R. Aiello, A. R. Hardy, M. W. Westneat, M. E. Hale, *Integr. Comp. Biol.* **2018**, 58, 844.  
[4] H. Kagermann, W. Wahlster, J. Helbig, *Securing the future of German manufacturing industry: Recommendations for implementing the strategic initiative INDUSTRIE 4.0: Final report of the Industrie 4.0 Working Group*, **2013**, <http://en.acatech.de/publication/recommendations-for-implementing-the-strategic-initiative-industrie-4-0-final-report-of-the-industrie-4-0-working-group/>.  
[5] T. Stock, G. Seliger, *Opportunities of Sustainable Manufacturing in Industry 4.0. Procedia CIRP*, **2016**, 40, 536.  
[6] S. Wang, J. Wan, Di Li, C. Zhang, *Int. J. Distrib. Sens. Networks* **2016**, 12, 3159805.  
[7] K. Zhuo, T. Liu, L. Zhou, *Industry 4.0: Towards Future Industrial Opportunities and Challenges*, in *12th International Conference on Fuzzy Systems*, Zhangjiajie, China, August **2015**, pp. 2147–2152.  
[8] M. Brettel, N. Friederichsen, M. Keller, M. Rosenberg, *Int. J. Inform. Commun. Eng.* **2014**, 8, 38.  
[9] M. Wollschlaeger, T. Sauter, J. Jasperneite, *IEEE Ind. Electron. Mag.* **2017**, 11, 17.  
[10] T. Sekitani, Y. Noguchi, K. Hata, T. Fukushima, *Science* **2008**, 321, 1468.  
[11] T. Someya, T. Sekitani, S. Iba, Y. Kato, H. Kawaguchi, T. Sakurai, *Proc. Natl. Acad. Sci. U. S. A.* **2004**, 101, 9966.  
[12] V. Maheshwari, R. Saraf, *Angew. Chem.* **2008**, 120, 7926.  
[13] C. Wittenberg, *IFAC-PapersOnLine* **2016**, 49, 420.  
[14] *Distributed Control Architecture for Smart Surfaces* (Eds: K. Boutoustous, G. J. Laurent, E. Dedu, L. Matignon, J. Bourgeois, N. LeFort-Piat), The 2010 IEEE/RSJ International Conference on Intelligent Robotics and Systems, 18–22 Oct. 2010, Taipei, Taiwan **2010**.  
[15] B. J. Kane, G. T. A. Kovacs, A CMOS Compatible Traction Stress Sensing Element For Use In High Resolution Tactile Imaging, in *Proceedings of the International Solid-State Sensors and Actuators Conference – TRANSDUCERS '95*. International Solid-State Sensors and Actuators Conference – TRANSDUCERS '95, June 25–29, 1995, IEEE, Stockholm, Sweden **1995**, pp. 648–651.  
[16] *Development and Calibration of a Submillimeter Three-Component Force Sensor* (Eds: W. L. Jin, J. C. D. Mote), International Conference on Experimental Mechanics: Advances and Applications, 20 March, SPIE, Singapore, Singapore **1997**.  
[17] L. Wang, D. J. Beebe, *Sens. Actuators, A* **2000**, 84, 33.  
[18] J. Missinne, E. Bosman, B. van Hoe, G. van Steenberge, S. Kalathimekkad, P. van Daele, J. Vanfleteren, *IEEE Photonics Technol. Lett.* **2011**, 23, 771.  
[19] L. Löfdahl, M. Gad-el-Hak, *Meas. Sci. Technol.* **1999**, 10, 665.  
[20] R. Suresh, S. C. Tjin, *Sens. Actuators, A* **2005**, 120, 26.  
[21] T.-V. Nguyen, R. Kazama, H. Takahashi, T. Takahata, K. Matsumoto, I. Shimoyama, *J. Micromech. Microeng.* **2017**, 27, 075017.  
[22] K. Takei, T. Takahashi, J.C. Ho, H. Ko, A. G. Gillies, P. W. Leu, R. S. Fearing, A. Javey, *Nat. Mater.* **2010**, 9, 821.  
[23] Y. Q. Dong, J. W. Y. Lam, B. Z. Tang, *J. Phys. Chem. Lett.* **2015**, 6, 3429.  
[24] H. Ito, T. Saito, N. Oshima, N. Kitamura, S. Ishizaka, Y. Hinatsu, M. Wakeshima, M. Kato, K. Tsuge, M. Sawamura, *J. Am. Chem. Soc.* **2008**, 130, 10044.  
[25] N. D. Nguyen, G. Zhang, J. Lu, A. E. Sherman, C. L. Fraser, *J. Mater. Chem.* **2011**, 21, 8409.  
[26] D. R. T. Roberts, S. J. Holder, *J. Mater. Chem.* **2011**, 21, 8256.  
[27] G. Zhang, J. Lu, M. Sabat, C. L. Fraser, *J. Am. Chem. Soc.* **2010**, 132, 2160.  
[28] T. Ikawa, T. Shiga, A. Okada, *J. Appl. Polym. Sci.* **1997**, 66, 1569.  
[29] A. Seeboth, D. Loetzsch, R. Ruhmann, *Am. J. Mater. Sci.* **2012**, 1, 139.  
[30] S. H. Foulger, P. Jiang, A. C. Lattam, D. W. Smith, J. Ballato, *Langmuir* **2001**, 17, 6023.

- [31] X. Zhang, Z. Chi, Y. Zhang, S. Liu, J. Xu, *J. Mater. Chem. C* **2013**, *1*, 3376.
- [32] X. Luo, J. Li, C. Li, L. Heng, Y.Q. Dong, Z. Liu, Z. Bo, B. Z. Tang, *Adv. Mater.* **2011**, *23*, 3261.
- [33] A. N. Shipway, E. Katz, I. Willner, *ChemPhysChem* **2000**, *1*, 18.
- [34] S. Liu, Z. Tang, *J. Mater. Chem.* **2010**, *20*, 24.
- [35] S. Wintzheimer, T. Granath, M. Oppmann, T. Kister, T. Thai, T. Kraus, N. Vogel, K. Mandel, *ACS Nano* **2018**, *12*, 5093.
- [36] E. Llobet, *Sens. Actuators, B* **2013**, *179*, 32.
- [37] M. J. Ruedas-Rama, J. D. Walters, A. Orte, E. A. H. Hall, *Anal. Chim. Acta* **2012**, *751*, 1.
- [38] H. Sun, A. M. Scharff-Poulsen, H. Gu, K. Almdal, *Chem. Mater.* **2006**, *18*, 3381.
- [39] A. Burns, P. Sengupta, T. Zedayko, B. Baird, U. Wiesner, *Small* **2006**, *2*, 723.
- [40] N. Korin, M. Kanapathipillai, B. D. Matthews, M. Crescente, A. Brill, T. Mammoto, K. Ghosh, S. Jurek, S. A. Bencherif, D. Bhatta, A. U. Coskun, C. L. Feldman, D. D. Wagner, D. E. Ingber, *Science* **2012**, *337*, 738.
- [41] T. Ballweg, C. Gellermann, K. Mandel, *ACS Appl. Mater. Interfaces* **2015**, *7*, 24909.
- [42] M. Oppmann, F. Miller, S. Thürauf, P. Groppe, J. Prieschl, C. Stauch, K. Mandel, *ACS Appl. Mater. Interfaces* **2018**, *10*, 14183.
- [43] C. Stauch, T. Ballweg, W. Stracke, R. Luxenhofer, K. Mandel, *J. Colloid Interface Sci.* **2017**, *490*, 401.
- [44] S. Zellmer, G. Garnweitner, T. Breinlinger, T. Kraft, C. Schilde, *ACS Nano* **2015**, *9*, 10749.
- [45] A. B. D. Nandiyanto, K. Okuyama, *Adv. Powder Technol.* **2011**, *22*, 1.
- [46] K. Ratajczak, M. Stobiecka, *J. Phys. Chem. B* **2017**, *121*, 6822.
- [47] T. R. Sathe, A. Agrawal, S. Nie, *Anal. Chem.* **2006**, *78*, 5627.
- [48] E. A. Bailey, G. K. Rollefson, *J. Chem. Phys.* **1953**, *21*, 1315.
- [49] L. S. Forster, D. Dudley, *J. Phys. Chem.* **1962**, *66*, 838.
- [50] M. M. Martin, L. Lindqvist, *J. Lumin.* **1975**, *10*, 381.
- [51] R. Sjöback, J. Nygren, M. Kubista, *Spectrochim. Acta Part A* **1995**, *51*, L7.
- [52] N. Negishi, M. Fujino, H. Yamashita, M. A. Fox, M. Anpo, *Langmuir* **1994**, *10*, 1772.
- [53] M. Beija, C. A. M. Afonso, J. M. G. Martinho, *Chem. Soc. Rev.* **2009**, *38*, 2410.
- [54] R. F. Kubin, A. N. Fletcher, *J. Lumin.* **1982**, *27*, 455.
- [55] M. J. Snare, F. E. Treloar, K. P. Ghiggino, P. J. Thistlethwaite, *J. Photochem.* **1982**, *18*, 335.
- [56] S. Lis, *J. Alloys Compd.* **2002**, *341*, 45.
- [57] T. M. Reineke, M. Eddaoudi, M. Fehr, D. Kelley, O. M. Yaghi, *J. Am. Chem. Soc.* **1999**, *121*, 1651.
- [58] X. J. Zhao, J. H. Yang, Y. Liu, P. F. Gao, Y. F. Li, *RSC Adv.* **2014**, *4*, 2573.
- [59] R. F. Chen, J. R. Knutson, *Anal. Biochem.* **1988**, *172*, 61.
- [60] I. L. Arbeloa, *J. Chem. Soc., Faraday Trans. 2* **1981**, *77*, 1735.
- [61] T. W. Kim, J.-H. Park, J.-I. Hong, *Bull. Korean Chem. Soc.* **2007**, *28*, 1221.
- [62] J. Wu, W. Liu, J. Ge, H. Zhang, P. Wang, *Chem. Soc. Rev.* **2011**, *40*, 3483.
- [63] L. Stryer, *Annu. Rev. Biochem.* **1978**, *47*, 819.
- [64] P. Bag, U. Flörke, K. Nag, *Dalton Trans.* **2006**, 3236.
- [65] J. A. Kaduk, *Acta Crystallograph. Sect. B Struct. Sci.* **2000**, *56*, 474.
- [66] C. Scherdel, T. Scherb, G. Reichenauer, *Carbon* **2009**, *47*, 2244.
- [67] C. Stauch, S. Späth, T. Ballweg, R. Luxenhofer, K. Mandel, *J. Colloid Interface Sci.* **2017**, *505*, 605.
- [68] C. Stumm, K. Szielasko, T. Granath, C. Stauch, K. Mandel, *Mater. Today Commun.* **2018**, *16*, 174.
- [69] K. Mandel, F. Hutter, C. Gellermann, G. Sextl, *Colloids Surf. A* **2011**, *390*, 173.
- [70] K. Mandel, M. Straßer, T. Granath, S. Dembski, G. Sextl, *Chem. Commun.* **2015**, *51*, 2863.
- [71] A. Flegler, M. Schneider, J. Prieschl, R. Stevens, T. Vinnay, K. Mandel, *RSC Adv.* **2016**, *6*, 57236.

Copyright WILEY-VCH Verlag GmbH & Co. KGaA, 69469 Weinheim, Germany, 2019.

**ADVANCED  
FUNCTIONAL  
MATERIALS**

## Supporting Information

for *Adv. Funct. Mater.*, DOI: 10.1002/adfm.201901193

**Expanding the Horizon of Mechanochromic Detection by  
Luminescent Shear Stress Sensor Supraparticles**

*Susanne Wintzheimer, Jakob Reichstein, Sarah Wenderoth,  
Sebastian Hasselmann, Maximilian Oppmann, Marcel T.  
Seuffert, Klaus Müller-Buschbaum, and Karl Mandel\**

WILEY-VCH

Copyright WILEY-VCH Verlag GmbH &amp; Co. KGaA, 69469 Weinheim, Germany, 2019.

## Supporting Information

**Expanding the horizon of mechanochromic detection by luminescent shear stress sensor supraparticles***Susanne Wintzheimer, Jakob Reichstein, Sarah Wenderoth, Sebastian Hasselmann, Maximilian Oppmann, Marcel T. Seuffert, Klaus Müller-Buschbaum, Karl Mandel\****Approximation of the impact energy during shear stress experiments (ball milling experiments):**

For the approximation of the impact energy acting on the TOS samples during ball milling experiments, the following assumptions were made, based on outcomes of earlier studies:<sup>[S1-S5]</sup> The impact energy on a sample by ZrO<sub>2</sub> balls of a diameter of 5 mm or 10 mm is the same at low ball-filling ratios (i.e., 0.1).<sup>[S1]</sup> The impact energy is independent of the milling sample.<sup>[S2]</sup> The rotational speed of the vessel is the same as the rotational speed of the mill.<sup>[S1, S2]</sup> The impact energy E<sub>i</sub> is linearly dependent on the volume of the grinding beaker (**Figure S1**: developed based on the variations of beaker dimensions at a ball-filling grade of 0.26 and 550 rpm rotational speed).<sup>[S1]</sup>

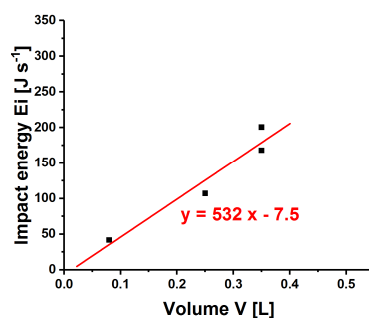


**Figure S1.** Impact energy E depending on the volume V of the grinding beaker during ball milling experiments.

WILEY-VCH

Additionally, it is expected that  $E_i$  is proportional to the milling speed<sup>[S2-S5]</sup> and to the filling grade.<sup>[S1]</sup> The calculated  $E_i$  as function of different ball-filling grades, rotational speeds and beaker volumes are listed in **Table S1**. It is evident that  $E_i$  is mainly influenced by the change in beaker size. Transferring these results to the experimental conditions of the grinding of TOSf with a rotational speed of  $600 \text{ min}^{-1}$  (**Figure S2**), a ball-filling grade of 0.07, a beaker volume of 0.045 L and 5 mm  $\text{ZrO}_2$  balls, the acting impact energy can be approximated to be  $15 \text{ Js}^{-1}$ .

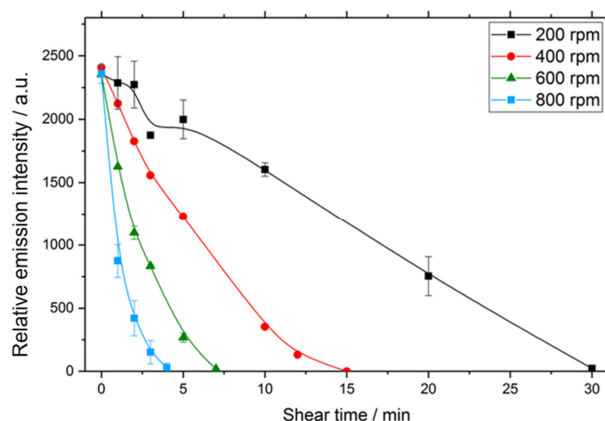


**Figure S2.** Variation of the milling speed (in rpm): Emission intensity drops at 510 nm (excited at 485 nm) of the TOSf (charcoal, silica, fluorescein) depending on the shear time.

Interestingly, the curve progression of the relative emission intensity over the shear time (especially at higher rotational speed) corresponds well with the curve progression of the normalized median diameter of grinded samples.<sup>[S2-S4]</sup> The curve first rapidly decreases in the initial stage of grinding and then tends to level off as the grinding progresses.<sup>[S2-S4]</sup>

The approximate work  $W_{t=0} = E_{i,600\text{rpm}} \cdot t_{t=0}$  which is needed in order to decrease the emission intensity of the sensor down to zero is  $6.3 \text{ kJ}$  ( $=7 \text{ min} \cdot 60 \text{ s min}^{-1} \cdot 15 \text{ Js}^{-1}$ ). This implies that the approximate impact energy acting at 200 rpm (Figure S2) rotational speed is  $E_{i,200\text{rpm}} = 3.5 \text{ Js}^{-1}$  ( $= 6300 \cdot 1800^{-1} \text{ Js}^{-1}$ ).

**Table S1.**  $E_i$  evolution during adaptation of measured values from other publications to our experimental conditions and equations used for the calculations.

used equations	conditions for the development of the equation ball-filling grade	ball-filling grade [-] / rotational speed [ $\text{min}^{-1}$ ] / beaker volume [L] / diameter of $\text{ZrO}_2$	$E_i$ evolution during adaptation of measured values from other

## WILEY-VCH

	[ $\cdot$ ] / rotational speed [ $\text{min}^{-1}$ ] / beaker volume [L]	balls [mm]	publications to our experimental conditions [ $\text{J s}^{-1}$ ]
based on [S1]:			
<b>experimentally measured values</b>		<b>0.26 / 550 / 0.25 / 10</b>	<b><math>E_i = 107</math></b>
$E_i = 532 \text{ J s}^{-1} \text{ L}^{-1} \cdot V - 7.5$	0.26 / 550 / -	0.26 / 550 / 0.045 / 10	$E_i = 16$
$E_i(550 \text{ min}^{-1}) = 0.57 \cdot E_i(650 \text{ min}^{-1})$	0.26 / - / 0.25	0.26 / 650 / 0.045 / 10	$E_i = 28$
$E_i(0.26) = 1.4 \cdot E_i(0.1)$	- / 650 / 0.25	0.1 / 650 / 0.045 / 10	$E_i = 20$
based on [S2]:			
<b>experimentally measured values</b>		<b>0.5 / 600 / 0.045 / 10</b>	<b><math>E_{w(20g)} = 1.25</math>, <math>E_{w(12g)} = 2.08</math></b>
$E_i = w \cdot E_w$ (sample weight $w$ , specific impact energy $E_w$ )		0.5 / 600 / 0.045 / 10	$E_i = 25$
<b>experimentally measured values</b>		<b>0.5 / 400 / 0.045 / 10</b>	<b><math>E_{w(20g)} = 0.37</math> <math>E_{w(12g)} = 0.62</math></b>
$E_i = w \cdot E_w$ (sample weight $w$ , specific impact energy $E_w$ )		0.5 / 400 / 0.045 / 10	$E_i = 7.4$

**Table S2.** Calculation of the approximate work that is done in order to result in a 50 % decrease of the initial emission intensity  $I$  of a TOS after a certain time  $t_{I=50\%}$ .

TOS sample	$t_{I=50\%}$ [min]	$W_{I=50\%}$ [J]
TOS-f	5.4	1134
TOS-c	24.6	5166
TOS-i	3.5	735
TOS-r	1.5	315
TOS-L	9.2	1932
TOS-M	0.74	155

**Table S3.** Calculation of the approximate work that is done in order to result in a decrease of the initial emission intensity  $I$  by 10 % after a certain time  $t_{I=90\%}$  or distance  $s_{I=90\%}$  ( $=2 \cdot t \cdot c$ ) in the case of TOS-f powder sample (determined by ball milling) and TOS-f coating (determined by crockmeter test), respectively.

TOS sample	$t_{I=90\%}$ [min]	$s_{I=90\%}$ [m]	$W_{I=90\%}$ [J]
TOS-f	0.5	-	105 ( $W = E_i \cdot t$ )
TOS-f coating	-	1.12	80 ( $W = F \cdot s$ )

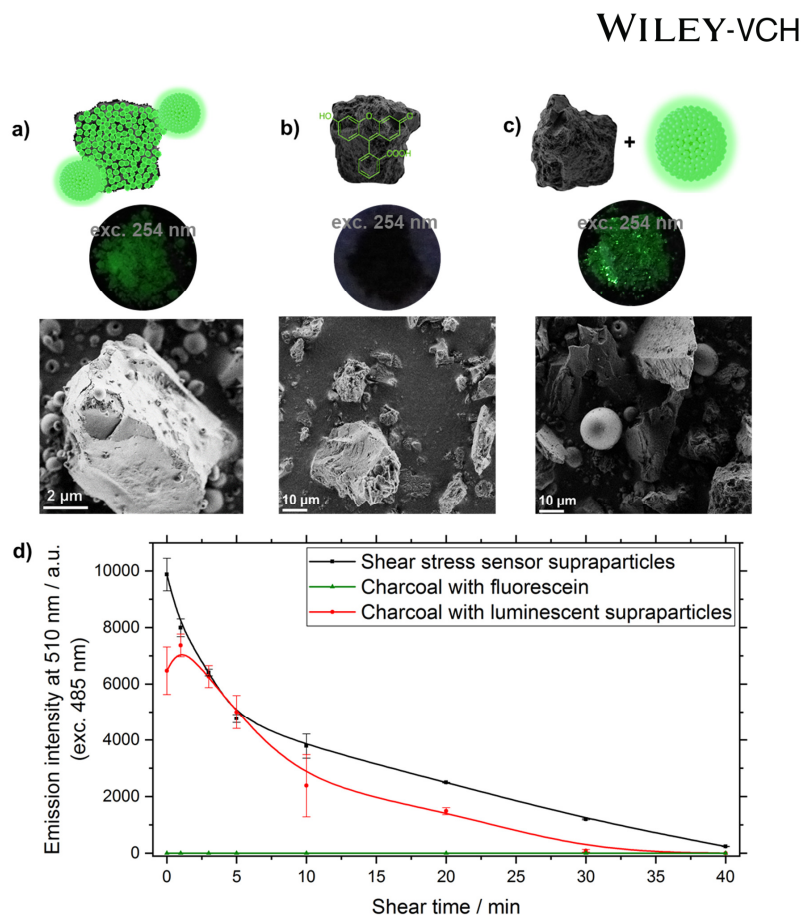


**Figure S3.** Scheme, photographs under UV irradiation and SEM images of a) TOSf, b) charcoal mixed with fluorescein, c) charcoal mixed with spray-dried silica-fluorescein supraparticles, d) Emission intensity reductions for 510 nm (excited at 485 nm) of the systems shown in a) to c) depending on the shear time.

WILEY-VCH

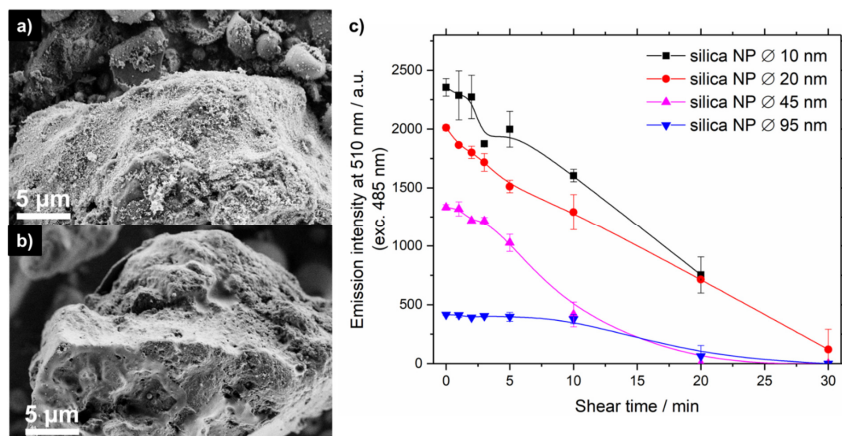
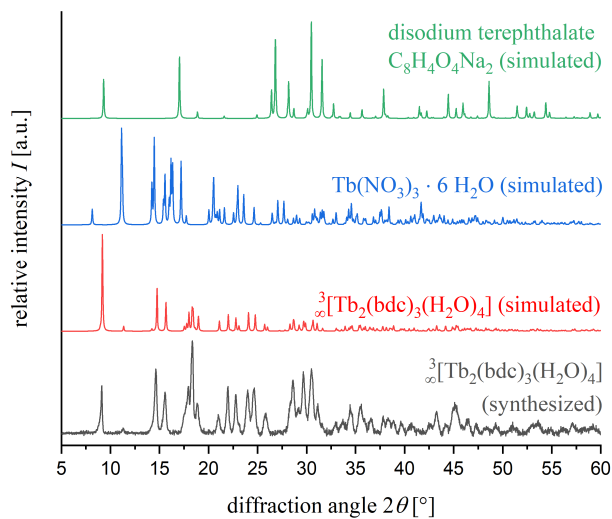


**Figure S4.** Exemplary SEM images of TOSs (charcoal, silica, fluorescein with quencher particles in spotlight) with silica nanoparticles with a diameter of a) 95 nm or b) 10 nm as well as the emission intensity of TOSs with varied sizes of the silica nanoparticle satellites (10 nm, 20 nm, 45 nm, 90 nm in diameter) at 510 nm (excited at 485 nm) depending on the shear time.



WILEY-VCH

**Figure S5.** Comparison of the measured X-ray powder diffraction pattern of  ${}^3[\text{Tb}_2(\text{bdc})_3(\text{H}_2\text{O})_4]$  and simulated diffraction patterns of  ${}^3[\text{Tb}_2(\text{bdc})_3(\text{H}_2\text{O})_4]$ ,<sup>[36]</sup> terbium nitrate hexahydrate<sup>[37]</sup> and disodium terephthalate<sup>[38]</sup> using single crystal X-ray data.

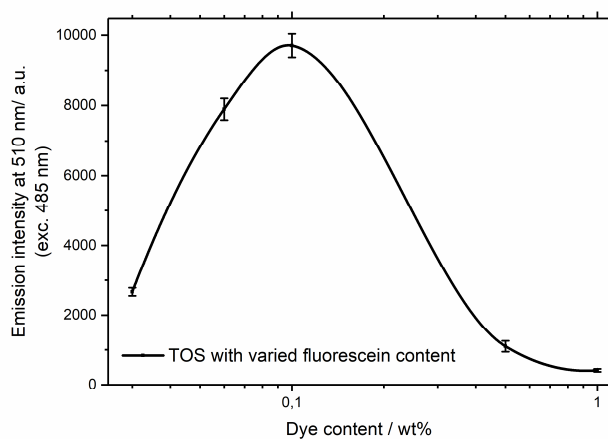
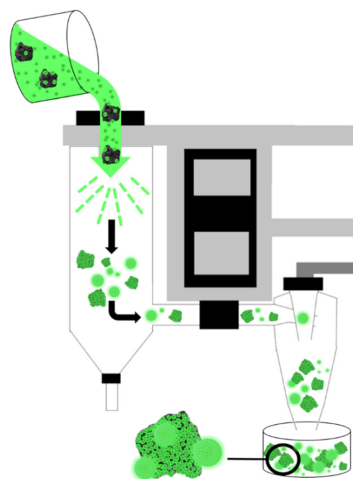


**Figure S6.** Optimization of luminescence emission intensity at 510 nm (excited at 485 nm) of the TOS depending on the fluorescein content, i.e. ratio of fluorescein to silica and charcoal particles.

WILEY-VCH



**Scheme S1.** Principle of the TOS formation via spray-drying by evaporation-induced self-assembly.

**Supporting video V1.** Confocal fluorescence microscopy of TOS-f (charcoal core, 10 nm silica particles, fluorescein) in non-sheared state video of a 3D closeup view of one supraparticle from different viewing angles.

[S1] Funk, Birgit (31.12.2015): Ressourceneffiziente chemische Synthese – Prozessentwicklung in Kugelmöhlen für lösungsmittelfreie Reaktionen (RESPEKT). DBU-final report-AZ-29622-31. Jena.

[S2] Mio, Hiroshi; Kano, Junya; Saito, Fumio (2004): Scale-up method of planetary ball mill. In: *Chemical Engineering Science* 59, S. 5909–5916.

[S3] Kano, Junya; Mio, Hiroshi; Saito, Fumio (2000): Correlation of grinding rate of gibbsite with impact energy of balls. In: *AIChE J.* 46 (8), S. 1694–1697. DOI: 10.1002/aic.690460820. [S4] Kano, J.; Mio, H.; Saito, F.; Miyazaki, M. (2001): Correlation of grinding rate of gibbsite with impact energy in tumbling mill with mono-size balls. In: *Minerals Engineering* 14 (10), S. 1213–1223. DOI: 10.1016/S0892-6875(01)00138-8.

[S5] Mio, Hiroshi; Kano, Junya; Saito, Fumio; Kaneko, Kantaro (2004): Optimum revolution and rotational directions and their speeds in planetary ball milling. In: *Int. J. Miner. Process.* 74S, S. 85–92.

[S6] Reineke, Theresa M.; Eddaoudi, Mohamed; Fehr, Michael; Kelley, Douglas; Yaghi, O. M. (1999): From Condensed Lanthanide Coordination Solids to Microporous Frameworks Having Accessible Metal Sites. In: *J. Am. Chem. Soc.* 121 (8), 1651–1657. DOI: 10.1021/ja983577d.

**WILEY-VCH**

[S7] Moret, Emmanuel; Bünzli, Jean-Claude G.; Schenk, Kurt J. (1990): Structural and luminescence study of europium and terbium nitrate hexahydrates. In: *Inorganica chimica acta* 178 (1), 83–88. DOI: 10.1016/S0020-1693(00)88138-4.

[S8] Kaduk, James A. (2000): Terephthalate salts: salts of monopositive cations. In: *Acta Crystallogr B Struct Sci* 56 (3), 474–485. DOI: 10.1107/S0108768199014718.

## REVIEW

## Supraparticles for Sustainability

Susanne Wintzheimer, Jakob Reichstein, Philipp Groppe, Andreas Wolf, Bastian Fett, Huanhuan Zhou, Rosa Pujales-Paradela, Franziska Miller, Stephan Müssig, Sarah Wenderoth, and Karl Mandel\*

The indispensable transformation to a (more) sustainable human society on this planet heavily relies on innovative technologies and advanced materials. The merits of nanoparticles (NPs) in this context are demonstrated widely during the last decades. Yet, it is believed that the impact of particle-based nanomaterials to sustainability can be even further enhanced: taking NPs as building blocks enables the creation of more complex entities, so-called supraparticles (SPs). Due to their evolving phenomena coupling, emergence, and colocalization, SPs enable completely new material functionalities. These new functionalities in SPs can be utilized to render six fields, essential to human life as it is conceived, more sustainable. These fields, selected based on an entropy-rate-related definition of sustainability, are as follows: 1) purification technologies and 2) agricultural delivery systems secure humans “fundamental needs.” 3) Energy storage and conversion, as well as 4) catalysis enable the “basic comfort.” 5) Extending materials lifetime and 6) bringing materials back in use ensure sustaining “modern life comfort.” In this review article, a perspective is provided on why and how the properties of SPs, and not simply properties of individual NPs or conventional bulk materials, may grant attractive alternative pathways in these fields.

just means the ability to exist constantly.<sup>[1]</sup>

As far as humankind is concerned, it is often defined as living in a way that is not at the expense of future generations.<sup>[2]</sup> Harmonizing these two demands one can state that the fulfillment of actual human needs (from the very basic to advanced ones), which is required or at least demanded for our continuance of existence, must not sacrifice the well-being of future human generations. All aspects of sustainability may be categorized into environmental, technical, socioethical, and economic concerns, which are all closely interconnected.<sup>[3]</sup> To reduce complexity, we restrict ourselves to an environmental and technical view in this review on chemical systems. More precisely, we focus on the question of how artificially synthesized objects can contribute to sustainability not only in the environment but also in technical systems and processes that are required to fulfill all human needs in modern life.

## 1. Introduction

Sustainability is more important than ever to assure future of humankind. In a most simplified definition, sustainability

This demands to define sustainability in this regard on a fundamental level for which we refer to Lineweaver's and Townes O'Brien's article “The Cosmic Context of the Millennium Development Goals: Maximum Entropy and Sustainability.”<sup>[4]</sup> The authors state that due to the second law of thermodynamics, any system increases in entropy, causing dissipation of energy (into heat) and matter (elements are spread from concentrated reservoirs all over the system, i.e., the planet).<sup>[4]</sup> However, the sun as major source provides energy to constantly revert this dissipation: With sunlight, biological systems are capable to assemble small molecules into more complex units, biomass is created, and eventually, for instance converted into useful chemical energy reservoirs (e.g., oil). Or, as another example, the sunlight also drives evaporation of water in the oceans, wind—also driven by the sun—carries the moist air to a sink such as a mountain ridge where it accumulates as rain that fills up depleted freshwater reservoirs.

The crucial point is—as the authors outline—that one has to consider the *rate* of entropy. There is a “sustainable” rate of entropy  $(dS/dt)_{\text{sustainable}}$ , i.e., a rate at which the “power” provided by the sun can ensure that there is sufficient inversion, keeping the balance between created order and occurring disorder.<sup>[4]</sup> Hence, for a sustainable living, the rate of entropy on our planet should be minimized.

Dr. S. Wintzheimer, J. Reichstein, P. Groppe, H. Zhou, Dr. R. Pujales-Paradela, F. Miller, S. Müssig, Prof. K. Mandel  
Department of Chemistry and Pharmacy  
Inorganic Chemistry  
Friedrich-Alexander University Erlangen-Nürnberg (FAU)  
Egerlandstrasse 1, D91058 Erlangen, Germany  
E-mail: karl.mandel@fau.de

Dr. S. Wintzheimer, A. Wolf, B. Fett, Prof. K. Mandel  
Fraunhofer-Institute for Silicate Research  
ISC  
Neunerplatz 2, D97082 Würzburg, Germany  
S. Wenderoth

Chair of Chemical Technology of Materials Synthesis  
Julius-Maximilians-University Würzburg  
Röntgenring 11, D97070 Würzburg, Germany

 The ORCID identification number(s) for the author(s) of this article can be found under <https://doi.org/10.1002/adfm.202011089>.

© 2021 The Authors. Advanced Functional Materials published by Wiley-VCH GmbH. This is an open access article under the terms of the Creative Commons Attribution License, which permits use, distribution and reproduction in any medium, provided the original work is properly cited.

DOI: 10.1002/adfm.202011089

However, our modern society optimizes processes toward a maximum gain rate and thus artificially increases this rate of entropy generation, and therefore dissipation, that it holds

$$(dS/dt)_{\text{current}} > (dS/dt)_{\text{sustainable}} \quad (1)$$

Considering once again the second law of thermodynamics, stating that entropy increase is inevitable, one could think that a higher rate of entropy increase may be the natural state every system converges to. However, this is not true as the authors clearly demonstrate that overall, it is decisive for how long entropy in a system can be generated.<sup>[4]</sup>

Consequently, one has to consider the integral of 1) over time. However, there is a constraint in the integral: if the rate exceeds the chance of a system to “regenerate,” there is a defined point in time  $t$  where the system collapses, see Equation (2).<sup>[5]</sup>

$$S_{\text{sus}} = \int_0^{t_{\text{sustainable}}} (dS/dt)_{\text{sustainable}} dt > S_{\text{collapse}} = \int_0^{t_{\text{collapse}}} (dS/dt)_{\text{current}} dt \quad (2)$$

A “sustainable” system possesses not only a low rate of entropy increase but also its integral over time can be infinitely extended. This yields a higher overall entropy and thus, fulfilling the second law of thermodynamics better, is the sustainable rate that keeps the ecosystem alive (Equation (3)).<sup>[4]</sup>

$$t_{\text{sustainable}} (dS/dt)_{\text{sustainable}} > t_{\text{collapse}} (dS/dt)_{\text{current}} \quad (3)$$

From these considerations follows that an intact ecosystem increases in entropy and thus causes dissipation of any form of resources. However, this proceeds at a rate, where this state can be infinitely extended if an external source of energy is able to renew the condensed reservoirs of resources. Vice versa, a nonintact, thus nonsustainable system is at a state of a too high rate of entropy increase.

Having identified the rate of entropy as the measure for sustainability, one can state that a contributor to sustainability either works against entropy/dissipation increase, using constantly existing forms of energy (sunlight), or helps to decelerate the rate of entropy increase by acting as a storage system, which delays depletion and dissipation.

Based on this, it is possible to identify six fields where materials can contribute to sustainability according to this definition.

- 1) Purification technologies: As clean water/freshwater is key in our life, reduction of entropy in this system, i.e., inverting water pollution obviously follows the definition. The same holds for air pollution.
- 2) Agricultural delivery systems: They help to reduce entropy in soil and groundwater, i.e., reduce their pollution.
- 3) Energy storage and conversion: To convert natural resources such as sunlight into energy we can work with, or transform other forms of energy into stored chemical or electrical energy, obviously helps to create systems that can revert entropy and thus is sustainable according to the definition.
- 4) Catalysis: Catalysts help to increase the order in a system (e.g., transform several molecules into another, desired, typically higher-ordered compound) and thus, fulfill the definition (less energy is needed to create something of reduced entropy).

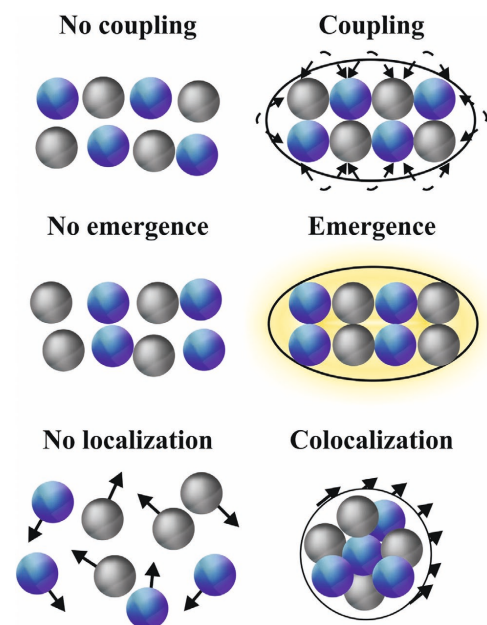
- 5) Extending materials lifetime: Dissipation is decelerated as substances are kept in use for a longer time.
- 6) Bringing materials back in use: Dissipation is reduced as substances are kept in a cycle of use and reuse.

Going back to the simplified definitions of sustainability mentioned in the very first sentences of this Introduction section, sustainability is the ability to exist constantly due to fulfillment of human needs without sacrificing the well-being of future generations for it. Following this interpretation, the review is structured into the three main sections: “fundamental needs,” “basic comfort,” and “modern life comfort.” Consequently, the identified six fields where materials can contribute to sustainability are classified into these sections. 1) Purification technologies and 2) agricultural delivery systems secure humans “fundamental needs.” 3) Energy storage and conversion, as well as 4) catalysis sustain our “basic comfort.” 5) Extending materials lifetime and 6) bringing materials back in use ensure sustaining “modern life comfort.”

In the last two decades, nanoobjects (nanoparticles) attracted a lot of interest not only due to some unexpected properties that fascinated scientists, but also practically as it turned out that they can significantly contribute to the above listed topics of sustainability in a way that is often superior to bulk materials.<sup>[6,7]</sup> What all nanoparticles (NPs) have in common is that by transforming the bulk materials to the nanoscale, a) more objects, b) more spatially distributed spots, and c) more surface per gram of material is obtained—with obvious advantages for most application fields. Additionally, true nanoproperties such as quantum effects might emerge.<sup>[8]</sup>

There were many breakthroughs reported with NPs. Yet, we believe, there is more that can be achieved by going one step further. This next step is to consider the large variety of NPs, tailored in size, shape and composition and therefore in their unique properties, as “the atoms of tomorrows materials”/as the atoms for more complex materials.<sup>[9]</sup> Just as in supramolecular chemistry,<sup>[10]</sup> more complex architectures could reveal even more advantageous properties.

Based on existing literature (such as<sup>[11,12]</sup> to name but a few), we recently made an attempt<sup>[13]</sup> to thoroughly define the term supraparticle to include any forms of complex particles made of nanobuilding blocks.<sup>[14]</sup> Additionally, we outlined, that by combining individual NPs to more complex entities, three new and unique types of properties and thus functionalities can be obtained—which are impossible to achieve with individual NPs. These are coupling, emergence, and colocalization (**Scheme 1**).<sup>[13]</sup> Coupling describes the strong interaction between electrons in NPs within a supraparticle (SP) due to their close proximity, while emergence arises from a specific structure within a SP rather than from intrinsic properties of the individual building blocks. Colocalization specifies that different NPs with distinct properties in a SP form a distinguishable common entity with either combined or superimposed properties that can be moved, as well as removed, concentrated, and observed individually. SPs are fundamentally defined as described in **Scheme 2**.<sup>[13]</sup> SPs are entities that have been created from colloiddally dispersed NPs as starting materials. Processes are excluded where the constituent particles are only transient stages and thus not accessible for analysis, modification, or exchange.<sup>[15]</sup> SPs are obtained in a dispersed form, for instance, in a colloid, powder, microcomposite, etc. This



**Scheme 1.** Functionality in supraparticles. Supraparticles exhibit additional functional properties compared to their building blocks. These are based on coupling, emergence, and colocalization. Reproduced with permission.<sup>[13]</sup> Copyright 2018, American Chemical Society.

distinguishes them from NP arrangements that are infinitely extended in one, two, or three dimensions.<sup>[16]</sup> Different to randomly agglomerated NPs,<sup>[17]</sup> a consistent structural motif prevails amongst the obtained SPs, such as crystal packing, fractal dimension, connectivity to the nearest neighbor, defined average size or shape. This results in the creation of additional functionality (coupling, emergence, or colocalization). A more detailed definition and comparison to other terms used for assemblies of NPs, are addressed in an own review article.<sup>[13]</sup>

In this review article, we point out, where SPs were reported to contribute to “sustainability” according to the definition described in this section. We work out why and how particularly the properties of SPs (and not simply individual NPs) yield unique contributions to the different fields of application.

While in some fields, the development of SPs to achieve superior functionalities is already significantly advanced, some other fields are to date rarely explored. Despite literature is barely available in the latter case, we consider certain fields as especially interesting for SP employment. This is why we included these in the review as a more conceptual part.

## 2. Supraparticles for Sustainability

As already pointed out in the Introduction, sustainability in a most simple definition means the ability to exist constantly. For

living beings first, the basic needs must be secured, namely, water to drink, air to breathe, and food to gain energy from. For human beings in a society, second, basic comfort must be sustained to enable mobility, heating, lighting, etc., which all fundamentally depend on electrical energy. Third, our modern world is not only energy but also materials dependent, i.e., “a materials world.”

### 2.1. Fulfillment of Basic Needs

Guaranteeing the fulfillment of our basic needs not only means to ensure sufficient provision with water, air, and food, but also to secure their cleanliness and thus an appropriate state for consumption. This is why technologies that purify water and air, as well as agricultural delivery systems, reducing unwanted overdosing, contribute to sustainability.

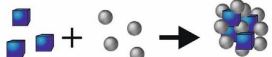
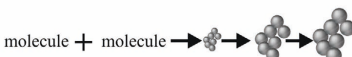
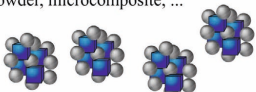
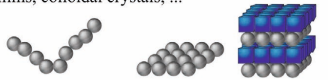
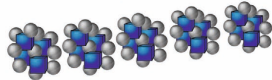
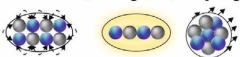
#### 2.1.1. Purification Technologies

One of the most apparent ways to visualize humanity’s (unsustainable) imprint on earth is through pollution of air and water. Since the beginning of the anthropogenic era, human activities have been relentlessly reducing the availability and quality of fresh air and clean water. As both of them are part of the same hydrologic cycle, contamination spreads and makes the imprint of humankind now truly global. Driven by the rapid population growth, fossil fuel-powered economy, and resource-intensive lifestyle, our impact is still accelerating and approaching a critical point with irreversible changes for our planet, like loss of biodiversity and climate change.<sup>[18]</sup> Not last, human health is directly threatened by the increasing contamination of air and water.<sup>[19]</sup>

To restore the natural balance and reduce humanity’s imprint, purification technologies will provide a critical contribution to the ultimate goal of a sustainable use of air and water. Most traditional treatment technologies are energy and chemical intensive, as well as ineffective in removing key trace contaminants. For these reasons, there has been a great interest in developing new materials to meet these new needs, especially in the field of nanomaterials.<sup>[20]</sup>

In the following, we critically discuss benchmark technologies for air and water purification and outline the contribution of specific nanomaterials to provide clean air and water. Based on this, we highlight where the use of SPs yields more sustainable purification technologies.

**Air:** Air pollution denotes the contamination of indoor and outdoor air by organic and inorganic substances. These pollutants can be classified into three main groups: gaseous pollutants, microorganisms, and particulate matter. Gaseous contaminants include volatile organic compounds, carbon monoxide, nitrogen-containing and sulfur-containing compounds. Microorganisms are bacteria, viruses and fungi and particulate matter describes all solid organic and inorganic pollutants.<sup>[21]</sup> Air pollution is combated by its prevention or its removal. Most material-based solutions currently focus on the removal of contaminants either from flue gases or from air. However, in order to efficiently eliminate pollutants, they first have to be locally

Supraparticles:	Excluded particles:
Entity consisting of defined particles created from colloiddally dispersed nanoparticles as the starting material 	Constituent particles are only transient stages that are not accessible for analysis, modification, or exchange 
Are obtained in a dispersed form as colloid, powder, microcomposite, ... 	Self-assembled nanoparticle arrangements infinitely extended in 1D, 2D or 3D as fibers, films, colloidal crystals, ... 
A consistent structural motif prevails among all particles: size, shape or internal structure 	Randomly agglomerated nanoparticles 
Their structural motif creates additional functionality: colocalization, emergence, coupling 	

Scheme 2. Definition of supraparticles and particles excluded from this definition.<sup>[13]</sup>

detected, identified, and quantified. This is why sensors or indicators for the control of air quality are of eminent importance.

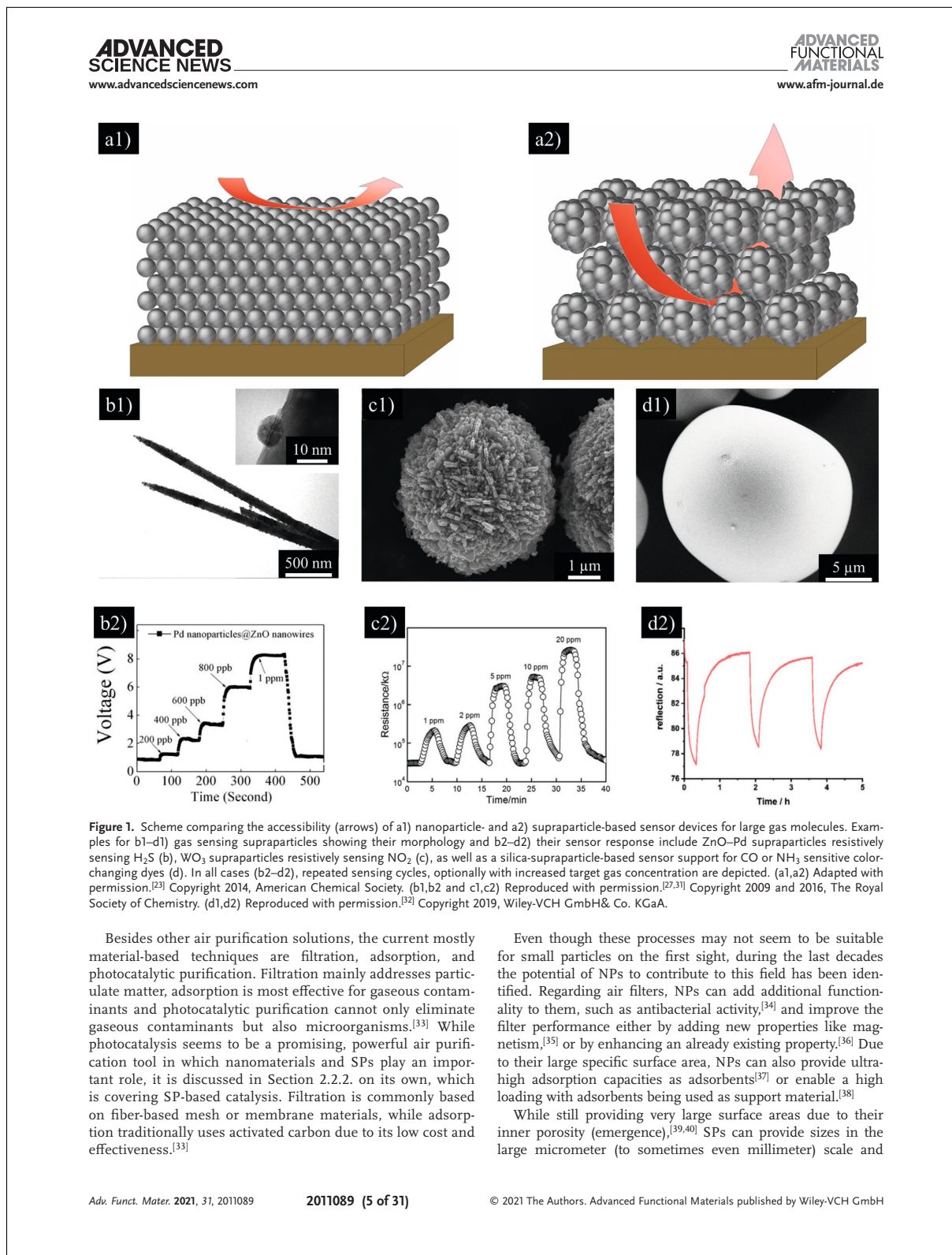
Herein, sensor development is mainly concentrated on the monitoring and detection of gaseous contaminants. While there certainly exist many sensor devices based on bulk materials, NPs have also been identified to provide numerous convenient features for their application as sensors and indicators. They offer the ability to synthesize them in almost any type of material, size, or shape and with any chemical surface modification, often showing unique physical, chemical, or electronic nanoderived properties.<sup>[7,22]</sup> This permits a precise control of sensitivity and selectivity, as well as response time to physical or chemical parameters. Furthermore, they enable the bottom-up fabrication of flexible sensors due to their small size, which is advantageous over complicated, multistep top-down processes.<sup>[7]</sup> Finally yet importantly, films with well-controlled porosity can be generated from NPs by precise adjustment of interparticle distances allowing the maximum interaction of a device with its environment.<sup>[7,23]</sup> More detailed information about nanosensors can be found in excellent review articles.<sup>[7,22,24,25]</sup>

Going one step further, using NPs as building blocks to create SPs for gas sensor applications adds several advantages to these materials, while still profiting from the aforementioned features. While NPs easily aggregate during device construction, e.g., during coating fabrication, resulting in a decrease in porosity, SPs maintain their large surface area within their structure (emergence).<sup>[26]</sup> Furthermore, the micrometer-size of these spheres also provides large pores within coatings, which

are needed for the detection of, e.g., large molecular gases, while retaining the preferred (crystal) size of containing NPs (Figure 1a).<sup>[23]</sup> Based on the colocalization of building blocks, SPs also enable the combination of several materials in close contact, which often improves sensitivity and selectivity or adds supplementary functionalities to the systems.<sup>[27–29]</sup>

Several SP-based sensors for the detection of gases like H<sub>2</sub>, CO, NO<sub>2</sub>, O<sub>2</sub>, or NH<sub>3</sub> have already been developed.<sup>[23,26,28,29,30]</sup> A highly sensitive H<sub>2</sub>S gas sensor consisting of ZnO nanowires decorated with Pd NPs was presented by Zhang et al. (Figure 1b1).<sup>[27]</sup> The sensor response is measured via the changed resistance in presence of the gas compared to pure air (Figure 1b2). NO<sub>2</sub> can for instance be detected with the help of WO<sub>3</sub> SPs consisting of nanorods also by changes in sensor resistance (Figure 1c).<sup>[31]</sup> A SP-based support for CO or NH<sub>3</sub> sensitive molecules assembled by differently sized silica NPs was shown by Wintzheimer et al. (Figure 1d1).<sup>[32]</sup> The gas-sensitive dye was loaded onto the SP after its fabrication and was thus able to operate in dry state instead of only in solution showing, e.g., the presence of NH<sub>3</sub> with a modified reflection intensity (Figure 1d2) and a color shift.

SPs as gas detecting materials as well as matrix for gas sensitive molecules often provide a superior sensitivity and selectivity compared to nano- or bulk materials and are thus promising for the detection of gaseous air contaminants. A precise detection of air pollution will enable the systematic application of air purification technologies in order to provide clean air to human beings at long sight.



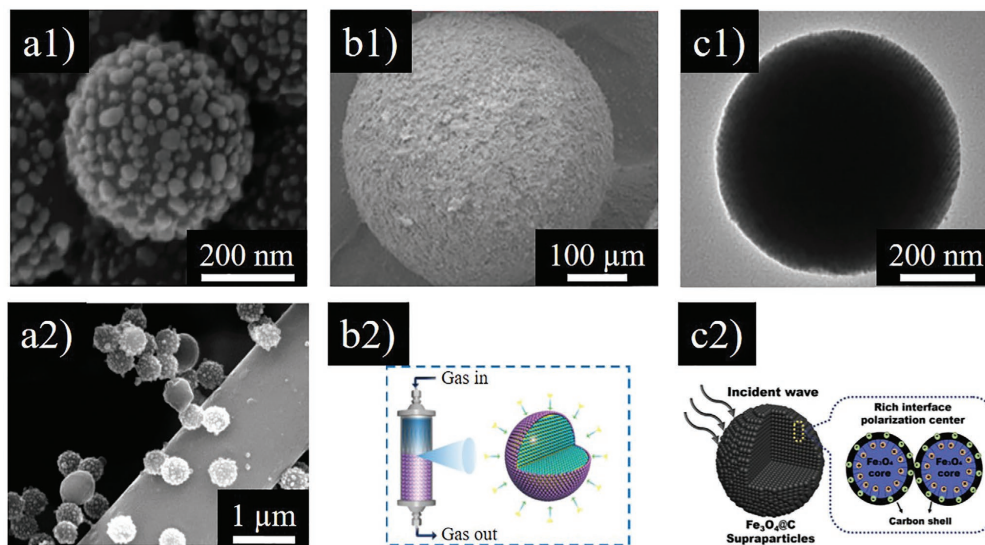


**Figure 2.** Supraparticles used in air purification systems. a1) Silica-gold supraparticles coated on filter fibers adding antibacterial activity to the system. a2) Their activity was demonstrated against *Escherichia coli* bacteria. b1) Silica-based hydrophilic-hydrophobic liquid-solid amine-containing supraparticles for b2) CO<sub>2</sub> sorption in fixed bed reactors. c1) Supraparticles consisting of carbon-coated iron oxide nanoparticles Fe<sub>3</sub>O<sub>4</sub>@C for c2) the absorption of electromagnetic waves. (a1,a2) Reproduced with permission.<sup>[43]</sup> Copyright 2014, The Royal Society of Chemistry. (b1,b2) Reproduced with permission.<sup>[41]</sup> Copyright 2019, Springer Nature AG & Co. KGaA. (c1,c2) Reproduced with permission.<sup>[44]</sup> Copyright 2020, Elsevier.

can thus be directly utilized for gas adsorption processes in common industrially used fixed or fluidized bed reactors.<sup>[41,42]</sup> Furthermore, their larger sizes compared to NPs also enable a better incorporation without aggregation into filters and a longer sustainment in those.<sup>[43]</sup>

Ko et al., for example, presented SPs consisting of silica cores and gold NP satellites, which are ideal for the coating of air filter fibers due to their size around 400 nm (Figure 2a), and proved an additional antibacterial activity of these coated filters (Figure 2a2).<sup>[43]</sup> For CO<sub>2</sub> capture, MgO SPs were developed providing a large active surface area due to their inner structure and rough surface. Coated with a thin layer of alkali metal salts, they showed a rapid sorption rate and high sorption capacity.<sup>[40]</sup> Rong et al. created a very pioneering liquid–solid SP by the assembly of hydrophobic silica NPs around a liquid marble (Figure 2b1), which contained hydrophilic silica NPs assembled with a liquid CO<sub>2</sub> adsorbing amine. This system exhibited a very high sorption capacity and rate, as well as long-term stability with reduced amine loss in fixed bed reactors (Figure 2b2).<sup>[41]</sup> Another SP system addresses the pollution of air by electromagnetic waves, which are emitted by electronic devices and harm human health.<sup>[44]</sup> Carbon-coated iron oxide NPs (Fe<sub>3</sub>O<sub>4</sub>@C) assembled into larger entities efficiently absorb these waves due to their supraparticulate structure (Figure 2c).<sup>[44]</sup>

These few examples impressively demonstrate the potential of SPs for the development of improved air purification systems due to their advantageous size range and high surface area.

**Water:** Along with unpolluted air, safe and clean water is mandatory for humankind. It is the origin of life and covers around 70% of the earth's surface. However, only a very small fraction (0.04%) is accessible for use. Thus, scarcity of clean water is highlighted as one of the biggest challenges of this century.<sup>[45]</sup> Besides the impact of climate change, inefficient water management, increasing demand, and increasing pollution are accelerating water shortage.<sup>[46]</sup> Typical, harmful pollutants are specific organic constituents (e.g., pesticides, dyes, pharmaceuticals), heavy metals (e.g., arsenic, lead), high salinity, pathogenic microorganisms and biomolecules, high turbidity from inorganic matter, or a combination of these.<sup>[47]</sup>

The diversity of pollutants, combined with substantial local differences of water quality across the world, e.g., hardness and alkalinity, makes the purification of water particularly challenging. In order to tackle this, flaws of existing treatment technologies have to be discovered and novel approaches must be developed. More sustainable water purification technologies require a focus not only on improved efficiency but also on other aspects such as a reduced use of primary resources (land, infrastructure), reusability, recyclability, scalability or low costs. Hereafter, we will discuss different important subcategories of water purification technologies: recognition (sensors), disinfection, and decontamination.

Following the goal to detect harmful contaminants in water, the ability to detect water pollution has improved with technological advances,<sup>[48]</sup> resulting in a broad range of sensors with various signal outputs and application sites within the

distribution systems.<sup>[24,49]</sup> Water quality monitoring has evolved manual, off-line control in laboratories to modern online or inline sensors connected via Wi-Fi.<sup>[50]</sup> The benefits of these novel techniques are a reduction of analysis time and costs, as well as a greatly increased detection rate enabling real-time water control.<sup>[51]</sup> The implementation of these techniques, however, still has to overcome some barriers. Hence, off-line chromatographic and spectroscopic methods for organic and inorganic chemicals remain the golden standard for water quality monitoring for now.<sup>[52]</sup>

Nanotechnology-enabled sensors can significantly contribute to the aforementioned transition not only by replacing many existing water quality sensors but also by enabling widespread low-cost measurements over the entire distribution system.<sup>[49]</sup> This may for instance permit continuous monitoring based on small-scale sensors connected to the Internet of Things.<sup>[53]</sup> Additionally, nanomaterial-based sensors potentially lead to rapid analysis times and particularly low detection limits enabling the treatment of previously untreatable contaminations.

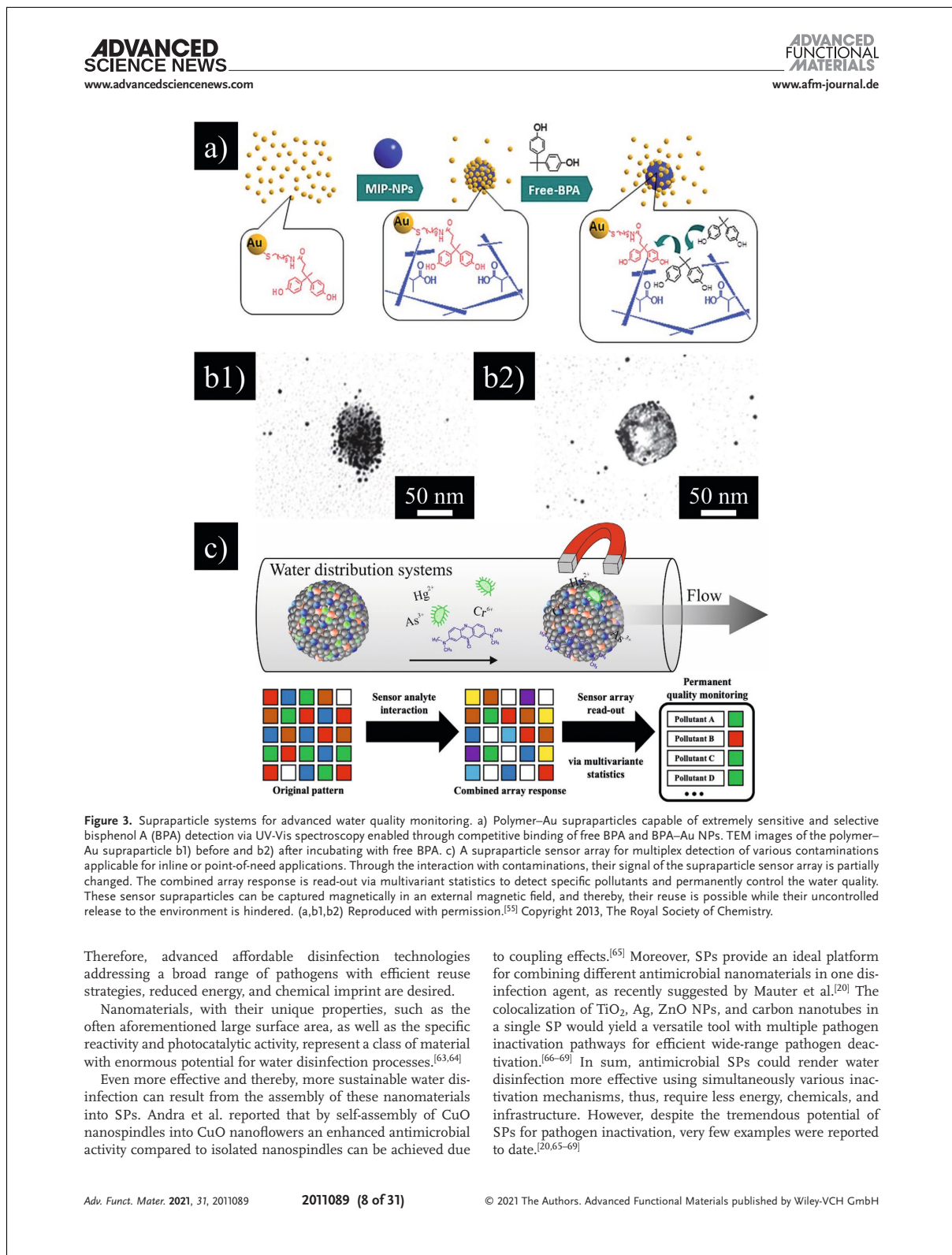
Although nanosensors have already expanded the horizon of existing technology, we believe that the use of SPs may enable even more sustainable water quality management. Therefore, we highlight some examples of these SP systems in the following section. Plastics are nowadays present in all field of our daily routine. However, there is a growing concern about their release of small toxic molecules, such as Bisphenol A.<sup>[54]</sup> Uchida et al. designed one promising localized-surface-plasmon-resonance-based SP sensor for the detection of this compound.<sup>[55]</sup> The SP consists of a polymer NP together with Bisphenol A-modified gold satellite NPs (Figure 3a). While the SP core exhibits imprinted cavities for selective binding of Bisphenol A, the gold NPs act as a signal transducer and due to this core-shell interaction, a new sensor functionality emerges. Whenever free Bisphenol A molecules are present, they competitively bind to the cavities and replace the gold NPs. This results in the disassembly of the SP (Figure 3b) and thus, a signal change is detectable by simple UV-Vis measurements instead of commonly applied enzyme-linked immunosorbent assays. These SPs show outstanding selectivity and enhance the previously reported sensitivity of bulk polymer sensors by a factor of 120 000.<sup>[55]</sup> Besides introducing new detection pathways, SPs provide an ideal platform to combine multiple functionalities within one complex entity and thereby, improve water sensor performance. Inline nanosensors have the ultimate advantage of continuous surveillance of the water quality due to permanent interaction with the analyte.<sup>[56]</sup> However, large quantities of sensors are required for sufficient signal intensity and the release of nanosensor materials into the distribution system must be avoided.<sup>[57]</sup> To overcome this issue, Wehner et al. used the colocalization of two functional building blocks, a superparamagnetic Fe<sub>3</sub>O<sub>4</sub>/SiO<sub>2</sub> SP core and different luminescent lanthanide-containing metal-organic frameworks (MOFs) as the shell.<sup>[58]</sup> Thereby, target substances can be detected by read-out of the luminescence signal of the MOF-based shell. The magnetic core enables the collection of the MOF@SPs by an external magnetic field and thus, achieves a strong increase of the luminescence signal, while avoiding water pollution due to sensor material release.<sup>[58]</sup> Similarly, Kim et al. proposed a wash-free sandwich immunoassay using the interaction of

magnetic iron oxide and photoluminescent ZnS:Mn SPs.<sup>[35]</sup> By luminescent detection of the target substance and magnetic harvesting of the sensor particles, they provide a cost-effective method with high sensitivity, specificity, and good reproducibility without time-consuming signal amplification steps. Furthermore, this system is capable of multiplex detection by simply adding a second photoluminescent Cd-doped ZnS SP.<sup>[35]</sup> Besides continuous surveillance of water quality within the distribution system by inline sensor technology, there is an increasing interest in developing analysis methods for the detection of pollutions in remote areas.<sup>[49,57]</sup> To develop simple, portable, and low-cost technologies for bioanalysis, smartphone-based solutions are an emerging platform.<sup>[59]</sup> Tran et al. recently presented a smartphone-based imaging platform for selective cell isolation and quantification and claimed that this technology may also serve as tool for pathogen detection.<sup>[60]</sup> The key to this technology is an SP system consisting of magnetic iron oxide NPs as core surrounded by photoluminescent quantum dots. The magnetic core enables the isolation of the target for a smartphone-based detection of the optical properties of the SPs.<sup>[60]</sup> Considering the increasing number of identified harmful contaminants in water, water quality monitoring should focus on multiplex detection of pollutants by semiselective methods like pattern recognition.<sup>[48,61]</sup> Thereby, selective analyte recognition is achieved through the interaction of an analyte with a sensor array. Subsequently, the combined response is assessed utilizing multivariate statistics resulting in a target selective sensor signal.<sup>[61]</sup> The development of an SP sensor array based on the colocalization of various selective nanosensors and magnetic NPs would generate a powerful tool for inline and point-of-use water quality monitoring (Figure 3c). This SP could be captured magnetically for signal augmentation and would enable a simultaneous detection of a broad range of harmful and toxic water contaminants, e.g., heavy metal ions, pathogens, and organic pollutants.

The aforementioned systems exemplarily show that SPs have a high potential to contribute significantly to the future of water quality control. They could increase the selectivity and sensitivity of existing sensors, which enables the identification of previously unrecognizable pollutants. Additionally, SPs could facilitate new detection pathways and allow for multiplex detection of contaminants.

The logical consequence of increasing industrial and urban water pollution, as well as the rising global population, is a decreasing available fraction of freshwater per person. In order to fight the accelerating scarcity of usable water, amplified reuse and recycling of wastewater is without alternatives. Besides improved water quality control, this requires advanced purification, i.e., disinfection technologies.

Despite the large improvement in water disinfection technology during the last century, pathogen-contaminated water remains the main cause for waterborne illnesses, particularly in developing countries. The current disinfection technology is based on multiple chemical disinfection steps using chlorine or chloramine and additional germicidal ozone or UV treatments to widen the range of pathogen deactivation.<sup>[61]</sup> Along with growing concerns about toxic byproducts formed during halogenated disinfection processes, these methods are chemical-, as well as energy-intensive and require extensive infrastructure.<sup>[62]</sup>



Besides the ever-present problem of pathogens, human-derived pollutants in water, such as pesticides, dyes, and pharmaceuticals, have a detrimental effect on human health and ecosystems.<sup>[70]</sup> Current water decontamination processes include physicochemical separation (adsorption, membrane filtration, and chemical precipitation or coagulation) and chemical oxidation through reactive radicals produced in advanced oxidation processes. These conventional treatment methods lack effectiveness and selectivity, remain chemical- and energy-intensive, and generate harmful chemical byproducts, as well as waste, which requires additional treatment steps, and thus, causing extra costs.<sup>[20,71]</sup> Therefore, new technologies are demanded that increase cost efficiency, enhance selectivity toward key trace pollutants, require fewer chemicals and less energy while enabling different application areas.

Nanoadsorbents gained tremendous interest as they offer significant improvements over conventional ones, mainly due to their high specific surface area, as it has already been mentioned before, which leads to a high adsorption capacity. Their tunable pore size and their functional surface chemistry enables selective and target specific adsorption of, e.g., toxic heavy metal ions or herbicides.<sup>[64,72]</sup> Driven by the extensive research effort in this field, nanomaterials with impressive adsorption capacity and highly effective catalytic degradation of pollutants have been developed, to date.

However, through the combination of various NPs in one SP decontamination agent the performance, applicability and sustainability of treatment processes to real water matrices are likely to be further improved.<sup>[20,47,73]</sup> Numerous SPs for wastewater decontamination were developed that use enhanced catalytic properties or smart combinations of catalytic and other functional building blocks. As catalysis is a very broad topic, we have devoted Section 2.2.2 of its own to it, where systems and performance for this purpose are described in more detail. For the design of advanced adsorbent systems, many SPs combine magnetic NPs with other nanomaterials: Sylvester et al. proficiently incorporated small iron oxide NPs into durable highly porous polymer microbeads.<sup>[74]</sup> These hybrid SPs combine the excellent handling, flow characteristics, and attrition resistance of conventional ion exchange materials with the outstanding affinity of iron oxide NPs for arsenic. Furthermore, several researchers combined the magnetic properties of iron oxide with highly effective adsorbent materials, like zeolitic frameworks<sup>[75]</sup> or carbon-based nanomaterials,<sup>[76]</sup> to enable their recovery and reusability. These SPs can be used for efficient decontamination of wastewater from toxic, volatile organic compounds,<sup>[77]</sup> heavy metal ions,<sup>[78]</sup> and dyes.<sup>[79]</sup> To enhance the sustainability of these systems, such compounds can be synthesized via upcycling of agricultural or household waste, like tea waste, and therefore, might be cost-effective adsorbents of the future.<sup>[80]</sup> After successful magnetic harvesting of adsorbents, multiple regeneration pathways for adsorbents have been proposed. Besides extracting the agents and subsequent reactivation via washing procedures or energy-intensive thermal treatment, additional building blocks are utilized to create more practical and sustainable regeneration methods. For instance, carbon coatings or NPs facilitate effective in situ electrocatalytic or electrochemical regeneration.<sup>[81,82]</sup> For electrocatalytic denitrification of lake water, Su et al. prepared carbon-coated Fe<sub>3</sub>O<sub>4</sub>

SPs via self-assembly of oleic acid capped iron oxide NPs with subsequent carbonization (Figure 4a1).<sup>[81]</sup> Thereby, a hierarchical structure of Fe<sub>3</sub>O<sub>4</sub> NPs with a rough carbon surface was obtained (Figure 4a2). As a result, these SPs achieved an excellent removal capacity for nitrate (Figure 4a3). Furthermore, the rough carbon surface allowed the electrocatalytic conversion of adsorbed NO<sub>3</sub><sup>-</sup> to N<sub>2</sub> and NH<sub>4</sub><sup>+</sup>. Besides recovery granted by colocalization of magnetic NPs and adsorbents, the assembly of NPs to hierarchically structured, porous SPs leads to significant improvements in adsorption capacity and kinetics.<sup>[83]</sup> Oppmann et al. designed reusable SPs from iron oxide and silica NPs that show a capillary effect due to emergence of the nano building blocks taking up dye from wastewater within 1 min (Figure 4b).<sup>[84]</sup> By tuning the size of the used silica NPs from 100 to 10 nm the equilibrium time and adsorption capacity can be tailored toward a specific application. Even more sustainable water treatment results from processes designed not only for extraction of contaminants but also for recovery and reuse of valuable substances.<sup>[85]</sup> In this context, nanoporous sorbents and SPs<sup>[86]</sup> may provide a smart answer to remove target substances, like phosphate, from water, as recently reviewed by Othman et al.<sup>[87]</sup> Furthermore, the removal and recovery of heavy metal ions using SPs consisting of superparamagnetic iron oxide NPs confined in a silica matrix has been shown.<sup>[88]</sup> The captured target substances can be desorbed and enriched in an acidic solution, and thereby, the SPs are regenerated. Adding layered double hydroxide ion exchangers to the above-described SP system, phosphate ions are efficiently adsorbed and magnetically recollected from municipal wastewater in laboratory to pilot-scale applications.<sup>[89]</sup> To close the loop, the captured phosphate was successfully transformed into struvite, a solid fertilizer product.

As a brief summary of this section, SPs provide a versatile platform (Figure 4c) to render water disinfection and decontamination processes more sustainable by improving their efficiency while reducing chemicals and energy consumption. They further grant novel pathways to provide clean and safe water. Additionally, SPs can be a tool to recover substances from wastewater and keep resources in circulation.

### 2.1.2. Agricultural Delivery Systems

While the preservation of clean air and water definitely is the basis for the long existence of humankind, one should not forget that the provision of food is of the same importance. As nowadays large parts of it are provided to us by agriculture, this section will focus on the potential contribution of SPs to a sustainable agriculture. In this context, sustainability can be understood as the seek for yield increase with the help of biocides, herbicides or fertilizers while trying not to compromise the cleanliness of soil, groundwater, and crop. An approach to address this challenge are delivery systems that provide the needed substance over long term with controlled release rates and minimized uncontrolled dissipation.

Concerning current material solutions, NP-based systems have already been reported by several groups to be applied as biocide, herbicide or fertilizer delivery systems. They have structural advantages like large surface areas, modifiable surface and

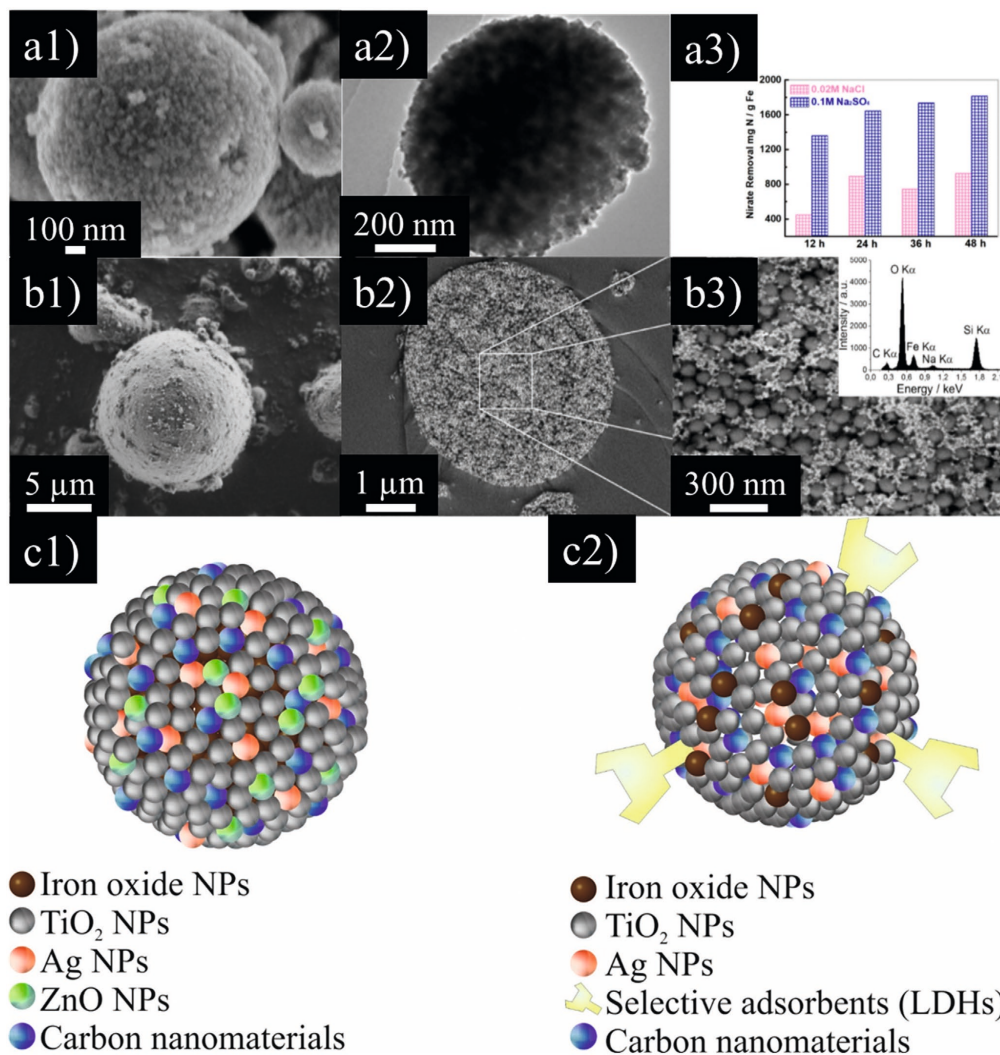


**Figure 4.** Supraparticles for advanced water disinfection and decontamination. a1) SEM and a2) TEM images of carbon-coated iron oxide supraparticles for electrocatalytic denitrification of water. a3) These supraparticles achieved a nitrate removal capacity of up to 1816 mg N g<sup>-1</sup> Fe in 0.1 M Na<sub>2</sub>SO<sub>4</sub> system in 100 mg L<sup>-1</sup> nitrate solution within 48 h. SEM images of raspberry-like iron oxide silica supraparticles for rapid and efficient dye uptake: b1) detail, b2) cross-section, b3) cross-section detail, and EDX measurement (inset). c1) Supraparticle consisting of colocalized antimicrobial building blocks, e.g. TiO<sub>2</sub>, Ag, ZnO NPs and carbon nanomaterials, as shell and iron oxide nanoparticles as their core for wide-range pathogen deactivation and magnetic recovery; c2) multifunctional magnetic supraparticle for simultaneous disinfection and decontamination to provide safe and clean water in a one-step process that allows for inline and point-of-use water treatment. Such a supraparticle may consist of TiO<sub>2</sub>, Ag, and iron oxide NPs, as well as selective adsorbents, e.g., layered double hydroxides (LDHs) and CNTs. (a1–a3) Reproduced with permission.<sup>[81]</sup> Copyright 2019, American Chemical Society. (b1–b3) Reproduced with permission.<sup>[84]</sup> Copyright 2018, Wiley-VCH GmbH & Co. KGaA.

stability, and thus superior loading capacity. For example, Gao et al.<sup>[90]</sup> showed that mesoporous organosilica NPs used for pesticide delivery, have a longer *Sclerotinia* disease protection

window on plants, which provides a solution for precisely managing plant disease and farming. Appell et al. also concluded that nanomaterials can deliver bioactive substances directly to

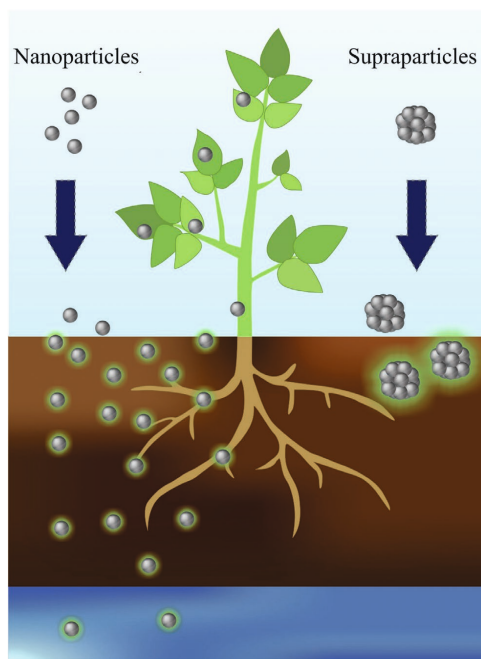


**Figure 5.** Supraparticle as an efficient means to decrease the accumulation in soil, plants or groundwater of nanomaterials, which are used as delivery systems.

target points through controlled release and thus, can reduce the use of agrochemicals.<sup>[91]</sup>

However, over the years, concerns arose about the bioaccumulation of nanomaterials in soil and groundwater and about the resulting unwanted uptake of potentially toxic NPs by humans. This consequently limited their use as agricultural delivery systems.<sup>[92]</sup> Furthermore, NPs are easily taken up by plants and therefore, may even contaminate human food sources.<sup>[93]</sup> Health concerns<sup>[94]</sup> surely not only restrict the application of NPs in agriculture but also in most of the other fields discussed in this review article. The use of SPs, providing larger particle sizes (typically in the microscale), may help to overcome these worries. The handling of any powders containing NPs within SPs reduces dust formation being thus easier and safer.<sup>[95]</sup> Furthermore, SPs are unlikely to cross most biological barriers and are not taken up by most cell types reducing their health hazard.<sup>[96]</sup>

This is also why the use of SPs, as assemblies of NPs, for agricultural delivery systems has a high potential: they still provide the advantages of nanomaterials while increasing the particle size for a safer handling and less material dissipation (Figure 5). A pioneering example of SPs for agricultural delivery systems was presented by Mattos et al.<sup>[97]</sup> Millimetric scaled SPs were assembled by biogenic silica particles and cellulose nanofibrils. Compared to NPs, SPs presented lower mobility,

which is associated with the size, and higher UV protection, as the “external” surface area-to-bulk ratio is decreased. Another example regarding the superior properties of SPs was reported by Xie et al. They designed a superhydrophobic biopolymer-coated slow-release fertilizer through self-assembly, which showed extended slow-release longevity (100 days more than unmodified ones) and superior durability in soil environment.<sup>[98]</sup> Additionally, SPs possess a high loading capacity due to their high porosity (emergence) and thus, higher delivery efficiency compared to NP delivery systems.<sup>[99]</sup>

It is also noteworthy that while most other of the SP-based delivery systems found in literature so far are used for medical purposes, their working principle may easily be transferred to agricultural purposes. For instance, Wang et al. investigated mesoporous silica SPs for innerear drug delivery and demonstrated that the concept of using these SPs as carriers is transferable to other delivery systems.<sup>[99]</sup> The creation of SPs may enable the triggered release of substances by blocking the guest-molecule carrying pores of a porous particle with removable NPs. Zhu et al. summarized various controlled-release delivery systems based on mesoporous silica materials and nanoparticulate gatekeepers, working via pH-response, ATP, as well as glutathione- and H<sub>2</sub>O<sub>2</sub>-responsive mechanisms.<sup>[100]</sup> Similar to these approaches, Torney et al. loaded a mesoporous silica NP with a gene and its chemical inducer, using gold NPs as caps of the ends, subsequently releasing the chemicals and triggering gene expression via removal of the gold NPs.<sup>[101]</sup> Also NP-raspberry-like containers were reported, which can be applied to carry and release antimicrobials in a controlled manner.<sup>[102]</sup>

All in all, SPs have a promising perspective toward sustainability in the field of agricultural delivery systems. When applied in herbicide/biocide/fertilizer delivery systems, they may help to reduce the use of agrochemicals and thus, decrease damage to water and soil. Additionally, compared to NPs, they are less likely to cause food contamination, as a result of their larger size.

## 2.2. Basic Comfort

Beyond fulfilled fundamental needs, such as clean water, life quality increases with access to (electrical) energy.

### 2.2.1. Energy Storage and Conversion

The “sustainable” generation of energy, which is the commonly used term for what is the conversion of various energy forms from the renewables wind, water, and sunlight into electrical energy, is heavily driven by materials development. In the context of electrical energy generation, SPs are not yet playing an important role. However, with regard to water and wind as energy sources, SPs may be considered as alternative design approaches for rare-earth element-free permanent magnets in the future.<sup>[103]</sup> For solar cells, SPs seem to be of interest for several types of photovoltaic technologies like perovskite or quantum dot solar cells.<sup>[104]</sup> For instance, Zhou et al. incorporated Cu<sub>9</sub>S<sub>5</sub>@SiO<sub>2</sub> SPs in a hole transport layer of a perovskite

solar cell. Besides improving the transport capacity and the electrical conductivity, the strong light scattering and reflection properties of the SPs increased the light trapping within the device, resulting in greater absorption efficiencies.<sup>[105]</sup> Especially in the field of quantum dot solar cells, where a well-defined assembly of quantum dots is an essential criterion to make use of coupling mechanisms, SPs may contribute to the ongoing process of implementing the promising theoretical capacity of the technology into well-performing photovoltaic devices.<sup>[106]</sup> A key issue in quantum dot solar cells is the extraction of photo-excited charge carriers before trapping or recombination. In order to tackle this challenge, Ojha et al. conjugated graphene sheets with SPs composed of CdS quantum dots. This coupling provided more stable excitons as well as ultrafast electron transfer from the photoexcited CdS quantum dots to the graphene sheets, leading to improved charge separation efficiencies.<sup>[107]</sup>

Since generation and usage of electrical energy are usually separated by time and location, intelligent distribution and efficient storage are key factors for a sustainable handling of energy. The further improvement of energy storage devices like batteries, supercapacitors, and fuel cells is therefore inevitable to tackle these challenges on the entire scale, from stabilizing the electric grid down to mobility topics and more sustainable portable electronic devices. In order to enhance the performance of such energy storage devices, the application of SPs has indeed attracted increasing interest in recent years.

In the versatile field of batteries, it is especially the lithium-ion technology that stands out with high energy and power densities. On top of that, the efficient conversion from electrical into chemical energy and vice versa, as well as the extremely

low self-discharge rate prevent energy dissipation and guarantee entropy conservation. However, there is still a large gap between the performance of modern lithium-ion batteries and the theoretical potential of the technology. The following section displays how SPs and their unique properties help to reduce this gap.

The electrodes, the key components of every battery, are responsible to convert electrical into chemical energy via a redox reaction accompanied by storage and release of lithium-ions. In order to have both, high energy and power densities, the active materials of the electrodes need to possess high specific capacities, as well as high ionic and electronic conductivities. On top of that, some active materials undergo significant changes in volume while storing and releasing lithium-ions, causing mechanical stress in the electrode.<sup>[108–110]</sup> In order to cope with volume changes and to allow electrolyte wetting, electrodes are commonly designed as porous layers including micrometer-sized active material particles, conductive carbon to improve the electronic conductivity and polymer binders (Figure 6a). However, active materials generally possess poor conductivities and dense micrometer-sized particles still represent long pathways for lithium-ions and electrons, which significantly limits the electrode performance. Thus, the logic step is to go down to the nanoscale, i.e., NPs, to create higher surface areas and shorter pathways (Figure 6b).<sup>[111]</sup> Furthermore, in theory nanoporous structures are able to cope better with volume changes than micrometer-sized particles that will crack under high mechanical stress.<sup>[112]</sup>

Yet, by reducing the particle size to the nanoscale, new challenges arise, including uncontrolled aggregation, increased moisture absorption, and broad particle size distributions that lead to higher demands of binder, as well as drastically

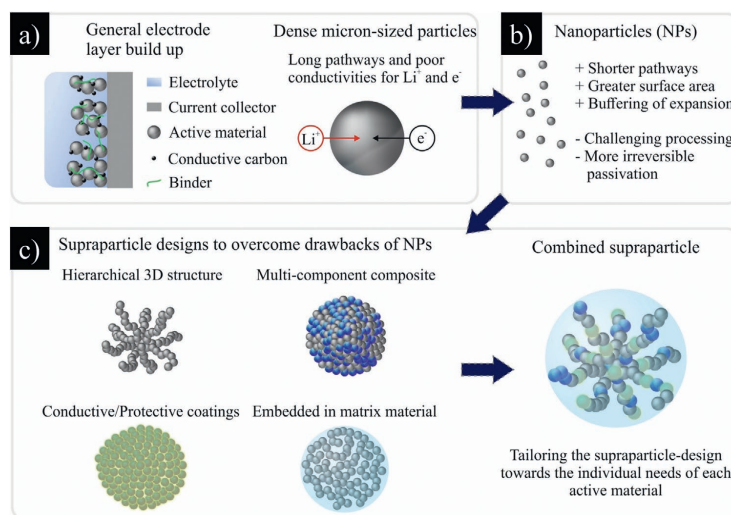


**Figure 6.** Superiority of supraparticle employment as active material in lithium-ion batteries. a) General build-up of an electrode layer and the issues of dense micrometer-sized particles. b) Nanoparticles (NPs) and the pros and cons as active material. c) Most common designs for supraparticles and the example of a supraparticle that combines various design approaches.

varying rheological properties of electrode slurries.<sup>[113]</sup> Liu et al. prepared carbon-coated NPs of the cathode material  $\text{LiFe}_{0.6}\text{Mn}_{0.4}\text{PO}_4/\text{C}$  (here: positive electrode) and compared them with SPs that were produced by spray-drying of these NPs. Besides the advantages in terms of processing, these particles exhibited an increased tap density that resulted in a significantly higher volumetric energy density.<sup>[111]</sup> On top of the processing advantages that result from this controlled colocalization, a well-defined design can greatly enhance the electrochemical properties of SPs. By spray-drying an aqueous dispersion of  $\text{LiFePO}_4$  nanorods with glucose, Yoo et al. synthesized SPs with micro- and mesopores. The combination of carbon coating and the hierarchical 3D structure lead to an outstanding performance at high current densities due to improved conductivities.<sup>[114]</sup> Two further commonly used design approaches for SPs in batteries are multicomponent composites and the embedment of the NP building blocks in a matrix material (Figure 6c). Since every active material has its unique properties, the design of the SP can be tailored toward the individual needs of each active material to overcome the specific challenges and make use of its full potential.

Lithium–sulfur batteries are promising candidates for high energy density batteries. However, the insulating nature of sulfur, volume changes during charging and discharging, as

well as the dissolution of polysulfides have represented strong limits to the technology so far.<sup>[115]</sup> Park et al. tackled these challenges by preparing graphitic carbon– $\text{TiO}_2$  composites via a pilot-scale spray-drying process.<sup>[108]</sup> After etching of embedded iron NPs, mesoporous SPs with vacancies for sulfur infiltration were obtained. The porous graphitic matrix coped well with volume changes and provided high conductivity, while the embedded  $\text{TiO}_2$  NPs were able to chemically trap polysulfides. The colocalization of these different components within one SP leads to excellent rate capability and cycle performance.<sup>[108]</sup>

While the previous examples of SPs in electrode active materials were all related to cathode materials, the potential of SPs to improve anode properties is considered to be even greater. This is a consequence of the challenges that arise due to the formation of irreversible passivation layers.<sup>[116]</sup> Since for most anode materials the lithiation and delithiation take place outside of the electrochemical stability window of the electrolyte, a passivation layer is formed during the first cycles. The formation of this so-called solid electrolyte interphase (SEI) layer consumes parts of electrolyte and active material, whereby a higher surface area of the active material leads to an increased material consumption.<sup>[117]</sup> Hence, the increased surface area of NPs represents one of the major drawbacks in terms of irreversible passivation for anode materials (Figure 7a).

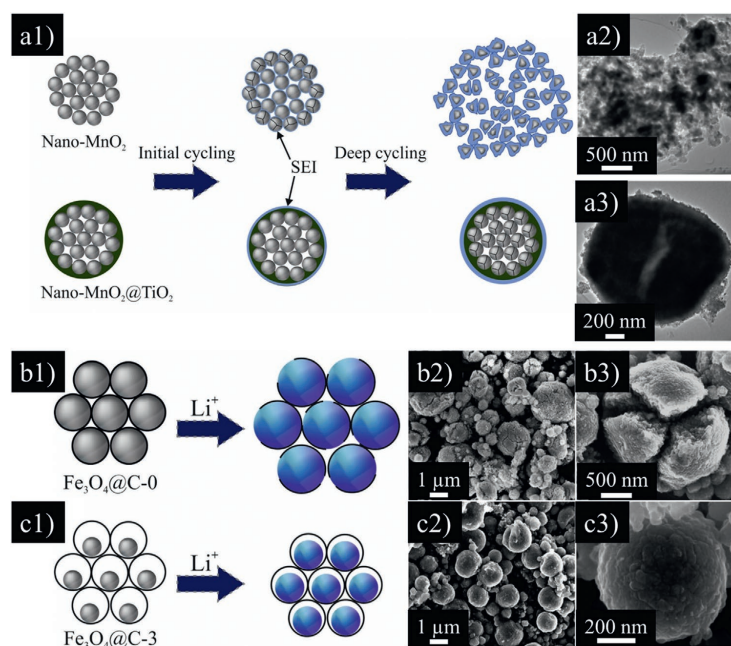


**Figure 7.** Schematic illustration of a) SEI formation on  $\text{MnO}_2$  nanoparticles compared to  $\text{nano-MnO}_2/\text{TiO}_2$  supraparticles and a2,a3) corresponding SEM images after 200 cycles. Scheme of b1) pomegranate-like arranged  $\text{Fe}_3\text{O}_4/\text{C}$  nanoparticles and the resulting breaking of the carbon coating due to lithiation, which leads to cracks in the supraparticle on the microscale, displayed by b2,b3) SEM images. Through etching, c1) time-controlled voids in the nanosized yolk-shell structure buffer the expansion, which prevents cracks in the microstructure, displayed by c2,c3) SEM images. a1–a3) and (b1–c3) Reproduced with permissions.<sup>[117,228]</sup> Copyright 2018, Elsevier.

Cao et al. approached this challenge by coating SPs consisting of MnO<sub>2</sub> NPs with TiO<sub>2</sub> NPs that prevent the direct contact of primary anode active material MnO<sub>2</sub> with the electrolyte. The SEI layer (Figure 7a1) formed on the surface of these micrometer-sized SPs and grew only slightly in diameter after deep cycling, while single MnO<sub>2</sub> NPs possessed a thick passivation layer, which resulted in significant loss of capacity.<sup>[117]</sup>

A very similar observation was made by Lee et al. for Fe<sub>2</sub>O<sub>3</sub> NPs as anode material, where the geometric confinement of the nanosized building blocks in SPs improved the cycle stability and rate capability.<sup>[118]</sup> However, even as NP-based material, Fe<sub>2</sub>O<sub>3</sub> suffers from volume changes during lithiation and de-lithiation. Resulting cracks due to mechanical stress in the microstructure expose fresh active material surfaces (Figure 7b), which are consequently passivated leading to more loss of capacity.<sup>[109]</sup> Han et al. tackled this challenge by fabricating a pomegranate-like SP consisting of yolk-shell Fe<sub>2</sub>O<sub>3</sub>@C NPs. The well-defined void in the nanosized yolk-shell structure (Figure 7c) allows a buffering of the volume changes to prevent cracking of the microsphere.<sup>[119]</sup>

Further approaches to overcome the drawbacks of Fe<sub>2</sub>O<sub>3</sub> NPs through adjusted SP designs include the embedment into a graphene matrix<sup>[120]</sup> as well as the work of Xiong et al., who prepared hollow composite microspheres consisting of Fe<sub>2</sub>O<sub>3</sub> NPs and a crossing net of carbon nanotubes that stabilized these SPs during volume changes.<sup>[121]</sup>

While most commercial lithium-ion batteries still rely on graphite as anode material, the next generation is proposed to be a composite of graphite and silicon NPs due to the outstanding specific capacity of ≈3580 mAh g<sup>-1</sup> for silicon, which is about ten times higher than graphite.<sup>[122]</sup> However, most of the previously discussed challenges for anode materials like volume changes and irreversible passivation are present for silicon as well, and even on a larger scale. In case of full lithiation, silicon undergoes a change in volume of up to 300%.<sup>[110,112]</sup> The reoccurring cracks cause increasing passivation and consumption of the active material, which is why a short cycle life is the main issue for silicon. A large number of different SP designs have been reported to overcome these major drawbacks of silicon. Most common are various forms of hierarchical composites containing carbon-coated silicon NPs and carbon nanorods,<sup>[123]</sup> often relying on spray-drying as the processing method of choice.<sup>[116,124]</sup> To provide an easy conception of the 3D structure, these SPs are sometimes described as raspberry-like,<sup>[125]</sup> pomegranate-like,<sup>[126]</sup> or watermelon-inspired.<sup>[127]</sup> One major advantage of silicon is its extensive abundance. In light of sustainability, the work of Zhang et al. stands out due to its unique way of producing silicon NPs out of rice husk, a common high output agricultural waste.<sup>[128]</sup> SPs containing these low-cost silicon NPs as well as carbon nanotubes showed remarkable electrochemical performance.

SPs have also been reported for more exotic anode active materials like micrometer-sized assemblies of ZnS/CoS/CoS<sub>2</sub>@N-doped NPs,<sup>[129]</sup> spray-dried mesoporous mixed Cu-Ni-oxide@graphene nanocomposites,<sup>[130]</sup> and nanoporous TiNb<sub>2</sub>O<sub>7</sub>/C composite microspheres.<sup>[131]</sup> Closely related to the lithium-ion technology are sodium-ion batteries that generally possess lower energy densities. However, the availability of sodium is much greater than that of lithium, where natural

reservoirs are limited. Therefore, the sodium ion technology is expected to play a crucial role for sustainable energy storage systems in the future.<sup>[132,133]</sup> Due to similar physicochemical characteristics of sodium and lithium, most of the main challenges in sodium ion batteries are analog to the herein described issues with lithium-ion batteries, like low conductivities of active materials, as well as volume expansion and the resulting increasing SEI formation on anodes. Hence, the potential that SPs offer to improve this type of battery is comparable to the lithium ion technology. With regard to cathode materials, Shan et al., for instance, produced SPs consisting of Na<sub>4</sub>Mn<sub>9</sub>O<sub>18</sub> rods, carbon nanotubes, and reduced graphene oxide via spray-drying. Via this SP approach, the system exhibited significantly improved conductivities.<sup>[133]</sup> Similar beneficial aspects, leading to enhanced cycle life and rate performance, could be observed for graphene-scaffolded Na<sub>2</sub>V<sub>3</sub>(PO<sub>4</sub>)<sub>3</sub> SPs.<sup>[134]</sup> In order to cope with volume changes at the anode, SPs that are described as hollow microspheres were reported as promising candidates. For example, Choi et al. prepared hollow SeFe<sub>2</sub>/graphitic carbon spheres with interconnected multicavities,<sup>[135]</sup> whereas Xie et al. synthesized hollow SPs consisting of carbon coated Na<sub>2</sub>Ti<sub>3</sub>O<sub>7</sub> rods.<sup>[136]</sup> Alternatively, Kim et al. reported metal sulfide/carbon composite SPs that were synthesized via spray-pyrolysis with NaCl NPs as templates to obtain cubic nanocavities in the final SPs. In case of MoS<sub>2</sub>/C these particles showed good rate performance and delivered high reversible capacity.<sup>[137]</sup>

As mentioned at the beginning of this section, next to batteries, also supercapacitors and fuel cells play an important role regarding energy storage devices. Supercapacitors have a key function whenever the required power densities exceed the capabilities of batteries. Compared to batteries, SPs have only been reported on few occasions in this field of research. However, these cases are good examples of how SPs can improve certain characteristics, like energy density<sup>[138]</sup> or conductivities of active materials.<sup>[139]</sup> For instance, Yan et al. prepared double-layered yolk-shell SPs where NiCo<sub>2</sub>S<sub>4</sub>-Ni<sub>9</sub>S<sub>8</sub> NPs are embedded into an amorphous carbon matrix<sup>[140]</sup> and Jeyaranjan et al. reported ternary scalable hierarchical microspheres composed of polyaniline nanofibers, reduced graphene oxide and cerium oxide nanorods with significantly improved reversibility of the pseudocapacitive characteristics leading to a greatly extended cycle life.<sup>[141]</sup>

With regard to fuel cells, SPs can play a key role in the fields of hydrogen production and oxygen evolution reaction.<sup>[142]</sup> Similar to supercapacitors, SPs in fuel cells have not been part of extensive research yet, but several examples can be found that underline the future potential of SPs for the technology.<sup>[143,144]</sup> The improved catalytic properties of these SPs, that are decisive for their application in fuel cells, will be covered in the following section.

### 2.2.2. Catalysis

In order to use energy in a sustainable way, it is necessary to develop more efficient approaches to convert and to store energy, but also to reduce the consumption of energy for certain chemical/physical processes. The efficiency of such a process can be seen as a measure for its sustainability, taking factors

like reaction rate, required amount of energy and chemicals, selectivity, and yield into account. All these factors are affected by materials that exhibit catalytic activity. The catalysis process itself describes the acceleration of a chemical/physical reaction by reducing the energy barrier the educts must overcome to form a product in a lower energy state.<sup>[145]</sup>

Nowadays, the chemical industry, as one of the biggest energy-consuming branches, takes our society above “basic human needs” to a higher level of comfort. Thus, the use of catalysts in industrial chemistry is stringently required heading toward a more sustainable society. Furthermore, most industrial established reactions rely on the use of catalysts to be economically feasible.<sup>[146]</sup> In the last years of the 20th century Anastas et al. already introduced the term “green chemistry” summing up 12 requirements for sustainable energy development in this industrial field.<sup>[147]</sup> The most relevant requirements regarding catalysis are energy efficiency, employment of less toxic chemicals, waste prevention and the use of renewable raw materials (in this case catalysts).<sup>[148]</sup> More than two decades later, the urge to shift the development toward sustainability became even larger due to the aggravating global climate crisis. This underlines the research efforts to develop new efficient catalytic materials.

Today, around 80% of economically important chemical reactions involve heterogeneous catalysis.<sup>[149]</sup> In this case, the catalyst itself acts in another phase than the reactants of the catalyzed reaction, e.g., liquid reactants with solid catalyst. In contrast to homogeneous catalysis, the heterogeneous approach brings along advantages like simple removal of the catalyst, efficient recovery, as well as high control over the material structure and properties itself.<sup>[150]</sup> One field of intense research effort in heterogeneous catalysis are NPs. Due to the possibility to precisely control size, as well as structure achieving a high surface area and due to the broad range of available materials, NPs exhibit excellent potential in catalytic applications. Still, there are several problems related to their use. The removal of NPs from reactions is usually rather complicated and they tend to agglomerate due to their high surface energy, which deteriorates their efficiency. Furthermore, they exhibit size-dependent physical, biological, and environmental dangers.<sup>[151]</sup> The assembly of individual NPs into SPs targets to overcome most of these disadvantages. Further, by confining the particles to distinct entities, new properties can arise due to their coupling.<sup>[152]</sup> One should mention in this context that NP deposition on a micrometer-sized support, which has already been used in catalysis for decades, cannot be considered as SP fabrication as usually no cooperative interplay between two components and no organized structure are achieved.<sup>[149]</sup> The phenomenon emergence is also crucial for the application of SPs in catalysis as it describes their inner porosity yielding high surface areas and controlled particle morphologies. Dependent of the resulting SP structure (dense, hollow, hierarchical porous, composite nanostructured) the performance of the catalyst is thus directly influenced.<sup>[149]</sup> However, this has been recently excellently reviewed by Gradon et al.<sup>[149]</sup> focusing on how to precisely control the structure and morphology of SPs in aerosol-based assembly methods aiming for new catalytic materials and will thus not be discussed in detail herein. Another recently released review article by Hou et al. outlined

different methods to create SPs for various catalytic fields.<sup>[153]</sup> This is why in the following, we only outline a few examples of systems that are of particular importance in light of sustainability.

As already noted, energy conversion systems particularly rely on the efficiency of involved chemical or physical reactions. In fuel cell applications, reactions like hydrogen evolution, oxygen evolution reaction, and oxygen reduction reaction play a crucial role.<sup>[142]</sup> Electrocatalytically active SPs can greatly affect those reactions. Ro et al. designed efficient electrocatalytically active SPs made of bimetallic Pt/Ni NPs loaded on  $\text{Fe}_3\text{O}_4/\text{SiO}_2$ .<sup>[143]</sup> The SPs featured efficient  $\text{H}_2$  production up to over 96% of the theoretically estimated value by converting  $\text{NaBH}_4$  into hydrogen. Their catalytic activity was comparable to these of the single NPs. Using bimetallic Pt/Ni NPs as catalytic species in the SPs reduced the amount of needed noble metal while maintaining a sufficient catalytic activity (Figure 8a). In sight of their magnetic properties, the SPs could be easily recycled by exploiting the colocalization properties of the single entities. Thus, multiple cycles were performed to test the stability and recyclability. The SPs showed less than 25%  $\text{H}_2$  conversion after 5 cycles due to aggregation of the surface NPs. Therefore, an additional  $\text{TiO}_2$  shell was added for the protection of the loaded Pt/Ni NPs leading to an enhanced stability with a  $\text{H}_2$  conversion of 94% after 5 cycles.<sup>[143]</sup> In proton exchange membrane fuel cells electrocatalysts with high efficiency are needed. Porous Pt/C SPs with a 3D pore network and high Pt loading were fabricated to enhance the catalytic activity. The electrochemical characterization showed that the high surface area and the Pt distribution inside the network increased the electrocatalytic performance of the SPs beyond those of the single materials.<sup>[144]</sup>

Another elegant strategy to produce a sustainable energy source is photocatalytic hydrogen evolution (PHE).<sup>[154,155]</sup> Recently, Li et al. developed  $\text{CoFe}_2\text{O}_4/\text{ZnIn}_2\text{S}_4$  SPs that exhibit efficient PHE up to  $800 \mu\text{mol h}^{-1} \text{g}^{-1}$ .<sup>[154]</sup> This was achieved by creating a p–n junction on the individual particles due to the combination of p-type  $\text{CoFe}_2\text{O}_4$  NPs and n-type  $\text{ZnIn}_2\text{S}_4$  microparticles. The PHE performance of these SPs was superior in comparison to the single particles. Because of the increased light absorption and the effective charge carrier separation at the p–n junction (due to coupling effects within the SPs), the particles were also used as efficient photodegradation agents for decomposing organic volatile compounds in water. Furthermore, the  $\text{CoFe}_2\text{O}_4/\text{ZnIn}_2\text{S}_4$  SPs exhibited excellent photostability and recyclability up to 5 cycles for PHE and photodegradation.<sup>[154]</sup>

As mentioned above, photocatalytic reactions can not only support energy storage and conversion but also greatly influence water purification by decomposing pollutants, i.e., dyes, volatiles or toxic chemicals. Herein, the catalytic reaction is based on the absorption and use of sunlight's energy, which is one of the main sustainable energy sources for humankind. Many materials are already known, that exhibit photocatalytic properties, i.e.,  $\text{ZnO}$ ,<sup>[156]</sup>  $\text{NiO}$ ,<sup>[156]</sup> carbon-based materials,<sup>[157]</sup>  $\text{Fe}_3\text{O}_4$ ,<sup>[158]</sup> or  $\text{Bi}_2\text{MoO}_6$ ,<sup>[159]</sup> and  $\text{BiVO}_4$ .<sup>[160]</sup> A well-established photocatalyst among these is titanium dioxide ( $\text{TiO}_2$ ).<sup>[156,161,162,163]</sup> Due to its wide bandgap, it is well suited for the absorption of solar light. The active surface area of catalytic materials is an important

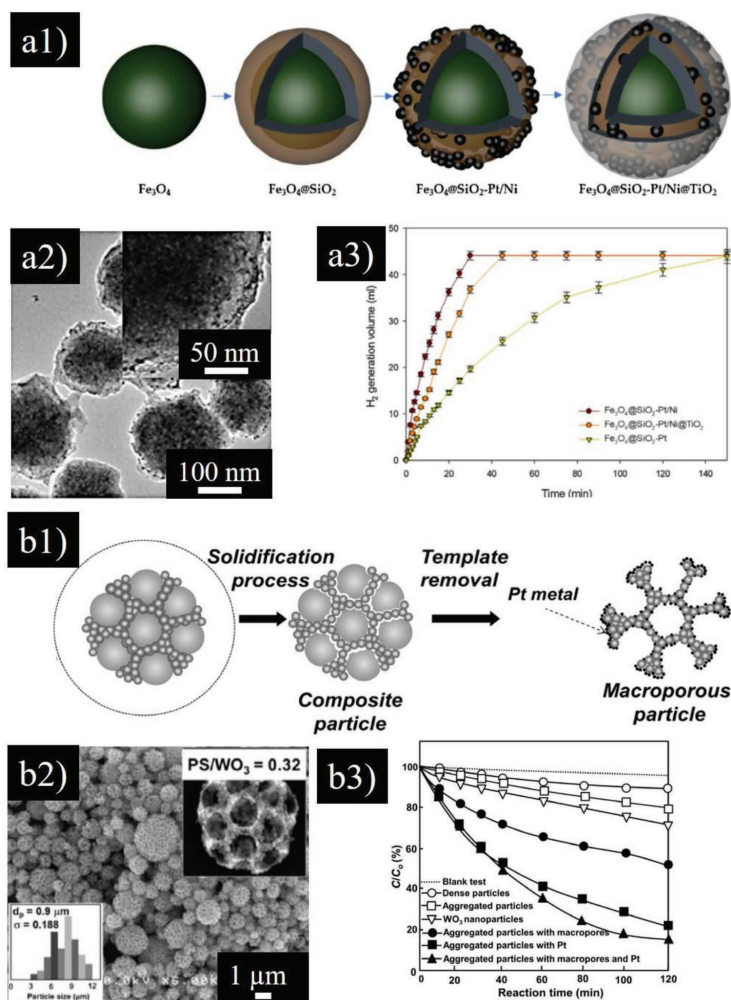


**Figure 8.** a1) Particle design scheme of  $\text{Fe}_3\text{O}_4@SiO_2-Pt/Ni@TiO_2$  supraparticles and a2) the corresponding TEM images. a3) Catalytic  $H_2$  gas generation from 0.05 M  $\text{NaBH}_4$  solution with 1 wt% Pt/Ni modified supraparticles. b1) Supraparticle formation process of macroporous Pt-modified  $\text{WO}_3$  supraparticles via template removal. b2) Exemplary SEM images of spray-dried particles with a PS/ $\text{WO}_3$  ratio of 0.32 after template removal and the resulting particle size distribution. b3) Photocatalytic activity shown in photodegradation profiles of rhodamine B of different particle designs. (a1–a3) Adapted with permission.<sup>[143]</sup> Copyright 2019, Elsevier. (b1–b3) Reproduced with permission.<sup>[166]</sup> Copyright 2015, American Chemical Society.

factor influencing its reactivity and efficiency. In order to increase the available catalytic surface,  $\text{TiO}_2$  NPs in combination with polystyrene NPs were used as precursor materials for highly porous  $\text{TiO}_2$  SPs. Liu et al. synthesized porous  $\text{TiO}_2$  SPs by a surface-mediated fabrication method and subsequent removal of polystyrene and used these structures as catalysts for photodegradation of rhodamine B.<sup>[164]</sup> The precise control of pore size and distribution throughout the SPs enables a

photocatalytic activity comparable to single NPs while allowing easy removal from the treated solution.<sup>[162]</sup> This improvement in catalytic behavior can be ascribed to the emergence property of the synthesized SPs. A similar approach was conducted with  $\text{WO}_3$  as photocatalyst (Figure 8b).<sup>[165,166]</sup> By adding Pt NPs to the porous  $\text{WO}_3$  SPs a photodegradation profile superior to the one of single  $\text{WO}_3$  NPs was achieved.<sup>[166]</sup> In another approach, magnetic NPs were added to the photocatalytic SPs. Herein,

Fe<sub>3</sub>O<sub>4</sub> was used as a core coated with SiO<sub>2</sub> and afterward with TiO<sub>2</sub> NPs. By implementing the SiO<sub>2</sub> shell around the Fe<sub>3</sub>O<sub>4</sub> core photodissolution of magnetite by TiO<sub>2</sub> was prevented. The final SPs exhibited photodegradation of methylene red in water while easy magnetic removal and reuse were possible.<sup>[167]</sup> The combination of Fe<sub>3</sub>O<sub>4</sub> and TiO<sub>2</sub> NPs was also investigated by Shi et al.<sup>[163]</sup> In an autoclave synthesis they combined these materials forming a supraparticulate structure. By precise control of the reaction temperature, the absorbance ability of the SPs in the visible solar spectrum was optimized. Next to excellent reusability and improved degradation efficiency compared to commercial TiO<sub>2</sub> NPs, the photocatalytic performance of the SPs is enhanced by applying an external magnetic field. This leads to the directional arrangement of magnetic particles, resulting in improved solar absorption of the SPs.<sup>[163]</sup>

The catalytically supported synthesis of industrially important chemicals by SPs (suing our definition) is a not yet intensively studied field. We believe that there is a high potential for SPs to advance into this field of catalytic application. In the following, we outline research topics, which partly involve SPs as catalysts or could also be addressed by this approach. Catalysis supported synthesis of organic chemicals can promote reactions like the hydrogenation of organic compounds, aldol reactions, or epoxidation.<sup>[168–170]</sup>

The hydrogenation of CO<sub>2</sub> to methanol or olefins is a recently intensively studied topic as it faces the challenge to effectively lower the carbon amount in the atmosphere. Yet, it remains a challenge to utilize CO<sub>2</sub> because of its low reactivity.<sup>[168]</sup> Fe<sub>3</sub>O<sub>4</sub> microspheres were used as catalysts and modified with different Mn contents for CO<sub>2</sub> conversion. The designed SPs exhibited excellent hydrogenation of CO<sub>2</sub> toward light olefins. With this approach, a yield and selectivity of 19% and 46%, respectively, to light olefins and an overall CO<sub>2</sub> conversion of 45% was achieved by modifying the iron oxide with 9% Mn. Herein, manganese acted as a promoter of the CO<sub>2</sub> adsorption and the activation of the C=O bonding while the Fe-based material initiated the reduction of CO<sub>2</sub> to CO.<sup>[171]</sup> The close proximity of these materials resulted in a coupling effect of the electronical properties, thus leading to sufficient reaction. In another approach porous Sn/TiO<sub>2</sub>/graphite carbon microparticles were used for the photocatalytically stimulated reaction of CO<sub>2</sub> and water to CO and CH<sub>4</sub>. The efficient absorption of light and the good catalytic performance was assigned to the unique composition and structural characteristics of the material.<sup>[172]</sup>

Au@Fe<sub>3</sub>O<sub>4</sub> SPs with a porous structure were designed to efficiently catalyze epoxidation of styrene. The loading of Au NPs onto Fe<sub>3</sub>O<sub>4</sub> particles led to a further enhanced selective oxidation of styrene with a maximum conversion of up to 95%.<sup>[170]</sup> Furthermore, porous Pd@Ni<sub>3</sub>Si<sub>4</sub>O<sub>10</sub>(OH)<sub>2</sub> SPs were synthesized by Zhang et al. for advanced styrene hydrogenation<sup>[173]</sup> and Yang et al. utilized porous Ti/Zr microspheres with reasonable cycle stability for the efficient synthesis of  $\gamma$ -valerolactone, an important platform molecule and biofuel additive, from biobased ethyl levulinate.<sup>[174]</sup> Niu et al. used Fe<sub>3</sub>O<sub>4</sub>@Fe(OH)<sub>3</sub> SPs as efficient catalysts for the reaction between different aldehydes and ketones at room temperature. It was shown that the OH-groups of the Fe(OH)<sub>3</sub> shell showed good catalytic activity in aldol reactions, while the magnetic Fe<sub>3</sub>O<sub>4</sub> core enabled easy removal and reusability.<sup>[169]</sup>

All the above-mentioned work can contribute significantly to a more sustainable development of our modern society. The catalytically supported reactions, i.e., the conversion of CO<sub>2</sub> or the purification of water by photodegradation, are just the obvious contributions. By creating SPs, properties related to sustainability develop even further, like magnetically removable and reusable catalysts, porous systems for less material in use or by substituting rare and cost-intensive materials (noble metal catalysts). The unsophisticated removal and the reuse of these SPs make them suitable for a sustainable resource management. Besides, the greatest advantages are the simultaneous retention and the improvement in their catalytic behavior, which arises from their structural and morphological uniqueness.

### 2.3. Material-Based Modern Life Comfort

The use of energy in the form of electricity for the operation of our countless commodities has become an integral part of everyday life in our society. While resource efficiency with respect to “energy” is already part of heavy research efforts, little has been put into systematically investigating material wear and disposal.

Mass production and increasing purchasing power in the course of industrialization led to the formation of a consumer society whose consumption behavior is characterized by a wasteful “take-make-dispose” pattern, i.e., in which durable goods are treated like consumable goods, at cost of environmental pollution and destruction.<sup>[175]</sup> Ubiquitous seduction marketing and even cultural norms trigger us to buy more and more products that we would not necessarily need to fulfill our basic needs. Once a product breaks down, it is either financially unviable to be repaired it or it is simply not designed to be fixable. Consequently, large amounts of goods end up as useless waste in landfills, which results in an enormous loss of valuable material. Therefore, this state-of-the-art linear economic model, which is designed for throughput rather than reusability, cannot be defined as sustainable, since it only functions based on the assumption that resources are permanently available. This does not correspond to reality and therefore does not contribute to the ability to exist constantly.

A novel alternative strategy to address this issue is the concept of circular economy, a system in which ideally waste does not exist. Products are consequently designed to last and are optimized for circulating in closed loops. These loops such as reuse, repair, remanufacture, refurbishment or recycling extend the product's life cycle and improve resource productivity. This production approach is not only sustainable but also paves the way to resilient economic growth and a systemic answer to reducing dependencies on resource markets due to net material savings, less price volatility, and supply risk.<sup>[176]</sup>

#### 2.3.1. Extending Materials Lifetime

In order to avoid waste in the first place, it would be advantageous to design products to last. Due to their characteristic coupling, emergence, and colocalization effects, SPs can contribute

to the development of long lasting products, for example, within coatings or as an alternative to pigments.

**"Anti-X" Coatings:** Most modern products use coatings on their surfaces to protect the materials they are made of and thus, enhance their durability. While antiscratch, antiwear or anticorrosion coatings prevent damage of the coated material, antifouling, antisoiling, self-cleaning, and antifogging coatings mainly avoid a regular cleaning of the material with its potentially negative effects of mechanical and chemical stress on their lifetime.

Nowadays, NPs are already regularly used for coating products. They can provide the same intrinsic properties as their bulk counterparts, such as UV absorption by ZnO or the high refractive index in case of TiO<sub>2</sub>, while showing less light scattering due to their size, which enables the creation of transparent coatings.<sup>[177]</sup> However, for the development of coatings where surface wetting plays a dominant role, i.e., for coatings that should provide an easy removal—or prevent the accumulation—of substances like oil, water, or dirt on them, the use of NPs often does not result in the desired surface structure of the coating. This is when SPs provide a promising alternative due to their larger size dimensions.<sup>[178]</sup> Coatings that require this feature are for example anti-corrosion coatings avoiding water accumulation, self-cleaning coatings enabling easy dirt, water, or oil removal, antisoiling coatings preventing dirt deposition, or antifogging coatings tackling fogging by water vapor. The minimization of surface wetting by diverse matters can be realized via superhydrophobic or superamphiphobic (e.g., for self-cleaning applications)<sup>[179]</sup> but also via superhydrophilic (e.g., for antifogging applications)<sup>[180]</sup> surfaces.

Raspberry-like SPs consisting of one larger surrounded by many smaller spherical particles have gained increasing attention in the coating community due to their unique structure.<sup>[181]</sup> Coatings based on raspberry-like SPs provide a dual-size roughness due to a coarse structure of about 10 to 20 μm and a finer structure on top of it of about 0.1 to 1 μm.<sup>[182]</sup> This structure, mimicking a lotus leaf surface, increases the liquid-repelling of a material.<sup>[178,183]</sup> Furthermore, the raspberry-like particle structure provides many re-entrant surfaces, which are surfaces hidden under overhangs, on the bottom half of each SP. These enable a vertical stabilization of droplets hindering their sagging into cracks and air pockets of the rough coating structure.<sup>[181,183]</sup> Both mentioned characteristic functional properties of these SPs are counted among the phenomenon of emergence.

As examples for SP-based coatings, raspberry-like silica-poly(divinylbenzene-co-glycidylmethacrylate) SPs were developed for superhydrophobic coatings,<sup>[184]</sup> poly(ethyl methacrylate)-silica ones for antifouling coatings,<sup>[185]</sup> hollow silica<sup>[186]</sup> (Figure 9a), and polystyrene-silica<sup>[180]</sup> (Figure 9b) ones for antifogging coatings, as well as polystyrene ones for superamphiphobic coatings<sup>[181]</sup> (Figure 9c).

While dual-size hierarchical structures could also be produced via layer by layer assembly, templating methods, chemical vapor deposition, lithography or plasma etching, the use of SPs is of advantage as no specialized equipment is needed for the coating procedure.<sup>[178]</sup> In comparison to the application of simple spherical (micro)particles, which would also yield a coating with rough surface structure, raspberry-like SPs provide

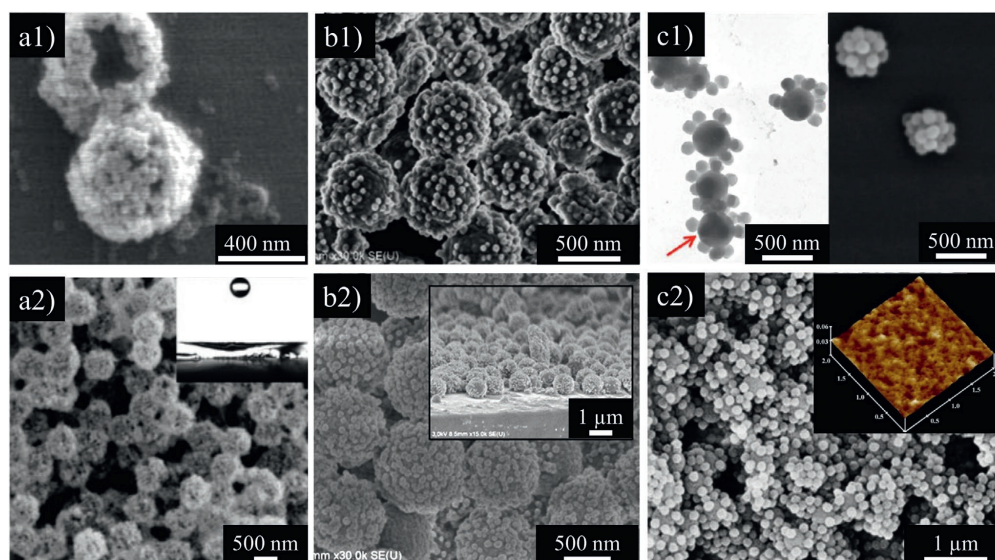


**Figure 9.** a1) Raspberry-like hollow silica and b1) polystyrene-silica supraparticles for antifogging coatings, as well as c1) polystyrene ones for superamphiphobic coatings and a2,b2,c2) the respective coatings made thereof. (a1,a2) Reproduced with permission.<sup>[186]</sup> Copyright 2008, Wiley-VCH GmbH & Co. KGaA. (b1,b2) Reproduced with permission.<sup>[180]</sup> Copyright 2020, Elsevier. (c1,c2) Reproduced with permission.<sup>[181]</sup> Copyright 2014, American Chemical Society.

the unique hierarchical dual-size roughness as well as many more re-entrant surfaces on their bottom halves.<sup>[181]</sup>

**Photonic Colors:** In contrast to other functional surface coatings, paints/pigments mostly meet rather aesthetic purposes than a certain surface property. Furthermore, paints and their use are deeply connected to mankind starting from cave paintings in the Stone Age.<sup>[187]</sup>

This is why colorants are ubiquitous in modern society and everyday life as they are used for many applications like food, clothing, cosmetics or paints.<sup>[188]</sup> The controlled tuning of hue and coloring effects, which is essential to fulfill various aesthetic needs, is achieved by the regulation of scattering and absorption properties of the colorant.<sup>[189]</sup> For manmade colored products, absorption is usually manipulated using organic dyes and pigments. Although they offer a broad variety of colors, there are several drawbacks, such as photo- or chemical-bleaching.<sup>[190,191]</sup> Additionally, in order to achieve different hues and optical effects, molecular dyes often have to be combined with supplementary compounds. A broad range of colors hence results in a multitude of chemical compounds, which increases costs of production and requires higher numbers of toxicity tests when brought into contact with the human body, for instance.<sup>[189]</sup>

Besides the coloration of fabricated products, astonishing examples and a large variety of colors are found in nature.<sup>[192]</sup> All living organisms, such as animals and plants, as well as several minerals show coloration effects, often caused by their structure.<sup>[187,193,194]</sup> These structurally colored materials, also called photonic pigments or photonic balls in the case of spherically shaped SPs, are of great interest in current research and could potentially replace conventionally used dyes and pigments in many applications.<sup>[195]</sup> Structural color is a phenomenon originating from scattering light wavelength-selectively rather than from absorption.<sup>[196]</sup> It arises from materials featuring either controlled shape, layering, roughness, porosity or arrangement of colloidal NPs. Focusing on NP-based objects, structural coloration is a striking example of an emergent property in SPs.<sup>[197]</sup> It is achieved by a periodic arrangement of colloidal NPs that serve as building blocks with sizes in the scale of the wavelength of visible light, i.e., by the creation of individual colloidal lattice planes. This repetitive structure interacts with visible light.<sup>[187,198]</sup> Thus, scattering appears due to Bragg's law, i.e., a certain wavelength shows angle-dependent, constructive interference depending on the primary particle size.<sup>[12,196,199]</sup> This effect appears macroscopically as coloration to the human eye. The wavelength of the constructive interference and hence of the coloration is shiftable over the entire visible spectrum by adjusting the size of the colloidal building blocks, which are often composed of silica or polymers.<sup>[197]</sup> In contrast to organic dyes or inorganic pigments, which result in coloration effects due to absorption and, thus, rely on the materials chemistry, structural coloration can be generated based on a single inert material.<sup>[190]</sup>

Incoherent light scattering significantly reduces color purity and brightness. Moreover, the combination of structural elements on the scale of visible light with light-absorbing molecular features has been shown to increase the brightness and clear hue. An important method to overcome the undesired influence of incoherent scattering events is to

add a wide-band absorbing component, such as carbon black or iron oxide to the colloidal system.<sup>[193]</sup> The black absorbing species absorbs light over the entire visible region due to its intrinsic material properties, thus purifying and increasing the color saturation of the photonic pigment. Therefore, vivid colored pigments can be tailored by the combination of NPs with controlled size and a black absorbing species. In addition to the absorption of undesired incoherently scattered light, these second species of building blocks can be used to tune the inter-scattering distance, i.e., the distance between silica NPs within the SPs.

Recently, Jiang et al. published their work on the addition of iron oxide NPs as the second particle species, which serve as a black absorber and spacer between the scattering silica NPs (Figure 10a). They were able to adjust the SPs color by controlling the size of the silica NPs and the addition of iron oxide NPs permitted a better manipulation of the resulting hue and brightness of the tailored color (Figure 10a1,a2).<sup>[194]</sup> The absorbing species does not have to be black necessarily; it needs to absorb incoherently scattered light over the complete optical spectrum. Therefore, besides iron oxide NPs, silver NPs are well suited as additive for color purification as well. Lai et al. succeeded in the synthesis of different colored photonic pigments (Figure 10b1,b2) by the assembly of different sized polystyrene NPs (Figure 10b3), which is another striking example of the emergent property of structural coloration in SPs assembled from smaller, nanoscale building-blocks. The hue and the brightness of these were significantly increased by the addition of silver NPs (Figure 10b1).<sup>[200]</sup>

While photonic SPs can be generated via colloidal assembly in a slowly evaporating droplet,<sup>[12,194,201]</sup> microfluidic fabrication is also suitable for the creation of structural colors.<sup>[202]</sup> Park et al. have shown that microfluidic techniques can generate microcapsules containing densely packed particles, such as polystyrene/poly(*N*-isopropylacrylamide-co-acrylic-acid) core-shell particles (Figure 10c1,c3). The core size and hence the size of scatterers, as well as the shell diameter can be well controlled, which enables the precise adjustment of the wavelength of coherently scattered light and thus, the coloration of the microcapsules (Figure 10c1,c2).<sup>[190]</sup>

Comparing photonic pigments to conventional chemically colored pigments, photonic pigments exhibit some major advantages, especially in terms of (mechanical, chemical, thermal, ...) stability and thus in terms of sustainability.<sup>[191,203]</sup> Since the coloring effects are generated from scattering events with nanostructured features and the nanoscale building blocks often consist of chemical- and photostable materials, photonic pigments usually offer nonfading properties. Therefore, they keep their intense color and brightness over time.<sup>[196]</sup> On the contrary, chemicals of conventional colorants eventually degrade and this can cause environmental pollution and can add additional future work, as well as costs for repainting.<sup>[191,199]</sup> Therefore, the lifetime of products painted with photonic pigments as colorant can be increased dramatically. Furthermore, in contrast to conventionally used pigments, photonic pigments are not composed of any heavy metals or carcinogenic substances.<sup>[195,204]</sup> Finally yet importantly, photonic pigments made from biological, environmentally benign, nanoparticulate building blocks offer a great, futuristic alternative to conquer

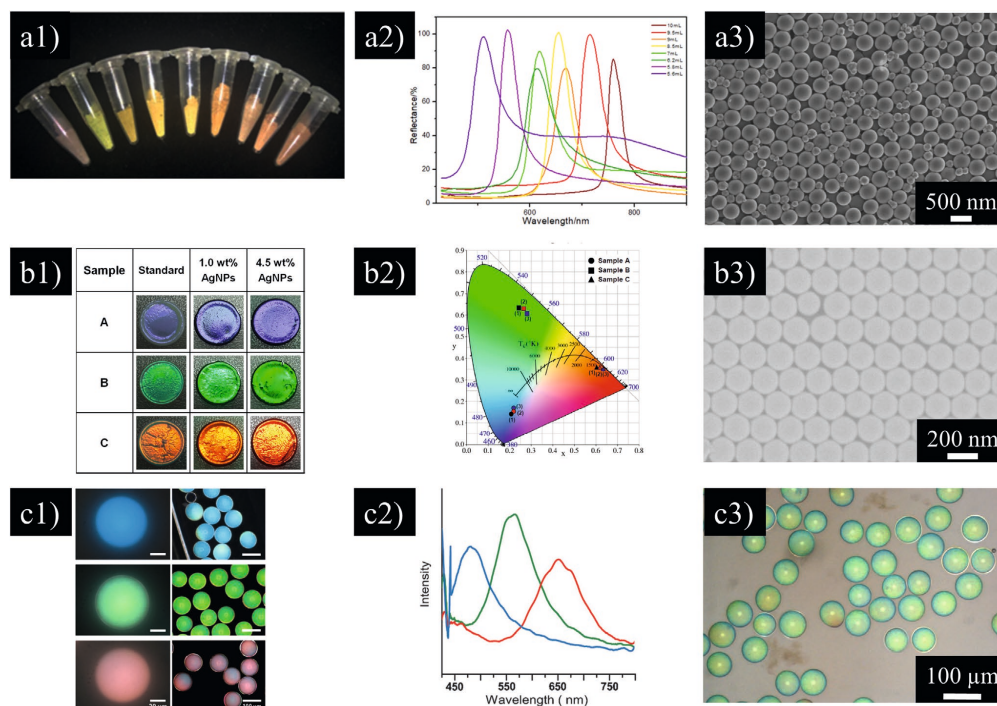


**Figure 10.** Examples of photonic coloration as an emergent property of supraparticles. a1) Different colors from iron oxide-silica supraparticles composed of differently sized silica spheres with iron oxide NPs, a2) corresponding reflection spectra, and a3) SEM image of iron oxide-silica supraparticles. b1) Photonic pigments made from supraparticles consisting of polystyrene nanoparticles with different sizes and silver nanoparticle satellites. Silver nanoparticles were used as absorbing species for increased hue and brightness. b2) Chromaticity diagram of different types of silver-polystyrene supraparticles, as well as b3) SEM image of photonic pigments made from polystyrene and 4.5 wt% silver nanoparticles (sample A in b1). c1) Photonic microcapsules consisting of a core-shell structure with different shell thicknesses in order to realize blue, green, and red coloration, c2) reflectance spectra of the microcapsules, and c3) an optical image of the photonic pigments. (a1–a3) Reproduced with permission.<sup>[194]</sup> Copyright 2020, AIP Publishing. (b1–b3) Reproduced with permission.<sup>[200]</sup> Copyright 2020, MDPI Open Access Journals. (c1–c3) Reproduced with permission.<sup>[190]</sup> Copyright 2014, Wiley-VCH GmbH & Co. KGaA.

the rising demands for sustainable, stable, and nontoxic colorants.<sup>[187,193,199,203]</sup>

### 2.3.2. Bringing Materials Back in Use

While the extension of materials lifetime certainly should be the goal for all products in use, wear, and tear or damage, caused by environmental influences, cannot be completely prevented.

Hence, easy maintenance to keep a product in working condition via simple detection and replacement of broken components must be implemented to avoid functional obsolescence and subsequently material dissipation. Once a product cannot be repaired anymore, at least the recycling and reuse of its material components is desired to save limited resources on our planet

*Sensors for Easy Repair:* The use of sensor or indicator materials reporting physical or chemical damage due to, e.g., mechanical

stress, temperature, aggressive solvents, pH changes or chemical gases is of increasing importance for the sustainable use of products as it enables defect indication of sub-micrometer sized components and, thus, their targeted repair.

For the development of sensor materials for harmful environmental triggers, NPs are already known to offer various outstanding properties in this regard compared to bulk materials. Besides their advantages already outlined in this review before (Section 2.1.1.), the possibility to miniaturize sensors<sup>[28]</sup> enables their integration into smallest product components and into almost any type of material, which is crucial for the development of sustainable sensor-equipped products.

As sensors are desired to detect several different triggers, SPs exhibit a variable platform to bottom-up design the desired properties and thereby possess functionalities that go beyond the single NP properties. This has been explained in detail for gas sensing applications (Section 2.1.1) but also holds for every type of sensor leading to high sensitivity and selectivity of these

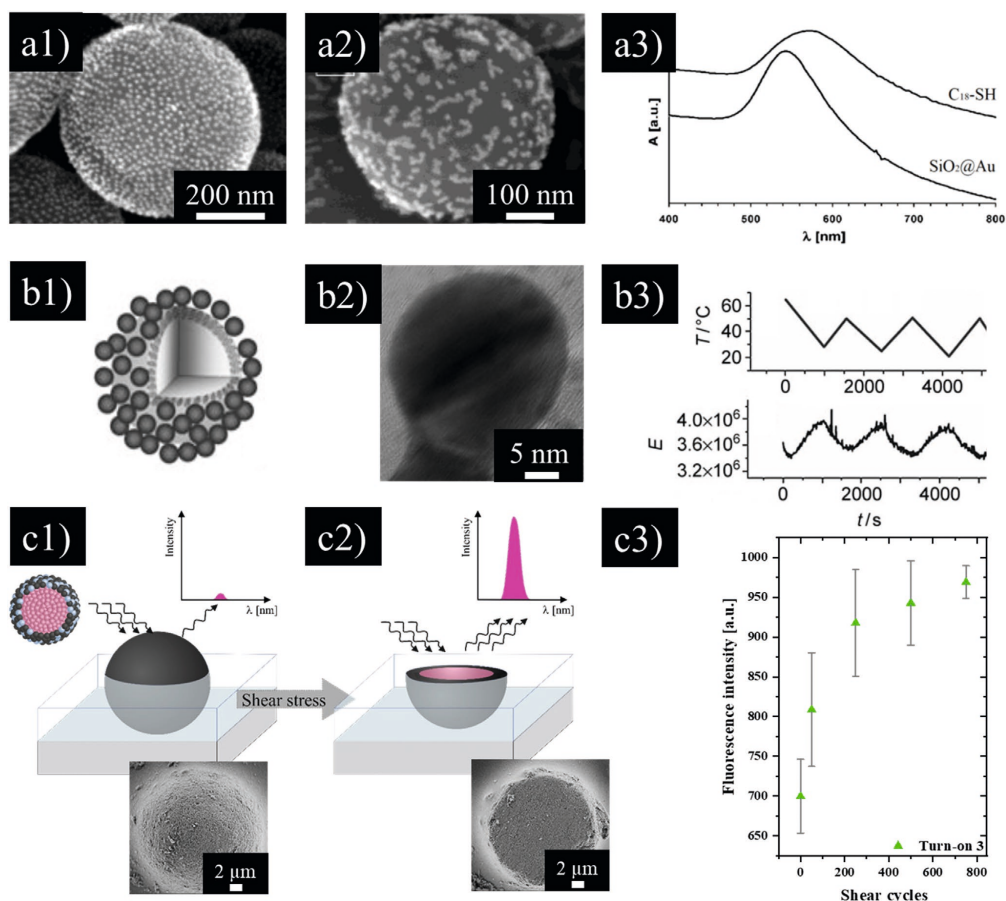


**Figure 11.** SEM images of silica-gold supraparticles as sensors for alkanethiols in a1) the as-prepared state and a2) after contact to propanethiol showing a3) a color change in the visible wavelength range dependent of the analyte type. Scheme of b1) Au-poly(ethylene glycol)-CdTe supraparticles, as well as b2) TEM. b3) This sensor indicates temperature changes via luminescence intensity variations. Scheme and SEM images of dye-doped silica-iron oxide supraparticles as shear stress indicators in c1) the as-prepared state and c2) after abrasion reporting c3) the damage via an increase in fluorescence intensity. (a1–a3) Reproduced with permission,<sup>[205]</sup> Copyright 2004, American Chemical Society. (b1,b2 and c1–c3) Reproduced with permission,<sup>[206,207]</sup> Copyright 2005 and 2020, Wiley-VCH GmbH & Co. KGaA.

SPs. A few research groups<sup>[205–207]</sup> even demonstrated that SP-based sensors can provide a response to analyte binding or mechanical forces through structural reorganization or fragmentation of their components which is an advanced sensor behavior in comparison to nanomaterial-based sensors that normally show a direct change of their physical properties.

In this context, Osterloh et al. prepared silica-gold SPs via electrostatic self-assembly as sensors for various linear chain alkanethiols.<sup>[205]</sup> They show a color change in presence of the analyte due to reorganization of the gold NPs on the silica core particle (Figure 11a). Examples of gas detecting

SPs have already been described in Section 2.1.1. extensively and may be easily transferred to sensor applications for easy product maintenance. An SP-based pH sensor has been created through the embedding of magnetic NPs and indicator dyes within a polymer particle by a miniemulsion solvent evaporation technique.<sup>[28]</sup> A temperature-sensitive SP was shown by Lee et al. based on CdTe NPs connected to a gold NP by poly(ethylene glycol) derivatives.<sup>[206]</sup> It monitors temperature changes between 20 and 60 °C via variation of the luminescence intensity (Figure 11b). Cold chain breach indicating magnetic supraparticulate microrods have been described by Müssig

et al.<sup>[208]</sup> Besides other mechanical stress indicator SPs,<sup>[209]</sup> a shear indicator based on hierarchically structured luminescent dye-doped silica NPs and iron oxide NPs assembled via spray-drying has been established.<sup>[207]</sup> It reports damages, e.g., by an increase in fluorescence signal (Figure 11c).

In summary, sensor and reporter SPs may play a key role in the development of easy maintenance products in the future due to their high sensitivity and selectivity based on the phenomena of emergence and colocalization offering high porosity as well as the combination of diverse materials within a sensor. However, also sustainable, repair-friendly product design needs to become the standard to make these SPs a powerful tool.

*Tracer-Based Sorting as Recycling Aid:* Once materials are not working properly anymore and cannot be repaired, their recycling and reuse are desired to save limited resources on our planet and thereby act sustainably. A major challenge for recycling is the automated sorting of different materials, such as polymers, to receive a high purity recycle.<sup>[210]</sup> If polymers are not sorted properly, the resulting recycle exhibits insufficient material properties and limits its reusability.<sup>[211]</sup> Thus, the efficient sorting of different materials is a crucial step for the recycling of waste streams.

The direct sorting utilizes intrinsic properties of the materials such as density, near-infrared fingerprint or magnetism but is often unsuitable for automated recycling especially when composite materials are to be recycled.<sup>[212]</sup> An alternative is the addition of a tracer into materials.<sup>[211]</sup> This tracer-based sorting often utilizes microparticles which are incorporated into plastics during their production and enables the identification of plastic by distinct (most frequently optical) signals during sorting and recycling.<sup>[213]</sup>

To cope with the mixed nature of the waste and thereby increase the recovery rates, tracers with more than one detectable signal are desired.<sup>[212]</sup> In contrast to NPs or microparticles, SPs represent a flexible platform to create multifunctional tracers. Furthermore they permit signal variations<sup>[214]</sup> and thereby to distinguish and sort different materials. Several reviews focus on the idea of object identification with nano- or microscale tracers in general.<sup>[215]</sup> In terms of SPs for recycling, only one publication from our group was found to date where SPs were described to contribute to recycling, indicating high capabilities for future contributions in this field.<sup>[216]</sup> Therein, a magnetic SP is suggested to enable sorting and identification of dark plastics. By variation of the composition, different magnetic fingerprints are resolved via magnetic particle spectroscopy (Figure 12a). Such a magnetic signal is advantageous for colorful and dark materials because it is not inferred by light absorption in the visible range and can thus be detected from within materials. Although not explicitly mentioned in many manuscripts, other SPs exhibit potential for their utilization in recycling as well.

One principle of signal variation is a structural variation within SPs. These codes are often referred to as graphical codes. It is important to note that the graphical signal is resolved within one SP rather than the arrangement of multiple SPs. Because materials in waste streams are often shredded the code generated by the spatial arrangement of microparticles may thereby be destroyed. A defined pattern of different materials is used to generate a barcode information, which is resolved, for

instance, due to different reflectance, sizes or magnetic properties. Progress in this field is well reported in other articles and is thus not further discussed herein.<sup>[217]</sup>

A SP that combines such a graphical patterning with a spectral signal was shown by Lee et al. Herein, the use of rare-earth upconverting nanocrystals reduces spectral interference from the sample due to large anti-Stokes shifts.<sup>[218]</sup> Such upconverting luminescent spectral signatures can be tailored by variations of lanthanide composition, dopant concentration, mass content,<sup>[219]</sup> or by addition of dyes into the SP (Figure 12b),<sup>[220]</sup> yielding a fluorescent resonant energy transfer due to coupling.

SPs based on encoded silica beads<sup>[221]</sup> (Figure 12c) or polymers<sup>[222]</sup> with quantum dots are another class of luminescent signal carriers. The different colors of various quantum dots are resolved via fluorescence imaging or fluorescence spectroscopy. Gao et al. suggested to detect the optical properties of quantum dot encoded polystyrene beads with flow cytometry, yielding a rapid readout. However, this system was only demonstrated in liquids and might be limiting for recycling applications.<sup>[223]</sup>

Song et al.<sup>[224]</sup> utilized the flexibility of SPs by layer-by-layer assembly of quantum dot NPs around gold NP cores. Thereby, both the intrinsic optical and plasmonic properties of quantum dots and gold NPs are preserved and enable the detection of both signals due to colocalization within the SP.

As an alternative to layer-by-layer assembly or swelling techniques, microfluidic syntheses of quantum dot encoded SPs were reported<sup>[225,226]</sup> as a simple and cost-effective method.<sup>[225]</sup> The microfluidic synthesis of barcode particles in general is reviewed in another excellent article.<sup>[227]</sup>

As SPs provide the possibility for variation of its NP building blocks, it facilitates the incorporation of quantum dots into microbeads in defined ratios. The resulting signal represents the ratio of incorporated quantum dots due to their colocalization and is thus controlled by the structure of the SP.<sup>[228]</sup> A similar principle was used to create luminescent IDs based on different rare-earth doped CaF<sub>2</sub> NPs that were assembled into SPs in defined ratios (Figure 12d).<sup>[229]</sup>

As an alternative to optical signals, SPs based on surface-enhanced Raman spectroscopy (SERS/SERSS)-encoded NPs<sup>[230]</sup> or encapsulated DNA<sup>[231]</sup> were reported. In order to decode the DNA via quantitative real-time PCR and Sanger sequencing, the SPs were equipped with magnetic NPs that enable the magnetic collection of the tracer. While DNA codes provide a large variety of possible codes and need only a very small amount of tracer, they are to date still expensive to decipher.

Magnetic iron oxide NPs were also combined with quantum dots<sup>[232]</sup> or upconverting nanocrystals<sup>[233]</sup> yielding multifunctional SPs. Thereby, the optical fingerprint of the SPs was maintained while adding the possibility of magnetic separation<sup>[233]</sup> or enabling magnetic resonance imaging.<sup>[232]</sup> Another work expanded this even further and presented a dual-mode encoded magnetic SP by combination of fluorescence reporters and SERS probes<sup>[234]</sup> and thereby represents a true multisensor tracer which will be desired for future recycling applications.

These examples show the high potential of SPs for tracer-based sorting as recycling aids and may thus inspire more researchers to focus on their development and implementation into recyclable materials.

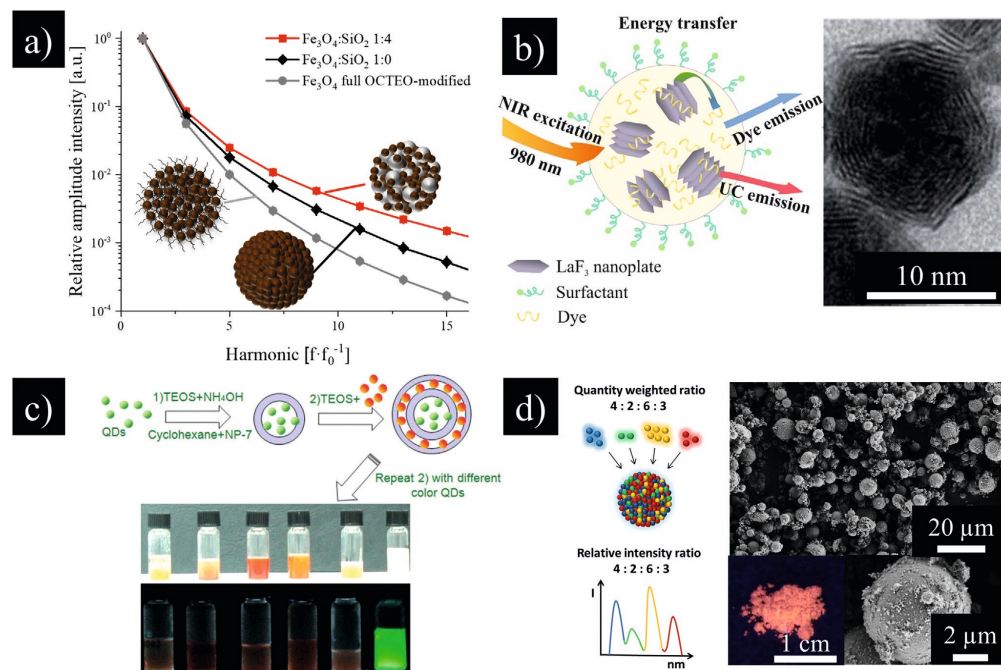


**Figure 12.** Supraparticles based on different physical properties enable a signal variation that can be used as unique ID. a) Magnetic fingerprints can be achieved via structural variation of supraparticles and identified by magnetic particle spectroscopy. b) Supraparticles assembled by rare earth doped  $\text{LaF}_3$  nanoplates and loaded with fluorescent dyes show tunable upconversion fluorescence codes. c) Silica spheres can be optically encoded by different layers of quantum dots. d) Different optical fingerprints are obtained from ratiometric mixing of differently rare earth doped  $\text{CaF}_2$  nanoparticles within a supraparticle. (a) Reproduced with permission.<sup>[216]</sup> Copyright 2019, Wiley-VCH GmbH & Co. KGaA. (b,<sup>[220]</sup> c)<sup>[221]</sup> Reproduced with permission. Copyright 2014 and 2011, The Royal Society of Chemistry. (d) Reproduced with permission.<sup>[229]</sup> Copyright 2019, American Chemical Society.

All in all, the use of SPs in products may not only enhance their durability, resulting in fewer product damages and a prolonged product lifetime, but also enable their easy maintenance as well as the recycling of their components. This can ultimately help us to bring the abstract concept of circular economy to life.

### 3. Conclusion

Sustaining existence of humans on our planet Earth in the future demands serious efforts in many fields and dimensions. Technology is a crucial and in fact key contributor to secure the fulfillment of human needs in line with ensuring the ability for us to exist constantly, i.e., to achieve a sustainable living on the planet. As outlined, for any technology, advanced materials are decisive contributors on all levels to secure “fundamental needs,” as well as to enable “basic” and even “modern life comfort” in the future as (at least the industrialized) nations are taking it for granted today. Focus in this review was put on how the merits of NPs to contribute to sustainability can be enhanced further by combining them to entities called SPs. By doing so, three fundamental new properties, namely, coupling,

emergence, and colocalization occur and yield new functionalities. These contribute to the defined sustainability topics “purification technologies,” “agricultural delivery systems,” “energy storage and conversion,” “catalysis,” “materials with extended lifetime,” and “materials brought back in use.”

In the fields of “energy storage” and “catalysis,” the combination of NPs to SPs to enhance properties or even achieve completely new functionalities has been already and is currently even more heavily in the focus of research and impressive systems were reported.

In the other fields studied in this review, we see great potential for SPs to contribute to sustainability, which, however, has not yet been fully unlocked to date. Recent, pioneering articles, however, give an idea of the impressive properties and ultimate functionalities that can be achieved by exploiting the potential to unite building blocks in unique combinations in SPs. For these—in our view—to date neglected fields—we suggested concepts in this review article in hope of spiking the creativity of other researchers to create new systems in the near future.

Several general challenges for establishing the use of SPs in these different fields of sustainability that should be particularly

addressed in future are, according to the authors' perspective, as follows:

- From a scientific perspective, many assembly processes are still not very well understood and the obtained SPs are thus only achieved via empirical studies. Calculations and simulations could help to fully understand SP formation and predict emergent sample properties. This would ultimately enable the tuning of internal or external assembly parameters to engineer SPs in a very reliable and predictable fashion.<sup>[235]</sup>
- Regarding the transition from chemical lab-scale SP synthesis to industrial fabrication, the main challenges are fabrication time, scalability, and cost. Many assembly processes require large time as NPs have to come together, rearrange and form ordered structures, which are kinetically restricted processes due to small diffusion rates of the building blocks.<sup>[236]</sup> A high number of SP syntheses are difficult to scale-up due to primary NP yield, matter transport at larger volumes, or the presence of competing processes, which scale up differently.<sup>[235]</sup> Finally, the added value of the use of SPs compared to NPs or random agglomerates to an application must equal out the surely higher fabrication costs of these materials.<sup>[236]</sup>
- In order to truly contribute to sustainability, also the fabrication processes of SPs should be as little energy-consumptive and the starting, as well as processing materials, as green, abundantly available and recoverable as possible. Furthermore, the reuse and recycling of SPs themselves after their application in a specific field should be critically reviewed.

In general, we see that the increase in SP research during the last years was enormous and we think that SPs as versatile functional systems have just started their triumph. Thus, borrowing the words of Feynman,<sup>[237]</sup> we think particularly with respect to contributing to technologies for sustainability, one can state that there is "plenty of room" at the supra-nano-level.

## Acknowledgements

This work was financially supported by the BMBF (NanoMatFutur grant 03XP0149), which is gratefully acknowledged. J.R. and S.M. acknowledge their scholarship funding of the German Federal Environmental Foundation (DBU).

Open access funding enabled and organized by Projekt DEAL.

## Conflict of Interest

The authors declare no conflict of interest.

## Keywords

nanomaterials, nanoparticles, supraparticles, sustainability

Received: January 7, 2021  
Published online: February 1, 2021

- [1] P. E. Shaw, L. Newby, *Regul. Stud.* **1998**, *32*, 863.  
[2] G. H. Brundtland, *Environ. Policy Law* **1985**, *14*, 26.

- [3] T. Kuhlman, J. Farrington, *Sustainability* **2010**, *2*, 3436.  
[4] *Nanotechnology Toward the Sustainable* (Ed: T. A. Faunce), Pan Stanford Publishing, Singapore **2015**.  
[5] B. D. Fath, *Int. J. Des. Nat. Ecodyn.* **2017**, *12*, 1.  
[6] a) T. Pradeep, Anshup, *Thin Solid Films* **2009**, *517*, 6441; b) X. Hu, G. Li, J. C. Yu, *Langmuir* **2010**, *26*, 3031.  
[7] M. Segev-Bar, H. Haick, *ACS Nano* **2013**, *7*, 8366.  
[8] E. Roduner, *Chem. Soc. Rev.* **2006**, *35*, 583.  
[9] S. C. Glotzer, M. J. Solomon, *Nat. Mater.* **2007**, *6*, 557.  
[10] J.-M. Lehn, *Chem. Soc. Rev.* **2017**, *46*, 2378.  
[11] a) Y. Xia, Z. Tang, *Chem. Commun.* **2012**, *48*, 6320; b) T. Wang, D. LaMontagne, J. Lynch, J. Zhuang, Y. C. Cao, *Chem. Soc. Rev.* **2013**, *42*, 2804; c) J. Guo, W. Yang, C. Wang, *Adv. Mater.* **2013**, *25*, 5196; d) E. Piccinini, D. Pallarola, F. Battaglini, O. Azzaroni, *Mol. Syst. Des. Eng.* **2016**, *1*, 155; e) D. Lawless, S. Kapoor, D. Meisel, *J. Phys. Chem.* **1995**, *99*, 10329; f) O. D. Velev, K. Furusawa, K. Nagayama, *Langmuir* **1996**, *12*, 2374.  
[12] V. Rastogi, S. Melle, O. G. Calderón, A. A. García, M. Marquez, O. D. Velev, *Adv. Mater.* **2008**, *20*, 4263.  
[13] S. Wintzheimer, T. Granath, M. Oppmann, T. Kister, T. Thai, T. Kraus, N. Vogel, K. Mandel, *ACS Nano* **2018**, *12*, 5093.  
[14] Z. Xue, P. Wang, A. Peng, T. Wang, *Adv. Mater.* **2019**, *31*, 1801441.  
[15] a) A. Othman, P. Vargo, S. Andrescu, *ACS Appl. Nano Mater.* **2019**, *2*, 7008; b) Y. Zhang, W. Qiu, Y. Ma, Y. Luo, Z. Tian, G. Cui, F. Xie, L. Chen, T. Li, X. Sun, *ACS Catal.* **2018**, *8*, 8540.  
[16] a) Z. Mao, H. Xu, D. Wang, *Adv. Funct. Mater.* **2010**, *20*, 1053; b) Z. Xue, C. Yan, T. Wang, *Adv. Funct. Mater.* **2019**, *29*, 1807658.  
[17] E. W. Chuan Lim, R. Feng, *J. Chem. Phys.* **2012**, *136*, 124109.  
[18] a) G. Shaddick, M. L. Thomas, P. Mudu, G. Ruggeri, S. Gumy, *npj Clim. Atmos. Sci.* **2020**, *3*, 7; b) S. J. Lade, W. Steffen, W. de Vries, S. R. Carpenter, J. F. Donges, D. Gerten, H. Hoff, T. Newbold, K. Richardson, J. Rockström, *Nat. Sustain.* **2020**, *3*, 119.  
[19] T.-T. Chau, K.-Y. Wang, *Sci. Rep.* **2020**, *10*, 2321.  
[20] M. S. Mauter, I. Zucker, F. Perreault, J. R. Werber, J.-H. Kim, M. Elimelech, *Nat. Sustainability* **2018**, *1*, 166.  
[21] H. Ren, P. Koshy, W.-F. Chen, S. Qi, C. C. Sorrell, *J. Hazard. Mater.* **2017**, *325*, 340.  
[22] A. Bigdeli, F. Ghasemi, H. Golmohammadi, S. Abbasi-Moayed, M. A. F. Nejad, N. Fahimi-Kashani, S. Jafarnejad, M. Shahrajabian, M. R. Hormozi-Nezhad, *Nanoscale* **2017**, *9*, 16546.  
[23] K. Suematsu, Y. Shin, Z. Hua, K. Yoshida, M. Yuasa, T. Kida, K. Shimano, *ACS Appl. Mater. Interfaces* **2014**, *6*, 5319.  
[24] G. T. Chandran, X. Li, A. Ogata, R. M. Penner, *Anal. Chem.* **2017**, *89*, 249.  
[25] Z. Farka, T. Juřík, D. Kovář, L. Trnková, P. Skládal, *Chem. Rev.* **2017**, *117*, 9973.  
[26] G. Zhu, C. Xi, H. Xu, D. Zheng, Y. Liu, X. Xu, X. Shen, *RSC Adv.* **2012**, *2*, 4236.  
[27] Y. Zhang, Q. Xiang, J. Xu, P. Xu, Q. Pan, F. Li, *J. Mater. Chem.* **2009**, *19*, 4701.  
[28] G. Mistlberger, A. L. Medina-Castillo, S. M. Borisov, T. Mayr, A. Fernández-Gutiérrez, J. F. Fernandez-Sanchez, I. Klimant, *Microchim. Acta* **2011**, *172*, 299.  
[29] K. Koren, G. Mistlberger, D. Aigner, S. M. Borisov, A. Zankel, P. Pölt, I. Klimant, *Monatsh. Chem.* **2010**, *141*, 691.  
[30] a) N. Singh, R. K. Gupta, P. S. Lee, *ACS Appl. Mater. Interfaces* **2011**, *3*, 2246; b) C. Pannek, T. Vetter, M. Oppmann, C. Weber, A. Eberhardt, M. Dold, M.-L. Bauersfeld, M. Henfling, S. Trupp, B. Schug, J. Wöllenstein, K. Mandel, *Sens. Actuators, B* **2020**, *306*, 127572; c) S. Bai, K. Zhang, L. Wang, J. Sun, R. Luo, D. Li, A. Chen, *J. Mater. Chem. A* **2014**, *2*, 7927.  
[31] Y. Shen, W. Wang, X. Chen, B. Zhang, D. Wei, S. Gao, B. Cui, *J. Mater. Chem. A* **2016**, *4*, 1345.

- [32] S. Wintzheimer, M. Oppmann, M. Dold, C. Pannek, M.-L. Bauersfeld, M. Herfling, S. Trupp, B. Schug, K. Mandel, *Part. Part. Syst. Charact.* **2019**, *36*, 1900254.
- [33] G. Liu, M. Xiao, X. Zhang, C. Gal, X. Chen, L. Liu, S. Pan, J. Wu, L. Tang, D. Clements-Groome, *Sustain. Cities Soc.* **2017**, *32*, 375.
- [34] Y. H. Joe, D. H. Park, J. Hwang, *J. Hazard. Mater.* **2016**, *301*, 547.
- [35] J. Kim, S. C. Hong, G. N. Bae, J. H. Jung, *Environ. Sci. Technol.* **2017**, *51*, 11967.
- [36] S. Wang, X. Zhao, X. Yin, J. Yu, B. Ding, *ACS Appl. Mater. Interfaces* **2016**, *8*, 23985.
- [37] A. K. Sinha, K. Suzuki, M. Takahara, H. Azuma, T. Nonaka, K. Fukumoto, *Angew. Chem., Int. Ed.* **2007**, *46*, 2891.
- [38] S. Meth, A. Goepfert, G. K. S. Prakash, G. A. Olah, *Energy Fuel* **2012**, *26*, 3082.
- [39] Z. Liu, Z. Li, X. Xie, S. Yang, J. Fei, Y. Li, Z. Xu, H. Liu, *Environ. Sci. Technol.* **2020**, *54*, 604.
- [40] T. Harada, T. A. Hatton, *Chem. Mater.* **2015**, *27*, 8153.
- [41] X. Rong, R. Ettelaie, S. V. Lishchuk, H. Cheng, N. Zhao, F. Xiao, F. Cheng, H. Yang, *Nat. Commun.* **2019**, *10*, 1854.
- [42] W. Choi, K. Min, C. Kim, Y. S. Ko, J. W. Jeon, H. Seo, Y.-K. Park, M. Choi, *Nat. Commun.* **2016**, *7*, 12640.
- [43] Y.-S. Ko, Y. H. Joe, M. Seo, K. Lim, J. Hwang, K. Woo, *J. Mater. Chem. B* **2014**, *2*, 6714.
- [44] L. Su, J. Ma, F. Zhang, Y. Fan, W. Luo, L. Wang, W. Jiang, J. Yang, *J. Materiomics* **2021**, *7*, 80.
- [45] M. Kumm, J. H. A. Guillaume, H. de Moel, S. Eisner, M. Flörke, M. Porkka, S. Siebert, T. I. E. Veldkamp, P. J. Ward, *Sci. Rep.* **2016**, *6*, 38495.
- [46] F. Pulizzi, W. Sun, *Nat. Nanotechnol.* **2018**, *13*, 633.
- [47] P. J. J. Alvarez, C. K. Chan, M. Elimelech, N. J. Halas, D. Villagrán, *Nat. Nanotechnol.* **2018**, *13*, 634.
- [48] L. Guerrini, E. Garcia-Rico, N. Pazos-Perez, R. A. Alvarez-Puebla, *ACS Nano* **2017**, *11*, 5217.
- [49] P. J. Vikesland, *Nat. Nanotechnol.* **2018**, *13*, 651.
- [50] K. Saravanan, E. Anusuya, R. Kumar, H. L. Son, *Environ. Monit. Assess.* **2018**, *190*, 556.
- [51] Y. Chen, D. Han, *Automat. Constr.* **2018**, *89*, 307.
- [52] *Standard Methods for the Examination of Water and Wastewater*, American Public Health Association, Washington, DC **2017**.
- [53] A. Nayyar, V. Puri, D.-N. Le, *J. Nanosci. Nanotechnol.* **2017**, *7*, 4.
- [54] C. A. Staples, P. B. Dome, G. M. Klecka, S. T. Oblock, L. R. Harris, *Chemosphere* **1998**, *36*, 2149.
- [55] A. Uchida, Y. Kitayama, E. Takano, T. Ooya, T. Takeuchi, *RSC Adv.* **2013**, *3*, 25306.
- [56] F. Mochi, L. Burratti, I. Fratoddi, I. Venditti, C. Battocchio, L. Carlini, G. Iucci, M. Casalboni, F. de Matteis, S. Cascardi, S. Nappini, I. Pis, P. Proposito, *Nanomaterials* **2018**, *8*, 488.
- [57] P. Westerhoff, A. Atkinson, J. Fortner, M. S. Wong, J. Zimmerman, J. Gardea-Torresdey, J. Ranville, P. Herckes, *Nat. Nanotechnol.* **2018**, *13*, 661.
- [58] T. Wehner, M. T. Seuffert, J. R. Sorg, M. Schneider, K. Mandel, G. Sextl, K. Müller-Buschbaum, *J. Mater. Chem. C* **2017**, *5*, 10133.
- [59] C. Vietz, M. L. Schütte, Q. Wei, L. Richter, B. Lalkens, A. Ozcan, P. Tinnefeld, G. P. Acuna, *ACS Omega* **2019**, *4*, 637.
- [60] M. V. Tran, K. Susumu, I. L. Medintz, W. R. Algar, *Anal. Chem.* **2019**, *91*, 11963.
- [61] M. K. Nakhleh, H. Amal, R. Jeries, Y. Y. Broza, M. Aboud, A. Gharra, H. Ivgi, S. Khatib, S. Badarnah, L. Har-Shai, L. Glas-Marmor, I. Lejbkovicz, A. Miller, S. Badarny, R. Winer, J. Finberg, S. Cohen-Kaminsky, F. Perros, D. Montani, B. Girerd, G. Garcia, G. Simonneau, F. Nakhoul, S. Baram, R. Salim, M. Hakim, M. Gruber, O. Ronen, T. Marshak, I. Doweck, O. Nativ, Z. Bahouth, D. Shi, W. Zhang, Q. Hua, Y. Pan, L. Tao, H. Liu, A. Karban, E. Koifman, T. Rainis, R. Skapars, A. Sivins, G. Ancans, I. Liepniece-Karele, I. Kikuste, I. Lasina, I. Tolmanis, D. Johnson, S. Millstone, J. Fulton, J. Wells, L. Wilf, M. Humbert, M. Leja, M. Leja, N. Peled, H. Haick, *ACS Nano* **2017**, *11*, 112.
- [62] M. A. Shannon, P. W. Bohn, M. Elimelech, J. G. Georgiadis, B. J. Mariñas, A. M. Mayes, *Nature* **2008**, *452*, 301.
- [63] Q. Li, S. Mahendra, D. Y. Lyon, L. Brunet, M. V. Liga, D. Li, P. J. J. Alvarez, *Water Res.* **2008**, *42*, 4591.
- [64] X. Qu, J. Brame, Q. Li, P. J. J. Alvarez, *Acc. Chem. Res.* **2013**, *46*, 834.
- [65] S. Andra, R. Ramoorthy, M. Muthalagu, *Mater. Res. Express* **2018**, *5*, 065043.
- [66] S. Maleki Dizaj, A. Mennati, S. Jafari, K. Khezri, K. Adibkia, *Adv. Pharm. Bull.* **2015**, *5*, 19.
- [67] K. R. Raghupathi, R. T. Koodali, A. C. Manna, *Langmuir* **2011**, *27*, 4020.
- [68] Z.-m. Xiu, Q.-b. Zhang, H. L. Puppala, V. L. Colvin, P. J. J. Alvarez, *Nano Lett.* **2012**, *12*, 4271.
- [69] M. Cho, H. Chung, W. Choi, J. Yoon, *Appl. Environ. Microb.* **2005**, *71*, 270.
- [70] R. P. Schwarzenbach, B. I. Escher, K. Fenner, T. B. Hofstetter, C. A. Johnson, U. von Gunten, B. Wehrli, *Science* **2006**, *313*, 1072.
- [71] S. Baruah, M. Najam Khan, J. Dutta, *Environ. Chem. Lett.* **2016**, *14*, 1.
- [72] a) H. Park, A. May, L. Portilla, H. Dietrich, F. Münch, T. Rejek, M. Sarcletti, L. Banspach, D. Zahn, M. Halik, *Nat. Sustainability* **2020**, *3*, 129; b) N. Wu, H. Wei, L. Zhang, *Environ. Sci. Technol.* **2012**, *46*, 419.
- [73] D. Copic, L. Maggini, M. de Volder, *Adv. Mater.* **2018**, *30*, 1706503.
- [74] P. Sylvester, P. Westerhoff, T. Möller, M. Badruzzaman, O. Boyd, *Environ. Eng. Sci.* **2007**, *24*, 104.
- [75] L. Zhou, P. Su, Y. Deng, Y. Yang, *J. Sep. Sci.* **2017**, *40*, 909.
- [76] M. S. Mauter, M. Elimelech, *Environ. Sci. Technol.* **2008**, *42*, 5843.
- [77] L. C. A. Oliveira, R. V. Rios, J. D. Fabris, V. Garg, K. Sapag, R. M. Lago, *Carbon* **2002**, *40*, 2177.
- [78] a) A. K. Mishra, S. Ramaprabhu, *J. Phys. Chem. C* **2010**, *114*, 2583; b) V. Chandra, J. Park, Y. Chun, J. W. Lee, I.-C. Hwang, K. S. Kim, *ACS Nano* **2010**, *4*, 3979.
- [79] a) L. Ai, H. Huang, Z. Chen, X. Wei, J. J. Jiang, *Chem. Eng. J.* **2010**, *156*, 243; b) L. Ai, C. Zhang, Z. Chen, *J. Hazard. Mater.* **2011**, *192*, 1515.
- [80] T. Madrakian, A. Afkhami, M. Ahmadi, *Spectrochim. Acta, Part A* **2012**, *99*, 102.
- [81] L. Su, D. Han, G. Zhu, H. Xu, W. Luo, L. Wang, W. Jiang, A. Dong, J. Yang, *Nano Lett.* **2019**, *19*, 5423.
- [82] a) M. Schneider, A. Tschöpe, D. Hanselmann, T. Ballweg, C. Gellermann, M. Franzreb, K. Mandel, *Part. Part. Syst. Charact.* **2020**, *37*, 1900487; b) M. Schneider, T. Ballweg, L. Groß, C. Gellermann, A. Sanchez-Sanchez, V. Fierro, A. Celzard, K. Mandel, *Part. Part. Syst. Charact.* **2019**, *36*, 1800537.
- [83] a) Y. Liu, Y. Wang, S. Zhou, S. Lou, L. Yuan, T. Gao, X. Wu, X. Shi, K. Wang, *ACS Appl. Mater. Interfaces* **2012**, *4*, 4913; b) H. U. Lee, S. C. Lee, Y.-C. Lee, S. Vrtnik, C. Kim, S. Lee, Y. B. Lee, B. Nam, J. W. Lee, S. Y. Park, S. Y. Lee, J. Lee, *J. Hazard. Mater.* **2013**, *262*, 130; c) Y. Yu, Y. Li, Y. Wang, B. Zou, *Langmuir* **2018**, *34*, 9359; d) Q. Zhang, Y. Zhang, J. Chen, Q. Liu, *Nanoscale Res. Lett.* **2019**, *14*, 104.
- [84] M. Oppmann, M. Wozar, J. Reichstein, K. Mandel, *ChemNanoMat.* **2018**, *6*, 141.
- [85] P. Pati, S. McGinnis, P. J. Vikesland, *Environ. Sci. Nano* **2016**, *3*, 1133.
- [86] A. J. Fijneman, J. Höglblom, M. Palmlöf, G. With, M. Persson, H. Friedrich, *Adv. Funct. Mater.* **2020**, *30*, 2002725.
- [87] A. Othman, E. Dumitrescu, D. Andreescu, S. Andreescu, *ACS Sustainable Chem. Eng.* **2018**, *6*, 12542.

- [88] a) K. Mandel, F. Hutter, C. Gellermann, G. Sextl, *ACS Appl. Mater. Interfaces* **2012**, *4*, 5633; b) K. Mandel, F. Hutter, C. Gellermann, G. Sextl, *Sep. Purif. Technol.* **2013**, *109*, 144.
- [89] a) K. Mandel, A. Drenkova-Tuhtan, F. Hutter, C. Gellermann, H. Steinmetz, G. Sextl, *J. Mater. Chem. A* **2013**, *1*, 1840; b) A. Drenkova-Tuhtan, M. Schneider, M. Franzreb, C. Meyer, C. Gellermann, G. Sextl, K. Mandel, H. Steinmetz, *Water Res.* **2017**, *109*, 77; c) E. Rott, M. Nouri, C. Meyer, R. Minke, M. Schneider, K. Mandel, A. Drenkova-Tuhtan, *Water Res.* **2018**, *145*, 608.
- [90] Y. Gao, Y. Liang, H. Dong, J. Niu, J. Tang, J. Yang, G. Tang, Z. Zhou, R. Tang, X. Shi, Y. Cao, *ACS Sustainable Chem. Eng.* **2020**, *8*, 5716.
- [91] *ACS Symposium Series* (Eds.: B. Park, M. Appell), American Chemical Society, Washington, DC **2013**.
- [92] G. E. Batley, J. K. Kirby, M. J. McLaughlin, *Acc. Chem. Res.* **2013**, *46*, 854.
- [93] a) X. Ma, J. Geisler-Lee, J. Geiser-Lee, Y. Deng, A. Kolmakov, *Sci. Total Environ.* **2010**, *408*, 3053; b) C. M. Rico, S. Majumdar, M. Duarte-Gardea, J. R. Peralta-Videoa, J. L. Gardea-Torresdey, *J. Agric. Food Chem.* **2011**, *59*, 3485.
- [94] a) A. B. Sengul, E. Asmatulu, *Environ. Chem. Lett.* **2020**, *18*, 1659; b) M. Ajdary, M. Moosavi, M. Rahmati, M. Falahati, M. Mahboubi, A. Mandegary, S. Jangjoo, R. Mohammadinejad, R. Varma, *Nanomaterials* **2018**, *8*, 634; c) V. Srivastava, D. Gusain, Y. C. Sharma, *Ind. Eng. Chem. Res.* **2015**, *54*, 6209.
- [95] C. Pecharrorman, A. Esteban-Cubillo, R. Torrecillas, J. S. Moya, *Int. J. Nanotechnol.* **2007**, *4*, 282.
- [96] D. S. Kohane, *Biotechnol. Bioeng.* **2007**, *96*, 203.
- [97] B. D. Mattos, B. L. Tardy, W. L. E. Magalhães, O. J. Rojas, *J. Controlled Release* **2017**, *262*, 139.
- [98] J. Xie, Y. Yang, B. Gao, Y. Wan, Y. C. Li, D. Cheng, T. Xiao, K. Li, Y. Fu, J. Xu, Q. Zhao, Y. Zhang, Y. Tang, Y. Yao, Z. Wang, L. Liu, *ACS Nano* **2019**, *13*, 3320.
- [99] Y. Wang, A. K. Wise, J. Tan, J. W. Maina, R. K. Shepherd, F. Caruso, *Small* **2014**, *10*, 4244.
- [100] C.-L. Zhu, X.-W. Wang, Z.-Z. Lin, Z.-H. Xie, X.-R. Wang, *J. Food Drug Anal.* **2014**, *22*, 18.
- [101] F. Torney, B. G. Trewyn, V. S.-Y. Lin, K. Wang, *Nat. Nanotechnol.* **2007**, *2*, 295.
- [102] T. Ballweg, C. Gellermann, K. Mandel, *ACS Appl. Mater. Interfaces* **2015**, *7*, 24909.
- [103] J. Cui, M. Kramer, L. Zhou, F. Liu, A. Gabay, G. Hadjipanayis, B. Balasubramanian, D. Sellmyer, *Acta Mater.* **2018**, *158*, 118.
- [104] a) J. S. van der Burgt, J. J. Geuchies, B. van der Meer, H. Vanrompay, D. Zanaga, Y. Zhang, W. Albrecht, A. V. Petukhov, L. Filion, S. Bals, I. Swart, D. Vanmaekelbergh, *J. Phys. Chem. C* **2018**, *122*, 15706; b) D. Vanmaekelbergh, L. K. van Vugt, H. E. Bakker, F. T. Rabouw, B. de Nijs, R. J. A. van Dijk-Moes, M. A. van Huis, P. J. Baesjou, A. van Blaaderen, *ACS Nano* **2015**, *9*, 3942.
- [105] X. Zhou, Z. Li, X. Deng, B. Yan, Z. Wang, X. Chen, S. Huang, *Nanotechnology* **2019**, *30*, 445401.
- [106] P. V. Kamat, *J. Phys. Chem. Lett.* **2013**, *4*, 908.
- [107] K. Ojha, T. Debnath, P. Maity, M. Makkar, S. Nejati, K. V. Ramanujachary, P. K. Chowdhury, H. N. Ghosh, A. K. Ganguli, *J. Phys. Chem. C* **2017**, *121*, 6581.
- [108] G. D. Park, J. Lee, Y. Piao, Y. C. Kang, *Chem. Eng. J.* **2018**, *335*, 600.
- [109] G. Guo, L. Ji, X. Shen, B. Wang, H. Li, J. Hu, D. Yang, A. Dong, *J. Mater. Chem. A* **2016**, *4*, 16128.
- [110] D. S. Jung, T. H. Hwang, S. B. Park, J. W. Choi, *Nano Lett.* **2013**, *13*, 2092.
- [111] W. Liu, P. Gao, Y. Mi, J. Chen, H. Zhou, X. Zhang, *J. Mater. Chem. A* **2013**, *1*, 2411.
- [112] Y. Zhang, K. Li, P. Ji, D. Chen, J. Zeng, Y. Sun, P. Zhang, J. Zhao, *J. Mater. Sci.* **2017**, *52*, 3630.
- [113] B. Huang, X. Zheng, X. Fan, G. Song, M. Lu, *Electrochim. Acta* **2011**, *56*, 4865.
- [114] J. W. Yoo, K. Zhang, V. Patil, J. T. Lee, D.-W. Jung, L. S. Pu, W. Oh, W.-S. Yoon, J. H. Park, G.-R. Yi, *Mater. Express* **2018**, *8*, 316.
- [115] J. He, K. Zhou, Y. Chen, C. Xu, J. Lin, W. Zhang, *Mater. Today Energy* **2016**, *1–2*, 11.
- [116] L. Chen, X. Xie, B. Wang, K. Wang, J. Xie, *Mater. Sci. Eng., B* **2006**, *131*, 186.
- [117] Z. Cao, X. Chen, L. Xing, Y. Liao, M. Xu, X. Li, X. Liu, W. Li, *J. Power Sources* **2018**, *379*, 174.
- [118] S. H. Lee, S.-H. Yu, J. E. Lee, A. Jin, D. J. Lee, N. Lee, H. Jo, K. Shin, T.-Y. Ahn, Y.-W. Kim, H. Choe, Y.-E. Sung, T. Hyeon, *Nano Lett.* **2013**, *13*, 4249.
- [119] D. Han, G. Guo, Y. Yan, T. Li, B. Wang, A. Dong, *Energy Storage Mater.* **2018**, *10*, 32.
- [120] a) G. Backert, B. Oschmann, M. N. Tahir, F. Mueller, I. Lieberwirth, B. Balke, W. Tremel, S. Passerini, R. Zentel, *J. Colloid Interface Sci.* **2016**, *478*, 155; b) G.-W. Zhou, J. Wang, P. Gao, X. Yang, Y.-S. He, X.-Z. Liao, J. Yang, Z.-F. Ma, *Ind. Eng. Chem. Res.* **2013**, *52*, 1197.
- [121] J. Xiong, Y. Yang, J. Zeng, J. Wang, J. Zhao, *J. Mater. Sci.* **2018**, *53*, 16447.
- [122] H. Sohn, D. H. Kim, R. Yi, D. Tang, S.-E. Lee, Y. S. Jung, D. Wang, *J. Power Sources* **2016**, *334*, 128.
- [123] a) G. D. Park, J. H. Choi, D. S. Jung, J.-S. Park, Y. C. Kang, *J. Alloys Compd.* **2020**, *821*, 153224; b) S. Li, X. Qin, H. Zhang, J. Wu, Y.-B. He, B. Li, F. Kang, *Electrochim. Commun.* **2014**, *49*, 98; c) X. Men, T. Wang, B. Xu, Z. Kong, X. Liu, A. Fu, Y. Li, P. Guo, Y.-G. Guo, H. Li, X. S. Zhao, *Electrochim. Acta* **2019**, *324*, 134850; d) A. Magasinski, P. Dixon, B. Hertzberg, A. Kvit, J. Ayala, G. Yushin, *Nat. Mater.* **2010**, *9*, 353; e) M. Zhang, X. Hou, J. Wang, M. Li, S. Hu, Z. Shao, X. Liu, *J. Alloys Compd.* **2014**, *588*, 206; f) J. Bae, *J. Solid State Chem.* **2011**, *184*, 1749.
- [124] a) M. Li, X. Hou, Y. Sha, J. Wang, S. Hu, X. Liu, Z. Shao, *J. Power Sources* **2014**, *248*, 721; b) Q. Pan, P. Zuo, S. Lou, T. Mu, C. Du, X. Cheng, Y. Ma, Y. Gao, G. Yin, *J. Alloys Compd.* **2017**, *723*, 434.
- [125] C. Ma, Z. Wang, Y. Zhao, Y. Li, J. Shi, *J. Alloys Compd.* **2020**, *844*, 156201.
- [126] a) J. Lin, J. He, Y. Chen, Q. Li, B. Yu, C. Xu, W. Zhang, *Electrochim. Acta* **2016**, *215*, 667; b) N. Liu, Z. Lu, J. Zhao, M. T. McDowell, H.-W. Lee, W. Zhao, Y. Cui, *Nat. Nanotechnol.* **2014**, *9*, 187.
- [127] Q. Xu, J.-Y. Li, J.-K. Sun, Y.-X. Yin, L.-J. Wan, Y.-G. Guo, *Adv. Energy Mater.* **2017**, *7*, 1601481.
- [128] Y.-C. Zhang, Y. You, S. Xin, Y.-X. Yin, J. Zhang, P. Wang, X.-s. Zheng, F.-F. Cao, Y.-G. Guo, *Nano Energy* **2016**, *25*, 120.
- [129] W. Cheng, H. Di, Z. Shi, D. Zhang, *J. Alloys Compd.* **2020**, *831*, 154607.
- [130] L. Lefrançois Perreault, F. Colò, G. Meligrana, K. Kim, S. Fiorilli, F. Bella, J. R. Nair, C. Vitale-Brovarone, J. Florek, F. Kleitz, J. Florek, F. Kleitz, C. Gerbaldi, *Adv. Energy Mater.* **2018**, *8*, 1802438.
- [131] G. Zhu, Q. Li, Y. Zhao, R. Che, *ACS Appl. Mater. Interfaces* **2017**, *9*, 41258.
- [132] X. Wu, J. Ma, Q. Ma, S. Xu, Y.-S. Hu, Y. Sun, H. Li, L. Chen, X. Huang, *J. Mater. Chem. A* **2015**, *3*, 13193.
- [133] Z. Shan, Y. He, T. Tan, Y. Zhang, X. Wang, *Solid State Sci.* **2019**, *94*, 77.
- [134] J. Zhang, Y. Fang, L. Xiao, J. Qian, Y. Cao, X. Ai, H. Yang, *ACS Appl. Mater. Interfaces* **2017**, *9*, 7177.
- [135] J. H. Choi, S.-K. Park, Y. C. Kang, *Small* **2019**, *15*, 1803043.
- [136] F. Xie, L. Zhang, D. Su, M. Jaronic, S.-Z. Qiao, *Adv. Mater.* **2017**, *29*, 1700989.
- [137] J. K. Kim, S.-K. Park, J.-S. Park, Y. C. Kang, *J. Mater. Chem. A* **2019**, *7*, 2636.
- [138] J. Huang, Y. Xiao, Z. Peng, Y. Xu, L. Li, L. Tan, K. Yuan, Y. Chen, *Adv. Sci.* **2019**, *6*, 1900107.

- [139] Y. Liu, C. Yu, H. Che, Z. Guo, J. Mu, X. Zhang, A. Liu, *J. Colloid Interface Sci.* **2021**, 581, 485.
- [140] Y. Yan, A. Li, C. Lu, T. Zhai, S. Lu, W. Li, W. Zhou, *Chem. Eng. J.* **2020**, 396, 125316.
- [141] A. Jeyaranjan, T. S. Sakthivel, C. J. Neal, S. Seal, *Carbon* **2019**, 151, 192.
- [142] Y. Li, H. Wang, C. Priest, S. Li, P. Xu, G. Wu, *Adv. Mater.* **2020**, 2000381.
- [143] G. Ro, D. K. Hwang, Y. Kim, *J. Ind. Eng. Chem.* **2019**, 79, 364.
- [144] R. Balgis, W. Widiyastuti, T. Ogi, K. Okuyama, *ACS Appl. Mater. Interfaces* **2017**, 9, 23792.
- [145] C. Descorme, P. Gallezot, C. Geantet, C. George, *ChemCatChem* **2012**, 4, 1897.
- [146] G. Prieto, H. Tüysüz, N. Duyckaerts, J. Knossalla, G.-H. Wang, F. Schüth, *Chem. Rev.* **2016**, 116, 14056.
- [147] P. Anastas, N. Eghbali, *Chem. Soc. Rev.* **2010**, 39, 301.
- [148] R. A. Sheldon, I. Arends, U. Hanefeld, *Green Chemistry and Catalysis*, John Wiley & Sons, New York **2007**.
- [149] L. Gradon, R. Balgis, T. Hirano, A. M. Rahmatika, T. Ogi, K. Okuyama, *J. Aerosol Sci.* **2020**, 149, 105608.
- [150] E. Drioli, L. Giorno, *Membrane Operations: Innovative Separations and Transformations*, Wiley-VCH, Weinheim, Germany **2009**.
- [151] a) M. J. Ndolomingo, N. Bingwa, R. Meijboom, *J. Mater. Sci.* **2020**, 55, 6195; b) K. Parveen, V. Banse, L. Ledwani, *AIP Conf. Proc.* **1724**, 1, 020048.
- [152] D. Luo, X. Qin, Q. Song, X. Qiao, Z. Zhang, Z. Xue, C. Liu, G. Mo, T. Wang, *Adv. Funct. Mater.* **2017**, 27, 1701982.
- [153] K. Hou, J. Han, Z. Tang, *ACS Mater. Lett.* **2020**, 2, 95.
- [154] C. Li, H. Che, P. Huo, Y. Yan, C. Liu, H. Dong, *J. Colloid Interface Sci.* **2021**, 581, 764.
- [155] R. Shi, Y. Cao, Y. Bao, Y. Zhao, G. I. N. Waterhouse, Z. Fang, L.-Z. Wu, C.-H. Tung, Y. Yin, T. Zhang, *Adv. Mater.* **2017**, 29, 1700803.
- [156] H. Karimi-Maleh, B. G. Kumar, S. Rajendran, J. Qin, S. Vadivel, D. Durgalakshmi, F. Gracia, M. Soto-Moscoco, Y. Orooji, F. Karimi, *J. Mol. Liq.* **2020**, 314, 113588.
- [157] R. D. Tentu, S. Basu, *Curr. Opin. Electrochem.* **2017**, 5, 56.
- [158] L. Li, Y. Chu, Y. Liu, L. Dong, *J. Phys. Chem. C* **2007**, 111, 2123.
- [159] J. Di, J. Xia, M. Ji, H. Li, H. Xu, H. Li, R. Chen, *Nanoscale* **2015**, 7, 11433.
- [160] S. Lardhi, L. Cavallo, M. Harb, *J. Phys. Chem. Lett.* **2020**, 11, 5497.
- [161] a) A. B. D. Nandiyanto, F. Iskandar, K. Okuyama, *Chem. Eng. J.* **2009**, 152, 293; b) S. Wooh, H. Huesmann, M. N. Tahir, M. Paven, K. Wichmann, D. Vollmer, W. Tremel, P. Papadopoulos, H.-J. Butt, *Adv. Mater.* **2015**, 27, 7338.
- [162] F. Iskandar, A. B. D. Nandiyanto, K. M. Yun, C. J. Hogan, K. Okuyama, P. Biswas, *Adv. Mater.* **2007**, 19, 1408.
- [163] L. Shi, X. Wang, Y. Hu, Y. He, *Sol. Energy* **2020**, 196, 505.
- [164] W. Liu, M. Kappel, H.-J. Butt, *ACS Nano* **2019**, 13, 13949.
- [165] A. B. D. Nandiyanto, O. Arutanti, T. Ogi, F. Iskandar, T. O. Kim, K. Okuyama, *Chem. Eng. Sci.* **2013**, 101, 523.
- [166] O. Arutanti, A. B. D. Nandiyanto, T. Ogi, T. O. Kim, K. Okuyama, *ACS Appl. Mater. Interfaces* **2015**, 7, 3009.
- [167] A. L. Costa, B. Ballarin, A. Spegini, F. Casoli, D. Gardini, *J. Colloid Interface Sci.* **2012**, 388, 31.
- [168] S. Kattel, P. Liu, J. G. Chen, *J. Am. Chem. Soc.* **2017**, 139, 9739.
- [169] F. Niu, L. Zhang, S.-Z. Luo, W.-G. Song, *Chem. Commun.* **2010**, 46, 1109.
- [170] C. Huang, H. Zhang, Z. Sun, Y. Zhao, S. Chen, R. Tao, Z. Liu, *J. Colloid Interface Sci.* **2011**, 364, 298.
- [171] J. Jiang, C. Wen, Z. Tian, Y. Wang, Y. Zhai, L. Chen, Y. Li, Q. Liu, C. Wang, L. Ma, *Ind. Eng. Chem. Res.* **2020**, 59, 2155.
- [172] W. Zhang, J. Qian, Y. Lei, C. Zhang, J. Ma, *Environ. Sci. Pollut. Res. Int.* **2020**, 27, 22631.
- [173] T. Wang, C. Liu, X. Ma, W. Zhu, X. Lv, H. Zhang, *Nanomaterials* **2019**, 9, 998.
- [174] T. Yang, H. Li, J. He, Y. Liu, W. Zhao, Z. Wang, X. Ji, S. Yang, *ACS Omega* **2017**, 2, 1047.
- [175] *Lahti Cleantech Annual Review* (Ed: K. Cura), Lahti **2016**.
- [176] A. M. King, S. C. Burgess, W. Ijomah, C. A. McMahon, *Sustain. Dev.* **2006**, 14, 257.
- [177] *ACS Symposium Series*, Vol. 1008 (Ed: R. H. Fernando), American Chemical Society, Washington, DC **2009**.
- [178] Z. Ye, Y. Chen, X. Yang, W. Hu, H. Ye, *Colloids Surf., A* **2017**, 514, 251.
- [179] X. Fan, L. Niu, Y. Wu, J. Cheng, Z. Yang, *Appl. Surf. Sci.* **2015**, 332, 393.
- [180] G. Sun, M. Fan, L. Chen, J. Luo, R. Liu, *Colloids Surf., A* **2020**, 589, 124458.
- [181] W. Jiang, C. M. Grozea, Z. Shi, G. Liu, *ACS Appl. Mater. Interfaces* **2014**, 6, 2629.
- [182] W. Ming, D. Wu, R. van Benthem, G. de With, *Nano Lett.* **2005**, 5, 2298.
- [183] X. Han, J. Peng, S. Jiang, J. Xiong, Y. Song, X. Gong, *Langmuir* **2020**, 36, 11044.
- [184] T. Song, T. Liu, X. Yang, F. Bai, *Colloids Surf., A* **2015**, 469, 60.
- [185] S. Pan, M. Chen, L. Wu, *J. Colloids Interface Sci.* **2018**, 522, 20.
- [186] X. Liu, X. Du, J. He, *Chem. Phys. Chem* **2008**, 9, 305.
- [187] E. S. A. Goerlitzer, R. N. Klupp Taylor, N. Vogel, *Adv. Mater.* **2018**, 30, 1706654.
- [188] a) F. Delgado-Vargas, O. Paredes-Lopez, *Natural Colorants for Food and Nutraceuical Uses*, CRC Press, Boca Raton, FL **2003**; b) G. Pfaff, P. Reynders, *Chem. Rev.* **1999**, 99, 1963.
- [189] N. Koay, I. B. Burgess, T. M. Kay, B. A. Neger, M. Miles-Rossouw, T. Shirman, T. L. Vu, G. England, K. R. Phillips, S. Utech, N. Vogel, M. Kolle, J. Aizenberg, *Opt. Express* **2014**, 22, 27750.
- [190] J.-G. Park, S.-H. Kim, S. Magkiriadou, T. M. Choi, Y.-S. Kim, V. N. Manoharan, *Angew. Chem., Int. Ed.* **2014**, 53, 2899.
- [191] J. M. Clough, E. Guimard, C. Rivet, J. Sprakel, T. E. Kodger, *Adv. Opt. Mater.* **2019**, 7, 1900218.
- [192] R. Vaz, M. F. Frasco, M. G. F. Sales, *Nanoscale Adv.* **2020**, 2, 5106.
- [193] M. Sakai, H. Kim, Y. Arai, T. Teratani, Y. Kawai, Y. Kuwahara, K. Abe, Y. Kuwana, K. Ikeda, K. Yamada, Y. Takeoka, *ACS Appl. Nano Mater.* **2020**, 3, 7047.
- [194] Y. f. Jiang, A. Zheng, S. j. Zheng, W. m. Liu, L. Zhuang, *J. Appl. Phys.* **2020**, 128, 103106.
- [195] M. Sakai, T. Seki, Y. Takeoka, *ACS Sustainable Chem. Eng.* **2019**, 7, 14933.
- [196] R. Ohnuki, M. Sakai, Y. Takeoka, S. Yoshioka, *Langmuir* **2020**, 36, 5579.
- [197] N. Vogel, S. Utech, G. T. England, T. Shirman, K. R. Phillips, N. Koay, I. B. Burgess, M. Kolle, D. A. Weitz, J. Aizenberg, *Proc. Natl. Acad. Sci. USA* **2015**, 112, 10845.
- [198] T. Sai, B. D. Wilts, A. Sicher, U. Steiner, F. Scheffold, E. R. Dufresne, *Chimia* **2019**, 73, 47.
- [199] D.-S. Choi, J.-H. Choi, C.-Y. Lee, *Appl. Sci.* **2020**, 10, 420.
- [200] C.-F. Lai, Y.-C. Wang, *Crystals* **2016**, 6, 61.
- [201] J. Wang, U. Sultan, E. S. A. Goerlitzer, C. F. Mbah, M. Engel, N. Vogel, *Adv. Funct. Mater.* **2020**, 30, 1907730.
- [202] D. Dendukuri, P. S. Doyle, *Adv. Mater.* **2009**, 21, 4071.
- [203] Y. Takeoka, S. Yoshioka, M. Teshima, A. Takano, M. Harun-Ur-Rashid, T. Seki, *Sci. Rep.* **2013**, 3, 2371.
- [204] J. L. Blatti, *J. Chem. Educ.* **2017**, 94, 211.
- [205] F. Osterloh, H. Hiramatsu, R. Porter, T. Guo, *Langmuir* **2004**, 20, 5553.
- [206] J. Lee, A. O. Govorov, N. A. Kotov, *Angew. Chem., Int. Ed.* **2005**, 44, 7439.
- [207] S. Wenderoth, T. Granath, J. Prieschl, S. Wintzheimer, K. Mandel, *Adv. Photonics Res.* **2020**, 1, 2000023.

- [208] S. Müssig, T. Granath, T. Schembri, F. Fidler, D. Haddad, K.-H. Hiller, S. Wintzheimer, K. Mandel, *ACS Appl. Nano Mater.* **2019**, *2*, 4698.
- [209] a) S. Wintzheimer, S. Müssig, S. Wenderoth, J. Prieschl, T. Granath, F. Fidler, D. Haddad, K. Mandel, *ACS Appl. Nano Mater.* **2019**, *2*, 6757; b) S. Wintzheimer, J. Reichstein, S. Wenderoth, S. Hasselmann, M. Oppmann, M. T. Seuffert, K. Müller-Buschbaum, K. Mandel, *Adv. Funct. Mater.* **2019**, *29*, 1901193.
- [210] S. P. Gundupalli, S. Hait, A. Thakur, *Waste Manage* **2017**, *60*, 56.
- [211] J. Woidasky, J. Moeslein, P. Wendler, D. Kirchenbauer, D. Wacker, G. Gao, C. Lang-Koetz, *Chem. Ing. Tech.* **2020**, *92*, 441.
- [212] S. R. Ahmad, *Environ. Technol.* **2004**, *25*, 1143.
- [213] G. Gao, A. Turshatov, I. A. Howard, D. Busko, R. Joseph, D. Hudry, B. S. Richards, *Adv. Sustainable Syst.* **2017**, *1*, 1600033.
- [214] a) Y. Xia, Z. Tang, *Adv. Funct. Mater.* **2012**, *22*, 2585; b) L. Scarabelli, M. Schumacher, D. Jimenez de Aberasturi, J.-P. Merkl, M. Henriksen-Lacey, T. Milagres de Oliveira, M. Janschel, C. Schmidtke, S. Bals, H. Weller, L. M. Liz-Marzán, *Adv. Funct. Mater.* **2019**, *29*, 1809071.
- [215] a) S. Shikha, T. Salafi, J. Cheng, Y. Zhang, *Chem. Soc. Rev.* **2017**, *46*, 7054; b) D. Paunescu, W. J. Stark, R. N. Grass, *Powder Technol.* **2016**, *291*, 344.
- [216] S. Müssig, F. Fidler, D. Haddad, K.-H. Hiller, S. Wintzheimer, K. Mandel, *Adv. Mater. Technol.* **2019**, *4*, 1900300.
- [217] a) D.-S. Wang, A. Mukhtar, K.-M. Wu, L. Gu, X. Cao, *Materials* **2019**, *12*, 3908; b) B. C. Park, Y. K. Kim, *Met. Mater. Int.* **2017**, *23*, 413.
- [218] J. Lee, P. W. Bisso, R. L. Srinivas, J. J. Kim, A. J. Swiston, P. S. Doyle, *Nat. Mater.* **2014**, *13*, 524.
- [219] Q. Zhang, X. Wang, Y. Zhu, *J. Mater. Chem.* **2011**, *21*, 12132.
- [220] L. Bao, H. You, L. Wang, L. Li, R. Qiao, Y. Zhang, Y. Zhong, Y. Xiong, Z. Li, *J. Mater. Chem. C* **2014**, *2*, 8949.
- [221] Q. Ma, I. C. Serrano, E. Palomares, *Chem. Commun.* **2011**, *47*, 7071.
- [222] a) J. Yang, S. R. Dave, X. Gao, *J. Am. Chem. Soc.* **2008**, *130*, 5286; b) Y. Zhang, A. R. Clapp, *RSC Adv.* **2014**, *4*, 48399.
- [223] X. Gao, S. Nie, *Anal. Chem.* **2004**, *76*, 2406.
- [224] F. Song, P. S. Tang, H. Durst, D. T. Cramb, W. C. W. Chan, *Angew. Chem., Int. Ed.* **2012**, *51*, 8773.
- [225] X.-H. Ji, N.-G. Zhang, W. Cheng, F. Guo, W. Liu, S.-S. Guo, Z.-K. He, X.-Z. Zhao, *J. Mater. Chem.* **2011**, *21*, 13380.
- [226] C.-G. Yang, L. Cheng, W.-Q. Ye, D.-H. Zheng, Z.-R. Xu, *Colloids Surf., A* **2020**, *588*, 124373.
- [227] Y. Zhao, Y. Cheng, L. Shang, J. Wang, Z. Xie, Z. Gu, *Small* **2015**, *11*, 151.
- [228] M. Han, X. Gao, J. Z. Su, S. Nie, *Nat. Biotechnol.* **2001**, *19*, 631.
- [229] F. Miller, S. Wintzheimer, T. Reuter, P. Groppe, J. Prieschl, M. Retter, K. Mandel, *ACS Appl. Nano Mater.* **2020**, *3*, 734.
- [230] C. Fernández-López, C. Mateo-Mateo, R. A. Alvarez-Puebla, J. Pérez-Juste, I. Pastoriza-Santos, L. M. Liz-Marzán, *Langmuir* **2009**, *25*, 13894.
- [231] M. Puddu, D. Paunescu, W. J. Stark, R. N. Grass, *ACS Nano* **2014**, *8*, 2677.
- [232] Q. Ma, Y. Nakane, Y. Mori, M. Hasegawa, Y. Yoshioka, T. M. Watanabe, K. Gonda, N. Ohuchi, T. Jin, *Biomaterials* **2012**, *33*, 8486.
- [233] Y. Zhang, C. Dong, L. Su, H. Wang, X. Gong, H. Wang, J. Liu, J. Chang, *ACS Appl. Mater. Interfaces* **2016**, *8*, 745.
- [234] R. Li, Y. Zhang, J. Tan, J. Wan, J. Guo, C. Wang, *ACS Appl. Mater. Interfaces* **2016**, *8*, 9384.
- [235] J. K. Stolarczyk, A. Deak, D. F. Brougham, *Adv. Mater.* **2016**, *28*, 5400.
- [236] O. D. Velev, S. Gupta, *Adv. Mater.* **2009**, *21*, 1897.
- [237] R. P. Feynman, *Eng. Sci.* **1960**, *23*, 22.



**Susanne Wintzheimer** is postdoc and group manager of the Supraparticle Group at the Friedrich-Alexander University Erlangen-Nürnberg, Germany, since 2020. Since 2021, she additionally is Scientific Head of the Particle Technology Group at the Fraunhofer Institute for Silicate Research ISC in Würzburg, Germany. She holds a Ph.D. in chemistry (graduated: 2017) from the University of Bordeaux, France. Her research interest is especially in the combination of organic and inorganic molecules and inorganic nanoparticles within supraparticles. To date she has published about 18 papers.



**Jakob Reichstein** studied functional materials at the Julius-Maximilians University of Würzburg, Germany, and received his M.Sc. degree in 2019. Consecutively, he started his Ph.D. with Prof. K. Mandel. Currently, he is a Ph.D. scholarship holder of the German Federal Environmental Foundation (DBU) and research associate in Inorganic Chemistry at the Friedrich-Alexander University Erlangen-Nürnberg. His research focuses on sensor-, and indicator supraparticles based on various luminescent nanoparticles for recording harmful environmental triggers.



**Philipp Groppe** is a Ph.D. candidate in the group of Prof. K. Mandel and research associate in Inorganic Chemistry at the Friedrich-Alexander University Erlangen-Nürnberg, Germany. He studied functional materials at the Julius-Maximilians-University Würzburg, Germany and graduated with a M.Sc. in 2020. His current research focuses on the assembly of porous supraparticles and their beneficial use in various applications, such as in catalysis or as adsorber materials.



**Andreas Wolf** is a PhD candidate working within a cooperation of the Fraunhofer Institute for Silicate Research ISC in Würzburg and the group of Prof. Karl Mandel at the Friedrich-Alexander University Erlangen-Nürnberg. He has been a research assistant at ISC since 2014 and contributed to different projects in the field of lithium-ion batteries. After further work on various topics at the University of New Mexico, the BMW Group and the Norwegian Institute for Energy Technology he finished his Masters degree in material science at the Julius-Maximilians University Würzburg in 2020. His current focus lies on recycling of lithium-ion batteries.



**Bastian Fett** is currently doing his Ph.D. in the group of Prof. Karl Mandel at the Fraunhofer-Institute for Silicate Research. He graduated with an M.Sc. in the fields of materials science and entrepreneurship from the Technical University Darmstadt, Germany, and the Aalto University, Finland, in 2019. His current research focuses on new materials for perovskite-based tandem solar cell applications by working on both, contact and absorber materials.



**Huanhuan Zhou** joined the Supraparticle Group as a Ph.D. candidate in October 2020. She obtained her master's degree from National Center for Nanoscience and Technology, University of Chinese Academy of Sciences in 2020. Her research focuses on the design of spray-dried supraparticles.



**Rosa Pujales-Paradela** is a postdoctoral researcher and research associate in the Professorship for Inorganic Chemistry (Prof. Mandel) at the Friedrich-Alexander University Erlangen-Nürnberg, Germany. She completed her Ph.D. studies in the University of Coruña, Spain, on the design of novel contrast agents for their use in magnetic resonance imaging (MRI) applications in 2019. Her current research focuses on the combination of different materials into porous supraparticle structures for their use in diverse applications, e.g., optical and magnetic markers, adsorbents, and purification.



**Franziska Miller** is a Ph.D. candidate and research associate in Prof. K. Mandel's research group at the Friedrich-Alexander University Erlangen-Nürnberg, Germany. She studied Nanoscience at the Eberhard Karls University Tübingen, Germany and received her M.Sc. in 2018. As part of her studies, she contributed to different projects in the field of functional nano- and supraparticles at the Fraunhofer-Institute for Silicate Research ISC in Würzburg, Germany. Her research focus is currently on the synthesis and characterization of optical ID marker supraparticles assembled from nanoparticle building blocks with distinct optical properties.



**Stephan Müssig** is a Ph.D. scholarship holder of the German Federal Environmental Foundation (DBU) and research associate in Inorganic Chemistry at the Friedrich-Alexander University Erlangen-Nürnberg, Germany. He graduated with an M.Sc. from the Julius-Maximilians University Würzburg, Germany in 2018. His research focus is currently on magnetic nano- and supraparticles on his way to create a magnetic marker technology for various applications.



**Sarah Wenderoth** studied chemistry at the Saarland University, Germany, and received her M.Sc. in 2018. Since then, she is a Ph.D. candidate at the Julius-Maximilians University Würzburg. Her current research focuses on the field of synthesis and functionalisation of nanoparticles, and their assembly into supraparticles to create smart and communicating surfaces with respect to mechanical shear stress.



**Karl Mandel** is Professor for Inorganic Chemistry at the Friedrich-Alexander University Erlangen-Nürnberg, Germany, since 2020, and Head of the Particle Technology Group at the Fraunhofer Institute for Silicate Research ISC in Würzburg, Germany, since 2014. He holds a Ph.D. in chemistry (graduated: 2013) from the Julius-Maximilians University Würzburg, Germany. His research interest is in creating supraparticles—mostly via spray-drying—to find new and unexpected properties and employing them as smart objects to contribute to sustainability.



### Erklärung zur Autorenschaft

Abrasion Indicators for Smart Surfaces Based on a Luminescence Turn-On Effect in Supraparticles, Sarah Wenderoth, Tim Granath, Johannes Prieschl, Susanne Wintzheimer, Karl Mandel, Advanced Photonics Research, 2020, 1, 2000023  
 Detaillierte Darstellung der Anteile an der Veröffentlichung (in %)

**Sarah Wenderoth (S. We., Hauptautor), Tim Granath (T.G.), Johannes Prieschl (J. P.), Susanne Wintzheimer (S. Wi.) , Karl Mandel (K. M.), korrespondierender Autor)**

Autor	S. We.	T. G.	J. P.	S. Wi.	K. M.	$\Sigma$ in Prozent
Konzept	10 %			9 %	6 %	25 %
Synthese Nanobausteine	6 %					6 %
Entwicklung Eisenoxid-Nanopartikel		5 %				5 %
Sprüh Trocknung	10 %					10 %
Charakterisierung der Schichten	20 %		3 %			23 %
Verfassen der Veröffentlichung	10 %	2 %		8 %	3 %	23 %
Korrektur der Veröffentlichung	3 %			2 %		5 %
Koordination der Veröffentlichung	1 %			1 %	1 %	3 %
<b>Summe</b>	<b>60 %</b>	<b>7 %</b>	<b>3 %</b>	<b>20 %</b>	<b>10 %</b>	<b>100%</b>



### Erklärung zur Autorenschaft

Optically sensitive and magnetically identifiable supraparticles as indicators of surface abrasion, Sarah Wenderoth, Stephan Müssig, Emille Genin, Karine Heuzé, Florian Fidler, Daniel Haddad, Susanne Wintzheimer, Karl Mandel, Nano Letters, 2022, 22, 7, 2762-2768  
 Detaillierte Darstellung der Anteile an der Veröffentlichung (in %)

**Sarah Wenderoth (S. We., Hauptautor), Stephan Müssig (S. M., Hauptautor), Johannes Prieschl (J. P.), Emille Genin (E. G.), Karine Heuzé (K. H.), Florian Fidler (F. F.), Daniel Haddad (D. H.), Susanne Wintzheimer (S. Wi.), Karl Mandel (K. M., korrespondierender Autor)**

Autor	S. We.	S. M.	J. P.	E. G.	K. H.	F. F.	D. H.	S. Wi.	K. M.	Σ in Prozent
Konzept	11 %	11 %						2 %	3 %	27 %
Synthese magnetischer Bausteine		5 %								5 %
Synthese optischer Bausteine	3 %									3 %
Farbstoffmodifikation	4 %			4 %	4 %			1 %		13 %
Sprühtrocknung	2 %	3 %	2 %							7 %
Optische Charakterisierung der Schichten	5 %									5 %
Magnetische Charakterisierung der Schichten		6 %				3 %	1 %			10 %
Verfassen der Veröffentlichung	6 %	6 %		1 %	1 %	1 %	1 %	2 %	2 %	20 %
Korrektur der Veröffentlichung	3 %	3 %								6 %
Koordination der Veröffentlichung	1 %	1 %						1 %	1 %	4 %
<b>Summe</b>	<b>35 %</b>	<b>35 %</b>	<b>2 %</b>	<b>5 %</b>	<b>5 %</b>	<b>4 %</b>	<b>2 %</b>	<b>6 %</b>	<b>6 %</b>	<b>100 %</b>



## Erklärung zur Autorenschaft

Supraparticles with Mechanically Triggerable Color-Change-Effect to Equip Coatings with the Ability to Report Damage, Sarah Wenderoth, Andreas Eigen, Susanne Wintzheimer Johannes Prieschl, Andreas Hirsch, Marcus Halik, Karl Mandel, *Small*, 2022, 18, 2107513  
 Detaillierte Darstellung der Anteile an der Veröffentlichung (in %)

**Sarah Wenderoth (S.We., Hauptautor), Andreas Eigen (A.E., Hauptautor), Susanne Wintzheimer (S.Wi.), Johannes Prieschl (J.P.), Andreas Hirsch (A.H.), Marcus Halik (M.H., korrespondierender Autor), Karl Mandel (K.M., korrespondierender Autor)**

Autor	S.We.	A.E.	S.Wi.	J.P.	A.H.	M.H.	K.M.	$\Sigma$ in Prozent
Konzept	5%	5%	3%			3%	3%	19%
Synthese Nano- und Suprapartikel	3%							3%
Entwicklung PBI-PA-Farbstoff					3%			3%
Modifikation Suprapartikel mit PBI-PA-Farbstoff		10%						10%
Herstellung Schichten und Charakterisierung	8%			3%				11%
Verfassen der Veröffentlichung	10%	8%	3%		2%	2%	2%	27%
Korrektur der Veröffentlichung	8%	7%	2%			3%	3%	23%
Koordination der Veröffentlichung	2%		2%					4%
<b>Summe</b>	<b>36%</b>	<b>30%</b>	<b>10%</b>	<b>3%</b>	<b>5%</b>	<b>8%</b>	<b>8%</b>	<b>100%</b>



### Erklärung zur Autorenschaft

Spray-Dried Photonic Balls with a Disordered/Ordered Hybrid Structure for Shear-Stress Indication, Sarah Wenderoth, Gudrun Bleyer, Jakob Endres, Johannes Prieschl, Nicolas Vogel, Susanne Wintzheimer, Karl Mandel, *Small*, 2022, 18, 2203068  
 Detaillierte Darstellung der Anteile an der Veröffentlichung (in %)

**Sarah Wenderoth (S.We., Hauptautor), Gudrun Bleyer (G.B.), Jakob Endres (J.E.), Johannes Prieschl (J.P.), Nicolas Vogel (N.V.), Susanne Wintzheimer (S.Wi.), Karl Mandel (K.M., korrespondierender Autor)**

Autor	S.We.	G.B.	J.E.	J.P.	N.V.	S.Wi.	K.M.	$\Sigma$ in Prozent
Konzept	10%					3%	3%	16%
Synthese Nano- und Suprapartikel	5%		2%					7%
Charakterisierung Suprapartikel	6%	2%	2%	2%				12%
Diskussion und Interpretation der Ergebnisse	8%	3%			2%	4%	2%	19%
Erstellung Abbildungen	8%							8%
Verfassen der Veröffentlichung	10%					2%	1%	13%
Korrektur der Veröffentlichung	10%	3%			2%	3%	3%	21%
Koordination der Veröffentlichung	3%					1%		4%
<b>Summe</b>	<b>60%</b>	<b>8%</b>	<b>4%</b>	<b>2%</b>	<b>4%</b>	<b>13%</b>	<b>9%</b>	<b>100%</b>



### Erklärung zur Autorenschaft

Hollow Superparamagnetic Nanoparticle-Based Microballoons for Mechanical Force Monitoring by Magnetic Particle Spectroscopy, Susanne Wintzheimer, Stephan Müssig, Sarah Wenderoth, Johannes Prieschl, Tim Granath, Florian Fidler, Daniel Haddad, and Karl Mandel, ACS Applied Nano Materials, 2019, 2, 10, 6757-6762  
 Detaillierte Darstellung der Anteile an der Veröffentlichung (in %)

Autor	S. Wi.	S. M.	S. W.	J. P.	T. G.	F. F.	D. H.	K. M.	Σ in Prozent
Konzept	10 %	5 %	4 %					6 %	25%
Synthese Microballoons					3 %				3%
Scherversuche		2 %	2 %	2 %					6%
Charakterisierung mittels MPS		4 %				3 %	3 %		10%
Charakterisierung mittels Mikroskopie			2 %	2 %					4%
Verfassen der Veröffentlichung	10 %	6 %	5 %		2 %	2 %	2 %	3 %	30%
Korrektur der Veröffentlichung	8 %	3 %	2 %					2 %	15%
Koordination der Veröffentlichung	7 %								7%
<b>Summe</b>	<b>35 %</b>	<b>20 %</b>	<b>15 %</b>	<b>4 %</b>	<b>5 %</b>	<b>5 %</b>	<b>5 %</b>	<b>11 %</b>	<b>100%</b>

Susanne Wintzheimer (S. Wi., Hauptautor), Stephan Müssig (S. M.), Sarah Wenderoth (S. W.), Johannes Prieschl (J. P.), Tim Granath (T. G.), Florian Fidler (F. F.), Daniel Haddad (D. H.), Karl Mandel (K. M., korrespondierender Autor)



### Erklärung zur Autorenschaft

Expanding the Horizon of Mechanochromic Detection by Luminescent Shear Stress Sensor Supraparticles, Susanne Wintzheimer, Sarah Wenderoth, Sebastian Hasselmann, Maximilian Oppmann, Marcel T. Seuffert, Klaus Müller-Buschbaum, Karl Mandel, Advanced Functional Materials, 2019, 29, 1901193  
 Detaillierte Darstellung der Anteile an der Veröffentlichung (in %)

**Susanne Wintzheimer (S.Wi., Hauptautor), Jakob Reichstein (J.R.), Sarah Wenderoth (S.We.), Sebastian Hasselmann (S.H.), Maximilian Oppmann (M.O.), Marcel T. Seuffert (M.S.), Klaus Müller-Buschbaum (K.M.-B.), Karl Mandel (K.M., korrespondierender Autor)**

Autor	S. Wi.	J.R.	S. We.	S.H.	M.O.	M.S.	K.M.-B.	K.M.	Σ in Prozent
Konzept	5%	3%	3%		1%		2%	3%	17%
Herstellung und Charakterisierung der Partikel		12%	7%	2%		2%			23%
Verfassen der Veröffentlichung	16%	5%	10%		1%		2%	3%	37%
Korrektur der Veröffentlichung	5%	5%	5%				2%	3%	20%
Koordination der Veröffentlichung	2%							1%	3%
<b>Summe</b>	<b>28%</b>	<b>25%</b>	<b>25%</b>	<b>2%</b>	<b>2%</b>	<b>2%</b>	<b>6%</b>	<b>10%</b>	<b>100%</b>



### Erklärung zur Autorenschaft

Supraparticales for Sustainability, Susanne Wintzheimer, Jakob Reichstein, Philipp Groppe, Andreas Wolf, Bastian Fett, Huanhuan Zhou, Rosa Pujales-Paradela, Franziska Miller, Stephan Müssig, Sarah Wenderoth, Karl Mandel, Advanced Functional Materials, 2021, 31, 2011089  
 Detaillierte Darstellung der Anteile an der Veröffentlichung (in %)

Susanne Wintzheimer (S.Wi., Hauptautor), Jakob Reichstein (J.R.), Philipp Groppe (P.G.), Andreas Wolf (A.W.), Bastian Fett (B.F.), Huanhuan Zhou (H.Z.), Rosa Pujales-Paradela (R.P.), Franziska Miller (F.M.), Stephan Müssig (S.M.), Sarah Wenderoth (S.We.), Karl Mandel (K.M.)												
Autor	S.Wi.	J.R.	P.G.	A.W.	B.F.	H.Z.	R.P.	F.M.	S.M.	S.We.	K.M.	Σ in Prozent
Konzept	5%	1%	1%	1%	1%	1%	1%	1%	1%	1%	4%	18%
Erstellung der Texte	10%	3%	3%	3%	3%	3%	3%	3%	3%	2%	4%	40%
Erstellen der Abbildungen	1%	1%	1%	1%	1%	1%	1%	1%	1%	5%	1%	15%
Erstellen der Veröffentlichung	10%									3%	2%	15%
Korrektur der Veröffentlichung	5%										1%	6%
Koordination der Veröffentlichung	5%										1%	6%
<b>Summe</b>	<b>36%</b>	<b>5%</b>	<b>11%</b>	<b>13%</b>	<b>100%</b>							